

**An Integrated Approach
to Hyperpolarised
Magnetic Resonance**

Elizabeth Jane Fear

Doctor of Philosophy

University of York

Chemistry

August 2020

Abstract

Nuclear magnetic resonance spectroscopy (NMR) and Magnetic Resonance Imaging (MRI) play a vital role in science and medicine. Hyperpolarisation technologies, which amplify achievable signal, can unlock new MR applications. Here, a group of thienopyridazines were synthesised and hyperpolarised via Signal Amplification by Reversible Exchange (SABRE). Thienopyridazines are of medical interest due to their anti-cancer properties.

^1H -NMR signal enhancements of $10,130\text{-fold} \pm 230$ at 9.4 T ($\sim 33\%$ polarisation) were achieved, under optimal conditions and novel ^{15}N -labelling used to identify eight SABRE active complexes. Alongside high polarisation levels, long signal lifetimes are desired to warrant a longer window for MR observation. ^1H T_1 lifetimes for the thienopyridazines were found to be $\sim 18\text{-}40$ s. Long-lived state (LLS) approaches extended the magnetic lifetime of the shorter T_1 values to 40 s in the T[2,3-*d*]P regioisomer.

Following successful hyperpolarisation, the imaging potential of thienopyridazines was demonstrated. *In vivo* detection of a 2 mL bolus of hyperpolarised thienopyridazine (in organic solvent) injected into the subcutaneous space was accomplished. Although hyperpolarised signal in a non-toxic aqueous solution was proven feasible (through biphasic extraction), polarisation levels were lower (3%); thus *in vivo* detection following intravenous injection was not possible. Although SABRE excels in ^1H polarisation, imaging is confounded by the vast background signals from the water/fat pool.

Successful X-nuclei imaging utilised hyperpolarised ^{13}C -nicotinamide (via SABRE & dissolution Dynamic Nuclear Polarisation, d-DNP). d-DNP achieved ^{13}C polarisation levels of 13% (with apparent 15 s T_1) permitting easy detection in an *in vivo* cancer model. Equivalent SABRE polarisation was inferior ($\sim 0.17\%$) and only *in vitro* imaging was possible.

A final study developed next generation SABRE methods cascading polarisation from $p\text{-H}_2$, via an *N*-heterocyclic substrate, to platinum-phosphine complexes. Substrates with high polarisation and long lifetimes (e.g., methyl-4,6-*d*₂-nicotinate) proved to be effective for such polarisation relay and resulted in improved ^{31}P signal detection.



List of Contents

Abstract	3
List of Contents	5
List of Tables.....	13
List of Figures	17
Acknowledgements	39
Declaration	41
Chapter 1: Introduction	43
1.1 A Brief History of Molecular Imaging	44
1.2 Nuclear Magnetic Resonance	47
1.2.1 Physical basis	48
1.2.2 Excitation and Detection	51
1.2.3 Relaxation	52
1.2.4 Spatial Encoding	56
1.2.5 Spectroscopic Imaging	56
1.3 Hyperpolarisation	57
1.3.1 Spin Exchange Optical Pumping (SEOP)	58
1.3.2 Dynamic Nuclear Polarisation (DNP).....	58
1.3.3 Para-Hydrogen Induced Polarisation (PHIP)	60
1.4 Signal Amplification By Reversible Exchange	66
1.4.1 Practical Basis	67
1.4.2 Underlying Chemistry	67
1.4.3 Physical Basis	68
1.4.4 Scope of SABRE.....	70
1.4.5 Substrates used with SABRE in this thesis	72
1.5 Thesis overview	73

1.5.1	Thesis objectives	73
1.5.2	Thesis Structure.....	73
1.5.3	Relevant Publications.....	74
1.5.4	Contributions and Acknowledgements	74
Chapter 2: Synthesis and SABRE Optimisation of Thienopyridazines and Furopyridazines.....		75
2.1	Introduction	75
2.1.1	Biological Role of Thienopyridazines	76
2.2	Synthesis of Thienopyridazines.....	77
2.2.1	Characterisation of Thienopyridazines.	81
2.3	Characterisation of Thienopyridazines in the SABRE Process.....	82
2.3.1	Formation of $[\text{Ir}(\text{COD})(\text{IMes})(\text{T}[2,3\text{-}d]\text{P})]\text{Cl}$ – In activated pre-catalyst.	82
2.3.2	Formation of $[\text{Ir}(\text{H})_2(\text{COD})(\text{IMes})(\text{T}[2,3\text{-}d]\text{P})]\text{Cl}$ – Intermediates C and D	83
2.3.3	Formation of $[\text{Ir}(\text{H})_2(\text{IMes})(\text{T}[2,3\text{-}d]\text{P})_3]\text{Cl}$, SABRE active complex	84
2.4	Hyperpolarisation of Thienopyridazines using SABRE – Effect of Spin Isomers on Hyperpolarisation	85
2.4.1	Substrate Loading Comparisons	88
2.4.2	Polarisation Transfer Field.....	89
2.4.3	Type of Catalyst - Effect of Changing Carbene Backbone of Catalyst	93
2.4.4	Magnetic lifetimes (T_1) of Thienopyridazines	99
2.4.5	Effect of Para-Hydrogen Pressure on SABRE Signal Enhancements	101
2.4.6	Use of Fully Deuterated Isotopologue of Thienopyridazine as a Co-ligand to Reduce Substrate Relaxation	103
2.5	Effect on SABRE Hyperpolarisation when Sulfur is replaced with Oxygen.	105
2.5.1	Synthesis and Characterisation of Furo[2,3- <i>d</i>]pyridazine, F[2,3- <i>d</i>]P	106
2.5.2	Optimisation and a Comparison of Signal Enhancement Levels.....	108
2.6	Conclusions and Discussions	111

Chapter 3: Investigation of Long-Lived Singlet States.....	115
3.1 Introduction	115
3.2 Theory of Long-Lived Singlet States	116
3.2.1 NMR T_1 Relaxation.....	117
3.2.2 Singlet State as a store of polarisation	119
3.3 Extending Signal Lifetimes of 3,6-substituted pyridazines.....	122
3.3.1 T_1 and T_{LLS} of 3,6-Substituted Pyridazines in the Absence of a Catalyst	123
3.3.2 SABRE Hyperpolarisation of 3,6-substituted pyridazines - Shake and Drop Experiments	127
3.4 LLS of Thienopyridazines	130
3.4.1 T_1 and T_{LLS} of Thienopyridazines in the Absence of a Catalyst.....	130
3.4.2 Hyperpolarised long-lived states in thienopyridazines	134
3.5 SABRE hyperpolarisation and LLS of ^{13}C and ^{15}N nuclei.....	135
3.5.1 Polarisation of X nuclei – direct/indirect	137
3.5.2 Thieno[2,3- <i>d</i>]pyridazine: Carbon Singlet State Polarisation	138
3.5.3 Thieno[2,3- <i>d</i>]pyridazine: Nitrogen Singlet State Polarisation.....	143
3.6 Conclusions and Discussions	157
Chapter 4: SABRE-Relay: A versatile route to hyperpolarisation.....	161
4.1 Introduction	161
4.2 Theory - SABRE Relay with a square planar platinum complex.....	163
4.2.1 Square Planar Platinum Catalysts: Substitution reactions and the Trans effect	164
4.2.1 Ligand Bite Angle	166
4.3 Synthesis of platinum complexes	168
4.3.1 Synthesis of [Pt(OTf) $_2$ (dppm)].....	169
4.3.2 Synthesis of [Pt(OTf) $_2$ (dppe)]	171
4.4 Characterisation of Iridium and Platinum complexes	174

4.4.1	Characterisation of $[\text{Ir}(\text{H})_2(d_{22}\text{-IMes})(2,4\text{-}d_2\text{-nicotinamide})_3]\text{Cl}$, $[\text{Pt}(\text{OTf})(\text{dppm})(2,4\text{-}d_2\text{-nicotinamide})]\text{OTf}$, and free 2,4- d_2 -nicotinamide.....	174
4.4.2	Exchange of bound nicotinamide.....	178
4.4.3	Polarisation transfer to $[\text{Pt}(\text{OTf})(\text{dppm})(2,4\text{-}d_2\text{-nicotinamide})]\text{OTf}$	179
4.5	^{31}P SABRE-Relay polarisation using pyrimidine as a function of bidentate phosphine ligand.....	181
4.5.1	Effect of Deuterium Labelling within Pyrimidine	183
4.6	^{31}P SABRE-Relay Polarisation Using Pyrazine.....	186
4.6.1	Effect of $[\text{Pt}(\text{OTf})_2(\text{dppp})]$ loading on ^{31}P SNR.....	189
4.7	^{31}P SABRE-Relay using 4,6- d_2 -methyl nicotinate	189
4.8	^{31}P SABRE-Relay using thienopyridazines	192
4.9	Conclusions and Discussions	193
Chapter 5: Translation of SABRE from Benchtop to Imaging Facility.....		197
5.1	Introduction	197
5.2	Theory of SABRE Catalysis: Development for <i>in vivo</i> applications	197
5.2.1	Catalyst-separated hyperpolarisation (CASH) SABRE.....	201
5.3	CASH-SABRE with Thienopyridazines – A biphasic study	202
5.4	Cytotoxicity.....	206
5.4.1	Evaluating the biocompatibility of the extracted aqueous layer from the CASH-SABRE method	206
5.5	Magnetic Resonance Imaging	211
5.5.1	Standard Imaging Approaches for Hyperpolarisation	212
5.5.2	RARE imaging.....	214
5.5.3	Chemical Shift Imaging of T[2,3- d]P	218
5.5.4	Echoplanar Spectroscopic Imaging EPSI of T[2,3- d]P.	223
5.5.5	Ex-Vivo Imaging.....	225
5.6	Conclusion and Discussions.....	227

Chapter 6: Hyperpolarisation and MRS of ^{13}C nicotinamide using d-DNP and SABRE	233
6.1 Introduction	233
6.2 Theory: Nicotinamide	234
6.2.1 Biomedical applications of Nicotinamide	235
6.2.2 Nicotinamide biochemistry and metabolism	235
6.2.3 Nicotinamide and cancer	236
6.3 Theory: d-DNP	237
6.3.1 Biological Properties	237
6.3.2 Physical Properties	238
6.3.3 DNP Sample Preparation	239
6.4 d-DNP polarisation of nicotinamide and <i>in vivo</i> application	240
6.4.1 ^{13}C DNP of nicotinamide in the solid-state	241
6.4.2 d-DNP- MRS <i>in vivo</i> experiments with ^{13}C -nicotinamide	244
6.4.3 ^{13}C nicotinamide using d-DNP and the effect of deuteration on T_1 values	248
6.5 SABRE hyperpolarisation of ^{13}C nicotinamide	250
6.5.1 ^{13}C SABRE – NMR optimisation	251
6.5.2 MRI/S	255
6.6 Conclusions and Discussions	258
Chapter 7: Conclusions and Outlook	261
7.1 Key findings	262
7.1.1 Polarisation level	262
7.1.2 Magnetic Lifetimes	263
7.1.3 Biocompatibility & Imaging Potential	264
7.1.4 Benchmarking	265
7.1.5 Next generation catalysis for polarisation transfer	266

7.2	Relevance	267
7.3	Summary and Future Directions.....	270
Chapter 8:	Experimental	273
8.1	General Methods	273
8.2	General Procedures.....	273
8.2.1	NMR SABRE experiments	273
8.2.2	Signal Enhancement Factors Calculations and Errors	274
8.2.3	Percentage Polarisation	275
8.2.4	T_1 measurements using Inversion Recovery	276
8.2.5	Characterisation NMR experiments.....	276
8.3	Chapter 2 Methods: Synthesis of Thienopyridazines and Furopyridazines ...	277
8.3.1	Synthesis of Thieno[2,3- <i>d</i>]pyridazine ¹⁸¹	277
8.3.2	Synthesis of Thieno[3,4- <i>d</i>]pyridazine ¹⁸¹	278
8.3.3	Synthesis of Thieno[2,3- <i>c</i>]pyridazine ¹⁸⁴	280
8.3.4	Synthesis of Thieno[3,2- <i>c</i>]pyridazine (adapted from literature procedure Ball <i>et al.</i> , 2012) ¹⁸⁴	283
8.3.5	Novel synthesis of d_4 -thieno[2,3- <i>d</i>]pyridazine	285
8.3.6	One-Pot Synthesis of Furo[2,3- <i>d</i>]pyridazine ¹⁸³	286
8.4	Chapter 3 Methods: Long-Lived States.....	287
8.4.1	T_{LLS} measurements	288
8.4.2	Novel synthesis of ^{15}N labelled thieno[2,3- <i>d</i>]pyridazine.....	288
8.4.3	Novel synthesis of fully deuterated d_4 -thieno[2,3- <i>d</i>]pyridazine- $^{15}\text{N}_2$	289
8.5	Chapter 4 Methods: Synthesis of platinum complexes for SABRE-Relay	290
8.5.1	Synthesis of $[\text{Pt}(\text{Cl})_2(\text{PhCN})_2]$	290
8.5.2	Synthesis of $[\text{Pt}(\text{Cl})_2(\text{dppm})]$	290
8.5.3	Synthesis of $[\text{Pt}(\text{OTf})_2(\text{dppm})]$	290
8.5.4	Synthesis of $[\text{Pt}(\text{Cl})_2(\text{dppe})]$:.....	291

8.5.5	Synthesis of [Pt(OTf) ₂ (dppe)]:	291
8.6	Chapter 5 Methods: Translation of SABRE from benchtop to imaging facility	292
8.6.1	Biphasic- CASH-SABRE	292
8.6.2	Cytotoxicity Assays	292
8.6.3	MRI and MRS	293
8.7	Chapter 6 Methods: d-DNP hyperpolarisation	295
8.7.1	Cell Culture (CRUK)	295
8.7.2	Hyperpolarisation of ¹³ C nicotinamide (CRUK)	295
8.7.3	Hyperpolarised ¹³ C Spectroscopy (MRS) CSI <i>In Vivo</i> at 7 T (CRUK)	295
8.7.4	Hyperpolarised <i>T</i> ₁ of ¹³ C nicotinamide (CHyM)	298
8.7.5	Hyperpolarised SABRE Imaging Experiments	299
	Appendices	301
	Appendix 1: Characterisation of pre-catalysts [Ir(COD)(IMes)(T[2,3- <i>d</i>]P)]Cl A and B and intermediates [Ir(COD)(H) ₂ (IMes)(T[2,3- <i>d</i>]P)]Cl A and B	301
	Appendix 2 Characterisation data for eight SABRE active complexes.	307
	Appendix 3: Characterisation data of complexes formed during SABRE-Relay	308
	¹ H NMR characterisation of [Ir(H) ₂ (<i>d</i> ₂₂ -IMes)(2,4- <i>d</i> ₂ -nicotinamide) ₃]Cl:	308
	¹ H and ³¹ P NMR characterisation of [Pt(OTf)(dppm)(2,4- <i>d</i> ₂ -nicotinamide)]OTf:	308
	Abbreviations	309
	References	311



List of Tables

Table 2.1: Chemical structures and NMR characterisation data (^1H , ^{13}C and ^{15}N) for T[2,3- <i>d</i>]P and T[2,3- <i>c</i>]P in methanol- <i>d</i> ₄ and T[3,4- <i>d</i>]P and T[3,2- <i>c</i>]P in chloroform- <i>d</i> (500MHz).....	81
Table 2.2: Signal enhancements for shake and drop experiments of the thienopyridazines using [IrCl(COD)(IMes)] as catalyst in a 1:4 catalyst to substrate ratio in methanol- <i>d</i> ₄ . *Average values across two proton sites.	87
Table 2.3: Enhancement factors of the thienopyridazines with four different catalysts [IrCl(COD)(IMes)], [IrCl(COD)(<i>d</i> ₂₂ -IMes)], [IrCl(COD)(SIMes)] and [IrCl(COD)(<i>d</i> ₂₂ -SIMes)].....	96
Table 2.4: Enhancement factors of T[2,3- <i>d</i>]P with two new catalysts [IrCl(COD)(X)] and [IrCl(COD)(Y)].....	97
Table 2.5: T_1 measurements for all resonances for T[2,3- <i>d</i>]P in the absence of a catalyst and with [IrCl(COD)(IMes)], [IrCl(COD)(<i>d</i> ₂₂ -IMes)], [IrCl(COD)(SIMes)], [IrCl(COD)(<i>d</i> ₂₂ -SIMes)], [IrCl(COD)(X)] and [IrCl(COD)(Y)].....	100
Table 2.6: T_1 measurements for T[3,4- <i>d</i>]P, T[2,3- <i>c</i>]P, T[3,2- <i>c</i>]P in the absence of a catalyst and with [IrCl(COD)(IMes)], [IrCl(COD)(<i>d</i> ₂₂ -IMes)], [IrCl(COD)(SIMes)] and [IrCl(COD)(<i>d</i> ₂₂ -SIMes)].	101
Table 2.7: Table of NMR ^1H , ^{13}C and ^{15}N resonances for F[2,3- <i>d</i>]P dissolved in methanol- <i>d</i> ₄ (500 MHz spectrometer).....	108
Table 2.8: Chemical Shift difference of neighbouring ^1H , ^{13}C and ^{15}N nuclei in F[2,3- <i>d</i>]P and T[2,3- <i>d</i>]P	114
Table 3.1: Parameters used in the LLS pulse sequence to measure T_{LLS} of 3-NH ₂ -6-Cl-py, 3-Cl-6-OCH ₃ -pyridazine and 3-Cl-6-CF ₃ -py.....	124
Table 3.2: Summary of SABRE activity and comparative thermal lifetimes (T_1 and T_{LLS} in the absence of the catalyst) of the 3,6-substituted pyridazines	129
Table 3.3: Parameter settings for the LLS pulse sequence used to measure T_{LLS} in T[2,3- <i>d</i>]P, T[2,3- <i>c</i>]P and T[3,2- <i>c</i>]P.....	131

Table 3.4: Signal enhancement and relaxation data (T_1 and T_{LLS}) associated with thienopyridazines in the absence and in the presence of [IrCl(COD)(IMes)] in a 1:4 catalyst: substrate ratio using a high field spin-lock.	135
Table 4.1: ^1H SABRE polarisation level and T_1 values of pyrimidine, 2,5- d_2 -pyrimidine ¹³⁵ , 5 d -pyrimidine and 4,6- d_2 -pyrimidine. SABRE conditions: [IrCl(COD)(IMes)] 5 mM, substrate 20 mM, methanol- d_4 , 3 bar (g) $p\text{H}_2$ measured at 400 MHz. Errors in T_1 approximately 6%.	184
Table 4.2: Signal enhancement values, ϵ and T_1 values of ^1H and ^{31}P resonances with 10 eq. of deuterated isotopologues to 1 eq. of [IrCl(COD)](d_{22} IMes) and 1 eq. [Pt(OTf) $_2$ (dppp)] in methanol- d_4 . * indicates overlapping signal. n/a. Due to 1:10 ratio measurements of T_1 were compromised.	186
Table 4.3: S/N values and enhancement values obtained for ^{31}P hyperpolarised spectra acquired on samples containing increasing amounts of [Pt(OTf) $_2$ (dppp)] relative to a constant pz concentration of 100 mM.	189
Table 4.4: Enhancement values, ϵ and T_1 values of ^1H and ^{31}P resonances with 10 eq. of 4,6- d_2 -methyl nicotinate to 1 eq. of [IrCl(COD)](d_{22} IMes) & 1 eq. of [Pt(OTf) $_2$ (dppm)]/[Pt(OTf) $_2$ (dppe)] / [Pt(OTf) $_2$ (dppp)] in methanol- d_4	192
Table 5.1: T_1 values for T[2,3- d]P (18 mM) in methanol- d_4 , dichloromethane- d_2 and deuterium oxide. Signal enhancement and T_1 values for T[2,3- d]P (18mM) with [IrCl(COD)](d_{22} -SIMes)] (4.5 mM) in methanol- d_4 and chloroform- d_2	206
Table 6.1: Formulations of differing volumes of glycerol:water ratio and nicotinamide showing K_{BU} and the expected maximum amplitude. Maximum amplitude can be estimated after 60% of build up.	241
Table 8.1: <i>In vivo</i> murine tumour size used for imaging	296
Table 8.2: Variable FA used to estimate hyperpolarised ^{13}C T_1	298
Table A 1: ^1H , ^{13}C and ^{15}N resonances of pre-catalyst A measured at 233 K in methanol- d_4	302
Table A 2: ^1H , ^{13}C and ^{15}N resonances of pre-catalyst B measured at 233 K in methanol- d_4	303
Table A 3: ^1H , ^{13}C and ^{15}N resonances of intermediate C [Ir(COD)(H) $_2$ (IMes)(T[2,3- d]P)]Cl measured at 233 K in methanol- d_4 (500 MHz spectrometer).	305

Table A 4: ^1H , ^{13}C and ^{15}N resonances of intermediate D $[\text{Ir}(\text{COD})(\text{H})_2(\text{IMes})(\text{T}[2,3-d]\text{P})]\text{Cl}$ measured at 233 K in methanol- d_4 (500 MHz spectrometer). 306

Table A 5: Characterisation data for eight SABRE active complexes E-L 307



List of Figures

Figure 1.1: ^{13}C -pyruvate and ^{13}C -lactate images acquired from a breast cancer patient following i.v. injection of hyperpolarised $[1-^{13}\text{C}]$ - pyruvate. (A) Standard structural MR. (B) Hyperpolarised ^{13}C -pyruvate and (C) ^{13}C -lactate images. (D) LAC/PYR map showing tumour heterogeneity represents decreased delivery of hyperpolarised substrate at the tumour centre. (E and F) Dynamic (temporal resolution = 4 s) hyperpolarised ^{13}C -pyruvate and ^{13}C -lactate images. ⁷ Data adapted from Gallagher <i>et al.</i> (2020).....	43
Figure 1.2: Chemical structure of 2-deoxy-2(^{18}F)fluoro-D-glucose.	45
Figure 1.3: (a) Classical model of a spin system. Thermal energy results in spinning charge with angular momentum (I), generating a small magnetic dipole moment (μ). (b) Random orientation of spins in bulk matter in the absence of an external magnetic field resulting in a net magnetic moment of zero. (c) Spins in the presence of an external magnetic field aligned with and against magnetic field.	49
Figure 1.4: a) Magnetic field B_0 with spins precessing at the Larmor frequency aligned parallel or anti parallel (Classical view). b) Energy level diagram of a nucleus with $I = 1/2$ resulting in two energy levels $m = -1/2$ and $m = +1/2$ when placed in a magnetic field (Quantum view).	50
Figure 1.5: Excitation step where an RF pulse (of variable power and duration) can be applied at the Larmor frequency to tip the net magnetisation through an angle towards the transverse (XY) plane.	52
Figure 1.6: T_1 relaxation showing spins returning to the z direction immediately after a 90° pulse.	53
Figure 1.7: (a) T_1 relaxation curve. (b) T_1 weighted image. ⁶⁸ (c) T_2 relaxation curve. (d) T_2 weighted image. ⁶⁸	54
Figure 1.8: T_2 relaxation showing spins dephasing across the XY plane after a 90° pulse.	55
Figure 1.9: a) Boltzmann distribution at thermal equilibrium of nuclear spins across the higher energy level (β) and the lower energy level (α); b) Hyperpolarised nuclear spins.	57
Figure 1.10: Schematic drawing of the DNP polariser taken from the first d-DNP paper by Jan H Ardenkjaer-Larsen <i>et al.</i> ³ (1) DNP polariser; (2) vacuum pump; (3) VTI; (4)	

microwave source; (5) pressure transducer; (6) sample port; (7) microwave container; (8) sample holder; (9) sample container; (10) dissolution wand.	59
Figure 1.11: The four possible nuclear spin alignments of the nuclei in a molecule of hydrogen in a magnetic field.....	61
Figure 1.12: Hydrogenation of acrylonitrile using <i>p</i> -H ₂ to form propionitrile incorporating two <i>para</i> -H ₂ derived protons.....	62
Figure 1.13: a) Energy diagram showing the four possible spin alignments of H ₂ derived nuclei after hydrogenation of an asymmetric unsaturated bond. The black arrows indicate the spin-allowed transitions b) ¹ H NMR spectrum which arises from these transitions.	63
Figure 1.14: a) PASADENA effect with selective polarisation of αβ and βα energy states from <i>p</i> -H ₂ derived nuclei b) Corresponding ¹ H NMR spectrum showing PASADENA enhancements.	64
Figure 1.15: a) ALTADENA effect with selective polarisation of only the βα energy states from <i>p</i> -H ₂ derived nuclei b) Corresponding ¹ H NMR spectrum showing ALTADENA enhancements.	65
Figure 1.16: Adapted from Cavallari <i>et al.</i> (2018) (a) Chemical pathway showing the steps involved in the PHIP-SAH process. (I) Formation of ester using [1- ¹³ C]-pyruvate and propargylic alcohol; (II) hydrogenation of triple bond side arm using <i>p</i> -H ₂ ; (III) Polarisation transfer from receiving protons to the labelled carbon; (IV) Hydrolysis of ester and phase extraction. Orange arrows indicates reactions carried out in the organic phase; blue arrows indicate the passages which occur in the aqueous phase. (b) CSI images of pyruvate and lactate distribution in living mice after injection of a dose of HP [1- ¹³ C]-pyruvate. ¹¹¹ The spatial localisation of the metabolite is achieved by overlaying with a ¹ H structural image. The region of highest metabolite concentration appears white and lowest appears black.....	66
Figure 1.17: Crabtree-type catalyst first used for SABRE hyperpolarisation. The active complex is formed by the oxidative addition of H ₂ in the presence of excess pyridine.	67
Figure 1.18: Formation of SABRE active catalyst with H ₂ through hydrogenation of COD ligand. Catalytic SABRE cycle showing the transfer of polarisation from the <i>p</i> -H ₂ derived hydrides to the substrate.....	68
Figure 1.19: Chemical structure of [Pt(OTf) ₂ (dppm)] and [Pt(OTf) ₂ (dppe)].	74

Figure 2.1: Family of thienopyridazines (anti-cancer agents) ¹⁶⁰⁻¹⁶² : Thieno[2,3- <i>d</i>]pyridazine, (T[2,3- <i>d</i>]P), Thieno[3,4- <i>d</i>]pyridazine (T[3,4- <i>d</i>]P), Thieno[2,3- <i>c</i>]pyridazine (T[2,3- <i>c</i>]P), Thieno[3,2- <i>c</i>]pyridazine (T[3,2- <i>c</i>]P).....	76
Figure 2.2: Reaction scheme for the synthesis of T[3,4- <i>d</i>]P following methods developed by Montavon et al (2013) resulting in an overall yield of 39%.	78
Figure 2.3: Reaction scheme for the synthesis of T[2,3- <i>d</i>]P following methods developed by Montavon et al (2013) resulting in a final product yield of 77%.	78
Figure 2.4: Three step reaction scheme for the synthesis of T[2,3- <i>c</i>]P developed by C. Ball et al (2012) ¹⁸⁴	79
Figure 2.5: Adapted three step reaction scheme for the synthesis of T[3,2- <i>c</i>]P following methods developed by C. Ball et al (2012) ¹⁸⁴	80
Figure 2.6: Structures of pre-catalysts [Ir(COD)(IMes)(T[2,3- <i>d</i>]P)]Cl A and B indicating the two bound nitrogen resonances (green)	83
Figure 2.7: Structures of intermediates [Ir(COD)(H) ₂ (IMes)(T[2,3- <i>d</i>]P)]Cl C and D indicating the two bound nitrogen resonances	84
Figure 2.8: Predicted regioisomeric products E-L for [Ir(H) ₂ (IMes)(T[2,3- <i>d</i>]P) ₃]Cl.....	85
Figure 2.9: Comparison of the aromatic region of a ¹ H spectrum of T[2,3- <i>d</i>]P and [IrCl(COD)(IMes)] in a 4 to 1 ratio at thermal equilibrium (green - with vertical expansion 64 times) and under SABRE conditions at 3 bar(g) of <i>p</i> -H ₂ (black). Insert shows the hydride region of the ¹ H spectra.....	86
Figure 2.10: Effect on signal enhancement values when changing substrate to catalyst ratios. The substrate used was T[2,3- <i>d</i>]P and the catalyst [IrCl(COD)(IMes)] forming the active catalyst [Ir(H) ₂ (IMes)(T[2,3- <i>d</i>]P) ₃]Cl. The solvent used was methanol- <i>d</i> ₄ and measurements were made on a 400 MHz spectrometer at 298K. (a) Signal enhancements values measured per individual proton with 4, 6 and 8 eq. of T[2,3- <i>d</i>]P to 1 equivalent of catalyst [IrCl(COD)(IMes)]. (b) Normalised signal enhancement values per proton showing a linear decrease of enhancement with increased number of substrate equivalents.....	88
Figure 2.11: Effect on signal enhancement values when changing substrate to catalyst ratios. The substrate used was T[3,4- <i>d</i>]P and the catalyst [IrCl(COD)(IMes)] forming the active catalyst [Ir(H) ₂ (IMes)(T[3,4- <i>d</i>]P) ₃]Cl. The solvent used was methanol- <i>d</i> ₄ and	

measurements were made on a 400 MHz spectrometer at 298K. (a) Signal enhancements values measured per individual proton with 4, 6 and 8 eq. of T[3,4- <i>d</i>]P to 1 equivalent of catalyst [IrCl(COD)(IMes)]. (b) Normalised signal enhancement values per proton showing a linear decrease of enhancement with increased number of substrate equivalents.	89
Figure 2.12: Polarisation transfer field plot showing variation of signal enhancement for T[2,3- <i>d</i>]P at 298 K using the automated polariser. PTF plots for each resonance show a Gaussian distribution and give a single maximum at 60.4 +/- 0.6 G.....	91
Figure 2.13: Polarisation transfer field plot for T[3,4- <i>d</i>]P at 298 k using the automated polariser. PTF plots for each resonance show a Gaussian distribution and give a single maximum at 60.9 +/- 0.5 G.....	91
Figure 2.14: Polarisation transfer field plot for T[2,3- <i>c</i>]P at 298 k using the automated polariser. PTF plots for each resonance show a Gaussian fit and give three maxima at peak 1 = 13.30 +/- 4.48 G, peak 2 = 65.37 +/- 0.60 G and peak 3 = 109.778 +/- 0.13 G	92
Figure 2.15: Polarisation transfer field plot for T[3,2- <i>c</i>]P at 298 K using the automated polariser. PTF plots for each resonance show a Gaussian fit and give three maxima at peak 1 = 13.64 +/- 1.06, peak 2 = 60.81 +/- 0.62 and peak 3 = 109.36 +/- 0.81983	92
Figure 2.16: Hyperpolarised spectra for T[3,2- <i>c</i>]P achieved at 0G (blue) and 60 G (black). Positive magnitudes for H7 and H3 and negative magnitudes for H6 and H2 at 0 G (blue). Negative magnitudes for all resonances at 60 G (black)	93
Figure 2.17 – Structures of the four carbene ligands, IMes, SIMes, <i>d</i> ₂₂ -SIMes and <i>d</i> ₂₂ -SIMes used to study SABRE signal enhancement of a series of thienopyridazines.....	94
Figure 2.18: Signal enhancements of the resonances in each of the four thienopyridazines with the greatest enhancement and how these levels vary when changing the carbene backbone.	96
Figure 2.19: Structure of carbene X found in [IrCl(COD)(1,3-bis(4-chloro-2,6-dimethylphenyl)imidazol-2-ylidene)] and carbene Y found in [IrCl(COD)(1,3-bis(4-dimethylamino)-2,6-dimethylphenyl)imidazol-2-ylidene)].....	97
Figure 2.20: Graph showing the effect of a change of catalyst on the signal enhancement values of the four proton signals in T(2,3- <i>d</i>)P	98

Figure 2.21: T_1 measured for $H_7 = 38.2 \pm 0.2$ s of T[2,3- <i>d</i>]P in the absence of a catalyst using inversion recovery (20 points).....	100
Figure 2.22: Effect on signal enhancement values when changing <i>p</i> -H ₂ pressure. The substrate used was T[2,3- <i>d</i>]P and the catalyst [IrCl(COD)(IMes)] forming the active catalyst [Ir(H) ₂ (IMes)(T[2,3- <i>d</i>]P) ₃]Cl. The solvent used was methanol- <i>d</i> ₄ and measurements were made on a 400 MHz spectrometer at 298 K. (a) Signal enhancements values measured per individual proton with 3, 4 and 5 bar(g) of <i>p</i> -H ₂ pressure. (b) Normalised signal enhancement values per proton showing a linear increase of enhancement with increased <i>p</i> -H ₂ pressure.....	102
Figure 2.23: Reaction scheme for the synthesis of <i>d</i> ₄ -thieno[2,3- <i>d</i>]pyridazine (<i>d</i> ₄ -T[2,3- <i>d</i>]P).....	104
Figure 2.24: Bar chart to show increase in signal enhancement for T[2,3- <i>d</i>]P with the use of a co-ligand and the use of a co-ligand in combination with a 60 G handheld shaker.	105
Figure 2.25: Chemical Structure of Furo[2,3- <i>d</i>]pyridazine, F[2,3- <i>d</i>]P	106
Figure 2.26: One-Pot synthesis of F[2,3- <i>d</i>]P using methodology by S. Kessler et al. (2012)	106
Figure 2.27: ¹ H spectrum of Furo[2,3- <i>d</i>]pyridazine in methanol- <i>d</i> ₄ after recrystallization with hexane.	107
Figure 2.28: A comparison of the two substrate; T[2,3- <i>d</i>]P and F[2,3- <i>d</i>]P with the [IrCl(COD)(IMes)] catalyst and [IrCl(COD)(<i>d</i> ₂₂ SIMes)].	109
Figure 2.29: Furo[2,3- <i>d</i>]pyridazine and thieno[2,3- <i>d</i>]pyridazine with the respective electronegativity values of oxygen and sulphur shown in red italics.....	110
Figure 2.30: A comparison of a ¹ H spectrum of F[2,3- <i>d</i>]P and [IrCl(COD)(<i>d</i> ₂₂ -SIMes)] in a 4 to 1 ratio at thermal equilibrium (vertically magnified 256 times) (in green) and under SABRE conditions at 4 bar(g) of <i>p</i> -H ₂ (blue)	110
Figure 2.31: Increase in signal enhancement of the four proton resonances of F[2,3- <i>d</i>]P with [Ir(COD)(<i>d</i> ₂₂ -SIMes)Cl] in a 4 to 1 ratio in methanol- <i>d</i> ₄ with a change in pressure from 3 bar(g) to 4 bar(g)	111
Figure 3.1: Pyridazine based molecules used to study long-lived states. (a) ¹ H pairs (blue) targeted for the LLS in 3,6-disubstituted pyridazines where R = Cl and R' = NH ₂ , OCH ₃ ,	

CF ₃ (section 3.3) (b) the ¹ H pairs (blue) (section 3.4), ¹³ C pairs (orange) and ¹⁵ N pairs (green) shown are suitable targets in thienopyridazine (section 3.5).....	116
Figure 3.2: Energy levels of the spin states of <i>ortho</i> and <i>para</i> -spin isomers of hydrogen and their magnetic dependence. The blue arrows indicate the allowed transitions between the triplet states and the red arrows indicate the forbidden transitions between the singlet and the triplet energy states. ²²⁰	117
Figure 3.3: a) Pulse sequence in the field-cycling singlet experiment. b) Pulse sequence in the high field (spin lock) singlet experiment.	120
Figure 3.4: a) Typical stages of an NMR experiment to create singlet order, b) methods to perform the symmetry switching (i) through chemical reactions (ii) by magnetic fields	121
Figure 3.5: Diagram to show how spin populations are manipulated during the field-cycling singlet creation experiment	122
Figure 3.6: Chemical structures of three 3,6-substituted pyridazines studied. The proton pairs highlighted by the blue area indicate where the creation of a long-lived singlet state is possible.....	123
Figure 3.7: <i>T</i> ₁ graphs obtained using the inversion recovery method for H4 and H5 of 3-chloro-6-methoxy pyridazine. The black squares reflect experimental measurements whilst the solid line is the line of best fit based on equation 3.1. The blue circles highlight the proton in the structure, which the <i>T</i> ₁ value reflects.....	123
Figure 3.8: a) ¹ H NMR spectrum of 3-Cl-6-OCH ₃ -py in methanol- <i>d</i> ₄ with the two doublets arising from mutually coupled H4 and H5 as indicated. b) Characteristic up, down, down, up antiphase peaks observed in the read-out phase of the LLS experiment which is indicative of the pseudo-singlet state created.	125
Figure 3.9: Exponential decay curve of the singlet state created between H4 and H5 in 3-chloro-6-methoxy pyridazine using the LLS pulse sequence in high field. The black squares indicated the intensity of the combined anti-phase NMR signal from the pseudo singlet state in the read-out stage of the LLS experiment.....	126
Figure 3.10: <i>T</i> ₁ values of H4 and H5 measured by inversion recovery (blue) and <i>T</i> _{LLS} values of the pseudo-singlet state created between H4 and H5 using the LLS sequence (green) for 3-NH ₂ -6-Cl-py, 3-Cl-6-OCH ₃ -py and 3-Cl-6-CF ₃ -py	127

- Figure 3.11: Thermal and hyperpolarised ^1H NMR spectra of 3-NH₂-6-Cl-py with [Ir(COD)Cl(IMes)] in a 1:4 ratio of catalyst to substrate in methanol-*d*₄. Hyperpolarised peaks are shown for the free and bound substrate. In the free substrate, H5 shows a signal enhancement of -112 fold and H4 shows an enhancement of -61 fold..... 127
- Figure 3.12: Hydride region of the ^1H NMR spectrum for 3-NH₂-6-Cl-py with [Ir(COD)Cl(IMes)] as catalyst in *d*₄-methanol. The blue star shows the hydrides for the tri-substituted complex [Ir(H)₂(3-amino-6-chloropyridazine)₃(IMes)] and the red stars indicate the hydrides when the solvent is occupying one of the equatorial positions... 128
- Figure 3.13: ^1H T_1 decay curves measured by inversion recovery for (a) H2 (b) H3 (c) H4 (d) H7 of T[2,3-*d*]P at 9.4T..... 131
- Figure 3.14: (a) ^1H NMR spectrum of T[2,3-*d*]P in methanol-*d*₄ showing the 4 proton resonances including the two doublets arising from the mutually coupled H2 and H3. (b) Characteristic antiphase peaks observed in the read-out stage of the LLS experiment of the pseudo-singlet created between H2 and H3. The highlighted locations indicate both the NMR peaks and the protons within the molecule where the pseudo-singlet state has been created..... 132
- Figure 3.15: Stacked array of NMR spectra resulting from the LLS experiment showing the decay of the long-lived singlet in the read-out stage..... 132
- Figure 3.16: Exponential decay of the singlet state created between H2 and H3 in T[2,3-*d*]P using the LLS pulse sequence in high field. The black squares indicate the intensity of the combined NMR signal from the pseudo singlet state in the read-out stage of the LLS experiment..... 133
- Figure 3.17: Polarisation transfer to X nuclei. Iridium complex formed during SABRE with T[2,3-*d*]P. The red dotted line shows the transfer of polarisation directly to the carbon in the substrate and the blue dotted line shows the transfer of polarisation to the nitrogen in the substrate. The black arrow indicates the coupling in Hz between the hydrides. (n is second in plane T[2,3-*d*]P which is omitted to aid the reader)..... 138
- Figure 3.18: Thermal $^{13}\text{C}\{^1\text{H}\}$ spectrum of T[2,3-*d*]P in methanol-*d*₄ (8192 scans).... 139
- Figure 3.19: Shake and Drop 1 scan ^{13}C experiment of T[2,3-*d*]P and [IrCl(COD)(*d*₂₂-SIMes)] in a 4 to 1 ratio in methanol-*d*₄. A 60 G shaker was used with a shaking time of 10 s before transferring to a 500 MHz spectrometer for detection. 140

- Figure 3.20: Shake and Drop 1 scan Ineptrd $^{13}\text{C}\{^1\text{H}\}$ experiment on T[2,3-*d*]P with [IrCl(COD)(*d*₂₂-SIMes)] in a 4 to 1 ratio in methanol-*d*₄. The sample was shaken in a 60 G field (magnetic shaker) for 50 s before measurement in a 500 MHz spectrometer. . 141
- Figure 3.21: Shake and Drop 1 scan ^{13}C experiment of T[2,3-*d*]P and [IrCl(COD)(*d*₂₂-SIMes)] in a 4 to 1 ratio in methanol-*d*₄. The sample was shaken in the mu metal shield for 10 seconds before measurement in a 500 MHz spectrometer. 142
- Figure 3.22: Shake and Drop 1 scan $^{13}\text{C}\{^1\text{H}\}$ experiment of T[2,3-*d*]P and [IrCl(COD)(*d*₂₂-SIMes)] in a 4 to 1 ratio in methanol-*d*₄. The sample was shaken in the mu metal shield for 10 seconds before measurement in a 500 MHz spectrometer. 142
- Figure 3.23: a) Hyperpolarised 1 scan ^{15}N NMR spectrum (above) b) Analogous hyperpolarised $^{15}\text{N}\{^1\text{H}\}$ NMR experiment (1 scan) of non-labelled T[2,3-*d*]P and [IrCl(COD)(*d*₂₂-SIMes)] in a 4 to 1 ratio in *d*₄-methanol. The sample was shaken in a mu metal shield for 10 seconds before measurement in a 500 MHz spectrometer..... 144
- Figure 3.24: Reaction scheme for the novel synthesis of doubly labelled thieno[2,3-*d*]pyridazine- $^{15}\text{N}_2$ in 90% yield. 145
- Figure 3.25: a) ^{15}N Thermal scan (512 transients) of T[2,3-*d*]P- $^{15}\text{N}_2$ in methanol-*d*₄ measured on a 9.4 T spectrometer (no catalyst present). b) Model of AB system showing *J* couplings and chemical shift frequencies..... 146
- Figure 3.26: Precatalysts A and B showing the two possible modes of binding and the different nitrogen chemical shifts that arise. 148
- Figure 3.27: Eight possible regioisomers of [Ir(H)₂(*d*₂₂-SIMes)(thieno[2,3-*d*]pyridazine- $^{15}\text{N}_2$)₃]. The complexes within the rectangles indicate enantiomeric pairs..... 148
- Figure 3.28: Single scan hyperpolarised $^{15}\text{N}\{^1\text{H}\}$ NMR spectrum of doubly labelled ^{15}N -thieno[2,3-*d*]pyridazine achieved by precatalyst [Ir(COD)Cl(*d*₂₂SIMes)] when present in a 1:6 ratio in *d*₄-methanol solution after PT at Earth's field. Blue stars (bound nitrogen in axial position), Purple stars (uncoordinated nitrogen in axial position) yellow star (bound nitrogen in equatorial position) and green star (nitrogen in free substrate) 149
- Figure 3.29: Expansion of axially bound ligands in (a) ^{15}N hyperpolarised spectrum and (b) $^{15}\text{N}\{^1\text{H}\}$ hyperpolarised spectrum after PTF at earth's field. The different colours represent the six different ^{15}N signals as doublets with $J_{^{15}\text{N}-^{15}\text{N}}$ 150

- Figure 3.30: 2D ^{15}N ^1H HSQC (263K) of T[2,3- d]- $^{15}\text{N}_2$ with [Ir(Cl)(COD)(d_{22} -SIMes)] in methanol- d_4 after activation with H_2 . Used to identify the eight equatorially bound nitrogen resonances in complexes E-L. J_{NN} coupling identified by the dotted line and δ ^{15}N resonances identified by the midpoint of the solid line..... 151
- Figure 3.31: Assigned ^1H hydride NMR resonances and ^{15}N resonances of the eight regioisomers of [Ir(H) $_2$ (T[2,3- d]P- $^{15}\text{N}_2$) $_3$ (d_{22} -SIMes)] at 11.7 T. The complexes within the rectangles indicate enantiomeric pairs. Resonances arising from the ^{15}N in the equatorial position are donated in blue where N^1 is light blue and N^2 is dark blue. Resonances arising from the ^{15}N in the axial position are donated in green where N^1 is light green and N^2 is dark green..... 152
- Figure 3.32: Natural singlet state formed when shaking in earth's magnetic field. The characteristic singlet can be seen in both the free substrate (shown within blue oval) and in the bound peaks..... 153
- Figure 3.33:a) Thermal $^{15}\text{N}\{^1\text{H}\}$ NMR spectrum (16 transients) expansion vertically multiplied by 8; b) Single scan hyperpolarised $^{15}\text{N}\{^1\text{H}\}$ NMR spectrum of doubly labelled ^{15}N thieno[2,3- d]pyridazine achieved by precatalyst [Ir(COD)Cl(d_{22} SIMes)] when present in a 1:6 ratio in d_4 -methanol solution after PTF at -7mG. Blue stars (bound equatorial), yellow star (bound axial) and green star (free) 154
- Figure 3.34: Novel synthesis of d_4 -thieno[2,3- d]pyridazine- $^{15}\text{N}_2$. Deuteration was achieved by refluxing the previously synthesised thieno[2,3- d]pyridazine- $^{15}\text{N}_2$ in D_2O with base for 4 weeks. 95% deuteration was achieved across the four resonances 155
- Figure 3.35: Hyperpolarised single scan NMR at -7mG using [Ir(COD)Cl(d_{22} SIMes)] as pre-catalyst present in a 1:6 ratio in d_4 -methanol solution with (a) thieno[2,3- d]pyridazine- $^{15}\text{N}_2$ and (b) d_4 -thieno[2,3- d]pyridazine- $^{15}\text{N}_2$ 156
- Figure 4.1: a) Schematic depiction of SABRE-Relay using a transfer agent, NH_2R (where $\text{R} = \text{H}$ or CH_2Ph or $\text{CH}_2\text{CH}_2\text{Ph}$ etc). NH_2R relays its polarisation received from $p\text{-H}_2$ to the target substrate $\text{R}'\text{-H}$ (where $\text{R}' = \text{amide}$, carboxyl etc.) through proton exchange. b) Schematic depiction of SABRE-Relay with a second metal complex; substrate S_1 binds reversibly to metal complexes- M_1 and M_2 , while S_2 represents the final target which receives the relayed polarisation. 162
- Figure 4.2: Square planar substitution reaction where $\text{X} = \text{spectator ligand}$, $\text{L} = \text{leaving group}$ and $\text{Nu} = \text{nucleophile}$ 164

- Figure 4.3: Mechanism of an associative square planar substitution reaction involving a 5-coordinate trigonal bipyramid intermediate..... 165
- Figure 4.4: Bite angle: The ligand-metal-ligand angle of bidentate ligands.²⁵⁴ 167
- Figure 4.5: Postulated mechanism for the transfer of nuclear spin order into a second agent. The precatalyst [IrCl(COD)(*d*₂₂-IMes)] (M₁) is transformed into the active SABRE complex [Ir(H)₂(IMes)(S₁)₃] (M₁-S₁) by adding substrate S₁. S₁ then gains hyperpolarised Zeeman and singlet order via polarization transfer from *p*-H₂. In the second step, the ³¹P response of M₂-S₁ becomes hyperpolarised.¹⁶⁸ 168
- Figure 4.6: [Pt(OTf)₂(dppp)], proposed to exchange its triflates for polarised N-heterocycles..... 168
- Figure 4.7 : Synthetic pathway for the synthesis of [Pt(OTf)₂(dppp)] from PtCl₂. 169
- Figure 4.8: Chemical structures of [Pt(OTf)₂(dppm)] and [Pt(OTf)₂(dppe)] synthesised. 169
- Figure 4.9: NMR spectra of the [Pt(Cl)₂(dppm)] and [Pt(dppm)₂]Cl₂ in dichloromethane-*d*₂ a) ¹H and ¹H{³¹P} showing six aromatic regions, b) ¹H and ¹H{³¹P} showing two alkyl regions c) ³¹P{¹H} 400 scans showing two phosphorous signals. The resonances with a blue star indicate [Pt(dppm)₂]Cl₂ and the green star indicates [Pt(Cl)₂(dppm)]. 170
- Figure 4.10: NMR spectra of the [Pt(OTf)₂(dppm)] complex in dichloromethane-*d*₂ a) ¹H and ¹H{³¹P} showing three aromatic resonances, b) ¹H and ¹H{³¹P} showing one alkyl resonance c) ³¹P{¹H} 400 scans showing one phosphorous signal..... 170
- Figure 4.11: NMR spectra of the [Pt(Cl)₂(dppm)] complex in dichloromethane-*d*₂ a) ¹H and ¹H{³¹P} showing three aromatic resonances, b) ¹H and ¹H{³¹P} showing one alkyl resonance c) ³¹P{¹H} 200 scans showing one phosphorous signal..... 171
- Figure 4.12: NMR spectra of [Pt(Cl)₂(dppe)] and [Pt(dppe)₂]Cl₂ in chloroform-*d* a) ¹H and showing characteristic aromatic resonances, b) ¹H showing characteristic alkyl resonances c) ³¹P{¹H} 400 scans showing two phosphorous signals. The resonances with a blue star indicate [Pt(dppe)₂]Cl₂ and the green star indicates [Pt(Cl)₂(dppe)] 172
- Figure 4.13: NMR spectra of the [Pt(OTf)₂(dppe)] and [Pt(dppe)₂]Cl₂ in dichloromethane-*d*₂ a) ¹H showing characteristic aromatic resonances, b) ¹H showing characteristic alkyl resonances c) ³¹P{¹H} 400 scans showing two phosphorous signals.

The resonances with a blue star indicate $[\text{Pt}(\text{dpppe})_2]\text{Cl}_2$ and the green star indicate $[\text{Pt}(\text{OTf})_2(\text{dpppe})]$	173
Figure 4.14: $[\text{Pt}(\text{dppm})(\text{OTf})(2,4\text{-}d_2\text{-nicotinamide})]\text{OTf}$ (left) and $[\text{Ir}(\text{H})_2(d_{22}\text{-IMes})(2,4\text{-}d_2\text{-nicotinamide})_3]\text{Cl}$ (right). The symbol n represents a further substrate molecule occupying an equatorial site.....	174
Figure 4.15 : ^1H NMR spectrum showing the aromatic region of a methanol- d_4 solution containing $[\text{Pt}(\text{OTf})(\text{dppm})(2,4\text{-}d_2\text{-nicotinamide})]\text{OTf}$, $[\text{Ir}(\text{H})_2(d_{22}\text{-IMes})(2,4\text{-}d_2\text{-nicotinamide})_3]\text{Cl}$, and 10 eq. of 2,4- d_2 -nicotinamide at 298 K.	175
Figure 4.16 : ^1H NMR spectrum showing the aromatic region of a d_4 -methanol solution containing $[\text{Pt}(\text{OTf})(\text{dppm})(2,4\text{-}d_2\text{-nicotinamide})]\text{OTf}$, $[\text{Ir}(\text{H})_2(d_{22}\text{-IMes})(2,4\text{-}d_2\text{-nicotinamide})_3]\text{Cl}$, and 10 eq. of 2,4- d_2 -nicotinamide at 273 K.	175
Figure 4.17 : ^1H COSY NMR spectrum showing the aromatic region of a d_4 -methanol solution containing $[\text{Pt}(\text{OTf})(\text{dppm})(2,4\text{-}d_2\text{-nicotinamide})]\text{OTf}$, $[\text{Ir}(\text{H})_2(d_{22}\text{-IMes})(2,4\text{-}d_2\text{-nicotinamide})_3]\text{Cl}$, and 10 eq. of 2,4- d_2 -nicotinamide at 273 K.	176
Figure 4.18: $^{31}\text{P}\{^1\text{H}\}$ NMR spectrum of a d_4 -methanol solution containing $[\text{Pt}(\text{OTf})(\text{dppm})(2,4\text{-}d_2\text{-nicotinamide})]\text{OTf}$, $[\text{Ir}(\text{H})_2(d_{22}\text{-IMes})(2,4\text{-}d_2\text{-nicotinamide})_3]\text{Cl}$, and 10 eq. of 2,4- d_2 -nicotinamide.....	177
Figure 4.19: $^1\text{H}\{^{31}\text{P}\}$ NMR spectrum showing the aromatic region of a d_4 -methanol solution containing $[\text{Pt}(\text{OTf})(\text{dppm})(d_2\text{-}2,4\text{-nicotinamide})]\text{OTf}$, $[\text{Ir}(\text{H})_2(d_{22}\text{-IMes})(d_2\text{-}2,4\text{-nicotinamide})_3]\text{Cl}$, and 10 eq. of $d_2\text{-}2,4\text{-nicotinamide}$ (245 K).....	177
Figure 4.20: 1D selective EXSY NMR experiment showing exchange into the signal for the <i>meta</i> proton of free nicotinamide (δ 7.57) and the <i>meta</i> proton of bound 2,4- d_2 -nicotinamide in $[\text{Pt}(\text{OTf})(\text{dppm})(2,4\text{-}d_2\text{-nicotinamide})]\text{OTf}$ (δ 7.73, red star) on selective excitation of the <i>meta</i> proton of equatorially bound 2,4- d_2 -nicotinamide in $[\text{Ir}(\text{H})_2(d_{22}\text{-IMes})(2,4\text{-}d_2\text{-nicotinamide})_3]\text{Cl}$ (δ 7.27, blue star) after a delay time of 0.6 s (298K).	178
Figure 4.21: ^1H NMR spectra showing the aromatic region of a d_4 -methanol solution containing $[\text{Pt}(\text{OTf})(\text{dppm})(2,4\text{-}d_2\text{-nicotinamide})]\text{OTf}$, $[\text{Ir}(\text{H})_2(d_{22}\text{-IMes})(2,4\text{-}d_2\text{-nicotinamide})_3]\text{Cl}$, and 10 eq. of 2,4- d_2 -nicotinamide under (top) Boltzmann conditions (bottom) SABRE conditions.	179
Figure 4.22: ^{31}P NMR spectra of a solution containing 10 eq. of 2,4- d_2 -nicotinamide dissolved in methanol- d_4 with the $[\text{IrCl}(\text{COD})(d_{22}\text{-IMes})]$ and $[\text{Pt}(\text{OTf})_2(\text{dppm})]$ to observe SABRE-Relay derived hyperpolarised signal. (a) Signal acquired in Boltzmann	

- equilibrium conditions with 1 scan (b) similar signal after 400 scans using a $d1 = 1$ s. (c) Hyperpolarised signal acquired using 1 scan. 180
- Figure 4.23: a) Experimental scheme used for the original study.¹⁶⁸ Two protocols were used: In protocol 1 the sample is mixed with p -H₂ at low magnetic field (~ 6 mT and ~ 1 - 10 μ T) for the durations of τ_{LF1} and τ_{LF2} before moving to high field (τ_{tr}) for NMR observation. A simultaneous 90° pulse is applied to ^1H and ^{31}P prior to acquiring the ^{31}P signal with decoupling. In protocol 2, an M2S sequence²¹⁰, is applied between τ_{LF1} and τ_{LF2} ; b) $^{31}\text{P}\{^1\text{H}\}$ NMR spectra of the metal complexes formed using pyrimidine and pyrazine as substrate. 181
- Figure 4.24: ^1H NMR spectra of pyrimidine dissolved in methanol- d_4 solution with [IrCl(COD)(d_{22} -IMes)] and [Pt(OTf)₂(dppm)] to observe SABRE derived signal at 65 G mixing field (bottom) and corresponding signal acquired in Boltzmann equilibrium conditions (top) that is vertically magnified 32 times for comparison purpose..... 181
- Figure 4.25: $^{31}\text{P}\{^1\text{H}\}$ NMR single-scan spectra of [Pt(OTf)(dppm)(pyrimidine)]OTf; a) hyperpolarised using SABRE-Relay at 65 G, 1 average; b) acquired under Boltzmann equilibrium conditions, using 32 averages using 10 eq. of pyrimidine to 1 eq. of [IrCl(COD)(d_{22} -IMes)] & 1 eq. [Pt(OTf)₂(dppm)] in methanol- d_4 182
- Figure 4.26: $^{31}\text{P}\{^1\text{H}\}$ NMR spectra of [Pt(OTf)((dppe)(pyrimidine)]OTf (red), [Pt(OTf)(dppm)(pyrimidine)]OTf (blue), [Pt(OTf)(dppp)(pyrimidine)]OTf (green), hyperpolarised using SABRE-Relay, 1 average. Red) 10 eq. of pyrimidine to 1 eq. of [IrCl(COD)(d_{22} -IMes)] & 1 eq. [Pt(OTf)₂(dppe)] in methanol- d_4 . Blue) 10 eq. of pyrimidine to 1 eq. of [Ir(COD)Cl](d_{22} IMes) & 1 eq. [Pt(OTf)₂(dppm)] in methanol- d_4 . Green) 10 eq. of pyrimidine to 1 eq. of [IrCl(COD) (d_{22} -IMes)] & 1 eq. [Pt(OTf)₂(dppm)] in methanol- d_4 183
- Figure 4.27: Deuterated isotopologues of pyrimidine 2,5- d_2 -pyrimidine¹³⁵, 5- d -pyrimidine, 4,6- d_2 -pyrimidine and 4,5,6- d_3 -pyrimidine (unpublished) used in the SABRE-Relay process. 184
- Figure 4.28: $^{31}\text{P}\{^1\text{H}\}$ hyperpolarised NMR spectra showing S/N of a) [Pt(OTf)(dppp)(5- d -pyrimidine)]OTf, b) [Pt(OTf)(dppp)(4,6- d_2 -pyrimidine)]OTf c) [Pt(OTf)(dppp)(4,5,6- d_3 -pyrimidine)]OTf d) [Pt(OTf)(dppp)(2,5- d_2 -pyrimidine)]OTf hyperpolarised using SABRE-Relay, 1 average. 10 eq. of deuterated pyrimidine to 1 eq. of [IrCl(COD)(d_{22} -IMes)] & 1 eq. [Pt(OTf)₂(dppp)] in methanol- d_4 185

- Figure 4.29: Aromatic region of a ^1H NMR spectrum acquired on a sample prepared using 5 mM of $[\text{IrCl}(\text{COD})(d_{22}\text{-IMes})]$ and $[\text{Pt}(\text{OTf})_2(\text{dppp})]$ respectively with 20 eq. of pz in 0.6 mL MeOD. The formation of $[\text{Ir}(\text{H}_2)(\text{IMes})(\text{pz})_3]$ is indicated by resonances corresponding to pz protons bound to Ir in the equatorial sites of the complex (red - ortho to the bonding N centre and orange - meta to the bonding N centre) and resonances corresponding to pz protons bound to the Ir in the axial site of the complex (dark green - ortho to the bonding N centre and light green - meta to the bonding N centre). Another two resonances, located further downfield, are diagnostic for pz bound to the platinum complex (dark blue – ortho to the N binding centre and light blue – meta to the N binding centre)..... 187
- Figure 4.30: ^1H NMR spectra of pz: a). acquired in Boltzmann equilibrium conditions, spectrum (magnified 64 times), b). Corresponding hyperpolarised NMR spectrum under SABRE (single scan). 187
- Figure 4.31: ^{31}P NMR spectra of $[\text{Pt}(\text{dppp})(\text{OTf})(\text{pz})]\text{OTf}$: a). acquired in Boltzmann equilibrium conditions, using 32 averages, b). hyperpolarised using SABRE-Relay, 1 average. 188
- Figure 4.32: $^{31}\text{P}\{^1\text{H}\}$ hyperpolarised single scan of $[\text{Pt}(\text{dppp})\text{OTf}(4,6\text{-}d_2\text{-deuterated methyl nicotinate})]$ (blue stars) and $[\text{Pt}(\text{dppp})(4,6\text{-}d_2\text{-deuterated methyl nicotinate})_2]$ (red stars) formed with 10 eq. of 4,6- d_2 -deuterated methyl nicotinate to 1 eq. of $[\text{Ir}(\text{COD})\text{Cl}](d_{22}\text{IMes})$ & 1 eq. $[\text{Pt}(\text{OTf})_2(\text{dppp})]$ in methanol- d_4 . $p\text{-H}_2$ was added and the sample was shaken for 10 seconds in the stray field. 190
- Figure 4.33: $^{31}\text{P}\{^1\text{H}\}$ hyperpolarised single scan of $[\text{Pt}(\text{OTf})(\text{dppp})(4,6\text{-}d_2\text{-methyl nicotinate})]\text{OTf}$ and $[\text{Pt}(\text{dppp})(4,6\text{-}d_2\text{-methyl nicotinate})_2]$ (green) formed with 10 eq. of 4,6- d_2 -deuterated methyl nicotinate to 1 eq. of $[\text{IrCl}(\text{COD})(d_{22}\text{IMes})]$ & 1 eq. $[\text{Pt}(\text{OTf})_2(\text{dppp})]$ in methanol- d_4 . $^{31}\text{P}\{^1\text{H}\}$ hyperpolarised single scan of $[\text{Pt}(\text{OTf})(\text{dppm})(4,6\text{-}d_2\text{-methyl nicotinate})]\text{OTf}$ and $[\text{Pt}(\text{dppm})(4,6\text{-}d_2\text{-methyl nicotinate})_2]$ (blue) formed with 10 eq. of 4,6- d_2 -deuterated methyl nicotinate to 1 eq. of $[\text{IrCl}(\text{COD})(d_{22}\text{IMes})]$ & 1 eq. $[\text{Pt}(\text{OTf})_2(\text{dppm})]$ in methanol- d_4 . $^{31}\text{P}\{^1\text{H}\}$ hyperpolarised single scan of $[\text{Pt}(\text{OTf})(\text{dppe})(4,6\text{-}d_2\text{-methyl nicotinate})]\text{OTf}$ and $[\text{Pt}(\text{dppe})(4,6\text{-}d_2\text{-methyl nicotinate})_2]$ (red) formed with 10 eq. of 4,6- d_2 -methyl nicotinate to 1 eq. of $[\text{IrCl}(\text{COD})(d_{22}\text{IMes})]$ & 1 eq. $[\text{Pt}(\text{OTf})_2(\text{dppe})]$ in methanol- d_4 . $p\text{-H}_2$ was added to each sample and was shaken for 10 seconds in the stray field of a 9.4T magnet..... 191

- Figure 4.34: $^{31}\text{P}\{^1\text{H}\}$ thermal (400 scans) of $[\text{PtOTf}(\text{dppp})(\text{T}[2,3\text{-}d]\text{P})]\text{OTf}$ (blue stars) and $[\text{Pt}(\text{dppp})(\text{T}[2,3\text{-}d]\text{P})_2]$ (red stars) formed with 10 eq. of $\text{T}[2,3\text{-}d]\text{P}$ to 1 eq. of $[\text{Ir}(\text{COD})\text{Cl}](d_{22}\text{IMes})$ & 1 eq. $[\text{Pt}(\text{OTf})_2(\text{dppp})]$ (green stars) in methanol- d_4 193
- Figure 4.35: Molecular structures of the anti-cancer drugs a) cisplatin, b) carboplatin and c) oxaliplatin. 196
- Figure 4.36: Hypothesised route to hyperpolarise cisplatin through SABRE-Relay.... 196
- Figure 5.1: Metabolism of methanol to form formaldehyde and formic acid. Alcohol dehydrogenase is the primary enzyme for the oxidation of methanol to formaldehyde. Formaldehyde dehydrogenase is the principle enzyme involved in the oxidation of formaldehyde to formic acid.²⁶⁰ 198
- Figure 5.2: Structures of SABRE catalysts containing water soluble co-ligands (1 and 2)^{266, 267} and NHC ligands (3 and 4)^{266, 268}. 199
- Figure 5.3: Heterogeneous SABRE catalysts using polymer microbeads (5)²⁶⁹ and silica gel (6)²⁷⁰. 200
- Figure 5.4: Chemicals used to remove the SABRE metal catalyst: 3-mercaptopropyl-functionalised silica gel (7)²⁷¹ and Bathophenanthrolinedisulfonic acid disodium (BPS) (8) used to deactivate the catalyst followed through filtration using a DEAE Sephadex column.²⁶³ 200
- Figure 5.5: Representation of the biphasic CASH-SABRE process¹³⁸. The iridium catalyst remains in the organic phase whilst the polarised substrate transfers into the aqueous phase for subsequent extraction. 201
- Figure 5.6: 1D projection of the ^2H signal amplitude on the z direction (parallel to the magnet bore and the NMR sample tube). Deuterium profile showing the distribution of the two solvent phases (chloroform- d_2 & D_2O) in the magnet. 203
- Figure 5.7: 1D projection of the ^1H NMR signal as a function of time (128 repetitions) using a biphasic mixture of 4.5 mM $[\text{IrCl}(\text{COD})(d_{22}\text{SIMes})]$ and 18 mM $\text{T}[2,3\text{-}d]\text{P}$ in dichloromethane- d_2 and deuterium oxide a) under thermal conditions and b) hyperpolarised conditions with 3 bar (g) $p\text{-H}_2$. Dark red indicates areas of highest signal intensity and dark blue areas of lowest signal intensity. 203
- Figure 5.8: 1D projection of the ^1H NMR signal as a function of time (128 repetitions) using a biphasic mixture of 4.5 mM $[\text{IrCl}(\text{COD})(d_{22}\text{SIMes})]$ and 18 mM $\text{T}[2,3\text{-}d]\text{P}$ in

dichloromethane- d_2 and deuterium oxide (a) No acid, hyperpolarised signal located in organic layer at the bottom half of the biphasic sample. (b) adding 0.1 μl conc. HCl, hyperpolarised signal remains in the organic layer. (c) adding 0.65 μl conc. HCl, hyperpolarised signal is now located in the aqueous layer at the top half of the biphasic sample. Top row rotated to show planar view for ease. Bottom row shows decay of the hyperpolarised signal with time.	205
Figure 5.9: Diagram to show the various steps of the toxicity testing and MTT assay.	207
Figure 5.10: MTT assay showing the biochemical conversion by the healthy cells of MTT into Formazan crystals.	208
Figure 5.11: Viability of A549 cells with SABRE biphasic mixture using T[2,3- d]P and [IrCl(COD)(d_{22} SIMes)] at 4 time intervals 1 h (light blue), 3 h (dark blue), 6 h (light green) and 24 hours (dark green). Y-axis = percentage of healthy cells compared with the control. X-axis = percentage of solvent to be tested with respect to total volume of medium received by the cells. Results are taken across 3 separate experiments.	209
Figure 5.12: Viability of MCF7 cells with SABRE biphasic mixture using T[2,3- d]P and [IrCl(COD)(d_{22} SIMes)] at 4 time intervals 1 h (orange), 3 h (green), 6 h (purple) and 24 hours (yellow). Y-axis = percentage of healthy cells compared with the control. X-axis = percentage of solvent to be tested with respect to total volume of medium received by the cells. Results are taken across 3 separate experiments.	209
Figure 5.13: Cell Viability versus T[2,3- d]P concentration to estimate LD ₅₀ value for two cell lines: A549 (a) and MCF7 (b).	210
Figure 5.14: (a) A typical schematic of an FID-based CSI pulse sequence and (b) EPSI pulse sequence for MRI.	213
Figure 5.15: Thermally polarised RARE images of (a) 1 to 4 ratio of [IrCl(COD)(d_{22} SIMes)] and T[2,3- d]P in methanol- d_4 , (d) 1 to 20 ratio; (b) and (e) are the same thermal images as (a) and (d) but normalised with respect to the hyperpolarised images (c) and (f). In the hyperpolarised images (c) and (f) 3 bar(g) of $p\text{-H}_2$ was used and the sample shaken for 10 s in a 60 G shaker prior to measurement at 9.4 T. The diagram shows the experimental set up of the SABRE mixture within a 10 mm J. Young tube housed within a standard falcon tube.	215

Figure 5.16: (a) Experimental set up for RARE imaging using a head coil and a Siemens water/oil based head coil phantom with two inserts to house two 10 mm J. Young tubes containing the SABRE mixture (top) and water (bottom); (b) thermal RARE with 1:4 ratio of substrate to catalyst; (c) hyperpolarised RARE with 1:4 ratio of substrate to catalyst; (d) difference image between the hyperpolarised and thermal signals with 1:4 ratio of substrate to catalyst; (e) thermal RARE with 1:20 ratio of substrate to catalyst; (f) hyperpolarised RARE with 1:20 ratio of substrate to catalyst; (g) difference image between the hyperpolarised and thermal signals with 1:20 ratio of substrate to catalyst. Images (b), (c), (e) and (f) are signal normalised relative to the head coil phantom response..... 216

Figure 5.17: Chemical Shift artefacts (a) conceptually described and (b) MRI of a kidney showing dark bands and white bands that are characteristic of chemical shift artefacts;²⁸³ (c) chemical shift based image distortion caused by the 4.7 ppm and 8 ppm shifts of the resonant T[2,3-*d*]P peaks respectively (1:20 ratio at 3T); (d) image blurring (1:4 ratio at 9.4 T); (e) combination of image blurring and chemical shift artefacts (9.4 T) 217

Figure 5.18: ^1H 20° single pulse NMR spectrum showing hyperpolarised peaks from T[2,3-*d*]P alongside the peaks from the water/agar mixture measured using the preclinical 7T MRI system. Expansion shows the hyperpolarised T[2,3-*d*]P peaks measured using the preclinical 7T MRI system (black) and hyperpolarised T[2,3-*d*]P peaks measured using a 400 MHz NMR system (blue). 219

Figure 5.19: Set up of the hyperpolarised MR experiment on a 7 T preclinical scanner. a) ^1H high resolution FLASH reference scan shows the signal from the water before hyperpolarisation took place. b) Experimental set up with 10 mm Young's tube containing the sample surrounded by a falcon tube containing a water/agar mixture. c) Hyperpolarised CSI of sample in a 16 x16 grid with a 20 mm slice thickness. Integral analysis across the δ 9.82 and 9.65 peaks was overlaid (as a heat map) on ^1H FLASH reference data. d) Hyperpolarised CSI heat map with cubic spline interpolation of the original data using a factor of 4 to give a 64 x 64 grid with ROI's of water (blue) and hyperpolarised sample (red). e) Spectra produced from the ROI of the hyperpolarised sample (red) and the ROI of the water (blue). f) Image blocks showing the x,y and frequency domain of the hyperpolarised sample with hyperpolarised peaks at δ 9.82, 9.65, 8.27 and 7.76..... 220

- Figure 5.20: Hyperpolarised ^1H MR signal of thienopyridazine (90 mM) at slice thicknesses from 20 mm to 0.5 mm. (a) Gives the summed raw data of the hyperpolarised peaks (b) Gives the data on the same relative scale from 0 to 100. 221
- Figure 5.21:(a) Hyperpolarised CSI signal from T[2,3-*d*]P with a slice thickness of 0.5 mm (b) Signal at thermal equilibrium of T[2,3-*d*]P with a slice thickness of 0.5 mm showing only water (c) The difference from hyperpolarised signal – thermal signal leaving only the hyperpolarised T[2,3-*d*]P signal. 222
- Figure 5.22: Comparison of (a) CSI (1 mm slice thickness) and (b) EPSI (1 mm slice thickness) showing image maps of hyperpolarised T[2,3-*d*]P and spectra normalised to the water peak. Insert in CSI spectrum (a) shows the incurrence of the water peak within the hyperpolarised spectrum with a similar amplitude to the peak of interest. Insert in EPSI spectrum (b) shows a Nyquist ghost of the T[2,3-*d*]P peaks at δ 2.4. Experimental set up shows a 10 mm J. Young tube containing the SABRE solution surrounded by water in a falcon tube. 223
- Figure 5.23: EPSI a) odd and even echo analysis for T[2,3-*d*]P b) odd and even echo analysis for water c) Raw spectra showing N/2 ghost artefacts. d) Corrected spectra following odd/even analysis.²⁸⁶ Water peak is aliased to approximately δ 8.7, T[2,3-*d*]P peaks (H4 and H7) are aliased to approximately δ 6 - 6.5 as spectral width has been halved. e) Manual correction based on spatial position results in an adequate overall spectrum. 225
- Figure 5.24: *Ex-vivo* subcutaneous injection of T[2,3-*d*]P. (a) Site of injection into rat and ^1H structural scan of cross section of torso overlaid with hyperpolarised T[2,3-*d*]P. (b) Hyperpolarised spectrum immediately after injection. (c) Thermal spectrum 5 minutes after injection. (d) Difference between hyperpolarised and thermal spectra (e) Design matrix for GLM analysis using $y = \beta_1 * M_1 + \beta_2 * M_2 + \beta_3 * M_3 + \beta_4 * M_4 + \text{error}$. Resultant fitted parameter maps of (f) β_3 showing water and associated Nyquist ghost peak signal originates in surrounding soft muscle tissue (as expected) and (g) β_4 showing T[2,3-*d*]P signal localised to the subcutaneous space where the bolus hyperpolarised solution was injected. 226
- Figure 6.1: Chemical structure of ^{13}C -nicotinamide. 234
- Figure 6.2: Schematic description of nicotinamide metabolism³¹⁴ Enzymes 1 = nicotinamide-N-methyltransferase, 2 = aldehyde oxidase, 3-5 = nicotinamide

deamidase, 6 = nicotinamide phosphoribosyltransferase, 7 = NAMN adenylltransferase, 8 = nicotinamide synthetase, 9 = poly(ADP-ribose) synthetase, 10 = nicotinamide glycohydrolase, 11 = nicotinamide phosphoribosyltransferase (NAMPT). 236

Figure 6.3: Relationship between relaxation time vs correlation time T_1 and $T_2^{234, 328}$. 238

Figure 6.4: Radicals used in DNP a) TEMPO and b) OX063. 239

Figure 6.5: Dotarem – Gadolinium Chelate used in DNP to increase polarisation and shorten polarisation build up times. 240

Figure 6.6: Power spectrum of microwave frequency to determine optimum for polarisation. A starting frequency of 94.080 GHz was used through to 94.160 GHz. The step size used was 5 MHz and the step duration 300 s. a) Absolute sweep amplitude recorded using: Formulation A (light blue), Formulation B (red), Formulation C (orange), Formulation D (green), Formulation E (purple). Insert shows normalised raw signal showing positive and negative polarisation peaks related to the shape of the first derivative ESR spectrum. b) Normalised amplitude of combined sweeps with errors indicating optimum frequency was 94.105 GHz. Dotted line shows least square fitting across all samples to estimate peak frequency. 242

Figure 6.7: (a) Polarisation build up curves at 94.105 GHz using 100 μ l aliquots of Formulation C (orange), Formulation D (green), Formulation E (purple) and Formulation F (black) b) Corresponding normalised build up profiles. 244

Figure 6.8: (a) 3D surface map of the flux of hyperpolarised ^{13}C -nicotinamide in PDX breast tumour (formulation F). Series of 180 ^{13}C magnetic resonance spectra recorded through the tumour starting immediately after the injection of 0.4 ml of 67 mM hyperpolarised ^{13}C nicotinamide. Spectra were collected every second for a total of 3 minutes with TE = 1 s. (b) 1D plot (through δ 171) of arterial input of the hyperpolarised ^{13}C -nicotinamide and the subsequent decay. The crosses indicate the experimental values. The red line indicates a theoretical T_1 decay of 14 s. The green line indicates a T_1 decay of 14 with the loss of hyperpolarisation due to the 5° FA being used. Experimental points from 14 s to 60 s fit with an exponential decay accounting for a 5° FA to give a T_1 of 14.7 s. 246

Figure 6.9: (a) ^1H MRI scan of the axial cross section of tumour bearing mouse (6 mm slice). (b) CSI map of 32 x 32 points showing the distribution of the ^{13}C -nicotinamide across the axial cross section through tumour and mouse torso (40 mm x 40 mm 2D plane,

- 6 mm slice). The yellow colour shows the areas of most intensive hyperpolarised signal whilst the dark blue colour shows the areas of little or no hyperpolarised signal. (c) CSI image of original 32 x 32 interpolated to 128 x 128 overlaid on a ^1H anatomical MRI scan. The white/yellow colour shows the areas of most intensive hyperpolarised signal.247
- Figure 6.10: (a) Thermal spectrum of ^{13}C -nicotinamide vertically multiplied 64 times to be seen alongside the hyperpolarised spectrum using d-DNP. (b) ^{13}C FISP image of ^{13}C nicotinamide using d-DNP. Both the spectra and the image were measured on a 9.4 T magnet.....248
- Figure 6.11: T_1 values the carbonyl carbon of nicotinamide, 2,4- d_2 -nicotinamide, 2,5- d_2 -nicotinamide and 4,6- d_2 -nicotinamide measured in ethanol- d_6 using thermal inversion recovery (400 MHz NMR system).....249
- Figure 6.12: T_1 and percentage polarisation of ^{13}C nicotinamide, 4,6- d_2 -nicotinamide and ^{13}C methyl nicotinate in water/glycerol mixture. Hyperpolarisation was carried out using d-DNP and T_1 values were measured using a 1 shot hyperpolarised T_1 with variable flip angle protocol (400 MHz).....250
- Figure 6.13: Iridium complex formed during SABRE with ^{13}C nicotinamide and $[\text{IrCl}(\text{COD})(\text{X})]$. The red dotted line shows the transfer of polarisation directly to the carbon and the blue dotted line shows the transfer of polarisation to the protons in nicotinamide. The black line indicates the coupling between the hydrides. (n is second in plane nicotinamide that is missed to aid the reader).251
- Figure 6.14: SABRE hyperpolarised ^{13}C signal from a sample containing ^{13}C nicotinamide and $[\text{IrCl}(\text{COD})(\text{X})]$ (5mM) in a 10 to 1 ratio in methanol- d_4 with 3 bar G of $p\text{-H}_2$ using different polarisation transfer fields: mu metal shield, 8-fold signal enhancement (red), -2mG, 18-fold signal enhancement (green) and -9mG, 24-fold signal enhancement (blue).252
- Figure 6.15: ^{13}C nicotinamide and $[\text{Ir}(\text{COD})\text{Cl}(\text{X})]$ (5 mM) in a 10 to one ratio in ethanol- d_6 with 3 bar(g) of $p\text{-H}_2$. (a) Signal to noise ratios (black) and signal enhancement (red) at different shaking times using SABRE (b) Hyperpolarised ^{13}C signal resulting from a 50 s shake and drop experiment giving S/N = 5667 and signal enhancement = 169 (0.17% polarisation). Thermal signal is vertically multiplied x 2 (green) to be seen alongside the hyperpolarised signal (blue).....253

Figure 6.16: Ir(COD)Cl(X)] (5 mM) with 10 eq. of ^{13}C nicotinamide with SABRE PTF 60G (black) 211 ± 7 fold signal enhancement (based on thermal shake and drop experiment) and SABRE INEPTD 60G (red) 144 ± 9 fold signal enhancement (based on thermal INEPTD experiment).	254
Figure 6.17: Comparison of hyperpolarised ^{13}C signals resulting from 40 s shake and drop experiments using [Ir(COD)Cl(X)] (5 mM) with 10 eq. (blue) and 20 eq. (red) of ^{13}C nicotinamide in ethanol- d_6 at 60 G and 3 bar of $p\text{-H}_2$	255
Figure 6.18: Images of SABRE hyperpolarised ^{13}C nicotinamide using ([Ir(COD)Cl(X)] (5 mM) with 10 eq. of ^{13}C nicotinamide in ethanol- d_6 at 60 G and 3 bar(g) of $p\text{-H}_2$. (a) FISP hyperpolarised image. (b) FISP thermal image. (c) CSI image with corresponding spectrum of ^{13}C nicotinamide peak. (d) EPSI image with corresponding spectrum of ^{13}C nicotinamide peak revealing Nyquist ghost peak at ~ 200 ppm.	256
Figure 6.19: (a) ^{13}C 3D decay of ^{13}C nicotinamide under SABRE conditions (shaking at 60 G) measured at 3T. (b) Estimated T_1 calculation of decay = 14 s.....	257
Figure 6.20: Images of SABRE hyperpolarised ^{13}C nicotinamide using ([Ir(COD)Cl(X)] (5 mM) with 10 eq. of ^{13}C nicotinamide in ethanol- d_6 at 60 G and 3 bar of $p\text{-H}_2$ at 3 T. (a) ^1H reference scan including sketch of set up. (b) CSI raw data using 8×8 voxels, (c) CSI raw data using 16×16 voxels, (d) spectrum from CSI showing ^{13}C nicotinamide hyperpolarised peak. (e) overlay of CSI (using 16×16 voxels) on ^1H reference scan with interpolation (8x).....	257
Figure 8.1: Inversion recovery experiment to measure T_1 . A 180° pulse flips the bulk magnetisation into the $-z$ plane. As the signal relaxes the bulk magnetisation builds back up into the $+z$ plane. Interrogation with a 90° pulse at various time intervals τ and fourier transform (FT) gives rise to an NMR peak. Analysis of the integral of this peak as a function of τ yields T_1	276
Figure 8.2: LLS pulse sequence with delays $\mathbf{14J}$; $\mathbf{14J} + \mathbf{12\Delta\nu}$; $\mathbf{14\Delta\nu}$ and τ where J and $\Delta\nu$ denote the scalar-coupling constant and chemical shift difference between the associated spin pair in Hertz respectively. A Waltz-16 composite pulse of 1 KHz amplitude was used as the spin-lock (with duration τ) in all cases.	288
Figure 8.3: Schematic of the d-DNP-MRI process used to measure a hyperpolarised time course experiment of ^{13}C -nicotinamide within a tumour and a CSI distribution map of HP ^{13}C -nicotinamide within the mouse torso.....	297

Figure 8.4: Schematic of the d-DNP-NMR process used to measure polarisation levels and hyperpolarised T_1299

Figure A 1: Structures of pre-catalysts [Ir(COD)(IMes)(T[2,3-*d*]P)]Cl A and B.....301

Figure A 2: Structures of intermediates [Ir(COD)(H)₂(IMes)(T[2,3-*d*]P)]Cl C and D.304



Acknowledgements

I would like to thank my supervisor Prof. Simon Duckett for the opportunity to return to study as a mature student. Not every supervisor, and department, would have given this opportunity to a mother with two young children and for that I am very grateful. I also appreciate the support and understanding of Simon, Meghan (IPM) and the department, in particular to the members of the graduate office (Alice, Rachel and Sharon), when I needed to take a leave of absence. This support was critical and key to me being able to continue my studies after a period of illness. I thank the Marie Curie and the Europol network for giving me the opportunity to travel to different countries including Poland, Denmark and Israel and meet leading scientists and fellow students from the field of hyperpolarisation and MR.

A huge thanks goes to my best friends Cheryl, Ruth and Selina for their active encouragement to return to my studies and continued support throughout the four years. A great big thank you goes to Lenny! Jenny Lewis, my partner in crime throughout our crazy return to university. I could not have done it without you! I would like to thank all CHyM members past and present for their technical and moral support; Pete Richardson (physics guru), Vicki and Richard (technical assistance), Lyndsay and Denise (organisation queens), Anand (toxicity studies), Alexandra (3T MRI, pyrazine work), Soumya (long-lived states), Ben, Alistair, Will, Aminata, Wissam (Biphasic Studies) and Marianna. I thank the CHyM girls, Jenny, Kate, Olga, Barby and Emma for their constant support and our laughs and know that I have made friends for life. Huge thanks go to Pete and Phil for being top blokes and organic chemistry gurus! Particular thanks to Pete for chapter reading. A big thank you to Marie for teaching me about cell culture and MRI and becoming a good friend. Massive thanks to Aneurin for his continual support, mentoring and chapter reading; not to mention giving me a job and introducing me to the wonderful world of MRI and Star Wars! A huge thank you to my Mum and Dad for their constant support in every decision I make. A very special mention goes to my children, Cristian and Stella, and husband Filippo for being the absolute stars that they are!



Declaration

I declare that this thesis is a presentation of original work and I am the sole author. This work has not previously been presented for an award at this, or any other, University. All sources are acknowledged as references.



Chapter 1: Introduction

Magnetic resonance (MR) is a spectroscopic/imaging technique at the forefront of molecular profiling research used for the diagnosis of disease by tracing aberrant cellular function.^{1,2} MR can provide both fundamental molecular data (spectra), alongside macroscopic structural information (images), in a non-invasive and non-destructive manner. Although MR can detect and characterise molecular structure and function, the technique's inherent sensitivity is somewhat limited by low thermal polarisation between quantised energy states of the nuclei when exposed to a magnetic field (section 1.2). In order to overcome this limitation, it is typical to use strong magnetic fields (>7 T), high concentrations and signal averaging, all of which can be impractical to implement for *in-vivo* measurements.

An alternative approach, to increase the sensitivity of MR, involves physical manipulation of the magnetic state populations, so called hyperpolarisation.³ Indeed, it is now possible to track metabolic flux of specific molecules in the body using hyperpolarisation techniques.⁴⁻⁶ Recent research uses hyperpolarisation for the detection and conversion of ¹³C labelled pyruvate to lactate as a means to image tumour metabolism in breast cancer.⁷ Example hyperpolarised MR imaging data adapted from Gallagher et.al (2020) are shown in Figure 1.1. Such data will facilitate improved diagnostics and treatment response tracking, with substantial benefits to patients. MR enhanced with hyperpolarisation, is therefore emerging as a minimally invasive alternative to nuclear medicine for molecular imaging. It is now a major research area in imaging-bioscience.⁸

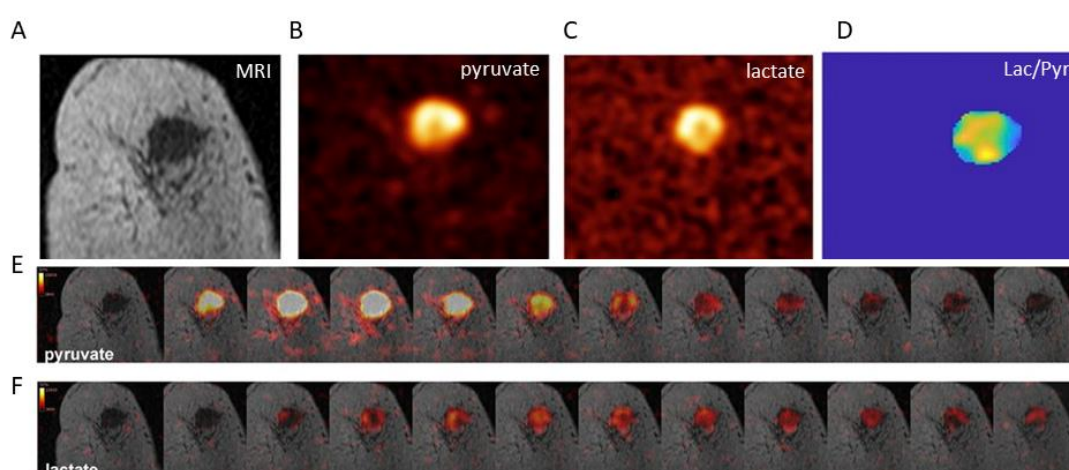


Figure 1.1: ¹³C-pyruvate and ¹³C-lactate images acquired from a breast cancer patient following i.v. injection of hyperpolarised [1-¹³C]- pyruvate. (A) Standard structural MR. (B) Hyperpolarised ¹³C-pyruvate and (C) ¹³C-lactate images. (D) LAC/PYR map showing tumour heterogeneity represents decreased delivery of hyperpolarised substrate at the tumour centre. (E and F) Dynamic (temporal resolution = 4 s) hyperpolarised ¹³C-pyruvate and ¹³C-lactate images.⁷ Data adapted from Gallagher *et al.* (2020).

1.1 A Brief History of Molecular Imaging

Over 100 years ago the discovery of X-rays revolutionised diagnostic medicine by enabling physicians to see, for the first time, structural images of the internal living body. Imaging of gross anatomical structure was further augmented through the invention of Computerised Tomography (CT) in 1967 by Sir Godfrey Hounsfield^{9, 10} and Magnetic Resonance Imaging (MRI) in 1973 by the American chemist Paul Lauterbur.¹¹ While CT finds wide usage¹² in modern medicine, X-ray exposure is high¹³ and it does not deliver the required functional molecular information (beyond perfusion of iodine-based contrast agents, which have known side effects¹⁴) for more subtle disease staging.

It was initially the evolution of complementary cutting-edge nuclear medicine which permitted deeper probing into the body on a molecular level. The combination of structural and functional information within the body is critically important to medicine for several reasons; (i) it helps to gain a better understanding of the biological pathways leading to disease; (ii) it helps with early diagnosis; (iii) it allows a quick assessment of the efficacy of drugs; and (iv) aids the selection of therapy chosen and effective personalised medical treatment.

In 1963, Kuhl and Edwards demonstrated that single photon emission computed tomography (SPECT) was a promising technique for tracking molecular function.^{15, 16} SPECT uses injectable radionuclides (molecules containing isotopes such as ^{99m}Tc, ¹¹¹In or ¹²³I) which emit gamma rays for subsequent detection outside the body. Localised function can be probed by creating radiolabelled ligands, the properties of which are designed to bind to certain types of healthy/diseased tissues. Modern gamma cameras, which rotate around the subject, produce 3D tomographic images that aid disease diagnosis. Today SPECT finds particular application in probing neuronal^{17, 18} and cardiac¹⁹ molecular function; albeit with relatively low spatial & temporal resolution.²⁰

In 1976, Hoffman and Phelps developed Positron Emission Tomography (PET)^{21, 22}, which uses radionuclides incorporated into biologically active molecules e.g. sugars, proteins or hormones.²³ 2-deoxy-2-(¹⁸F)fluoro-D-glucose (FDG),²⁴ a glucose analogue, in which a positron emitting radionuclide (¹⁸F) is introduced in place of the hydroxyl group at the 2 position of the glucose molecule (Figure 1.2), is one of the most widely used radioactive tracers. Following injection, the tracer collects in areas of the body where there are abnormal levels of chemical activity associated

with disease. As the radio-nucleotide decays (FDG $T_{1/2} = 109.7$ min), it emits a positron which upon annihilation with an electron produces a pair of high energy (511 keV) photons orientated at $\sim 180^\circ$ with respect to one another. Detection of near simultaneous multiple annihilation events by an array of photon scintillation detectors, around the subject, is used to produce 2D images. Resultant images are of higher spatial resolution than SPECT.^{20, 25}

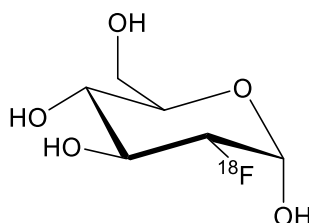


Figure 1.2: Chemical structure of 2-deoxy-2(^{18}F)fluoro-D-glucose.

In the specific case of FDG, after emitting a positron, ^{18}F decays to ^{18}O which binds to a labile proton. It is subsequently metabolised to glucose-6-phosphate labelled with a harmless non-radioactive “heavy oxygen”. Other common PET isotopes include ^{15}O ($T_{1/2} = 2.03$ min), ^{13}N ($T_{1/2} = 9.96$ min), ^{11}C ($T_{1/2} = 20.4$ min) which are used to monitor heart conditions,²⁶ neurodegenerative diseases²⁷ and cancer²⁸. Isotopes with much longer half-lives (e.g. ^{64}Cu ; $T_{1/2} = 12.7$ h), are also used. For example, ^{64}Cu -CuCB-bicyclam has been developed as a PET receptor imaging agent to target the chemokine C-X-C motif receptor 4 (CXCR4), which is important in cancer metastasis, in autoimmune diseases, and stem cell-based repair processes after stroke and myocardial infarction.²⁹

PET has also developed into a vital molecular imaging tool for the early staging of metastases^{30, 31}, assessing therapy response³² and monitoring disease reoccurrence.^{33, 34} Cancerous cells have a higher metabolic rate of glucose than normal cells known as the Warburg Effect³⁵. Thus, tumour cells show up as hot spots on ^{18}F FDG-PET scans.

It should be noted, however, that caution should be taken when interpreting FDG-PET images. Non-cancerous conditions such as lymph node response to inflammation/sarcoidosis^{36, 37} can be mistaken for cancer³⁸. Treatment assessment using ^{18}F FDG-PET is difficult in some organs (e.g., prostate and brain) due to both poor tumour and increased background uptake, respectively.²⁵ In addition, although the amount of injectable/ingestible tracer is on the pico to nanomolar scale it is radioactive and therefore PET is classed as invasive. A further disadvantage is the need for specialised equipment, in the form of a cyclotron³⁹, for synthesis of the biologically active radio-

nucleotide. Due to the radio-nucleotide half-life and the logistics of producing the agent, timing is crucial and there is little room for error. An advantage of PET is the high sensitivity, but this is coupled with the disadvantage that it is the incorporated radioisotope which is being recorded and so the molecule should not be metabolised rapidly (or should be metabolically trapped as with FDG).

Since 2001 combined PET and computerised tomography (CT) has replaced stand-alone PET.⁴⁰ CT adds detailed structural anatomy to the relatively low-resolution functional PET images.^{41, 42} In the clinic the combination of X-ray CT and PET images has led to improvements in tumour detection.⁴³ Recent research exploits ¹⁸F FDG-PET/CT to assess pneumonia/acute respiratory diseases in COVID-19 patients.^{44, 45}

Magnetic resonance imaging (MRI) produces anatomic images from thousands of voxels whose signals arise from bulk magnetic properties of tissue. The signal is based predominantly on the protons found in fat and water within the body. MRI has the advantage of offering higher spatial and temporal resolution over PET/SPECT and it does not expose the patient to any ionizing radiation. Combined PET/MRI modalities were developed in 1997 by Shao et al.⁴⁶ Specifically for neuroimaging, a combination of electroencephalography (EEG), PET and MRI has also been developed (Shah et al. 2012). The three techniques complement each other well; the strength of MRI is in structural–functional imaging, PET provides molecular imaging and EEG provides a temporal dimension where the other two modalities are weak.⁴⁷⁻⁴⁹

Magnetic Resonance Spectroscopy (MRS) is an MRI technique where spatial resolution is sacrificed to produce spectra from a smaller number of voxels identifying metabolite molecules differentiated by their chemical shifts (δ). It has therefore become a powerful technique for studying metabolism *in vivo*. ¹H MRS may be used to measure the levels of various abundant metabolites, including lactate, neutral lipids, choline and phospholipid metabolites, such as phosphocholine in oncology⁵⁰, or neurochemicals such as GABA and glutathione in neurodegenerative diseases.⁵¹⁻⁵⁴

Several metabolically relevant nuclei in addition to hydrogen (¹H) are MR active/visible allowing a range of metabolites in a variety of tissues to be detected including ¹³C and ³¹P which have long been used in the investigation of metabolic processes *in vivo*.⁵⁵ ³¹P can be used to observe energy metabolism by monitoring ATP, inorganic phosphate⁵⁶ and intracellular pH.⁵⁷ Measurement of ²³Na tissue concentration can be used to monitor tumorous tissue elimination after chemotherapy⁵⁸

and even whole body imaging⁵⁹ The non-invasive nature of MRS allows repeated experiments with no harm to the patient so that response to long-term treatment (drug therapy) and rapid intervention (e.g. exercise, insulin stimulation) can be assessed.

Due to its relative insensitivity, thermal MRS is often limited to regions where metabolites are in a high enough concentration to be detected, for example in the brain or tumours. However, even then the spatial and temporal resolution is limited and increasing the magnetic field strength can only help to a certain extent. Therefore, the need for hyperpolarisation techniques, such as dissolution-dynamic nuclear polarisation (d-DNP) which can increase ¹³C MRS sensitivity by 10,000-fold, is clear. This sensitivity increase has not only allowed detection of ¹³C labelled metabolites but also their metabolism and tissue distribution.^{3,4}

MRS combined with hyperpolarisation techniques provides a way to obtain both high-definition structural information and fast dynamic functional information to aid diagnosis with zero risk even with repeated measurements to the patients. At the moment these techniques are still in their infancy and therefore at present combinations with other imaging modalities can be complementary.

To understand how hyperpolarisation techniques can help to overcome the insensitivity in NMR and MRS a more in-depth examination is required of the underlying principles.

1.2 Nuclear Magnetic Resonance

The field of Nuclear Magnetic Resonance (NMR) spectroscopy exploits MR phenomenon to study chemical, physical and biological properties.⁶⁰ Since its introduction in 1946 by Bloch⁶¹ and Purcell⁶² NMR has become one of the leading analytical methods in chemistry. Both NMR and MRI play unique roles, the former as an analytical spectroscopic tool across the sciences, the latter primarily for clinical diagnostics across the medical specialities. However, the scientific basis underpinning both technologies is the same. In this section the physical basis of the nuclear magnetic resonance signal is described. Some of the basic imaging techniques employed in this thesis are outlined. A full understanding is based in quantum theory but by using some classical descriptions, it is much easier to grasp the complex scientific principles of NMR. This section is only intended as an overview and the author directs to '*Principles of Nuclear Magnetic Resonance Microscopy*'⁶³, '*Nuclear Magnetic Resonance*'⁶⁴ and '*Spin Dynamics: Basic of Nuclear Magnetic Resonance*'⁶⁵ if a full understanding is required.

1.2.1 Physical basis

Some nuclei have an intrinsic angular momentum known as spin and consequently possess a magnetic dipole moment that can be exploited in NMR and MRI. Hydrogen (^1H) provides the simplest nuclei to explain the NMR phenomenon. A positively charged proton, has thermal energy resulting in classical rotation/spin with angular momentum. In this classical model the rotating charge induces a small magnetic field and the nucleus possesses a magnetic dipole moment, $\boldsymbol{\mu}$ (Figure 1.3 a).

On a more realistic quantum level the system is described by the spin quantum number I . For any nuclei, the spin quantum number is determined by the number of unpaired protons and neutrons (each having spin $1/2$). For nuclei with $I = 0$ there is no angular momentum, no magnetic moment and therefore the nucleus is NMR silent. Any nucleus with $I > 0$ possesses spin and is therefore ‘NMR active’. Spin angular momentum, \mathbf{I} , is a vector quantity where both its direction and magnitude are quantised. A spin I nucleus has $2I + 1$ projections onto an axis e.g., the z axis. The z component of \mathbf{I} , i.e., I_z is quantised according to equation [1.1].

$$I_z = m\hbar \quad [1.1]$$

The magnetic quantum number, m has $2I+1$ values between $-I$ and $+I$ in integral steps therefore for a proton $m = +1/2$ and $-1/2$.

Spin angular momentum and the magnetic moment of a nucleus are related by the gyromagnetic ratio, γ (equation [1.2]).

$$\boldsymbol{\mu} = \gamma\mathbf{I} \quad [1.2]$$

where γ is a fundamental property of the specific nucleus (possessing a different value for every nuclear isotope), thereby acting as a unique fingerprint for identification.

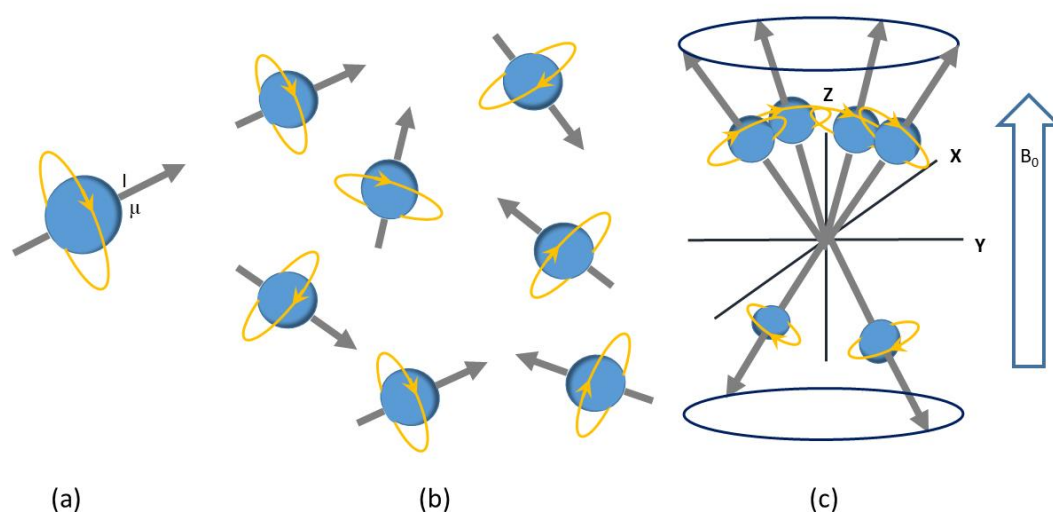


Figure 1.3: (a) Classical model of a spin system. Thermal energy results in spinning charge with angular momentum (l), generating a small magnetic dipole moment (μ). (b) Random orientation of spins in bulk matter in the absence of an external magnetic field resulting in a net magnetic moment of zero. (c) Spins in the presence of an external magnetic field aligned with and against magnetic field.

Any nucleus with an odd number of protons and/or neutrons (e.g., ^{13}C , ^{19}F , ^{31}P , ^{17}O) exhibits these essential spin properties. However, ^1H is often the target nucleus due to 99.985% isotopic abundance, high natural abundance (especially for *in-vivo* imaging)⁶⁶ and high gyromagnetic ratio.

In the absence of an external static magnetic field, the magnetic moments of bulk matter will be randomly orientated (Figure 1.3 b). Thus, there is no net nuclear magnetization. When placed in a static magnetic field (B_0), the individual magnetic moments align either parallel or anti-parallel to the field,⁶⁷ with a slight excess of spins in the parallel orientation (Figure 1.3 c).

Classical torque induces precession around B_0 (Figure 1.3 c) with an angular frequency ω_0 known as the Larmor frequency, which can be calculated using equation [1.3] where B_0 is the static magnetic field strength.

$$\omega_0 = \gamma B_0 \quad [1.3]$$

The Larmor frequency therefore is a characteristic property for a particular nucleus (defined by γ) and for the chemical environment of that nucleus (which changes local B_0).

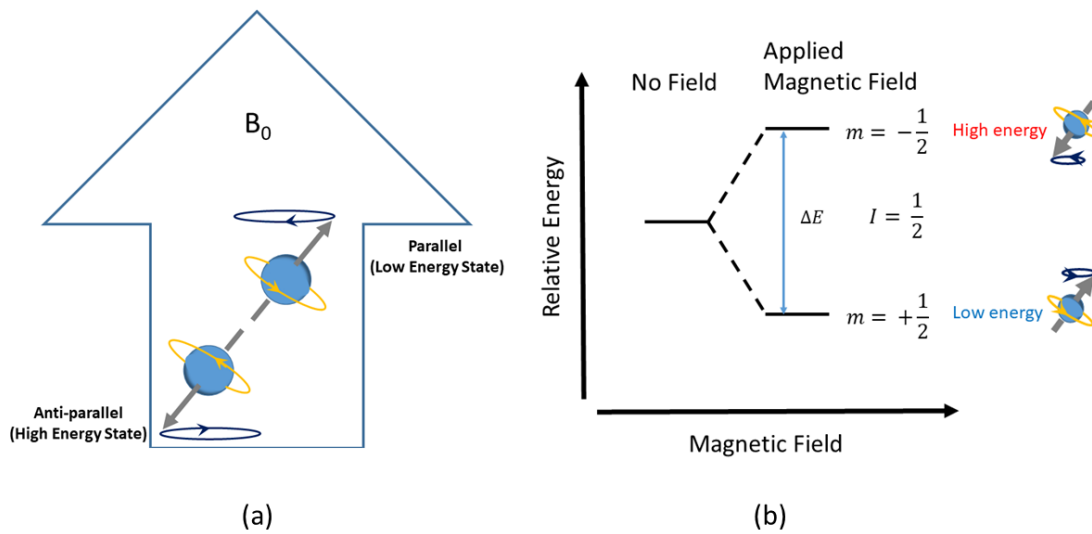


Figure 1.4: a) Magnetic field B_0 with spins precessing at the Larmor frequency aligned parallel or anti parallel (Classical view). b) Energy level diagram of a nucleus with $I = 1/2$ resulting in two energy levels $m = -1/2$ and $m = +1/2$ when placed in a magnetic field (Quantum view).

On a quantum level, spins have $2I + 1$ possible energy levels. The existence of these classical spin states is a consequence of the quantum ‘Zeeman Effect’ (Figure 1.4). For ^1H with spin $I = \frac{1}{2}$ there are therefore two possible energy levels (defined by magnetic quantum numbers $m = \frac{1}{2}$ and $m = -\frac{1}{2}$, termed α and β respectively). The difference in energy, ΔE , between two spin $\frac{1}{2}$ levels is given in equation [1.4].⁶⁴

$$\Delta E = \hbar\gamma B_0 \quad [1.4]$$

where $\hbar = h/2\pi$. Thermal energetics are such that there is a slight excess of spins in the lower energy state. Resultant state populations follow Boltzmann statistics at thermal equilibrium and the number of excess spins is given by equation [1.5].

$$\frac{n_{(m=-\frac{1}{2})}}{n_{(m=\frac{1}{2})}} = e^{-\Delta E/k_B T} \quad [1.5]$$

where $n_{(m=\frac{1}{2})}$ and $n_{(m=-\frac{1}{2})}$ are the lower and upper energy state populations respectively; k_B is Boltzmann’s constant and T is temperature. As thermal energy ($k_B T$) is much greater than the energy state difference (ΔE), the exponent in equation 1.4 can be expanded ($e^{-x} = 1 - x$) and the normalised population difference calculated as per equation [1.6].

$$\frac{n_{(m=\frac{1}{2})} - n_{(m=-\frac{1}{2})}}{n_{(m=\frac{1}{2})} + n_{(m=-\frac{1}{2})}} = \frac{\Delta E}{2k_B T} \quad [1.6]$$

For ^1H ($\gamma = 42.58 \text{ MHz/T}$) in a 9.4 T static magnetic field $\Delta E = 2.65 \times 10^{-25} \text{ J}$ (eqn. [1.3]). At 300 K the population difference can be calculated with equation [1.6] as 3.2×10^{-5} ; or 1 in $\sim 32,000$ extra nuclei in the low energy state. Thus, a net magnetization exists in the direction of the applied magnetic field (Figure 1.3c) defined as the z axis.

Although this population difference is extremely small, when imaging the human body with ^1H at standard clinical field strengths of 1.5 T, one can calculate that in a single voxel (imaging volume element) of 0.02 mL the number of excess protons would be 6.02×10^{15} (6 million billion) and, therefore, represents a significant signal for subsequent excitation and detection (section 1.2.2). The linear dependence of population difference (\sim net magnetisation) on the gyromagnetic ratio (through ΔE) is noted. Thus, NMR signal is inherently smaller for the other applicable nuclei (e.g. ^{13}C) even before considering differences in natural abundance. Nevertheless, this small low energy level population excess can be manipulated. Hyperpolarisation techniques for doing this will be explored in sections 1.3 & 1.4 and are the basis of this thesis.

The resultant net magnetization cannot be detected in the z axis (as it is dwarfed by the huge static magnetic field in the same direction). To detect this net magnetisation, it must be perturbed, by an oscillating magnetic field, B_1 (perpendicular to the static field, B_0 , and rotating at the same Larmor frequency), into the transverse (x - y) plane. This is done through a process of electromagnetic excitation.

1.2.2 Excitation and Detection

Net magnetization is perturbed into the x - y plane by a short Radio Frequency (RF) pulse emitted from a surrounding antenna. The frequency of this RF pulse must be ‘resonant’ to the Larmor frequency defining the energy difference between the spin states. Thus, only nuclei that precess with the same frequency as the RF pulse will be excited. In a rotating frame of reference, the effect is a rotation of the net magnetization around B_1 (the RF field) onto the transverse (x - y) plane (Figure 1.5); perpendicular to B_1 and B_0 . The angle of net magnetization rotation (determined by the pulse power and duration) is called the nutation or flip angle (FA). Following cessation of the RF pulse the precessing magnetisation vector will induce a time varying AC current in a receiving antenna/coil. The magnitude of this time oscillating current will reduce as

the system relaxes back to equilibrium. Fourier transformation of this time oscillating signal delivers the component Larmor frequencies (if multiple are present) as a spectrum.

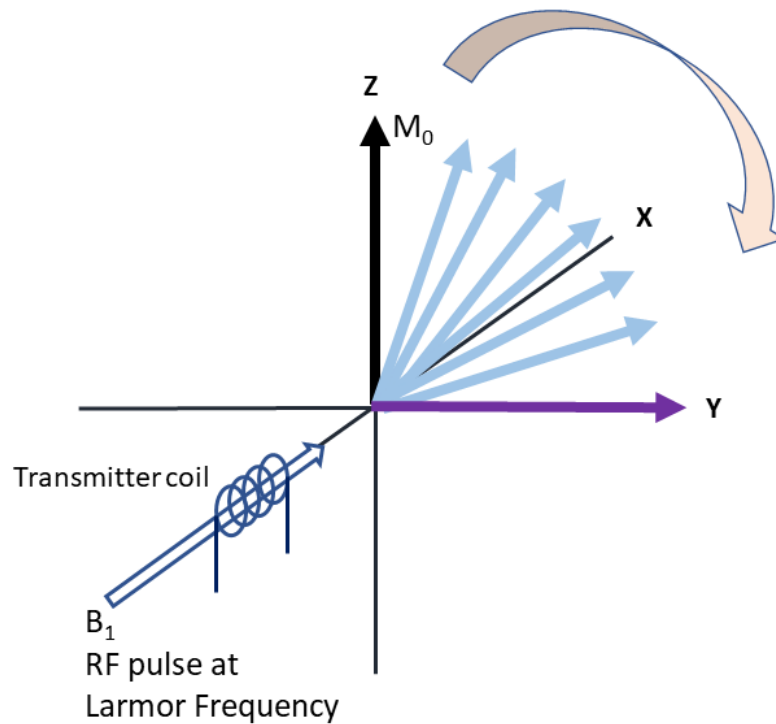


Figure 1.5: Excitation step where an RF pulse (of variable power and duration) can be applied at the Larmor frequency to tip the net magnetisation through an angle towards the transverse (XY) plane.

1.2.3 Relaxation

The relaxation of spins back to thermal equilibrium occurs via two key mechanisms; i) longitudinal (T_1) (Figure 1.6); and ii) transverse (T_2) relaxation (Figure 1.8). T_1 describes magnetisation evolution in the z direction while T_2 describes the x - y plane evolution (e.g., T_2 is not simply the loss of x - y magnetisation into the longitudinal, z plane). Note at thermal equilibrium the magnitude of the net magnetisation is defined as M_0 .

i) Longitudinal T_1 (spin-lattice) Relaxation

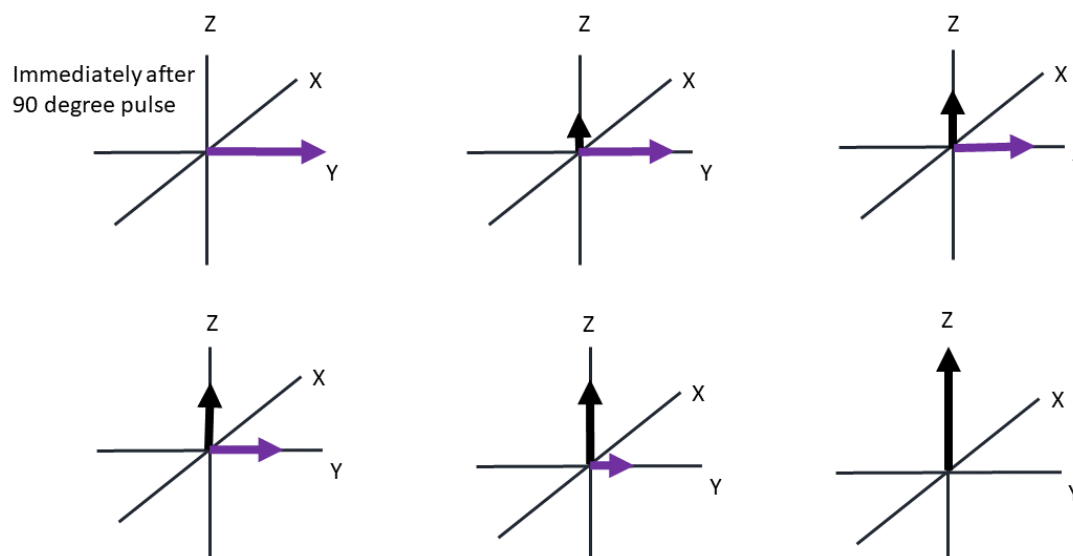


Figure 1.6: T_1 relaxation showing spins returning to the z direction immediately after a 90° pulse.

As soon as the excitation RF pulse stops (at $t = 0$), excited spins will return to the low energy state. The net magnetization relaxes back to align with the static magnetic field (z axis). Longitudinal magnetisation (M_z) reflects the z-component of the net magnetisation vector. Therefore, at $t = 0$, following a 90° excitation pulse, there is no longitudinal magnetization (high and low energy states are equally populated). T_1 is the time constant of ‘decay’ as the longitudinal magnetisation returns to a magnitude M_0 (Figure 1.7a); as described by equation [1.6].

$$M_z = M_0 \left(1 - e^{-\frac{t}{T_1}} \right) \quad [1.6]$$

In MRI, T_1 relaxation is very important. Not all protons are bound in the same way within the body. In fat tissue, for example, magnetically shielded ^1H atoms are found within large triglyceride molecules which rotate at an optimum rate efficient for T_1 . Fat therefore has a short T_1 value. Conversely magnetically deshielded ^1H atoms in small water molecules, spin more rapidly at a rate which is inefficient for T_1 relaxation. Water therefore has a longer T_1 value. By exploiting these differences in T_1 , image contrast between different tissues results when imaging at short repetition times (TR), as can be seen in Figure 1.7. For clarity repetition time is the amount of time between successive excitation pulses i.e., repeated measures required for spatial encoding (see section 1.2.4). At short TR tissues with long T_1 will not have relaxed to thermal equilibrium.

Therefore, subsequent excitations will result in signal attenuation for that tissue pool in contrast to those with short T_1 . The subsequent image is said to be T_1 weighted.

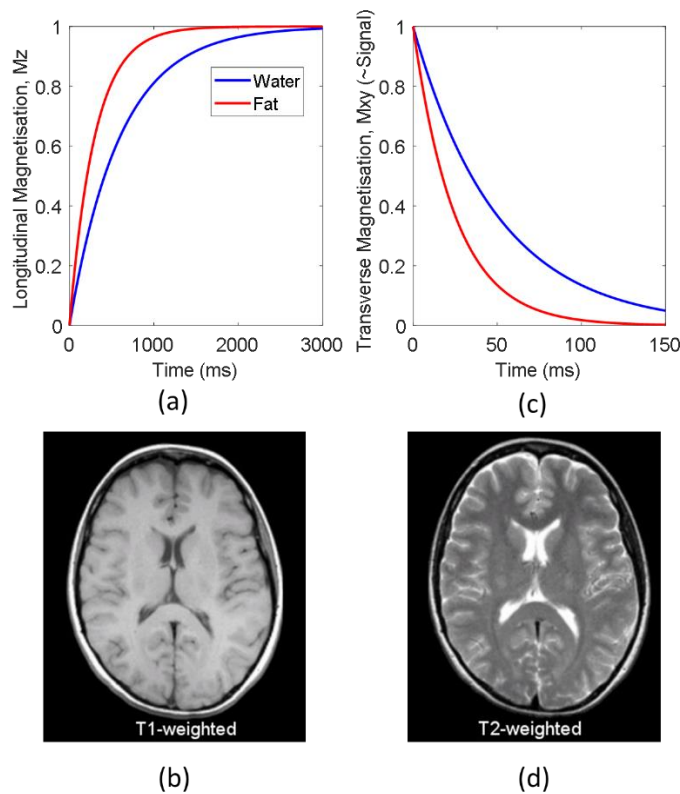


Figure 1.7: (a) T_1 relaxation curve. (b) T_1 weighted image.⁶⁸ (c) T_2 relaxation curve. (d) T_2 weighted image.⁶⁸

Note that full relaxation of the longitudinal magnetisation is on the order of seconds. Scanning at long TRs ($5 \times$ longest T_1) ensures excitation from thermal equilibrium for all tissues and therefore avoids T_1 weighting. Image contrast is now determined by T_2 relaxation, which occurs on a much faster (ms) time scale. Unfortunately, scans can take tens of minutes to complete (depending on the required resolution).

ii) Transverse T_2 (spin-spin) Relaxation

Following excitation with a 90° RF pulse (B_1), the magnetization vector rotates around B_1 into the x-y plane to be perpendicular to B_1 . At this time point ($t = 0$) the nuclei are all in phase (individual magnetic moments, be them in the high or low energy state, are all pointing in the same transverse direction). Immediately after the 90° pulse, the net magnetization continues to precess around the z-axis in the transverse x-y plane; but spins do not remain in phase for long. The magnetic moments of the individual spins influence each other (spin-spin interaction)

generating random local increases/decreases in field and thus slightly different precession frequencies (equation 1.2). The moments (precessing at different rates) begin to de-phase, thus reducing the transverse magnetisation vector. Eventually the spins will be completely dephased and there will be no transverse magnetisation and thus no current induced in the detector (Figure 1.8). In most biological tissues this process occurs on the order of milliseconds (much faster than spin-lattice relaxation).

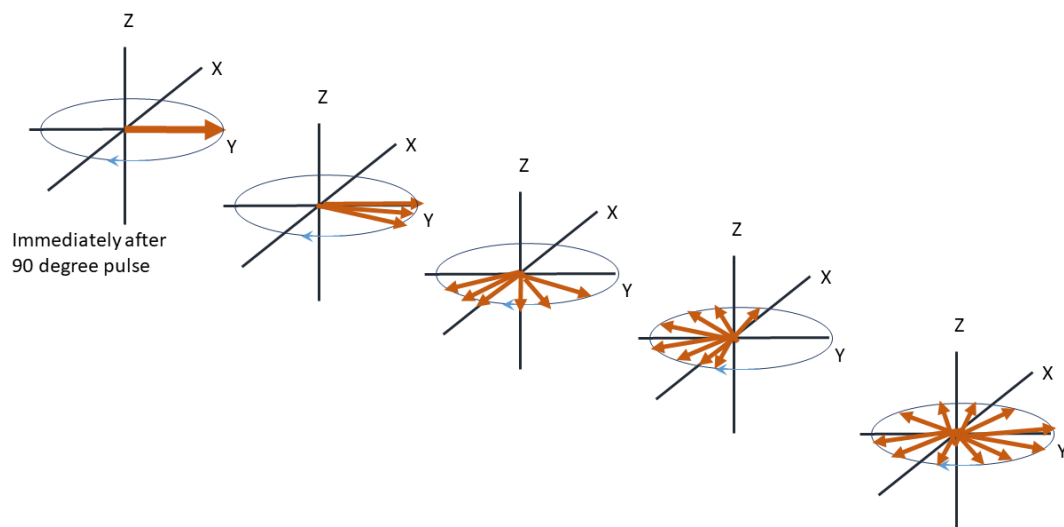


Figure 1.8: T_2 relaxation showing spins dephasing across the XY plane after a 90° pulse.

Following a 90° excitation pulse ($t = 0$) the net magnetization, M_0 , is flipped fully into the transverse plane. T_2 is the time constant of transverse M_{xy} signal decay described by:

$$M_{xy} = M_0 e^{-\frac{t}{T_2}} \quad [1.8]$$

Once again, when thinking in terms of MRI, T_2 depends on how the hydrogen proton is bound within its molecule and that again is different for each tissue. T_2 is therefore another parameter, which is used in MRI to obtain contrast.

As it is the precession of the transverse magnetisation that induces the AC current in the nearby detector; when dephasing occurs the magnitude of the current will decrease. This time decaying signal is called a Free Induction Decay (FID). It is noted that due to the presence of magnetic field inhomogeneities and chemical shift, NMR signal actually decays faster than T_2 times would predict. Extra dephasing, and thus signal decay caused by such effects is given a time constant T_2^* .

1.2.4 Spatial Encoding

Fourier transformation unravels the different oscillating components of the FID to obtain a spectrum as a function of frequency. The target nuclei in differing chemical environments resonate at slightly differing frequencies depending on the relative shielding/deshielding experienced and gives rise to chemical shift which is the basis of NMR. At this point, it is not possible to know where the different signals originated from, in a spatial sense. Spatial localisation in MRI is achieved through the introduction of varying magnetic field gradients.^{11, 69, 70} Resonant frequency is a linear function of the applied magnetic field (Larmor equation 1.2), therefore, if a linear magnetic field gradient is applied across the sample, the resonant frequency of the nucleus becomes a function of its spatial position within the applied gradient. Spatial encoding in standard MRI uses a single nuclear chemical environment (e.g., the abundant water pool within the body). Modern MRI systems employ three gradient coils to encode slice, frequency and phase information in ‘k-space’ (before 2D Fourier transform into an image). A full description of spatial encoding is beyond the scope of this thesis and the reader is referred to “Principles of MRI” by Friedman et al.⁷¹

1.2.5 Spectroscopic Imaging

As mentioned above MRI is employed in the medical specialities for diagnostic purposes, utilising the water protons (^1H) as a marker of gross changes in soft tissue anatomy (based on changes in T_1/T_2 relaxation). Today MRI remains unrivalled in the clinic for such purposes. However, as detailed in section 1.1, imaging structure alone limits application when considering relevant biochemistry.

Observing the body at a molecular level, with MRI, is much more complex as cell metabolites are present at $\sim 10\,000$ times lower concentration than tissue water.⁷² The imaging gradient coils can be pulsed in such a way, and the water pool signal suppressed with RF, to provide spectroscopic information from localised voxels within the body. Spatial resolution is lost but the gain in chemical shift resolution enables proton magnetic resonance spectroscopy (^1H MRS) to be used to assess localised metabolic properties⁵¹. Although there are advantages over anatomic imaging alone, on a typical clinical scanner detection requires low spatial (1 cm^3) and temporal resolutions (5-10 min) that mitigate for the low metabolite concentrations.⁷³ On these time scales MRS cannot relay more important dynamic information about metabolic flux. Without a method to increase the sensitivity of MR to the metabolites of interest it is a difficult technique to implement for real-

time metabolic imaging. MR signal enhancement by hyperpolarisation can temporarily help to overcome these limits by providing transient signal enhancements of several orders of magnitude.

1.3 Hyperpolarisation

NMR/MRI insensitivity is driven by low natural abundance (nano to micro molar concentrations) confounded by the low Boltzmann nuclear polarisation (equation 1.5). To overcome the low thermal polarisation of spin states, on a theoretical level, one needs to force more spins into the low energy state, thus increasing the net magnetisation and available signal for subsequent detection. On a simple level this can be done by cooling samples (to decrease $k_B T$) and/or by using stronger magnetic fields (to increase ΔE). However, such solutions are either very expensive (stronger superconducting magnets) and/or impractical (sample cooling) particularly when considering *in-vivo* MRI applications. One must therefore consider a more fundamental quantum manipulation to hyperpolarise the sample. Again the purpose being to produce a significant deviation away from the Boltzmann distribution, leading to a larger proportion of the nuclear spins in the low energy state to generate a larger net magnetisation (Figure 1.9) and thus signal.⁷⁴

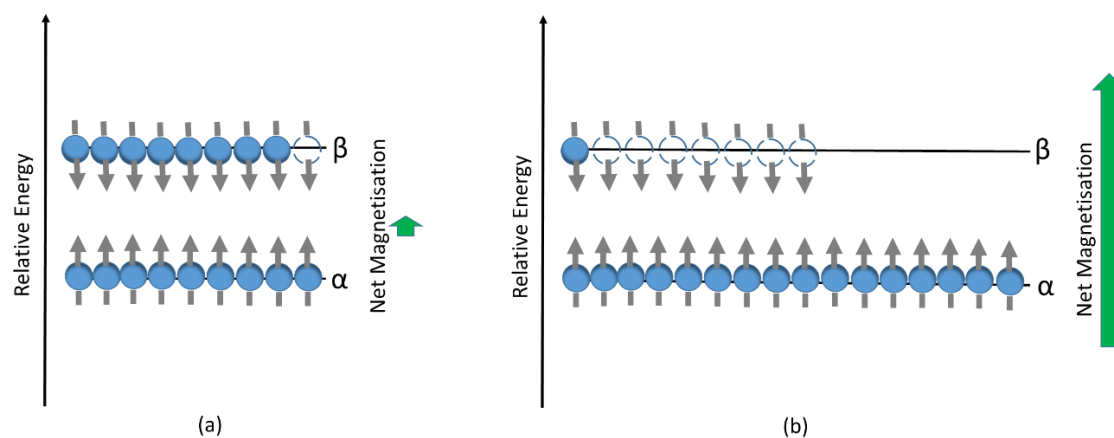


Figure 1.9: a) Boltzmann distribution at thermal equilibrium of nuclear spins across the higher energy level (β) and the lower energy level (α); b) Hyperpolarised nuclear spins.

The term ‘Hyperpolarisation’ (HP) is often used today to describe a collection of techniques manipulating spin populations including, spin exchange optical pumping (SEOP - used for nuclei in the gas phase); Dynamic Nuclear Polarisation (DNP – for the solid/liquid phase) and Para-Hydrogen Induced Polarisation (PHIP – for the gas/liquid phase). This thesis focuses on the application of the latter two techniques in the liquid phase.

1.3.1 Spin Exchange Optical Pumping (SEOP)

Optical pumping methods can be used for polarising noble gases (e.g. ^3He and ^{129}Xe , where polarisation can be increased dramatically to 30-50%⁷⁵ and 5-10%⁷⁶ respectively). Rubidium atoms (in the vapour phase) are spin polarised using circularly polarised laser light (795 nm). Polarisation is then transferred to the target nuclei through the hyperfine interaction during binary collisions⁷⁷. Direct optical pumping of the target nucleus is not practical, as the wavelength required to cause the electronic transition would be in the far ultraviolet (e.g., 58 nm for ^3He). Whilst the technique was originally devised for applications in basic and applied physics, hyperpolarized ^3He ⁷⁸ and the potentially cheaper and more versatile ^{129}Xe ^{79, 80} have been developed for clinical application with magnetic resonance imaging of lungs⁷⁸⁻⁸¹, sinuses⁸² and brain.⁸³ To take advantage of the different properties of the two gases and obtain ^1H images, simultaneous imaging of lung function and structure was carried out using a triple nuclear hybrid MR imaging set up.⁸¹ The cost and complexity of HP gas MRI has, to some extent, limited its widespread clinical use. Recent research using ^{19}F as the nuclei of choice in the form of inert fluorinated gases (79% sulfur hexafluoride (SF_6) or perfluoropropane (C_3F_8 or PFP⁸⁴) and 21% oxygen) may prove to be a more economical route as only thermal conditions are required without the expense and expertise required for HP lung studies.⁸⁵

1.3.2 Dynamic Nuclear Polarisation (DNP)

The underlying principle of DNP comes from Overhauser's theory developed in 1953,⁷⁴ which predicted that saturating an electron spin could dramatically polarise nuclear spins. This was demonstrated experimentally in 1956 with lithium and sodium containing ammonia in the liquid state (Overhauser effect).⁸⁶ At temperatures close to absolute zero (1 K), electron spin polarisation approaches 100%. Transfer of this electron spin polarisation to nuclear spins is then achieved by saturating the linked electron paramagnetic resonance (EPR) transition through microwave irradiation. The maximum theoretical enhancement resulting in the nuclear spin polarisation level for a proton is given by $\gamma_e/\gamma_{1\text{H}}$, which is ~ 660 , and uses the appropriate gyromagnetic ratio of the nucleus.⁸⁷ Since the introduction of the Overhauser effect, additional DNP mechanisms have been identified, namely the 'solid effect'⁸⁸, 'thermal mixing'⁸⁹ and the 'cross effect'⁹⁰. Major breakthroughs came when DNP was adapted to work in the liquid state in a process termed dissolution-DNP (d-DNP), thereby achieving significant increases in sensitivity ($>10\ 000$ -fold) for ^{13}C Magnetic Resonance Spectroscopy (MRS).³ Figure 1.10 shows the original d-DNP system developed by Ardenkjaer-Larsen and co-workers.³

During the d-DNP process ^{13}C – labelled biomolecules are mixed with small quantities of a stable organic radical (the source of free electron spins) and a “glassing agent”; this agent usually consists of a combination of two of the following: water, glycerol, DMSO, methanol or ethylene glycol. This mixture is cooled to approximately 1 K in a magnetic field (typically 3.35 T) and the electron spins are irradiated with microwaves to drive polarisation transfer from them to the ^{13}C nuclei within the biomolecule. The frozen sample is then rapidly dissolved in a preheated pressurised solution ($\sim 180^\circ\text{C}$ under 10-bar pressure). An optical sensor detects the presence of the polarised sample and high-pressure nitrogen gas pushes it out so that it can be injected into a phantom, cell suspension, animal or patient as required for subsequent detection with NMR/MRI.^{91, 92} The signal enhancement which can be achieved through d-DNP is defined by equation 1.9.

$$\varepsilon' = \varepsilon \cdot \frac{B_{DNP}}{B_{NMR}} \cdot \frac{T_{NMR}}{T_{DNP}} \quad [1.9]$$

where ε represents the solid-state DNP enhancement, B_{DNP} represents the strength of the DNP magnetic field, B_{NMR} represents the strength of the NMR detector magnetic field, T_{NMR} represents the temperature inside the NMR magnet and T_{DNP} represents the temperature inside the DNP. It is this temperature factor, which permits much greater enhancements in d-DNP.⁹³

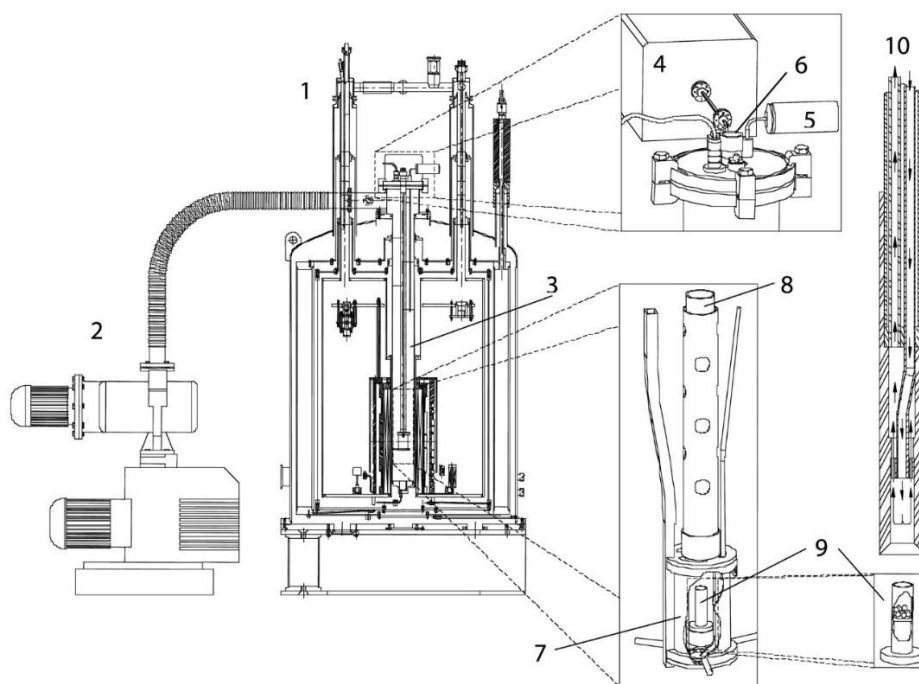


Figure 1.10: Schematic drawing of the DNP polariser taken from the first d-DNP paper by Jan H Ardenkjaer-Larsen *et al.*³ (1) DNP polariser; (2) vacuum pump; (3) VTI; (4) microwave source; (5) pressure transducer; (6) sample port; (7) microwave container; (8) sample holder; (9) sample container; (10) dissolution wand.

d-DNP has permitted *in vivo* imaging of ^{13}C metabolites and their conversion, giving ‘real time’ observation of metabolic flux within core biochemical pathways (such as glycolysis and the tricarboxylic acid (TCA) cycle).^{3, 94} Indeed MRS observation of metabolism at high spatial and temporal resolutions (2-5 mm and <1 s respectively) have now been achieved.⁹⁵

Over the last ten years, a range of molecules have been successfully hyperpolarised using d-DNP. The most successful of these d-DNP polarised agent is $[1-^{13}\text{C}]$ pyruvate, currently the only substrate that has been translated into the clinic to date for grading tumours.⁴ The success of this agent could be attributed to i) its clinical importance lying at the crossroads of two very important biochemical pathways, glycolysis and the tricarboxylic acid (TCA) cycle; (ii) the fact that it forms a “glass” as a neat liquid which means that extremely high concentrations can be achieved in the initial sample; (iii) it achieves high levels of polarisation; (iv) it has a long T_1 on two of its three carbon sites⁹⁶ and (v) associated metabolism is sufficiently fast to be observed within the ‘ T_1 window’ of detection. The current literature focus using d-DNP concerns imaging metabolism in tumours⁹⁷⁻⁹⁹ and cardiac tissue.¹⁰⁰⁻¹⁰⁵ d-DNP’s success, particularly when using pyruvate, is based upon the “Warburg effect”; introduced by Otto Warburg in 1924.³⁵ He hypothesised that tumour cells produce their energy mainly through the non-oxidative process of glycolysis rather than the normal oxidative breakdown of pyruvate in the TCA (Kreb’s) cycle occurring in the mitochondria. The high glycolysis rate of cancer cells give rise to an unusually high lactate concentration in tumours and it is this process that is probed when using hyperpolarised pyruvate.⁴

Other successful analytes include $[1,4-^{13}\text{C}_2]$ -fumarate, which has been shown to be a useful marker of tumour necrosis; ^{13}C -labelled bicarbonate for the *in vivo* mapping of pH; and ^{13}C -labelled urea as a marker of perfusion amongst others.^{91, 97, 99, 106}

While finding obvious clinical traction it is noted that d-DNP requires a sophisticated and expensive polariser (e.g., clinical SPINlab, GE Healthcare, costs approximately £2 million), limiting its use to few research laboratories. Moreover, it requires a relatively long polarisation step (approximately 1 hour - see chapter 6) with consequent large consumption of cryogenic liquids. d-DNP for hyperpolarisation is explored further in chapter 6.

1.3.3 Para-Hydrogen Induced Polarisation (PHIP)

At room temperature, there are two nuclear spin isomers of hydrogen, *ortho* (*o*-H₂) and *para* (*p*-H₂).¹⁰⁷ The *ortho* state is a triplet (with spin alignments $\alpha\alpha$, $(\alpha\beta+\beta\alpha)/\sqrt{2}$, and $\beta\beta$) while lower energy *p*-H₂ is the singlet form $((\alpha\beta-\beta\alpha)/\sqrt{2})$.

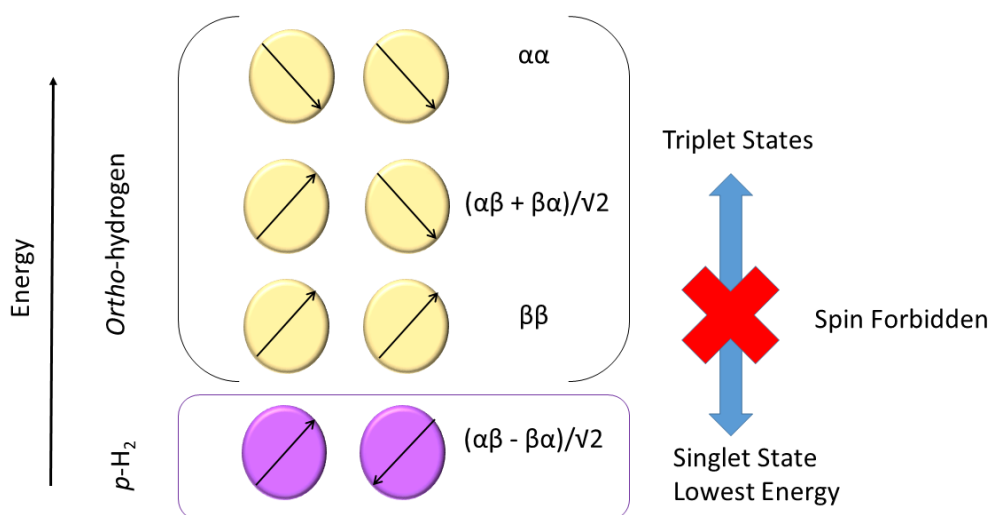


Figure 1.11: The four possible nuclear spin alignments of the nuclei in a molecule of hydrogen in a magnetic field.

It is the symmetrisation postulate of quantum mechanics that helps us to understand why there are two isomers. For a diatomic molecule, the total wave function is the product of individual wave functions representing translational (tra), vibrational (vib), rotational (rot), electronic (ele) and nuclear (nuc) quantised states.

Born-Oppenheimer equation
$$\Psi_{\text{tot}} = \Psi_{\text{tra}} \Psi_{\text{vib}} \Psi_{\text{rot}} \Psi_{\text{ele}} \Psi_{\text{nuc}} \quad [1.10]$$

Hydrogen is a fermion possessing a half-integer spin. The overall wave function of identical fermions must be antisymmetric in exchange of the nuclei. The $\Psi_{\text{tra}} \Psi_{\text{vib}} \Psi_{\text{ele}}$ contributions are all symmetric. In *o*-H₂ the $\alpha\alpha$ spin state is symmetrical as are the $\beta\beta$ and $(\alpha\beta + \beta\alpha)/\sqrt{2}$, therefore Ψ_{nuc} is symmetric. If the total wave function must be antisymmetric, Ψ_{rot} must be antisymmetric with rotational energy levels resulting from quantised angular momentum $J = 1, 3, 5$, etc. In *p*-H₂ the singlet state $(\alpha\beta - \beta\alpha)/\sqrt{2}$ is antisymmetric therefore Ψ_{nuc} is antisymmetric. Consequently, Ψ_{rot} has to be symmetric with $J = 0, 2, 4$, etc. *p*-H₂ therefore presents with the lowest rotational energy level ($J = 0$) and is therefore more stable than *o*-H₂. The energy separation between the two isomers is the difference in energy between the $J = 0$ and $J = 1$ rotational states ($120 \text{ cm}^{-1} = 730 \text{ J/mol}$) and it is this relatively large energy gap which allows the two forms to be easily separated. At room temperature (298 K), hydrogen consists of 75% *o*-H₂ and 25% *p*-H₂. With a reduction in temperature, conversion from *ortho* to the *para* state is favoured. This is, however, spin forbidden, and equilibration takes considerable time, but can be accelerated by adding a paramagnetic catalyst (iron oxide). On cooling to 20 K (liquid H₂), with an appropriate catalyst, *p*-H₂ can be generated at 99% purity. If the catalyst is then removed *p*-H₂ can be allowed to warm to room

temperature. As transitions to the *ortho* state are spin forbidden it will take the system several months (in a vacuum) to return to thermal equilibrium. This therefore provides a viable, relatively inexpensive means of storing *p*-H₂ for use in hyperpolarisation techniques such as *para*-hydrogen induced polarisation (PHIP) and signal amplification by reversible exchange (SABRE).

p-H₂ is NMR silent due to the absence of spin angular momentum ($I = 0$). The symmetry of the molecule must be broken before it can be detected. This can be done by incorporating/binding the hydrogen into two magnetically inequivalent environments. This has been achieved in two distinct methods. Weitekamp and Bowers (1986) were the first to theorise that *p*-H₂ could be used to increase NMR sensitivity¹⁰⁸ in a technique coined as *para*-hydrogen induced polarisation (PHIP). These predictions were experimentally proven a year later through the *para*-hydrogenation of acrylonitrile to propionitrile using [RhCl(PPh₃)₃].¹⁰⁹

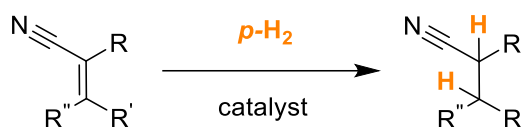


Figure 1.12: Hydrogenation of acrylonitrile using *p*-H₂ to form propionitrile incorporating two *para*-H₂ derived protons.

As described in section 1.2.1 the signal strength which is detected in an NMR experiment is dependent on the relative difference between the populations of magnetic energy levels that are probed. In the case of normal hydrogen, the four energy states are nearly equally populated at room temperature according to the Boltzmann distribution resulting in only 1 in 32,000 protons being observable in a 9.4 T (400 MHz) magnetic field. In the case of pure *p*-H₂, only one of the four potential spin configurations ($\alpha\beta + \beta\alpha$)/ $\sqrt{2}$ is populated leading to a large population difference between the four magnetic states in the product molecule.

When hydrogenation of an unsaturated bond is carried out with normal hydrogen, the resulting spin states of the two incorporated protons in the product are $\alpha\alpha$, $\alpha\beta$, $\beta\alpha$ and $\beta\beta$ and are populated according to the Boltzmann conditions. In the propionitrile example (Figure 1.12) the R groups are all different. Therefore, the incorporated protons derived from hydrogen are chemically inequivalent. Because of this inequivalence, the $\alpha\beta$ and $\beta\alpha$ spin states reside at slightly different energies. This leads to four possible energy transitions (Figure 1.13) giving the corresponding set of two small in-phase doublets in a resultant NMR spectrum.

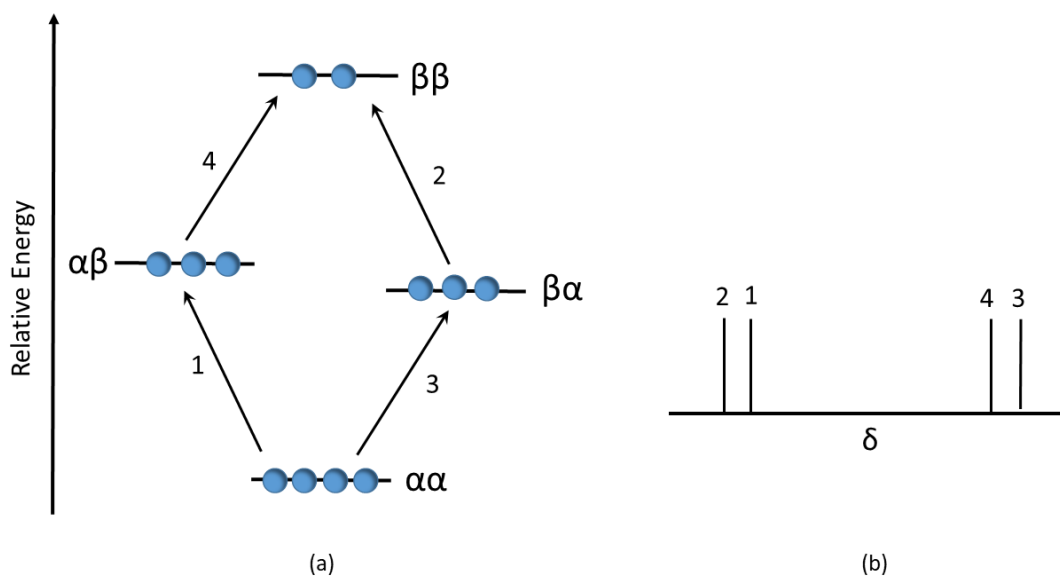


Figure 1.13: a) Energy diagram showing the four possible spin alignments of H_2 derived nuclei after hydrogenation of an asymmetric unsaturated bond. The black arrows indicate the spin-allowed transitions b) 1H NMR spectrum which arises from these transitions.

If the same reaction is carried out, but this time $p\text{-}H_2$ is used instead, the incorporated protons derived from the $p\text{-}H_2$ could retain the same nuclear spin alignment as $p\text{-}H_2$ itself $(\alpha\beta + \beta\alpha)/\sqrt{2}$. Two different phenomena, i) PASADENA and ii) ALTADENA, can then be observed depending on where the hydrogen addition takes place, in terms of magnetic field.

i) PASADENA

When *para*-hydrogenation of an unsaturated bond occurs at high field, this is termed '*para*- H_2 and synthesis allow dramatically enhanced nuclear alignment' (PASADENA)¹⁰⁹. Under these conditions both the $\alpha\beta$ and $\beta\alpha$ spin states are equally populated giving rise to four possible energy transitions (Figure 1.14). Transitions to the $\alpha\alpha$ spin state (1 and 3) are emissive, whereas the transitions to the $\beta\beta$ spin state are absorptive. This gives rise to an NMR spectrum containing two antiphase doublets, which are highly enhanced due to the initial larger population difference than that of the Boltzmann distribution.

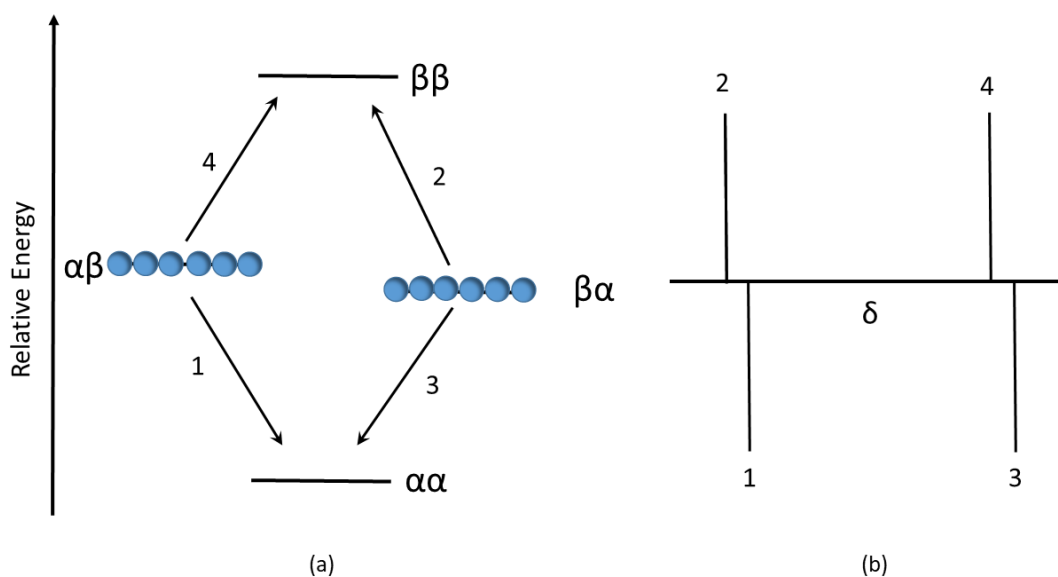


Figure 1.14: a) PASADENA effect with selective polarisation of $\alpha\beta$ and $\beta\alpha$ energy states from $p\text{-H}_2$ derived nuclei b) Corresponding ^1H NMR spectrum showing PASADENA enhancements.

ii) ALTADENA

When *para*-hydrogenation of an unsaturated bond occurs at low magnetic field, followed by its transfer and detection at high field it is termed ‘adiabatic longitudinal transfer after dissociation engenders nuclear alignment’ (ALTADENA). At low field, the spin system is strongly coupled. The eigenfunctions are the symmetry adapted singlet (S), and triplet (T_{+1} , T_0 and T_{-1}) states. As the transfer occurs adiabatically (i.e., without the populations being altered) the system continually adapts itself during the transition to the new field conditions. In this way it always remains in a state which corresponds to an eigenfunction of the relevant Hamiltonian. Therefore, at high field only one of the $\alpha\beta$ or $\beta\alpha$ becomes populated. Thus, the only transitions possible are 2 and 3 as can be seen in Figure 1.15. On a resulting NMR spectrum, this translates as two highly enhanced singlets with opposite phase (emission/absorption).

As the acronym suggests, the field variation is adiabatic which means that the field-dependent eigenstates of the system change so slowly that their populations remain the same. Consequently, both at high field and low field only one spin state is populated. The spins not only acquire multiplet polarisation (which is the same as in PASADENA) but also net polarisation. The total polarisation of the system is zero thus the spins carry polarisation of the same size but opposite sign.

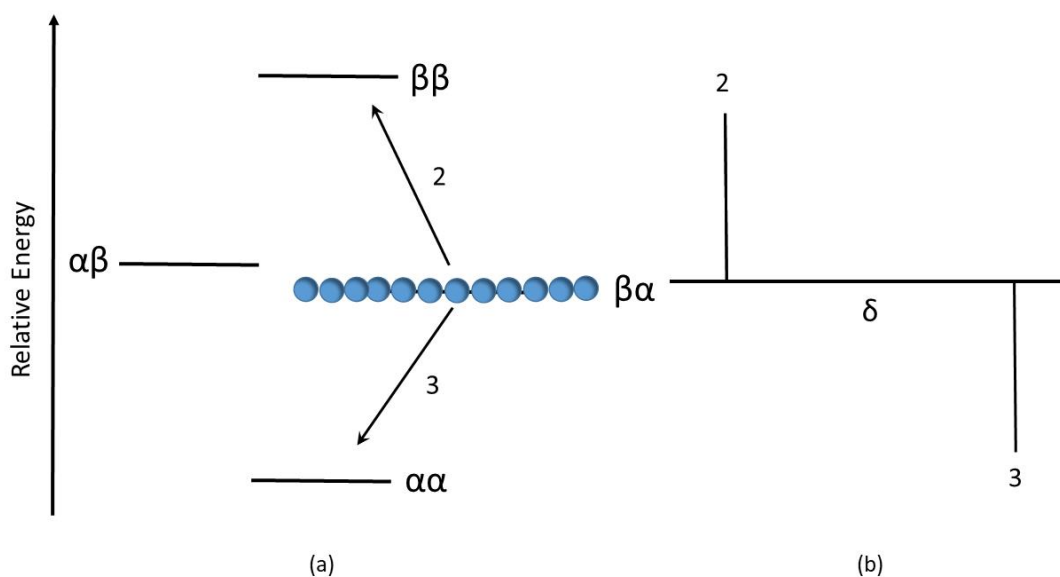


Figure 1.15: a) ALTADENA effect with selective polarisation of only the $\beta\alpha$ energy states from $p\text{-H}_2$ derived nuclei b) Corresponding ^1H NMR spectrum showing ALTADENA enhancements.

Although highly enhanced NMR signals are observed in PHIP, there is a necessity for the $p\text{-H}_2$ to be incorporated into the molecule through a chemical hydrogenation reaction. It therefore relies on the substrate of interest having an unsaturated bond for this technique to work.

To overcome this limitation the necessary unsaturated functionality was developed in the form of a molecular tag, which could be cleaved. The PHIP of some of the most important metabolic imaging reporters, such as pyruvate, only became possible therefore after the introduction of this Side Arm Hydrogenation (PHIP-SAH) technique.¹¹⁰ With further optimisation this led to the first *in vivo* metabolic imaging study using the PHIP-SAH hyperpolarized $[1\text{-}^{13}\text{C}]$ pyruvate detecting the response of the heart to altered metabolism in real time.¹¹¹ The polarisation transfer from the $p\text{-H}_2$ protons to the ^{13}C carboxylate signal was achieved via a magnetic field cycling approach. $6.2 \pm 0.3\%$ hyperpolarisation was observed on the ^{13}C carboxylate of allyl-pyruvate. It is important to note that manual processes to make the agent biocompatible took $\sim 55\text{--}60$ s. As the T_1 of $[1\text{-}^{13}\text{C}]$ pyruvate is 54 s only $3.5 \pm 0.5\%$ polarisation was retained at injection time. Nevertheless, this polarisation was demonstrated to be sufficient for carrying out *in vivo* ^{13}C studies.

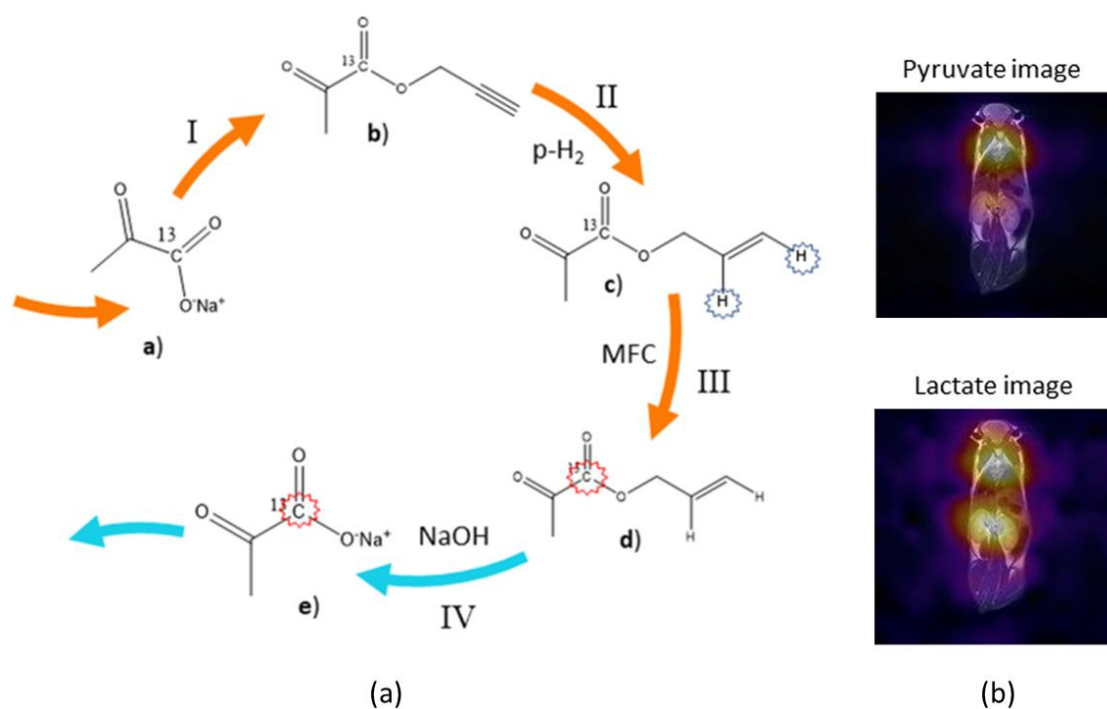


Figure 1.16: Adapted from Cavallari *et al.* (2018) (a) Chemical pathway showing the steps involved in the PHIP-SAH process. (I) Formation of ester using [1-¹³C]-pyruvate and propargylic alcohol; (II) hydrogenation of triple bond side arm using *p*-H₂; (III) Polarisation transfer from receiving protons to the labelled carbon; (IV) Hydrolysis of ester and phase extraction. Orange arrows indicates reactions carried out in the organic phase; blue arrows indicate the passages which occur in the aqueous phase. (b) CSI images of pyruvate and lactate distribution in living mice after injection of a dose of HP [1-¹³C]-pyruvate. ¹¹¹The spatial localisation of the metabolite is achieved by overlaying with a ¹H structural image. The region of highest metabolite concentration appears white and lowest appears black.

1.4 Signal Amplification By Reversible Exchange

Adams *et al.* (2009) demonstrated that the polarisation power of *p*-H₂ could also be utilised without changing the chemical identity of the agent (substrate) of interest. The technique is known as Signal Amplification by Reversible Exchange (SABRE).¹¹² A metal framework in the form of a magnetisation transfer catalyst, typically an octahedral iridium complex, is employed to temporarily, and reversibly, bind both *p*-H₂ and the substrate. The symmetry of the singlet state in *p*-H₂ is broken as the resulting *p*-H₂ derived hydrides are now chemically and/or magnetically inequivalent. With the correct resonance conditions, magnetisation can be simultaneously delivered from *p*-H₂ to the target substrate via long range scalar coupling in a matter of seconds. As the agent (substrate) is in excess, the bound polarised ligands are in continuous exchange with the free agent, so that a solution of hyperpolarised agent builds up rapidly (see 1.4.2).

1.4.1 Practical Basis

In a standard SABRE experiment the iridium polarisation transfer catalyst and agent (substrate) are dissolved in a solvent such as methanol- d_4 and placed in an NMR tube fitted with a J. Young's tap. The sample is degassed using a high vacuum Schlenk line and $p\text{-H}_2$ is introduced. The tube is manually shaken (10-30 s) to facilitate dissolution of $p\text{-H}_2$ into solution. This shaking process takes place in the stray field of the magnet (typically 60-80 G for ^1H - see section 1.4.3) where the correct resonance conditions are met for rapid polarisation transfer. Alternatively, an automated system can be used (described in section 8.2). In either case the hyperpolarised agent can then be detected with high field NMR/MRI.

1.4.2 Underlying Chemistry

Initial SABRE experiments were carried out using a Crabtree-type pre-catalyst, $[\text{Ir}(\text{COD})(\text{PCy}_3)(\text{py})]\text{BF}_4$ ¹¹²⁻¹¹⁴ (where COD = *cis,cis*-1,5-cyclooctadiene, Cy = cyclohexyl and py = pyridine) to allow transfer of polarisation from $p\text{-H}_2$ to N containing substrates (typically heterocycles). The reaction involves a temporary association of both the substrate and $p\text{-H}_2$ in the coordination sphere of a transition metal to form $[\text{Ir}(\text{H})_2(\text{PCy}_3)(\text{py})_3]\text{BF}_4$.

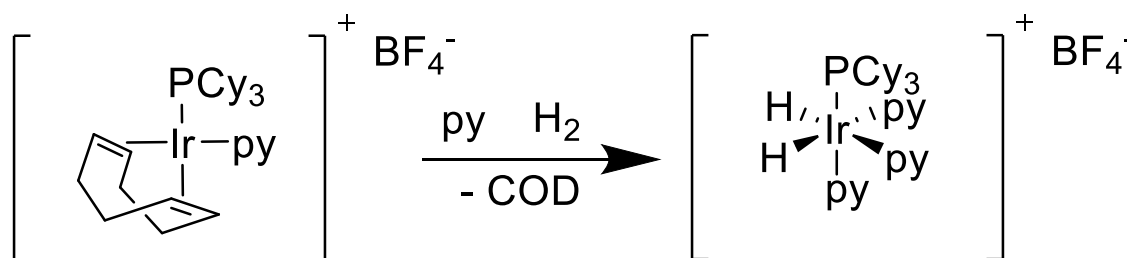


Figure 1.17: Crabtree-type catalyst first used for SABRE hyperpolarisation. The active complex is formed by the oxidative addition of H_2 in the presence of excess pyridine.

The iridium precatalyst is square planar with the iridium oxidation state being +1. The SABRE active complex becomes octahedral on addition of both the substrates and the $p\text{-H}_2$ and the oxidation state of iridium changes to +3. The originally bound COD is hydrogenated to form cyclo-octane (COA) which dissociates from the metal centre.

Later improvements to the system were made by the incorporation of N-heterocyclic carbenes (NHCs) as one of the ligands into the iridium catalyst.¹¹⁵ These strongly electron donating ligands have the effect of increasing the lability of both the hydrides and substrates thereby reducing the lifetime of the active catalyst.¹¹⁶ With a reduced lifetime, the process is more efficient allowing more polarised substrate to build up in solution in a shorter timescale. The most commonly used

catalyst is $[\text{IrCl}(\text{COD})(\text{IMes})]$, where IMes is 1,3-bis(2,4,6-trimethylphenyl)-imidazol-2-ylidene, which forms the SABRE active complex $[\text{Ir}(\text{H})_2(\text{IMes})(\text{sub})_3]\text{Cl}$ when excess $p\text{-H}_2$ and substrate are present (Figure 1.18).

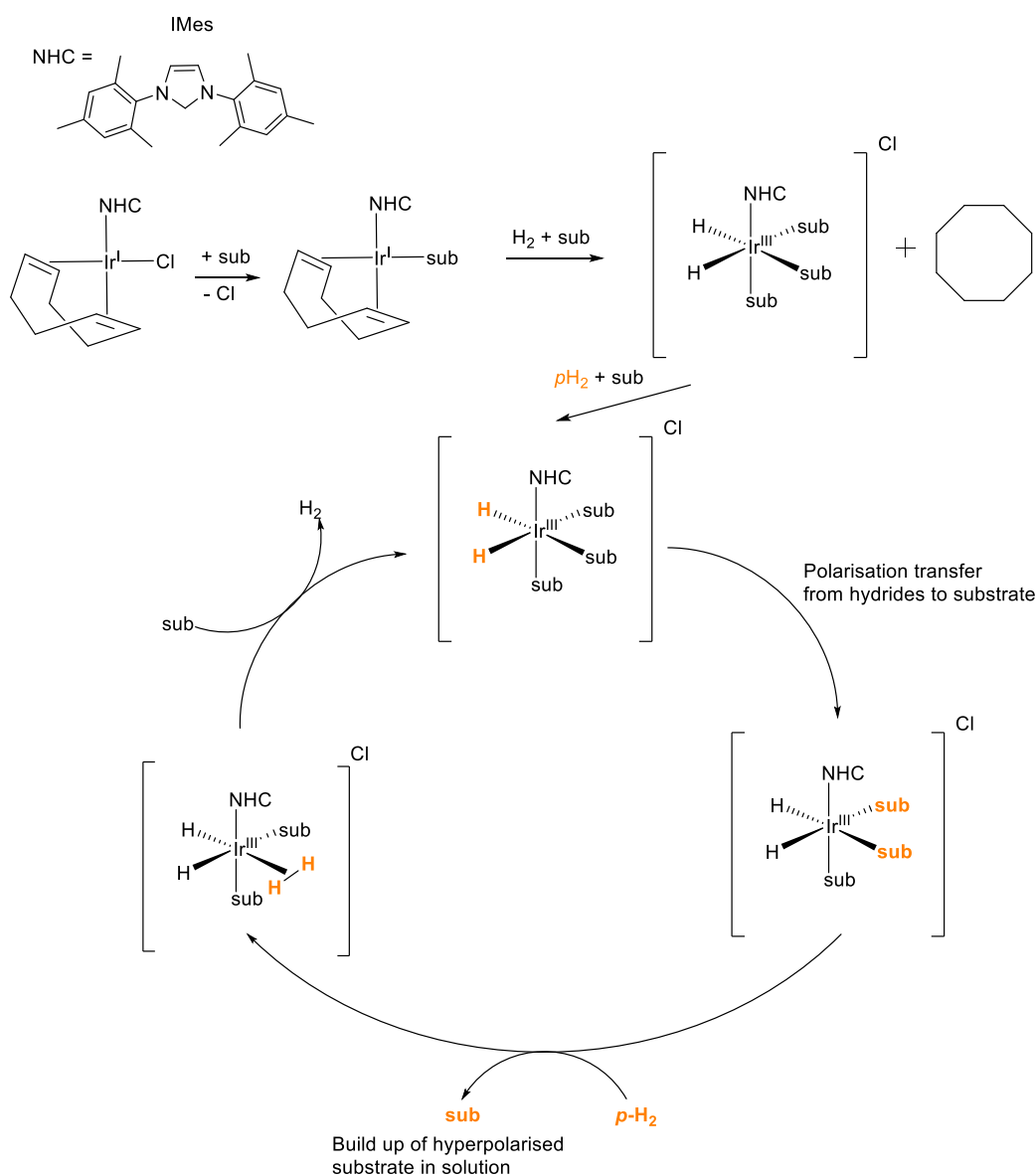


Figure 1.18: Formation of SABRE active catalyst with H_2 through hydrogenation of COD ligand. Catalytic SABRE cycle showing the transfer of polarisation from the $p\text{-H}_2$ derived hydrides to the substrate.

1.4.3 Physical Basis

In SABRE, the $[\text{Ir}(\text{H})_2(\text{IMes})(\text{sub})_3]\text{Cl}$ complex remains intact for a short period and polarisation transfer has to occur within this lifetime.^{112, 117} The efficiency of this transfer process therefore relies on the size of the couplings between the $p\text{-H}_2$ and target spins. In order for this transfer to occur, ^1H nuclei typically require a low magnetic field, in the range of 50-80 G^{115, 118} in order for

the chemical shift differences ($\Delta\delta_{\text{HH}}$) between the hydrides and the protons of the substrate to match the J_{HH} scalar coupling between the two hydrides (~ 5 to 10 Hz).¹¹⁵

The spin system behaviour involved in SABRE can be described through the density matrix theory which is obtained by solving the Liouville-von Neumann (LvN) equation.¹¹⁹ This uses a Hamiltonian which includes Zeeman and J -coupling interactions, a time-dependent magnetic field (which accounts for the time it takes to go from low field for polarisation outside of the magnet to high field within the magnet for detection) and also kinetic parameters which consider both chemical and relaxation processes. The density matrix theory gives an extensive description of how the nuclear spin system evolves with time and field but requires significant computation to solve, particularly if J -couplings and chemical shifts are not known. A second method based on level anti-crossings (LAC's) gives the same results but arguably delivers a clearer idea of SABRE polarisation.¹²⁰ LACs occur at magnetic fields where spin energy levels approach or cross one another. The levels at the crossing point split due to spin-spin interactions and therefore actual crossing is avoided; hence the 'anti' in LAC's. For polarisation transfer to occur, efficient mixing of the spin states is required. For efficient mixing of the spin states, strong coupling is necessary and LAC's define field regions where strong coupling occurs.

A pair of weakly coupled spins occur when the difference in their chemical shifts $\Delta\delta$ is much larger than the scalar coupling J between them, $\Delta\delta \gg J$. This is known as an AX-spin system. Conversely strongly coupled spins occur when $\Delta\delta < J$ or $\Delta\delta = J$ which is known as an AB-spin system. When $\Delta\delta$ is negligible, an A_2 system such as H_2 occurs.

In the AB system the eigenstates are mixed states of the two spins. If this system is placed in low field when $J \gg \Delta\delta$ the eigenstates begin to resemble the S and T_0 states (like those in H_2). When the system is moved to high fields where $J \ll \Delta\delta$ the eigenstates resemble the $\alpha\beta$ and $\beta\alpha$ states of the AX system.

Due to the mixing at low field the two spins cannot be distinguished from one another and therefore are polarised together. Therefore, having the sample at low field allows polarisation transfer to take place due to the strong coupling created there. An analysis based on LAC's gives both the magnetic field where SABRE polarisation will occur and the sign rules for the resulting magnetisation (i.e., whether the peak will be in-phase or anti-phase). As SABRE requires substrate and $p\text{-H}_2$ exchange at the iridium centre any variable that will affect this rate of exchange will have consequences on the efficiency of the polarisation transfer. The lifetime of the substrate

on the catalyst must be on the right timescale to obtain optimum polarisation build-up and limited loss of polarisation due to T_1 . Changes in temperature, $p\text{-H}_2$ concentration, substrate concentration and iridium concentration can all affect this rate of exchange.^{113, 115, 121} The polarisation transfer time (PTT - the shaking time that is used for the reaction to take place) and the polarisation transfer field (PTF - the magnetic field in which the sample is shaken) also have an effect on polarisation transfer efficiency.^{121, 122} Whilst LAC can be used on simple model systems to predict PTF values, more complicated substrates require an experimental approach for exact PTF. It is noted however that LAC theory gives a good starting point. Another key component for efficient optimisation is the nature of the carbene ligand.¹²³ Unfortunately, the above optimisation steps are substrate specific so although significant work has been carried out it is still difficult to establish optimum conditions for a specific substrate without significant optimisation studies.

1.4.4 Scope of SABRE

Since its inception in 2009, research on SABRE has developed it into a versatile hyperpolarisation technique. Although the focus of this thesis is on *in vivo* applications of hyperpolarised molecules, it is recognised that hyperpolarised NMR is a rapidly growing field of research.

In an industrial setting, reaction monitoring is an integral part of synthetic design, optimisation and scale up.¹²⁴ High field NMR spectrometers (9.4 T+) can be used for this purpose. Unfortunately, due to high purchase cost, running costs and space requirements uptake is limited. Benchtop spectrometers (1-2 T) are a much cheaper and compact alternative however, these instruments suffer from low sensitivity. This low sensitivity is confounded by often small amounts of available analyte or when detecting trace impurities for example in the pharmaceutical industry. Hyperpolarisation through a simple rapid and repeatable method such as SABRE could address this insensitivity.¹²⁵⁻¹³⁰ Recent research by Lehmkuhl *et al.* (2020) used SABRE to permit single scan ^1H , ^{13}C , ^{15}N and ^{19}F detection between 1 mT and 10 mT.¹³¹ Research by Hill-Casey *et al.* (2019) demonstrated Earth's field detection using *in situ* SABRE. ^1H polarization levels of up to 3.3% were reported.¹³² In fact SABRE detection can also be carried out at zero field.¹³³

In contrast to d-DNP, where the main focus is ^{13}C polarisation, the most extensive studies involving SABRE have been with ^1H polarisation.^{112, 134-137} Efforts have been concentrated in this area due to several reasons; specifically ^1H has a very high natural abundance and high gyromagnetic ratio (eq. 1.6). In addition, any potential imaging agent (based on an endogenous chemical) will undoubtedly have multiple proton sites in its structure and not require expensive

labelling. Aiding translation further, all clinical MRI systems are ^1H based and therefore there is no need for purchase of new coils tuned to heteronuclei resonances. Thus, clinical translation should be smooth if one can overcome biocompatibility issues through biphasic studies¹³⁸ or direct polarisation in water.¹³⁹

Traditionally SABRE works well with nitrogen containing heterocyclic rings (in organic solvents) due to the ability of the nitrogen to ligate easily with the iridium catalyst. Many substrates containing this motif have been examined (including pyridine¹³⁶, tuberculosis drugs^{134, 140}, pyridazine¹⁴¹, imidazole¹³⁷) but the substrate needs to be of biological relevance (in terms of exploring function rather than anatomy) and safe to administer. Much focus has been directed to nicotinamide, more commonly known as vitamin B3. Rayner et al (2017) explored the polarisation, longitudinal (T_1) lifetimes and imaging potential of nicotinamide, methyl nicotinate and a series of deuterated isotopologues.¹³⁵

Polarisation transfer normally occurs at low field with fast transfer to high field for detection. Specialised RF methods^{142, 143} have been developed to transfer polarisation and detect *in situ* at high field. Using these methods detection is immediate and recycling is possible making rapid repetitive measurements possible. This is less important for biomedical imaging but of relevance for sample testing.

Direct transfer of polarisation is also possible to heteronuclei¹¹² including ^{13}C ,¹⁴⁴⁻¹⁴⁷ ^{15}N ,^{133, 137, 145, 148-152} ^{31}P ¹⁵³ amongst others ^{19}F ,^{112, 154, 155} ^{29}Si ¹⁵⁶ and ^{119}Sn .¹⁵⁷ In most cases smaller magnetic fields (in the mG range) are required for direct transfer due to the much larger chemical shift difference between the hydrides and the heteronuclei of interest in the substrate. This will be looked at in more details in chapters 3 and 6. Although this thesis concentrates on ^1H SABRE studies, polarisation of X nuclei (^{15}N , ^{13}C and ^{31}P) has also been undertaken.

Despite low abundance and low gyromagnetic ratio, ^{15}N -nuclei have been of considerable interest in SABRE studies due to their T_1 values which are typically longer than ^1H . Much of the research has concentrated on direct polarisation transfer to ^{15}N which requires low micro-tesla magnetic fields¹³³ termed SABRE-SHEATH. Polarisation is achieved through the strong 2J -coupling between the hydride ligands and ^{15}N nuclei in the labelled substrate directly bound to the metal centre.¹⁴⁸ Through this method an extensive range of substrates have been hyperpolarised including *N*-heterocycles,^{137, 145, 149} nitriles,¹⁴⁹ Schiff bases¹⁵⁰ and diazene.¹⁴⁹ ^{15}N polarisation using the LIGHT-SABRE (low irradiation generation of high tesla-SABRE) method enables efficient

in magnet catalytic polarisation.¹⁵⁸ In terms of promising *in vivo* applications, the antibiotic metronidazole has been polarised to 20%¹⁵⁹ and ¹⁵N₂ diazines have been developed as biocompatible molecular tags.^{151, 152}

In contrast to d-DNP studies, the progression of ¹³C SABRE *in-vivo* has been somewhat hindered due to low polarisation levels. A 65-fold enhancement at 9.4 T (0.05% polarisation) was previously reported using ¹³C nicotinamide (isotopically labelled at the carbonyl carbon).¹⁴⁴ The SABRE-SHEATH technique was used to polarise ¹³C nuclei in pyridine-¹⁵N however only a 10-fold signal enhancement at 9.4 T were observed.¹⁴⁵ More recent research¹⁴⁶ shows how through the use of micro-tesla PTF and optimisation of temperature and concentration polarisation levels of ¹³C nuclei in pyridine-¹⁵N reached ~4.4%. It was noted that ¹³C polarisation in pyridine-¹⁴N was much lower than that achieved with pyridine-¹⁵N. This phenomenon was thought to arise from significant quadrupolar ¹⁴N-relaxation in the micro-tesla fields.¹⁴⁶

1.4.5 Substrates used with SABRE in this thesis

A series of structures called the *thienopyridazines* were identified as the compounds of choice for study here (chapter 2). These structures were chosen as firstly their chemical motif is found in some anti-cancer drugs¹⁶⁰⁻¹⁶² and therefore potentially a chemical molecule that is biocompatible. Secondly, they are based on N-heterocyclic organic molecules which, as stated above, represent ligands known to work well in the SABRE process. On a more structural basis, thienopyridazines were interesting molecules to use because of the presence of the sulphur atom. It was investigated whether this had any significant role to play in the overall polarisation or the binding mechanism involved in SABRE catalysis.

A series of *pyridazines* substituted in the 3 and 6 position were tested for their potential to create a long-lived state (chapter 3). These provided a simple model to explore long-lived states prior to experimentation with the target thienopyridazines.

Nicotinamide is an endogenous natural human metabolite (or endogenite).¹⁶³ It therefore exhibits low toxicity,¹⁶⁴ is free of side effects and very high doses have been tolerated by humans.¹⁶⁵ It plays a critical role in cellular biology as a precursor of the cofactor Nicotinamide Adenine Dinucleotide (NAD)¹⁶⁶ and it has been used as a therapeutic agent for a number of conditions including the prevention of neurocognitive conditions.¹⁶⁷ Importantly it contains a nitrogen containing heterocyclic molecule and therefore very amenable to the SABRE process.¹¹²

As stated above significant work has been carried out on ^1H SABRE of this molecule. In chapter 6 the ^{13}C signal of this molecule is investigated in both SABRE and its sister technology d-DNP.

1.5 Thesis overview

1.5.1 Thesis objectives

This thesis describes multidisciplinary research into the imaging potential of Signal Amplification by Reversible Exchange (SABRE) hyperpolarised compounds. Methods for the optimisation of this catalytic process for thienopyridazines are implemented. The aim is to test the functionalisation of these agents across a range of MRI field strengths – from clinically relevant 3 Tesla up to high field (9.4 T+). The work aims to satisfy the reader that SABRE hyperpolarisation is an important cost-effective imaging tool, offering a wide range of target compounds (over sister technologies such as Dynamic Nuclear polarisation), that has the potential to aid clinical diagnosis; the compounds described here offer future progression in this area.

1.5.2 Thesis Structure

Chapter 2 identifies a series of four compounds, thienopyridazines, that were used as hyperpolarised contrast agents (CA) using the SABRE technique. The suitability and potential clinical benefits of these compounds for future clinical application is discussed. A detailed description of their chemical synthesis is given followed by a sequential series of optimisation experiments with the aim to improve their overall hyperpolarisation level (and in turn imaging performance) using SABRE. This includes exploration of synthetic strategies to substitute various nuclei within a CA to see how SABRE efficiency and “magnetic lifetimes” of the synthesised CA is affected. One of the downsides of these molecules is the short polarisation lifetimes therefore **Chapter 3** exploits quantum methods or “long-lived singlet states” to further extend the magnetic lifetime of thienopyridazines for improved applicability in the clinic. The wider application of these methods is exemplified with a new series of compounds, 3,6-substituted pyridazines. Building on the challenges to hyperpolarisation outlined in the above work, **Chapter 4** details novel methods to relay hyperpolarisation from one metal catalyst to the ligands of a second metal catalyst; thereby opening the range of CA which can be hyperpolarised using SABRE. The process is exemplified using a range of catalysts and potential CAs. **Chapter 5** focuses on translating SABRE from the laboratory benchtop to the imaging facility. Methods for testing the toxicology of thienopyridazines are detailed. Furthermore, experiments are detailed to improve the biocompatibility of the CA solvent using biphasic separation. **Chapter 6** benchmarks SABRE

against a sister hyperpolarisation technology, dissolution dynamic nuclear polarisation (d-DNP). Chemical Shift Imaging (CSI) of vitamin B3, nicotinamide was carried out investigating the magnetic lifetime and imaging potential of this important biomolecule. **Chapter 7** provides discussion and critical analysis of the results of all the above experiments and describes potential future avenues to explore in synthesis, catalysis, toxicology/biocompatibility, and imaging of compounds for SABRE hyperpolarisation. Finally, **Chapter 8** details the experimental techniques used to enable imaging of hyperpolarised agents in the context of this work.

1.5.3 Relevant Publications

The work in chapter 4 is the basis for the publication: SABRE-Relay: A Versatile Route to Hyperpolarization published in *The Journal of Physical Chemistry Letters*, 2018, 9, 1112-1117. DOI: 10.1021¹⁶⁸

The synthesis of the two palladium complexes $[\text{Pt}(\text{OTf})_2(\text{dppm})]$ and $[\text{Pt}(\text{OTf})_2(\text{dppe})]$ and the characterisation and testing of these were my contribution to the paper.

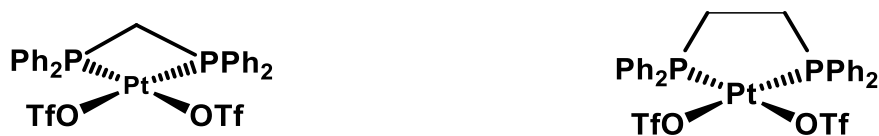


Figure 1.19: Chemical structure of $[\text{Pt}(\text{OTf})_2(\text{dppm})]$ and $[\text{Pt}(\text{OTf})_2(\text{dppe})]$.

The work is discussed in this chapter and extensions to this work are investigated.

1.5.4 Contributions and Acknowledgements

Dr Pete Rayner synthesised ^{13}C nicotinamide (chapter 6), the deuterated isotopologues of nicotinamide, deuterated methyl nicotinate (section 4.7) and all the iridium catalysts used within this thesis. In addition to synthesis, the ^{13}C thermal T_1 measurements of the deuterated isotopologues of nicotinamide were also carried out by Dr Pete Rayner.

Dr Philip Norcott synthesised the deuterated isotopologues of pyrimidine and measured the SABRE ^1H signal enhancements and T_1 values with $[\text{IrCl}(\text{COD})(\text{IMes})]$ (section 4.5.1). The work carried out on the pyrazine and platinum complexes (section 4.6) and the imaging on the 3T Siemens clinical scanner was carried out in collaboration with Dr Alexandra Olaru. Dr Alan Wright and Dr De-en Hu (CRUK, Cambridge) are UK Home Office personal license holders and helped complete the *in vivo* work in chapter 6.

Chapter 2: Synthesis and SABRE Optimisation of Thienopyridazines and Furopyridazines

2.1 Introduction

Cancer is one of the main threats in terms of global health, with 17 million new cases of cancer worldwide in 2018.¹⁶⁹ It is estimated that there will be 27.5 million new cases of cancer each year by 2040. With the UK incidence of cancer being rated higher than two-thirds of Europe and higher than 90% of the world there is an immediate need for action in terms of prevention and research.¹⁶⁹ Currently, tumour response to treatment is mainly assessed by traditional MRI methods through measurement of tumour size. However, visible reductions in tumour size may take weeks or months to present. Thus, there is a clear need to develop imaging techniques that are able to give earlier indications of treatment response.^{170, 171} One of the major challenges in understanding cancer metabolism and the role of treatments like chemotherapy is the complexity of the different biochemical/metabolic pathways involved. This is further exacerbated by the fact that metabolites within these pathways are present in such low concentrations (e.g. 5.50 mM fasting plasma glucose FPG)¹⁷² and therefore difficult to detect with traditional MR methods. Hyperpolarisation offers a route to overcome this problem. Hyperpolarised ¹³C MRI, based on d-DNP of pyruvate is already revolutionising cancer research and diagnosis.^{4, 91, 97} With a proven need, fundamental research is required to expand the scope of hyperpolarised NMR and MRI in the field of oncology.

To address this need, a family of thienopyridazines (Figure 2.1), with known anti-cancer properties,¹⁶⁰⁻¹⁶² were investigated as potential ¹H SABRE hyperpolarised agents. In addition to having anti-cancer properties, this class of compound also possess an N-heterocyclic ring, which should make them suitable ligands for coordination to the iridium SABRE catalyst.^{112, 135, 141} High signal enhancements combined with long T_1 values for the ¹H resonances would be the optimum scenario for a hyperpolarised agent for use in biomedical imaging.

In this chapter, the multistep synthesis of the thienopyridazine agents/substrates is discussed (section 2.2) and full NMR characterisation of these molecules is completed (section 2.3). Characterisation of the species created during the SABRE catalytic cycle are described, both in terms of the inactivated pre catalyst (section 2.3.2) and subsequent intermediate complexes, which form before the final product (section 2.3.3). SABRE performance is evaluated (section 2.4) and optimisation undertaken to increase signal enhancement. This includes the study of: i) substrate loading; ii) polarisation transfer field; iii) catalyst type (including an assessment of T_1 lifetimes);

iv) p -H₂ pressure; and v) the use of a deuterated co-ligand. A final study (section 2.5) investigates how substitution of an oxygen atom with a sulphur atom, to create a furopyridazine, affects SABRE polarisation in terms of nuclear electronegativity.

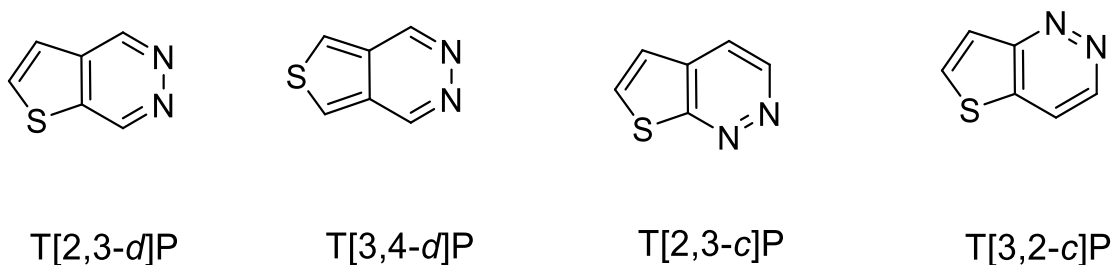


Figure 2.1: Family of thienopyridazines (anti-cancer agents)¹⁶⁰⁻¹⁶²: Thieno[2,3-*d*]pyridazine, (T[2,3-*d*]P), Thieno[3,4-*d*]pyridazine (T[3,4-*d*]P), Thieno[2,3-*c*]pyridazine (T[2,3-*c*]P), Thieno[3,2-*c*]pyridazine (T[3,2-*c*]P).

Two SABRE methods (i.e., shake and drop and the automated polariser - see section 8.2.1) were used to generate signal enhancement. The technique of choice is highlighted within the individual sections. All experiments were carried out using methanol-*d*₄ as the solvent. It is noted that to meet the overall aim to use these compounds as *in vivo* agents, it is necessary to move to a biocompatible solvent system. This problem will be investigated and addressed in chapter five.

2.1.1 Biological Role of Thienopyridazines

Over the last 40 years pyridazine chemistry has been of major research interest as derivatives exhibit a wide variety of biological roles including anti-inflammatory,^{173, 174} anticancer,^{175, 176} antiviral¹⁷⁷ and antimicrobial¹⁷⁸ activity. Specifically, the thienopyridazine motif can be found in many chemical agents that demonstrate anti-cancer activity. For example, the motif T[2,3-*d*]P is found in IκB Kinase (IKKs) inhibitors.^{161, 162} IκB kinases (IKK) and IKK-related kinases have an important role in regulating the immune response. Their mechanism of action is through nuclear factor-κB and IFN regulatory factor – dependent signalling transduction cascades. It has been demonstrated that these kinases are involved in the development of many human diseases, including cancer. Dysregulation of IKK activities leads to tumour survival, proliferation, migration and metastasis in human cancers.^{162, 179} Thieno[2,3-*c*]pyridazine (T[2,3-*c*]P) derivatives have also been synthesised and shown non-selective broad spectrum activity against all cancer lines.¹⁶⁰ Broad spectrum activity indicates that multiple pathways and targets involved in the proliferation of cancer are affected rather than a specific enzyme or pathway.¹⁸⁰ This type of mechanism of action is analogous to broad-spectrum antibiotics, which target multiple bacterial strains.

2.2 Synthesis of Thienopyridazines

Two main methods were used for the synthesis of the desired thienopyridazines; one route for the *-d* configuration and one for the *-c* configuration. A three step synthesis of thieno[3,4-*d*]pyridazine, T[3,4-*d*]P was conducted using adapted literature methods¹⁸¹ (Figure 2.2). The first step involved the reduction of the dicarboxylic acid to the diol. Two reagents for this reduction were tested: borane-tetrahydrofuran (BH₃.THF) and borane dimethylsulfide (BH₃.DMS). Despite literature precedent, BH₃.THF did not yield any of the desired product and only starting material was recovered (verified by LC-MS and ¹H NMR). However, BH₃.DMS, which has improved stability and higher solubility,¹⁸² gave an 85% yield of thiophene-3,4-diyldimethanol. Next, a Swern oxidation to form the dialdehyde was also successful and subsequent treatment of the crude product with hydrazine hydrate yielded the desired diazine. Contrary to the original method, step 3 was carried out without prior purification of the dialdehyde to try to minimise loss of product and a 46% yield of T[3,4-*d*]P resulted. It was found that 48 hours was required for the total consumption of starting material.

The synthesis of T[2,3-*d*]P was not reported in the same study, however, the previous methodology was applied here to form it. As the intermediate thiophene-2,3-dicarbaldehyde was commercially available, only the final step of the synthesis of the 1,2-diazine was required and this proved successful giving T[2,3-*d*]P in a 77% yield, as outlined in Figure 2.3. Two further methods for the synthesis of T[2,3-*d*]P from 2-thiophenecarboxaldehyde have been previously reported by Kessler *et al.* (2012), but both methods involved more complex synthesis with lower yields of 48% and 66%.¹⁸³ Their methodology however was used for the synthesis of furo[2,3-*d*]pyridazine, F[2,3-*d*]P (section 2.5.2).

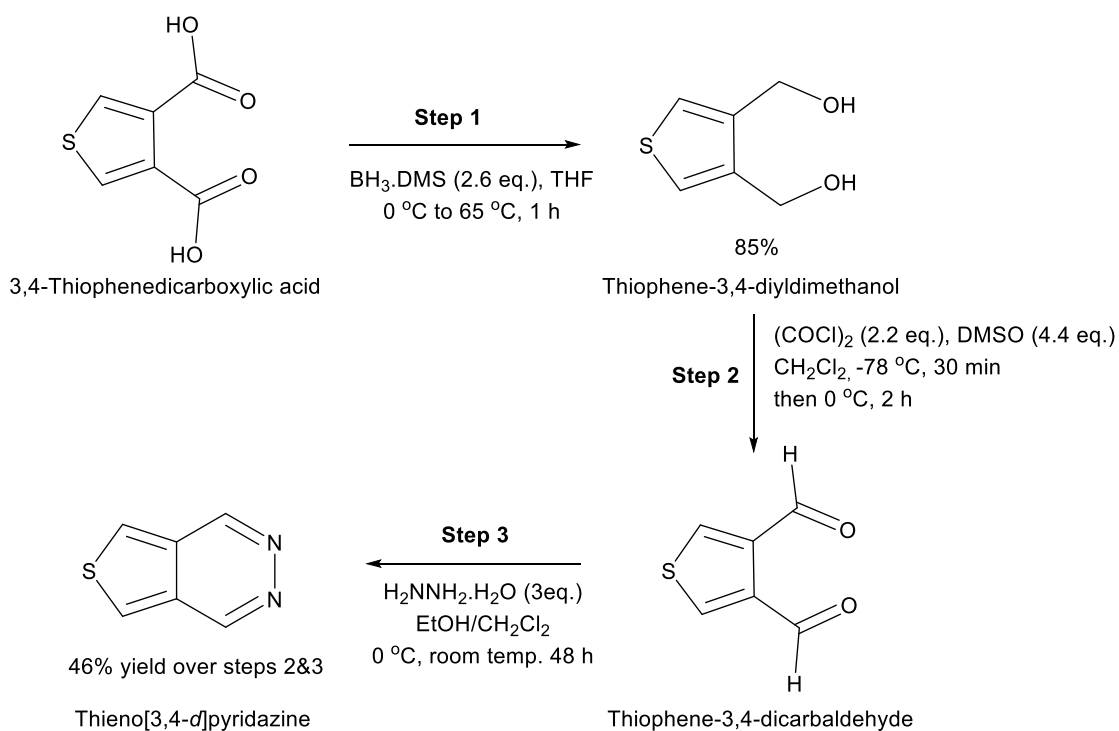


Figure 2.2: Reaction scheme for the synthesis of T[3,4-*d*]P following methods developed by Montavon et al (2013) resulting in an overall yield of 39%.

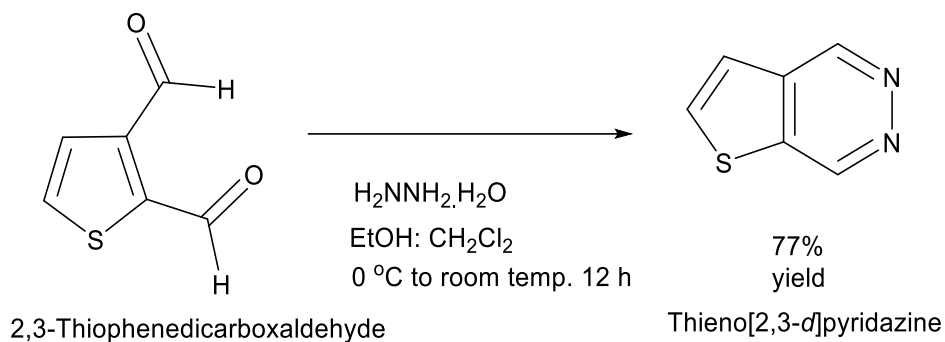


Figure 2.3: Reaction scheme for the synthesis of T[2,3-*d*]P following methods developed by Montavon et al (2013) resulting in a final product yield of 77%.

C. Ball *et al* (2012)¹⁸⁴ developed copper-catalysed tandem C-N bond formation methods to synthesise amongst other heterocycles, T[2,3-*c*]P. This methodology was used and the final three step synthesis is shown in Figure 2.4.

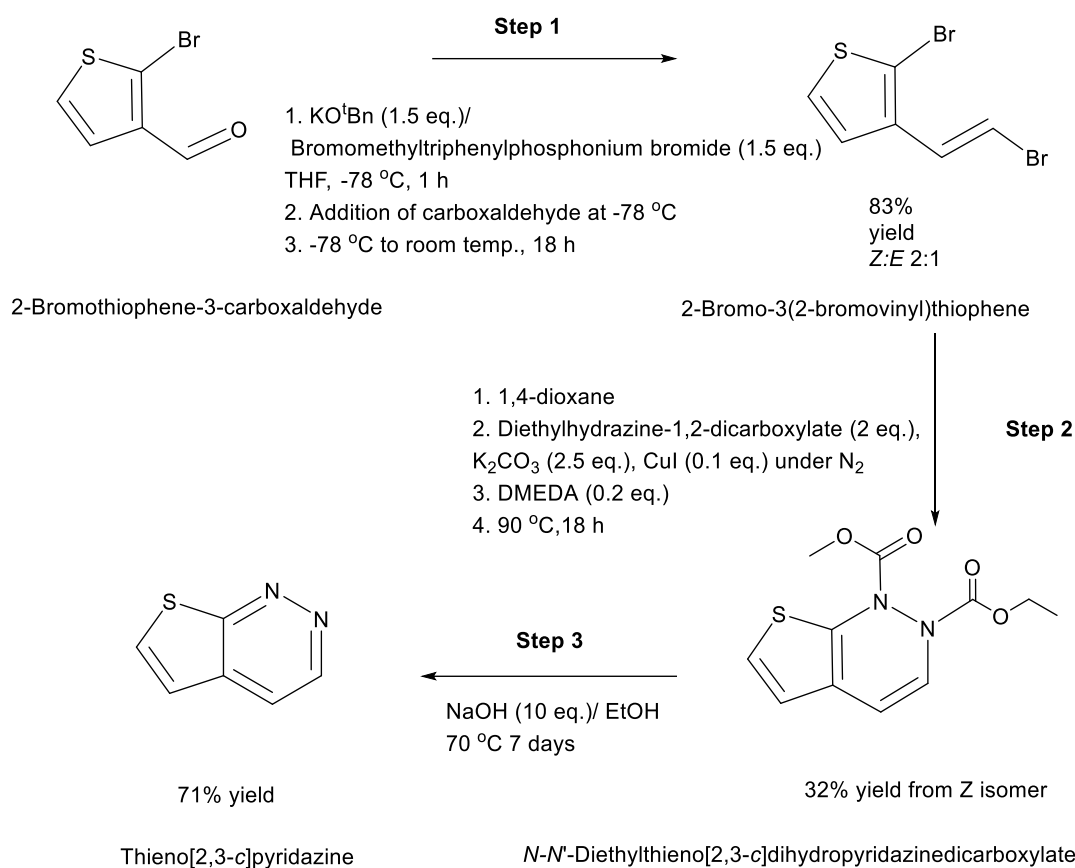


Figure 2.4: Three step reaction scheme for the synthesis of T[2,3-c]P developed by C. Ball *et al* (2012)¹⁸⁴

The main challenge was the production of *E* and *Z* isomers in the first step in a 1:2 ratio, which have almost identical retention factor values (*R_f*) of 0.47 and 0.39 (100% hexane). Consequently, the desired *Z* stereoisomer could not be isolated and a mixture of the stereoisomers was used in the second step. The two *E* and *Z* alkenes do not ionise therefore their formation in the first step and their reaction products in the second step were difficult to monitor with LC-MS. A ¹H NMR (400 MHz) of the crude reaction mixture after step 2 repeatedly showed that some of the *Z*-isomer starting material was still present whereas the *E*-isomer, which does not form the product, had reacted completely in other side reactions. Due to this mixture of starting material, product and impurities, product yield was low (32%) in comparison to literature values (53%).¹⁸⁴ Five equivalents of sodium hydroxide, alongside a much longer reaction time (7 days) compared with 16 hours reported by C. J. Ball (2012), were implemented to increase the yield of the final step to 71% compared with 58% as quoted in the literature.

Although the synthesis of T[3,2-*c*]P has not been previously reported in the literature by using this methodology, its synthesis was attempted using the same route as T[2,3-*c*]P. Pleasingly, this was successful, and the synthetic pathway is shown in Figure 2.5. As in the synthesis of T[2,3-*c*]P, one of the main challenges was the production of the *E* and *Z* stereoisomers in the first step. This time, the desired *Z* stereoisomer was in a slightly higher proportion, with 2.6:1 ratio compared with 2:1 in the synthesis of T[2,3-*c*]P but now with identical *R_f* values (*R_f* = 0.6 for both *E* and *Z* in 95:5 hexane:EtOAc). An impurity with a similar *R_f* value was also produced within the reaction (*R_f* = 0.52 in 95:5 hexane:EtOAc) but was successfully removed via flash column chromatography. In the second step, a further series of column chromatography purification steps were needed to remove the *E*-stereoisomer and side products and isolate the *N*-*N'*-diethylthieno[2,3-*c*]dihydropyridazinedicarboxylate. As this route is new for this particular compound, the yields cannot be directly compared to a literature value but the overall yield is comparable with that of T[2,3-*c*]P.

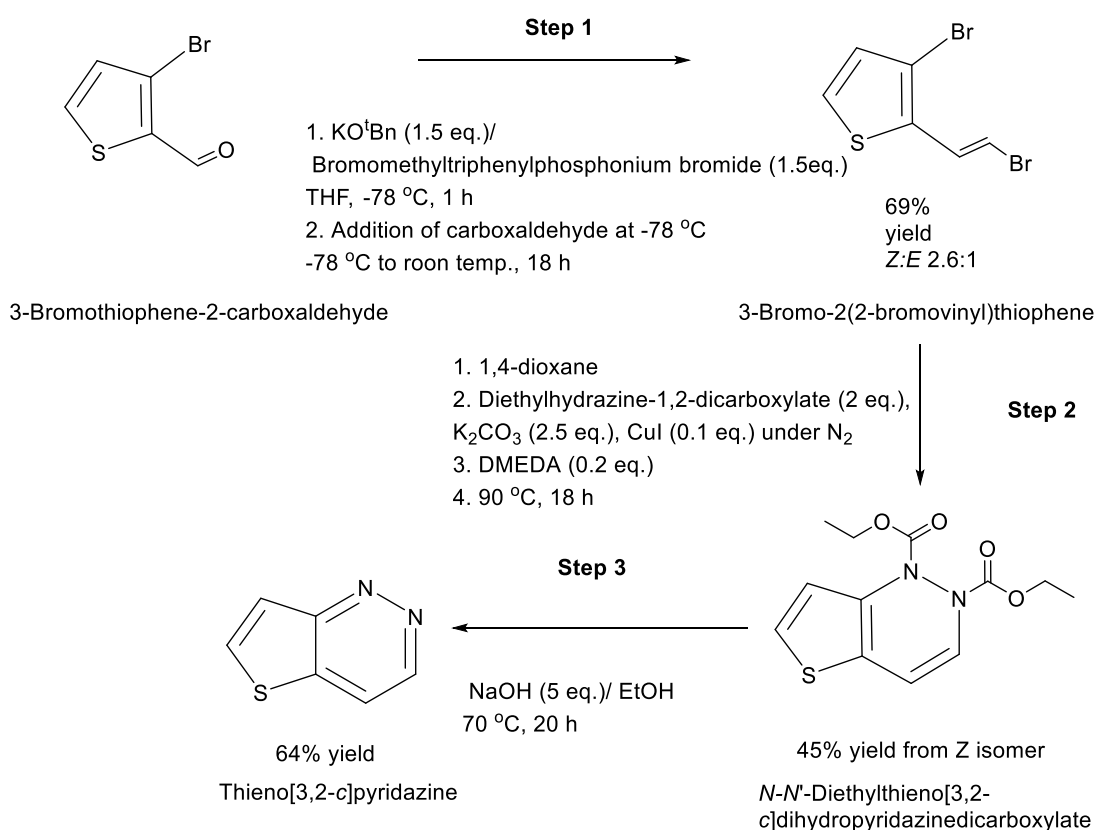
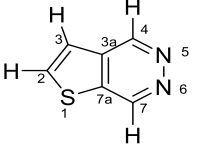
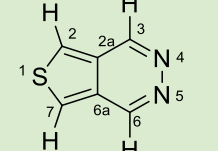
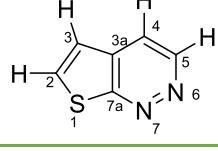
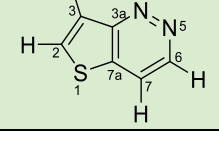


Figure 2.5: Adapted three step reaction scheme for the synthesis of T[3,2-*c*]P following methods developed by C. Ball *et al* (2012)¹⁸⁴

2.2.1 Characterisation of Thienopyridazines.

Full characterisation of the synthesised substrates was completed. Table 2.1 presents chemical structures and NMR characterisation data (^1H , ^{13}C and ^{15}N) for T[2,3-*d*]P and T[2,3-*c*]P in methanol-*d*₄ and T[3,4-*d*]P and T[3,2-*c*]P in chloroform-*d*. 2D ^1H and decoupled ^{13}C NMR spectra were used alongside homo-nuclear COrelation SpectroscopY (COSY) and Heteronuclear Multiple-Quantum Correlation (HMQC) spectra to obtain these data. It was important to use direct one bond and multiple bond couplings values in order to acquire this information. A HMQC proton-nitrogen spectrum was recorded to confirm the identity of protons in closest proximity to the nitrogen atoms.

Table 2.1: Chemical structures and NMR characterisation data (^1H , ^{13}C and ^{15}N) for T[2,3-*d*]P and T[2,3-*c*]P in methanol-*d*₄ and T[3,4-*d*]P and T[3,2-*c*]P in chloroform-*d* (500MHz)

Substrate	Nuc.	Resonance							
		2	3	3a	4	5	6	7	7a
	^1H	8.25, d	7.75, dd		9.63, d			9.79, ps	
	J_{HH}	5.34	5.34, 0.6		1.43				
	^{13}C	135.17	122.23	136.92	146.44			146.27	139.92
	^{15}N					355.04	354.36		
		2	3	3a	4	5	6	7	7a
	^1H	8.15, s		9.37, s			9.37, s		8.15, s
	J_{HH}								
	^{13}C	13.31	130.70	147.01			147.01	130.70	123.31
	^{15}N				347.70	347.70			
		2	3	3a	4	5	6	7	7a
	^1H	8.21, d	7.54, d		8.17, d	9.18, d			
	J_{HH}	5.92	5.92		5.65	5.65			
	^{13}C	135	120.95	135.02	120.95	144.95			165.90
	^{15}N						376.93	373.88	
		2	3	3a	4	5	6	7	7a
	^1H	7.91, dd	7.87, d				9.14, d	8.04, dd	
	J_{HH}	5.64, 0.74	5.64				5.74	5.74, 0.74	
	^{13}C	124.28	132.60	159.9			143.74	120.03	137.10
	^{15}N				393.95	391.62			

NMR characterisation of the pre-catalyst and intermediates formed with T[2,3-*d*]P in the SABRE catalytic cycle were then carried out to investigate the mechanism of binding involved with [IrCl(COD)(IMes)]. The leading hypothesis was that coordination to the metal centre would occur via the two nitrogen nuclei, as was demonstrated by Appleby *et al.*(2015) in the

detailed mechanistic study of pyridazine.¹⁴¹ However coordination of ligands through sulfur has also been demonstrated.^{185, 186}

2.3 Characterisation of Thienopyridazines in the SABRE Process

SABRE hyperpolarisation relies on reversible binding of the substrate to a metal catalyst. Understanding how binding occurs is important to optimise the polarisation transfer processes.^{112, 119, 187} In the case of the thienopyridazines, they possess both an *N*-heterocyclic ring and a *S*-heterocyclic ring. Lewis basic nitrogen containing molecules such as *N*-heterocycles and nitriles¹⁸⁸ have been found to be the most effective ligands for ¹H SABRE catalysis however, there have been examples where polarisation transfer has been successful with sulfur heterocycles.¹⁸⁵ It is possible, therefore, that binding could occur through both the nitrogen and sulfur nuclei in the thienopyridazines. As discussed in chapter one, SABRE involves the initial formation of a square planar pre-catalyst as one of the substrate molecules displaces the chloride ion of [IrCl(COD)(IMes)]. Addition of H₂ to the complex reduces the iridium and an octahedral intermediate formed with one substrate molecule. Next, the COD ligand is firstly reduced to COE and then completely displaced with two substrates occupying its former position. The first step was to investigate the formation of the pre-catalyst before H₂ is introduced (2.3.1). The second step was to investigate the reaction intermediates formed after addition of H₂ (2.3.2) and finally the SABRE active product (2.3.3).

2.3.1 Formation of [Ir(COD)(IMes)(T[2,3-*d*]P)]Cl – In activated pre-catalyst

An investigation of the inactivated precatalyst was undertaken using the precursor catalyst [IrCl(COD)(IMes)]. This was dissolved together with a four-fold excess of T[2,3-*d*]P, in methanol-*d*₄ to give the square planar complex [Ir(COD)(IMes)(T[2,3-*d*]P)]Cl. The chloride ligand is displaced by the thienopyridazine and acts as a counterion. It was expected that as either nitrogen site can bind to the iridium centre (through their lone pair of electrons) and as the substrate is asymmetrical, two possible pre-catalysts could form as shown in Figure 2.6. Multi nuclei 2D NMR experiments were carried out at 298 K and 233 K. The latter low temperature measurements slowed down dynamic interactions resulting in sharper peaks.

The number of bound peaks confirmed the presence of the two species (Figure 2.6). Analysis of the peak integrals showed that all bound resonances for each species were present in equal proportions. Therefore, it can be concluded that the substrate had an equal preference for binding

at each of the two nitrogen sites, which is unsurprising as there are limited steric and electronic differences between them. Figure 2.6 shows the structures of the two pre-catalysts, **A** and **B**, that are formed. Appendix 2.1 details characterisation data for the two species **A** and **B**. A NOESY interaction between protons at position 3 and 4 was observed and used to assign orientation. It was found that protons at positions 3 and 7 were coupled through a long range $^5J_{\text{HH}}$ coupling. No evidence was found for coordination through sulphur in the hydride region. The two bound nitrogen nuclei appear at δ 286.63 (complex **A**) and 285.52 (complex **B**) with their adjacent unbound nitrogen nuclei at δ 356.96 (complex **A**) and 359.97 (complex **B**) as confirmed by 2D NMR methods (see Appendix 1).

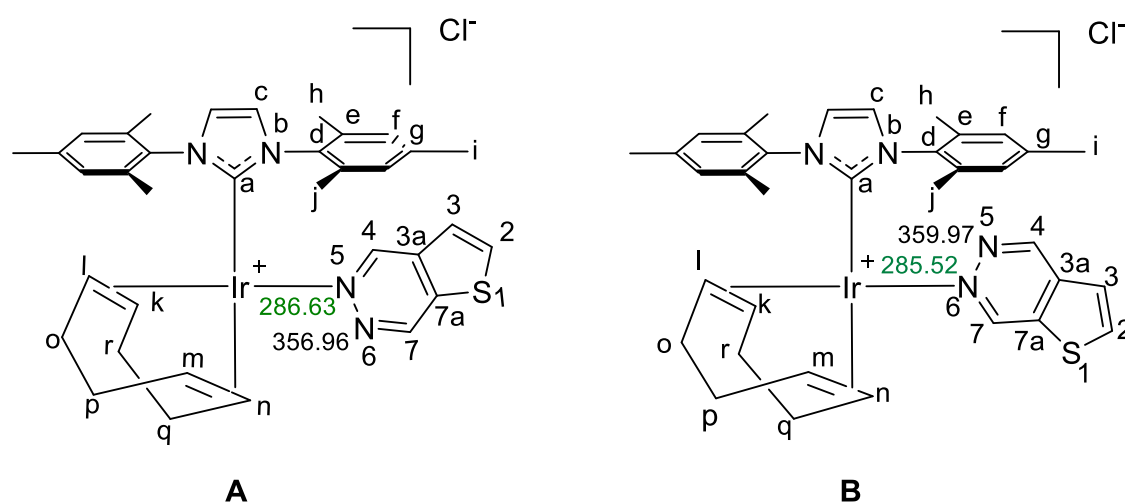


Figure 2.6: Structures of pre-catalysts $[\text{Ir}(\text{COD})(\text{IMes})(\text{T}[2,3\text{-}d]\text{P})]\text{Cl}$ **A** and **B** indicating the two bound nitrogen resonances (green)

2.3.2 Formation of $[\text{Ir}(\text{H})_2(\text{COD})(\text{IMes})(\text{T}[2,3\text{-}d]\text{P})]\text{Cl}$ – Intermediates **C** and **D**

In order to detect $[\text{Ir}(\text{H})_2(\text{COD})(\text{IMes})(\text{T}[2,3\text{-}d]\text{P})]\text{Cl}$, the intermediate formed in the SABRE cycle, H_2 addition was carried out at cold temperatures in the presence of 1.2 equivalents of substrate. Four chemically inequivalent hydride resonances were detected in the ^1H NMR (243 K). As displayed in Figure 2.7, these are assigned as two hydrides that are cis to one another at δ -13.87 and δ -17.62 for complex **C** and a further two hydrides that are cis to one another at δ -13.92 and δ -17.70 for complex **D**. The characterisation of these intermediates was extremely challenging due to their complexity. Resonances within the catalyst backbone and the COD ligand became non-equivalent but lead to very similar resonances in the ^1H and ^{13}C NMR. Nevertheless, diagnostic signals were seen for the two intermediates (Appendix 1).

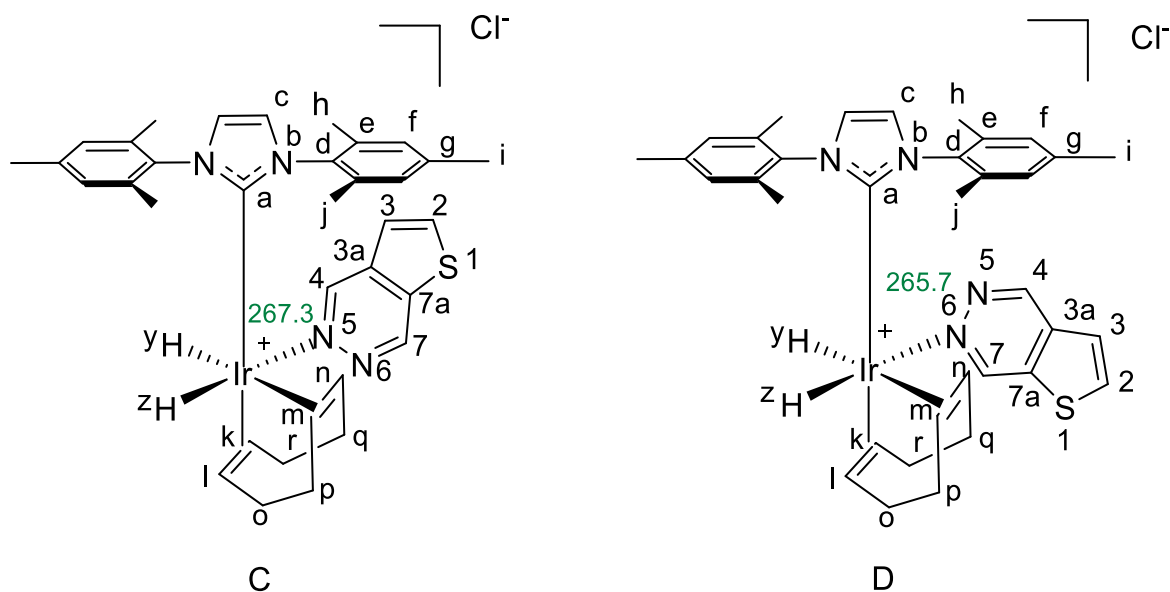


Figure 2.7: Structures of intermediates $[\text{Ir}(\text{COD})(\text{H})_2(\text{IMes})(\text{T}[2,3\text{-}d]\text{P})]\text{Cl}$ C and D indicating the two bound nitrogen resonances

From these results it is hypothesised that the two species interconvert via a haptotropic shift^{141, 189} where the binding to the iridium quickly switches between the two adjacent nitrogen sites. Only at low temperatures when the kinetics are much slower can these two species be distinguished. This phenomenon was previously observed for analogous iridium pyridazine complexes¹⁴¹. However, unlike pyridazine (which is symmetric), T[2,3-*d*]P being asymmetric adds additional complexity.

2.3.3 Formation of $[\text{Ir}(\text{H})_2(\text{IMes})(\text{T}[2,3\text{-}d]\text{P})_3]\text{Cl}$, SABRE active complex

After activation with H_2 is complete, the solution becomes pale yellow in colour indicating a change of oxidation state of the iridium centre and the presence of an octahedral SABRE active product. A complicated signal in the hydride region at $\delta -21.5$ was observed using ^1H NMR spectroscopy. This suggests the formation of several SABRE active complexes with overlapping resonances. The region at $\delta -21.5$ is typical of a hydride ligand *trans* to a nitrogen.¹⁹⁰ As hydride ligand signals are not observed in other regions of the NMR spectrum it can be concluded that binding occurs only through nitrogen and not through sulfur. When COD is hydrogenated, thienopyridazine can occupy three sites on the catalyst and hence there is the possibility of forming eight different species (Figure 2.8). In complexes E-H, four pairs of chemically equivalent but magnetically inequivalent hydrides would be expected and in complexes I-L four pairs of both chemically and magnetically inequivalent hydrides should result. All complexes should be SABRE active as the presence of magnetically inequivalent hydrides is the prerequisite

for polarisation transfer.^{117, 191} Only through the formation of inequivalent hydrides can the symmetry of *p*-H₂ be broken and latent polarisation released.

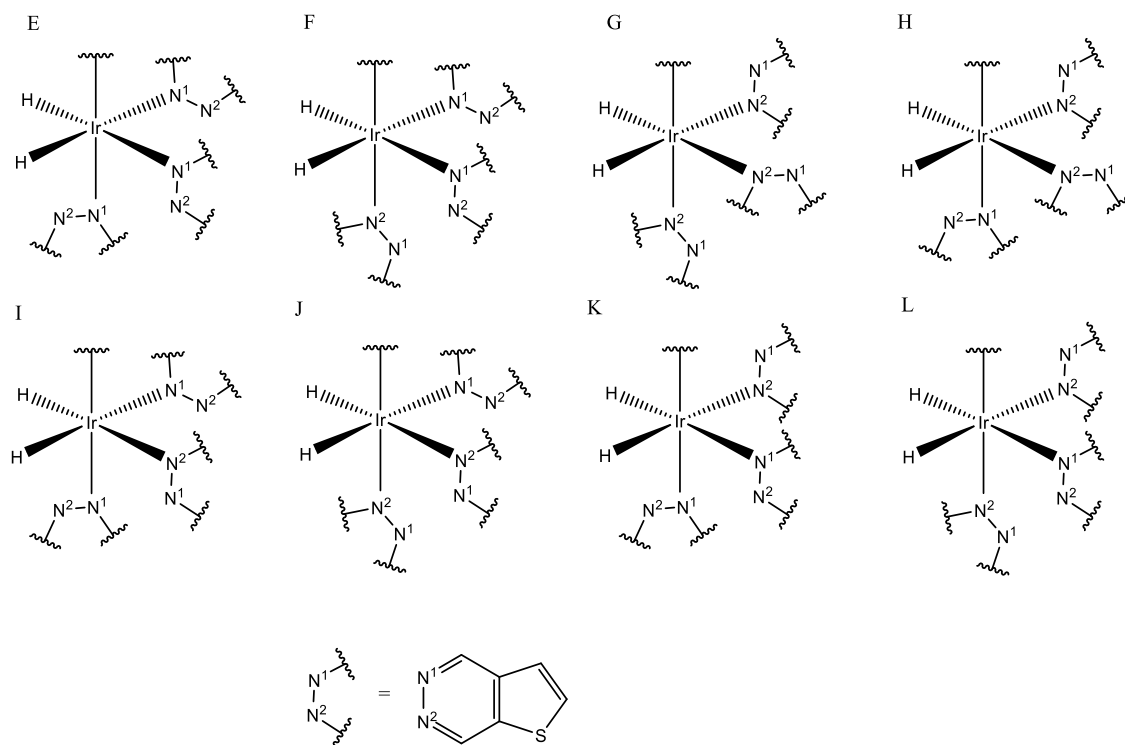


Figure 2.8: Predicted regioisomeric products E-L for [Ir(H)₂(IMes)(T[2,3-*d*]P)₃]Cl

Despite wide ranging efforts to characterise all of the regioisomeric products E-L, at this stage, it was not possible due to the complexity of the spectra. However, as reported in chapter 3, ¹⁵N-labelling of the two nitrogen nuclei to form thieno[2,3-*d*]pyridazine-¹⁵N₂ was carried out and allowed subsequent characterisation of the 8 complexes through ¹⁵N-¹H coupling. Therefore, it is possible to conclude that all regioisomers are formed during the SABRE activation process.

With the four compounds synthesised to an adequate yield and characterisation complete, the agents were tested for SABRE hyperpolarisation.

2.4 Hyperpolarisation of Thienopyridazines using SABRE – Effect of Spin Isomers on Hyperpolarisation

[IrCl(COD)(IMes)] has proved to be an efficient SABRE catalyst for many other substrates.¹¹⁵ SABRE polarisation of the synthesised thienopyridazines was therefore first attempted with [IrCl(COD)(IMes)] at 4.5 mM concentration in methanol-*d*₄ with a 4:1 substrate to catalyst ratio and 3 bar (g) *p*-H₂.

Catalyst activation was achieved by adding H₂ (3 bar (g)). Intermediate hydride peaks began to appear in all cases in a ¹H NMR spectrum (400 MHz) at δ -14.1 and -17.6. The intermediate hydride peaks disappeared leaving one multiplet signal present at δ -21.5. This suggested the presence of chemically different hydrides caused by the ligation of a nitrogen ligand. SABRE measurements were then carried out by replacing the H₂ with *p*-H₂. Figure 2.9 shows the aromatic region of a single scan ¹H NMR spectrum at thermal equilibrium, and one under hyperpolarised conditions of the SABRE complex [Ir(H)₂(IMes)(T[2,3-*d*]P)₃]. The thermal spectrum has been vertically magnified 64 times to be seen alongside the hyperpolarised spectrum. The insert shows the hydride region.

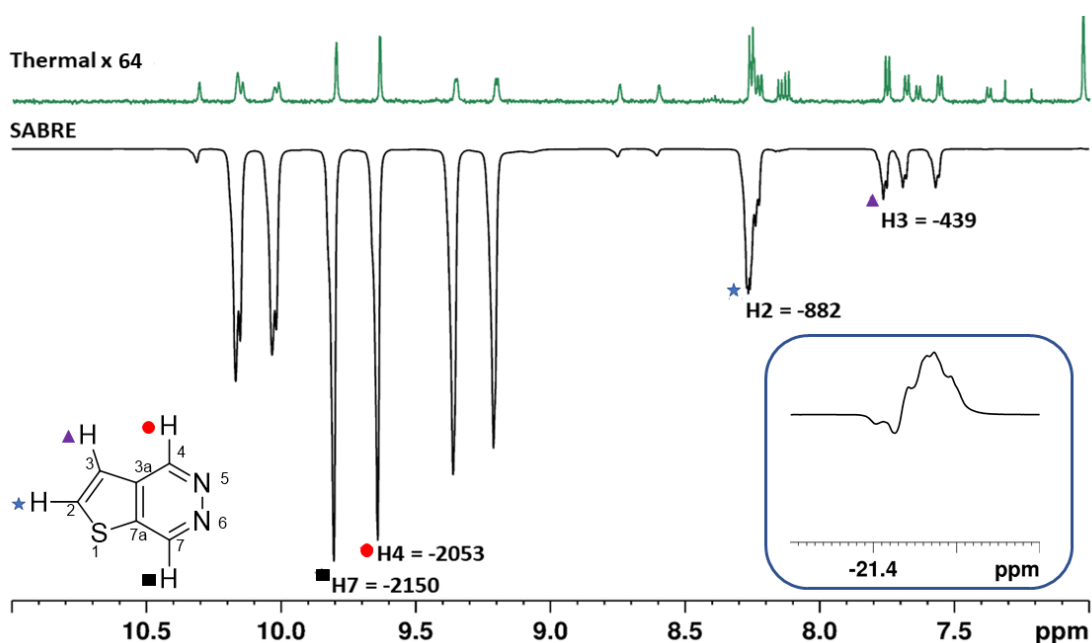
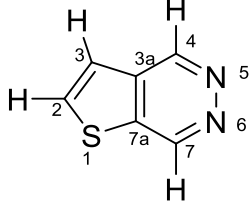
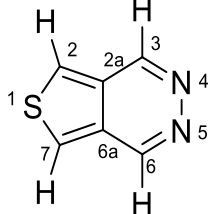
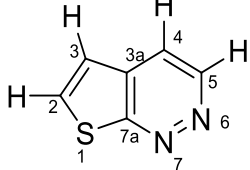
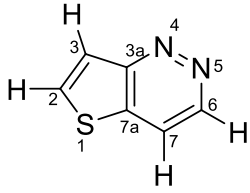


Figure 2.9: Comparison of the aromatic region of a ¹H spectrum of T[2,3-*d*]P and [IrCl(COD)(IMes)] in a 4 to 1 ratio at thermal equilibrium (green - with vertical expansion 64 times) and under SABRE conditions at 3 bar(g) of *p*-H₂ (black). Insert shows the hydride region of the ¹H spectra.

Each substrate showed large NMR signal enhancement values over those acquired under thermal conditions and confirm their suitability as potential SABRE contrast agents. The largest ¹H signal enhancement of each substrate were -2150 ± 67 (H7 in T[2,3-*d*]P), -1480 ± 21 (H3/H6 in T[3,4-*d*]P), -583 ± 19 (H5 in T[2,3-*c*]P), -822 ± 19 (H6 in T[3,2-*c*]P). Table 2.2 quantifies enhancement across all relevant resonances. Data show that T[2,3-*d*]P and T[3,4-*d*]P with the -*d* configuration and the highest level of symmetry, had the highest signal enhancements. The symmetrical T[3,4-*d*]P is less efficient than T[2,3-*d*]P which may suggest that the electronic effect of the thiophene ring may be significant or the T_1 of H3/H6 is much shorter than H4 and H7 in T[2,3-*d*]P.

Table 2.2: Signal enhancements for shake and drop experiments of the thienopyridazines using [IrCl(COD)(IMes)] as catalyst in a 1:4 catalyst to substrate ratio in methanol- d_4 . *Average values across two proton sites.

Substrate	Structure	Resonance	Enhancement Values (per proton)
T[2,3- <i>d</i>]P		H7 (N) 9.79	-2150 ± 67
		H4 (N) 9.63	-2053 ± 77
		H2 (S) 8.25	-882 ± 47
		H3 (S) 7.75	-439 ± 42
T[3,4- <i>d</i>]P		H3/H6 (N) 9.40	-1480 ± 21*
		H2/H7 (S) 8.58	-1138 ± 18*
T[2,3- <i>c</i>]P		H5 (N) 9.18	-583 ± 19
		H4 (N) 8.17	-384 ± 13
		H2 (S) 8.21	-174 ± 5
		H3 (S) 7.54	-39 ± 3
T[3,2- <i>c</i>]P		H6 (N) 9.14	-822 ± 19
		H7 (N) 8.41	-371 ± 14
		H2 (S) 8.24	-828 ± 20
		H3 (S) 7.86	-385 ± 18

From these results, it can be concluded that the position of the nitrogen atoms relative to the five-membered sulfur ring plays a role in the efficiency of spin polarisation transfer. In T[2,3-*c*]P and T[3,2-*c*]P one of the two possible nitrogen binding sites (position 7 in T[2,3-*c*]P and position 4 in T[3,2-*c*]P) is adjacent to the carbon of the fused rings and therefore sterically hindered when approaching the catalyst. From this data it can be hypothesised that this positioning could negatively affect the way the substrate can bind to the iridium centre compared with substrates T[2,3-*d*]P and T[3,4-*d*]P (where both nitrogen nuclei are not directly adjacent to the fused ring). It could also be hypothesised that the close proximity of the electronegative sulfur atom to the

two nitrogen atoms in T[2,3-*c*]P may contribute a negative effect on binding due to this substrate being polarised to a lesser degree than in T[3,2-*c*]P.

To date there are no generalised optimum conditions for the SABRE hyperpolarisation for any given substrate.¹²³ The SABRE reaction is substrate dependent and as such, a series of optimisation steps for thienopyridazines were investigated, including substrate loading comparison, polarisation transfer field, carbene type on the precursor catalyst and *p*-H₂ pressure.

2.4.1 Substrate Loading Comparisons

It has been demonstrated that SABRE signal enhancement levels are affected by substrate loading (i.e. the ratio of the substrate molecules to catalyst in terms of concentration).¹²¹ To investigate the effect of substrate loading, samples were made up using catalyst to substrate ratios 1:4, 1:6, and 1:8 for the two highest performing substrates in terms of signal enhancement, T[2,3-*d*]P and T[3,4-*d*]P. Figure 2.10 demonstrates that signal enhancements were optimised when four molar equivalents of substrate were present relative to iridium. This would be expected as there are three positions on the catalyst which the substrate can occupy, in addition to having one substrate in free solution for NMR detection. At low catalyst to substrate ratios the substrate is more likely to come into contact with the catalyst for reversible exchange. Both experimental data¹²¹ and theoretical models predict that large signal enhancements result with low substrate-to-catalyst ratios.¹⁸⁷

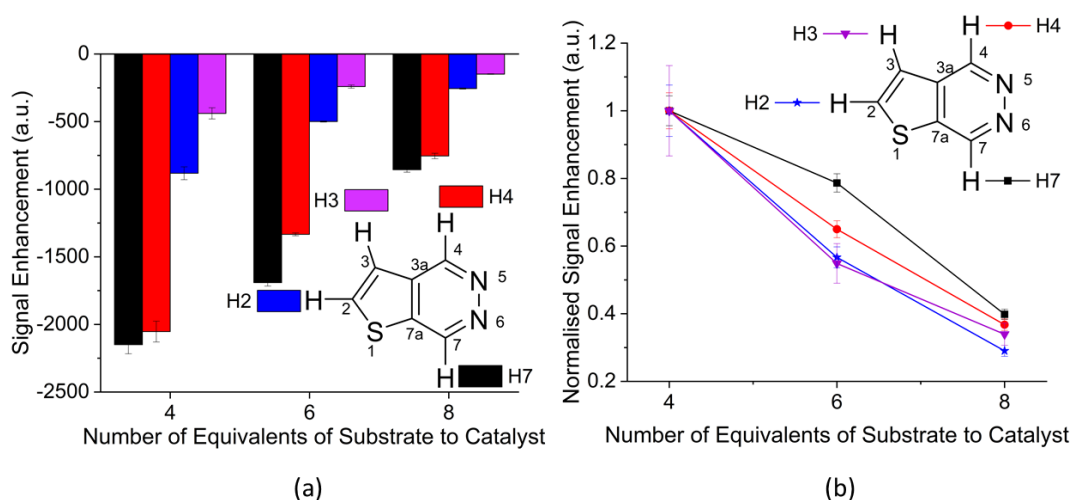


Figure 2.10: Effect on signal enhancement values when changing substrate to catalyst ratios. The substrate used was T[2,3-*d*]P and the catalyst [IrCl(COD)(IMes)] forming the active catalyst [Ir(H)₂(IMes)(T[2,3-*d*]P)₃]Cl. The solvent used was methanol-*d*₄ and measurements were made on a 400 MHz spectrometer at 298K. (a) Signal enhancements values measured per individual proton with 4, 6 and 8 eq. of T[2,3-*d*]P to 1 equivalent of catalyst [IrCl(COD)(IMes)]. (b) Normalised signal enhancement values per proton showing a linear decrease of enhancement with increased number of substrate equivalents.

The normalised data (Figure 2.11b) shows an almost linear dependence on the number of equivalents of substrate. An increase in number of equivalents shows a corresponding decrease in signal enhancement independent of proton site. All protons show over 50% reduction in signal enhancement when moving from four to eight equivalents.

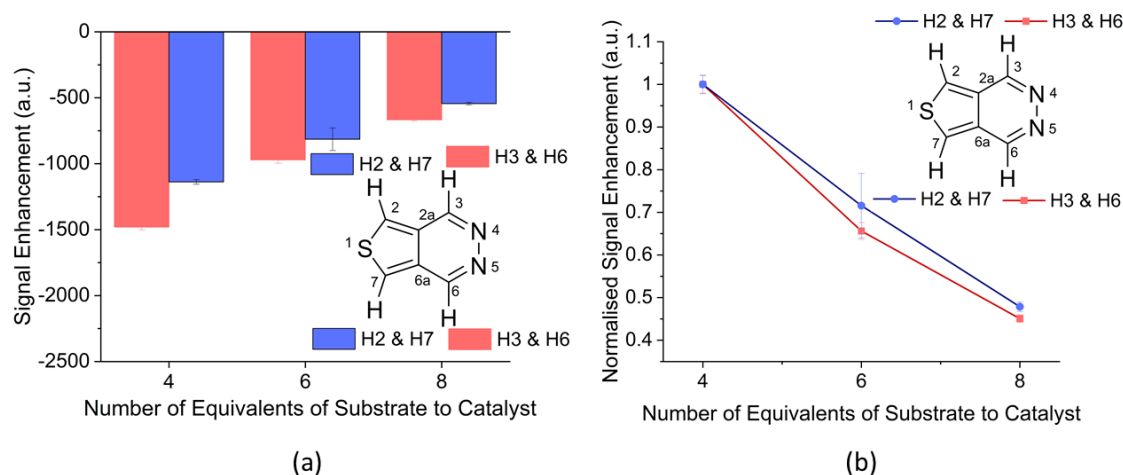


Figure 2.11: Effect on signal enhancement values when changing substrate to catalyst ratios. The substrate used was T[3,4-*d*]P and the catalyst [IrCl(COD)(IMes)] forming the active catalyst [Ir(H)₂(IMes)(T[3,4-*d*]P)₃]Cl. The solvent used was methanol-*d*₄ and measurements were made on a 400 MHz spectrometer at 298K. (a) Signal enhancements values measured per individual proton with 4, 6 and 8 eq. of T[3,4-*d*]P to 1 equivalent of catalyst [IrCl(COD)(IMes)]. (b) Normalised signal enhancement values per proton showing a linear decrease of enhancement with increased number of substrate equivalents.

The linear dependence of equivalence was also observed for all proton sites within T[3,4-*d*]P evidenced by the normalised data in Figure 2.11(b). The resonance for the equivalent protons again shows 50% reduction in signal enhancement when moving from four to eight equivalents of substrate to catalyst.

2.4.2 Polarisation Transfer Field

A study of the field dependence on the extent of hyperpolarisation on each of the four distinct protons of each of the four substrates was carried out. Previous studies on many hetero-aromatic substrates have identified that 65 Gauss is the optimum field for successful hyperpolarisation using the SABRE technique.^{112, 119} This is determined by the dominant hydride-hydride coupling. Obtaining this data was important to ensure that the subsequent ‘shake and drop’ experiments were conducted using the optimum Polarisation Transfer Field (PTF).¹⁹² In order for these results to be precise, a reversible flow polariser was used as described in chapter 8.2. Once again, a 1:4 catalyst to substrate ratio was used. For reproducibility, the automated system greatly exceeds the shake and drop experiments as experimental errors are reduced. In the shake and drop method,

shaking within the stray field of the spectrometer can mean that the field differs slightly each time. An average is taken of the values found in five to seven shakes to minimise this human error. However, this will still be a significant error compared with the flow system.

The hyperpolarisation values recorded using the automated system are, however considerably lower than those achieved with the shake and drop technique (e.g. -1300 vs -2150 signal enhancement for H7 in T[2,3-*d*]P using [IrCl (COD)(IMes)]). This is due to the limitations of the automated system; including firstly the fact that the sample is not degassed before entering the flow system. A sample is prepared in a standard sample vial, rather than a sealed Young's tube, before being injected into the flow system. It is likely that paramagnetic O₂ is introduced into the system, which can shorten T_1 lifetimes and consequently reduce the level of polarisation. The second reason is due to the reduced efficiency of *p*-H₂ delivery into solution. In the automated system, the *p*-H₂ is simply bubbled through the solution. During the 'shake and drop' technique there is vigorous shaking of the sample within the Young's tube which allows for more effective dissolution of the gas within the sample, leading to higher polarisation levels. The third reason is due to the length of the experiment. In the automated system, once the *p*-H₂ has been bubbled through there are several stages, which take approximately five to six seconds in total. The stages include normalising the pressure, transportation of the hyperpolarised solution and the settling period before the measurement is taken. Five to six seconds may seem insignificant but when the lifetime of some T_1 values is of the same order of magnitude, it can have a dramatic effect of detectable signal levels. The flow system cannot compete yet with the human efficiency of simply 'dropping' the Young's tube into the spectrometer.

The trend of hyperpolarisation achieved with the automated flow system agrees very well with the results achieved with the 'shake and drop' method. Within each substrate the protons are hyperpolarised to approximately the same ratio and the signal enhancement values are approximately double for the shake and drop technique when compared to the flow system.

Figure 2.12 to Figure 2.15 portray the resulting PTF data and show that all substrates yield their largest signal enhancements for all four free ligand spins between 60 and 70 G. It can be concluded that similar $^4J_{\text{HH}}$ couplings operate in all four substrates. PTF plots for the higher symmetry substrates, T[2,3-*d*]P and T[3,4-*d*]P, are unimodal with a single maxima at $60.4 \text{ G} \pm 0.6$ and $60.9 \text{ G} \pm 0.5$ respectively as predicted by the Level Anti-crossing approach LAC approach.^{120 193}

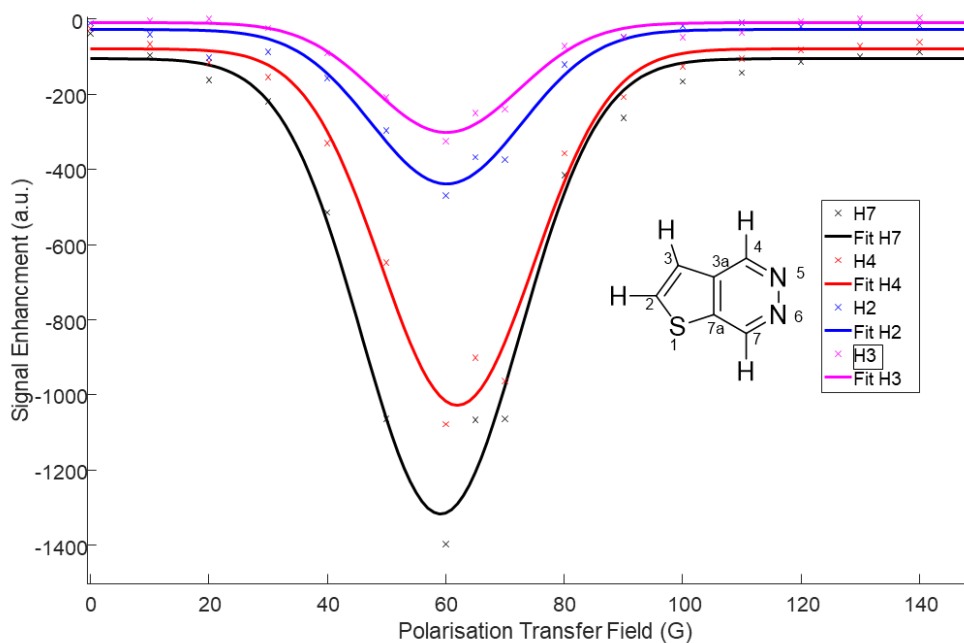


Figure 2.12: Polarisation transfer field plot showing variation of signal enhancement for T[2,3-*d*]P at 298 K using the automated polariser. PTF plots for each resonance show a Gaussian distribution and give a single maximum at 60.4 +/- 0.6 G

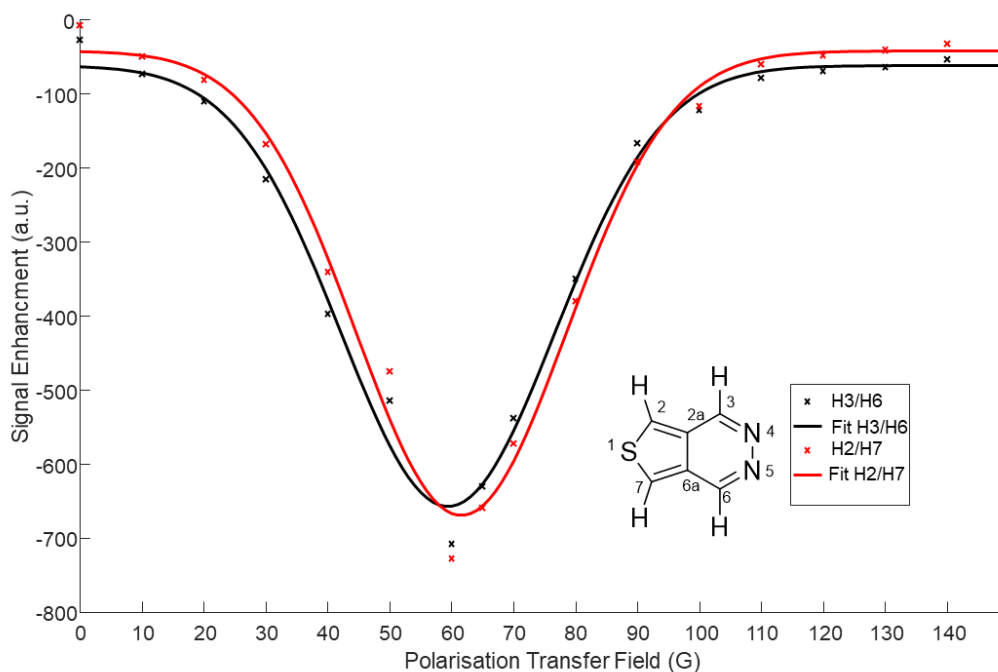


Figure 2.13: Polarisation transfer field plot for T[3,4-*d*]P at 298 K using the automated polariser. PTF plots for each resonance show a Gaussian distribution and give a single maximum at 60.9 +/- 0.5 G

When T[2,3-*c*] and T[3,2-*c*] were examined (Figure 2.14 and Figure 2.15) multimodal behaviour across polarisation field was observed. Three Gaussian functions were required to adequately fit

the resulting PTF profiles. This is inconsistent with the normal LAC suggestions.¹⁹⁴ Polarisation transfer was observed at lower fields; with positive amplitude for H7 and H3 and negative amplitude for H6 and H2 (Figure 2.16). This trend has been modelled in the LAC theory, however a phosphorous ligand was present in the SABRE catalyst.¹⁹⁴

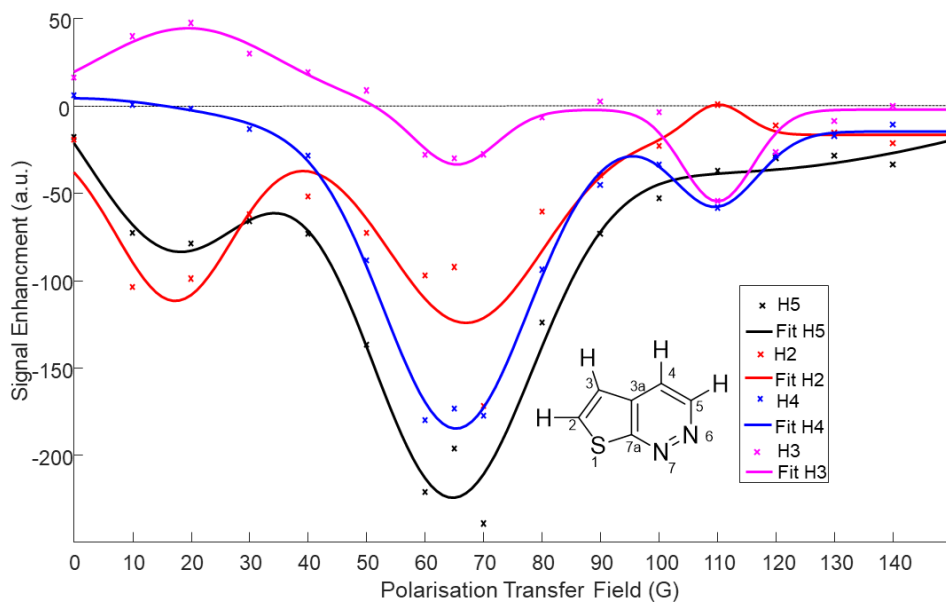


Figure 2.14: Polarisation transfer field plot for T[2,3-c]P at 298 k using the automated polariser. PTF plots for each resonance show a Gaussian fit and give three maxima at peak 1 = 13.30 +/- 4.48 G, peak 2 = 65.37 +/- 0.60 G and peak 3 = 109.778 +/- 0.13 G

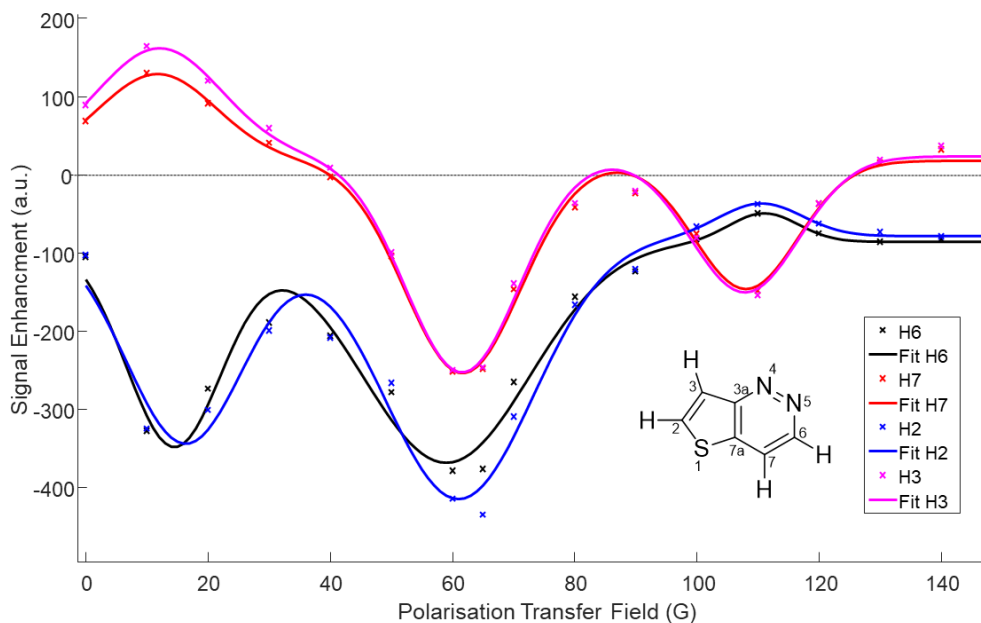


Figure 2.15: Polarisation transfer field plot for T[3,2-c]P at 298 K using the automated polariser. PTF plots for each resonance show a Gaussian fit and give three maxima at peak 1 = 13.64 +/- 1.06, peak 2 = 60.81 +/- 0.62 and peak 3 = 109.36 +/- 0.81983

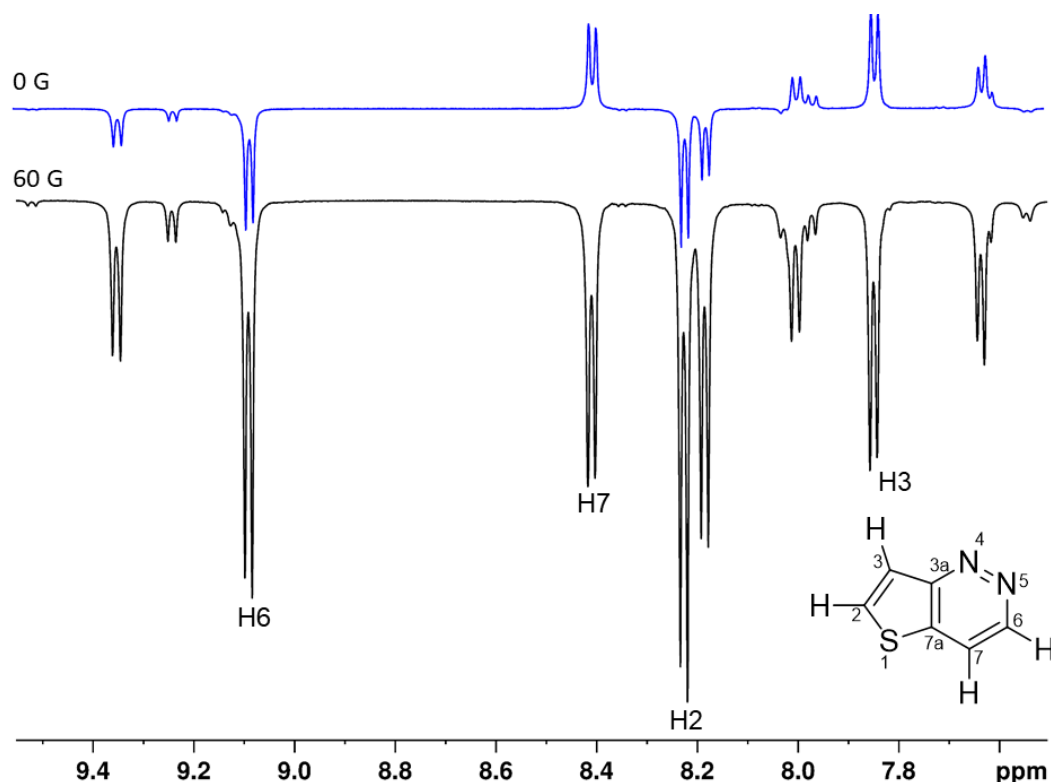


Figure 2.16: Hyperpolarised spectra for T[3,2-c]P achieved at 0G (blue) and 60 G (black). Positive magnitudes for H7 and H3 and negative magnitudes for H6 and H2 at 0 G (blue). Negative magnitudes for all resonances at 60 G (black)

The hydride region of the NMR spectra of all these samples is complex and consistent with several different SABRE active catalysts. One hypothesis to explain this behaviour is associated with the change in sign of the propagating J_{HH} couplings from the hydride to the protons in the ligand according to which of the two nitrogen binding sites is involved.^{118, 120, 193, 195} This sign change is brought about by the resulting variation of coupling bond-order and will, in turn, invert the sign of the population difference, thereby leading to a hyperpolarised signal of opposite phase. It has been recently confirmed experimentally and theoretically that the changes in coupling constants resulting from binding to iridium lead to complex PTF profiles when mixtures of species are present in solution.¹⁹⁶ Consequently, the resulting PTF profile should exhibit complex behaviour as contributions from the different forms of the catalyst combine together here to yield the resulting catalyst-averaged signal. This behaviour would require further very detailed theoretical and experimental study if a rigorous model were to be proposed. That was beyond the scope of this project.

2.4.3 Type of Catalyst - Effect of Changing Carbene Backbone of Catalyst

The catalyst [IrCl(COD)(IMes)] is often used in SABRE studies due to its rapid synthesis from commercially available starting materials. However, the choice of the carbene within the catalyst

is vital if strong signal enhancements are desired. Modifying the chemistry of the carbene changes steric, electronic and relaxation properties which affect exchange rates and polarisation build up in the free substrate.¹²³

The four catalyst precursors $[\text{IrCl}(\text{COD})(\text{IMes})]$,¹²¹ the saturated version of IMes, $[\text{IrCl}(\text{COD})(1,3\text{-bis}(2,3,6\text{-trimethylphenyl})\text{-}4,5\text{-dihydroimidazol-}2\text{-ylidene})]$, $([\text{IrCl}(\text{COD})](\text{SIMes})$ ¹²¹ and the partially deuterated version of both, $[\text{IrCl}(\text{COD})(d_{22}\text{-}1,3\text{-bis}(2,4,6\text{-trimethyl})\text{-imidazol-}2\text{-ylidene})]$ $([\text{IrCl}(\text{COD})(d_{22}\text{-IMes})]$ ¹⁹⁷ and $[\text{IrCl}(\text{COD})(d_{22}\text{-}1,3\text{-bis}(2,3,6\text{-trimethylphenyl})\text{-}4,5\text{-dihydroimidazol-}2\text{-ylidene})]$ $[\text{IrCl}(\text{COD})(d_{22}\text{-SIMes})]$ ¹³⁵ were therefore screened. The molecular structures of their parent NHC's are illustrated in Figure 2.17. Based on previous data¹³⁵ it was expected that the deuterated version $d_{22}\text{-IMes}$ would give the largest signal enhancement values. Although the rate of ligand exchange should be the same as IMes, deuterium labelling has been shown to increase the lifetime of the bound substrate polarisation and hence lead to more efficient SABRE.^{135, 140, 190, 197} It is also known that polarisation not only reaches those ligands in the equatorial positions but also in the axial position within the carbene framework. Replacing the protons of the carbene with deuterium prevents spin dilution and focuses the polarisation into the desired equatorial ligands. A series of samples were prepared to test the SABRE activity of these catalysts with the four thienopyridazines.

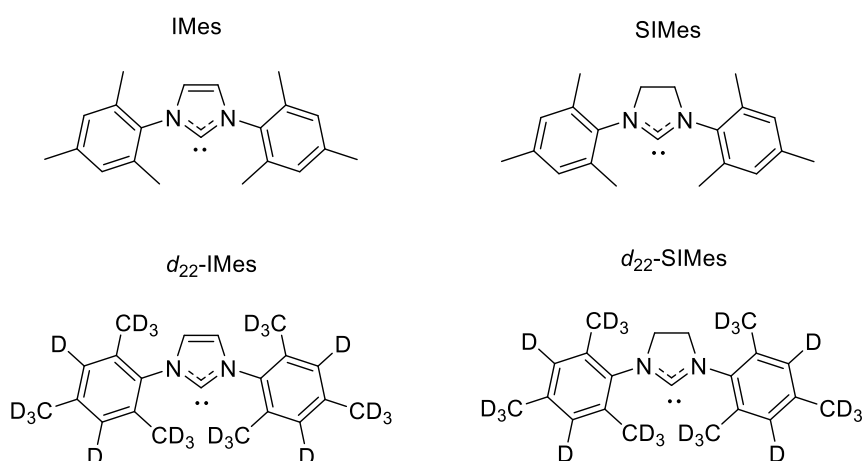


Figure 2.17 – Structures of the four carbene ligands, IMes, SIMes, $d_{22}\text{-SIMes}$ and $d_{22}\text{-SIMes}$ used to study SABRE signal enhancement of a series of thienopyridazines.

When $[\text{IrCl}(\text{COD})(\text{IMes})]$ was compared to $[\text{IrCl}(\text{COD})(\text{SIMes})]$, an increase in signal enhancement values from -2150 to -2673 for T[2,3- d]P resulted. This is a $\sim 25\%$ increase in signal enhancement. Data for all four substrates tested is collated in Table 2.3. It is hypothesised

that the increase in polarisation transfer efficiency is due to a more optimal lifetime of the transient active SABRE catalyst. This lifetime is inversely proportional to the rate of ligand dissociation and is predicted to be approximately 4.5 s^{-1} .¹⁸⁷ Additionally, it has been shown previously that increasing the buried volume^{198, 199} of the NHC ligand can increase ligand dissociation rates by steric effects.¹²³ The buried volume increases from 33.0% to 34.5% for $[\text{IrCl}(\text{COD})(\text{IMes})]^{200}$ and $[\text{IrCl}(\text{COD})(\text{SIMes})]^{200}$ respectively; therefore the SIMes ligand would cause an increased rate of T[2,3-*d*]P loss from the catalyst. This could result in more optimal ligand exchange dynamics and further experiments should be conducted in the future to prove this hypothesis.

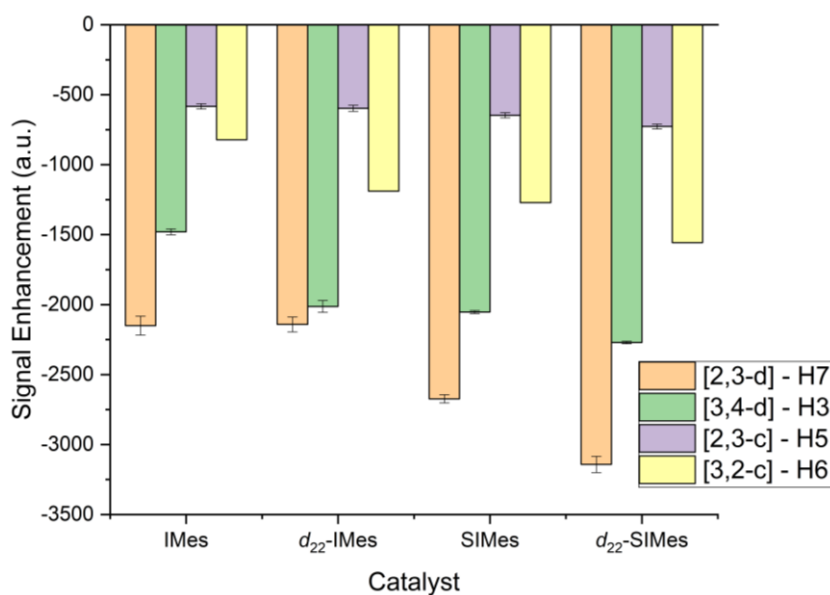
Using $[\text{IrCl}(\text{COD})(d_{22}\text{-IMes})]$ as the catalyst, T[2,3-*d*]P showed no significant difference in hyperpolarisation compared with its non-deuterated counterpart; all values being within error, e.g. -2141 ± 53 and -2150 ± 67 (H7). For T[3,4-*d*]P, $[\text{IrCl}(\text{COD})(d_{22}\text{-IMes})]$ does improve values compared with its non-deuterated counterpart bringing enhancement values in line with those achieved with $[\text{IrCl}(\text{COD})(\text{SIMes})]$ (e.g. -2013 ± 11 for H3/H6 -2053 ± 11 respectively). With T[2,3-*c*]P, $[\text{IrCl}(\text{COD})(d_{22}\text{-IMes})]$ gives slightly enhanced values (e.g. -597 ± 29 for H5) compared to $[\text{IrCl}(\text{COD})(\text{IMes})]$ (-583 ± 19 for H5) but $[\text{IrCl}(\text{COD})(\text{SIMes})]$ produces the highest values (-647 ± 18 for H5). Once again for T[3,2-*c*]P, $[\text{IrCl}(\text{COD})(d_{22}\text{-IMes})]$ does improve values (-1189 ± 3 for H6) compared with $[\text{IrCl}(\text{COD})(\text{IMes})]$ (-822 ± 19 for H6) but gives similar enhancements to those found with $[\text{IrCl}(\text{COD})(\text{SIMes})]$ (1271 ± 9 for H6).

The next step was to investigate the enhancements using the partially deuterated version of SIMes, $[\text{IrCl}(\text{COD})(d_{22}\text{-SIMes})]$. The general effect of the deuteration in SIMes is an increase in signal enhancement across all resonances. Maximal increases in signal enhancements between 10 and 22% were observed. An average enhancement of -3142 was recorded during a standard shake and drop experiment for H7 of T[2,3-*d*]P. In terms of percentage polarisation this equates to 9.8%.

For clarity, the resonances with the largest enhancements per substrate (T[2,3-*d*]P H7, T[3,4-*d*]P H3, T[2,3-*c*]P H5 and T[3,2-*c*]P H6) were plotted against the different catalysts as can be seen in Figure 2.18.

Table 2.3: Enhancement factors of the thienopyridazines with four different catalysts [IrCl(COD)(IMes)], [IrCl(COD)(*d*₂₂-IMes)], [IrCl(COD)(SIMes)] and [IrCl(COD)(*d*₂₂-SIMes)].

Substrate	Resonance (ppm)	Enhancement Factors Per Proton			
		IMes	SIMes	<i>d</i> ₂₂ -IMes	<i>d</i> ₂₂ -SIMes
T[2,3- <i>d</i>]P	H7 (N) 9.79	-2150 ± 67	-2673 ± 29	-2141 ± 53	-3142 ± 58
	H4 (N) 9.63	-2053 ± 77	-2489 ± 31	-1984 ± 50	-3072 ± 60
	H2 (S) 8.25	-882 ± 47	-1621 ± 57	-739 ± 78	-885 ± 33
	H3 (S) 7.75	-439 ± 42	-640 ± 29	-362 ± 16	-525 ± 21
T[3,4- <i>d</i>]P	H3/H6 (N) 9.40	-1480 ± 21	-2053 ± 11	-2013 ± 42	-2271 ± 9
	H2/H7 (S) 8.58	-1138 ± 18	-1623 ± 16	-1758 ± 47	-1787 ± 15
T[2,3- <i>c</i>]P	H5 (N) 9.18	-583 ± 19	-647 ± 18	-597 ± 29	-727 ± 17
	H4 (N) 8.17	-384 ± 13	-409 ± 21	-391 ± 31	-422 ± 7
	H2 (S) 8.21	-174 ± 5	-217 ± 13	-233 ± 22	-205 ± 4
	H3 (S) 7.54	-39 ± 3	-63 ± 6	-70 ± 8	-106 ± 2
T[3,2- <i>c</i>]P	H6 (N) 9.14	-822 ± 19	-1271 ± 9	-1189 ± 3	-1557 ± 40
	H7 (N) 8.41	-371 ± 14	-502 ± 12	-540 ± 28	-762 ± 23
	H2 (S) 8.24	-828 ± 20	-847 ± 32	-899 ± 29	-1121 ± 34
	H3 (S) 7.86	-385 ± 18	-548 ± 15	-477 ± 29	-745 ± 22

**Figure 2.18: Signal enhancements of the resonances in each of the four thienopyridazines with the greatest enhancement and how these levels vary when changing the carbene backbone.**

T[2,3-*d*]P was consistently the better performing substrate, with 30% higher signal enhancement over T[3,4-*d*]P with all catalysts except *d*₂₂-IMes. For this reason only T[2,3-*d*]P was carried forward for further experimentation with two new catalysts, [IrCl(COD)(1,3-bis(4-chloro-2,6-dimethylphenyl)imidazol-2-ylidene)],¹³⁵ [IrCl(COD)(X)] and [IrCl(COD)(1,3-bis(4-(dimethylamino)-2,6-dimethylphenyl)imidazol-2-ylidene)]¹³⁵ [IrCl(COD)(Y)] shown in Figure 2.19. Using these two catalysts the effect on signal enhancement due to the electronic properties of the carbenes were investigated. The presence of the chloro group in X has a –I inductive effect and results in a carbene which is more electron withdrawing than IMes. The presence of the –NMe₂ group has a +M mesomeric effect and results in a carbene which is more electron donating compared with IMes. These catalysts resulted in higher signal enhancements (over [IrCl(COD)(IMes)]) for methyl-4,6-*d*₂-nicotinate¹²³ in a study carried out by Rayner *et al.*(2018) with 60% increase in the case of [IrCl(COD)(X)] and 40% in the case of [IrCl(COD)(Y)].^{123 36}

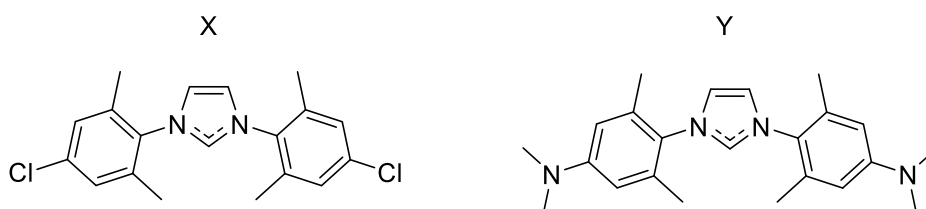


Figure 2.19: Structure of carbene X found in [IrCl(COD)(1,3-bis(4-chloro-2,6-dimethylphenyl)imidazol-2-ylidene)] and carbene Y found in [IrCl(COD)(1,3-bis(4-dimethylamino)-2,6-dimethylphenyl)imidazol-2-ylidene]

Resulting changes in signal enhancement level for T[2,3-*d*]P using these catalysts are shown in Table 2.4 and are compared with those achieved using the best performing catalyst [IrCl(COD)(*d*₂₂-SIMes)] from the previous study.

Table 2.4: Enhancement factors of T[2,3-*d*]P with two new catalysts [IrCl(COD)(X)] and [IrCl(COD)(Y)]

Substrate/Catalyst	Resonance (ppm)	Enhancement Factors Per Proton		
		X	Y	<i>d</i> ₂₂ -SIMes
T[2,3- <i>d</i>]P	H7 (N) 9.79	-757 ± 38	-1670 ± 45	-3142 ± 58
	H4 (N) 9.63	-640 ± 38	-1571 ± 49	-3072 ± 60
	H2 (S) 8.25	-357 ± 13	-572 ± 18	-885 ± 33
	H3 (S) 7.75	-143 ± 8	-283 ± 14	-525 ± 21

T[2,3-*d*]P has now been tested with six different catalysts in total and the results for each of the four resonances of T[2,3-*d*]P are shown in Figure 2.20.

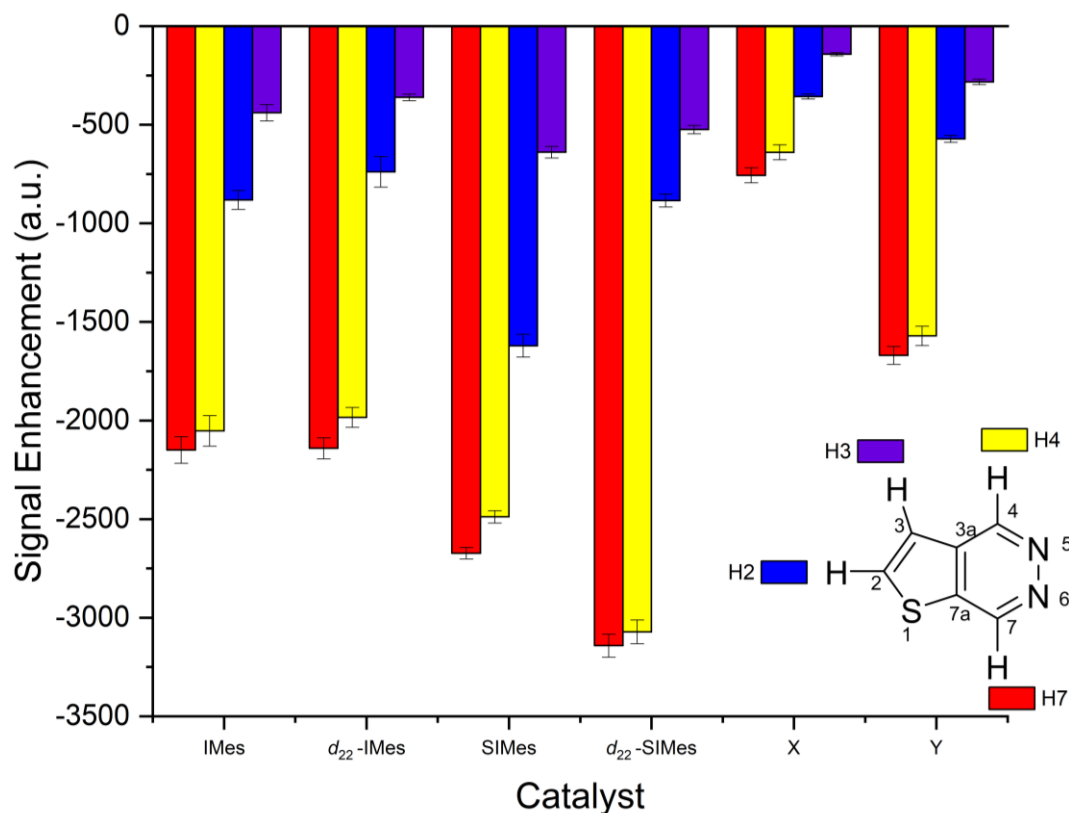


Figure 2.20: Graph showing the effect of a change of catalyst on the signal enhancement values of the four proton signals in T(2,3-*d*)P

In contrast to the signal improvements found with methyl-4,6-*d*₂-nicotinate¹²³ the signal enhancements achieved for T[2,3-*d*]P were generally inferior (65% in the case of [IrCl(COD)(X)] and 22% in the case of [IrCl(COD)(Y)] to those achieved with the traditional [IrCl(COD)(IMes)]. Due to the poor performance of these catalysts, further testing with the remaining three substrates was not carried out.

Data illustrates that the choice of catalyst is very substrate specific and that there are still many factors, that contribute to the success in each individual SABRE reaction to be able to predict or create generalised optimum conditions for a particular type of substrate. However, all catalysts tested with the IMes backbone have shown inferior results to those achieved with SIMes and confirms that the sterically bigger [IrCl(COD)(SIMes)] is favourable for thienopyridazines. A previous study¹²¹ has shown that there is an increase in the rate of substrate dissociation as a consequence of the change in percentage buried volume (%V_{bur}). This faster rate of dissociation

combined with the promotion of H₂ exchange may allow a faster build of hyperpolarised molecules in solution within the T_1 timeframe.

Results show that deuteration of the carbene prevents spin dilution in the active SABRE catalyst and therefore the substrates in the equatorial plane of the SABRE active complex demonstrate higher polarisation.

2.4.4 Magnetic lifetimes (T_1) of Thienopyridazines

There are two key parameters to consider when using hyperpolarised molecules in ¹H MRS. The overall magnitude of the hyperpolarised signal is extremely important, so that a signal may be observed against the huge background signal from water. Therefore, optimisation steps are critical to increase the signal enhancement and magnitude. The second parameter is the magnetic lifetime or T_1 of this transient hyperpolarised signal. High ¹H signal enhancements combined with long T_1 values for the ¹H resonances would give the optimum scenario to allow a large window of observable hyperpolarised signal for use in biomedical imaging.

An investigation into the magnetic lifetimes of the four resonances in each of the four substrates was carried out. The inversion recovery method (see chapter 8.2.4) was used to measure the longitudinal lifetime (T_1) for each of the resonances belonging to the four substrates, both with and without the four different catalysts present. Data were fit to an exponential decay model, as shown in equation 2.1, where M_z = magnetisation along the z axis at time, t , M_0 = magnetisation along the z axis at $t = 0$ and T_1 = decay time constant.

$$M_z = M_0 \left(1 - e^{-\frac{t}{T_1}} \right) \quad [2.1]$$

To measure the T_1 values without the catalyst present, methanol-*d*₄ samples were prepared in 5 mm Young's tubes with 18 mM of substrate and degassed. A suitable delay was applied between experiments to allow for five times the T_1 value to ensure full relaxation back to thermal equilibrium. To measure T_1 in the presence of the catalysts, samples were prepared with 4.5 mM of catalyst in methanol-*d*₄ with four equivalents of substrate in each case. After degassing, 3 bar(g) of *p*-H₂ was introduced into the Young's tube. In all cases, measurements were made using a 400 MHz spectrometer. An example of the collected data is shown in Figure 2.21 and tabulated results for all resonances of T[2,3-*d*]P with and without the six different catalysts studied can be found in Table 2.5.

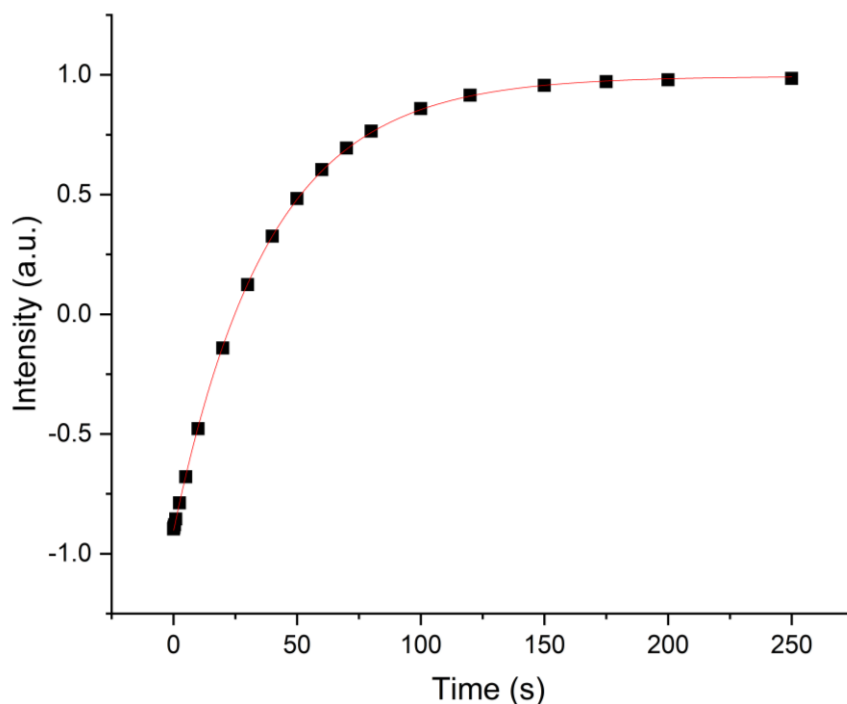


Figure 2.21: T_1 measured for H7 = 38.2 ± 0.2 s of T[2,3-*d*]P in the absence of a catalyst using inversion recovery (20 points).

Table 2.5: T_1 measurements for all resonances for T[2,3-*d*]P in the absence of a catalyst and with [IrCl(COD)(IMes)], [IrCl(COD)(*d*₂₂-IMes)], [IrCl(COD)(SIMes)], [IrCl(COD)(*d*₂₂-SIMes)], [IrCl(COD)(X)] and [IrCl(COD)(Y)]

Res (δ)	T_1 (s)						
	Sub. Alone	IMes	SIMes	<i>d</i> ₂₂ -IMes	<i>d</i> ₂₂ -SIMes	X	Y
H7 9.79	38.21 ± 0.18	7.28 ± 0.10	7.03 ± 0.10	9.22 ± 0.06	9.54 ± 0.13	9.61 ± 0.05	4.91 ± 0.08
H4 9.63	21.42 ± 0.09	5.13 ± 0.06	4.82 ± 0.06	5.77 ± 0.06	5.96 ± 0.06	6.45 ± 0.05	7.18 ± 0.11
H2 8.25	24.29 ± 0.14	7.50 ± 0.11	7.25 ± 0.11	7.26 ± 0.09	7.57 ± 0.11	9.25 ± 0.12	7.56 ± 0.13
H3 7.75	14.89 ± 0.24	4.64 ± 0.07	4.38 ± 0.03	4.68 ± 0.10	4.78 ± 0.05	5.56 ± 0.11	4.30 ± 0.03

Table 2.6 shows the tabulated T_1 values for [3,4-*d*]P, T[2,3-*c*]P, T[3,2-*c*]P with and without the four catalysts studied.

Table 2.6: T_1 measurements for T[3,4-*d*]P, T[2,3-*c*]P, T[3,2-*c*]P in the absence of a catalyst and with [IrCl(COD)(IMes)], [IrCl(COD)(*d*₂₂-IMes)], [IrCl(COD)(SIMes)] and [IrCl(COD)(*d*₂₂-SIMes)].

Substrate	Res. (δ)	T_1 (s)				
		Sub Alone	IMes	SIMes	<i>d</i> ₂₂ -IMes	<i>d</i> ₂₂ -SIMes
T[3,4- <i>d</i>]P	H3 9.40	25.86 \pm 0.17	5.44 \pm 0.07	5.67 \pm 0.04	6.98 \pm 0.06	6.83 \pm 0.05
	H2 8.58	29.10 \pm 0.21	9.41 \pm 0.10	9.69 \pm 0.09	10.94 \pm 0.11	11.74 \pm 0.10
T[2,3- <i>c</i>]P	H5 9.18	22.00 \pm 0.11	3.19 \pm 0.03	3.75 \pm 0.06	5.35 \pm 0.05	4.79 \pm 0.70
	H4 8.17	17.67 \pm 0.21	5.21 \pm 0.07	4.76 \pm 0.07	5.92 \pm 0.09	5.23 \pm 0.07
	H2 8.21	40.33 \pm 0.13	7.49 \pm 0.16	7.82 \pm 0.10	10.64 \pm 0.27	8.63 \pm 0.07
	H3 7.54	28.25 \pm 0.13	5.61 \pm 0.17	5.92 \pm 0.10	7.89 \pm 0.29	6.81 \pm 0.11
T[3,2- <i>c</i>]P	H6 9.14	17.91 \pm 0.08	2.9 \pm 0.05	2.87 \pm 0.04	4.19 \pm 0.10	3.56 \pm 0.05
	H7 8.41	20.58 \pm 0.06	4.96 \pm 0.07	4.33 \pm 0.15	6.44 \pm 0.01	5.01 \pm 0.17
	H2 8.24	26.72 \pm 0.03	6.36 \pm 0.08	6.91 \pm 0.07	8.02 \pm 0.06	7.30 \pm 0.06
	H3 7.86	25.72 \pm 0.06	4.32 \pm 0.03	4.73 \pm 0.03	6.02 \pm 0.08	5.50 \pm 0.03

The values show that the addition of the SABRE catalyst causes a vast reduction in the magnetic lifetime (from those measured with just the substrate alone); e.g. 38 to 7 s on H7 of T[2,3-*d*]P when using [IrCl(COD)(IMes)]. This is in agreement with all SABRE studies to date, demonstrating that the presence of the catalyst has a detrimental effect on the effective lifetimes of the proton resonances in the substrate.^{187, 201} In fact, the measured T_1 of the free substrate is actually a weighted average of the material in solution and that bound to the catalyst due to the exchange process.¹⁸⁷ If the catalyst could be removed after hyperpolarisation then the T_1 values would return to their original values recorded under thermal conditions.²⁰¹ This is explored in chapter five. There is a clear trend from the data in that the use of the deuterated catalysts extends the T_1 lifetime of all proton resonances e.g. 7 to 9 s on H7 of T[2,3-*d*]P when moving from [IrCl(COD)(IMes)] to [IrCl(COD)(*d*₂₂-IMes)] as the catalyst. Relaxation times of the bound substrate increases¹³⁶ which can be explained by a reduction in dipole-dipole relaxation in the active catalyst due to the presence of deuterium rather than protons. Due to the weighted averaging, the observed T_1 in the free material is also increased. While direct comparisons to other substrate systems in terms of enhancement are difficult the observed changes in T_1 values are in line with other studies reported in the literature.¹³⁵

2.4.5 Effect of Para-Hydrogen Pressure on SABRE Signal Enhancements

A study was carried out using T[2,3-*d*]P and [IrCl(COD)(*d*₂₂-SIMes)] (which have given the greatest enhancements to date) to confirm that using greater *p*-H₂ pressures would improve the

level of polarisation. As $p\text{-H}_2$ is a component of the catalytic process we can expect that during a standard SABRE experiment carried out at 3 bar(g) of pressure it is the limiting factor.¹³⁵ The productive catalytic cycle will eventually come to an end point when all of the $p\text{-H}_2$ has been converted to H_2 . To test this hypothesis, experiments were carried out changing only the pressure of the $p\text{-H}_2$ introduced into the standard 5mm J. Young tube to 4 bar(g) and 5 bar(g) with a constant exposure (shake) time of 10 seconds. The results should therefore reflect the increase in $p\text{-H}_2$ incorporation rate into the SABRE catalyst. The results shown in Figure 2.22 support the theory that an increase in $p\text{-H}_2$ pressure leads to a corresponding increase in SABRE enhancement.

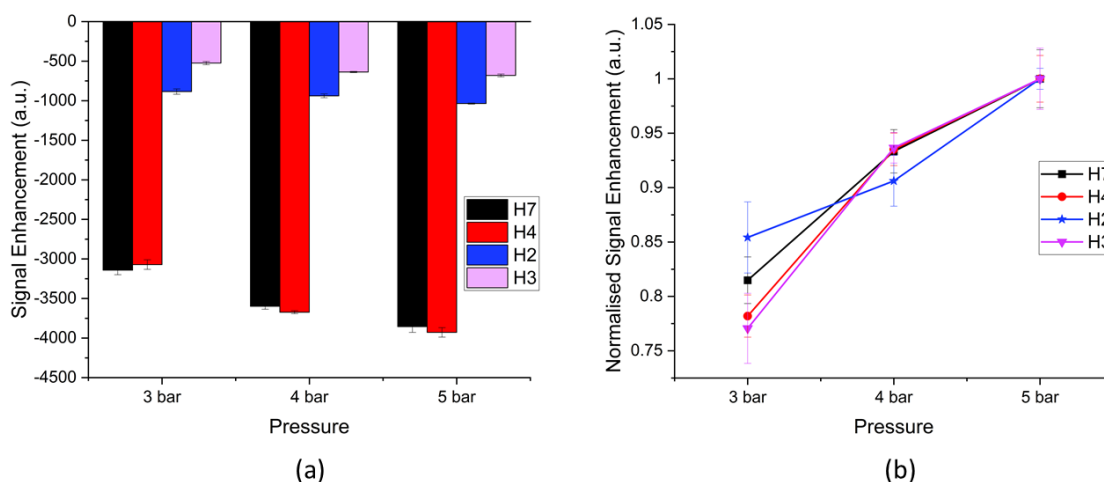


Figure 2.22: Effect on signal enhancement values when changing $p\text{-H}_2$ pressure. The substrate used was T[2,3- d]P and the catalyst [IrCl(COD)(IMes)] forming the active catalyst [Ir(H)₂(IMes)(T[2,3- d]P)₃]Cl. The solvent used was methanol- d_4 and measurements were made on a 400 MHz spectrometer at 298 K. (a) Signal enhancements values measured per individual proton with 3, 4 and 5 bar(g) of $p\text{-H}_2$ pressure. (b) Normalised signal enhancement values per proton showing a linear increase of enhancement with increased $p\text{-H}_2$ pressure.

Figure 2.22 b shows that increase in signal enhancement with $p\text{-H}_2$ pressure is independent of the proton site (with all normalised values within standard error at each pressure value) with a two bar decrease in pressure resulting in a 20% loss in signal enhancement across the substrate. It must be noted that using high pressures is not something that could be done on a routine basis as it is on the limit of safety standard for the glass 5mm tubes. The results show that there is a clear trend that with an increase in hydrogen pressure there is an increase in SABRE enhancements. One can hypothesise that if equipment allowed us to increase the pressure beyond 5 bar(g) there would be a corresponding increase in enhancement before a plateau at a given pressure at which point relaxation effects would dominate.

2.4.6 Use of Fully Deuterated Isotopologue of Thienopyridazine as a Co-ligand to Reduce Substrate Relaxation

Within the SABRE process there are three substrate molecules that bind to the iridium centre. Chapter one detailed that for symmetrical substrates only those in the equatorial plane, *trans* to the hydrides, receive polarisation through the scalar coupling network. The substrate in the axial plane, *trans* to the carbene, is unable to receive polarisation. In the case of asymmetrical substrates, the scalar coupling network also includes the carbene and the substrates in the axial position. In section 2.4.3 it was demonstrated that using selected deuteration of the carbene prevents spin dilution in the active SABRE catalyst and therefore the substrates in the equatorial plane of the SABRE active complex demonstrate higher polarisation. This phenomenon of reducing the spin dilution and increasing enhancements could also be applied to the substrates themselves. This has been demonstrated in previous studies using a fully deuterated isotopologue of the methyl nicotinate as a co-ligand.¹³⁵ It is hypothesised that the co-ligand, which cannot receive polarisation itself, statistically occupies two of the three possible binding sites. In this way the remaining protio substrate, *trans* to the hydrides, receives all the polarisation from the hydride ligands. In addition, the presence of the deuterated substrate may increase the relaxation times experienced by the protons in the active catalyst. Both effects would be expected to increase resultant proton polarisation over that achieved without the deuterated co-ligand. In the previous study an extremely high level of 50% polarisation was achieved in the H2 site of the selectively deuterated substrate methyl-4,6-*d*₂-nicotinate using a one to three ratio of substrate to co-ligand relative to the catalyst.¹³⁵

It was decided to test this hypothesis here by synthesising a fully deuterated version of T[2,3-*d*]P, *d*₄-thieno[2,3-*d*]pyridazine. It is noted that while polarisation of a single molecule may increase, dilution with the deuterated co-ligands may limit the advantages of this approach in terms of absolute signal gain.

2.4.6.1 Synthesis of a Deuterated Co-ligand, *d*₄-thieno[2,3-*d*]pyridazine

No known synthetic methodology for a fully deuterated T[2,3-*d*]P has been previously detailed. Hydrogen–deuterium exchange can easily occur with exchangeable protons with a suitable deuterium source such as D₂O.^{202, 203} To facilitate the exchange of non-exchangeable hydrogen atoms (such as those found in T[2,3-*d*]P), the use of acid, base or metal (Pd) catalysts, coupled with conditions of increased temperature and pressure, have been used (where the substrate is robust enough to the conditions and reagents employed).^{135, 136, 204, 205} As a first attempt, the

substrate was dissolved in an excess of D₂O in the presence of a base and refluxed. As shown in Figure 2.23 reflux in D₂O was carried out for a total of one month. The deuteration reaction was followed by LC-MS and additional D₂O and base were added accordingly. After one month, deuteration across the four positions had taken place to 95%. Despite this reaction being incredibly slow, it yielded the desired product in good yield and therefore no further optimisation was conducted.

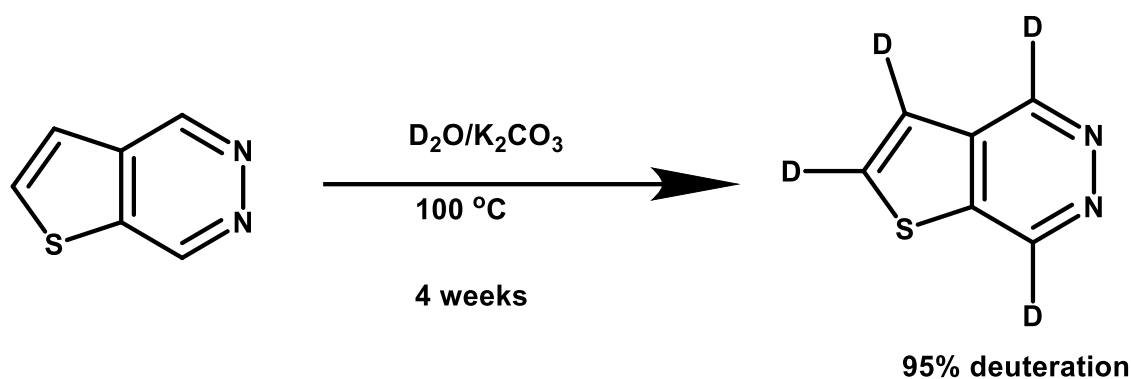


Figure 2.23: Reaction scheme for the synthesis of *d*₄-thieno[2,3-*d*]pyridazine (*d*₄-T[2,3-*d*]P)

2.4.6.2 Effect on Signal Enhancement Hyperpolarisation Levels using a Deuterated Co-ligand

SABRE shake and drop experiments were carried out under (i) standard conditions, i.e. 4.5 mM of [IrCl(COD)(*d*₂₂-SIMes)] in methanol-*d*₄ with four equivalents of T[2,3-*d*]P, 3 bar (g) H₂ and shaking in the stray field of the magnet; (ii) Using a co-ligand, i.e. 4.5mM of [IrCl(COD)(*d*₂₂-SIMes)] in methanol-*d*₄ with one equivalent of T[2,3-*d*]P and three equivalents of the deuterated co-ligand T[2,3-*d*]P-*d*₄ before shaking in the stray magnet field and (iii) using a co-ligand and a 60 G handheld magnetic shaker instead of shaking in the stray field.²⁰⁶

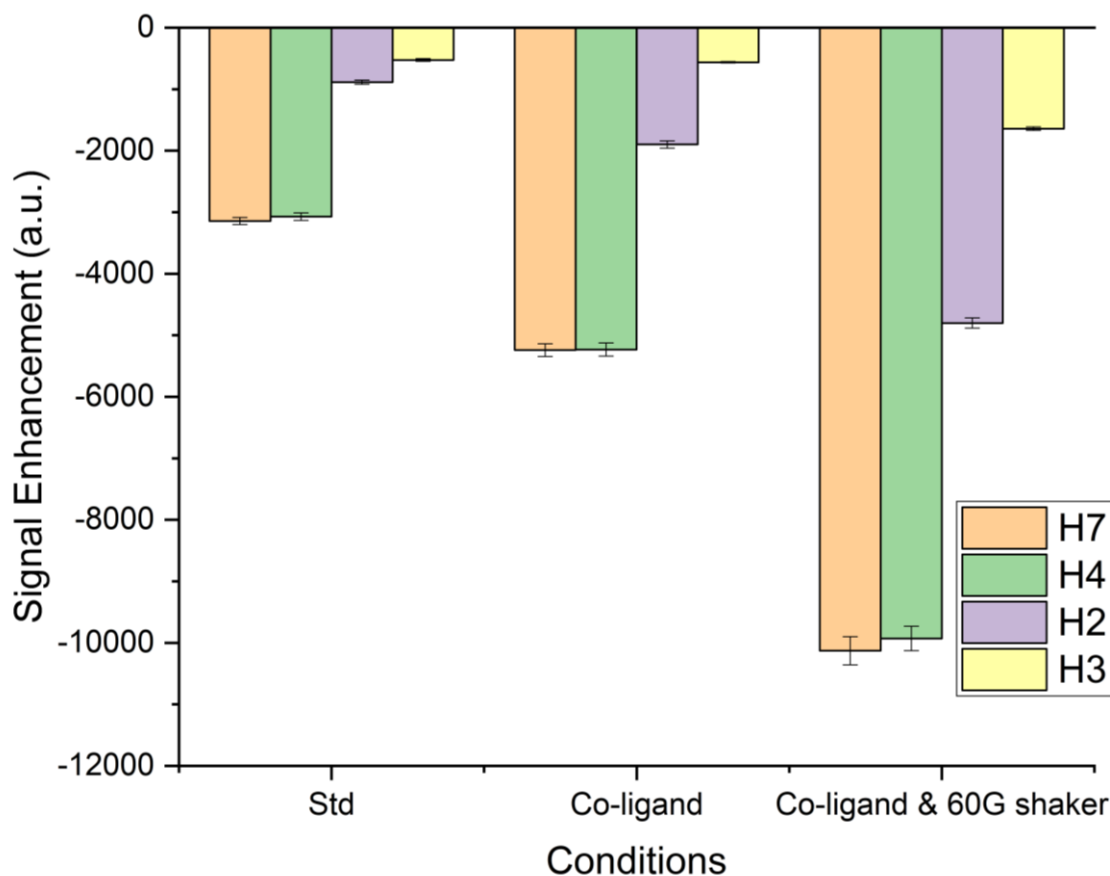


Figure 2.24: Bar chart to show increase in signal enhancement for T[2,3-*d*]P with the use of a co-ligand and the use of a co-ligand in combination with a 60 G handheld shaker.

The presence of a co-ligand allowed an increase (e.g., 66% on H7) in signal enhancement (-5240-fold for H7, 17% polarisation). As it was recognised that a variance in field occurs when shaking in the stray field of the magnet, a 60 G handheld magnet array shaker²⁰⁶ was employed resulting in a further increase (93% on H7) in signal enhancement of (-10,130-fold \pm 230 for H7, 33% polarisation). This resulted in a total increase of 223% in the level of signal enhancement seen for H7 from standard conditions to those using a deuterated co-ligand and 60 G handheld shaker. These implementations were the most successful in terms of optimisation steps.

2.5 Effect on SABRE Hyperpolarisation when Sulfur is replaced with Oxygen

As an extension to this work, it was decided to investigate the replacement of the sulphur atom with oxygen to form the corresponding furopyridazine to see how this would affect signal enhancement and T_1 values. As T[2,3-*d*]P was considered to be the most successful isomer in terms of both hyperpolarisation enhancement and length of magnetic lifetime it was decided to

carry out a direct comparison by synthesising the corresponding oxygen analogue, Furo[2,3-*d*]pyridazine, F[2,3-*d*]P, shown in Figure 2.25.

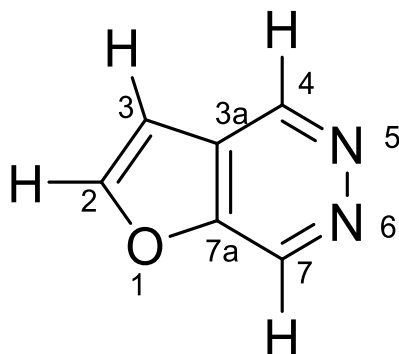


Figure 2.25: Chemical Structure of Furo[2,3-*d*]pyridazine, F[2,3-*d*]P

The aim was to investigate and compare how this change of atom could affect binding of the ligand to the catalyst, polarisation levels and magnetic lifetimes. In addition to understanding how a chemical change within a molecule can affect the SABRE process, the furopyridazine motif is also a feature in some antimicrobial drugs^{207, 208} and is therefore interesting when considering it as a possible *in vivo* imaging candidate.

2.5.1 Synthesis and Characterisation of Furo[2,3-*d*]pyridazine, F[2,3-*d*]P

A direct one-pot synthesis developed by Kessler *et al.* (2012) was followed for the synthesis of furo[2,3]pyridazine¹⁸³, F[2,3-*d*]P, as shown in Figure 2.26. The main step in their method was the transformation of an aromatic aldehyde into a directed ortho-metalation group (DMG). Usually an aldehyde is not classed as a DMG but when reacted with lithium amides, such as Lithium N,N,N'-trimethylethyldiamide (in step 1) they form α -aminoalkoxides which are moderate to good DMGs²⁰⁹. Lithium N,N,N'-trimethylethyldiamide was synthesised under nitrogen by dropwise addition of *n*-BuLi and N,N,N'-trimethylethyldiamine.

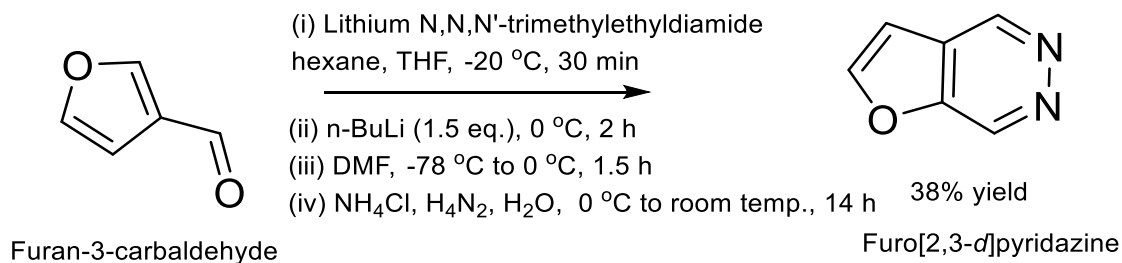


Figure 2.26: One-Pot synthesis of F[2,3-*d*]P using methodology by S. Kessler *et al.* (2012)

An additional purification step was required after column chromatography due to remaining impurities determined by NMR. A 38% yield of F[2,3-*d*]P was achieved after recrystallisation

using hexane. The purity was confirmed via ^1H NMR, MS and IR. ^1H NMR peaks at δ 9.62, 9.59, 8.25 and 7.1 ppm in Figure 2.27 arise from the four proton resonances in F[2,3-*d*]P. The additional purification step required could explain the lower yield achieved compared with the quoted literature value of 55%.

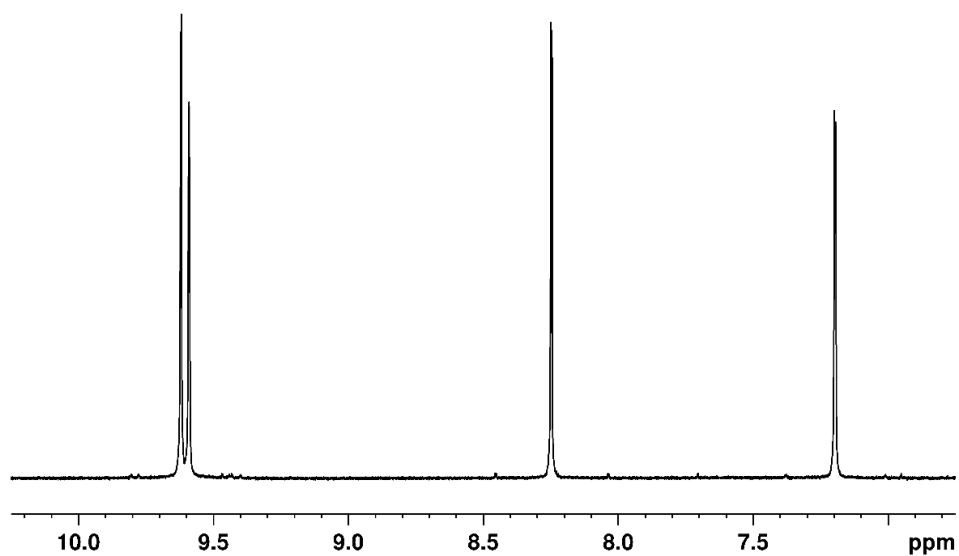


Figure 2.27: ^1H spectrum of Furo[2,3-*d*]pyridazine in methanol- d_4 after recrystallization with hexane.

Characterisation of furo[2,3-*d*]pyridazine was carried out in methanol- d_4 using a combination of 1D and 2D (COSY, NOESY, HMQC) NMR experiments. The ^1H , ^{13}C and ^{15}N chemical shifts are detailed in Table 2.7.

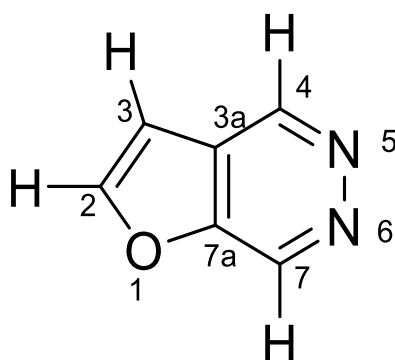


Table 2.7: Table of NMR ^1H , ^{13}C and ^{15}N resonances for F[2,3-*d*]P dissolved in methanol- d_4 (500 MHz spectrometer).

Res. No.	^1H - NMR (ppm)	^{13}C - NMR (ppm)	^{15}N - NMR(ppm)
2	8.25, d, $J_{\text{HH}} = 2.14$ Hz	150.1	
3	7.19, dd, $J_{\text{HH}} = 2.14$ Hz, 0.94Hz	104.7	
3a		126.7	
4	9.59, pseudo dd, $J_{\text{HH}} = 0.97, 1.29$ Hz	137.7	
5			367.3
6			362.7
7	9.62, d, $J_{\text{HH}} = 1.5$ Hz	146.7	
7a		153.2	

2.5.2 Optimisation and a Comparison of Signal Enhancement Levels

A shake and drop experiment carried out in methanol- d_4 with $[\text{IrCl}(\text{COD})(\text{IMes})]$ (4.5 mM), four equivalents of F[2,3-*d*]P and 3 bar(g) of *p*- H_2 revealed an increase in signal enhancement compared with T[2,3-*d*]P (e.g. -2609 ± 60 and -2150 ± 67 respectively for position H7). Using the optimum catalyst for T[2,3-*d*]P, $[\text{IrCl}(\text{COD})(d_{22}\text{-SIMes})]$, not only gave greater enhancements for F[2,3-*d*]P compared with the $[\text{IrCl}(\text{COD})(\text{IMes})]$ (e.g. -3470 ± 59 and -2609 ± 60 respectively for position H7) but also showed greater signal enhancements than T[2,3-*d*]P under the same conditions (e.g. -3470 ± 59 and -3142 ± 58 respectively for position 7), as can be seen in Figure 2.28.

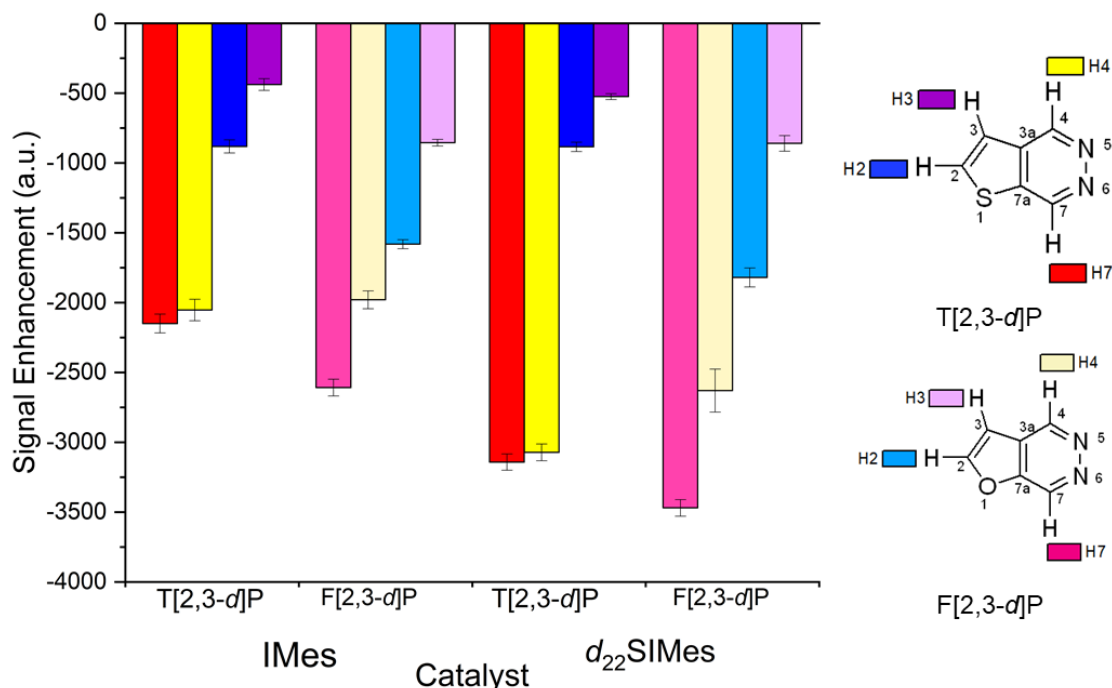


Figure 2.28: A comparison of the two substrate; T[2,3-*d*]P and F[2,3-*d*]P with the [IrCl(COD)(IMes)] catalyst and [IrCl(COD)(d_{22} SIMes)].

In the case of T[2,3-*d*]P, the levels of signal enhancement on protons 4 and 7, those with 4J coupling to the hydrides, appear to receive similar polarisation, with H7 having a slightly increased level over H4 (e.g. -3142 ± 58 for H7 and -3072 ± 60 for H4 with [IrCl(COD)(d_{22} SIMes)]). However, in F[2,3-*d*]P, the difference in polarisation levels in the corresponding H4 and H7 positions show a more significant bias towards H7 (e.g. -3470 ± 59 for H7 and -2630 ± 154 for H4). This phenomenon could be explained in terms of the electronegativities of the atoms involved (Figure 2.29). In T[2,3-*d*]P, sulfur has the same electronegativity value as carbon ($\chi = 2.5$ on the Pauling scale). However, in the case of F[2,3-*d*]P, oxygen has a higher electronegativity value ($\chi = 3.5$). It is hypothesised that during the haptotopic shift between the two nitrogens that with the presence of the more electronegative oxygen there is a preference to spend longer on N6 than N5 and this is why H7 receives more polarisation. It could also be explained in terms of an increase in exchange rate due to the electronegativity of the oxygen.

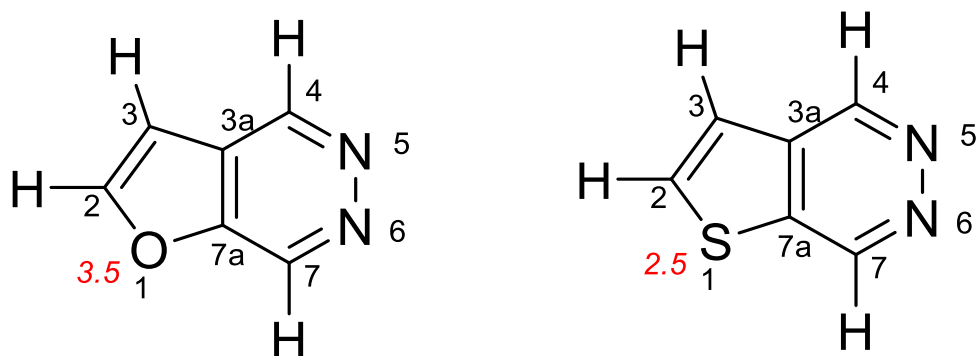


Figure 2.29: Furo[2,3-*d*]pyridazine and thieno[2,3-*d*]pyridazine with the respective electronegativity values of oxygen and sulphur shown in red italics

As in the case of T[2,3-*d*]P, shake and drop SABRE experiments were carried out on F[2,3-*d*]P to investigate the effect on signal enhancement levels when increasing the *p*-H₂ pressure. The results show even with an increase in pressure from 3 bar(g) to 4 bar(g) (Figure 2.30 spectra and Figure 2.31) there was a considerable increase in the overall polarisation levels (-3470 ± 59 and -4617 ± 147 for H7 respectively). Although F[2,3-*d*]P has not been tested with 5 bar(g), it would be expected that the trend would continue and further increases in enhancement levels should be achievable. F[2,3-*d*]P shows a better pressure response than T[2,3-*d*]P as an increase from 3 to 4 bar results in a 33% increase in signal enhancement compared with 16%.

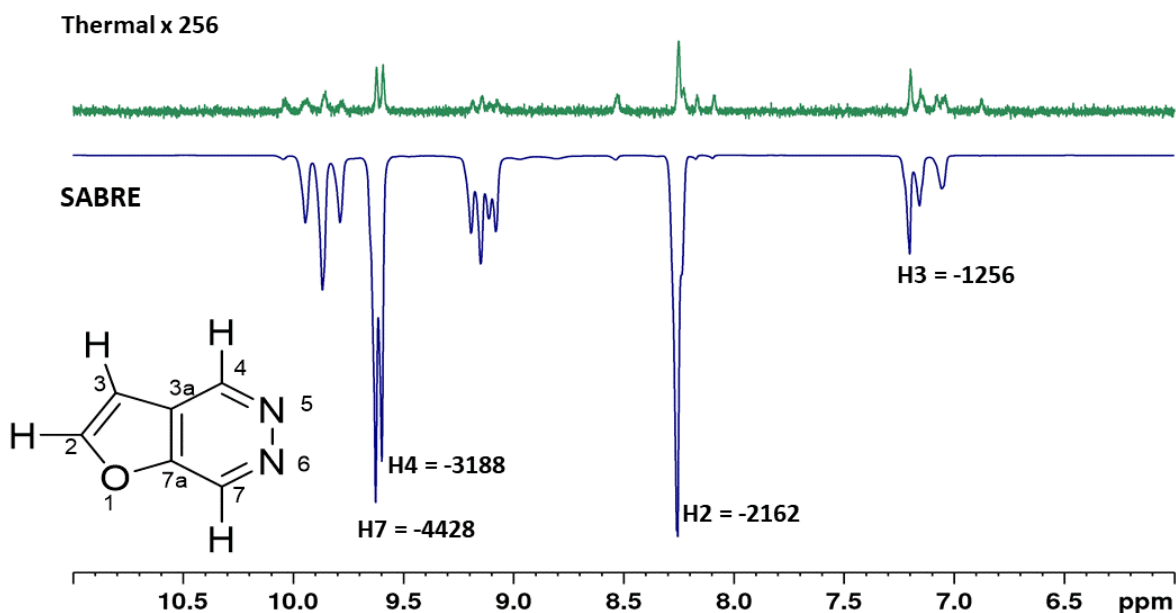


Figure 2.30: A comparison of a ¹H spectrum of F[2,3-*d*]P and [IrCl(COD)(*d*₂₂-SIMes)] in a 4 to 1 ratio at thermal equilibrium (vertically magnified 256 times) (in green) and under SABRE conditions at 4 bar(g) of *p*-H₂ (blue)

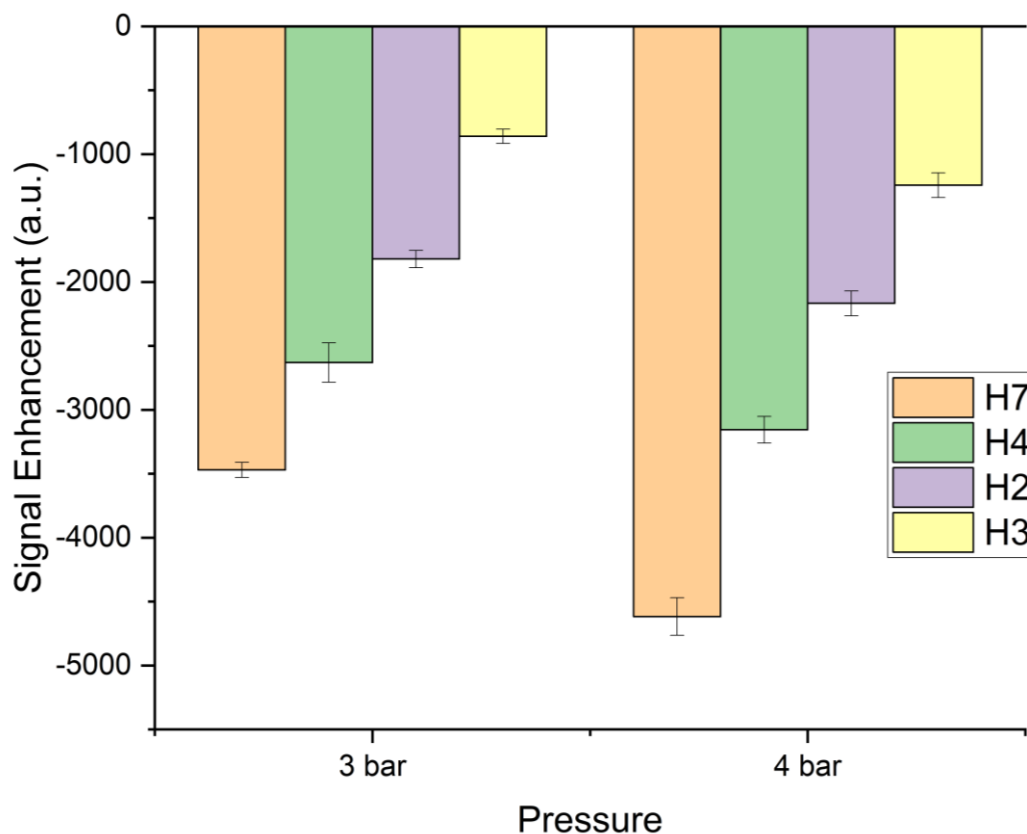


Figure 2.31: Increase in signal enhancement of the four proton resonances of F[2,3-*d*]P with [Ir(COD)(*d*₂₂-SIMes)Cl] in a 4 to 1 ratio in methanol-*d*₄ with a change in pressure from 3 bar(g) to 4 bar(g)

2.6 Conclusions and Discussions

In this chapter, the multistep synthesis of the thienopyridazine agents/substrates was discussed (section 2.2) and T[2,3-*d*]P, T[3,4-*d*]P, T[2,3-*c*]P, T[3,2-*c*]P were synthesized in good yields by adapting two methodologies. Characterisation of the species created during the SABRE catalytic cycle with T[2,3-*d*]P were described, both in terms of the inactivated pre catalyst and subsequent intermediate complexes upon activation. In both cases complex spectra resulted. On cooling it was found that in both the precatalyst and the intermediate, two different forms of the SABRE complexes were present. This was dependent on which nitrogen was bound to the iridium metal centre and confirmed that a haptotropic shift was occurring at 298 K. Analysis of the respective peak integrals showed that the forms were present in equal proportion.

SABRE performance was evaluated (section 2.4) and all four thienopyridazines showed high levels of signal enhancement compared with those found under thermal conditions. The optimum conformation for the greatest SABRE signal enhancements was found to be the T[2,3-*d*]P arrangement.

Several optimisation steps were investigated to increase SABRE ^1H signal enhancement. Substrate loading studies revealed the optimum catalyst to substrate ratio was shown to be 1:4 with a linear decrease with increase in concentration. This is in agreement with theoretical models.¹⁸⁷

When the PTF of each of the thienopyridazines were investigated all four substrates demonstrated maximum polarisation transfer at ~ 60 G. In the $-d$ conformation the field plot showed a single Gaussian distribution from 0 to 140 G with one maximum peak at 60 G indicating one mechanism of polarisation transfer through 4J coupling. The $-c$ conformation exhibited a more complicated pattern where the data was fitted to three Gaussians and where three maxima were measured at ~ 13 G, 60-65 G and ~ 110 G. It was interpreted that three different polarisation transfer pathways were at work.

When the identity of the carbene backbone was changed to vary the lifetime of the active complex, it was the more flexible, sterically bulky SIMes, which consistently gave the highest signal enhancements across the substrate range. Although it is unusual for $[\text{IrCl}(\text{COD})(\text{SIMes})]$ to be the better mediator of polarisation transfer compared with $[\text{IrCl}(\text{COD})(\text{IMes})]$, there have been other rare examples where this is the case.¹⁹⁰

Deuteration of the catalyst resulted in both improved signal enhancements and longer T_1 values consistent with less spin dilution and reduced dipole-dipole relaxation respectively due to the presence of deuterium. Observations from NMR spectra revealed that considerable polarisation is measured in the bound ligands. Optimal conditions would require that the bulk of the polarisation be transferred to the free ligands. The use of the unsaturated SIMes catalyst has made significant improvements within all substrates studied in this project to date. From previous studies,¹²¹ SIMes is known to have a faster rate of exchange compared with its unsaturated analogue. It can be hypothesised that a catalyst that provides an even greater rate of exchange could result in more of the polarisation building up in the free substrate in solution and less polarisation being measured on the bound substrate. Further catalyst design in the future using the SIMes backbone may allow even greater polarisation levels to be achieved.

Maximum ^1H longitudinal (T_1) lifetimes was found in T[2,3-*d*]P to be 38 s (H7 without catalyst) and 10 s (H7 with catalyst). $p\text{-H}_2$ pressure proved to be the limiting factor in the catalytic cycle. Increases in gas pressure results in a linear increase in signal enhancement (e.g. -3142 ± 57 at 3

bar (g), -3599 ± 36 at 4 bar (g) and -3856 ± 73 at 5 bar (g) in T[2,3-*d*]P). This supports theoretical predictions.¹⁸⁷

A novel, fully deuterated version of T[2,3-*d*]P was synthesised and employed as a co-ligand in a 1:3:1 catalyst to co-ligand to substrate ratio to afford higher signal enhancements (66% increase). The co-ligand does not receive polarisation itself and therefore focusses the polarisation on the ¹H-sites of the one protio substrate in the active SABRE catalyst. Although signal enhancement was increased per protio substrate, absolute signal gain is not increased due to the reduction in concentration of NMR visible protons. If it were possible to extract the highly polarised protio molecules to form a concentrated sample, then this would be beneficial but as yet this is not technically feasible. The deployment of handheld magnetic shakers tuned to a specific field (~60 G) allowed for greater mixing of *p*-H₂ in solution and a much more accurate PTF to facilitate optimum polarisation transfer and consequently 93% higher signal enhancements.

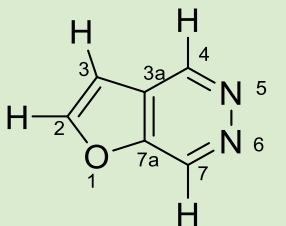
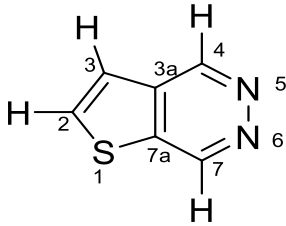
A final study (section 2.5) showed the successful one-pot synthesis with the furo-derivative, F[2,3-*d*]P. SABRE enhancements proved to be even greater than those found in T[2,3-*d*]P (21% on H7). Increased signal enhancements were also observed with the change of catalyst from [IrCl(COD)(IMes)] to [IrCl(COD)(*d*₂₂-SIMes)] (33% on H7) and with increase in *p*-H₂ pressure from 3 bar(g) to 4 bar(g) (33%). F[2,3-*d*]P shows a better pressure response than T[2,3-*d*]P as an increase from 3 to 4 bar results in a 33% increase in signal enhancement compared with 16%. Thermal *T*₁ values for F[2,3-*d*]P were longer than T[2,3-*d*]P (H7 = 38 ± 1 s, H4 = 6 ± 1 s, H3 = 39 ± 1 s and H2 = 29 ± 1 s).

It has been demonstrated that all of the four synthesised thienopyridazines and furopyridazine are SABRE active and bind through the nitrogen atoms. Although sulphur and oxygen have been shown to bind to iridium in other substrates such as methanol and DMSO¹⁸⁶, there is no evidence of this in the thienopyridazines and furopyridazine. It can be concluded that nitrogen atoms have a much preferable binding affinity for the iridium than sulphur and oxygen in these molecules.

In each case, hydrides appeared as overlapping signals in only one region of the spectrum at δ -21.5 indicative of binding through nitrogen. Due to the presence of adjacent nitrogen nuclei, these molecules exhibit the ability to perform a haptotropic shift with the iridium metal centre and consequently provides two possible pathways of polarisation transfer through ⁴*J* coupling to the hydrides.

In conclusion both the thienopyridazines and furopyridazines are promising candidates for SABRE hyperpolarisation. Combined with their biological activity they present as interesting SABRE hyperpolarised probes to observe disease state in real time through MRS(I). However, it is acknowledged that the short T_1 times, in the presence of the heavy metal catalyst, present a limitation for such application. To address the limitations of T_1 , chapter three will investigate the phenomenon of long-lived singlet states to store hyperpolarisation and extend magnetic lifetimes. It has been demonstrated that molecules, which exhibit pairs of neighbouring nuclei sharing a mutual J coupling and a small chemical shift difference, can be manipulated using RF and changes in field to form pseudo singlet states with an increased lifetime over T_1 .²¹⁰⁻²¹⁴ When examining the chemical shift difference of proton, carbon and nitrogen pairs within T[2,3-*d*]P and F[2,3-*d*]P it is clear that T[2,3-*d*]P is the more favourable of the two as can be seen by the values shown in Table 2.8. It is for this reason and that fact that T[2,3-*d*]P is the target molecule of this study (anti-cancer properties) that despite the slightly higher signal enhancements and longer T_1 times achieved with F[2,3-*d*]P, T[2,3-*d*]P was taken forward for singlet state studies in chapter three.

Table 2.8: Chemical Shift difference of neighbouring ^1H , ^{13}C and ^{15}N nuclei in F[2,3-*d*]P and T[2,3-*d*]P

Substrate	$\Delta\delta$ ^1H (ppm)	$\Delta\delta$ ^{13}C (ppm)	$\Delta\delta$ ^{15}N (ppm)
	H2-H3 = 1.1 ppm	C3a-C7a = 26.5 ppm	N5-N6 = 4.6 ppm
	H2-H3 = 0.50 ppm	C3a-C7 = 3.0 ppm	N5-N6 = 0.7 ppm

As indicated throughout the chapter, methanol- d_4 was used as the solvent of choice to facilitate SABRE; however, it is a clear that this solvent cannot be used *in-vivo* applications. Chapter five shows the challenges involved in transferring these optimised results of T[2,3-*d*]P into a solvent system, which is amenable for *in vivo* use. It is noted that F[2,3-*d*]P is much less soluble in water than T[2,3-*d*]P and is another reason why this substrate was not investigated further.

Chapter 3: Investigation of Long-Lived Singlet States

3.1 Introduction

Translation of SABRE hyperpolarisation from benchtop to clinical MRI remains a major research aim of the Centre for Hyperpolarised Magnetic Resonance. ^1H NMR signals of up to 60% 135 ^1H magnetic state purity have been recorded using the SABRE technique; but these are transient signals which decay exponentially with time as the nuclear spins relax back to thermal equilibrium. This lifetime is characterised by the time constant T_1 , known as the longitudinal, or spin-lattice, relaxation time constant. For many molecules amenable to the SABRE technique, the ^1H T_1 is on the order of seconds, although for X-nuclei it can be longer. The decay of polarisation is important as it limits the period available for subsequent MR detection and thus needs to be overcome when considering the creation of sustainable hyperpolarisation for use *in vivo*.

Chapter 2 described the optimisation steps needed to increase overall SABRE hyperpolarisation of the target thienopyridazines. Polarisation levels of up to 30% were described for T[2,3-*d*]P. However, the short T_1 's reported (~ 9 s in the presence of the catalyst) limit the window over which they can be detected. Final signal detection (as a function of this time-based decay) in the clinical domain is reduced, due to the need for quality control processes, and subsequent transport to the patient for *in vivo* injection. Despite these delays, the T_1 value of the carbonyl carbon in pyruvate (~ 60 s *in vitro*,²¹⁵ 30-40 s *in vivo*^{72, 97}) is sufficient (with 20% polarisation) for detection *in vivo* by ^{13}C dissolution-DNP-MRS. Such existing DNP based frameworks give a benchmark for the likely requirements for successful *in vivo* SABRE hyperpolarised biomolecule detection.

This chapter concentrates on exploring long-lived singlet state (LLS) methods^{210-212, 216, 217} to extend nuclear spin state lifetimes. The theory behind generation of LLS is given in section 3.2. ^1H LLS in the pyridazine motif (Figure 3.1a), are first investigated in the context of a simplified proof of principle model (section 3.3). Once the formation of a LLS has been established in this simple model, application to the more complex thienopyridazines (Figure 3.1b) is investigated (section 3.4). The pair of quaternary carbons, fusing the two rings and the two adjacent nitrogen nuclei in the parent pyridazine ring, are identified as potential targets for ^{13}C and ^{15}N LLSs. Section 3.5 therefore, investigates SABRE polarisation potential of these sites. Imaging of these nuclei would have the benefit of high contrast-to-noise ratios and no background signal.²¹⁸ ^{13}C hyperpolarised MRS is already used clinically⁴ and imaging of ^{15}N has also been proved possible pre-clinically.²¹⁹ Synthetic strategies are investigated to create a ^{15}N labelled version of

thienopyridazine with the aim of improving ^{15}N LLS signal detection and to aid in the full characterisation of the complexes formed. A final study involves the synthesis of a fully deuterated ^{15}N version of thienopyridazine with the aim of limiting T_1 relaxation, thus extending signal lifetimes.

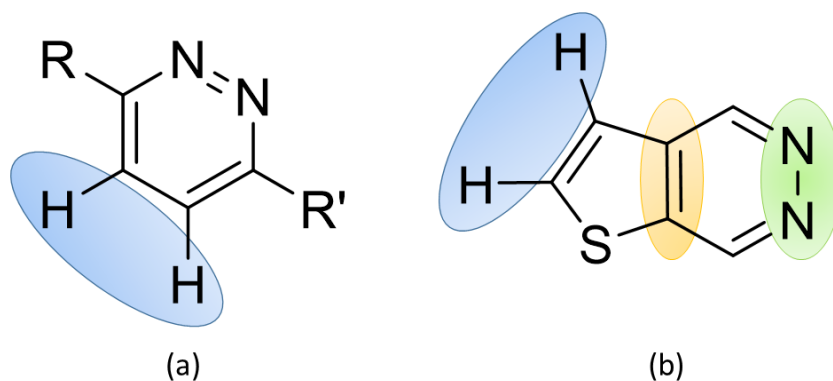


Figure 3.1: Pyridazine based molecules used to study long-lived states. (a) ^1H pairs (blue) targeted for the LLS in 3,6-disubstituted pyridazines where $\text{R} = \text{Cl}$ and $\text{R}' = \text{NH}_2, \text{OCH}_3, \text{CF}_3$ (section 3.3) (b) the ^1H pairs (blue) (section 3.4), ^{13}C pairs (orange) and ^{15}N pairs (green) shown are suitable targets in thienopyridazine (section 3.5).

3.2 Theory of Long-Lived Singlet States

The concept of long-lived nuclear singlet states was introduced in the context of *o*- H_2 and *p*- H_2 in chapter one. For two nuclear spins that are coupled, singlet and triplet spin order can occur. The triplet spin isomer (e.g., *o*- H_2) has total angular momentum, $I = 1$ and as such, in the presence of a magnetic field, the angular momentum projection along the z axis can have three values $m_I = -1, 0$ and $+1$. These three energy eigenstates are degenerate at zero field. When placed in a magnetic field the different states separate, with the energy difference increasing with increasing field (Figure 3.2). For *o*- H_2 , transitions between these energy states gives rise to a single NMR peak at δ 4.5 ppm. Due to the transitions being of identical energy, the scalar J coupling is unobservable.

In contrast, the singlet state (e.g., *p*- H_2) is non-magnetic, meaning its energy is independent of magnetic field (total angular momentum, $I = 0$). Transitions between the singlet state and the triplet manifold are symmetry forbidden. True singlets like *p*- H_2 are therefore ‘NMR silent’.

To help understand how singlet states can help prolong hyperpolarisation signals one must first appreciate the different signal relaxation mechanisms.

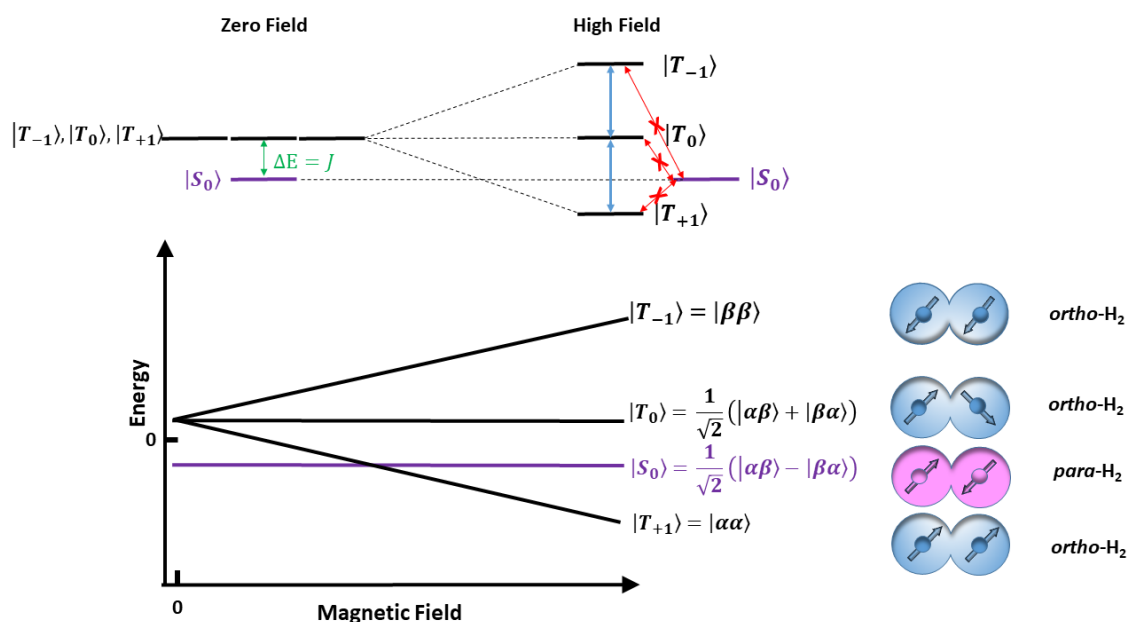


Figure 3.2: Energy levels of the spin states of *ortho* and *para*-spin isomers of hydrogen and their magnetic dependence. The blue arrows indicate the allowed transitions between the triplet states and the red arrows indicate the forbidden transitions between the singlet and the triplet energy states.²²⁰

3.2.1 NMR T_1 Relaxation

When a non-equilibrium state is created (by excitation with a radio frequency pulse in an NMR experiment) the excited spins decay back to thermal equilibrium. This is known as longitudinal relaxation. The decay is described by a time constant, T_1 . Mechanisms of longitudinal relaxation include i) Dipole-dipole; ii) Spin rotation; iii) Chemical Shift Anisotropy; and iv) Paramagnetic interactions.

- Dipole-Dipole Relaxation

In chapter one a nuclear spin was conceptually described as a tiny magnet with a north and south pole (a dipole) creating an electromagnetic field. A dipole-dipole interaction results when two of these nuclei are located less than 6 Angstroms apart. In the liquid phase, the dominant nuclear relaxation mechanism is due to inter-nuclear Dipole-Dipole (DD) couplings that evolve through random molecular motion. This interaction is inversely proportional to the sixth power of distance between the dipoles. Hence, intramolecular DD coupling is much stronger than the corresponding intermolecular effect. This is the main relaxation mechanism responsible for T_1 relaxation.

- Spin rotation

Spin rotation relaxation occurs when the nuclear spins within a molecule interact with the local magnetic fields caused by the rotational angular momentum of the molecule.^{138, 221, 222} The effect is therefore highly dependent upon molecular symmetry.

- Chemical Shift Anisotropy

Relaxation due to chemical shift anisotropy (CSA) occurs due to fluctuations in the anisotropic chemical shift interaction which each spin experiences through incoherent motion. CSA relaxation is proportional to the square of the magnetic field strength (B_0^2) therefore this mechanism of relaxation is more important at higher fields. CSA effects also depend upon molecular symmetry.

- Paramagnetic Relaxation

Paramagnetic effects concern unpaired electrons, which have magnetic moments that are 658 times bigger than a proton nucleus. Paramagnetic effects on nuclear spins are dramatic and often rapid relaxation ensues. In the context of *p*-H₂, paramagnetic effects provide a route to break the symmetry of H₂ when interacting with a surface. Breaking of symmetry allows interconversion between otherwise forbidden transitions, and therefore it is easier for the system to lose energy and T_1 is reduced. Singlet states have been shown to be between two and three times less sensitive to paramagnetic relaxation than conventional nuclear magnetisation.²²³

Within the triplet manifold, dipole-dipole interactions are the dominant relaxation mechanism and the measurable signal returns to thermal equilibrium quickly ($T_1 \sim 9$ s for the target thienopyridazines, in the presence of the catalyst). For singlet states there is no role for intra-nuclear dipole-dipole coupling. Direct decay (dependent upon molecular symmetry) primarily only occurs through spin rotation, chemical shift anisotropy and paramagnetic interactions. However, singlet-triplet interconversion (although spin forbidden and hence slow) exchanges spin population from the singlet state to the triplet state from where it can rapidly decay (via dipole-dipole interactions). The overall decay of the singlet state is defined by the time constant T_S and this is much longer than T_1 .

For symmetric molecules like H₂, spin rotation and CSA do not affect relaxation. As such, *p*-H₂ has a lifetime on the order of months compared with a few seconds in *o*-H₂. In molecules with

less symmetry than H_2 , spin rotation relaxation and CSA can shorten T_S to the order of 100s of seconds. However, this will still be longer than the T_1 . Hence, spin population transition into the singlet state presents as a promising route to store hyperpolarisation.

There are, however, two major limitations. The number of molecules with pairs of isolated chemically equivalent spins like $p\text{-H}_2$ is limited. Secondly, with precisely symmetrical spins, the lack of interaction with the field means that the signal from the ‘protected’ singlet state cannot be observed with standard NMR unless the field breaks the symmetry between the spins. There is now a growing field in NMR accessing pseudo-singlet states. A pseudo-singlet state describes when singlet order is imposed (via field cycling or spin locking – see 3.2.2) upon a pair of nuclei which are not isolated but are near chemical equivalence. When under singlet order, a population difference exists between the states of this nuclear pair (i.e., with higher population enforced in singlet than triplet state). Akin to any singlet state, slow singlet-triplet conversion means the system will exhibit a longer magnetic state lifetime. Thus, magnetisation is stored. Importantly here, the ordering process is reversible, and the system can return to a normal state (with triplet population) to be observed when required.

3.2.2 Singlet State as a store of polarisation

In 2004, Levitt *et al.*^{210, 211} pioneered the use of singlet states to store polarisation. It was stated that to create a long-lived pseudo singlet state a molecule must contain a pair of spin $\frac{1}{2}$ nuclei (of the same isotopic type), a difference in chemical shift, $\Delta\delta$, and a mutual scalar coupling, J . In this case the pseudo-singlet state is not an eigenstate and as such without intervention would evolve into states prone to T_1 relaxation mechanisms. The decay of such states can be described by the time constant T_{LLS} .

At high field, a pair of spins that have different chemical shifts are described classically as ‘weakly coupled’, or an AX system (i.e., if chemical shift differences are large compared to the coupling between them, $\Delta\delta > J$). The two spins are said to be far from equivalence. If these spins are then forced into a pseudo-eigenstate, for example by moving them to low field (where $\Delta\delta$ is reduced) they become ‘strongly coupled’. In this regime their resonances overlap and so can be described more appropriately as being near to equivalence. The spins begin to resemble an AA’ system (i.e., the nuclei are chemically equivalent but are not magnetically equivalent) and form a pseudo-singlet state. This state negates dipole-dipole relaxation preserving the signal from associated fast T_1 decay.²¹¹ After a period of time the system is returned to high field for NMR observation.²¹¹

^{216, 224} This AX to AA' to AX system behaviour is exploited in a field cycling singlet state experiment (Figure 3.3a).

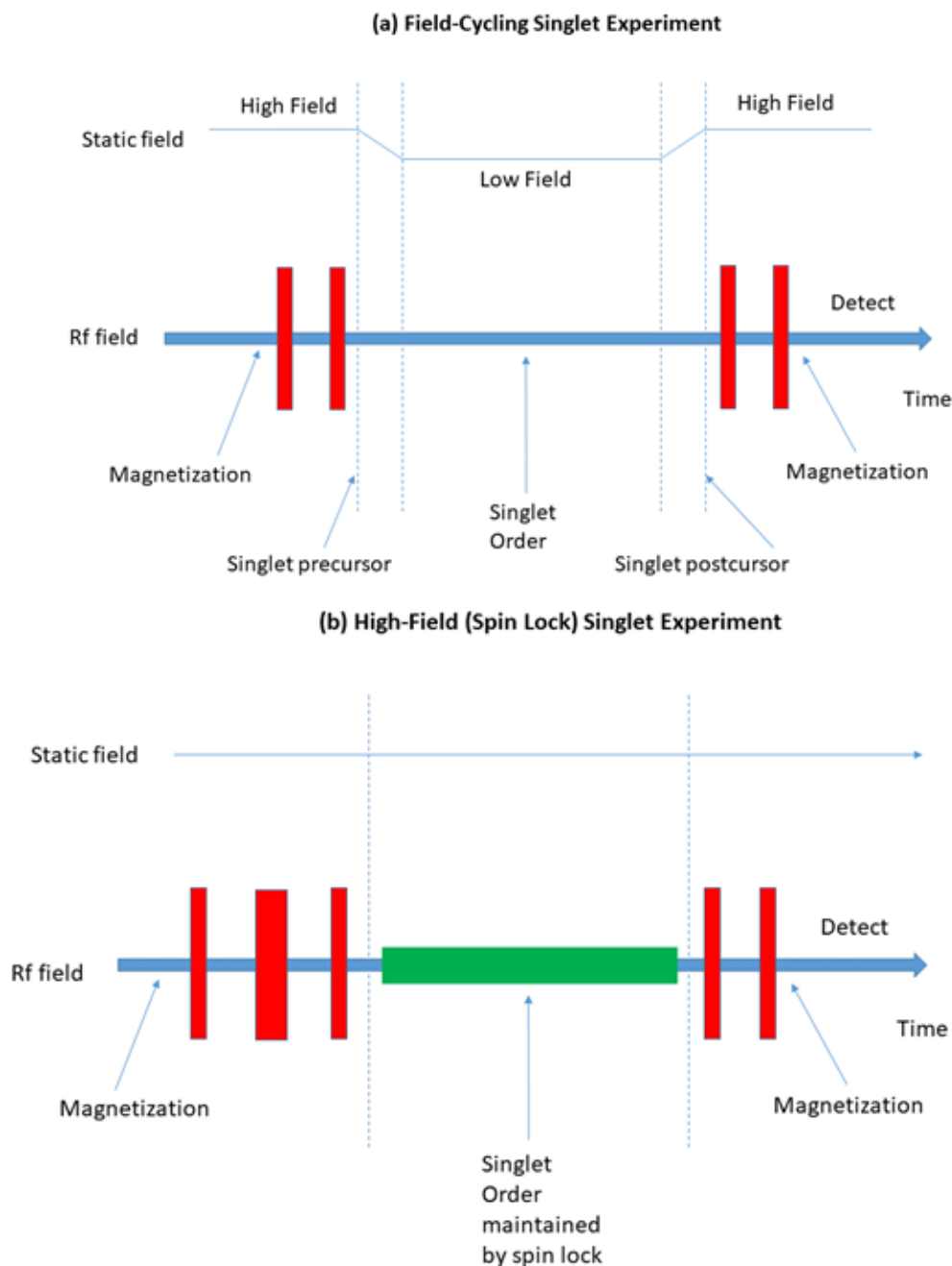


Figure 3.3: a) Pulse sequence in the field-cycling singlet experiment. b) Pulse sequence in the high field (spin lock) singlet experiment.

For ‘weakly coupled’ systems a pseudo singlet state can also be achieved via multiple spin echoes; known as a spin locking technique^{210, 217}(Figure 3.3b). The train of spin echoes effectively removes the frequency difference between the spins causing them to have near equivalence. The system demonstrates AA' behaviour, thereby preventing singlet-triplet transitions.²¹⁰

Symmetry switching can be achieved through either a chemical reaction²²⁵ (utilised to change the electronic environment of the nuclei), or by changing the magnetic field (Figure 3.4 b). Symmetry switching in SABRE uses both a chemical reaction (catalysis) and changes in magnetic field (polarisation transfer ~6 mT to measurement field 9.4 T).

In summary, a typical LLS experiment involves three stages; preparation, storage of the singlet and observation (as illustrated in Figure 3.4a²¹²). In stage one, the symmetry of the pair of nuclei is broken so that singlet-triplet transitions are allowed. Through specific RF excitation (coupled with evolution under chemical shift and J -coupling) transitions create a population imbalance between $\alpha\beta$ and $\beta\alpha$ spin states (Figure 3.5). In stage two, symmetry is imposed to prevent singlet-triplet transitions. This can be achieved by lowering the field or through spin locking (see above). The “protected” singlet order then decays with a time constant T_{LLS} . This is longer than the longitudinal relaxation time constant T_1 ,^{224, 226} helping preserve polarisation for longer. In stage three, the symmetry is broken again to restore singlet-triplet transitions and an NMR signal can be observed.

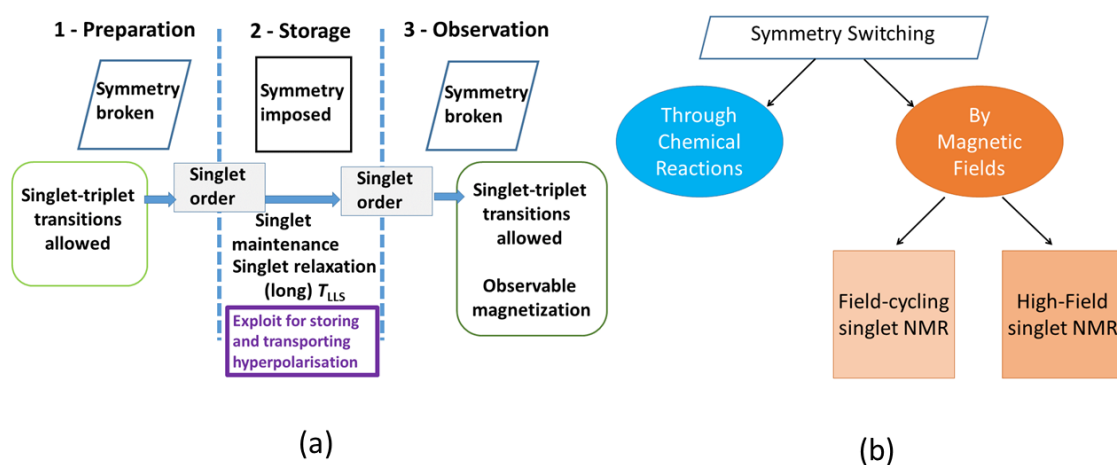


Figure 3.4: a) Typical stages of an NMR experiment to create singlet order, b) methods to perform the symmetry switching (i) through chemical reactions (ii) by magnetic fields

Longer lifetime nuclear singlet order has been exploited in various different fields such as geometry determination to detect protein folding and unfolding²²⁷; to observe molecular diffusion²²⁸ but arguably the most promising application of singlet NMR is to extend the lifetime of nuclear spin hyperpolarisation produced by PHIP, in the form of SABRE^{147, 168, 229-231}, and dissolution-DNP.¹³⁸

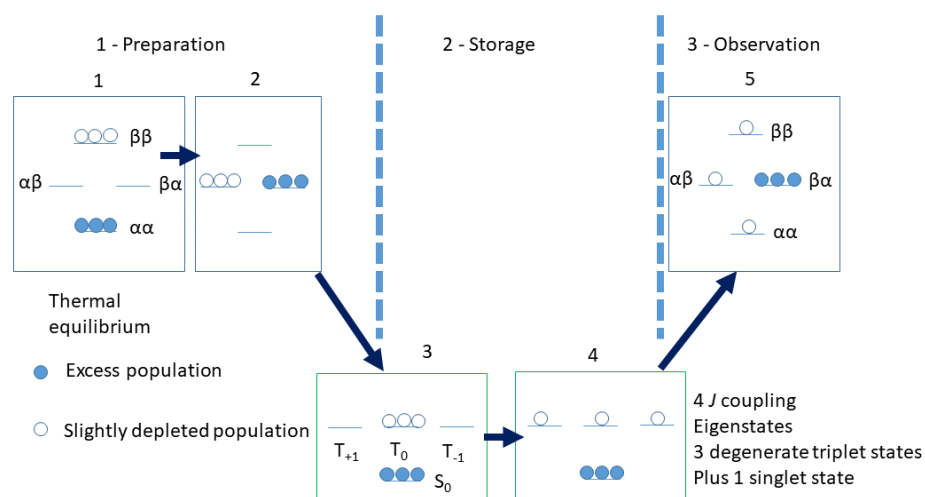


Figure 3.5: Diagram to show how spin populations are manipulated during the field-cycling singlet creation experiment

Field cycling between high and low fields can be hard to achieve in practise. The spin-lock method (Figure 3.3b), where the sample remains in the detection magnet, is a more practical solution and was therefore implemented here.

The following sections investigate whether singlet states can be created in the target pyridazine based substrates to overcome the limitations of short signal lifetimes.

3.3 Extending Signal Lifetimes of 3,6-substituted pyridazines

The LLS behaviour of three pyridazine-based molecules, 3-amino-6-chloropyridazine (3-NH₂-6-Cl-py), 3-chloro-6-methoxypyridazine (3-Cl-6-OCH₃-py) and 3-chloro-6-(trifluoromethyl)pyridazine (3-Cl-6-CF₃-py) was investigated (Figure 3.6).

The pyridazine motif was initially tested because it represents a simple model (parent ring of the thienopyridazines upon which this thesis is focused) with isolated proton pairs that weakly couple to one another (for creating a possible pseudo-singlet state). In addition, they feature nitrogen heteroatoms and therefore should be amenable to the SABRE hyperpolarisation mechanism.

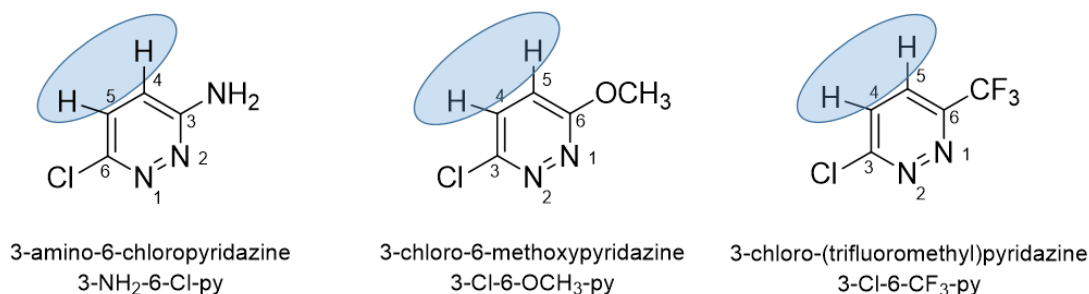


Figure 3.6: Chemical structures of three 3,6-substituted pyridazines studied. The proton pairs highlighted by the blue area indicate where the creation of a long-lived singlet state is possible.

3.3.1 T_1 and T_{LLS} of 3,6-Substituted Pyridazines in the Absence of a Catalyst

18 mM d_4 -methanol samples of the three pyridazines (Figure 3.6) were prepared and degassed prior to NMR measurement. ^1H T_1 values were measured using an inversion recovery approach at 9.4 T (Chapter 8.2.4). Representative T_1 recovery curves for the H4 and H5 sites in 3-Cl-6-OCH₃-pyridazine are shown in Figure 3.7. Relaxation data were fitted to equation 3.1 where M_{xy} is the transverse magnetisation/signal at time τ , M_0 is the magnetisation at $\tau = 0$ and T_1 is the longitudinal relaxation time constant.

$$M_{xy} = M_0 \left(1 - 2e\left(\frac{-\tau}{T_1}\right)\right) \quad [3.1]$$

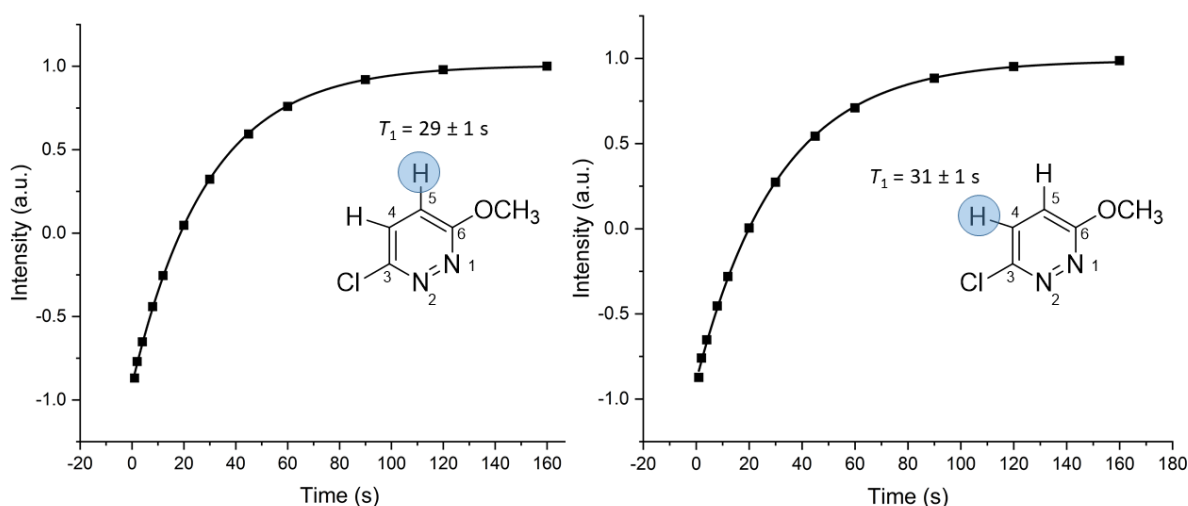
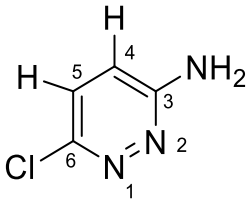
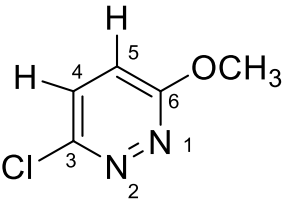
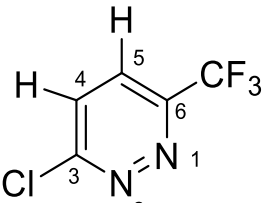


Figure 3.7: T_1 graphs obtained using the inversion recovery method for H4 and H5 of 3-chloro-6-methoxy pyridazine. The black squares reflect experimental measurements whilst the solid line is the line of best fit based on equation 3.1. The blue circles highlight the proton in the structure, which the T_1 value reflects.

Estimated decay time constants T_1 for all substrates serve as a benchmark to which any observed LLS extension in lifetime can be compared (see section 3.3.2 below).

The spin locking pulse sequence used for generation of the pseudo-singlet LLS is detailed in section 8.4.1. J -couplings and chemical shifts were measured in hertz from simple ^1H NMR spectra at 9.4 T (Table 3.1). These parameters were used as priors for setting the appropriate pulse delays in the spin locking sequence (Figure 8.2).

Table 3.1: Parameters used in the LLS pulse sequence to measure T_{LLS} of 3-NH₂-6-Cl-py, 3-Cl-6-OCH₃-pyridazine and 3-Cl-6-CF₃-py.

Substrate/ Parameters			
$\Delta\delta$ H4-H5 (Hz)	161.5	171.0	27.7
J_{HH} H4-H5 (Hz)	9.3	9.3	8.9

In order to encode T_{LLS} relaxation, a series of NMR experiments were completed in which the storage time, τ , was varied from 0 to 400 s. The presence of the singlet state at the point of read-out was evidenced by the characteristic up, down, down, up antiphase signal seen for the two doublets (Figure 3.8) in the associated NMR experiment.

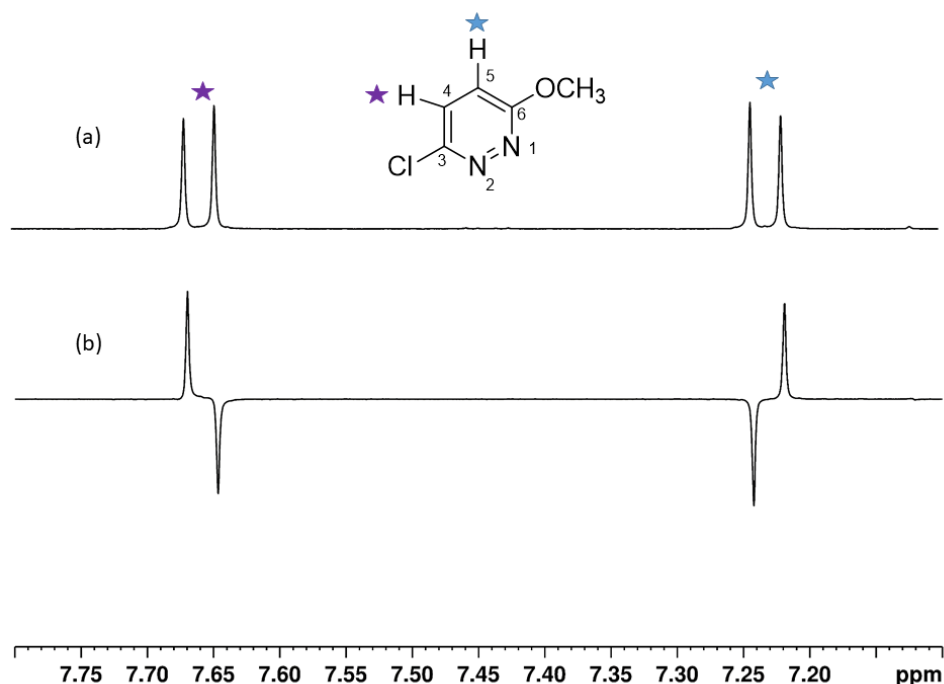


Figure 3.8: a) ¹H NMR spectrum of 3-Cl-6-OCH₃-py in methanol-*d*₄ with the two doublets arising from mutually coupled H4 and H5 as indicated. b) Characteristic up, down, down, up antiphase peaks observed in the read-out phase of the LLS experiment which is indicative of the pseudo-singlet state created.

The summed peak intensity (integrals of antiphase peaks combined in absolute mode) was plotted against storage time, τ , in Figure 3.9. Assuming 100% efficiency, in terms of singlet storage, magnetisation is expected to decay as a mono exponential with time constant T_{LLS} . The resultant T_{LLS} for 3-Cl-6-OCH₃-py was 82 ± 2.1 s (r^2 value of 0.996). This magnetisation lifetime is 2.7 times longer than the baseline $T_1 \sim 30 \pm 1.4$ s and therefore presents compelling evidence of the benefit of creating a pseudo singlet state for potential storage of hyperpolarisation. It was observed that the first few data points show a faster rate of relaxation. In the literature it is common to neglect the first few points in the associated data in order to remove this effect.¹⁶⁸ However, this such non mono-exponential behaviour, could be due to imperfections in the sequence or due to possible contributions from the triplet state manifold. These data were therefore also fitted to a bi-exponential equation:

$$M_{xy} = M_0 e\left(\frac{-\tau}{T_T}\right) + M_0 e\left(\frac{-\tau}{T_{LLS}}\right) \quad [3.2]$$

where M_{xy} is the detected magnetisation/signal at time τ , M_0 is the magnetisation associated with the indicated state at $\tau = 0$, T_T is the faster relaxation rate due to residual relaxation within the triplet manifold or imperfections in the sequence and T_{LLS} is the long-lived singlet relaxation.

Fitting to the bi-exponential decay equation extended T_{LLS} to 108 ± 9.8 s for 3-Cl-6-OCH₃-py and improved the r^2 fit to 0.999. T_T was found to be 26 ± 6.9 s, within error of the average T_1 for the proton sites in 3-chloro-6-methoxypyridazine. The relative contributions of $M_0(T_T)$ and $M_0(T_{LLS})$ are 0.82 and 2.95, thus the spin lock experiment was 77% efficient in creating the pseudo-singlet state.

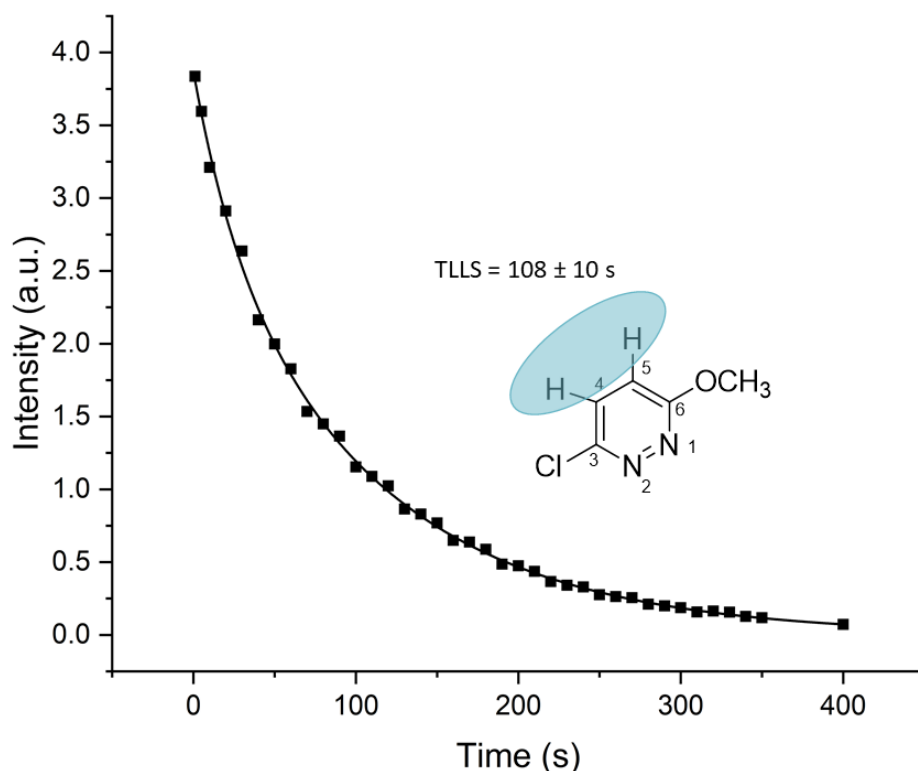


Figure 3.9: Exponential decay curve of the singlet state created between H4 and H5 in 3-chloro-6-methoxypyridazine using the LLS pulse sequence in high field. The black squares indicated the intensity of the combined anti-phase NMR signal from the pseudo singlet state in the read-out stage of the LLS experiment.

Similar T_1 and T_{LLS} measurements were recorded for all three substrates. Once again, for 3-NH₂-6-Cl-py and 3-Cl-6-CF₃-py, a bi-exponential equation gave the best fit, however, the T_T decay was much faster than the measured T_1 decay of either of the individual spins. For 3-NH₂-6-Cl-py and 3-Cl-6-CF₃-py the relaxation time T_T was 7 ± 1 s and 5 ± 1 s respectively. T_{LLS} decays of 43 ± 3 s ($r^2 = 0.998$, bi-exponential) and 84 ± 6 s ($r^2 = 0.999$, bi-exponential) were obtained, respectively. Again, the longevity of this signal (2.5 to 3.5 times T_1) is commensurate with the successful creation of a long-lived-state in both cases.

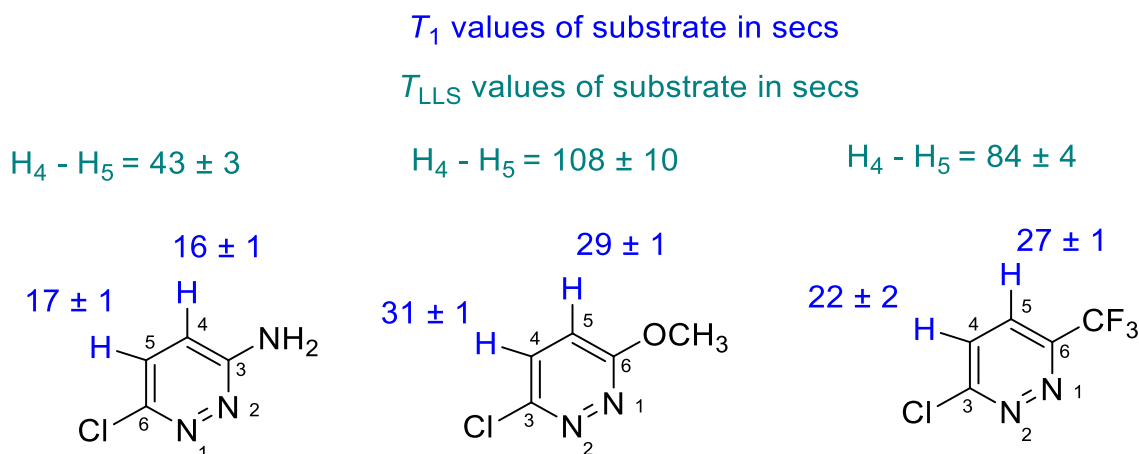


Figure 3.10: T_1 values of H4 and H5 measured by inversion recovery (blue) and T_{LLS} values of the pseudo-singlet state created between H4 and H5 using the LLS sequence (green) for 3-NH₂-6-Cl-py, 3-Cl-6-OCH₃-py and 3-Cl-6-CF₃-py

3.3.2 SABRE Hyperpolarisation of 3,6-substituted pyridazines - Shake and Drop Experiments

As shown in section 3.3.1, the three pyridazine substrates exhibit long pseudo singlet state lifetimes ($T_{LLS} \sim 40$ to 110s). To test that these agents could also be polarised with SABRE, shake and drop experiments were carried out with the precursor catalyst [IrCl(COD)(IMes)] in a 4:1 ratio at 9.4 T. 3-NH₂-6-Cl-py yielded hyperpolarisation with limited signal enhancements of -112 fold for the H5 signal and -61 fold for H4 (Figure 3.11).

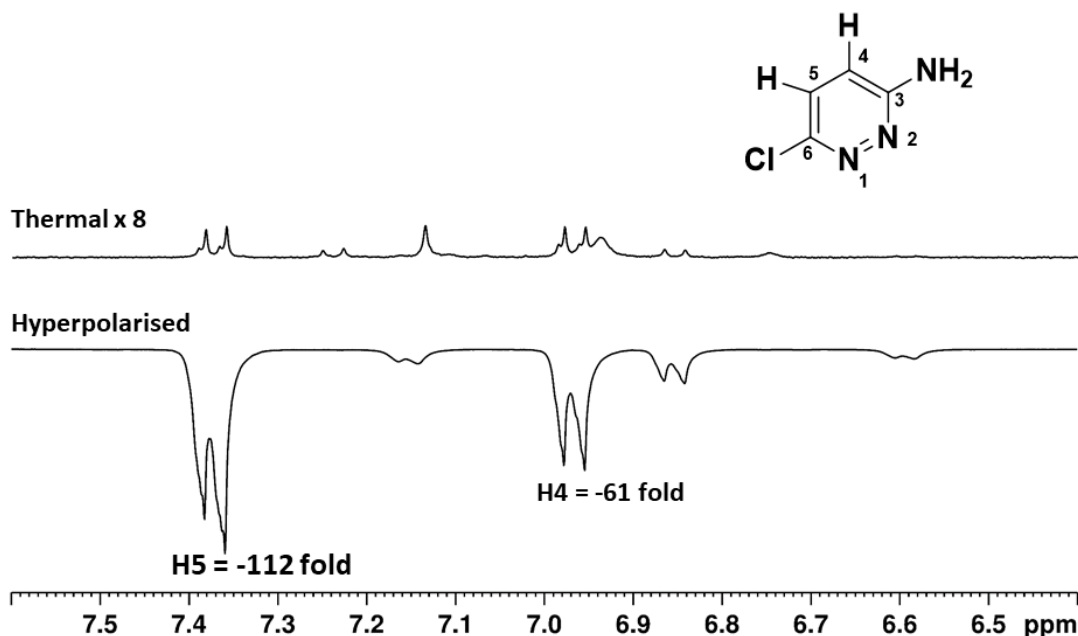


Figure 3.11: Thermal and hyperpolarised ¹H NMR spectra of 3-NH₂-6-Cl-py with [Ir(COD)Cl(IMes)] in a 1:4 ratio of catalyst to substrate in methanol-*d*₄. Hyperpolarised peaks are shown for the free and bound substrate. In the free substrate, H5 shows a signal enhancement of -112 fold and H4 shows an enhancement of -61 fold.

The hydride region of this spectrum is shown in Figure 3.12 and contains a narrow peak at $\delta -22.1$ consistent with the formation of the tris-substituted complex $[\text{Ir}(\text{H})_2(3\text{-NH}_2\text{-6-Cl-py})_3(\text{IMes})]$. The two broad hydride peaks also present suggest the formation of a further complex. The hydride yielding the signal at $\delta -21.9$ in this species will be *trans* to 3-NH₂-6-Cl-py whilst that at $\delta -29.65$ is *trans* to oxygen. This is evidence that the methanol-*d*₄ solvent is acting as a ligand. When amine binding to iridium has been studied in SABRE the corresponding hydride signals appear at around $\delta -22$. Hyperpolarisation enhancements are an order of magnitude smaller than those seen for the thienopyridazines detailed in chapter 2. This is due to weak binding and rapid exchange, effects consistent with the detection of the methanol adduct.

Hyperpolarised x 8 - Hydride region

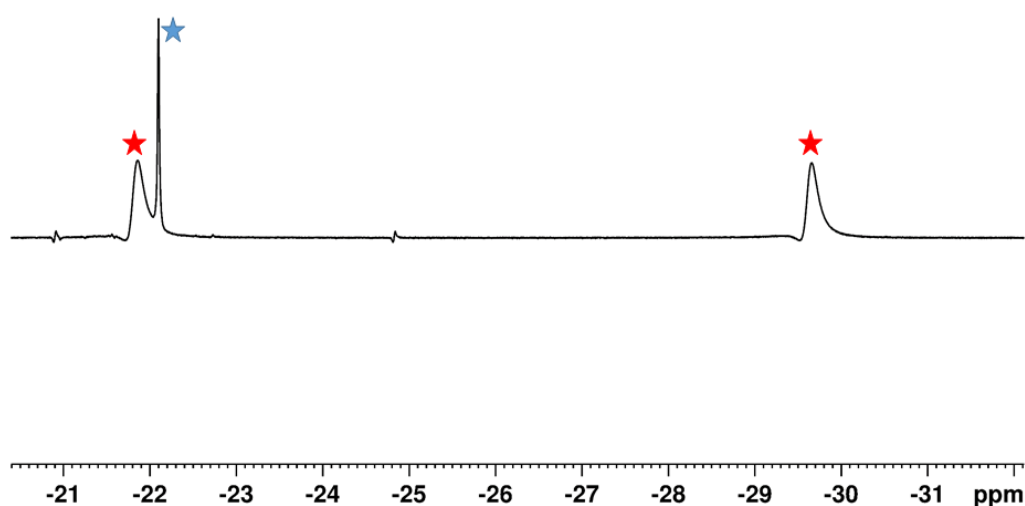


Figure 3.12: Hydride region of the ¹H NMR spectrum for 3-NH₂-6-Cl-py with $[\text{Ir}(\text{COD})\text{Cl}(\text{IMes})]$ as catalyst in *d*₄-methanol. The blue star shows the hydrides for the tris-substituted complex $[\text{Ir}(\text{H})_2(3\text{-amino-6-chloropyridazine})_3(\text{IMes})]$ and the red stars indicate the hydrides when the solvent is occupying one of the equatorial positions.

In contrast, while the corresponding ¹H NMR spectrum of the 3-Cl-6-OCH₃-py system showed hydride ligand signals but essentially no substrate signal enhancements, 3-Cl-6-CF₃-py failed to yield any hydride ligand signals and does not activate the catalyst. Following these observations, the alternative catalyst $[\text{IrCl}(\text{COD})(\text{SIMes})]$ was used with both substrates to see if it would permit SABRE hyperpolarisation. A very small signal enhancement (-15) was again measured for 3-chloro-6-methoxypyridazine. No hydride ligands were observed for 3-Cl-6-CF₃-py. A summary of these SABRE results and the relaxation lifetimes for these 3,6-substituted pyridazines is shown in Table 3.2.

Table 3.2: Summary of SABRE activity and comparative thermal lifetimes (T_1 and T_{LLS} in the absence of the catalyst) of the 3,6-substituted pyridazines


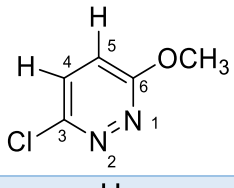
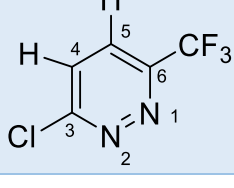
Substrate	$\Delta\delta$ H4-H5 (Hz)	J_{HH} H4-H5 (Hz)	SABRE ϵ lMes	SABRE ϵ sIMes	T_1 substrate alone (s)	T_{LLS} substrate alone (s)
	161.5	9.3	H5 = -117 H4 = -31		H5 = 17 ± 1 H4 = 16 ± 1	H4-H5 = 43 ± 3
	171	9.3	No SABRE	H4 = -15 H5 = 0	H4 = 31 ± 1 H5 = 29 ± 1	H4-H5 = 108 ± 10
	27.74	8.98	No SABRE	No SABRE	H4 = 22 ± 2 H5 = 27 ± 1	H4-H5 = 84 ± 4

Table 3.2 shows that SABRE activity for the 3,6-substituted pyridazines is lower in terms of signal enhancement when compared to the thienopyridazines. Polarisation transfer occurs through a 4J coupling from hydride to an *ortho* proton resonance in the substrate. In the case of the 3,6-disubstituted pyridazines the *ortho* position is occupied and therefore a weaker 5J coupling from the hydride to the *meta* position would take place. It has been shown previously that polarisation efficiency decreases if no $^4J_{HH}$ coupling is present in the active catalyst and a smaller $^{5/6}J_{HH}$ needs to be used instead.¹³⁵ This could account in part for the lower signal enhancement levels observed. However, even the protons which are distant from the nitrogen binding site in the thienopyridazines, with a 6J coupling with the hydrides, have higher signal enhancements. It is hypothesised that the additional steric bulk and the electron withdrawing nature of the functional groups next to the binding site for the 3,6-substituted pyridazines was detrimental to their SABRE performance.

Although SABRE hyperpolarisation performance was poor for the 3,6-substituted pyridazines, it remains that application of spin lock LLS techniques in this motif demonstrated extended polarisation lifetimes (2.5 times for 3-NH₂-6-Cl-py; 3.5 times for OCH₃ and 3.1 times for 3-Cl-6-CF₃-py). It was important to test whether such singlet states could be generated in the target thienopyridazine substrates and if this would influence polarisation performance (section 3.4).

3.4 LLS of Thienopyridazines

Results presented in section 3.3 provide evidence that for the pyridazine motif, pseudo LLS can be achieved for polarisation storage. However, the additional steric bulk and electron withdrawing effects of the functional groups next to the binding site for the 3,6-substituted pyridazines was detrimental to their SABRE performance. Interestingly additional steric bulk in the form of a fused thiophene ring is not a significant issue for the thienopyridazines as signal enhancement levels up to $-10,000$ can be achieved. The creation of analogous long-lived states in the synthesised thienopyridazines was therefore tested.

3.4.1 T_1 and T_{LLS} of Thienopyridazines in the Absence of a Catalyst

T_1 values were estimated for all proton sites in each of the four thienopyridazine substrates detailed in chapter 2. Inversion recovery results for T[2,3-*d*]P and subsequent T_1 estimates (ranging from 18-49 s) are exemplified in Figure 3.13. LLS preparation using the spin locking approach requires neighbouring weakly coupled protons exhibiting a $\Delta\delta > J$ coupling. It was recognised that the pairs of protons H2/H3 in T[2,3-*d*]P, H2/H3 and H4/H5 in T[2,3-*c*]P and H2/H3 and H6/H7 in T[3,2-*c*]P could be potential sites for the creation of LLS. Their J coupling values are given alongside their chemical shift difference in Table 3.3.

T[3,4-*d*]P is symmetric and therefore does not possess neighbouring proton spins with a mutual J coupling. It was therefore not amenable to generation of an LLS with spin locking and was not considered further.

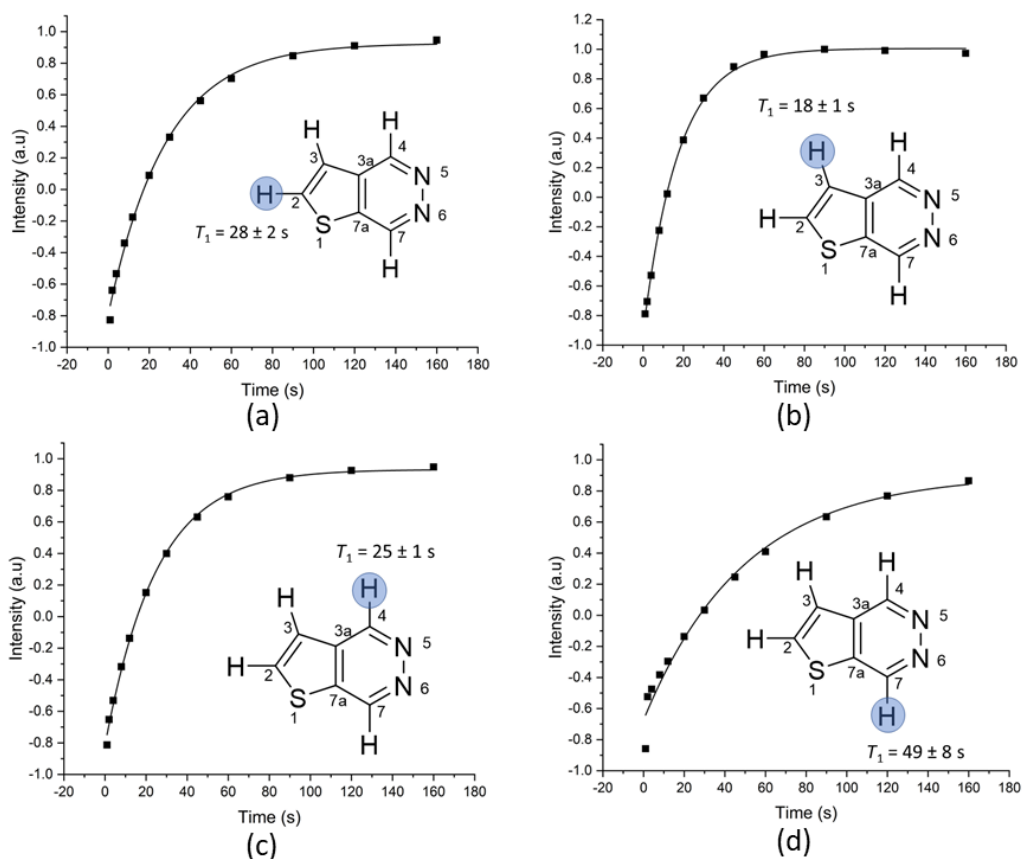


Figure 3.13: ^1H T_1 decay curves measured by inversion recovery for (a) H2 (b) H3 (c) H4 (d) H7 of T[2,3-*d*]P at 9.4T.

Table 3.3: Parameter settings for the LLS pulse sequence used to measure T_{LLS} in T[2,3-*d*]P, T[2,3-*c*]P and T[3,2-*c*]P.

Substrate/ Parameter				
	[2,3- <i>d</i>]	[3,4- <i>d</i>]	[2,3- <i>c</i>]	[3,2- <i>c</i>]
J-coupling constant (Hz)	$J_{\text{H2H3}} = 5.3$	-	$J_{\text{H2-H3}} = 5.94$ $J_{\text{H4-H5}} = 5.64$	$J_{\text{H2-H3}} = 5.69$ $J_{\text{H6-H7}} = 5.73$
Chemical shift difference $\Delta\delta$ (Hz)	$\text{H}_2\text{-H}_3 = 202.5$	-	$\text{H}_2\text{-H}_3 = 252.25$ $\text{H}_4\text{-H}_5 = 405.04$	$\text{H}_2\text{-H}_3 = 149.39$ $\text{H}_6\text{-H}_7 = 273.97$

Figure 3.14 a shows a thermal ^1H NMR spectrum of the four protons of T[2,3-*d*]P with protons H2 and H3 observed as doublets at δ 8.23 and δ 7.75. Figure 3.14 b shows the results

of a spin locked LLS experiment (storage time of 1 s before the readout). The antiphase peaks are a characteristic fingerprint of the singlet state generation.

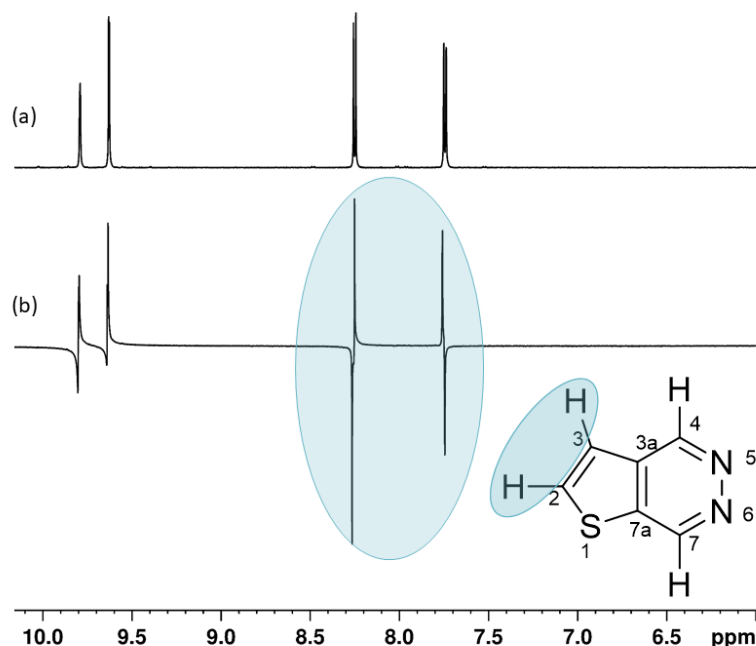


Figure 3.14: (a) ^1H NMR spectrum of T[2,3- d]P in methanol- d_4 showing the 4 proton resonances including the two doublets arising from the mutually coupled H2 and H3. (b) Characteristic antiphase peaks observed in the read-out stage of the LLS experiment of the pseudo-singlet created between H2 and H3. The highlighted locations indicate both the NMR peaks and the protons within the molecule where the pseudo-singlet state has been created

Twenty spin lock experiments were run with increasing storage time (Figure 3.15). The resonances at δ 9.80 and δ 9.64, which are not involved in the singlet state, decay rapidly through scalar coupling relaxation. The resonances at δ 8.23 and δ 7.75 have a much longer lifetime indicative that singlet storage has been achieved.

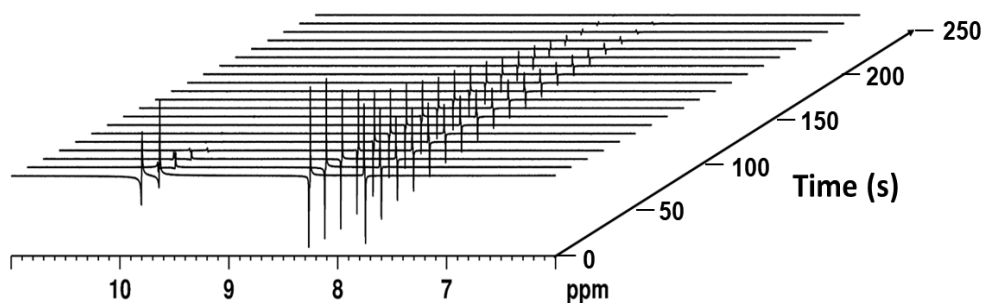


Figure 3.15: Stacked array of NMR spectra resulting from the LLS experiment showing the decay of the long-lived singlet in the read-out stage

Figure 3.16 shows the results of fitting these data to determine the T_{LLS} between H2 and H3 of T[2,3-*d*]P. Assuming 100% singlet state generation efficiency a mono-exponential fit results in a T_{LLS} of 26 s ($r^2 = 0.988$). A bi-exponential model fit with both T_T and T_{LLS} floating, resulted in the first part of the curve yielding an apparent T_T of 7 ± 1 s. The second part of the curve enabled the lifetime of the pseudo singlet state to be estimated at 40 ± 3 s (r^2 value improved to 0.998).

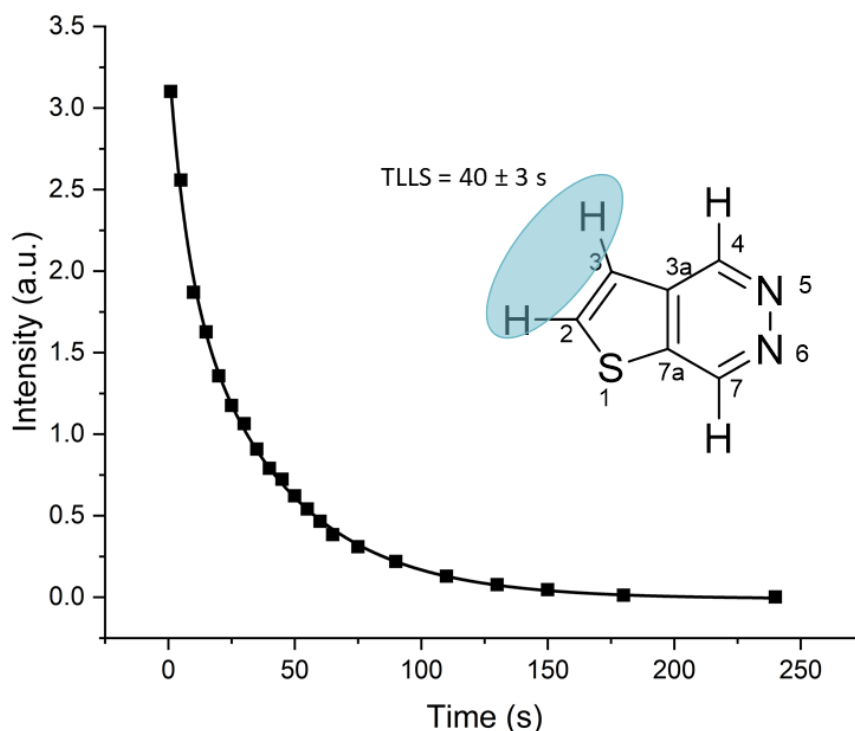


Figure 3.16: Exponential decay of the singlet state created between H2 and H3 in T[2,3-*d*]P using the LLS pulse sequence in high field. The black squares indicate the intensity of the combined NMR signal from the pseudo singlet state in the read-out stage of the LLS experiment.

The individual proton T_1 values for H2 and H3 were 28 and 18 s, respectively. Although not representative of the estimated T_T the T_{LLS} value is longer at 40 seconds. Hence, we can predict that a short-lived singlet state had been created, although its lifetime extension is just ~ 1.7 times that of the average T_1 , presumably due to small couplings to other proton sites (H4 and H7).

For T[2,3-*c*]P and T [3,2-*c*]P the T_{LLS} values did not indicate any increase in the overall lifetimes. T[2,3-*c*]P with individual T_1 values of 38 ± 3.8 s (H2) and 28 ± 1.0 s (H3) gave a T_{LLS} of 32 ± 1.6 s. T[3,2-*c*]P with individual T_1 values of 26 ± 0.8 s (H2) and 25 ± 0.7 s

(H3) gave a T_{LLS} of 22 ± 1.5 s. This is evidence that the singlet state created here was not ‘long-lived’.

3.4.2 Hyperpolarised long-lived states in thienopyridazines

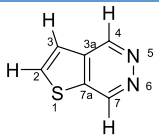
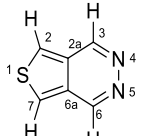
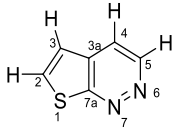
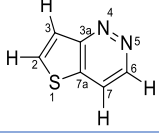
Chapter two showed that in contrast to the 3,6-substituted pyridazines, the thienopyridazines demonstrate excellent SABRE activity with over 2,000 fold signal enhancement (compared to 113 for pyridazine) being achieved for an individual proton resonance under standard SABRE conditions using $[\text{IrCl}(\text{COD})(\text{IMes})]$. Optimisation steps increased this figure to 10,000-fold.

Despite the relatively short T_{LLS} values compared with T_1 for the thienopyridazines, hyperpolarisation experiments combined with long-lived state measurements were attempted for T[2,3-*d*]P, T[2,3-*c*]P and T[3,2-*c*]P.

For this study, an automated flow system was used due to the number of experiments involved. Highest enhancements are achieved when using a 1:4 catalyst to substrate ratio (section 2.4.1). As such, this ratio was implemented here for long-lived state exploration. The sample was initially held at 65 G and bubbled with *p*-H₂ for SABRE polarisation. The sample was then shuttled into a high field NMR system and the spin locking pulse sequence, with variable storage delay, was applied before readout.

The estimated T_{LLS} values for the different samples are given in (Table 3.4), alongside their T_1 values as measured by inversion-recovery. For comparison, the T_{LLS} values and T_1 values are also shown for the substrate without the SABRE catalyst. It can be noted that the lifetimes are dramatically decreased when the catalyst is present in the ratio of 1:4 (catalyst: substrate) which is typical for SABRE measurements. Catalyst dilution or sequestration would enable the value to return to that recorded without the catalyst.

Table 3.4: Signal enhancement and relaxation data (T_1 and T_{LLS}) associated with thienopyridazines in the absence and in the presence of $[\text{IrCl}(\text{COD})(\text{IMes})]$ in a 1:4 catalyst: substrate ratio using a high field spin-lock.

Substrate	Res.	Sig. Enhanc.	Substrate Alone		Hyperpolarised substrate with catalyst	
			T_1 (s)	T_{LLS} (s)	T_1 (s)	T_{LLS} (s)
	H7	-2150 ± 67	49.45 ± 8.10	-	7.28 ± 0.10	-
	H4	-2053 ± 77	24.88 ± 0.94	-	5.13 ± 0.06	-
	H2	-882 ± 47	27.87 ± 1.50	40.02 ± 2.89	7.50 ± 0.11	9.00 ± 0.43
	H3	-439 ± 42	17.53 ± 0.40		4.64 ± 0.07	
	H3	-1480 ± 21	25.86 ± 0.17	-	5.44 ± 0.07	-
	H2	-1138 ± 18	29.10 ± 0.21	-	9.41 ± 0.10	-
	H5	-583 ± 19	21.10 ± 0.49	-	3.19 ± 0.03	-
	H4	-384 ± 13	18.48 ± 0.16	-	5.21 ± 0.07	-
	H2	-174 ± 5	38.08 ± 3.82	32.21 ± 1.64	7.49 ± 0.16	2.34 ± 0.4
	H3	-39 ± 3	28.24 ± 1.04		5.61 ± 0.17	
	H6	-822 ± 19	18.68 ± 0.18	-	2.90 ± 0.05	3.21 ± 0.05
	H7	-371 ± 14	20.08 ± 0.41	-	4.96 ± 0.07	
	H2	-828 ± 20	25.80 ± 0.80	21.69 ± 1.51	6.36 ± 0.08	5.20 ± 1.25
	H3	-385 ± 18	25.13 ± 0.77		4.32 ± 0.03	

The T_{LLS} measurements were carried out in high field using a ‘spin-lock’ to reduce the chemical shift difference and impose symmetry. Although this is a very effective and simple method, the field cycling experiment where the sample is physically transported into low field has been shown to be more effective at reducing the chemical shift difference. Unfortunately, it was not possible to implement on the TPs. When attempts were made to remove the sample adiabatically from high field to low field, the decay time shortening effect of the catalyst at the 1:4 loading was too severe, and no signal could be detected at the read-out stage. This is not surprising given the extremely short T_1 estimates in the presence of the catalyst (see Table 3.4). In the future it might be sensible to repeat these measurements with a lower loading to increase lifetime but obviously the hyperpolarisation level will fall. There have been many recent advances in catalyst design¹²³ and a more comprehensive catalysis study would also be warranted.

3.5 SABRE hyperpolarisation and LLS of ^{13}C and ^{15}N nuclei

While SABRE can hyperpolarise X-nuclei,¹¹² focus to date has concentrated on proton.^{112, 123, 135} There are clear advantages for hyperpolarising protons not least with a natural abundance of 99.98% there is no requirement for expensive synthetic labelling. In addition, high- γ nuclei, such as ^1H , can be observed more readily with NMR. There are several reasons why this is the case.

The first is that the nuclear magnetic moment μ is proportional to γ . A large gyromagnetic ratio indicates a large magnetic moment and therefore a strong NMR signal. Secondly, at thermal equilibrium, the Boltzmann polarisation is proportional to the splitting of the Zeeman energy levels, which is in turn is proportional to γ . For a given field and polarisation level, the signal detected by NMR is proportional to γ^3 . Therefore with $\gamma^{1\text{H}}$ four times that of $\gamma^{13\text{C}}$ a 64-fold gain in ^1H signal intensity results over ^{13}C .⁶⁵ In addition, the 1.109% natural abundance of ^{13}C results in further signal penalty. The story is similar for ^{15}N . Again, a low 0.37% natural abundance results in a large sensitivity penalty. This is exacerbated by the low gyromagnetic ratio for ^{15}N ($-2.712 \times 10^7 \text{ rad s}^{-1} \text{ T}^{-1}$). In general terms, this means that the signal to noise ratio for a ^1H measurement is 264,000-fold greater than that of ^{15}N at the same magnetic field.

On a more practical note all magnetic resonance scanners in hospital settings are always equipped with RF coils for ^1H MRI. Although capable of imaging other nuclei, the extra investment in additional RF coils tuned to a different frequency is often not made. Therefore, wide scale clinical application of X-nuclei technology is currently limited.

Despite the advantages of ^1H detection, there are challenges when arriving at the imaging stage for hyperpolarisation. One of the main problems with using a hyperpolarised proton signal is the background signal of water in the body which is several orders of magnitude stronger than that of metabolites. This can lead to a distorted baseline and off resonance signals. Water suppression, and optimised shimming strategies would be needed to observe the signal derived from the exogenous hyperpolarised agent. The presence of multiple resonances from the hyperpolarised substrates would also need to be accounted for. Non-standard imaging approaches, and specific pulse sequences (e.g. multi point DIXON imaging²³²) are therefore required to aid detection. Another important consideration is the effect of paramagnetic O_2 dissolved in the blood. Paramagnetic O_2 has a much larger effect on ^1H compared with ^{13}C .²³³ This is due to the larger gyromagnetic ratio of ^1H . To date, most *in-vivo* hyperpolarisation experiments concentrate on X-nuclei imaging to avoid these complications.

The thienopyridazines contain both carbon and nitrogen sites which would be amenable for X-nuclei imaging/polarisation. Following relatively unsuccessful long-lived state storage in the ^1H sites of the thienopyridazine substrates, further experiments exploring LLS in the X-nuclei sites (^{13}C and ^{15}N) were investigated. Establishing LLS enhanced X-nuclei SABRE hyperpolarisation would make the technique comparable to the DNP benchmarks. There are several steps to

consider to achieve this goal. The first step is to establish if SABRE polarisation is possible for X nuclei and if any signal enhancements are observed at natural abundance. There are two possible routes to achieve this either directly to the X nuclei or indirectly through ^1H polarisation transfer. Once established that polarisation is possible, a second step to consider is synthetic labelling of the X nuclei to increase signal. If synthetic labelling strategies are possible the third step would be to use long-lived state techniques to increase magnetic lifetimes.

3.5.1 Polarisation of X nuclei – direct/indirect

Polarisation to X nuclei may be carried out in two ways. One involves indirect transfer of the polarisation via ^1H . In this case, the PTF would be at 60 G, which was found to be optimal for ^1H polarisation (chapter 2.4.2). A second method involves direct transfer to the X nuclei at a specific PTF. When considering the matching conditions for SABRE transfer of magnetisation through the iridium catalyst from the hydrides to ^{13}C nuclei directly, the J coupling between the hydrides (~ 8 Hz) and the chemical shift difference ($\Delta\nu$ in Hz) between H and X nuclei must match. As such, the PTF must also be changed accordingly. In an 11.7 T magnet, ^1H resonates at 500 MHz whereas ^{13}C resonates at a lower frequency of 125 MHz (due to their different gyromagnetic ratios). The exact chemical shift difference is not essential as in the case of ^1H SABRE because they are now separated on the order of MHz. The correct field for magnetisation transfer, B_{PTF} , can be calculated using equation 3.3:

$$B_{PTF} = \frac{J_{HH}}{\Delta\nu_{HX}} \cdot B_0 \quad [3.3]$$

where J_{HH} is the J coupling in hertz between the para-hydrogen derived hydrides (8 Hz), $\Delta\nu_{HX}$ is the frequency difference between the hydrides and the polarised X-nuclei (375 MHz for ^{13}C at 11.7 T) and B_0 is the strength of the detection field (e.g., 11.7 T).

Using equation 3.3 the polarisation transfer field required for polarisation exchange is extremely small ~ 2.5 mG. Similarly, the PTF for ^{15}N is ~ 2 mG.

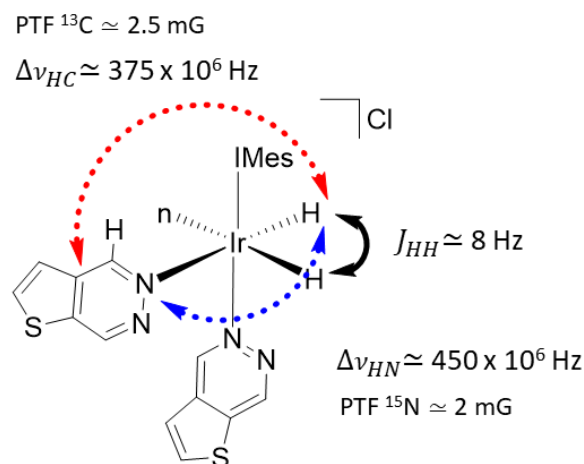


Figure 3.17: Polarisation transfer to X nuclei. Iridium complex formed during SABRE with T[2,3-*d*]P. The red dotted line shows the transfer of polarisation directly to the carbon in the substrate and the blue dotted line shows the transfer of polarisation to the nitrogen in the substrate. The black arrow indicates the coupling in Hz between the hydrides. (*n* is second in plane T[2,3-*d*]P which is omitted to aid the reader)

Long lived hyperpolarisation of ^{13}C hyperpolarised within T[2,3-*d*]P was investigated first (section 3.5.2) followed by ^{15}N (section 3.5.3).

3.5.2 Thieno[2,3-*d*]pyridazine: Carbon Singlet State Polarisation

Metabolites used in ^{13}C MRS generally contain ^{13}C labelled quaternary carbons as they usually exhibit longer T_1 lifetimes (9 – 60 s). This is due to the absence of strong carbon-proton couplings to provide a source of relaxation.²³⁴ The most commonly used metabolite used in d-DNP MRS, ^{13}C pyruvate is a prime example with the carbonyl carbon(s) being labelled.⁹⁷ The thienopyridazines each contain two quaternary carbons at the fusion point of the two rings and it is hypothesised that these would exhibit longer T_1 lifetimes than the other four carbon atoms present. In addition to being quaternary carbons, they are also adjacent to one another and therefore it is expected that they would possess a mutual large J_{CC} coupling, a requirement for LLS creation. A second requirement for the successful creation of a LLS is that $\Delta\delta$ between the two carbons in the pair needs to be small. Previous characterisation in section 2.3 revealed that T[3,4-*d*]P is symmetrical so the two central carbons have identical chemical shifts. In this case a singlet state is created but as the symmetry cannot be broken it will always remain NMR silent. In the case of T[2,3-*c*]P, T[3,2-*c*]P and F[2,3-*d*]P, $\Delta\delta$ is large between the central carbons at $\Delta\delta$ 30.88, $\Delta\delta$ 16.16 and $\Delta\delta$ 26.5 respectively. Only in the case of T[2,3-*d*]P is $\Delta\delta$ small with a value of δ 2.98. It is hypothesised, therefore, that these two central carbons would be ideal

candidates for the creation of LLS. For this reason only T[2,3-*d*]P was investigated for SABRE hyperpolarised carbon signals.

The thermal based resonances of the six carbon atoms in T[2,3-*d*]P, can be seen in Figure 3.18.

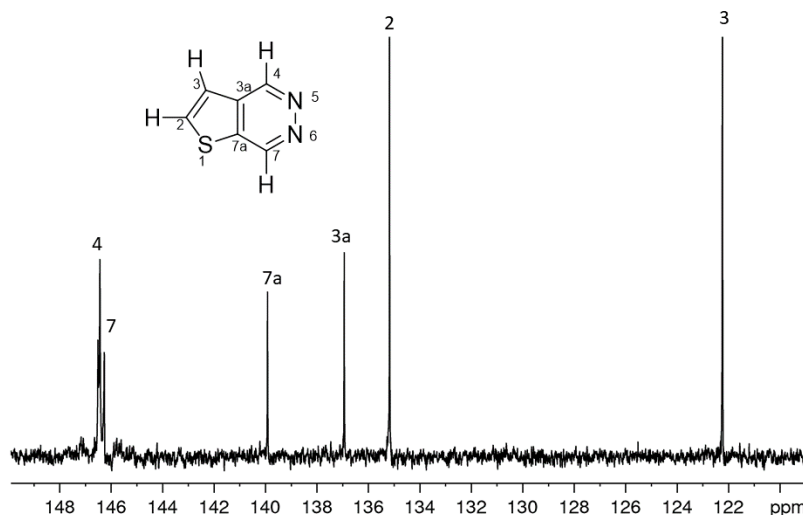


Figure 3.18: Thermal $^{13}\text{C}\{^1\text{H}\}$ spectrum of T[2,3-*d*]P in methanol- d_4 (8192 scans)

The chemical shift difference for sites 3a and 7a (the central quaternary carbons) is $\Delta\delta_{\text{CC}} = 2.98$ ppm which is equivalent to 375 Hz when recorded on a 500 MHz (11.74 T) spectrometer. By comparison to related ^{13}C labelled pyridazine molecules¹⁴⁷, the predicted J_{CC} of 3a and 7a would be in the range of 58-60 Hz. Hence, the long-lived state of T[2,3-*d*]P could be created in a 1 T field which would be readily accessible using a benchtop spectrometer.

As a proof of concept, the ^{13}C SABRE hyperpolarisation of T[2,3-*d*]P was conducted using molecules at natural abundance. ^{13}C NMR SABRE shake and drop experiments (section 8.2.1) were carried out on the unlabelled T[2,3-*d*]P with $[\text{Ir}(\text{COD})\text{Cl}(d_{22}\text{SIMEs})]$ in an 4:1 ratio at 3 bar in methanol- d_4 . Polarisation was attempted both indirectly (via ^1H) and directly to ^{13}C nuclei. With ^1H SABRE the thermal signal, although small, can still be observed in a single scan using the same receiver gains value of the hyperpolarised experiment. A direct comparison of signal enhancement can therefore be calculated. This is not the case for ^{13}C based SABRE therefore values are now quoted as signal to noise ratios (S/N).

Indirect transfer of polarisation (i.e., through ^1H) to ^{13}C at the optimised PTF of 60 G (chapter 2.4.2) resulted in a hyperpolarised spectrum (see Figure 3.19). It can be noted that only the

carbons, 3a and 7a of the free substrate were observed. This agrees with the original hypothesis that only the quaternary carbons have a long enough lifetime to be observed during hyperpolarisation experiments. The remaining hyperpolarised signals arise from the carbon nuclei in the bound ligands. Although 60 G shows hyperpolarised signals with S/N of 126, they exhibit anti-phase behaviour, a typical observation when the polarisation is relayed through the protons.

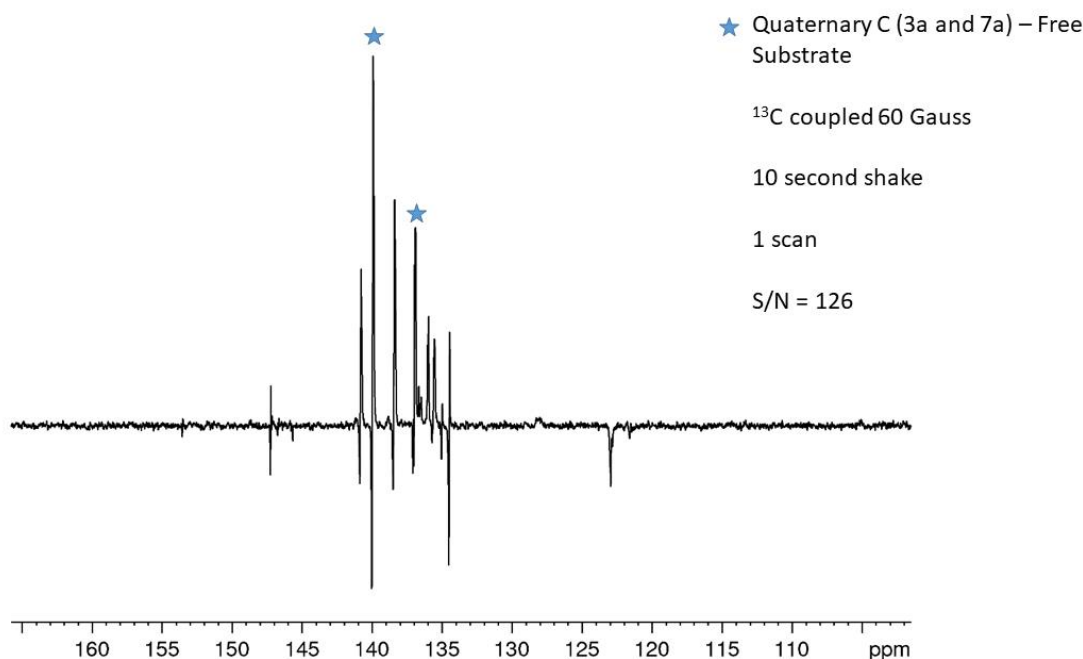


Figure 3.19: Shake and Drop 1 scan ^{13}C experiment of T[2,3- d]P and [IrCl(COD)(d_{22} -SIMes)] in a 4 to 1 ratio in methanol- d_4 . A 60 G shaker was used with a shaking time of 10 s before transferring to a 500 MHz spectrometer for detection.

In order to prove this anti-phase characteristic is associated with a proton coupling and hence obtain phased signals (during polarisation transfer from protons at a PTF of 60 G) whilst simultaneously improving S/N an INEPT (insensitive nuclei enhanced by polarisation transfer) experiment was carried out. This pulse sequence was originally created as a signal enhancement method.^{65, 235} It involves the transfer of polarisation from spins with a large Boltzmann population difference to spins of interest with a smaller Boltzmann population difference, thereby increasing the signal intensity of low gamma nuclei. The disadvantage of this method is that the duration of the pulse sequence is longer than that of a direct 90° pulse experiment, so relaxation during the experiment could lead to a lower enhancement in the read-out stage. Using an INEPT approach, improvements (~ 1.2 times) were seen in signal to noise of the quaternary carbons. Across two experiments S/N was 147 ± 6 when shaking for 10 seconds. This increased to 207 ± 13 when the sample was shaken for 50 seconds (Figure 3.20). While an interesting general trend was found

(an increase in S/N with increasing shaking time) it is noted that further experiments would be required to improve accuracy across shake times before drawing a definitive conclusion here. It is difficult to manually shake to a consistent level for 50 s and an automated approach should be adopted to explore this.

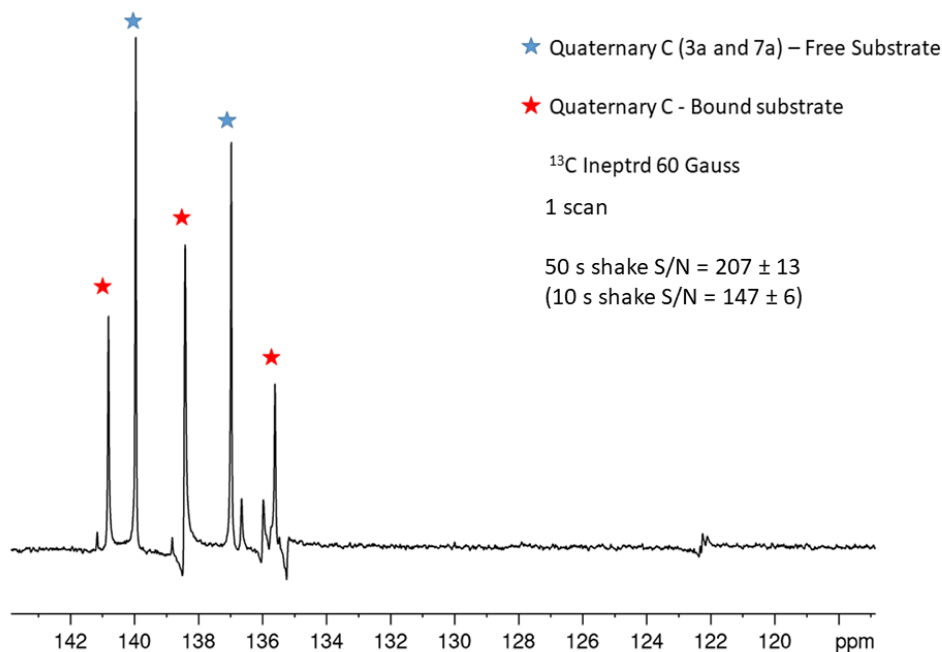


Figure 3.20: Shake and Drop 1 scan Ineptd ¹³C{¹H} experiment on T[2,3-*d*]P with [IrCl(COD)(*d*₂₂-SIMes)] in a 4 to 1 ratio in methanol-*d*₄. The sample was shaken in a 60 G field (magnetic shaker) for 50 s before measurement in a 500 MHz spectrometer.

Direct polarisation transfer to ¹³C nuclei was also explored (in fields on the order of mG). The samples (n = 2) were shaken inside a mu-metal shield, which reduces the magnetic field by ~1000 fold, prior to insertion into the 500 MHz spectrometer. This is predicted to lead to direct transfer to ¹³C and result in both free and bound peaks being in-phase. In agreement with this prediction the resulting spectrum showed in-phase peaks with S/N of 91 ± 3 (Figure 3.21).

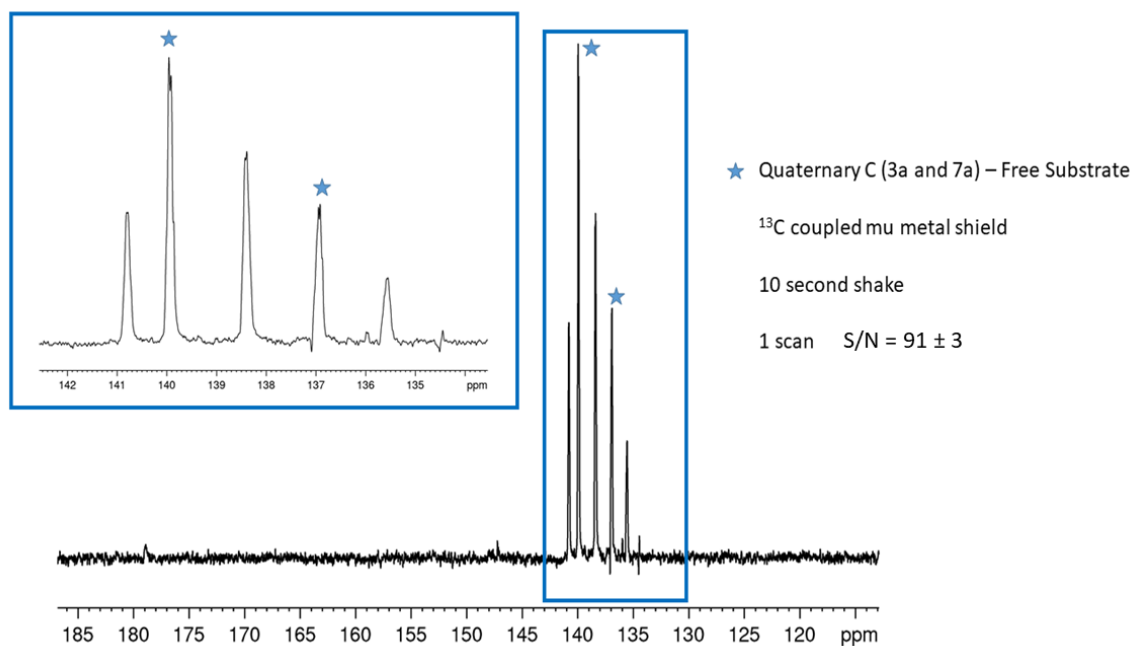


Figure 3.21: Shake and Drop 1 scan ^{13}C experiment of T[2,3-*d*]P and [IrCl(COD)(*d*₂₂-SIMes)] in a 4 to 1 ratio in methanol-*d*₄. The sample was shaken in the mu metal shield for 10 seconds before measurement in a 500 MHz spectrometer.

When repeated with proton decoupling an improvement in S/N to 232 ± 6 was observed (Figure 3.22). Due to the additional weight and cumbersome nature of the mu-metal shield the effects of extending shake times were not explored. Again, developing an automated system to complete this study would be of benefit in the future.

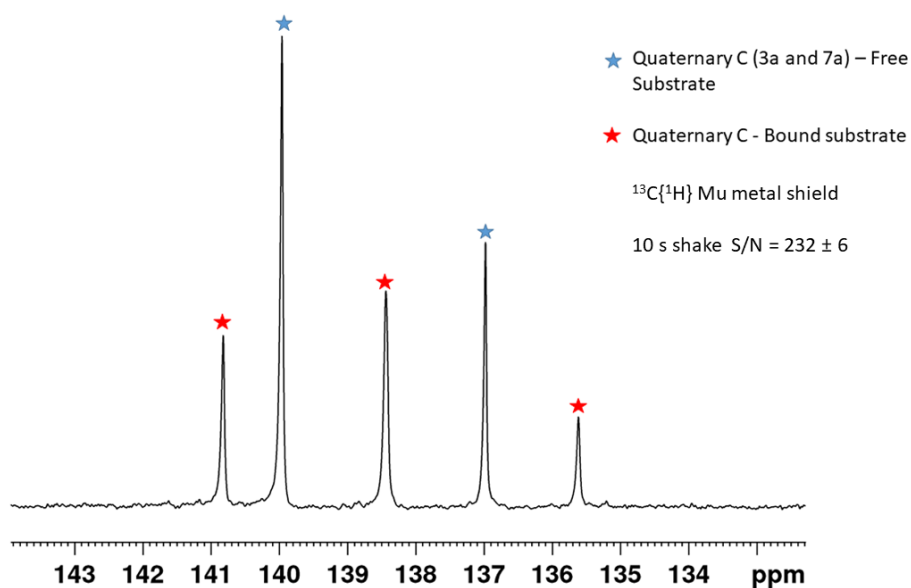


Figure 3.22: Shake and Drop 1 scan $^{13}\text{C}\{^1\text{H}\}$ experiment of T[2,3-*d*]P and [IrCl(COD)(*d*₂₂-SIMes)] in a 4 to 1 ratio in methanol-*d*₄. The sample was shaken in the mu metal shield for 10 seconds before measurement in a 500 MHz spectrometer.

Optimum conditions to give the best signal to noise values (>200) were either with a standard ^{13}C decoupled 10s shake and drop experiment (using the mu-metal shield; $S/N = 232 \pm 6$) or an INEPT experiment (with refocusing for multiplicity and decoupling) following sample shaking for 50 s in a 60 Gauss magnetic array shaker ($S/N = 207 \pm 13$). This confirms that while SABRE transfer via proton is more efficient than the direct route when refocussing or INEPT is involved the extra delays result in the latter being optimal.

If it were possible to introduce ^{13}C labelled carbons into these two positions, with 100% abundance as opposed to the actual 1.109% present, one could estimate S/N values will increase to 22,000 if we retain the same efficiency. This assumes T_1 saturation and T_2 peak broadening are not considered.

Thus, if the synthesis of the $^{13}\text{C}_2$ isotopologue could be achieved a hyperpolarised long-lived state would be readily accessible. Unfortunately, ^{13}C labelling of sites between two fused rings would be synthetically very challenging (and warrants a whole separate project). Due to this limitation, investigations turned to the ^{15}N nuclei within T[2,3-*d*]P.

3.5.3 Thieno[2,3-*d*]pyridazine: Nitrogen Singlet State Polarisation

High field (500 MHz) ^{15}N NMR single scan hyperpolarised spectra of non-labelled T[2,3-*d*]P with and without decoupling are shown in Figure 3.23. The precursor catalyst used was $[\text{IrCl}(\text{COD})(d_{22}\text{-SIMes})]$, in a methanol- d_4 solvent with substrate to catalyst ratio of 4:1. To obtain direct polarisation transfer to the nitrogen, the sample was shaken with $p\text{-H}_2$ in a mu-metal shield. The two nitrogen resonances were observed at δ 354.98 and δ 354.47 giving $\Delta\delta_{\text{NN}} = 0.51$ ppm (corresponding to 26 Hz at 11.74 T). A thermally polarised NMR spectrum of the same sample was run, but after 4000 scans a ^{15}N signal was still not visible. For the decoupled $^{15}\text{N}\{^1\text{H}\}$ SABRE only one scan is required to obtain a signal with S/N of 5, thus confirming the benefit of hyperpolarisation.

As expected, these two nitrogen resonances are very close to one another in terms of chemical shift. Consequently, if this system could be ^{15}N labelled, second order effects would be expected to produce an AB pattern of doublets due to the presence of strong coupling (if $J_{\text{NN}} > 13$ Hz). At fields lower than 3 T, the corresponding singlet state should therefore be well preserved. As described in section 3.2.2, the effect of chemical shift can be overcome with the use of a radio frequency spin-lock. This involves the deposition of energy into the sample and is not likely to be practical for human MRI studies with ^1H nuclei. It may however be possible for ^{15}N detection

which requires less RF power. This is referred to normally as the Specific Absorption Rate (SAR) and there are serious limitations imposed on MRI by this property to prevent local heating.

It is noted that only resonances from the free nitrogen were observed. No ^{15}N signals were detected for the bound ligands.

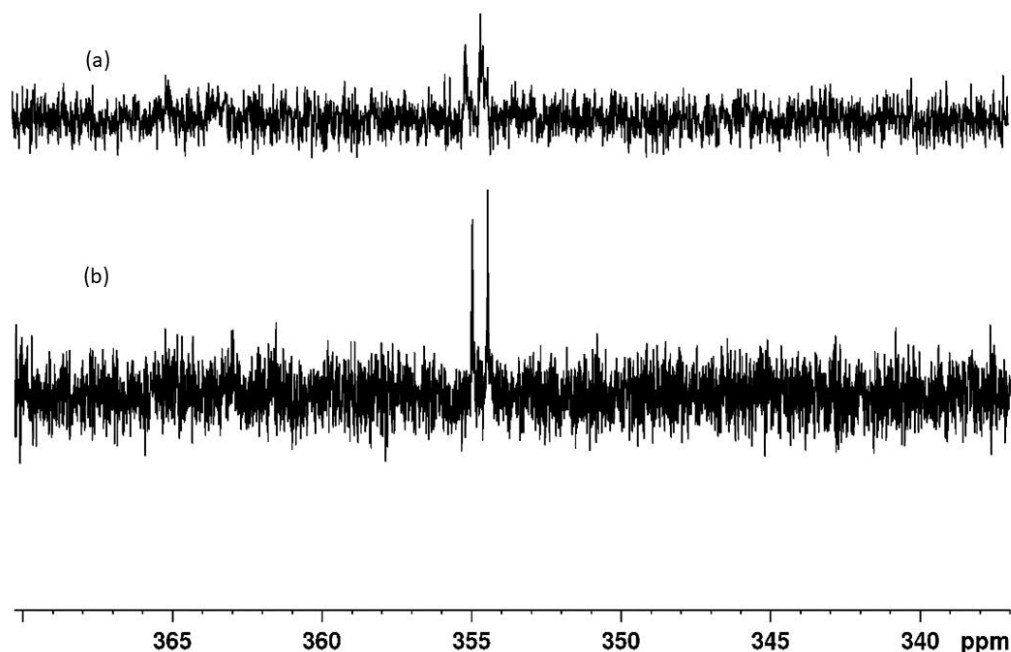


Figure 3.23: a) Hyperpolarised 1 scan ^{15}N NMR spectrum (above) b) Analogous hyperpolarised $^{15}\text{N}\{^1\text{H}\}$ NMR experiment (1 scan) of non-labelled T[2,3-*d*]P and [IrCl(COD)(*d*₂₂-SIMes)] in a 4 to 1 ratio in *d*₄-methanol. The sample was shaken in a mu metal shield for 10 seconds before measurement in a 500 MHz spectrometer.

From the calculations of PTF for ^{15}N , we would expect 2 mG to be the optimum field for direct transfer. Experiments were conducted to vary the field within the shield, using a DC driven coil, but this provided no benefit in terms of S/N. Due to this technical difficulty, experiments continued with the mu-metal shield alone.

It was hypothesised that synthetic ^{15}N labelling of the T[2,3-*d*]P would result in considerable signal enhancement benefits (100% abundance compared with 0.37% natural abundance). With the increased sensitivity of ‘labelled’ samples, detection of bound ^{15}N signals should be possible. Furthermore, the potential production of a ^{15}N - ^{15}N singlet state in the free material could be quantified in terms of signal lifetime.

3.5.3.1 Synthetic labelling of thieno[2,3-*d*]pyridazine-¹⁵N₂

Synthesis of non-labelled T[2,3-*d*]P via hydrazine hydrate was detailed in section 2.2 and resulted in a 77% yield. Here, the process was modified and completed using ¹⁵N₂-hydrazine sulfate and in the reaction with 2,3-thiophenedicarboxaldehyde. This resulted in a 90% yield of thieno[2,3-*d*]pyridazine-¹⁵N₂ (T[2,3-*d*]P-¹⁵N₂). The increased yield is reflective of the production of water during imine formation and the fact that dry hydrazine sulfate was the better reducing agent (Figure 3.24)

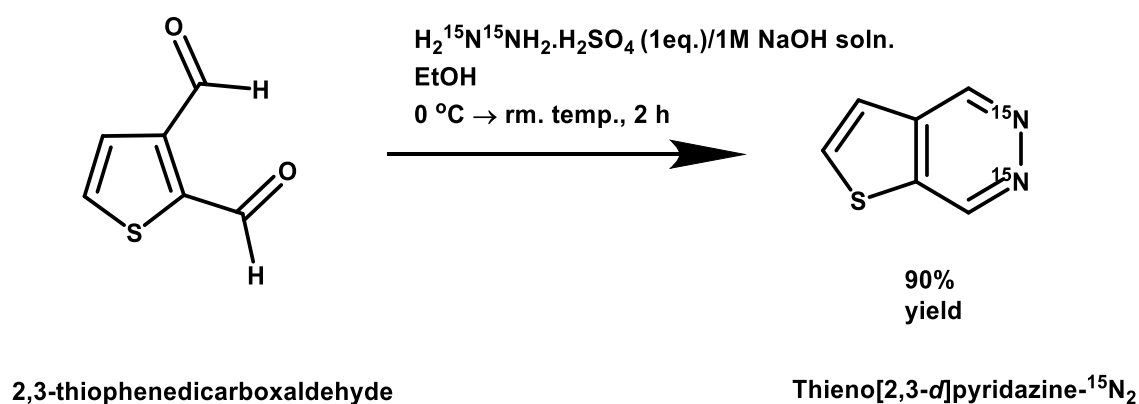


Figure 3.24: Reaction scheme for the novel synthesis of doubly labelled thieno[2,3-*d*]pyridazine-¹⁵N₂ in 90% yield.

Figure 3.25(a) shows the resulting thermally polarised ¹⁵N NMR spectrum of this product, which was measured with just 512 repetitions.

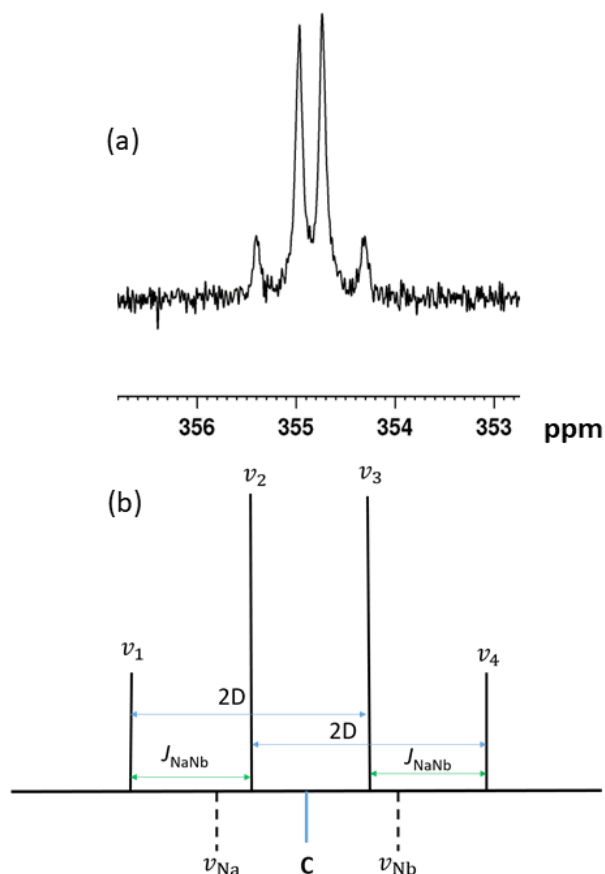


Figure 3.25: a) ^{15}N Thermal scan (512 transients) of T[2,3- d]P- $^{15}\text{N}_2$ in methanol- d_4 measured on a 9.4 T spectrometer (no catalyst present). b) Model of AB system showing J couplings and chemical shift frequencies.

As predicted, the ^{15}N NMR spectrum of T[2,3- d]P- $^{15}\text{N}_2$ exhibited an AB pattern and a signal ‘roofing’ effect was observed. The four peaks of this higher order coupling spectrum represent a combination of all the spins in the system. Consequently, the four peaks can be analysed to yield $J_{\text{Na-Nb}}$ according to equation 3.4:

$$|J_{\text{Na-Nb}}| = (v_1 - v_2) = (v_3 - v_4) \quad [3.4]$$

Where $v_{(1-4)}$ represents the frequencies of the four peaks as shown in Figure 3.25. This results in $|J_{\text{Na-Nb}}| = 21.43$ Hz at 11.74 T. In the unlabelled sample the chemical shift difference between the nitrogens was measured as $\Delta\delta_{\text{NaNb}} = 0.51$ ppm (corresponding to 25.86 Hz at 11.74 T) but this could also be calculated in the labelled sample using equation 3.5:

$$\Delta\nu = (v_{\text{Na}} - v_{\text{Nb}}) = \sqrt{[(v_1 - v_2)(v_3 - v_4)]} \quad [3.5]$$

$$= \sqrt{[(2D)^2 - J^2]}$$

$$v_{Na} = C + \frac{\Delta\nu}{2}$$

$$v_{Nb} = C - \frac{\Delta\nu}{2}$$

The chemical shift difference and the J coupling are almost equal to one another in this system and therefore would appear to be ideal candidates for the formation of a singlet state at low field.

Data shows that the optimum substrate to catalyst ratio for signal enhancement is 1:4 (section 2.4.1). However, the presence of the catalyst has a detrimental affect on the T_1 lifetimes (section 3.4.2). To try to reduce this effect on T_1 without greatly affecting signal enhancement a sample was prepared using [Ir(COD)Cl(d_{22} -SIMes)] as the SABRE precatalyst with a 1:6 catalyst to substrate ratio in d_4 -methanol. Shake and drop experiments were carried out on this sample in conjunction with the mu-metal shield and the variable field solenoid to probe SABRE across an array of PTF values, including 2 mG which was calculated as the optimum field for polarisation transfer. The earth's field (0.5 G) was also used to try to create a LLS. All experiments resulted in the collection of a highly complex series of ^{15}N NMR spectra suggestive of multiple species and multiple binding sites.

This result is not surprising, as section 2.3.2 detailed the formation of the T[2,3- d]P derived adduct [Ir(COD)(IMes)(T[2,3- d]P)]Cl which exists as two structural isomers which differ according to the nitrogen binding site. These two forms can be readily distinguished by their bound nitrogen NMR signals which appear at δ 286.6 (A) and δ 285.5 (B) alongside their un-bound nitrogen partner which yield signals at δ 357.0 (A) and δ 360.0 (B) respectively (Figure 3.26). Peak integration revealed that these two forms exist in equal proportions, and as they interconvert, they must have similar free energies.

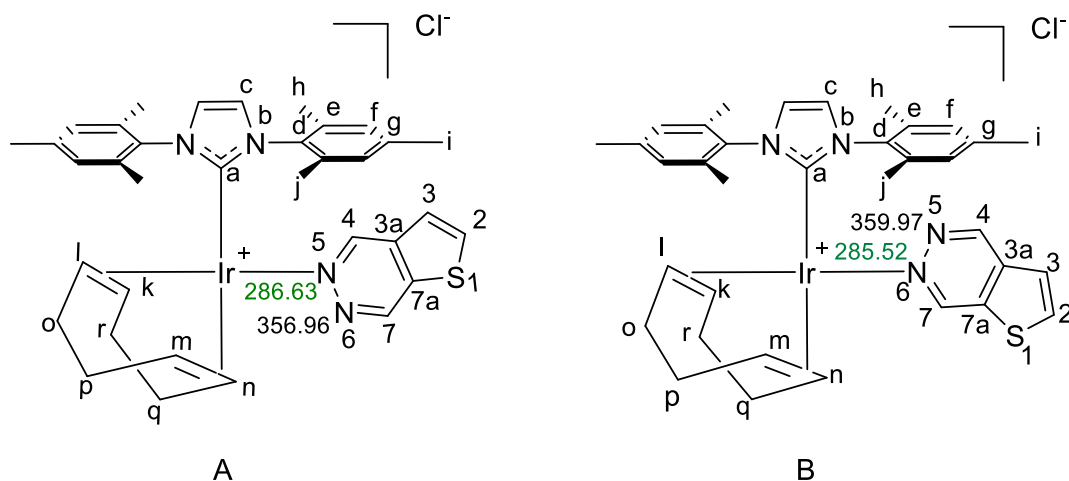


Figure 3.26: Precatalysts A and B showing the two possible modes of binding and the different nitrogen chemical shifts that arise.

Although the final SABRE active catalyst, $[\text{Ir}(\text{H})_2(\text{IMes})(\text{sub})_3]$, was not characterised in chapter two, a broad multiplet was observed at $\delta -21.5$ indicating there is a complex mixture of products.

Due to the asymmetry of T[2,3-*d*]P, eight isomers can form as depicted in Figure 3.27.

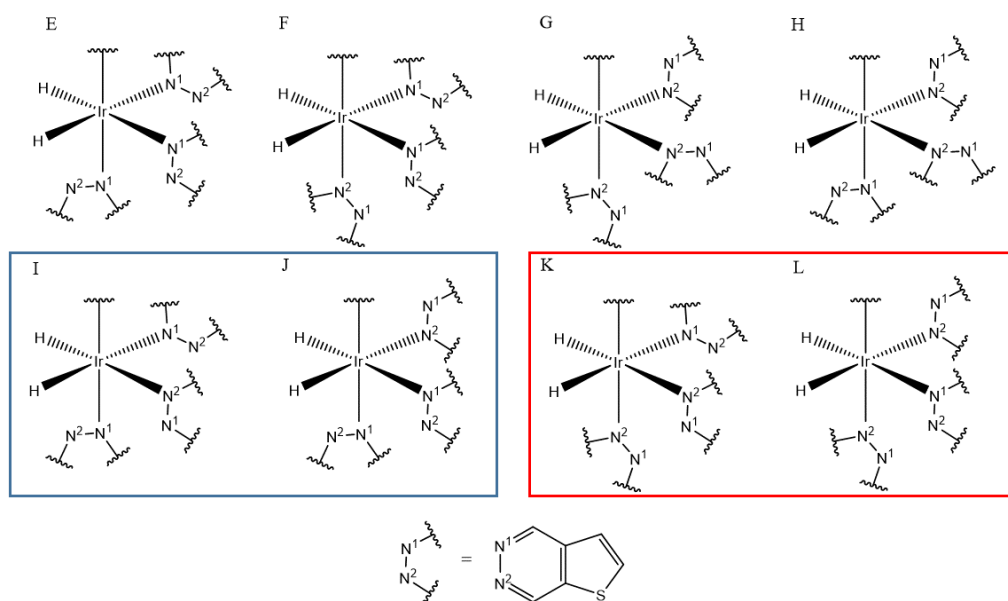


Figure 3.27: Eight possible regioisomers of $[\text{Ir}(\text{H})_2(d_{22}\text{-SIMes})(\text{thieno}[2,3\text{-}d]\text{pyridazine-}^{15}\text{N}_2)_3]$. The complexes within the rectangles indicate enantiomeric pairs.

Of these eight forms, two are enantiomeric pairs (blue and red boxes). Consequently, just six distinct forms should be seen by NMR spectroscopy. Collectively these would be predicted to yield 26 different ^{15}N resonances. The corresponding SABRE $^{15}\text{N}\{^1\text{H}\}$ NMR spectrum after transfer at 0.5 G PTF and detection at 11.7 T confirmed this complexity. The observation of signals in two regions, centred at $\delta 285$ and $\delta 305$, suggested the successful detection of bound

^{15}N resonances for ligands *trans* to NHC (axial) and *trans* to hydride (equatorial) respectively in accordance with previous studies on pyridine.²³⁶ The further rationalisation of this result was achieved by recording a series of 1D and 2D NMR spectra. According to the theory of SABRE, a singlet state shared between the two nitrogen centres in T[2,3-*d*]P should be created which upon NMR interrogation should lead to pairs of signals with opposite phase after a 90° excitation pulse. Analysis of the SABRE result started by recording a $^{15}\text{N}\{^1\text{H}\}$ NMR spectrum after such a pulse. The expected phase behaviour was observed with the bound ligand signals in accordance with this hypothesis, as shown in Figure 3.28. It contained strong ^{15}N signals for the axially bound T[2,3-*d*]P ligands (δ 280, blue star) alongside weak signals for the corresponding equatorial ligands (yellow star). The weak signals seen for the equatorially bound ligands were consistent with decoherence of the ^{15}N singlet state through coupling to the hydride ligands and rapid exchange with the catalyst. The strong signals derived from the axial ligands reflects their slow exchange and weak hydride coupling. The signals centred on δ 365 arise from the uncoordinated nitrogen centres of these axial ligands (purple star).

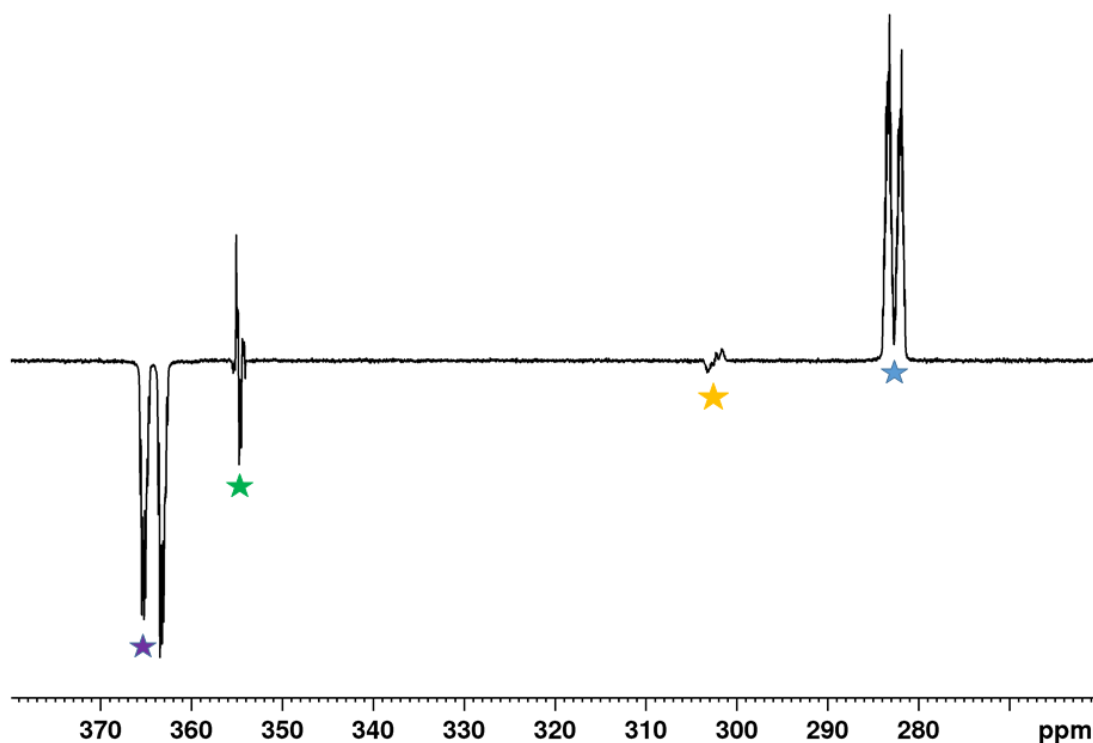


Figure 3.28: Single scan hyperpolarised $^{15}\text{N}\{^1\text{H}\}$ NMR spectrum of doubly labelled ^{15}N -thieno[2,3-*d*]pyridazine achieved by precatalyst [Ir(COD)Cl(d_{22} SIMes)] when present in a 1:6 ratio in d_4 -methanol solution after PT at Earth's field. Blue stars (bound nitrogen in axial position), Purple stars (uncoordinated nitrogen in axial position) yellow star (bound nitrogen in equatorial position) and green star (nitrogen in free substrate)

Figure 3.29 shows an expansion of these spectral regions which demonstrates the ability of SABRE to unravel a very complex response within a single scan measurement. The two regions are each made up of three sets of doublets where $J_{15N-15N}$ varies between 18 and 20 Hz. The adjacent nitrogen partners to these resonances appear within two similarly complex patterns at δ 365.5 and δ 363. The splitting pattern profiles differ within these peaks because the corresponding chemical shifts are different.

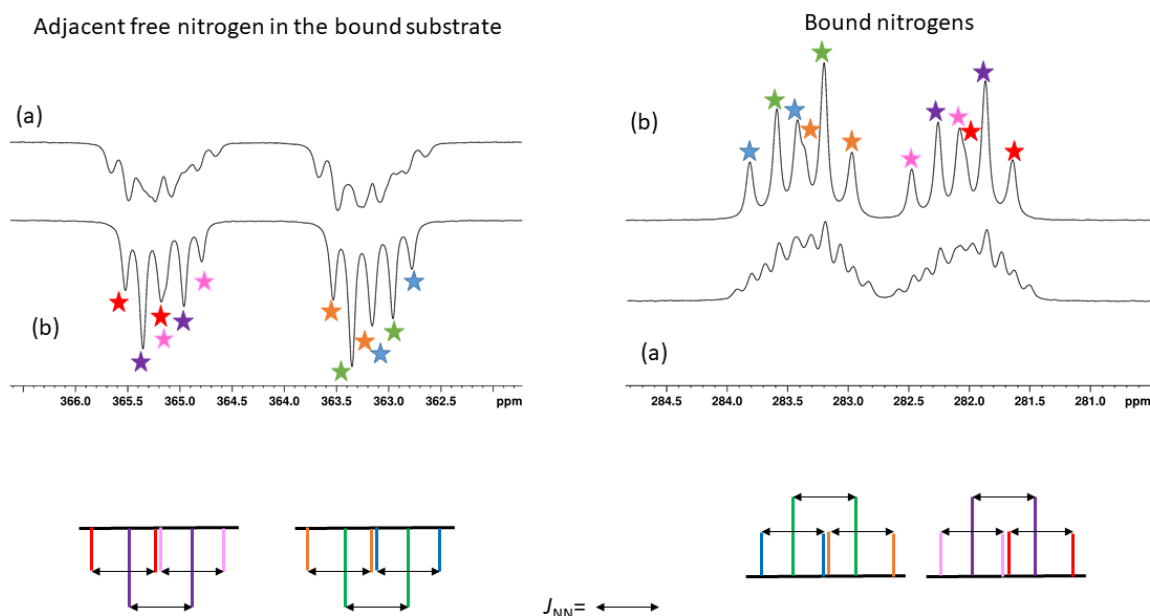


Figure 3.29: Expansion of axially bound ligands in (a) ^{15}N hyperpolarised spectrum and (b) $^{15}\text{N}\{^1\text{H}\}$ hyperpolarised spectrum after PTF at earth's field. The different colours represent the six different ^{15}N signals as doublets with $J_{15\text{N}-15\text{N}}$

Although these spectra show quite clearly the signals arising from the bound and adjacent uncoordinated nitrogen in the axial positions, the equatorially bound ligands were not easily distinguished. The equatorially bound nitrogen signals were present but weak. The uncoordinated nitrogen partners were absent. A much more thorough analysis was required to locate these and to fully characterise and confirm the existence of the eight regioisomers predicted.

A series of low temperature (263K) ^1H - ^{15}N Heteronuclear Single Quantum Correlation (HSQC) experiments were carried out under thermal equilibrium to characterise these isomers. These NMR spectra revealed that the ^{15}N signals from the uncoordinated nitrogen centres of the equatorial ligands overlapped with the signals arising from those in the axial ligands. By collecting appropriate data, it was possible to connect the hydride ligands of the six isomers to discrete ^{15}N resonances through the associated *trans* J_{HN} couplings of 18-20 Hz and thereby identify the equatorial ligands (Figure 3.30).

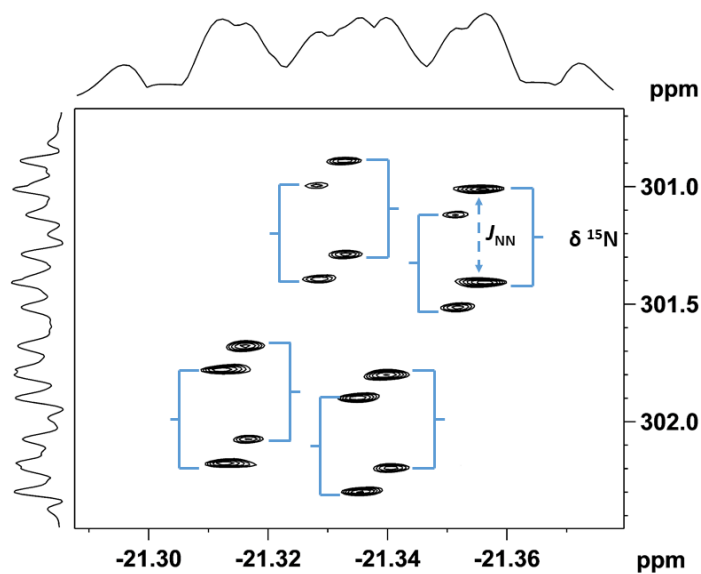


Figure 3.30: 2D ^{15}N ^1H HSQC (263K) of T[2,3- d]- $^{15}\text{N}_2$ with [Ir(Cl)(COD(d_{22} -SIMEs) in methanol- d_4 after activation with H_2 . Used to identify the eight equatorially bound nitrogen resonances in complexes E-L. J_{NN} coupling identified by the dotted line and $\delta^{15}\text{N}$ resonances identified by the midpoint of the solid line

Connections between the ligands ^{15}N and ^1H resonances then allowed signals to be attributed to unique axial ligands. By using a longer polarisation transfer delay it proved possible to identify connections between the hydride ligands and the remote ^{15}N centres in T[2.3- d]P. Characterisation data for the eight isomers is presented in appendix 2, where complete assignments were possible.

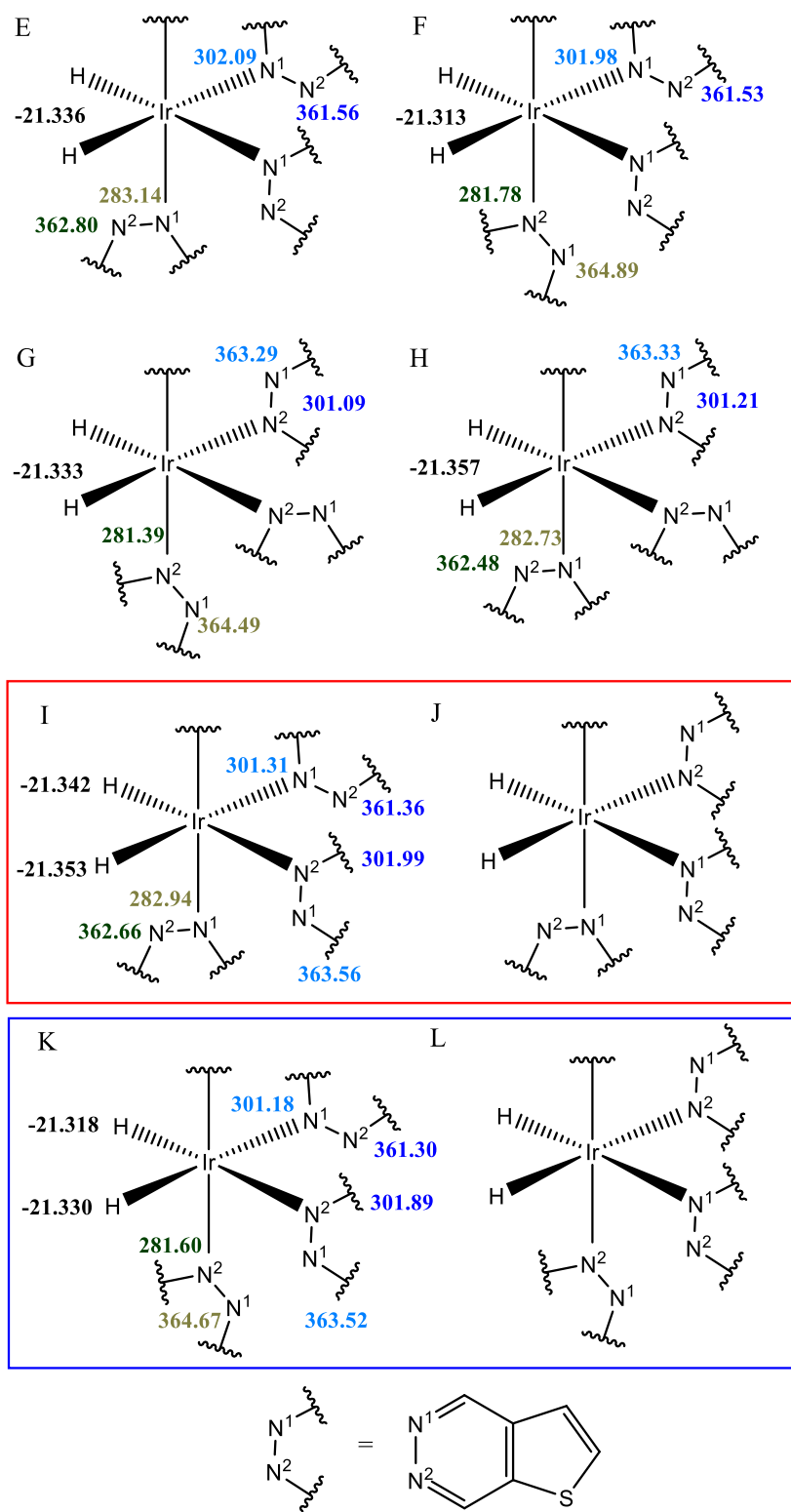


Figure 3.31: Assigned ^1H hydride NMR resonances and ^{15}N resonances of the eight regioisomers of $[\text{Ir}(\text{H})_2(\text{T}[2,3\text{-}d]\text{P-}^{15}\text{N}_2)_3](d_{22}\text{-SiMes})$ at 11.7 T. The complexes within the rectangles indicate enantiomeric pairs. Resonances arising from the ^{15}N in the equatorial position are donated in blue where N¹ is light blue and N² is dark blue. Resonances arising from the ^{15}N in the axial position are donated in green where N¹ is light green and N² is dark green.

Figure 3.31 links the hydride resonances for the equivalent hydrides in complexes E-H and the inequivalent hydrides in complexes I-L to the ^{15}N resonances of bound T[2,3-*d*]P. The increased intensity of the signals for the two pairs of enantiomers is reflective of their higher proportion. It must be noted that the chemical shifts listed for these inequivalent hydride ligands reflect the peak positions for the intense inner lines of their AB multiplets. As the associated smaller outer peaks lie only just above the noise, their exact chemical shifts were not calculated.

The ^{15}N NMR resonances arising from the free substrate appeared to be more complicated as they did not have the characteristic down, down, up, up peak pattern. Instead, a down, up, down, up pattern presented. In an experiment using a small flip angle (e.g. 10°) it was expected that either the two inner or the two outer peaks would disappear,¹⁵¹ however, this did not occur.

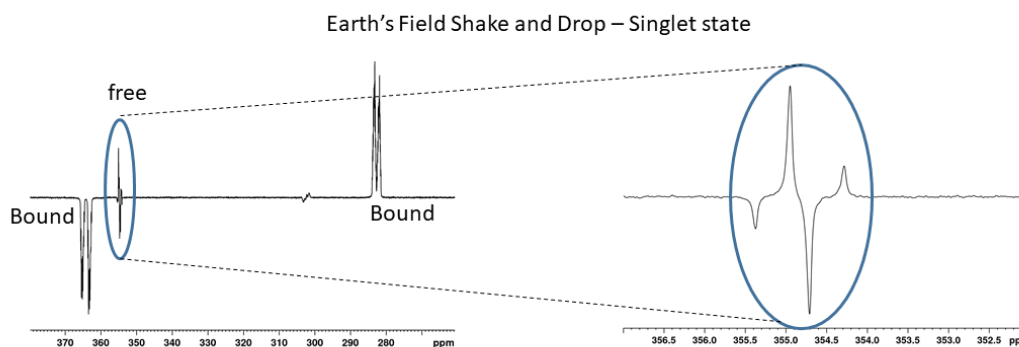


Figure 3.32: Natural singlet state formed when shaking in earth's magnetic field. The characteristic singlet can be seen in both the free substrate (shown within blue oval) and in the bound peaks.

When the substrate is bound to the catalyst, first order character exists, and the predicted singlet appearance is observed. However, given the evidence of complicated second order character within the multiplet signal arising from the free substrate, the exact appearance of these spectra was not further analysed.

To explore the LLS behaviour of the synthesised labelled product a field cycling approach was undertaken. Samples were shaken with $p\text{H}_2$ in the earth's field for 10 s and then stored in the mu metal shield for various time periods. Storage in the mu metal shield will collapse the chemical shift difference. After 90 s of storage a hyperpolarised response was observed. The two signals

were not antiphase with respect to one another but instead both possessed the same phase which is indicative of direct magnetisation. It appeared that using the mu metal shield was sufficient to achieve this matching condition and cause direct hyperpolarisation into the nitrogen. In practice, at all of the polarisation transfer fields tested free ^{15}N -thieno[2,3-*d*]pyridazine signals alongside the corresponding ligand bound signals were observed. When the mu metal shield was employed with a solenoid to try and polarise nitrogen directly, signals were seen with varying intensities according to field. The field which gave the largest enhancement was at -7 mG.

A maximum ^{15}N signal enhancement of -2166 fold ($\text{S/N} = 1063.80$) was recorded for the free material with a -7 mG field. Figure 3.33 compares the $^{15}\text{N}\{^1\text{H}\}$ single hyperpolarised scan and 16-scan thermally polarised NMR spectrum (at a relative 8 x vertical expansion).

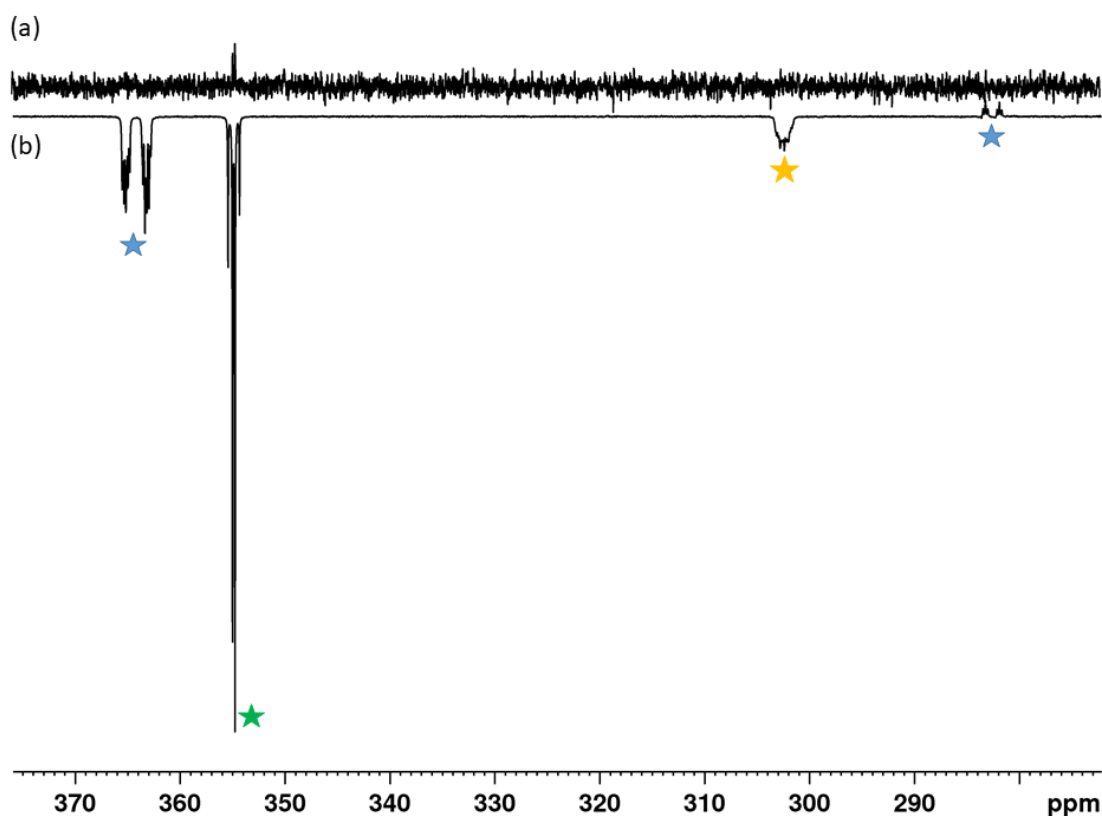


Figure 3.33: a) Thermal $^{15}\text{N}\{^1\text{H}\}$ NMR spectrum (16 transients) expansion vertically multiplied by 8; b) Single scan hyperpolarised $^{15}\text{N}\{^1\text{H}\}$ NMR spectrum of doubly labelled ^{15}N thieno[2,3-*d*]pyridazine achieved by precatalyst $[\text{Ir}(\text{COD})\text{Cl}(d_{22}\text{SImes})]$ when present in a 1:6 ratio in d_4 -methanol solution after PTF at -7 mG. Blue stars (bound equatorial), yellow star (bound axial) and green star (free)

The neighbouring spin $1/2$ protons could also be a source of relaxation and therefore a further extension was to synthesise and test a fully deuterated version of the ^{15}N labelled

thienopyridazine. It has previously been proved that by replacing the protons with the quadrupolar deuterium ($I=1$) T_1 lifetimes can increase.¹³⁵

3.5.3.2 Synthesis of d_4 -thieno[2,3-*d*]pyridazine- $^{15}\text{N}_2$

The synthesis of d_4 -thieno[2,3-*d*]pyridazine- $^{15}\text{N}_2$ was novel; therefore the deuteration reaction was initially tested on the less expensive non-labelled form of T[2,3*d*]P. This reaction was previously described (section 2.4.5) where it was used to demonstrate polarisation enhancement using a fully deuterated co-ligand. T[2,3-*d*]P was refluxed in D_2O in the presence of a base. Although the four-week preparation time was lengthy, ~95% deuteration was achieved. The successful synthesis was then repeated with the more expensive labelled thieno[2,3-*d*]pyridazine- $^{15}\text{N}_2$ molecule (following formation as described in section 3.5.3.1). This synthetic route could be improved, in terms of efficiency and overall deuteration, but as the molecule was used to simply demonstrate proof of principle for reducing relaxation effects, optimisation of the reaction was beyond the scope of this thesis.

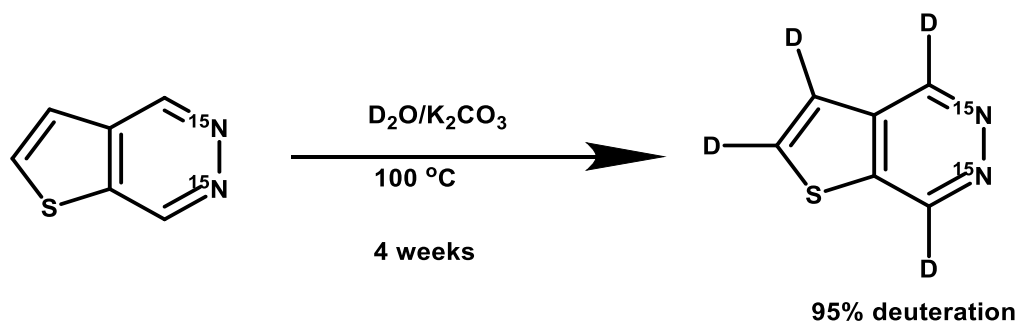


Figure 3.34: Novel synthesis of d_4 -thieno[2,3-*d*]pyridazine- $^{15}\text{N}_2$. Deuteration was achieved by refluxing the previously synthesised thieno[2,3-*d*]pyridazine- $^{15}\text{N}_2$ in D_2O with base for 4 weeks. 95% deuteration was achieved across the four resonances

SABRE hyperpolarisation experiments were repeated with d_4 -thieno[2,3-*d*]pyridazine- $^{15}\text{N}_2$ under the same conditions i.e. 1:6 catalyst to substrate ratio, 3 bar (g) *p*- H_2 in methanol- d_4 .

Hyperpolarisation at -7 mG once again showed a large signal enhancement of -8291 (2.7% polarisation and S/N 2697.16) compared with -2167 (0.71% polarisation and S/N 1063.80) for the non-deuterated version (see Figure 3.35). This result confirmed that the polarisation (at -7 mG) must be going directly through to nitrogen and dispersing across the hydrogen sites (spin dilution effect). In the case of the fully deuterated form the polarisation remains on the nitrogen nuclei and is therefore higher.

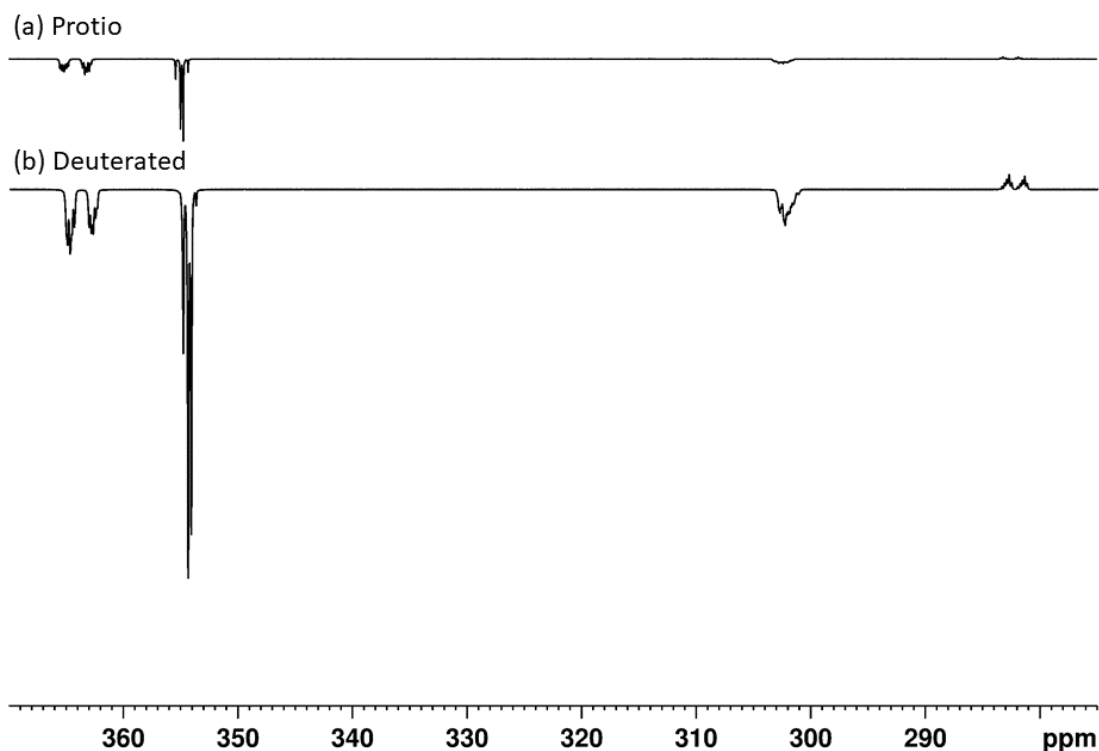


Figure 3.35: Hyperpolarised single scan NMR at -7mG using $[\text{Ir}(\text{COD})\text{Cl}(d_{22}\text{SIMes})]$ as pre-catalyst present in a 1:6 ratio in d_4 -methanol solution with (a) thieno[2,3-*d*]pyridazine- $^{15}\text{N}_2$ and (b) d_4 -thieno[2,3-*d*]pyridazine- $^{15}\text{N}_2$

3.5.3.3 Magnetic Lifetimes

The lifetime of the hyperpolarised signal of free T[2,3-*d*]P- $^{15}\text{N}_2$ was measured at 11.7 T using repeated 10° flip angle interrogation after shaking at -7mG . T_1 was found to be 6 s. It is noted that the relatively short T_1 value is a function of the catalyst still being in solution during measurement. This value was verified by running a thermal inversion recovery T_1 experiment also in the presence of the catalyst which yielded the same value. The hypothesis was that by deuterating at all four proton sites, the T_1 of the hyperpolarised nitrogen nuclei would increase. Relaxation through coupled protons is six times more efficient than that of deuterium. However for d_4 -T[2,3-*d*]pyridazine- $^{15}\text{N}_2$ the T_1 was also found to be 6 s. Hence whilst deuteration improved signal enhancement compared with its protio counterpart, it had no effect on the lifetime in the presence of the catalyst. It can be concluded that the presence of the catalyst even in a 1:6 ratio is the dominant source of relaxation in both cases.

The lifetime of the hyperpolarised signal was also measured after shaking at earth's field. As the singlet state should be present at any field it was thought that the lifetime of the singlet state could be measured at this field. The lifetime measured was only 3 s after shaking in the earth's field and

immediately transferring to high field for measurement. Similar findings were observed for the deuterated version.

3.6 Conclusions and Discussions

Here the effect of using singlet state nuclear spin order as a mechanism for protecting and storing hyperpolarisation from the relaxation mechanisms responsible for T_1 decay was explored. In perfectly symmetrical molecules like H_2 the singlet state can in fact be separated from its triplet states as a stable spin isomer, $p\text{-}H_2$ (with a lifetime in the order of months under the right conditions). Work by Levitt et.al. (2004)^{210, 211} has shown that singlet state phenomenon are not limited to systems with both a high degree of symmetry and spin isomerism; but can be pseudo-achieved in a much wider range of molecules.^{210-213, 224, 237}

The 3,6-substituted pyridazines showed a marked extension in lifetime using the long-lived state high field spin lock approach. An effective three times increase in signal lifetimes was observed. In particular, the methoxy-substituted pyridazine having already substantial T_1 values of 31 and 29 seconds yields a T_{LLS} value of over 100 seconds. When considering eventual clinical MR detection of such agents this permits more time for both quality assurance procedures and detection. However, hyperpolarisation levels in these simple motifs proved to be very low or non-existent (in the fluoro-substituted molecule). SABRE inactivity can be explained in terms of both electronic (mesomeric, M/inductive, I) and steric effects (A value, general representation of steric bulk) of the substituents yielding poor ligands for catalysis.

For the three pyridazine motifs tested, the presence of $-I$ chloride results in a deactivating inductive effect reducing the ability of the nitrogen centres within the N-heterocyclic ring to bind. The amino group (NH_2) is one of the most electron-donating of functional groups tested, due to $+M$ resonance effects, and this would act to offset the effect of the Cl. Overall, the stronger $+M$ effect of the amino groups must contribute enough electron density into the aromatic ring and the nitrogens so that they are able to bind into the iridium centre, albeit weakly, allowing limited polarisation transfer (-117-fold enhancement on H5). In terms of steric effects Cl has an A value of 0.43 whereas $-NH_2$ is larger with an A value of 1.6.

The methoxy group ($-OCH_3$) although not as strongly activating as the amino group should still donate electron density due to resonance effects ($+M$). However, with the competing $-I$ effect of the chlorine this may explain the SABRE inactivity in the case of 3-chloro-6-methoxypyridazine.

In terms of sterics, the A value for $-\text{OCH}_3$ is relatively small (0.6) compared with the $-\text{NH}_2$ and CF_3 .

Fluorine is the most electronegative atom with a value of 4.0 on the Pauling scale. CF_3 therefore is one of the most deactivating groups, through induction effects, second only to NO_2 . With three fluorine atoms drawing the electron density away from the bonding nitrogens, plus the chlorine substituent on the opposite site, these two negative effects could prevent binding into the metal centre. The A value for CF_3 is also large at 2.1. So, both sterics and electronic effects may contribute to the inactivity as a SABRE ligand.

In addition, these motifs with substituents at the 3 and 6 position, adjacent to the two nitrogen sites, could prevent polarisation crossing the spin system. However, previous data²³¹ suggests this should not be a problem as other related molecules deuterated in these positions still polarise.

Conversely the thienopyridazines showed high levels signal enhancement (over 2000 fold for H7 and H4 of T[2,3-*d*]P) but a pseudo long-lived state could only be created in T[2,3-*d*]P on resonances H2 and H3. There was a small extension of their lifetimes with the T_{LLS} compared to their individual T_1 lifetimes. It must be noted, however, that firstly this extension is on the two resonances, H2 and H3, receiving the least polarisation when hyperpolarised with ~880-fold and ~450-fold enhancements respectively compared with over 2000-fold enhancements in H4 and H7. Secondly the T_{LLS} lifetime, of 40 s was less than the individual T_1 of H7 which receives the most hyperpolarisation. The T_{LLS} method for thienopyridazines with regard to ^1H singlet states was not able to extend the overall hyperpolarisation lifetimes of these particular molecules. This is because there are more spins involved in the system, the situation is much more complex when considering the effect of the J couplings and the interplay of other relaxation mechanisms. Singlet relaxation times can be reduced if one of the nuclei in the singlet state pair is also coupled to another nucleus. Out-of-pair J couplings can cause interconversion of the singlet with the set of triplet states which then relax due to dipole-dipole coupling. It has been demonstrated that the singlet state can be protected from this mechanism only if the intrapair J coupling is much larger than the difference of the two out-of-pair couplings.²³⁸ In addition the spin-locking method is hard to achieve in the case of large chemical shift differences. It may be that the chemical shift differences were too large in the thienopyridazine proton pairs for spin locking to be efficient.

The T_{LLS} measurements were carried out in high field using a 'spin-lock' to reduce the chemical shift difference and impose symmetry. Although this is a very effective and simple method, the

field cycling experiment where the sample is physically transported into low field usually has been shown in many situations to be more effective at reducing the chemical shift difference.

Although field cycling has been shown to provide better LLS values it was not possible in this case as when attempts were made to remove the sample adiabatically from high field to low field the effect of the catalyst at the 1:4 loading was too severe and no signal could be detected at the read-out stage. This is not surprising given the extremely short T_1 estimates in the presence of the catalyst (Table 3.4). In the future it might be sensible to repeat these measurements with a higher excess of substrate to increase lifetime but obviously the hyperpolarisation level will fall. There have been many recent advances in catalyst design¹²³ and a more comprehensive study of catalyst would also be warranted.

Investigations into X nuclei showed that carbon hyperpolarisation is possible for T[2,3-*d*]P with the two quaternary carbons being easily seen in a single SABRE hyperpolarised experiment. Conditions were optimised to achieve the highest signal to noise/signal enhancement, and it was observed that these two central carbons resonances with their similar chemical shifts could be candidates for a singlet pair. The difficulty here was that ^{13}C labelled carbons would be required to try and create and test this singlet. However the synthesis of T[2,3-*d*]P- $^{13}\text{C}_2$ was beyond the scope of this thesis.

Nitrogen hyperpolarisation was shown to be possible with the two nitrogen nuclei observed in a single scan in the non-labelled T[2,3-*d*]P. In the case of nitrogen, novel synthetic steps were undertaken to create the doubly labelled T[2,3-*d*]P- $^{15}\text{N}_2$. It was identified that the $\Delta\delta$ between the nitrogens was 25.86 Hz and that $J_{\text{NN}} = 21.43$ Hz. It was hypothesised that with these conditions the creation of a singlet state would be possible. Indeed, natural occurring singlet states were created and observed in both the free and bound peaks.

Remarkably, when ^{15}N labelling was introduced into the molecule it became possible through an extensive series of low temperature (263 K) ^1H - ^{15}N Heteronuclear Single Quantum Correlation (HSQC) 2D NMR experiments to characterise the eight SABRE active complexes that were predicted in chapter two. Upon binding, the catalyst breaks the symmetry of the thienopyridazine

ligand giving definitive proof of the existence of the singlet state and all ^{15}N signals were readily visible.

Novel synthetic steps were also taken to synthesise the fully deuterated version, $d_4\text{-T}[2,3\text{-d}]\text{P-}^{15}\text{N}_2$, in an effort to increase polarisation levels and increase magnetic lifetimes. Hyperpolarisation at -7 mG showed a large signal enhancement of -8291 (2.7% polarisation and S/N 2697.16) compared with -2167 (0.71% polarisation and S/N 1063.80) for the non-deuterated version. Although low field storage proved to be difficult, work carried out by Theis et al. (2016) demonstrates that in systems such as these ^{15}N long lived singlet states can be generated at 0.4 and 0.6 T.¹⁵¹ ^{15}N NMR has the potential to be highly diagnostic as chemical shift reflects a good indicator of structure.

It is clear that the creation of pseudo singlet states between pairs of nuclei is possible and the associated decay constant T_{LLS} can be longer than the individual T_1 lifetimes. However, in terms of hyperpolarised biomolecular imaging there are limitations. When considering the creation of pseudo long-lived states using MRI directly, both the high field spin lock method and the field-cycling method may be impractical. The use of multiple spin echo sequences (i.e., the spin lock stage) could potentially exceed safe power levels and rapidly shuttling a patient from high field (the MRI scanner) to low field (outside the MRI scanner) is unrealistic. However, research has shown that rapid field-cycling in MRI is now possible.²³⁹ To date no important hyperpolarised metabolite has demonstrated a sufficiently long lived singlet lifetime in a biologically relevant media to warrant clinical translation. $^{13}\text{C}_2$ -labelled pyruvate appeared to be a promising target, however, the increase in lifetime observed at low field²¹³ was not observed at the higher fields required for medical imaging. Labelling the anaesthetic gas, nitrous oxide to form $^{15}\text{N}_2\text{O}$ was also identified as a potential candidate as a 20 minute T_s was recorded in solution.²²⁴ Unfortunately, in the gas phase this lifetime was reduced dramatically by very efficient nuclear spin-rotation relaxation. The prospect of hyperpolarised singlet states in the future of MR imaging is still a huge and exciting prospect but more research and development are required to make this clinically accessible.

Chapter 4: SABRE-Relay: A versatile route to hyperpolarisation

4.1 Introduction

The catalytic process upon which SABRE hyperpolarisation depends has been illustrated and expanded through the presented work on the target thienopyridazine molecules (Chapter 2). By optimisation of both the synthesis and polarisation conditions, a 10,128-fold \pm 228 (33% polarisation) ^1H NMR signal enhancement was achieved for T[2,3-*d*]P. Whilst the NMR signal enhancements observed using traditional SABRE may reach impressive levels of polarisation, they are in one sense “limited” to resonances corresponding to nuclei on substrates that bind reversibly to iridium, which are typically *N*-heterocycles, nitriles,¹⁸⁸ Schiff bases and diazirines.^{151, 240} There has been considerable success with *N*-heterocycles, in particular *d*₂-methylnicotinate and *d*₂-nicotinamide¹³⁵ which have now been taken through to *in vivo* experimentation. Recently reported studies have proven that important metabolites such as pyruvate²⁴¹ and acetate²⁴² are also now amenable to direct SABRE transfer. However, to be able to extend SABRE to include other biologically important classes of substrates, alternative methods were required to overcome the requirement of binding the target substrate to the iridium catalyst. In essence, relaying the polarisation through an intermediate.

Two particular methods have proven to be successful in relaying hyperpolarisation; so called SABRE-Relay.^{168, 243} In one method the polarisation is relayed from a hyperpolarised proton on a carrier molecule/transfer agent (usually ammonia or an amine) to a proton on the substrate of choice through a process of proton exchange. This technique has extended the classes of compounds that can be hyperpolarised through SABRE to potentially any molecule containing functionality with an exchangeable proton (Figure 4.1a).²⁴³ In an alternative method, the polarisation created through SABRE is cascaded through a hyperpolarised substrate intermediate onto the remote ligands of a second metal complex (Figure 4.1b).¹⁶⁸

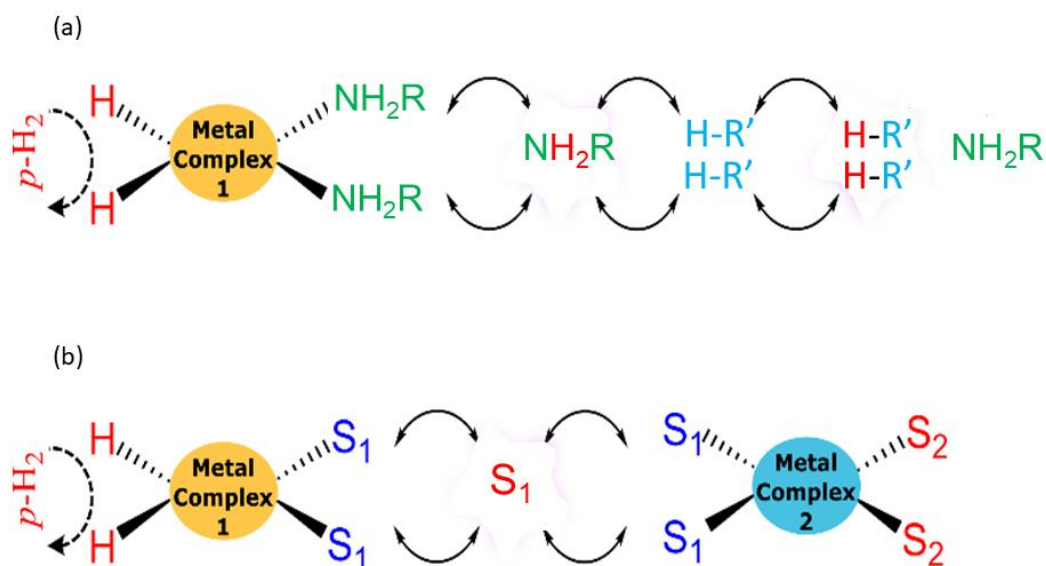


Figure 4.1: a) Schematic depiction of SABRE-Relay using a transfer agent, NH_2R (where $\text{R} = \text{H}$ or CH_2Ph or $\text{CH}_2\text{CH}_2\text{Ph}$ etc). NH_2R relays its polarisation received from $p\text{-H}_2$ to the target substrate $\text{R}'\text{-H}$ (where $\text{R}' = \text{amide}$, carboxyl etc.) through proton exchange. b) Schematic depiction of SABRE-Relay with a second metal complex; substrate S_1 binds reversibly to metal complexes- M_1 and M_2 , while S_2 represents the final target which receives the relayed polarisation.

In this chapter, the development of the latter method, using a second platinum-based catalyst, will be investigated. The theory behind this technique will be discussed in section 4.2. At the time of joining the project no work had been published. The initial concept was demonstrated by two post-doctoral researchers within the group using the platinum catalyst, $[\text{Pt}(\text{OTf})_2(\text{dppp})]$. The techniques used for the synthesis and characterisation of the platinum catalysts will be described in section 4.3 and can also be found in the first published SABRE-Relay work (Roy *et al.*, 2018) of which I am a co-author.¹⁶⁸ Full characterisation of the SABRE-Relay process including the two metal complexes formed will be exemplified in section 4.4 which are also detailed in Roy *et al.* (2018). The work carried out in the remaining sections extended and optimised the work of the original published data. In Section 4.5 a comparison of pyrimidine and its deuterated isotopologues will be investigated in terms of their efficiency as ligands for polarisation transfer in this method. Pyrazine will be investigated as a ligand for the SABRE-Relay process in section 4.6 and shows how the process is affected in terms of substrate loading. Deuterated methyl nicotinate has proved to be the substrate with the highest polarisation to date in SABRE studies¹³⁵. In section 4.7, a study will investigate if the high ^1H polarisation levels in deuterated methyl nicotinate can be carried through to give high levels of signal enhancement in the remote ^{31}P

ligands on the second metal complex. A final study, in section 4.8, will investigate the thienopyridazines and investigate their suitability as polarisation transfer ligands in this process.

4.2 Theory - SABRE Relay with a square planar platinum complex

The SABRE process relies on singlet state $p\text{-H}_2$ as a source of polarisation. Polarisation transfers through a metal complex, M_1 , into a substrate S_1 . Through a detailed understanding of spin polarisation transfer mechanisms, Roy *et al.* (2018) recognised polarisation on S_1 would be subsequently transferred, via J coupling, to the ‘scaffold’ of the second metal complex, M_2 . In turn this would enhance the NMR resonances of a substrate (S_2) also bound upon M_2 . As the second agent, S_2 , never actually comes into contact with $p\text{-H}_2$, a key requirement is that hyperpolarized S_1 has a long lifetime. Thus, it was hypothesised that larger molecules which also exhibit pseudo-singlet state behaviour (see chapter 3) could be used as a secondary/intermediate source of polarisation.

Roy *et al.* (2018) went on to demonstrate that 2,6- d_2 -nicotinamide and 2,4- d_2 -nicotinamide (both of which contain two neighbouring “isolated” protons and thus can form a pseudo-singlet state) could relay polarisation and enhance sensitization of the ^{31}P nuclei within a second metal complex $[\text{Pt}(\text{OTf})_2(\text{dppp})]$. When 4,5,6- d_3 -nicotinamide was used (which cannot form a singlet state) no ^{31}P hyperpolarisation was observed.¹⁶⁸ Whilst clearly demonstrating a possible mechanism for the polarisation relay observed it was recognised that several other well-defined mechanisms for polarisation transfer could also be possible. One example is the incoherent spin polarisation induced nuclear Overhauser effect (SPINOE). This mechanism was responsible for the single spin based ^{129}Xe hyperpolarisation into a second agent.²⁴⁴ Another possible mechanism presents through coherent single spin Zeeman order transfer.^{245, 246}

Here, the original study is extended upon by expanding the portfolio of both platinum metal complexes and transfer intermediates. Therefore, a detailed understanding of square planar platinum catalysts is required.

4.2.1 Square Planar Platinum Catalysts: Substitution reactions and the Trans effect

Square planar d^8 based transition-metal complexes containing weak donor ligands, particularly platinum and palladium complexes of the type $[MX_2L_2]$ ($M = Pd$ or Pt , $X =$ anionic ligand, $L =$ weak donor ligand), are valuable starting materials in organometallic chemistry. Their usefulness lies in the ease with which the donor ligand may be displaced.²⁴⁷

In Figure 4.1b the pre-catalyst used for metal complex 1 was $[IrCl(COD)(d_{22}\text{-Imes})]$. This complex was chosen as it generally gives good signal enhancements for a wide range of substrates. Metal complex 2 was a square planar platinum complex, $[Pt(OTf)_2(dppp)]$. The second complex needs to be easily substituted by the hyperpolarised substrate. In this case, triflate groups are labile leaving groups and the chelated phosphine group provides stability for the complex. In addition, it has NMR active phosphorous atoms present to probe for hyperpolarisation transfer.

Square planar $Pt(II)$ complexes have been studied extensively due to the ability to isolate suitable precursors and then introduce a reagent to achieve substitution where the reaction is sufficiently slow as to be followed by traditional spectroscopic methods such as UV and NMR. For NMR, slow reactions can be followed easily as a series of spectra can be recorded provided the gap between spectra is greater than a few seconds. For faster reactions that are not reversible, stop-flow in UV is normally used. Generally such complexes undergo substitution via an associative mechanism (Figure 4.2) where both bond-breaking and bond-making can be important.²⁴⁸

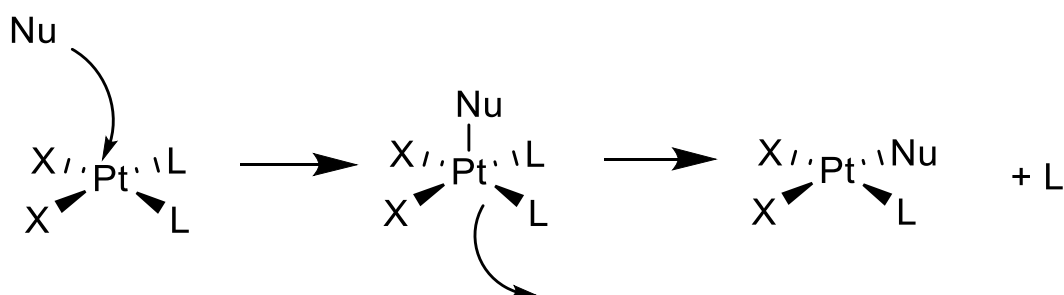


Figure 4.2: Square planar substitution reaction where X = spectator ligand, L = leaving group and Nu = nucleophile.

Provided the reaction does not proceed by slow solvent substitution (e.g., in the presence of water), these reactions are first-order in complex, first-order in the entering group and second-order overall. The rate constants may vary widely with the identity of the nucleophile. The sensitivity of the reaction to the entering nucleophile in contrast to its insensitivity to the leaving

group indicates that the nucleophile is the major factor determining the overall activation energy.²⁴⁹ This behaviour is expected in an associative substitution as the reaction passes through an activated complex with increased coordination number. As the stereochemistry is retained during this process, an activated complex which is a 5-coordinate trigonal bipyramid (Figure 4.3) structure is involved.^{249, 250}

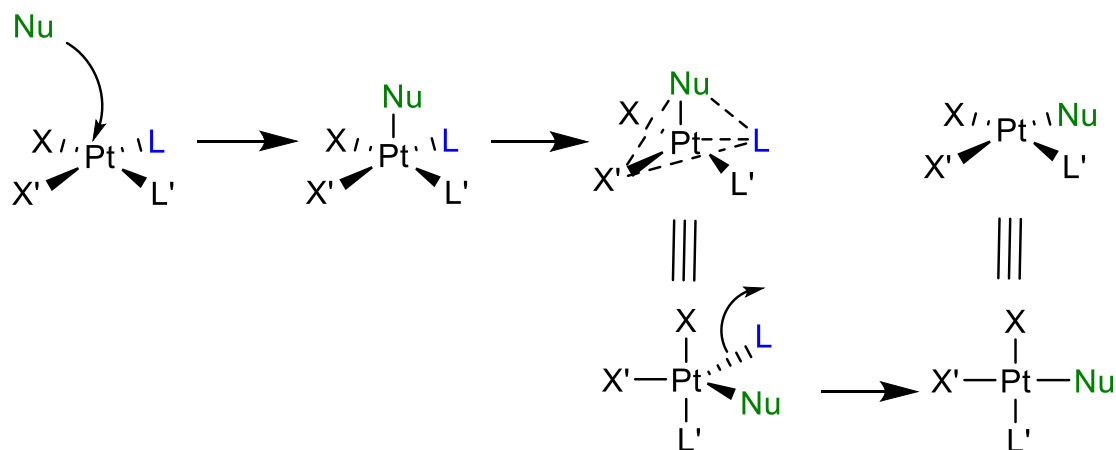
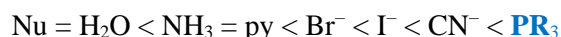


Figure 4.3: Mechanism of an associative square planar substitution reaction involving a 5-coordinate trigonal bipyramid intermediate.

Factors affecting the rate of substitution

- 1) **The entering group (Nu).** The rate of substitution is proportional to the nucleophilicity of the entering group, i.e., for Pt(II), the rate increases in the order:



hard

soft

This trend is element specific and consistent with Pt(II) being a soft metal centre. There is no correlation with other properties of nucleophiles, such as basicity, redox potentials or pKa. The most important factor is the polarizability or “softness”

- 2) **The leaving group (L).** The same principle applies but now in reverse.

Thus, good entering groups (good nucleophiles) are usually poor (non-labile) leaving groups. A triflate group is an excellent example of a labile leaving group.

- 3) **The nature of spectator ligands in the complex.**

- a) The trans effect

A spectator ligand is present in the complex and not lost during the reaction (X and X' in Figure 4.3). Most good nucleophiles are good reaction accelerators if they occupy a trans position as a spectator ligand. The trans effect can be defined as the ability of a ligand to direct the replacement of the ligand trans to it and is only applicable to reactions involving square planar complexes. The incoming ligand will add trans to the ligand farthest to the left on the trans-series and essentially arises from the competition between ligands for the same orbital.

Trans effect series:^{251, 252}

CO, CN⁻, C₂H₄ > **PR₃** > H⁻ > CH₃⁻ > C₆H₅⁻ > NO₂⁻, SCN⁻, I⁻, Br⁻ > Cl⁻ > py, NH₃ > H₂O

The rate of this substitution is therefore effected by the nature of the ligand opposite to it within the coordination sphere, known as the trans effect.²⁵³

Square planar substitution reactions generally occur slowly due to the loss of crystal field stabilization energy during the formation of the intermediate trigonal bipyramidal complex. The loss of crystal field stabilization energy (CFSE) increases going down the group with 4d and 5d metals being much slower. For this reason most square planar substitution kinetic studies are exemplified by Pt(II) complexes.

b) Chelate effect

Bidentate ligands and multidentate ligands readily substitute/exchange in place of monodentate ligands because they create a more stable complex. This is known as the chelate effect. The reasons for this lie in the increase in entropy S on releasing independent molecules into solution. ΔS is therefore positive and reactions tend towards entropy increase. The corresponding enthalpy change (ΔH) is negligible (~ 0) if similar coordinate bonds are broken and formed. Overall Gibb's free energy ΔG shown in equation [4.1] will always be negative due to a small/negligible ΔH and positive T (in Kelvin) and ΔS values.

$$\Delta G = \Delta H - T\Delta S \quad [4.1]$$

The exchange always happens readily as it is feasible at any temperature.²⁵⁰

4.2.1 Ligand Bite Angle

The steric properties of diphosphines are determined by the substituents on the phosphorous atoms (i.e., the 4 phenyl groups in this case) and the length of the carbon bridge between the two

phosphorus atoms. Generally, the most stable complexes form when there is a five-membered ring (i.e., when the bridge between the two phosphorous atoms consists of two carbon atoms as in 1,3-bis(diphenylphosphino)ethane, dppe). This is the case for both octahedral and square-planar complexes in which the “metal-preferred”¹³⁸ P-M-P angle is $\sim 90^\circ$.²⁵⁴

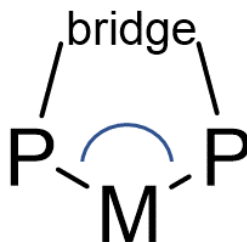


Figure 4.4: Bite angle: The ligand-metal-ligand angle of bidentate ligands.²⁵⁴

Bidentate ligands have played an important role in the development of catalytic applications of metal organic complexes. The synthesis of dppe was reported as early as 1959.²⁵⁵ Here three different bidentate phosphine ligands will be incorporated into the platinum complexes where the number of carbon atoms in the bridge ranges from 1 to 3. This will change the bite angles of the bidentate phosphine ligand and consequently the angles of the orbitals.

By comparing the SABRE-Relay reaction with each of these complexes using the same substrate, the effect of bite angle within the platinum complex on the ^{31}P hyperpolarised signal enhancements can be examined. The substrate can then be changed to see if the trend changes.

As platinum is NMR active, characterisation of the complexes formed is facilitated. Platinum complexes also undergo ligand exchange without degrading in the presence of oxygen. Figure 4.5 shows the proposed mechanism and the complexes formed in the SABRE-Relay process in more detail.

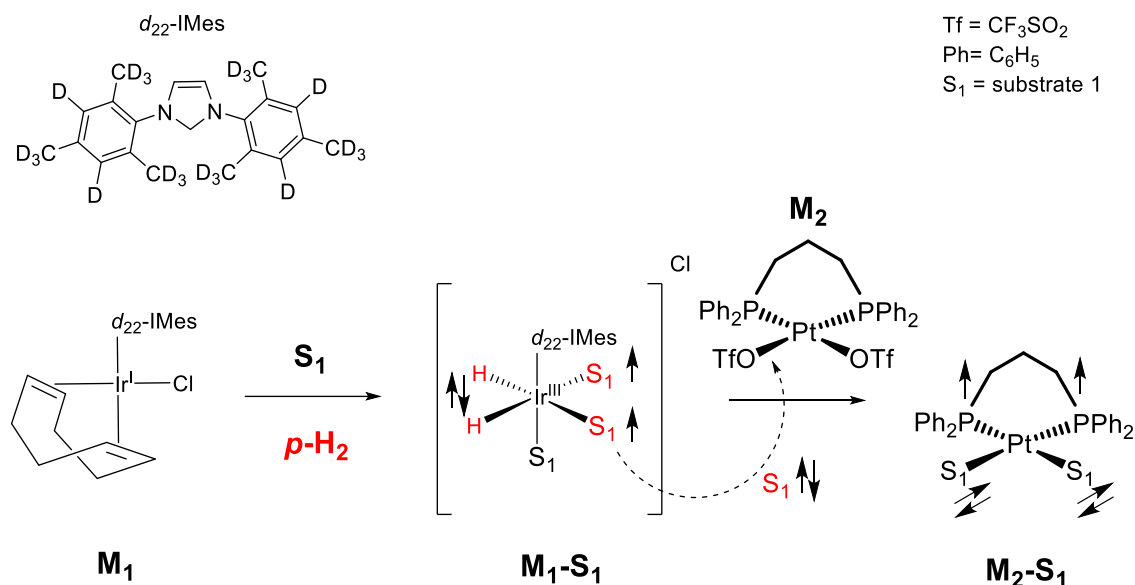


Figure 4.5: Postulated mechanism for the transfer of nuclear spin order into a second agent. The precatalyst $[\text{IrCl}(\text{COD})(d_{22}\text{-IMes})]$ (M_1) is transformed into the active SABRE complex $[\text{Ir}(\text{H})_2(\text{IMes})(\text{S}_1)_3]$ ($\text{M}_1\text{-S}_1$) by adding substrate S_1 . S_1 then gains hyperpolarised Zeeman and singlet order via polarization transfer from $p\text{-H}_2$. In the second step, the ^{31}P response of $\text{M}_2\text{-S}_1$ becomes hyperpolarised.¹⁶⁸

4.3 Synthesis of platinum complexes

The first of the platinum complexes investigated for this process is shown in Figure 4.6. It is a platinum complex chelated by bidentate 1,3-bis(diphenylphosphino)propane (dppp) and two triflate ligands. Once the triflate ligands have been displaced, they act as anions and stabilise any positive platinum complexes that result.

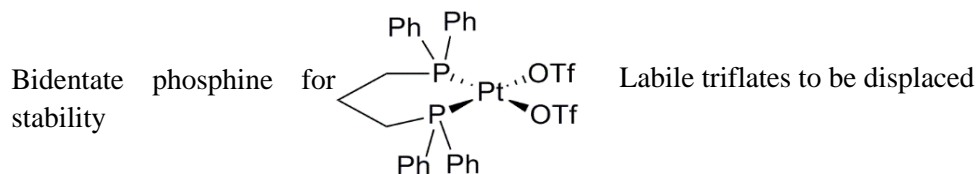


Figure 4.6: $[\text{Pt}(\text{OTf})_2(\text{dppp})]$, proposed to exchange its triflates for polarised N-heterocycles.

$[\text{Pt}(\text{OTf})_2(\text{dppp})]$, was prepared according to the pathway shown in Figure 4.7 which was adapted from synthetic procedures in the literature.^{256, 257}

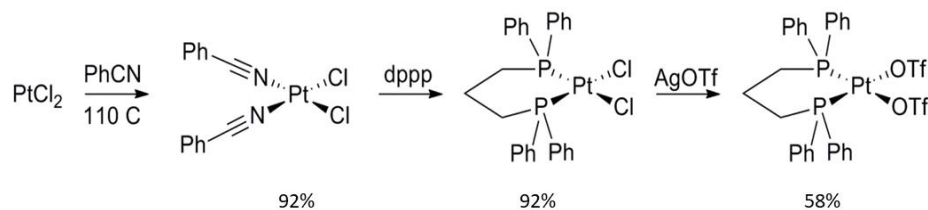


Figure 4.7 : Synthetic pathway for the synthesis of $[\text{Pt}(\text{OTf})_2(\text{dppp})]$ from PtCl_2 .

As this procedure was shown to be successful, the synthesis of the two further complexes shown in Figure 4.8, was attempted using 1,3-bis(diphenylphosphino)methane (dppm) and 1,3-bis(diphenylphosphino)ethane (dppe).



Figure 4.8: Chemical structures of $[\text{Pt}(\text{OTf})_2(\text{dppm})]$ and $[\text{Pt}(\text{OTf})_2(\text{dppe})]$ synthesised.

4.3.1 Synthesis of $[\text{Pt}(\text{OTf})_2(\text{dppm})]$

Synthesis of $[\text{Pt}(\text{OTf})_2(\text{dppm})]$ following the same procedure as the synthesis of $[\text{Pt}(\text{OTf})_2(\text{dppp})]$ was found to be confounded by an impurity. At the second stage, where the chloride complex $[\text{Pt}(\text{Cl})_2(\text{dppm})]$ is formed, ^1H NMR revealed six aromatic resonances and two alkyl resonances (Figure 4.9 a and b). As this is a symmetric complex, only three aromatic resonances derived from *ortho*, *meta* and *para* protons of the phenyl rings would be expected. Where one region was expected for the two alkyl protons, two were seen at δ 4.70 and δ 4.53 each appearing as triplets due to phosphorous coupling. Integration revealed two species present in a ratio of 20:7. The major form with signals at δ 4.53 ($-\text{CH}_2$), δ 7.98 (*ortho*), δ 7.53 (*meta*), and δ 7.59 (*para*) and the minor form with signals at δ 4.70 ($-\text{CH}_2$), δ 7.53 (*ortho*) (this signal lies under the *meta* signal of the major form), δ 7.32 (*meta*) and δ 7.48 (*para*) respectively. $^{31}\text{P}\{^1\text{H}\}$ NMR spectrum revealed a peak at δ -64.21 but also a much smaller peak at δ -37.6 (Figure 4.9 c). Once again, due to the symmetry of the molecule only one phosphorous resonance was expected. The smaller phosphorous signal at δ -37.6 was identified as the bis-substituted complex $[\text{Pt}(\text{dppm})_2]\text{Cl}_2$.

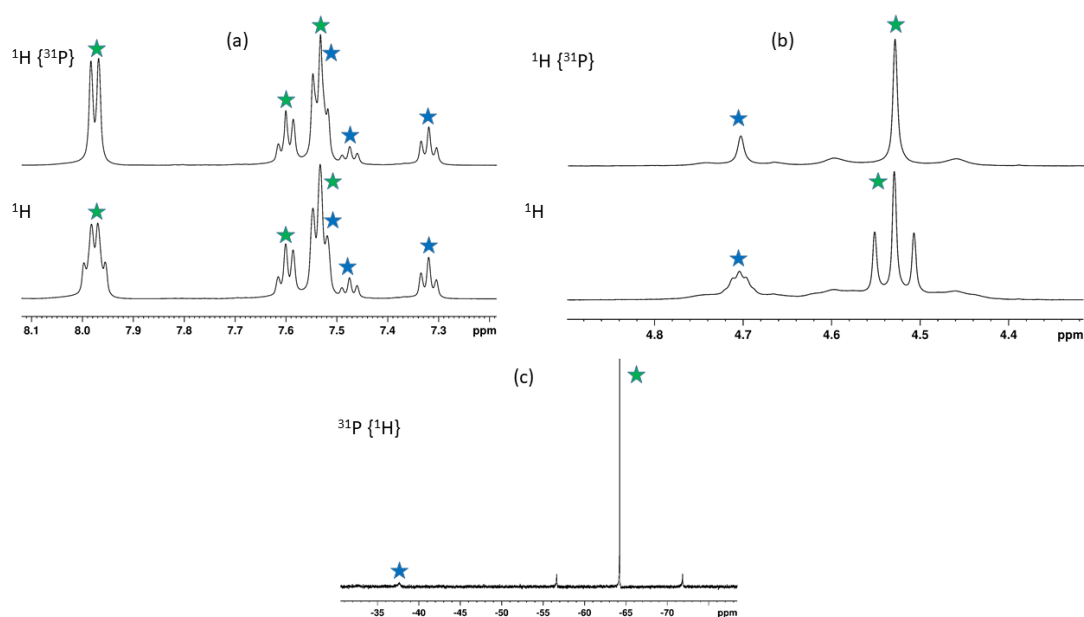


Figure 4.9: NMR spectra of the $[\text{Pt}(\text{Cl})_2(\text{dppm})]$ and $[\text{Pt}(\text{dppm})_2]\text{Cl}_2$ in dichloromethane- d_2 a) ^1H and $^1\text{H}\{^{31}\text{P}\}$ showing six aromatic regions, b) ^1H and $^1\text{H}\{^{31}\text{P}\}$ showing two alkyl regions c) $^{31}\text{P}\{^1\text{H}\}$ 400 scans showing two phosphorous signals. The resonances with a blue star indicate $[\text{Pt}(\text{dppm})_2]\text{Cl}_2$ and the green star indicates $[\text{Pt}(\text{Cl})_2(\text{dppm})]$.

$[\text{Pt}(\text{dppm})_2]\text{Cl}_2$ was a minor product and was not carried through to the final product. Continued synthesis only formed $[\text{Pt}(\text{OTf})_2(\text{dppm})]$; confirmed by the detection of only one ^{31}P peak (Figure 4.10 c) and three ^1H aromatic resonances (Figure 4.10 a). Complete characterisation data for $[\text{Pt}(\text{OTf})_2(\text{dppm})]$ is given in section 8.5.3

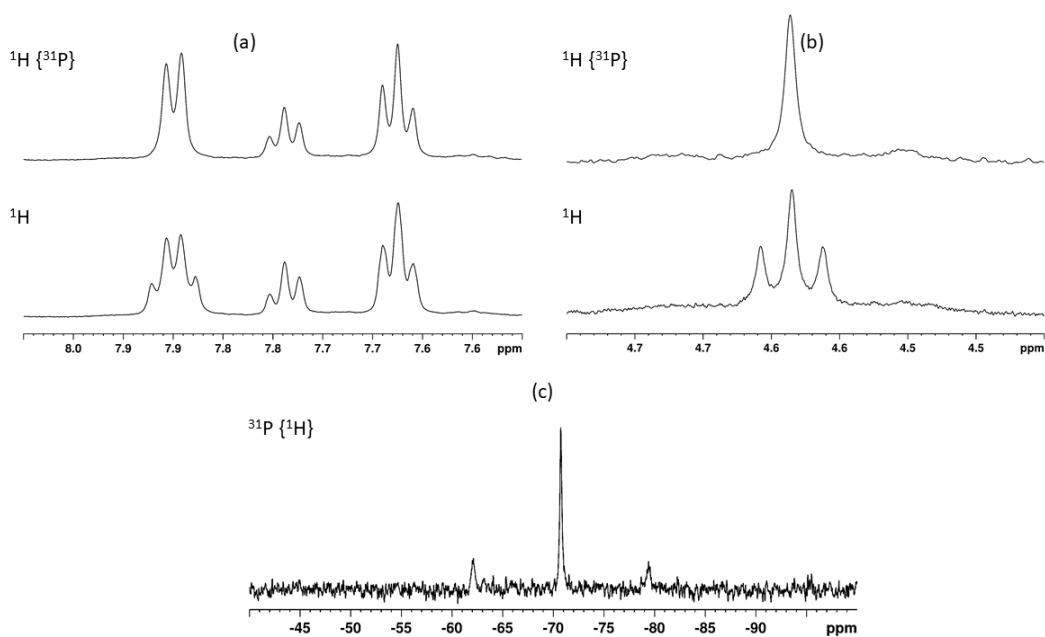


Figure 4.10: NMR spectra of the $[\text{Pt}(\text{OTf})_2(\text{dppm})]$ complex in dichloromethane- d_2 a) ^1H and $^1\text{H}\{^{31}\text{P}\}$ showing three aromatic resonances, b) ^1H and $^1\text{H}\{^{31}\text{P}\}$ showing one alkyl resonance c) $^{31}\text{P}\{^1\text{H}\}$ 400 scans showing one phosphorous signal.

Improved yield for the synthesis of the intermediate $[\text{Pt}(\text{Cl})_2(\text{dppm})]$, required 1.05 equivalents of dppm (as opposed to 1.1 equivalents above) under much slower addition. Under these conditions $[\text{Pt}(\text{Cl})_2(\text{dppm})]$ was isolated showing one ^{31}P signal (Figure 4.11 c) and the absence of the bis-substituted by-product. Full characterisation data for $[\text{Pt}(\text{Cl})_2(\text{dppm})]$ is given in section 8.5.2

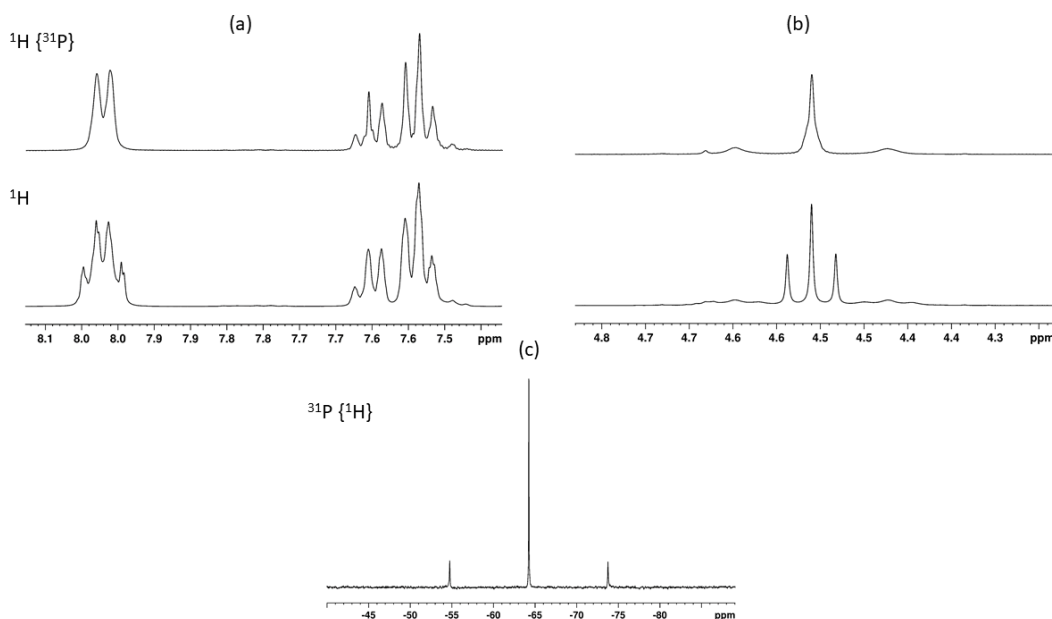


Figure 4.11: NMR spectra of the $[\text{Pt}(\text{Cl})_2(\text{dppm})]$ complex in dichloromethane- d_2 a) ^1H and $^1\text{H}\{^{31}\text{P}\}$ showing three aromatic resonances, b) ^1H and $^1\text{H}\{^{31}\text{P}\}$ showing one alkyl resonance c) $^{31}\text{P}\{^1\text{H}\}$ 200 scans showing one phosphorous signal.

4.3.2 Synthesis of $[\text{Pt}(\text{OTf})_2(\text{dppe})]$

Synthesis of the intermediate $[\text{Pt}(\text{Cl})_2(\text{dppe})]$ also exhibited by-product contamination. Phosphorous NMR revealed the presence of two phosphorous signals, each with their own platinum satellites (Figure 4.12c). *cis*- $\text{PtCl}_2(\text{dppe})$ is observed at δ 41.53 with $J_{\text{P-Pt}} = 3620$ Hz. $[\text{Pt}(\text{dppe})_2]\text{Cl}_2$ is observed at δ 47.73 with $J_{\text{P-Pt}} = 2362$ Hz.²⁵⁸ A COSY ^1H NMR spectrum revealed that peaks at δ 7.32 and 7.72 belonged to one complex and those at δ 7.55 and 7.89 belonged to another. A ^{31}P -optimised HMQC NMR spectrum showed that proton signals at δ 3.37, 7.72, 7.32 were coupled to the phosphorus resonance at δ 47.26 $[\text{Pt}(\text{dppe})_2]\text{Cl}_2$. Proton signals at δ 2.37, 7.89 and 7.55 are coupled to the phosphorous resonance at δ 41.28 *cis*- $\text{PtCl}_2(\text{dppe})$. Integration showed that *meta* and *para* resonances of $[\text{Pt}(\text{Cl})_2(\text{dppe})]$ overlapped. In addition $[\text{Pt}(\text{dppe})_2]\text{Cl}_2$ was found to be the major product in a 1.75:1 ratio. Characterisation data of $[\text{Pt}(\text{Cl})_2(\text{dppe})]$ is given in section 8.5.4

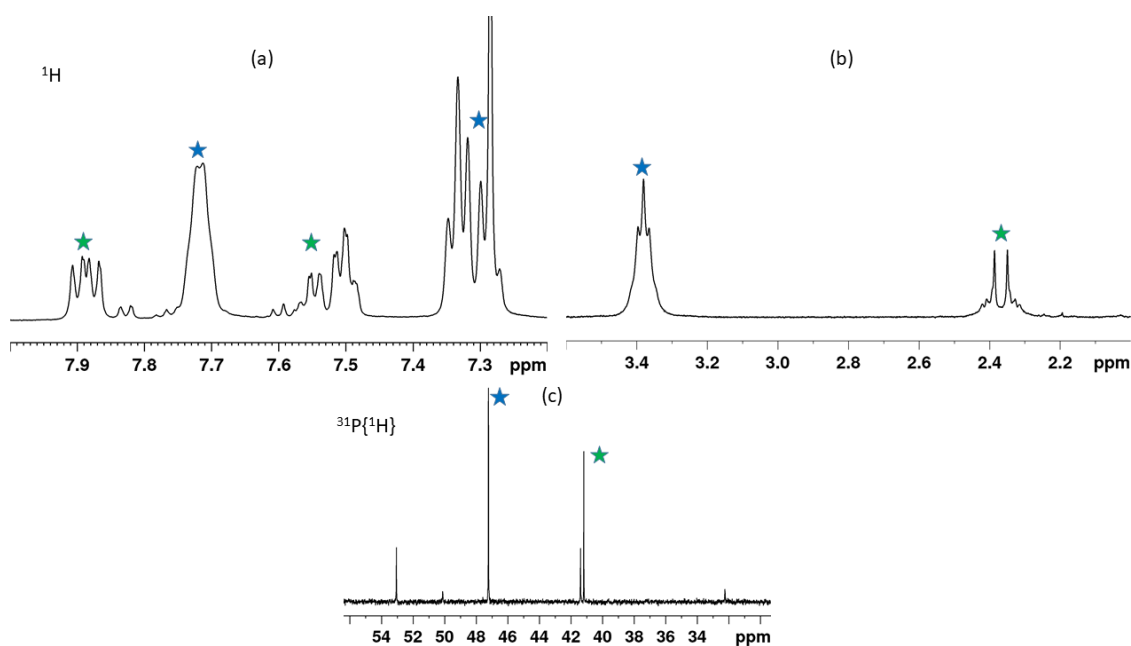


Figure 4.12: NMR spectra of $[\text{Pt}(\text{Cl})_2(\text{dppe})]$ and $[\text{Pt}(\text{dppe})_2]\text{Cl}_2$ in chloroform-*d* a) ^1H and showing characteristic aromatic resonances, b) ^1H showing characteristic alkyl resonances c) $^{31}\text{P}\{^1\text{H}\}$ 400 scans showing two phosphorous signals. The resonances with a blue star indicate $[\text{Pt}(\text{dppe})_2]\text{Cl}_2$ and the green star indicates $[\text{Pt}(\text{Cl})_2(\text{dppe})]$

Synthesis was continued through to the final stage and after addition of the silver triflate, a mixture of $[\text{Pt}(\text{OTf})_2(\text{dppe})]$ and $[\text{Pt}(\text{dppe})_2]\text{Cl}_2$ was collected in a ratio of 20:3. Unfortunately, the impurity, $[\text{Pt}(\text{dppe})_2]\text{Cl}_2$, did carry through to this final stage with $[\text{Pt}(\text{OTf})_2(\text{dppe})]$ being the major product (Figure 4.13). Full characterisation of $[\text{Pt}(\text{OTf})_2(\text{dppe})]$ can be found in section 8.5.5. As $[\text{Pt}(\text{dppe})_2]\text{Cl}_2$ is a stable species the potential substrate molecules would be unable to displace either of the dppe ligands. As such $[\text{Pt}(\text{dppe})_2]\text{Cl}_2$ would remain as an inert bystander in the SABRE-Relay process.

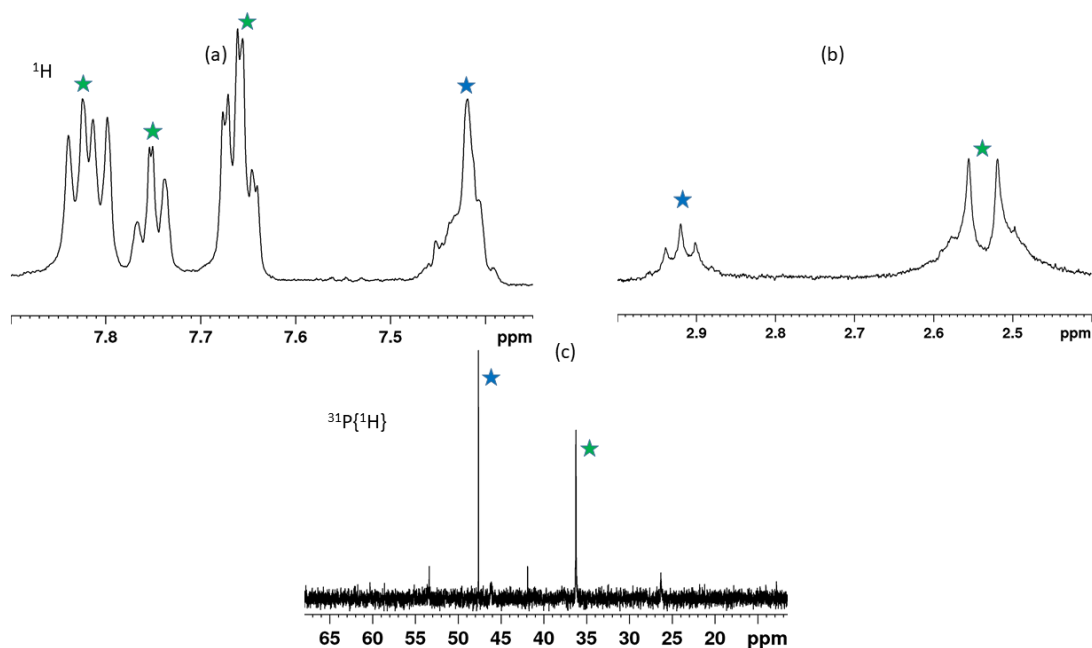


Figure 4.13: NMR spectra of the $[\text{Pt}(\text{OTf})_2(\text{dppe})]$ and $[\text{Pt}(\text{dppe})_2]\text{Cl}_2$ in dichloromethane- d_2 a) ^1H showing characteristic aromatic resonances, b) ^1H showing characteristic alkyl resonances c) $^{31}\text{P}\{^1\text{H}\}$ 400 scans showing two phosphorous signals. The resonances with a blue star indicate $[\text{Pt}(\text{dppe})_2]\text{Cl}_2$ and the green star indicate $[\text{Pt}(\text{OTf})_2(\text{dppe})]$

Repetition with 1.05 equivalents of dppe (as opposed to 1.1 equivalents) under much slower addition still resulted in $[\text{Pt}(\text{dppe})_2]\text{Cl}_2$ as a major product. However a higher proportion (ratio of 6:5) of the target $[\text{Pt}(\text{Cl})_2(\text{dppe})]$ resulted.

For subsequent hyperpolarisation experiments samples were prepared containing 5mM of $[\text{IrCl}(\text{COD})(d_{22}\text{-IMes})]$, 5 mM of the different platinum complexes ($[\text{Pt}(\text{OTf})_2(\text{dppm})]$, $[\text{Pt}(\text{OTf})_2(\text{dppe})]$ and $[\text{Pt}(\text{OTf})_2(\text{dppp})]$) with 10 equivalents of the different target substrates tested (2,4- d_2 -nicotinamide, pyrimidine, deuterated isotopologues of pyrimidine, 4,6- d_2 -deuterated methyl nicotinate and T[2,3- d]P). It was hypothesised that the hyperpolarised substrate would undergo a substitution reaction with the square planar platinum complex displacing the labile triflate ligand(s) resulting in a new mono or bis-substituted square planar complex.

A two-stage process was adopted. Stage one investigated if standard SABRE would still be feasible in the presence of additional platinum complexes. Once confirmed, stage two characterised the bound ligands formed (using ^1H NMR) to investigate exchange between the free and bound ligand pools in both metal complexes.

4.4 Characterisation of Iridium and Platinum complexes

Full characterisation of the SABRE-Relay process was exemplified with 2,4- d_2 -nicotinamide as the intermediate substrate (S_1) between the $[\text{IrCl}(\text{COD})(d_{22}\text{-IMes})]$ and $[\text{Pt}(\text{OTf})_2(\text{dppm})]$. 2,4- d_2 -nicotinamide has a T_{LLS} for the proton pair H5 and H6 of 29.0 ± 3.5 s compared with individual T_1 values of 13.3 ± 0.4 and 9.5 ± 0.4 s respectively¹⁶⁸. Data here could then be compared to previously published work using $[\text{Pt}(\text{OTf})_2(\text{dppp})]$ as the second metal complex.¹⁶⁸

4.4.1 Characterisation of $[\text{Ir}(\text{H})_2(d_{22}\text{-IMes})(2,4\text{-}d_2\text{-nicotinamide})_3]\text{Cl}$, $[\text{Pt}(\text{OTf})(\text{dppm})(2,4\text{-}d_2\text{-nicotinamide})]\text{OTf}$, and free 2,4- d_2 -nicotinamide.

On addition of H_2 to a methanol- d_4 sample of $[\text{Ir}(\text{COD})(d_{22}\text{-IMes})\text{Cl}]$, $[\text{Pt}(\text{dppm})(\text{OTf})_2]$ and 10 equivalents of 2,4- d_2 -nicotinamide, the transition metal complexes shown in Figure 4.14 were observed to form, and were characterised by thermal based NMR spectroscopy.

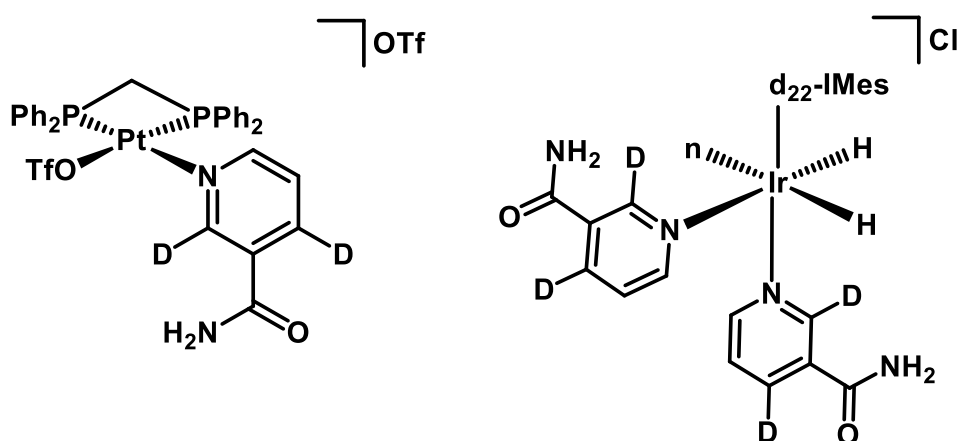


Figure 4.14: $[\text{Pt}(\text{dppm})(\text{OTf})(2,4\text{-}d_2\text{-nicotinamide})]\text{OTf}$ (left) and $[\text{Ir}(\text{H})_2(d_{22}\text{-IMes})(2,4\text{-}d_2\text{-nicotinamide})_3]\text{Cl}$ (right). The symbol n represents a further substrate molecule occupying an equatorial site.

The proton resonances for the free 2,4- d_2 -nicotinamide in solution were clearly identifiable at δ 8.70 (ortho) and δ 7.57 (meta) (Figure 4.15). A singlet in the hydride region at δ -22.65 confirmed the formation of $[\text{Ir}(\text{H})_2(d_{22}\text{-IMes})(2,4\text{-}d_2\text{-nicotinamide})_3]\text{Cl}$, in which the hydride ligands are chemically equivalent. Furthermore, the singlet at δ 7.13 corresponded to the two NCH protons on the backbone of $d_{22}\text{-IMes}$. As there were no other singlets in the aromatic region, only one iridium carbene complex was present in solution.

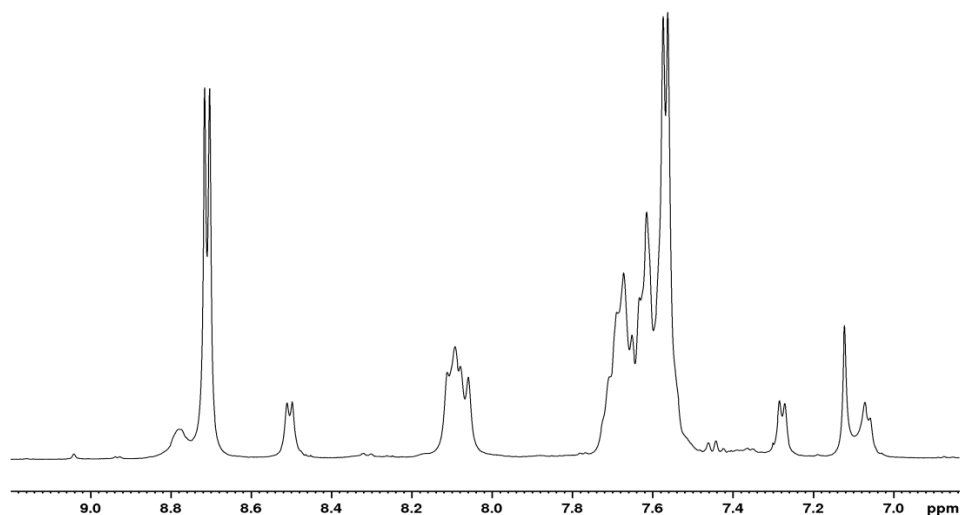


Figure 4.15 : ^1H NMR spectrum showing the aromatic region of a methanol- d_4 solution containing $[\text{Pt}(\text{OTf})(\text{dppm})(2,4\text{-}d_2\text{-nicotinamide})]\text{OTf}$, $[\text{Ir}(\text{H})_2(d_{22}\text{-IMes})(2,4\text{-}d_2\text{-nicotinamide})_3]\text{Cl}$, and 10 eq. of 2,4- d_2 -nicotinamide at 298 K.

On cooling to 273 K the individual resonances become more distinct (Figure 4.16). This demonstrated that at room temperature there is exchange between the free 2,4- d_2 -nicotinamide and the bound platinum and bound iridium.

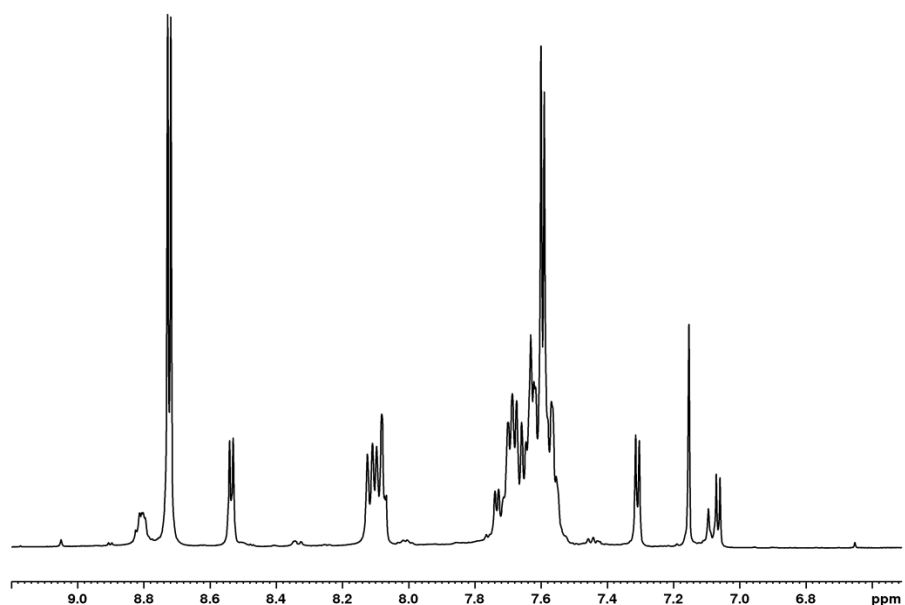


Figure 4.16 : ^1H NMR spectrum showing the aromatic region of a d_4 -methanol solution containing $[\text{Pt}(\text{OTf})(\text{dppm})(2,4\text{-}d_2\text{-nicotinamide})]\text{OTf}$, $[\text{Ir}(\text{H})_2(d_{22}\text{-IMes})(2,4\text{-}d_2\text{-nicotinamide})_3]\text{Cl}$, and 10 eq. of 2,4- d_2 -nicotinamide at 273 K.

The doublet at δ 8.50, with a J_{HH} coupling value of 5.5 Hz, corresponded to the *ortho* protons of the iridium bound 2,4- d_2 -nicotinamide ligands positioned *trans* to hydride ligands (equatorial). In

the corresponding COSY NMR spectrum (Figure 4.17) a cross peak was observed between this signal and another at δ 7.28. This corresponded to the *meta* proton of the same bound 2,4- d_2 -nicotinamide ligands. The smaller doublet at δ 8.08, also with a J_{HH} coupling value of 5.5, corresponded to the iridium bound 2,4- d_2 -nicotinamide ligands positioned *trans* to d_{22} -IMes (axial). A cross peak was observed between this signal and another at δ 7.06, which corresponded to the *meta* proton of the same bound 2,4- d_2 -nicotinamide ligand. ^1H NMR characterisation of $[\text{Ir}(\text{H})_2(d_{22}\text{-IMes})(2,4\text{-}d_2\text{-nicotinamide})_3]\text{Cl}$ is given in Appendix 3.

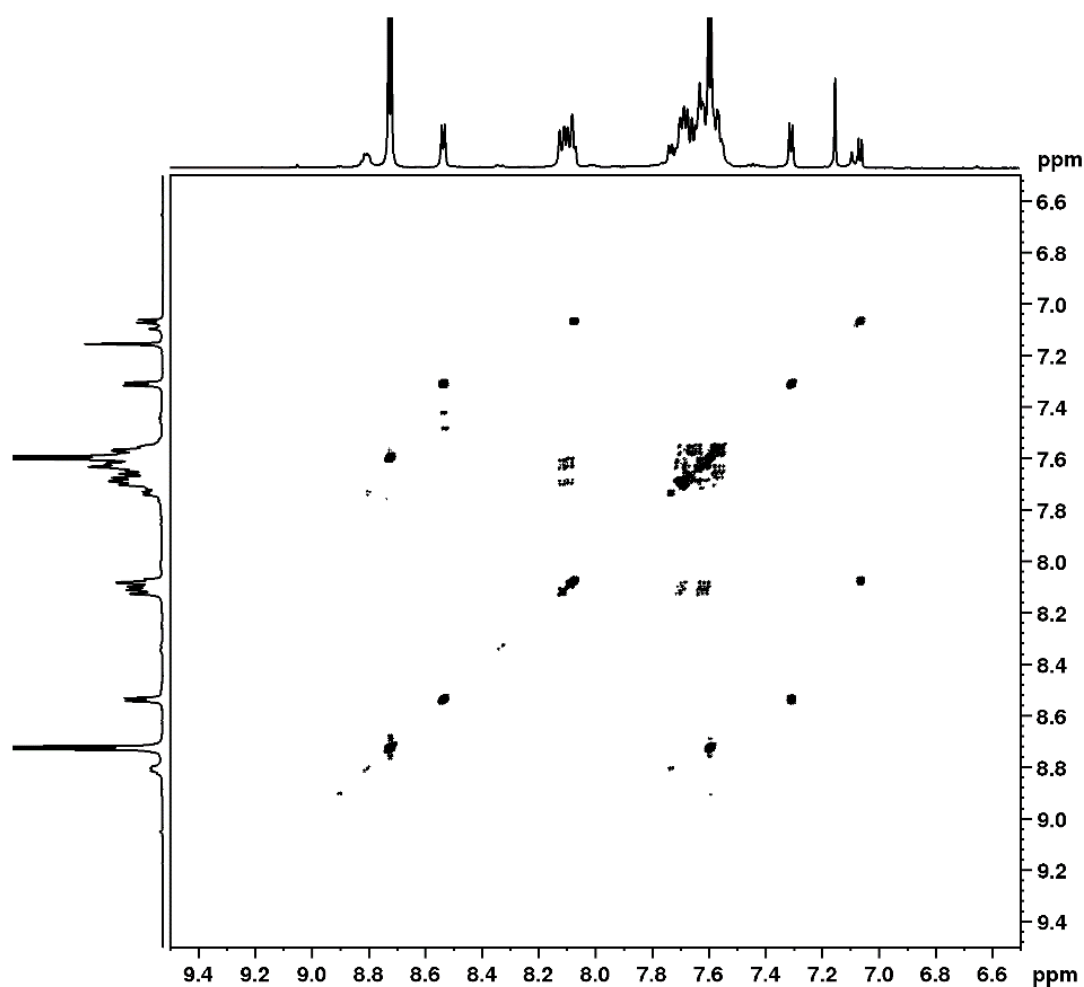


Figure 4.17 : ^1H COSY NMR spectrum showing the aromatic region of a d_4 -methanol solution containing $[\text{Pt}(\text{OTf})(\text{dppm})(2,4\text{-}d_2\text{-nicotinamide})]\text{OTf}$, $[\text{Ir}(\text{H})_2(d_{22}\text{-IMes})(2,4\text{-}d_2\text{-nicotinamide})_3]\text{Cl}$, and 10 eq. of 2,4- d_2 -nicotinamide at 273 K.

The $^{31}\text{P}\{^1\text{H}\}$ NMR spectrum is shown in Figure 4.18. The two doublets at δ -64.39 and -57.35 were both split by J_{PP} constants equal to 69.6 Hz and J_{PPt} constants equal to 2900 Hz (giving rise to the small satellites), which was consistent with the chemically inequivalent ^{31}P nuclei in the proposed platinum complex (shown in Figure 4.14).

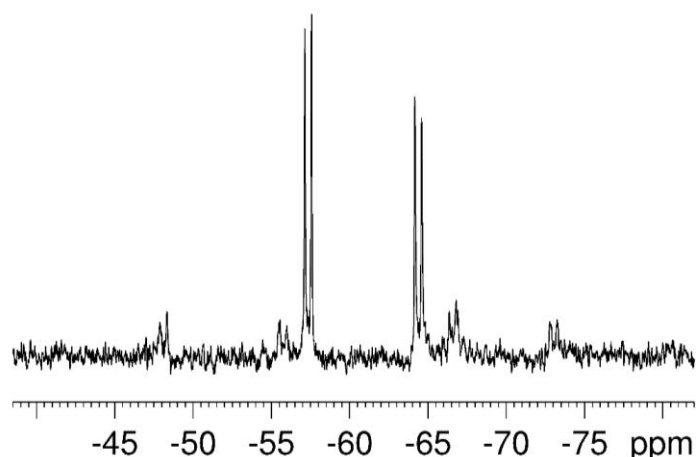


Figure 4.18: $^{31}\text{P}\{^1\text{H}\}$ NMR spectrum of a d_4 -methanol solution containing $[\text{Pt}(\text{OTf})(\text{dppm})(2,4-d_2\text{-nicotinamide})]\text{OTf}$, $[\text{Ir}(\text{H})_2(d_{22}\text{-IMes})(2,4-d_2\text{-nicotinamide})_3]\text{Cl}$, and 10 eq. of $2,4-d_2\text{-nicotinamide}$.

On decoupling the ^1H nuclei to phosphorus, the splitting was simplified for some of the NMR signals in the aromatic region. Further cooling to 245 K separated the peaks further (Figure 4.19). The doublet of doublets at δ 8.83 reduced to a doublet, confirming that this signal was split by $J_{\text{HP}} = 3.1$ Hz and $J_{\text{HH}} = 5.5$ Hz. This resonance corresponded to the *ortho* proton of the platinum bound $2,4-d_2\text{-nicotinamide}$ ligand, which coupled to a doublet at δ 7.75, also with $J_{\text{HH}} = 5.5$ Hz, corresponding to the *meta* proton of the same $2,4-d_2\text{-nicotinamide}$ ligand.

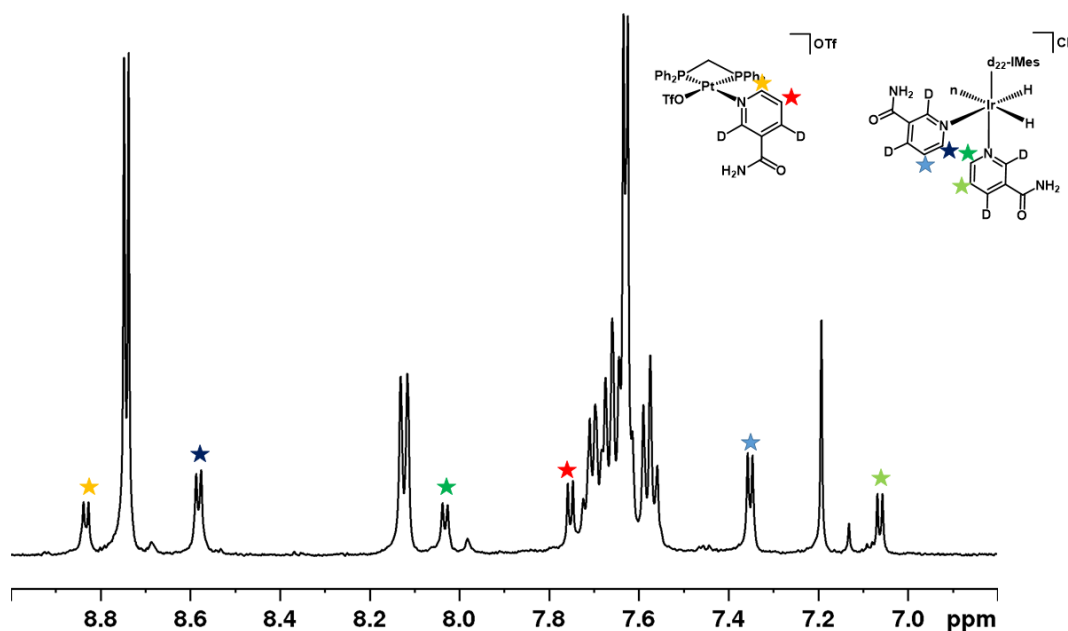


Figure 4.19: $^1\text{H}\{^{31}\text{P}\}$ NMR spectrum showing the aromatic region of a d_4 -methanol solution containing $[\text{Pt}(\text{OTf})(\text{dppm})(d_2\text{-}2,4\text{-nicotinamide})]\text{OTf}$, $[\text{Ir}(\text{H})_2(d_{22}\text{-IMes})(d_2\text{-}2,4\text{-nicotinamide})_3]\text{Cl}$, and 10 eq. of $d_2\text{-}2,4\text{-nicotinamide}$ (245 K).

A cross peak observed in ^{31}P -optimised HMQC spectra confirmed that the ^1H NMR signal at δ 8.03 coupled to the ^{31}P NMR peak at δ -64.39 . This was confirmed as the ^{31}P nucleus positioned

trans to the bound nicotinamide. Cross peaks in ^{31}P -optimised HMQC, and COSY NMR spectra allowed ^1H and ^{31}P characterisation of the platinum complex found in Appendix 3.

Characterisation data showed that a SABRE active catalyst did indeed form in the presence of the platinum-based complex. In addition, bound 2,4- d_2 -nicotinamide ligands were observed in both the iridium and platinum complexes. To show that these complexes exchange on the right timescale, EXchange SpectroscopY (EXSY) experiments were completed to demonstrate magnetisation transfer. By exciting either bound peak, EXSY data should confirm exchange through equilibration.

4.4.2 Exchange of bound nicotinamide

Selective irradiation of the signal for the *meta* proton of equatorially bound 2,4- d_2 -nicotinamide in $[\text{Ir}(\text{H})_2(\text{d}_{22}\text{-IMes})(2,4\text{-}d_2\text{-nicotinamide})_3]\text{Cl}$ at δ 7.27 showed polarisation transfer into both the *meta* proton belonging to the free 2,4- d_2 -nicotinamide and the *meta* proton of platinum bound 2,4- d_2 -nicotinamide (Figure 4.20). This demonstrated that the complexes exchange on an appropriate timescale for NMR.

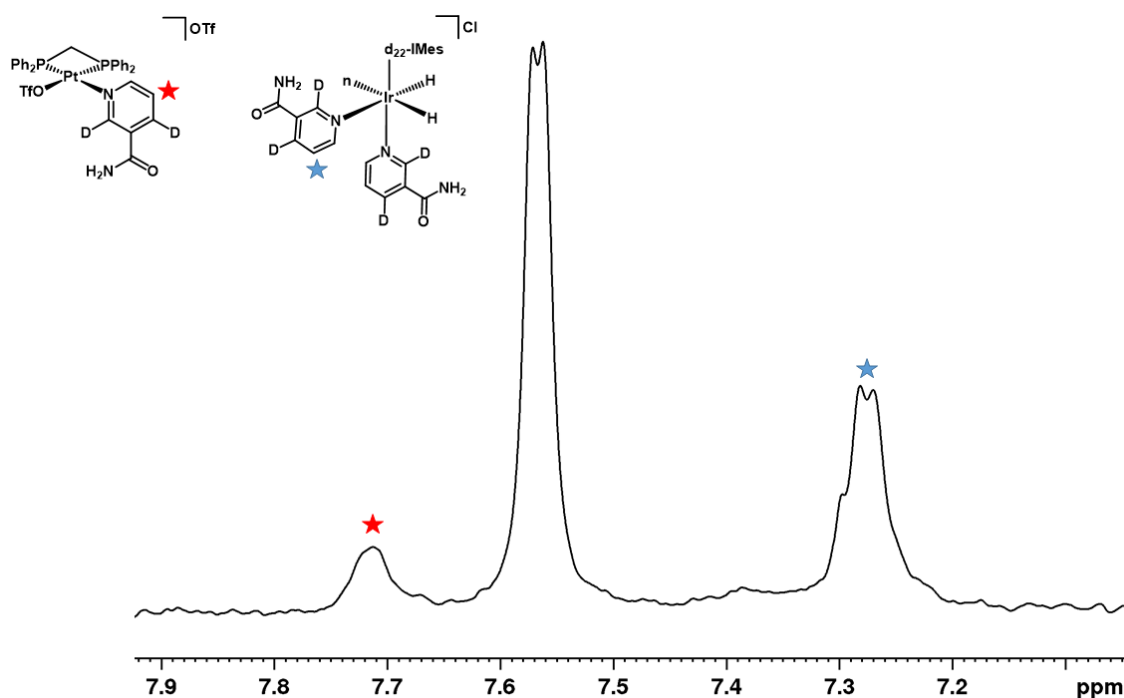


Figure 4.20: 1D selective EXSY NMR experiment showing exchange into the signal for the *meta* proton of free nicotinamide (δ 7.57) and the *meta* proton of bound 2,4- d_2 -nicotinamide in $[\text{Pt}(\text{OTf})(\text{dppm})(2,4\text{-}d_2\text{-nicotinamide})]\text{OTf}$ (δ 7.73, red star) on selective excitation of the *meta* proton of equatorially bound 2,4- d_2 -nicotinamide in $[\text{Ir}(\text{H})_2(\text{d}_{22}\text{-IMes})(2,4\text{-}d_2\text{-nicotinamide})_3]\text{Cl}$ (δ 7.27, blue star) after a delay time of 0.6 s (298K).

4.4.3 Polarisation transfer to [Pt(OTf)(dppm)(2,4-*d*₂-nicotinamide)]OTf

Replacement of hydrogen gas with 3 bar (g) *p*-H₂, and shaking at 65 G, led to hyperpolarisation of many of the resonances in the acquired 400MHz ¹H NMR spectra. The hyperpolarised resonances in the aromatic region are shown in Figure 4.21. Notably, the peaks at δ 8.8 and 7.75 (labelled with *), corresponding to the protons of platinum bound nicotinamide which have been shown to undergo exchange, were enhanced in absolute magnitude over their expected level. The *ortho* ¹H resonance was enhanced 130-fold, whilst the *meta* was enhanced 100-fold.

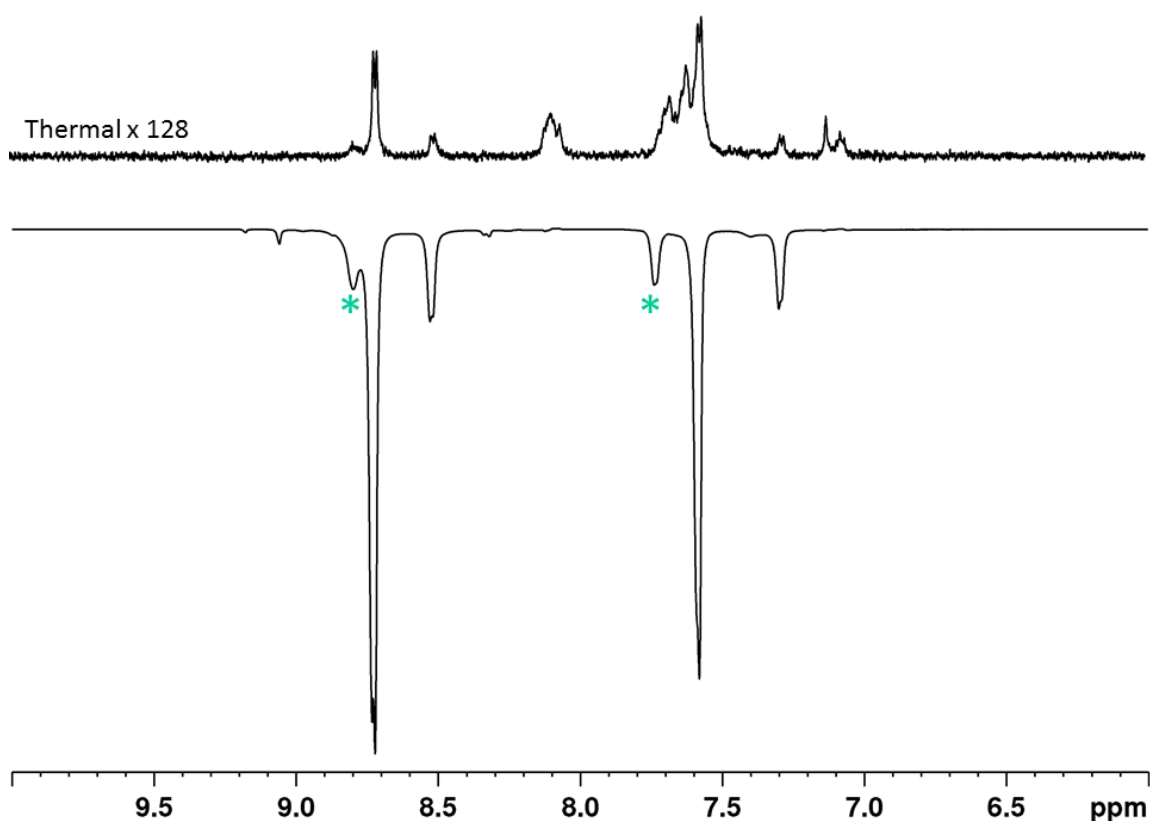


Figure 4.21: ¹H NMR spectra showing the aromatic region of a *d*₄-methanol solution containing [Pt(OTf)(dppm)(2,4-*d*₂-nicotinamide)]OTf, [Ir(H)₂(*d*₂₂-IMes)(2,4-*d*₂-nicotinamide)₃]Cl, and 10 eq. of 2,4-*d*₂-nicotinamide under (top) Boltzmann conditions (bottom) SABRE conditions.

In addition, a small hyperpolarised ³¹P signal was also observed under single scan conditions (see in Figure 4.22c). The spectrum confirmed that the relayed transfer of spin-order, from *p*-H₂, into spins of the second platinum complex, (that do not interact with it) was achieved.

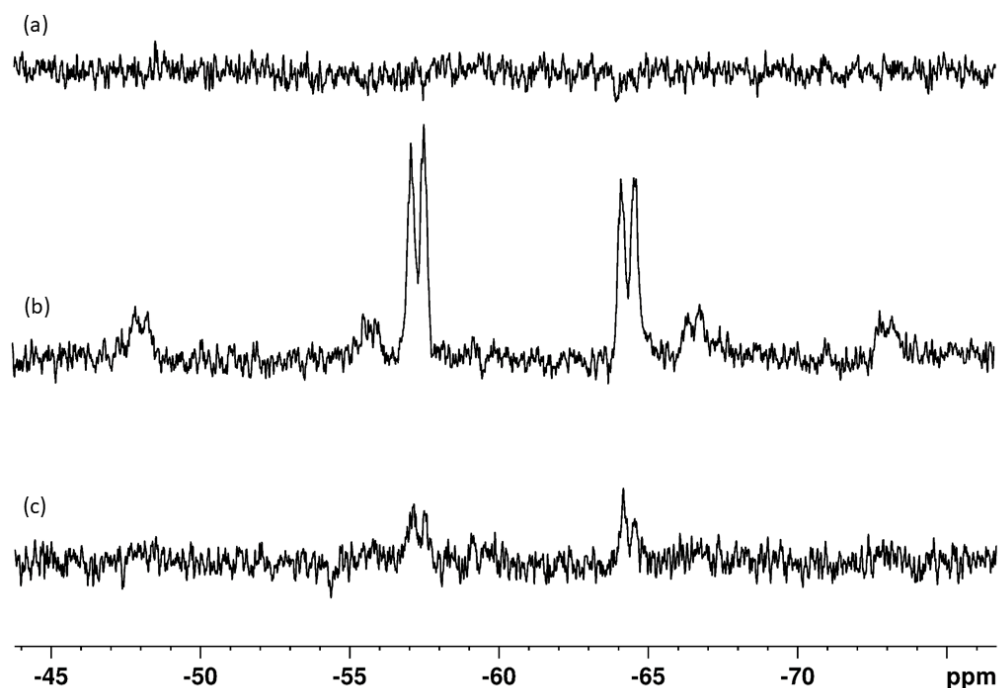


Figure 4.22: ^{31}P NMR spectra of a solution containing 10 eq. of 2,4- d_2 -nicotinamide dissolved in methanol- d_4 with the $[\text{IrCl}(\text{COD}) (d_{22}\text{-IMes})]$ and $[\text{Pt}(\text{OTf})_2(\text{dppm})]$ to observe SABRE-Relay derived hyperpolarised signal. (a) Signal acquired in Boltzmann equilibrium conditions with 1 scan (b) similar signal after 400 scans using a $d_1 = 1$ s. (c) Hyperpolarised signal acquired using 1 scan.

Two experimental protocols (shown in a) were developed for achieving these ^{31}P NMR signal enhancements.¹⁶⁸ A simpler version using just one 60 G PTF was employed here because it gave better results than either of the previously reported methods.

Once confirmation of the polarisation transfer into the synthesised Pt metal complexes was confirmed with the nicotinamide model, other intermediates substrates were tested. These included pyrimidine, pyrazine, 4,6- d_2 -methyl nicotinate and T[2,3- d]P. Two of the most successful substrates were pyrimidine and pyrazine and a typical set of results are shown in Figure 4.23b. For this reason, these substrates were examined in more detail in conjunction with two further polarisation receiving complexes. 4,6- d_2 -methyl nicotinate was also investigated as this has been the most successful substrate to date in terms of both polarisation levels and T_1 lifetime. Thienopyridazines were also tested in this role.

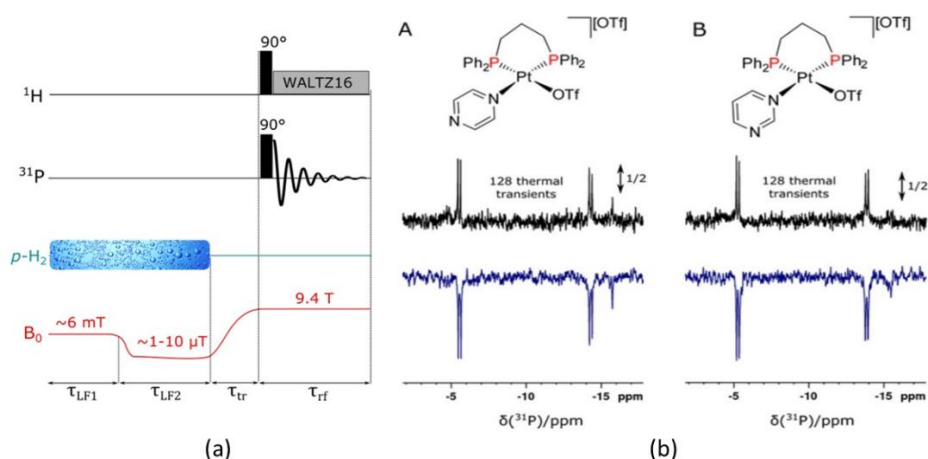


Figure 4.23: a) Experimental scheme used for the original study.¹⁶⁸ Two protocols were used: In protocol 1 the sample is mixed with *p*-H₂ at low magnetic field (~6 mT and ~1-10 μT) for the durations of τ_{LF1} and τ_{LF2} before moving to high field (τ_{tr}) for NMR observation. A simultaneous 90° pulse is applied to ¹H and ³¹P prior to acquiring the ³¹P signal with decoupling. In protocol 2, an M2S sequence²¹⁰, is applied between τ_{LF1} and τ_{LF2} ; b) ³¹P{¹H} NMR spectra of the metal complexes formed using pyrimidine and pyrazine as substrate.

4.5 ³¹P SABRE-Relay polarisation using pyrimidine as a function of bidentate phosphine ligand

A series of standard shake and drop experiments were undertaken. Samples were prepared in methanol-*d*₄ using 5 mM of both [IrCl(COD)(*d*₂₂IMes)] and the platinum complex. 50 mM of substrate were used in each case. The samples were prepared in inert conditions due to the presence of the triflate ligand in the platinum complex. The samples were then degassed and *p*-H₂ was added. The polarisation transfer step took 10 seconds. Figure 4.24 and Figure 4.25 show the resulting ¹H and ³¹P spectra respectively.

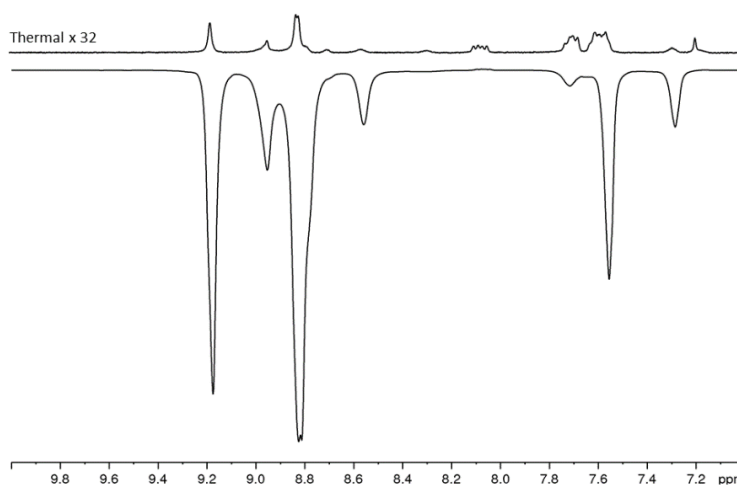


Figure 4.24: ¹H NMR spectra of pyrimidine dissolved in methanol-*d*₄ solution with [IrCl(COD)(*d*₂₂-IMes)] and [Pt(OTf)₂(dppm)] to observe SABRE derived signal at 65 G mixing field (bottom) and corresponding signal acquired in Boltzmann equilibrium conditions (top) that is vertically magnified 32 times for comparison purpose.

Based on comparison of appropriate pyrimidine spectra without the platinum complex it can be deduced that the peak at δ 7.65 is likely to be an enhanced pyrimidine resonance within the platinum product.

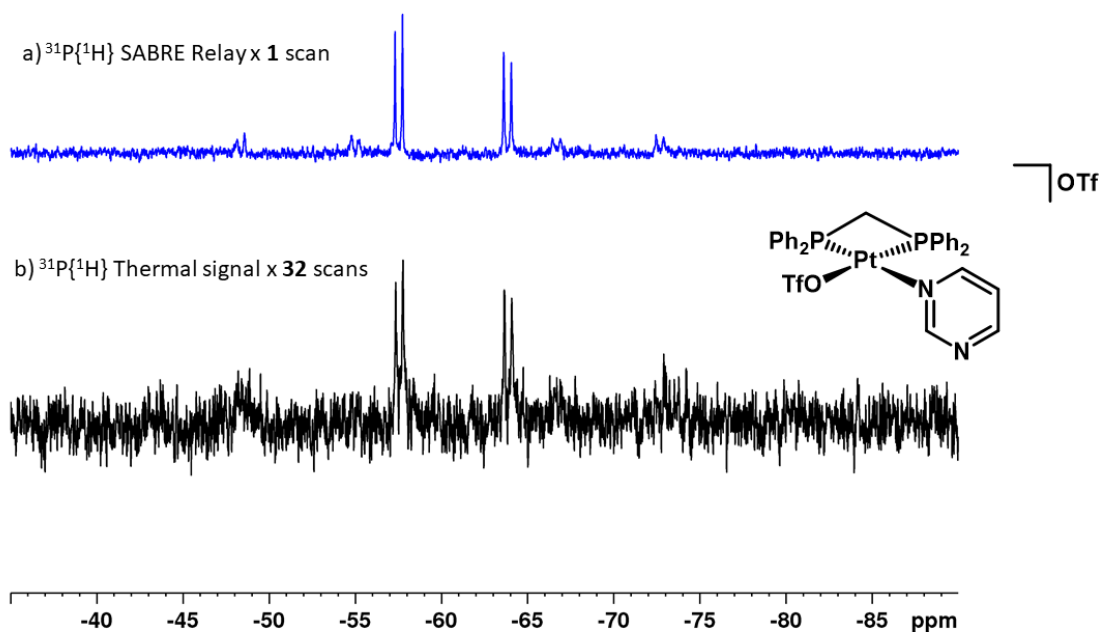


Figure 4.25: $^{31}\text{P}\{^1\text{H}\}$ NMR single-scan spectra of $[\text{Pt}(\text{OTf})(\text{dppm})(\text{pyrimidine})]\text{OTf}$; a) hyperpolarised using SABRE-Relay at 65 G, 1 average; b) acquired under Boltzmann equilibrium conditions, using 32 averages using 10 eq. of pyrimidine to 1 eq. of $[\text{IrCl}(\text{COD})(d_{22}\text{-lMes})]$ & 1 eq. $[\text{Pt}(\text{OTf})_2(\text{dppm})]$ in methanol- d_4 .

Figure 4.25 shows that the two doublets arising from the inequivalent-coupled phosphorous nuclei of $[\text{Pt}(\text{OTf})(\text{dppm})(\text{pyrimidine})]\text{OTf}$ are clearly enhanced. Even the platinum satellites of each of the signals are observed in a single hyperpolarised scan. This is in comparison to 32 averages (under Boltzmann conditions) where the platinum satellites cannot be distinguished from noise. Further tests using $[\text{Pt}(\text{OTf})_2(\text{dppe})]$ and $[\text{Pt}(\text{OTf})_2(\text{dppp})]$ were completed. The resulting overlaid hyperpolarised NMR spectra are shown in Figure 4.26.

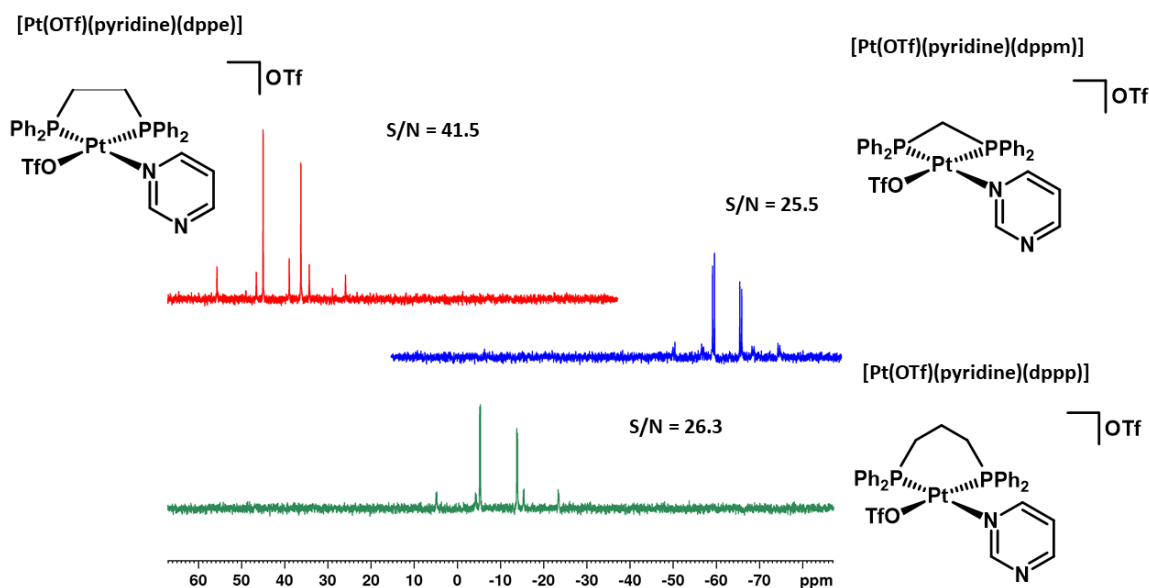


Figure 4.26: $^{31}\text{P}\{^1\text{H}\}$ NMR spectra of $[\text{Pt}(\text{OTf})(\text{dpe})(\text{pyrimidine})]\text{OTf}$ (red), $[\text{Pt}(\text{OTf})(\text{dppm})(\text{pyrimidine})]\text{OTf}$ (blue), $[\text{Pt}(\text{OTf})(\text{dppp})(\text{pyrimidine})]\text{OTf}$ (green), hyperpolarised using SABRE-Relay, 1 average. Red) 10 eq. of pyrimidine to 1 eq. of $[\text{IrCl}(\text{COD})(d_{22}\text{-IMes})]$ & 1 eq. $[\text{Pt}(\text{OTf})_2(\text{dpe})]$ in methanol- d_4 . Blue) 10 eq. of pyrimidine to 1 eq. of $[\text{Ir}(\text{COD})\text{Cl}](d_{22}\text{-IMes})$ & 1 eq. $[\text{Pt}(\text{OTf})_2(\text{dppm})]$ in methanol- d_4 . Green) 10 eq. of pyrimidine to 1 eq. of $[\text{IrCl}(\text{COD})(d_{22}\text{-IMes})]$ & 1 eq. $[\text{Pt}(\text{OTf})_2(\text{dppm})]$ in methanol- d_4 .

As shown in Figure 4.26 all three platinum complexes are enhanced by the SABRE-Relay process, with platinum satellites clearly seen in each case. When pyrimidine is used as the substrate, a platinum complex containing the dpe ligand results in the most efficient relayed signal gain with a signal to noise value of 41.4. This is almost twice that found when using the dppp based complex ($S/N = 26.3$). This indicates that the bite angle of the square planar platinum complex must affect the ligand exchange rates, with the dpe ligand being optimal.

4.5.1 Effect of Deuterium Labelling within Pyrimidine

With pyrimidine leading to good ^{31}P signal enhancements under SABRE-Relay, the effect of deuterium labelling within the adduct was explored. There were two main hypotheses tested: i) if a long-lived singlet state (ie. the presence of two adjacent ^1H atoms with a mutual J coupling) was essential for the SABRE-Relay process to take place and ii) how T_1 lifetimes and polarisation level effects the SABRE-Relay process. With deuterium labelling, the T_1 values of the remaining ^1H resonances would be extended and thus should improve the polarisation level. It was hypothesised that higher ^1H polarisation levels and longer ^1H T_1 lifetimes on the substrate would enable the build-up of more ^{31}P polarisation in the phosphine ligands of the adduct. Ligand exchange rates would be expected to remain the same.

Here only the dppp complex was tested as synthesis was proven to be more straightforward (over dppe). A series of four deuterated pyrimidine isotopologues including 2,5-*d*₂-pyrimidine¹³⁵ (Figure 4.27) were tested. The *T*₁ values and ¹H polarisation levels are given in Table 4.1. It must be noted that in this study the catalyst to substrate ratio used was 1:4 as opposed to the 1:10 ratio used in these studies.

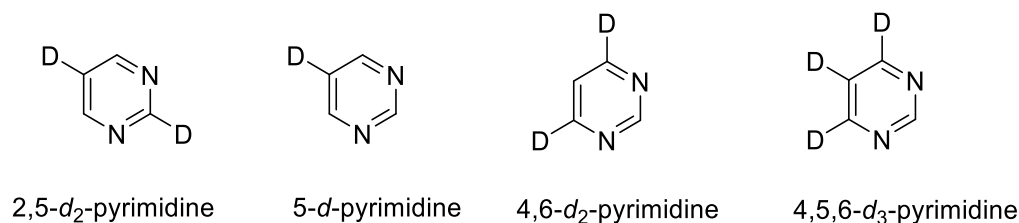


Figure 4.27: Deuterated isotopologues of pyrimidine 2,5-*d*₂-pyrimidine¹³⁵, 5-*d*-pyrimidine, 4,6-*d*₂-pyrimidine and 4,5,6-*d*₃-pyrimidine (unpublished) used in the SABRE-Relay process.

Table 4.1: ¹H SABRE polarisation level and *T*₁ values of pyrimidine, 2,5-*d*₂-pyrimidine¹³⁵, 5-*d*-pyrimidine and 4,6-*d*₂-pyrimidine. SABRE conditions: [IrCl(COD)(IMes)] 5 mM, substrate 20 mM, methanol-*d*₄, 3 bar (g) *p*H₂ measured at 400 MHz. Errors in *T*₁ approximately 6%.

Substrate	<i>T</i> ₁ (no cat.) /s	<i>T</i> ₁ (with cat.) /s	Polarisation Level (%)
	H2 77.5 H4/H6 39.0 H5 29.0	H2 6.0 H4/H6 20.0 H5 16.5	H2 1.9 H4/H6 1.6 H5 1.3
	129.0	34.5	3.6
	H2 126.0 H4/6 121.0	H2 22.0 H4/6 33.0	H2 2.8 H4/6 2.8
	H2 78.5 H5 109.9	H2 30.0 H5 72.0	H2 1.7 H5 1.6
	H2 141.1	H2 28.0	H2 6.0

¹H and ³¹P single scan hyperpolarised NMR spectra were recorded. The ³¹P results showed that all the deuterated pyrimidines were successful intermediates for the SABRE-Relay process. It is

the singly deuterated pyrimidine, 5-*d*-pyrimidine which afforded the best signal to noise values ($S/N = 42.2 \pm 2.1$), followed by 4,6-*d*₂-pyrimidine (31.2 ± 1.7), and then non-deuterated pyrimidine ($S/N = 26.9 \pm 1.5$). It can be noted that in all of the deuterated cases there are no directly neighbouring proton pairs where a singlet state could be created. In the case of 5-*d*-pyrimidine all three protons at positions 2, 4 and 6 are isolated from one another either by a nitrogen or a deuterium atom. In the case of 4,5,6-*d*₃-pyrimidine there is only one proton, so a singlet state is not possible here. This represents the first direct evidence that a singlet state is not required for SABRE-Relay

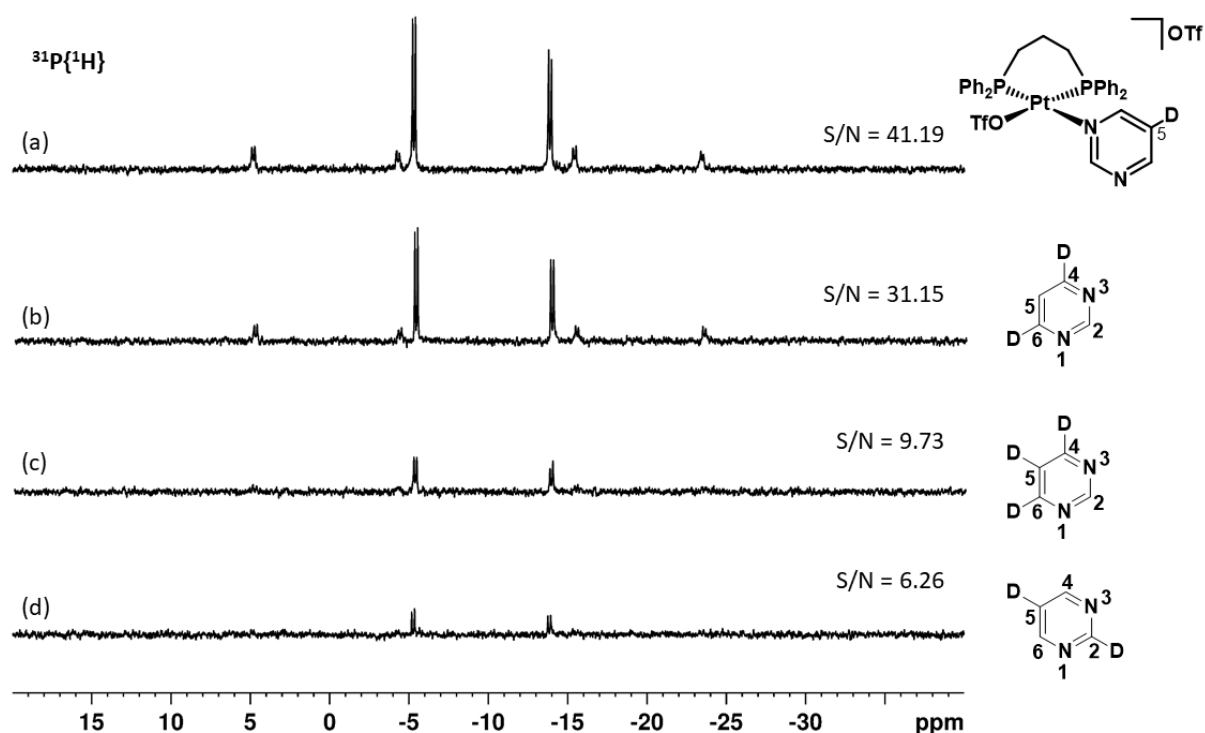
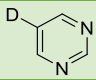
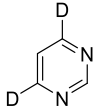
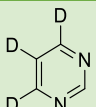
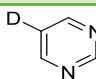


Figure 4.28: $^{31}\text{P}\{^1\text{H}\}$ hyperpolarised NMR spectra showing S/N of a) $[\text{Pt}(\text{OTf})(\text{dppp})(5\text{-}d\text{-pyrimidine})]\text{OTf}$, b) $[\text{Pt}(\text{OTf})(\text{dppp})(4,6\text{-}d_2\text{-pyrimidine})]\text{OTf}$ c) $[\text{Pt}(\text{OTf})(\text{dppp})(4,5,6\text{-}d_3\text{-pyrimidine})]\text{OTf}$ d) $[\text{Pt}(\text{OTf})(\text{dppp})(2,5\text{-}d_2\text{-pyrimidine})]\text{OTf}$ hyperpolarised using SABRE-Relay, 1 average. 10 eq. of deuterated pyrimidine to 1 eq. of $[\text{IrCl}(\text{COD})(d_{22}\text{-IMes})]$ & 1 eq. $[\text{Pt}(\text{OTf})_2(\text{dppp})]$ in methanol-*d*₄.

The protons of 5-*d*-pyrimidine possess both high ^1H signal enhancement recorded in the SABRE-Relay process ($H_2 = -1623 \pm 60$ ($5.2 \pm 0.2\%$), $H_{4/6} = -794 \pm 38$ ($2.6 \pm 0.1\%$)) and long T_1 values ($H_2 = 16.3 \pm 0.1$ s, $H_{4/6} = 24.2 \pm 0.2$ s in the SABRE-Relay mixture (Table 4.2); $H_2 = 126$ s, $H_{4/6} = 121$ s recorded in the absence of a catalyst - Table 4.1). It can be hypothesised that this combination of factors leads to the increased polarisation on the phosphorous ligand and consequently gives a high S/N value of 41.9.

Table 4.2: Signal enhancement values, ϵ and T_1 values of ^1H and ^{31}P resonances with 10 eq. of deuterated isotopologues to 1 eq. of $[\text{IrCl}(\text{COD})](d_{22}\text{IMes})$ and 1 eq. $[\text{Pt}(\text{OTf})_2(\text{dppp})]$ in methanol- d_4 . * indicates overlapping signal. n/a. Due to 1:10 ratio measurements of T_1 were compromised.

Sub	^1H T_1 (s) (free)	^1H ϵ	^{31}P T_1 (s) (bound)	^{31}P ϵ
	H2 16.3 ± 0.1 H4/H6 24.2 ± 0.2	H2 -1623.3 ± 60.3 H4/H6 -794.6 ± 38.4	$\delta -5.3 = 2.4 \pm 0.1$ $\delta -13.9 = 2.4 \pm 0.2$	$\delta -5.3 = 20.5 \pm 0.9$ $\delta -13.9 = 19.6 \pm 0.9$
	H2 16.0 ± 0.1 H5 $42.5 \pm 0.8^*$	H2 -1575.7 ± 23.7 H5 -995.1 ± 13.7	$\delta -5.3 = 2.7 \pm 0.2$ $\delta -13.9 = 2.5 \pm 0.1$	$\delta -5.3 = 13.9 \pm 0.6$ $\delta -13.9 = 11.2 \pm 0.2$
	H2 - n/a	H2 -1123.7 ± 49.2	$\delta -5.3 = 2.1 \pm 0.1$ $\delta -13.9 = 2.0 \pm 0.1$	$\delta -5.3 = 5.0 \pm 0.3$ $\delta -13.9 = 4.3 \pm 0.2$
	H4/H6 - n/a	H4/H6 -1030.6 ± 49.4	$\delta -5.3 = 2.9 \pm 0.2$ $\delta -13.9 = 2.8 \pm 0.2$	$\delta -5.3 = 2.8 \pm 0.2$ $\delta -13.9 = 3.2 \pm 0.2$

4.6 ^{31}P SABRE-Relay Polarisation Using Pyrazine.

Pyrazine gives a single ^1H resonance. When binding to the catalysts this symmetry is broken giving two distinct resonances (Figure 4.29).

The SABRE-Relay polarisation transfer method was used in this work to investigate the existence of long-lived singlet states in the pyrazine (pz) molecule. In order to investigate the efficiency of the SABRE-Relay polarization transfer method, a sample containing 20 equivalents of pz to 5 mM of $[\text{IrCl}(\text{COD})(d_{22}\text{-IMes})]$ and 5 mM of $[\text{Pt}(\text{OTf})_2(\text{dppp})]$ in 0.6 mL methanol- d_4 was prepared. After adding H_2 at 3 bar (g), the formation of $[\text{Ir}(\text{H}_2)(\text{IMes})(\text{pz})_3]$ was confirmed by the presence of pz resonances in the aromatic region which are diagnostic for the ligand bound in the equatorial (δ 8.4, 8.35) and axial (δ 8.28, 8.20) sites of the Ir complex (Figure 4.29) and by a single hydride resonance, typical for equivalent hydrogen atoms bound on a tris-substituted complex, at δ -22.17.

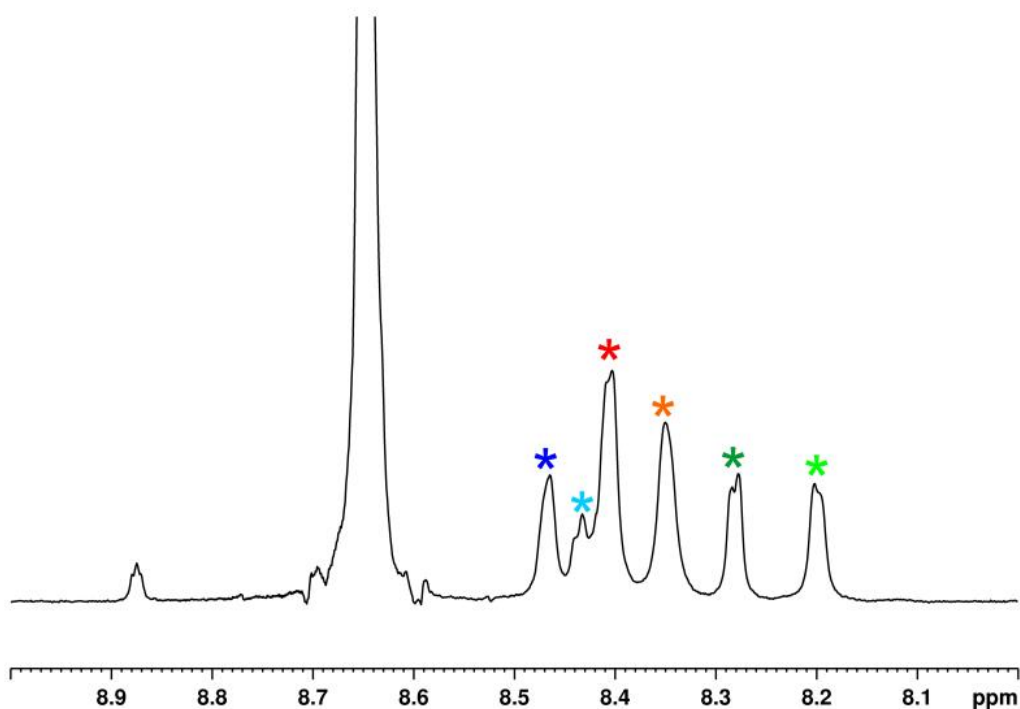


Figure 4.29: Aromatic region of a ^1H NMR spectrum acquired on a sample prepared using 5 mM of $[\text{IrCl}(\text{COD})(d_{22}\text{-IMes})]$ and $[\text{Pt}(\text{OTf})_2(\text{dppp})]$ respectively with 20 eq. of pz in 0.6 mL MeOD. The formation of $[\text{Ir}(\text{H}_2)(\text{IMes})(\text{pz})_3]$ is indicated by resonances corresponding to pz protons bound to Ir in the equatorial sites of the complex (red - ortho to the bonding N centre and orange - meta to the bonding N centre) and resonances corresponding to pz protons bound to the Ir in the axial site of the complex (dark green - ortho to the bonding N centre and light green - meta to the bonding N centre). Another two resonances, located further downfield, are diagnostic for pz bound to the platinum complex (dark blue – ortho to the N binding centre and light blue – meta to the N binding centre).

When $p\text{-H}_2$ was added to the sample and shaken in the stray field of the magnet at ~ 6.5 mT, a strong ^1H SABRE response was detected following a one-shot interrogation using a 90° RF pulse (Figure 4.30).

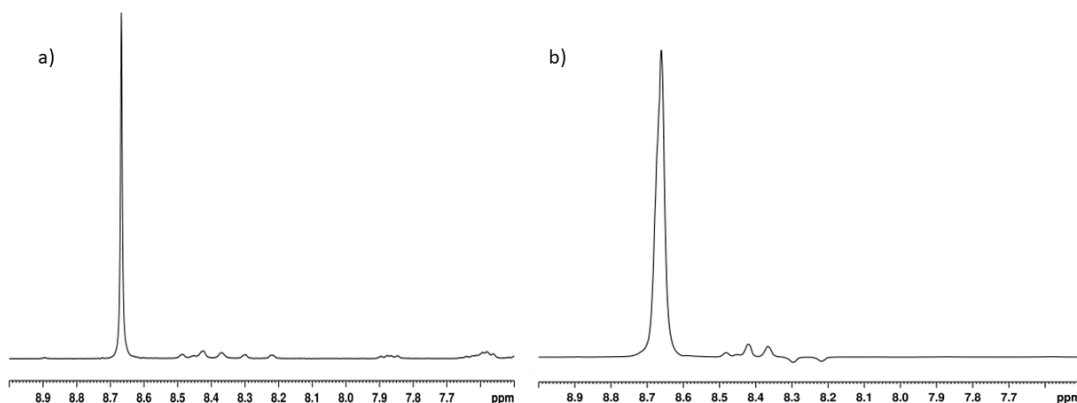


Figure 4.30: ^1H NMR spectra of pz: a). acquired in Boltzmann equilibrium conditions, spectrum (magnified 64 times), b). Corresponding hyperpolarised NMR spectrum under SABRE (single scan).

The free pz resonance was enhanced to approximately 200-fold and smaller enhancements were observed for all the bound pz resonances, as well as for the phenyl groups of the platinum complex (1-fold up to 3.5-fold), and the iridium carbene backbone (5-fold) /methyl protons. Interestingly, the pz peaks bound to iridium in the axial position were antiphase and enhanced by -84-fold and -77-fold respectively, while their counterparts in the equatorial sites were in phase and exhibited a lower enhancement, of 24-fold and 32-fold, respectively. This is potential evidence that either the concentration of the sample or the temperature at which the experiment was performed (298 K) does not lead to optimal exchange.

When running a ^{31}P proton decoupled one-shot NMR measurement under Boltzmann equilibrium conditions, no signal was detected from either of the ^{31}P resonances in the platinum complex. However, a longer experiment, with 32 averages and a magnetization recovery time of 50 s, allowed for the detection of the ^{31}P peaks and their corresponding Pt satellites (Figure 4.31a). In order to investigate the possibility of polarisation transfer from $p\text{-H}_2$ via the iridium catalyst and pz to the platinum complex, one-shot ^{31}P proton decoupled experiments were carried out after adding 3 bar(g) of $p\text{-H}_2$ to the sample. Polarisation transfer was successfully mediated by the iridium catalyst and pz and the two ^{31}P resonances of $[\text{PtOTf}(\text{dppp})(\text{pz})]\text{OTf}$ appeared strongly enhanced (Figure 4.31b), the S/N of the hyperpolarised spectrum being 10 times higher than its Boltzmann equilibrium counterpart.

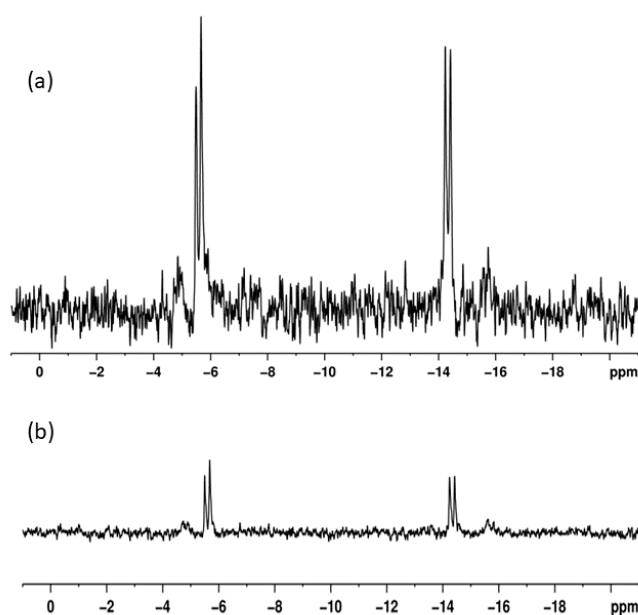


Figure 4.31: ^{31}P NMR spectra of $[\text{Pt}(\text{dppp})(\text{OTf})(\text{pz})]\text{OTf}$: a). acquired in Boltzmann equilibrium conditions, using 32 averages, b). hyperpolarised using SABRE-Relay, 1 average.

4.6.1 Effect of [Pt(OTf)₂(dppp)] loading on ³¹P SNR.

In order to investigate the influence of the [Pt(OTf)₂(dppp)] loading on the efficiency of the polarisation transfer process, three samples were analysed containing 5 mM of [IrCl(COD)(*d*₂₂-Imes)], 20 equivalents of pz and increasing amounts of [Pt(OTf)₂(dppp)] (1.25 mM, 2.5 mM and 5.0 mM). Each sample was polarised using 3 bar(g) of *p*-H₂ and a ~6.5 mT polarisation transfer field and a minimum of five ³¹P proton decoupled NMR spectra were acquired immediately after the polarisation transfer process. The ³¹P enhancement values were calculated using the S/N values determined for both hyperpolarised and Boltzmann equilibrium condition spectra, respectively. The results, presented in Table 4.3 show by reducing the relative amount of [Pt(OTf)₂(dppp)] the signal enhancement values were dramatically increased. It is noted however, that the best absolute S/N (11.5 ± 1.4) is obtained when working at high loadings.

Table 4.3: S/N values and enhancement values obtained for ³¹P hyperpolarised spectra acquired on samples containing increasing amounts of [Pt(OTf)₂(dppp)] relative to a constant pz concentration of 100 mM.

Amount[Pt(OTf) ₂ (dppp)]/ mM	S/R _{hyp} δ = -5.6	ε δ = -5.6	S/R _{hyp} δ = -14.3	ε δ = -14.3
1.25	4.8 ± 1.3	13.9 ± 3.5	3.5 ± 0.6	9.1 ± 1.6
2.50	8.2 ± 0.8	6.8 ± 0.6	6.2 ± 0.4	7.2 ± 0.5
5.00	11.5 ± 1.4	6.1 ± 0.7	9.2 ± 0.8	5.4 ± 0.5

4.7 ³¹P SABRE-Relay using 4,6-*d*₂-methyl nicotinate

As discussed in chapter one the deuterated methyl nicotinate used in this study is the best performing substrate molecule for SABRE in terms of polarisation level and lifetime.¹³⁵ 4,6-*d*₂-deuterated methyl nicotinate reacts with [Pt(OTf)₂(dppp)] to form the mono-substituted platinum complex [Pt(OTf)(dppp)(4,6-*d*₂-methyl nicotinate)] (as can be seen in Figure 4.32) which yields two doublet phosphorous signals at δ -5.07 and -14.31 with ¹⁹⁵Pt satellites. However, in contrast to the other substrates studied, 4,6-*d*₂-methyl nicotinate also forms the bis-substituted platinum complex [Pt(dppp)(4,6-*d*₂-methyl nicotinate)₂] where both triflate ligands are displaced, giving rise to a singlet phosphorous signal at δ -15.0 with its corresponding satellites.

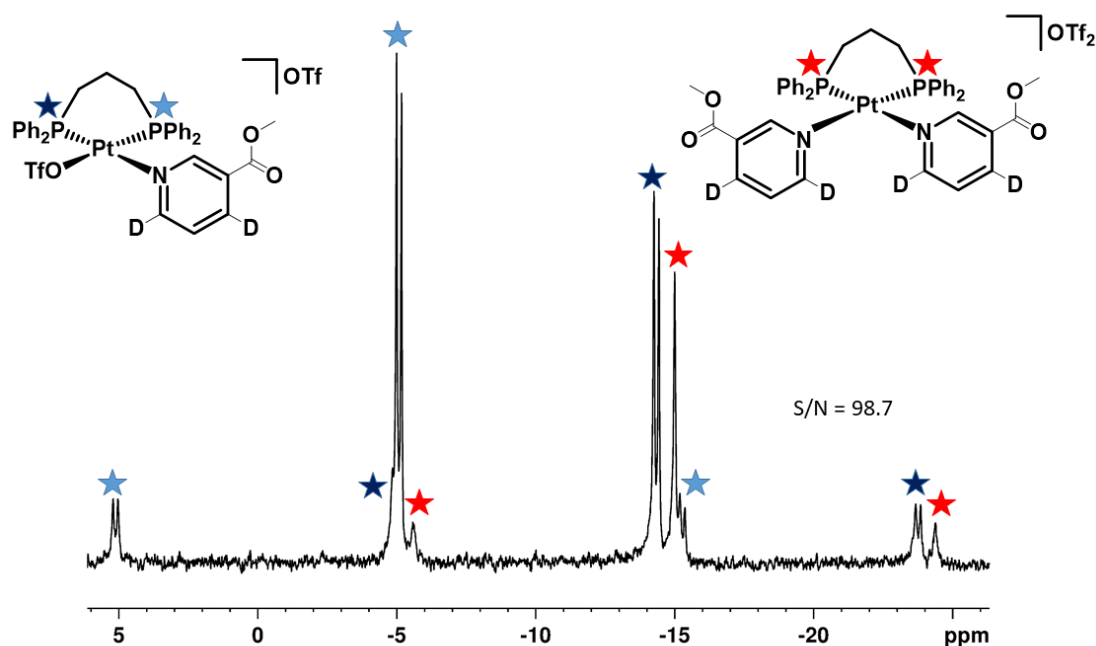


Figure 4.32: $^{31}\text{P}\{^1\text{H}\}$ hyperpolarised single scan of $[\text{Pt}(\text{dppp})\text{OTf}(4,6\text{-}d_2\text{-deuterated methyl nicotinate})]$ (blue stars) and $[\text{Pt}(\text{dppp})(4,6\text{-}d_2\text{-deuterated methyl nicotinate})_2]$ (red stars) formed with 10 eq. of 4,6- d_2 -deuterated methyl nicotinate to 1 eq. of $[\text{Ir}(\text{COD})\text{Cl}](d_{22}\text{IMes})$ & 1 eq. $[\text{Pt}(\text{OTf})_2(\text{dppp})]$ in methanol- d_4 . $p\text{-H}_2$ was added and the sample was shaken for 10 seconds in the stray field.

All three platinum complexes were tested using this substrate intermediate (Figure 4.33). The signal to noise value recorded using 4,6- d_2 -methyl nicotinate peaked at $S/N = 99 \pm 5$.

The formation of the bis-substituted complex indicates that the binding of 4,6- d_2 -methyl nicotinate is stronger than any of the other substrates studied to date. As described in section 4.2.1, the rate of substitution is proportional to the nucleophilicity of the entering group. It would suggest that 4,6- d_2 -methyl nicotinate was a better nucleophile in comparison with the other substrates tested here. The mono and bis-substituted complexes were detected in the corresponding thermally polarised NMR spectra.

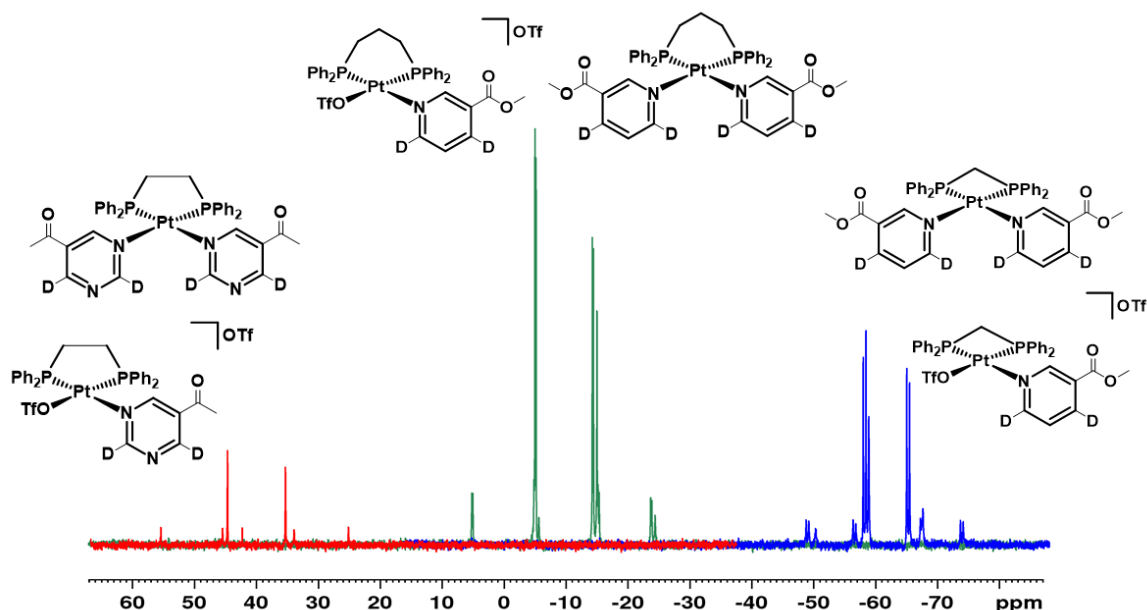


Figure 4.33: $^{31}\text{P}\{^1\text{H}\}$ hyperpolarised single scan of $[\text{Pt}(\text{OTf})(\text{dppp})(4,6\text{-}d_2\text{-methyl nicotinate})]\text{OTf}$ and $[\text{Pt}(\text{dppp})(4,6\text{-}d_2\text{-methyl nicotinate})_2]$ (green) formed with 10 eq. of 4,6- d_2 -deuterated methyl nicotinate to 1 eq. of $[\text{IrCl}(\text{COD})(d_{22}\text{IMes})]$ & 1 eq. $[\text{Pt}(\text{OTf})_2(\text{dppp})]$ in methanol- d_4 . $^{31}\text{P}\{^1\text{H}\}$ hyperpolarised single scan of $[\text{Pt}(\text{OTf})(\text{dppm})(4,6\text{-}d_2\text{-methyl nicotinate})]\text{OTf}$ and $[\text{Pt}(\text{dppm})(4,6\text{-}d_2\text{-methyl nicotinate})_2]$ (blue) formed with 10 eq. of 4,6- d_2 -deuterated methyl nicotinate to 1 eq. of $[\text{IrCl}(\text{COD})(d_{22}\text{IMes})]$ & 1 eq. $[\text{Pt}(\text{OTf})_2(\text{dppm})]$ in methanol- d_4 . $^{31}\text{P}\{^1\text{H}\}$ hyperpolarised single scan of $[\text{Pt}(\text{OTf})(\text{dppe})(4,6\text{-}d_2\text{-methyl nicotinate})]\text{OTf}$ and $[\text{Pt}(\text{dppe})(4,6\text{-}d_2\text{-methyl nicotinate})_2]$ (red) formed with 10 eq. of 4,6- d_2 -methyl nicotinate to 1 eq. of $[\text{IrCl}(\text{COD})(d_{22}\text{IMes})]$ & 1 eq. $[\text{Pt}(\text{OTf})_2(\text{dppe})]$ in methanol- d_4 . $p\text{-H}_2$ was added to each sample and was shaken for 10 seconds in the stray field of a 9.4T magnet.

When using 4,6- d_2 -methyl nicotinate as the substrate, the best performing complex proved to be the more sterically challenged $[\text{Pt}(\text{OTf})_2(\text{dppp})]$. This is consistent with the need for steric bulk to drive ligand exchange in the presence of 4,6- d_2 -methyl nicotinate but more rigorous discussion would require significantly more data.

Table 4.4: Enhancement values, ϵ and T_1 values of ^1H and ^{31}P resonances with 10 eq. of 4,6- d_2 -methyl nicotinate to 1 eq. of $[\text{IrCl}(\text{COD})](d_{22}\text{IMes})$ & 1 eq. of $[\text{Pt}(\text{OTf})_2(\text{dppm})]/[\text{Pt}(\text{OTf})_2(\text{dppe})]/[\text{Pt}(\text{OTf})_2(\text{dppp})]$ in methanol- d_4

Cat	^1H T_1 (s) (free)	^1H ϵ	^{31}P T_1 (s) (bound)	^{31}P ϵ	^{31}P ratio (Thermal)	^{31}P ratio (Hyp.)
dppm	H2 10 ± 1 H5 overlapping peaks	H2 -1861 ± 40 H5 -930 ± 15	doublet δ -57.3 1 ± 1 δ -64.3 1 ± 1 singlet δ -58.0 in the noise	doublet δ -57.3 28 ± 1.0 δ -64.3 26 ± 1.4 singlet δ -58.0 25 ± 1.5	doublet δ -57.3 = 1 δ -64.3 = 0.8 singlet δ -58.0 = 0.43	doublet δ -57.3 = 1 δ -64.3 = 0.8 singlet δ -58.0 = 0.45
dppe	H2 11 ± 1 H5 24 but overlapping peaks	H2 -1185 ± 34 H5 -1293 ± 33	doublet δ 45.1 3 ± 1 δ 35.7 3 ± 1 singlet δ 42.7 1.5 ± 1	doublet δ 45.1 14 ± 0.5 δ 35.7 13 ± 0.5 singlet δ 42.7 16 ± 2.5	doublet δ 45.1 = 1 δ 35.7 = 1 singlet δ 42.7 = 0.1	doublet δ 45.1 = 1 δ 35.7 = 1 singlet δ 42.7 = 0.1
dppp	H2 10 ± 1 H5 31 ± 1	H2 -1062 ± 54 H5 -857 ± 35	doublet δ -5.1 2 ± 1 δ -14.3 2 ± 1 singlet δ -15.0 2 ± 1	doublet δ -5.1 35 ± 1.7 δ -14.3 38 ± 1.6 singlet δ -15.0 34 ± 1.7	doublet δ -5.1 = 1 δ -14.3 = 0.8 singlet δ -15.0 = 0.47	doublet δ -5.1 = 1 δ -14.3 = 0.8 singlet δ -15.0 = 0.45

With dppm and dppe, the singlet indicating the bis-substituted complex appears in the middle of the two phosphorous signals from the mono-substituted complex in terms of chemical shift. When analysing the proportion of the platinum complexes in the thermal spectra the ratios show that using $[\text{Pt}(\text{OTf})_2(\text{dppm})]$ and $[\text{Pt}(\text{OTf})_2(\text{dppp})]$ results in a 1:0.23 of the mono-substituted to bis-substituted product (Table 4.4). However using $[\text{Pt}(\text{OTf})_2(\text{dppe})]$ results in a much smaller proportion of the bis-substituted product (1: 0.05). As this is measured under thermal conditions the amount of species in the equilibrium depends on the thermodynamic ground state. In all cases they were more stable in the mono-substituted form. The ratios of the hyperpolarised spectra are directly analogous to those in the thermal spectra in all three systems. In the hyperpolarised system the amount of each species is dependent on the kinetic exchange rate. This identical ratio of species observed under both thermal and hyperpolarised conditions shows that ^{31}P signal enhancement is directly proportional to the concentration of the species.

4.8 ^{31}P SABRE-Relay using thienopyridazines

As the target substrates in this thesis are the thienopyridazines, the SABRE-Relay process was attempted using T[2,3- d]P (synthesised isomer with the highest polarisation level – see chapter 2) and $[\text{Pt}(\text{OTf})_2(\text{dppp})]$. Unfortunately, no hyperpolarised ^{31}P signal was observed in a single scan. This could be explained by the low ^1H signal enhancements (~ 200) achieved using the ratios and catalysts of this particular method compared with >1000 -fold with 4,6- d_2 -methyl nicotinate and 5- d -pyrimidine. A thermal ^{31}P spectrum shown in Figure 4.34 revealed the presence of the

mono-substituted (indicated by the presence of doublets at $\delta -6.07$ and $\delta -14.26$) and the bis-substituted complexes (indicated by the singlet at -16.00). The presence of both these species shows that the steric bulk of T[2,3-*d*]P is not an issue for binding to platinum. However, the combination of a short T_1 and low polarisation under these conditions meant that no measurable ^{31}P hyperpolarisation was observed. Future experiments should explore relay of polarisation with the different iridium metal catalysts available, such as $[\text{Ir}(\text{Cl})(\text{COD})(d_{22}\text{-SIMes})]$, and implement the different optimisation steps which were detailed in chapter two.

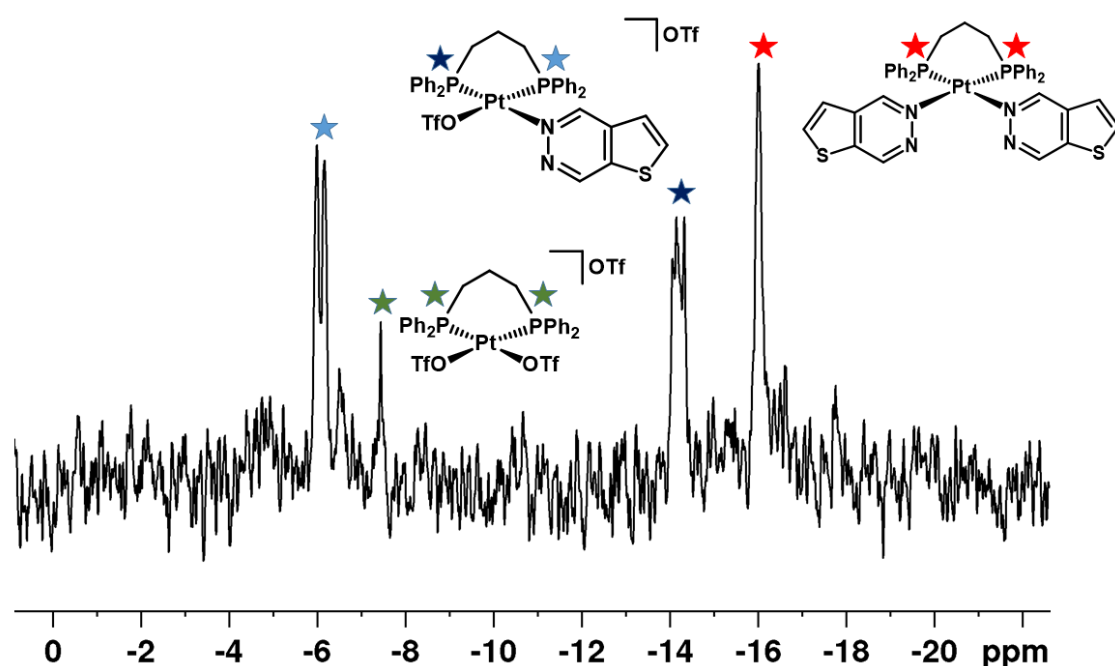


Figure 4.34: $^{31}\text{P}\{^1\text{H}\}$ thermal (400 scans) of $[\text{PtOTf}(\text{dppp})(\text{T}[2,3\text{-}d]\text{P})\text{OTf}]$ (blue stars) and $[\text{Pt}(\text{dppp})(\text{T}[2,3\text{-}d]\text{P})_2]$ (red stars) formed with 10 eq. of T[2,3-*d*]P to 1 eq. of $[\text{Ir}(\text{COD})\text{Cl}](d_{22}\text{IMes})$ & 1 eq. $[\text{Pt}(\text{OTf})_2(\text{dppp})]$ (green stars) in methanol- d_4 .

4.9 Conclusions and Discussions

Here a proof of principle study demonstrates that SABRE derived polarisation can be successfully cascaded into a second metal complex via a coherent transfer pathway using a series of different N-heterocycles. Enhanced ^{31}P NMR responses were measured in a metal complex which does not interact directly with $p\text{-H}_2$. These enhanced responses were recorded in a matter of seconds using simple single scan hyperpolarised experiments.

A novel aspect of this work is that SABRE-Relay can proceed without the creation of a singlet state at low field in the intermediate substrate. In the original study two protocols were used employing both field-cycling and a magnetisation to singlet state (M2S) pulse sequence¹⁶⁸ as it

was thought that these stages were necessary. However, all the hyperpolarised experiments performed in this chapter do not use a long-lived state based sequence and thus provides evidence that the SABRE-Relay process can take place as a standard shake and drop $^{31}\text{P}\{^1\text{H}\}$ experiment (with a PTF of 65 G).

The pyridine and deuterated pyrimidine studies show a general trend that the amount of phosphorous enhancement measured on the platinum catalyst increases with an increase in total proton polarisation across the free substrate molecule. It can be concluded that in general, substrate molecules which are able to bind to the platinum catalysts, with high SABRE ^1H polarisation levels and long T_1 can undergo SABRE-relay.

The detection of the mono and/or bis-substituted platinum complex appears to be substrate specific. In most cases it is the mono-substituted complex which forms, however in the case of d_2 -4,6-methyl nicotinate and T[2,3- d]P the bis-substituted complex is also formed. The formation of the bis-substituted complex indicates that the sterically bulkier d_2 -4,6-methyl nicotinate and T[2,3- d]P are better ligands for platinum than the sterically smaller substrates such as pyrimidine and pyrazine.

Disappointingly, T[2,3- d]P did not succeed in producing a hyperpolarised phosphorous signal in a single scan despite its ability to bind to the platinum catalyst. This lack of signal can be explained by a combination of the inherent shorter T_1 and lower ^1H signal enhancements compared to other substrates.

The work presented here provides a sound basis for much more detailed kinetic and thermodynamic studies of the equilibrium involved in the reaction. There is much potential to study different ratios of the catalysts and substrate and a whole library of iridium based SABRE catalysts have now been developed which could be tested in this process.¹²³ The ligand design of the platinum catalysts could be varied and could incorporate ligands which give phosphorous resonances which are much closer in chemical shift than those measured here. In this way a ^{31}P pseudo-singlet state could be created to extend the magnetic lifetime of the ^{31}P hyperpolarised signal.

It is expected that SABRE-Relay using a second-metal catalyst will be used in the future to enhance new classes of agents that are not amenable to the original SABRE hyperpolarisation route. With development, instead of the dppp bridged chelated ligands, it is feasible that the

platinum complexes could contain labile ligands. These, once polarised, could be separated from the platinum complex and used for *in vivo* MRS experimentation.

This method gave the first evidence that it is possible to cascade SABRE hyperpolarisation to a remote ligand, which is not bound to the SABRE active complex. This was a huge breakthrough which led to major method developments opening up the range and number of ligands that could be polarised by SABRE significantly in a technique termed SABRE-Relay using proton transfer.²⁴³ This first stage of this process involves “traditional” SABRE to hyperpolarise ammonia or an amine (the transfer agent). The labile, now hyperpolarised protons, of the amine can relay the hyperpolarisation through proton exchange into the target substrate. Polarisation of a wide range of chemically diverse agents with amide, alcohol, carboxylic acid and phosphate functionalities is now feasible. Importantly this means that some of the most significant endogenous molecules which have already been successfully used *in vivo* using d-DNP MRS have the potential to be hyperpolarised using the much simpler, more cost-effective SABRE method.

With the introduction of this new SABRE Relay process, one could argue that the method discussed in this chapter is obsolete, particularly when thinking about hyperpolarised imaging. The hyperpolarised phosphorous signal has a T_1 of $\sim 2/3$ s and the catalyst itself contains a heavy metal such as platinum therefore at first glance, would not appear suitable for clinical use. However, when considering cancer metabolism monitoring through the use of anti-cancer drugs, cis-platin and its derivatives (carboplatin and oxaliplatin) are some of the most common anti-cancer drugs on the market.²⁵⁹ Their structures shown in Figure 4.35 share many similarities with the platinum catalysts studied here, in that they both possess a platinum metal centre and exhibit square planar geometry.

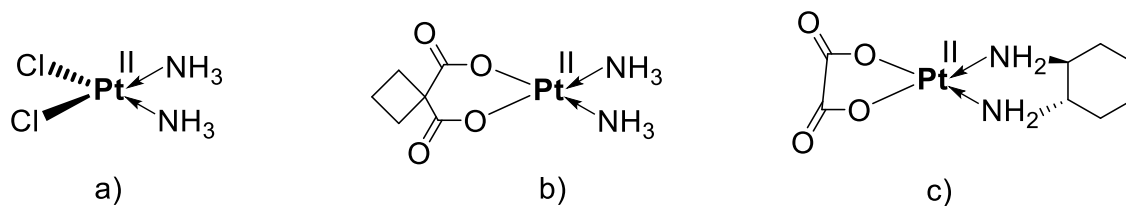


Figure 4.35: Molecular structures of the anti-cancer drugs a) cisplatin, b) carboplatin and c) oxaliplatin.

If SABRE Relay using proton transfer was used in combination with SABRE Relay using a second metal catalyst it could be possible to hyperpolarise cisplatin. The ammonia could be hyperpolarised by scalar coupling through the iridium catalyst. Once hyperpolarised, two possible mechanisms could be hypothesised. It could act as a carrier of hyperpolarisation to allow proton exchange with those in the ammonia ligands of cisplatin or the hyperpolarised ammonia molecule could displace the non-hyperpolarised ammonia ligand within cisplatin. On closer inspection, the latter is extremely unlikely as the Pt-NH₃ bonds are kinetically inert and thermodynamically stable. Labelled ¹⁵NH₃ could be employed so that hyperpolarised cisplatin could be detected through both ¹H and ¹⁵N NMR.

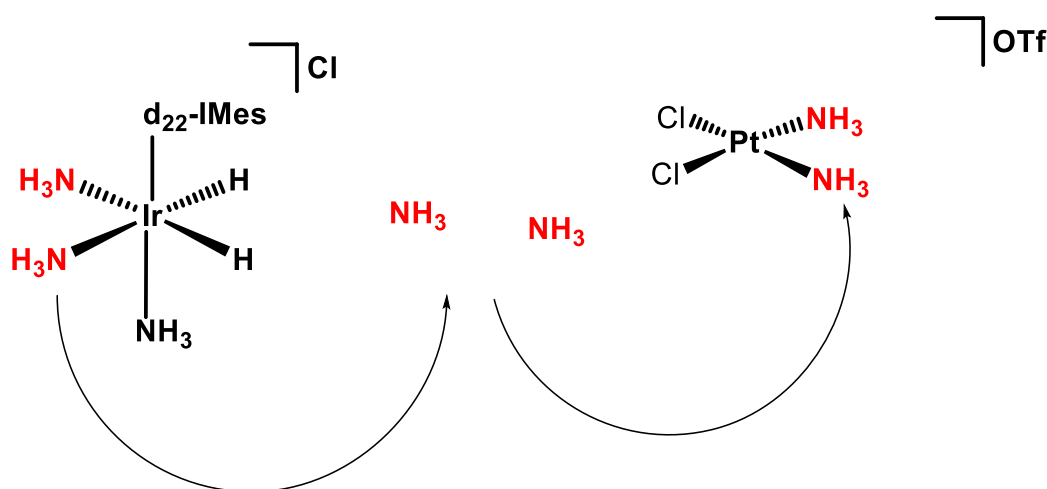


Figure 4.36: Hypothesised route to hyperpolarise cisplatin through SABRE-Relay.

Cisplatin is often used in combination with another anti-cancer drug fluorouracil to provide combined chemotherapy treatment for cancers of the gullet, head and neck. Unpublished work within our group hyperpolarising fluorine, carbon and proton atoms within fluorouracil using SABRE-Relay has been successfully carried out. A combined chemotherapy treatment which could be hyperpolarised and used in imaging could lead to the development of pharmacokinetic profiles of accumulation in tissues and tumours which could inform dosing regimes or new drug delivery mechanisms.

Chapter 5: Translation of SABRE from Benchtop to Imaging Facility

5.1 Introduction

Hyperpolarisation will find important application in the field of magnetic resonance imaging (MRI), where it can aid medical diagnosis (though metabolic profiling) and track associated treatment (directly by imaging drug delivery, or indirectly through a change in metabolic response). Indeed, hyperpolarised agents for use in oncology^{4,94} are now a clinical reality, through the development and rollout of d-DNP.³ This chapter focuses on the initial steps needed for translation of the SABRE method from the laboratory benchtop to the imaging facility. Research here concentrates on the target thienopyridazines as the substrate of interest.

The SABRE polarisation transfer process necessitates a solvent into which all three of the main constituents (catalyst, *p*-H₂ and target substrate) readily dissolve. Methanol-*d*₄ is the optimum solvent for achieving high SABRE enhancement values as solubility is high for both catalyst and *p*-H₂.¹³⁵ Unfortunately, this solvent is not biocompatible (see below). To overcome this limitation, the use of biphasic separation was explored. Biphasic separation (section 5.2) permits isolation of the hyperpolarised agent in an aqueous phase whilst the toxic iridium catalyst remains in the organic phase. This catalyst-separated hyperpolarisation (CASH) SABRE method¹³⁸ is implemented for T[2,3-*d*]P in section 5.3. Following successful separation of polarised thienopyridazine into an aqueous layer, cytotoxicity assays were carried out on two cell lines to verify biocompatibility (section 5.4). Finally, several different MR imaging methods were tested on preclinical and clinical based MRI systems to demonstrate improved ¹H detection (section 5.5).

5.2 Theory of SABRE Catalysis: Development for *in vivo* applications

A major consideration for the development of the SABRE method for medical diagnosis is solution/solvent biocompatibility. Finding a viable alternative to 100% methanol-*d*₄ is critical. Methanol is extremely toxic to humans.²⁶⁰ Oxidation of the alcohol within the body forms the metabolites formaldehyde and formic acid that are responsible for acidosis, blindness, and death; with a lethal ingested dose of just 1-2 mL/kg (Figure 5.1).²⁶¹

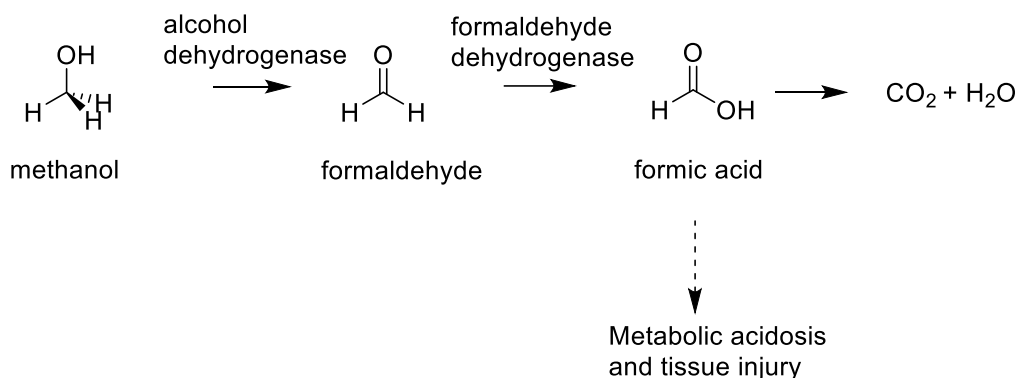


Figure 5.1: Metabolism of methanol to form formaldehyde and formic acid. Alcohol dehydrogenase is the primary enzyme for the oxidation of methanol to formaldehyde. Formaldehyde dehydrogenase is the principle enzyme involved in the oxidation of formaldehyde to formic acid.²⁶⁰

Direct SABRE polarisation in water would be ideal to meet biocompatibility requirements, however both the metal catalyst [IrCl(COD)(IMes)] and *p*-H₂²⁶² have poor solubility here. To reduce toxicity, previous studies have used solvent mixtures of ethanol-*d*₆ and D₂O.¹⁴⁴ However, the level of signal gain is reduced¹⁹²; and *T*₁ relaxation values were found to decrease relative to those in methanol.¹³⁵ The lower enhancement values reflect the change in ligand exchange kinetics.¹⁹² Cytotoxicity studies show a maximum of 30% ethanol can be tolerated before cell death occurs.²⁶³ Furthermore, *in-vivo* bolus injection of absolute ethanol into pigs (0.1mL/kg of body weight) is known to cause cardiovascular collapse.²⁶⁴ Ford *et al.* (1984) showed that when administered in both rats and dogs IV formulations greater than 10% propylene glycol and 30% ethanol produced hemoglobinuria/hemolysis *in vivo*.²⁶⁵ While their data did show that using saline rather than water can have slightly less haemolytic potential, the maximum 'acceptable' concentration of organic co-solvent was recommended to not exceed 25%. The wellbeing of any animals for *in-vivo* testing is paramount. Therefore, unpublished *in-vivo* rat studies (within the CHyM group) have been completed and demonstrate that only 300 µl of 30% ethanol solvents can be injected intravenously without altering physiological measures (blood pressure/breathing rate). Such low volumes, combined with the low signal enhancements in solvent mixtures, confounds the *in-vivo* application of SABRE hyperpolarisation

Other methods previously tested to achieve biocompatibility of SABRE, include the use of water-soluble catalysts (see Figure 5.2). Two studies used co-ligands to increase catalyst water solubility; a phosphine ligand containing hydrophilic arylsulfonate groups²⁶⁶ (1) and a diol moiety within the traditional COD ligand²⁶⁷ (2). Other studies have functionalised the NHC group with hydrophilic groups (shown in structures (3)²⁶⁶ and (4)²⁶⁸).

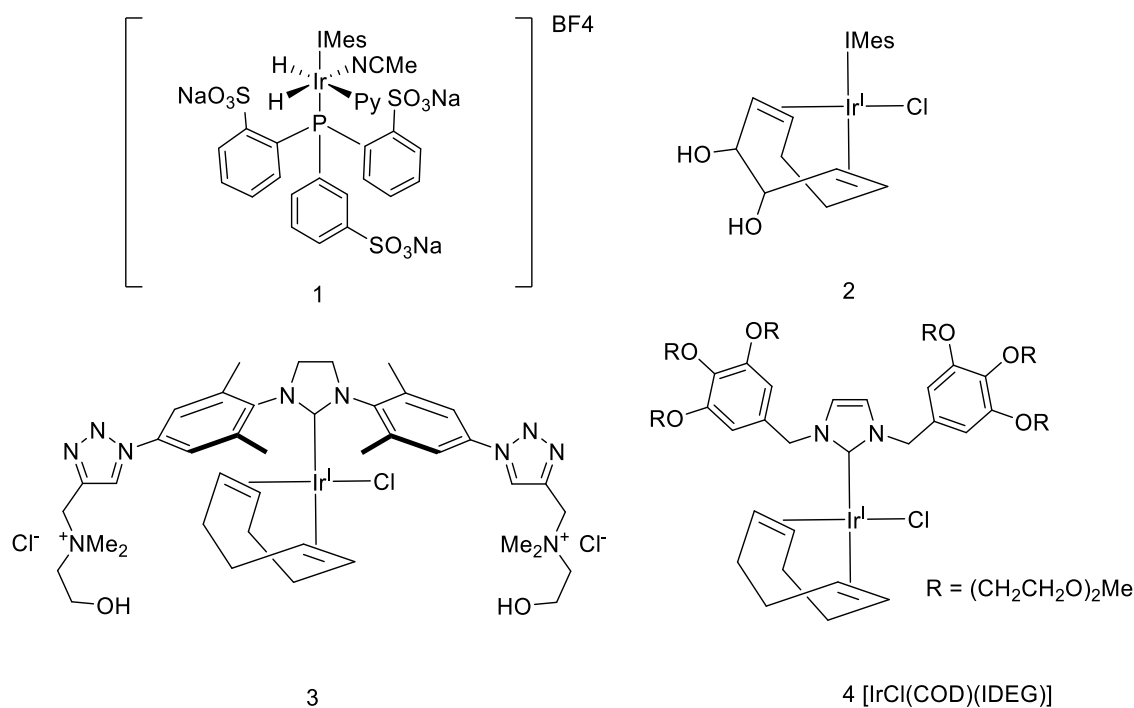


Figure 5.2: Structures of SABRE catalysts containing water soluble co-ligands (1 and 2)^{266, 267} and NHC ligands (3 and 4)^{266, 268}.

Although the pre-catalyst $[\text{IrCl}(\text{COD})(\text{IDEG})]$ (**4**) gave the most promising results with a range of substrates being hyperpolarised, a maximum of only 42-fold ^1H NMR signal enhancement was observed at 7 T.²⁶⁸ However, ^{15}N enhancement of 1000-fold was achieved at 7 T for ^{15}N -pyridine.²⁶⁸ Despite the ability to achieve reasonable X-nuclei SABRE catalysis in aqueous solutions, the toxic iridium would still need to be removed before *in vivo* use. One solution could be heterogeneous catalysis. With the iridium catalyst attached in the solid phase, it could easily be removed from the hyperpolarised solution after catalysis (Figure 5.3). In one study the catalyst was bonded to polymer microbeads (**5**) yielding a 5-fold ^1H enhancement for the *ortho* proton of pyridine at 9.4 T.²⁶⁹ In a second study the iridium-NHC catalyst was immobilised on silica gel (**6**), with polarisation transfer at low field, yielding a 100-fold ^{15}N signal enhancement in ^{15}N -pyridine at 9.4 T.²⁷⁰ However, in both cases methanol- d_4 was used as the solvent and hence the system remained bio-incompatible.

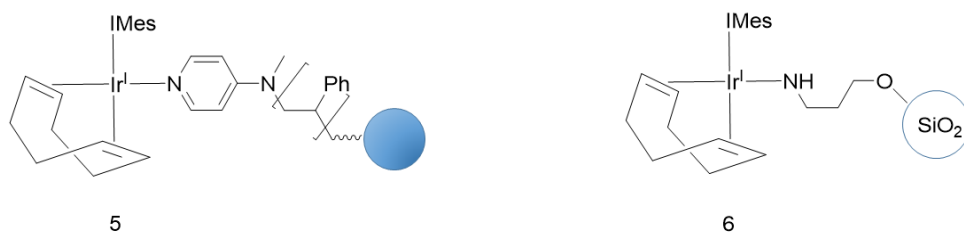


Figure 5.3: Heterogeneous SABRE catalysts using polymer microbeads (5)²⁶⁹ and silica gel (6)²⁷⁰.

An alternative two-stage process was reported using phase extraction and catalyst capture with a silica scavenging agent.²⁷¹ The most successful scavenger tested was the commercially available 3-mercaptopropyl-functionalised silica gel shown in Figure 5.4 (7). It was found that the significant concentration of thiol groups relative to the concentration of iridium in solution was a prerequisite for efficient and rapid metal capture.

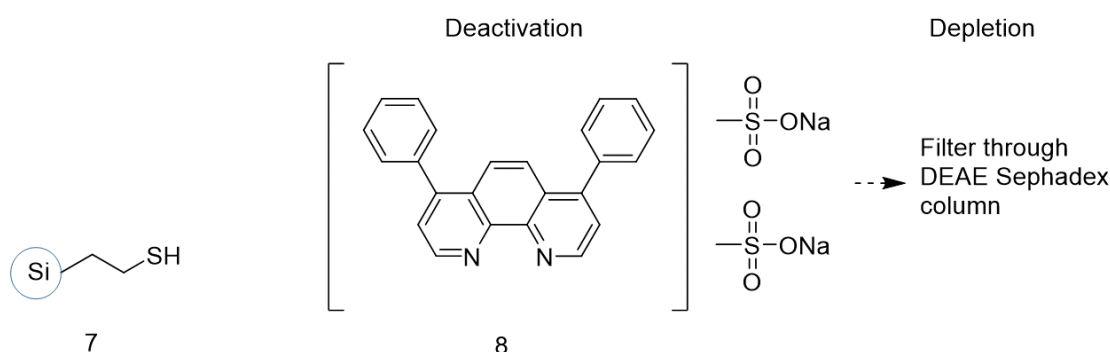


Figure 5.4: Chemicals used to remove the SABRE metal catalyst: 3-mercaptopropyl-functionalised silica gel (7)²⁷¹ and Bathophenanthroline disulfonic acid disodium (BPS) (8) used to deactivate the catalyst followed through filtration using a DEAE Sephadex column.²⁶³

Other approaches to remove the catalyst used a chelating ligand, bathophenanthroline sulfonic acid (BPS), which would irreversibly bind to the catalyst thereby deactivating it.²⁶³ Once chelated, ion-exchange chromatography using a Diethylaminoethyl (DEAE) Sephadex column enabled catalyst removal. This method yielded a 74 ± 21 -fold ^1H signal enhancement in methyl-4,6- d_2 -nicotinate with detection at 9.4 T. This represented a 30% decrease in signal relative to the standard SABRE sample in ethanol- d_6 /D₂O (30:70). This loss in polarisation can be attributed to relaxation effects due to the 12 s required to complete the activation and depletion steps.

A more promising route to biocompatibility involves biphasic catalysis. This method uses an organic phase and an aqueous phase. Ideally the iridium catalyst remains in the organic phase

whilst the polarised substrate ends in the aqueous phase for subsequent extraction. Optimisation of this process requires careful consideration of the solubility for each substrate used. Such biphasic separation, when applied to SABRE, was coined catalyst-separated hyperpolarisation via signal amplification by reversible exchange (CASH-SABRE)¹³⁸

5.2.1 Catalyst-separated hyperpolarisation (CASH) SABRE

Iali et al.¹³⁸ used CASH-SABRE to demonstrate NMR enhancements of substrates in D₂O increased considerably when compared to any of the methods outlined above. For example, using ethanol-*d*₆/D₂O (30:70) with BPS yielded a 74 ± 21 -fold ¹H signal enhancement when methyl-4,6-*d*₂-nicotinate was used as substrate at 9.4 T. In contrast a 3000-fold signal enhancement (~9.5% polarisation) per proton was reported for the same substrate in the D₂O layer of the biphasic system.¹³⁸ In methanol-*d*₄ values of 9.5% (H4) and 8.3% (H6) were recorded.¹³⁵ Inductively Coupled Plasma – Mass Spectrometry (ICP-MS) measurements from the aqueous layer only detected minimal catalyst contamination (1.5×10^{-6} mol dm⁻³) and minimal chloroform-*d*₃ contamination (0.06%).¹³⁸ The CASH-SABRE process is outlined in Figure 5.5.

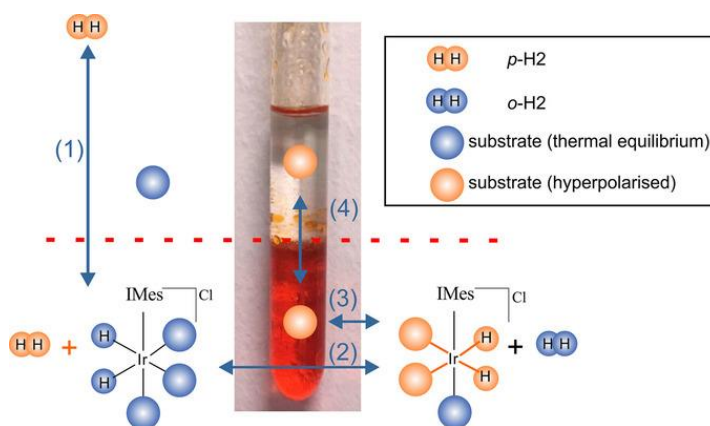


Figure 5.5: Representation of the biphasic CASH-SABRE process¹³⁸. The iridium catalyst remains in the organic phase whilst the polarised substrate transfers into the aqueous phase for subsequent extraction.

CASH-SABRE was exemplified with a number of different substrates (including pyrazine, 4,6-*d*₂-methyl nicotinate, 4,6-*d*₂-nicotinamide and pyridazine) at the 20-100 mM level together with [IrCl(COD)(IMes)] (5mM) in 0.3 mL (CDCl₃) and 0.3 mL (D₂O) and 0.16 w/v% NaCl).

Before activation with *p*-H₂, the catalyst resides in the organic phase and the substrate may be present in one phase or across both the aqueous phase and organic phase. Upon activation, and shaking the sample at ~65 G, SABRE polarisation takes place in the resulting emulsion. Once

separation occurs, free hyperpolarised substrate can be detected in both layers depending on the solubility of the substrate.

The implementation of saline as opposed to pure D₂O was a major breakthrough. Prior to this, full relaxation of the ¹H hyperpolarised signals in the substrate occurred before separation of the two layers was complete. The addition of other salts including NaCO₂Me, NH₄CO₂Me and NH₄Cl were attempted but NaCl proved to deliver the best separation times and enhancement levels.¹³⁸

Associated cytotoxicity assays using a 10% bolus volume of the isolated biphasic aqueous phase with 4,6-*d*₂-methyl nicotinate as substrate caused no observable changes within the A549 and MCF7 cell lines used.²⁶³

5.3 CASH-SABRE with Thienopyridazines – A biphasic study

A study using T[2,3-*d*]P was carried out to investigate if the CASH-SABRE method could be applied successfully as a route to improved bio-compatibility. 18 mM of T[2,3-*d*]P with 4.5 mM of [IrCl(COD)(*d*₂₂-SIMes)] (optimum catalyst for this substrate) was used across the two layers. Both substrate and catalyst were dissolved in 0.35 mL of dichloromethane-*d*₂ in a 5mm Young's tube. The solution was then degassed using freeze-pump-thaw cycling with liquid nitrogen. 0.35mL of aqueous D₂O and 2 mg NaCl (to aid separation) were then added to the sample (under an inert atmosphere in a glovebox) and degassed again under vacuum.

Due to the organic and aqueous phases being immiscible, the lower dichloromethane-*d*₂ layer maintained the original orange colour due to the presence of the pre-catalyst, whereas the aqueous layer remained colourless. With the addition of H₂ and upon shaking, the two layers first formed an emulsion and then separate into two distinct layers again after ~15 s. The lower dichloromethane-*d*₂ layer was pale yellow in colour indicating the presence of the active catalyst [Ir(H)₂(IMes)(T[2,3-*d*]P)₃] with the aqueous layer remaining colourless.

A 1D projection of the ²H signal amplitude across the length of the NMR sample tube (*z*-axis) was measured (Figure 5.6). This confirmed the spatial distribution/bi-phasic separation of the aqueous (D₂O) and organic (dichloromethane-*d*₂) layers.

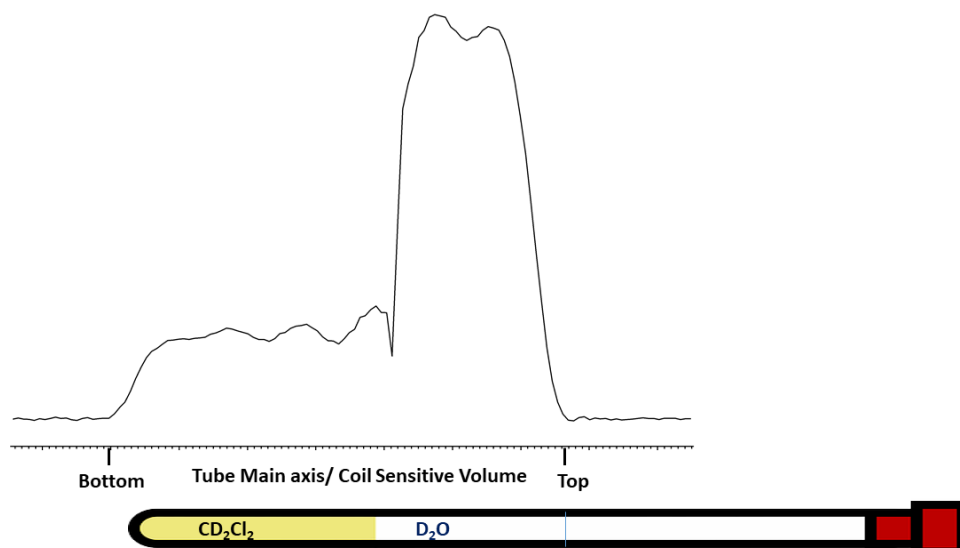


Figure 5.6: 1D projection of the ^2H signal amplitude on the z direction (parallel to the magnet bore and the NMR sample tube). Deuterium profile showing the distribution of the two solvent phases (chloroform- d_2 & D_2O) in the magnet.

A 1D projection was then recorded to show the corresponding ^1H NMR signal amplitude at thermal equilibrium (Figure 5.7a) and following hyperpolarisation (Figure 5.7b) (see section 8.6.1). No thermal signal was seen due to the low ^1H concentrations involved (Figure 5.7a). A hyperpolarised signal for T[2,3- d]P, decaying over time, was observed but was unfortunately confined to the dichloromethane- d_2 layer. This is direct evidence that T[2,3- d]P exhibits lower solubility in the D_2O phase.

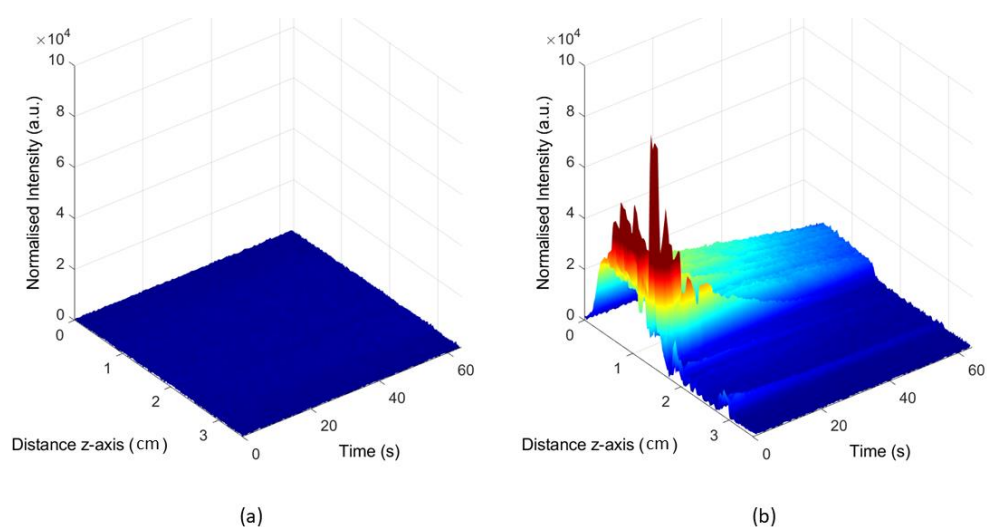


Figure 5.7: 1D projection of the ^1H NMR signal as a function of time (128 repetitions) using a biphasic mixture of 4.5 mM $[\text{IrCl}(\text{COD})(d_{22}\text{SIMes})]$ and 18 mM T[2,3- d]P in dichloromethane- d_2 and deuterium oxide a) under thermal conditions and b) hyperpolarised conditions with 3 bar (g) $p\text{-H}_2$. Dark red indicates areas of highest signal intensity and dark blue areas of lowest signal intensity.

One of the various techniques for the enhancement of solubility for poor water soluble drugs is pH adjustment.²⁷² To improve aqueous solubility via protonation, studies were completed using dilute acid. Samples were subsequently loaded with 0.1 μl and 0.65 μl of conc. HCl. These data show that at low HCl loadings the T[2,3-*d*]P hyperpolarised response is still derived from the chloroform-*d*₂ layer (pH 4) (Figure 5.8b) whilst for 0.65 μl HCl loading (pH 1.5) the hyperpolarised signal is observed within the aqueous phase (Figure 5.8c)

A 940-fold signal enhancement was observed (3% polarisation) for the T[2,3-*d*]P with 0.65 μl conc. HCl. As expected, there is a 70% reduction in the signal enhancement level compared to the corresponding data using methanol-*d*₄ as the solvent. Notwithstanding, when compared to the results presented in the original CASH-SABRE paper (pyrazine 790-fold, 5-methylpyrimidine 340-fold, 4,6-*d*₂-methyl nicotinate 3000-fold, 4,6-*d*₂-nicotinamide 260-fold and pyridazine 380-fold) this represented a promising result.

Unfortunately, subsequent shake and drop experiments using the same sample revealed a 7 times decrease in the levels of signal gain (data not shown). It is hypothesised that this effect is due to the HCl acid deactivating the catalyst. This limits repeatability for QA measures before possible *in-vivo* injection. It is therefore noted that this technique for T[2,3-*d*]P is somewhat limited to a single shot hyperpolarisation step with aqueous extraction.

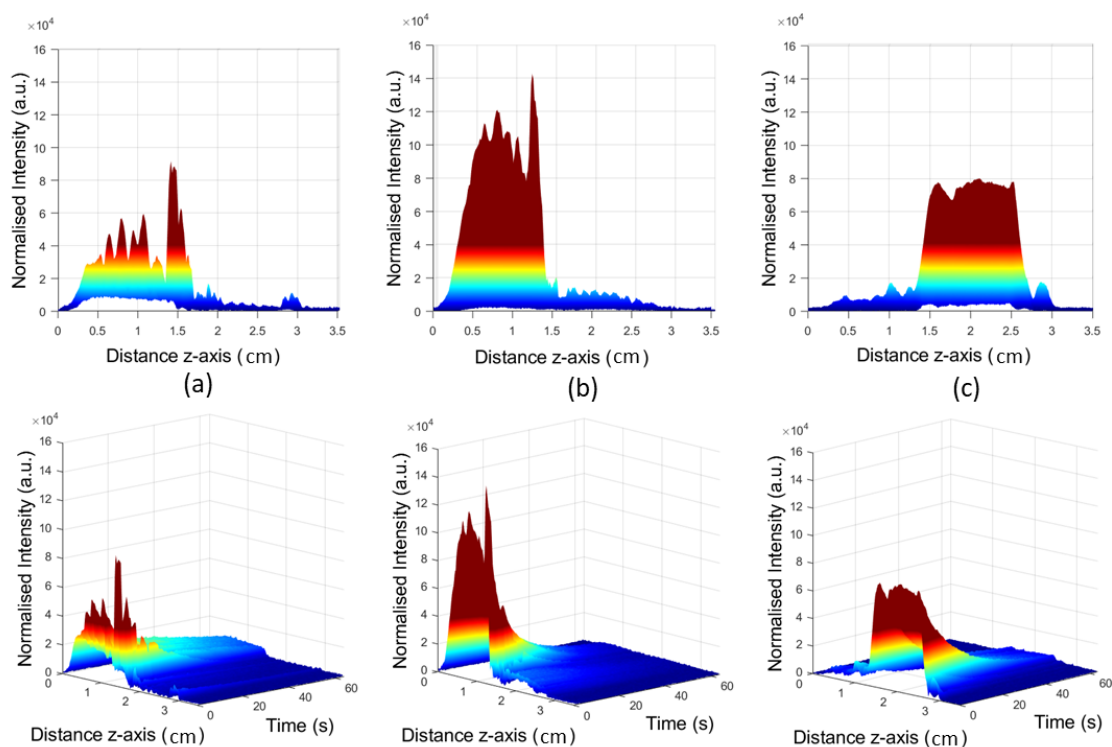


Figure 5.8: 1D projection of the ^1H NMR signal as a function of time (128 repetitions) using a biphasic mixture of 4.5 mM $[\text{IrCl}(\text{COD})(d_{22}\text{SIMes})]$ and 18 mM $\text{T}[2,3-d]\text{P}$ in dichloromethane- d_2 and deuterium oxide (a) No acid, hyperpolarised signal located in organic layer at the bottom half of the biphasic sample. (b) adding 0.1 μl conc. HCl, hyperpolarised signal remains in the organic layer. (c) adding 0.65 μl conc. HCl, hyperpolarised signal is now located in the aqueous layer at the top half of the biphasic sample. Top row rotated to show planar view for ease. Bottom row shows decay of the hyperpolarised signal with time.

Results confirm that $\text{T}[2,3-d]\text{P}$ can be hyperpolarised and separated into a biocompatible solvent using the CASH-SABRE method (under low acidity pH 1.5). The aqueous layer remained colourless throughout the experiments, potentially indicating the active catalyst was not soluble in the aqueous layer and remained in the organic layer. Although this was not confirmed with ICP-MS it is noted that unpublished data (within the CHyM group) shows that CASH-SABRE preparation for nicotinamide and 4,6- d_2 -nicotinamide formulations with $[\text{IrCl}(\text{COD})(1,3\text{-bis}(4\text{-chloro-2,6-dimethylphenyl)imidazol-2-ylidene})]$ catalyst resulted in $<5\text{ppm}$ Iridium in the aqueous layer (this was at the limit of detection in water). These samples of nicotinamide went on for pharmacokinetic study in rats following IV injection with no adverse effects (further indication of limited catalyst contamination using SABRE-CASH preparation).¹⁶⁴ Table 5.1 shows the enhancement factors and T_1 values achieved for SABRE hyperpolarised $\text{T}[2,3-d]\text{P}$ in both methanol- d_4 and dichloromethane- d_2 using a 4 to 1 ratio. There is a one third drop in signal enhancement moving from methanol- d_4 to dichloromethane- d_2 . Unfortunately, T_1 values in these solvents is shortened, by up to 60 s, due to the presence of the catalyst. However, as the polarised

substrate transfers to the deuterium oxide layer of the biphasic system T_1 values extend (see Table 5.1).

Table 5.1: T_1 values for T[2,3- d]P (18 mM) in methanol- d_4 , dichloromethane- d_2 and deuterium oxide. Signal enhancement and T_1 values for T[2,3- d]P (18mM) with [IrCl(COD)(d_{22} -SIMes)] (4.5 mM) in methanol- d_4 and chloroform- d_2 .

Res (δ)	T_1 (s) CD ₃ OD Substrate Alone	T_1 (s) CD ₃ OD SABRE 1:4 ratio	ϵ CD ₃ OD SABRE 1:4 ratio	T_1 (s) CD ₂ Cl ₂ Substrate Alone	T_1 (s) CD ₂ Cl ₂ SABRE 1:4 ratio	ϵ CD ₂ Cl ₂ SABRE 1:4 ratio	T_1 (s) D ₂ O Substrate Alone
H7	38.2 ± 0.2	9.5 ± 0.1	-3142 ± 58	72.2 ± 3.7	12.6 ± 0.1	-1157 ± 73	57.6 ± 0.2
H4	21.4 ± 0.1	6.0 ± 0.1	-3072 ± 60	46.0 ± 1.2	12.1 ± 0.1	-884 ± 52	23.9 ± 0.3
H2	24.3 ± 0.1	7.6 ± 0.1	-885 ± 33	49.6 ± 1.4	20.6 ± 0.1	-305 ± 29	22.1 ± 0.3
H3	14.9 ± 0.2	4.8 ± 0.1	-525 ± 21	36.6 ± 0.8	12.4 ± 0.1	-333 ± 29	13.2 ± 0.3

Subsequent biocompatibility of the aqueous layer was tested with cytotoxicity in cell assays.

5.4 Cytotoxicity

It is noted that T[2,3- d]P was synthesised in the laboratory and no existing cytotoxicity data was available. To ensure biocompatibility, the toxicity of T[2,3- d]P in the resultant CASH-SABRE aqueous layer was tested. Toxicity studies (for 3-24 hour exposure times) were carried out to assess how cell viability is affected with salt, acid and the substrate T[2,3- d]P.

5.4.1 Evaluating the biocompatibility of the extracted aqueous layer from the CASH-SABRE method

Cytotoxicity of the aqueous layer from the biphasic preparation was tested using two cell lines: A549 (lung cancer cells) and MCF7 (breast cancer cells). The required number of cells ($\sim 10^4$ per well) were seeded 24 h before treatment so that they were in exponential growth phase. Treatment involved exposure of the cells for 1, 3, 6 and 24 h to a series of percentage volumes of the extracted aqueous layer; 0%, 2.5%, 5%, 7.5% and 10%. Dilutions were prepared with D₂O before adding to the cells and medium. The final amount of the treatment was maintained at 10% in the total volume of the cell growth medium (i.e., 10 μ L in 100 μ L). Separate plates were prepared for each of the exposure times and triplicate sample wells were used for each condition. Triplicate sample wells of a control were also prepared containing cells and medium alone.

An MTT (3-(4,5-dimethylthiazol-2-yl)-2,5-diphenyltetrazolium Bromide) colorimetric assay was used to measure cell viability in this study. After incubation at desired time points (1 h, 3h, 6 h

and 24 h) the cell media was replaced with fresh media (100 μ L) containing 10 μ L of MTT (Figure 5.9). MTT is a yellow tetrazolium dye, which turns purple when it is reduced to an insoluble formazan. This reduction is carried out by oxidoreductase enzymes found inside cells, which are dependent on NADH or NADPH (Figure 5.10). The level of active oxidoreductase enzymes reflects the amount of cellular metabolic activity. Cells were incubated further for 4 h in a humidified atmosphere at 37 $^{\circ}$ C. The medium with MTT was then carefully aspirated, and the formed formazan crystals were solubilized in 100 μ L of dimethyl sulfoxide (DMSO). The absorbance of the coloured solution produced was quantified using a spectrophotometer set to a 600 nm wavelength. Data were compared to the absorbance of formazan in a control solution to determine if cellular metabolic activity had increased or decreased. Percentage viability of the various dilutions is compared to the control where only cell media is present.

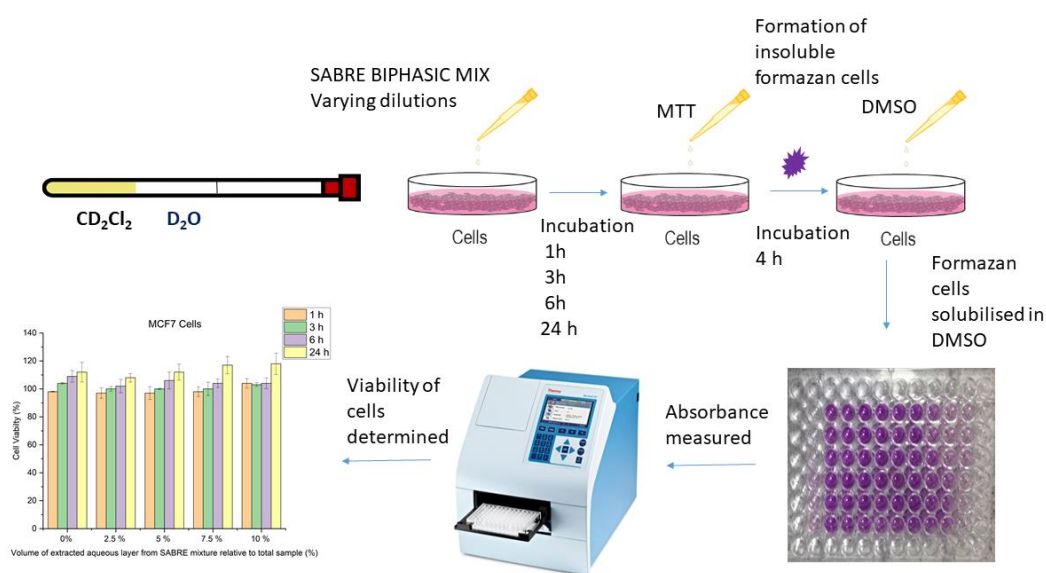


Figure 5.9: Diagram to show the various steps of the toxicity testing and MTT assay.

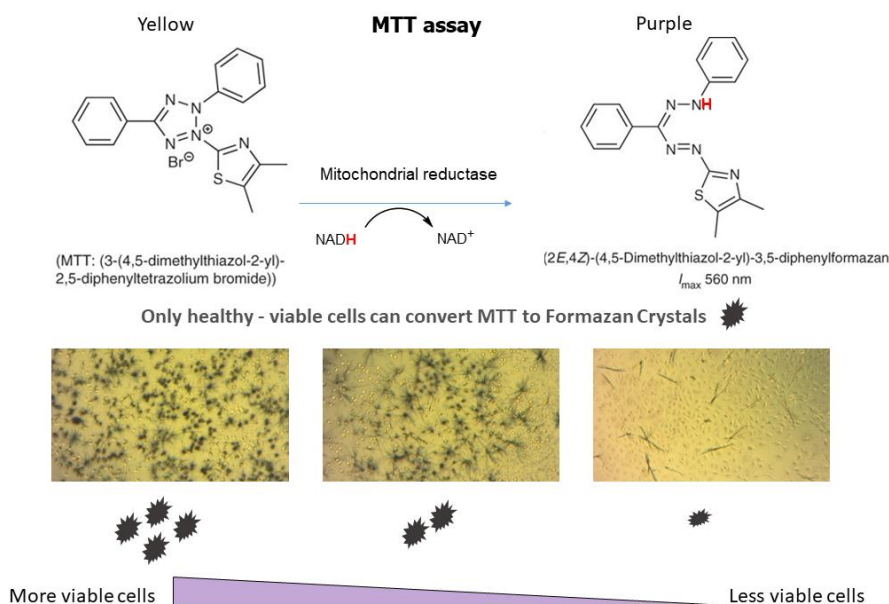


Figure 5.10: MTT assay showing the biochemical conversion by the healthy cells of MTT into Formazan crystals.

Figure 5.11 and Figure 5.12 show the response of the two cell lines studied using varying volumes of the extracted aqueous phase of the biphasic mixture containing T[2,3-*d*]P and [IrCl(COD) (*d*₂₂-SIMes)]. Results of the MTT assay show that treatment with the separated aqueous phase across the different bolus volumes did not decrease the viability of the A549 cells at any of the time points tested (Figure 5.11). All results are within standard error. The results show that although the aqueous phase in the biphasic mixture is acidic, the cells tolerate these conditions, a much unexpected positive response.

Results of the MTT assay show that treatment with the separated aqueous phase across the different bolus volumes did not decrease the viability of the MCF7 cells at any of the time points tested (Figure 5.12). The measure of cell viability is normalised to the cells without any treatment. Therefore, a cell viability of >100% (found at 24 hours) is an indicator that the cells were able to multiply and grow better in the presence of the treatment.

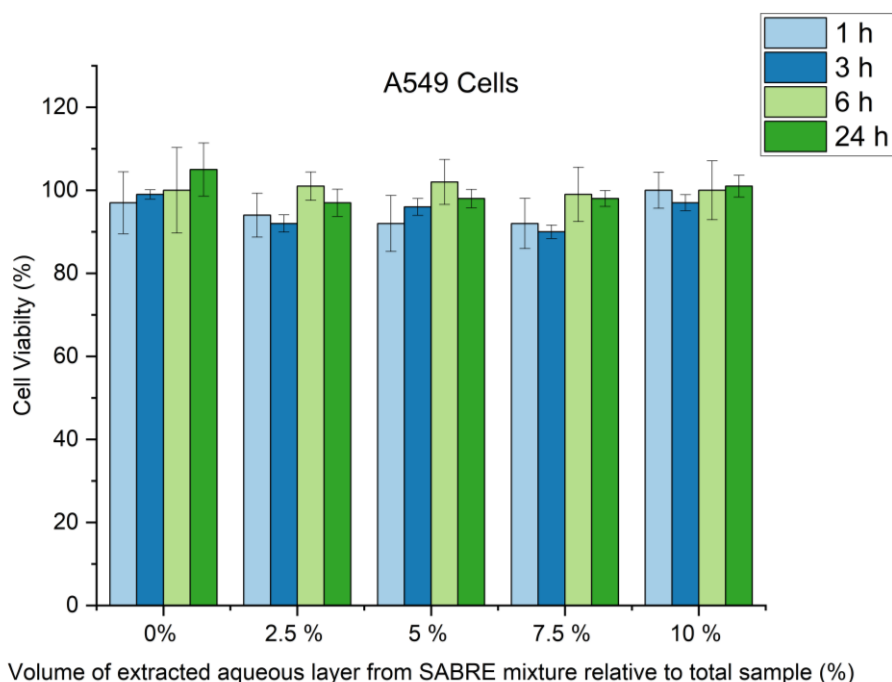


Figure 5.11: Viability of A549 cells with SABRE biphasic mixture using T[2,3-*d*]P and [IrCl(COD)(*d*₂₂SIMes)] at 4 time intervals 1 h (light blue), 3 h (dark blue), 6 h (light green) and 24 hours (dark green). Y-axis = percentage of healthy cells compared with the control. X-axis = percentage of solvent to be tested with respect to total volume of medium received by the cells. Results are taken across 3 separate experiments.

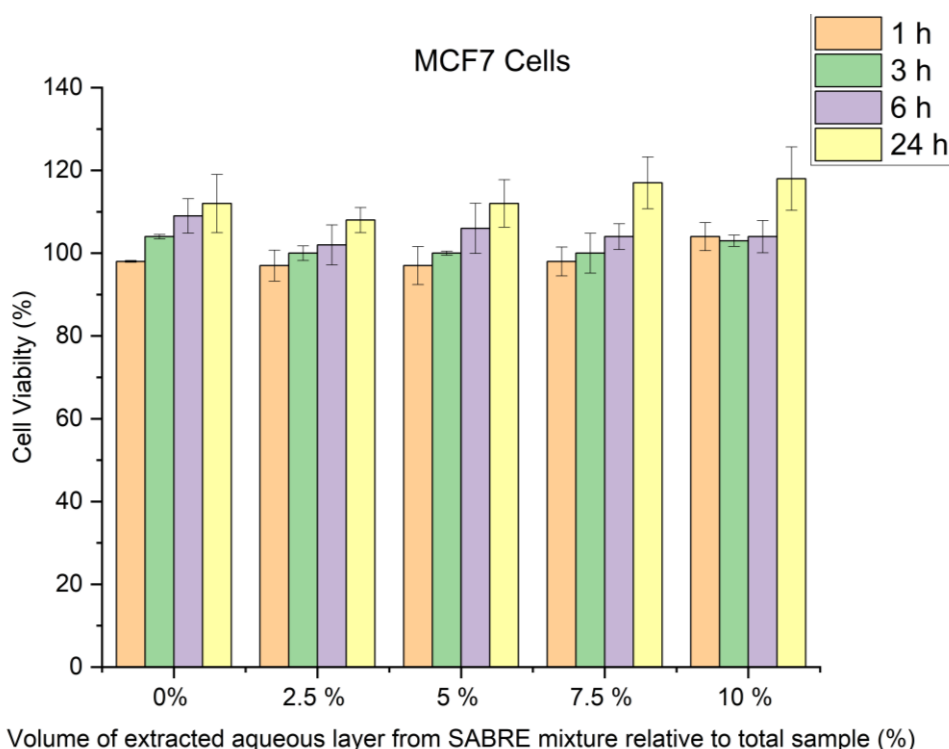


Figure 5.12: Viability of MCF7 cells with SABRE biphasic mixture using T[2,3-*d*]P and [IrCl(COD)(*d*₂₂SIMes)] at 4 time intervals 1 h (orange), 3 h (green), 6 h (purple) and 24 hours (yellow). Y-axis = percentage of healthy cells compared with the control. X-axis = percentage of solvent to be tested with respect to total volume of medium received by the cells. Results are taken across 3 separate experiments.

The precise concentration of the thienopyridazine which had transferred to the aqueous layer is not known exactly. If it assumed that the T[2,3-*d*]P is evenly distributed between the two layers we would expect 18 mM of substrate in the aqueous layer. However, from the biphasic experiments it appeared that upon the addition of the acid, the T[2,3-*d*]P was mainly concentrated in the D₂O layer as detailed in Figure 5.8 c. If we assume there is total transference there would be 36 mM of T[2,3-*d*]P in the aqueous layer. The maximum % volume of the extracted aqueous layer used in the cell viability MTT assay was 10% which would equate to 3.6 mM. It can be concluded that concentrations up to 3.6 mM of T[2,3-*d*]P can be tolerated by MCF7 and A549 cells, with up to 24 hours of exposure, and therefore at these concentrations can be assumed to be safe. However knowing the 50% intravenous lethal dose (LD₅₀) of T[2,3-*d*]P would be useful. The LD₅₀ is the amount of substance required (per body weight) to cause the death of 50% of a group of test animals (usually mice and rats). It is a way of measuring the acute toxicity of a substance.²⁷³ However, non-animal alternatives such as *in-vitro* cytotoxicity methods or computer-based structure-activity models have started to be approved.²⁷⁴ A wider concentration study was carried out on T[2,3-*d*]P alone to try and estimate the LD₅₀ values for the two cell lines (Figure 5.13).

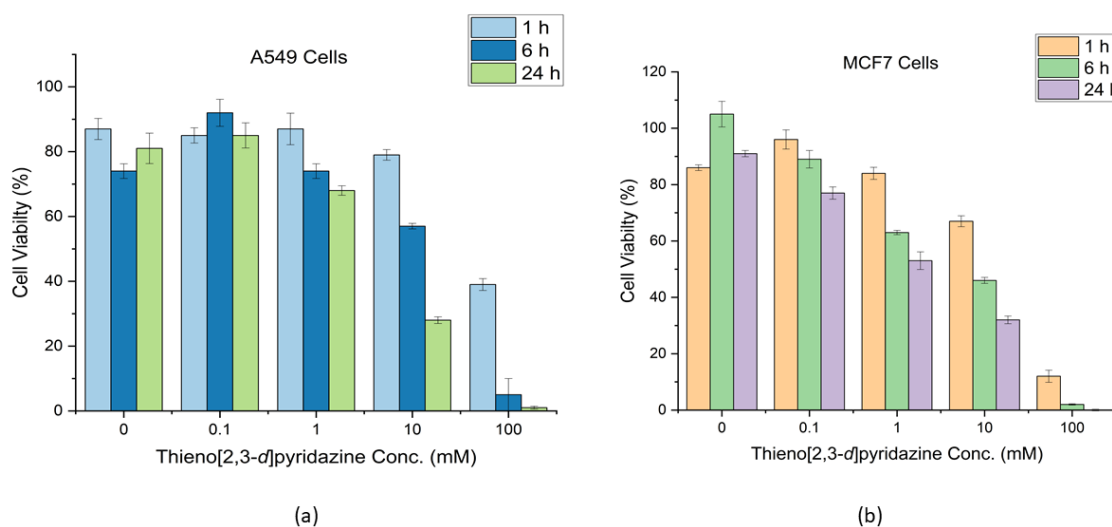


Figure 5.13: Cell Viability versus T[2,3-*d*]P concentration to estimate LD₅₀ value for two cell lines: A549 (a) and MCF7 (b).

Figure 5.13 suggests that concentrations around 10 mM approach the LD₅₀ for T[2,3-*d*]P and care would have to be taken to avoid these levels for any *in-vivo* protocol. It is noted that this was a single experiment showing lower overall cell viability to data presented in Figure 5.11 and Figure 5.12 (average of 4 experiments). It is unknown why this is the case and the experiment should be

repeated with a higher range of concentrations to accurately determine the LD₅₀. Equally it is not known if the cell death is caused by the toxicity of the aqueous SABRE layer or the actual anti-cancer properties of this agent. ICP-MS analysis of the aqueous layer should also be conducted in the future to determine the actual concentration of T[2,3-*d*]P. Furthermore, if an eventual *in vivo* protocol were developed a neutralisation step (due to the presence of the HCl, pH 1.5) would need to be included in the extraction procedure before injection.

With biocompatibility of our biphasic approach for T[2,3-*d*]P proven for concentrations lower than 10 mM through cytotoxicity assay, the next step before (pre)clinical roll-out into the imaging facility involved testing MR imaging/spectroscopy performance of this biomolecule in phantoms.

5.5 Magnetic Resonance Imaging

Due to the inherent low polarisation level of thermal ¹H MRI, coupled with the low concentration of metabolites *in-vivo* it can be difficult to detect functional bio-chemical processes occurring within cells. In addition there is limited dispersion along the chemical-shift dimension (0-12 ppm)²⁷⁵ combined with broad linewidths and splitting due to *J* coupling.⁵³ ¹H MRS can be carried out in the brain where certain metabolites such as GABA (a principal inhibitory neurotransmitter in the human brain) and Glutathione (the most abundant redox compound in the brain) are, in theory, at a high enough concentration (mM) to be detected. However, spectral editing techniques such as MEscher-Garwood Point RESolved Spectroscopy (MEGA-PRESS)²⁷⁶ are required to simplify the spectrum and often only one metabolite at a time can be edited alongside water suppression. Imaging longitudinal metabolic processes in health and disease under thermal polarisation conditions requires upwards of tens of minutes of signal averaging.²⁷⁷ Fast time resolved dynamic information of functional metabolism cannot be measured on these timescales. Gaining a better insight into the fast chemical processes occurring within the body in ‘real time’ can help to understand and diagnose disease states at a much earlier stage. In fact, the use of exogenous hyperpolarised contrast agents (using d-DNP) is already permitting MRS(I) based chemical elucidation in clinical settings.^{4, 278, 279}

There is a clear clinical need for hyperpolarisation. The SABRE method has advantages over d-DNP in terms of i) faster polarisation build up time (seconds compared with upwards of 40 minutes) and ii) polarisation of ¹H which all clinical systems can utilise. It is important therefore to investigate MR imaging performance of the T[2,3-*d*]P biomolecule in phantoms across relevant detection field strengths.

It is noted that all experiments from this point use SABRE in methanol- d_4 to take advantage of the 3 times increase in signal enhancement compared with the extracted aqueous layer of the biphasic system. The aim in these experiments was to test signal acquisition and not biocompatibility. Additionally, results are given in S/N.

5.5.1 Standard Imaging Approaches for Hyperpolarisation

Imaging approaches suitable for ^1H hyperpolarisation require fast k-space acquisition such as single shot Rapid Acquisition with Relaxation Enhancement (RARE), or chemical shift resolved magnetic resonance spectroscopic imaging (MRSI) sequences.

One of the major advantages of the RARE sequence over a traditional single spin echo sequence is that it is much faster, which is an obvious advantage when considering application to transient hyperpolarised signals. The increased speed of the RARE acquisition sequence is due to the ability to obtain more than one line of k-space, by applying multiple refocusing (180°) RF pulses, following a single excitation pulse. Encoding is achieved by changing the phase-encoding gradient between the resultant echoes. In addition, signal intensity can be maximised through centric encoding of k-space. Unfortunately, the sequence is not frequency specific and therefore multiple peaks can cause chemical shift artefacts. Selected deuteration could be applied to limit resultant resonances. However, it is noted that although attempted, targeted deuteration of the target T[2,3- d]P, to reduce spectral peaks, was synthetically challenging and not pursued further. For this reason, Magnetic Resonance spectroscopy sequences, which permit collection of both spatial and chemical shift data, were ideally suited for these hyperpolarised studies.

Indeed Magnetic Resonance Spectroscopic Imaging (MRSI) or Chemical Shift Imaging (CSI) has become the method of choice for localised spectroscopic analysis.²⁸⁰ CSI works by producing images which reveal the spatial distribution of various chemical species of interest in an image slice. A grid is used across a particular field of view where each pixel of the grid represents a chemical shift spectrum identical to those found in standard NMR. A typical CSI imaging sequence is shown in Figure 5.14 a.

Standard ^1H chemical shift imaging in the past has shown to be a better diagnostic tool than conventional MRI for certain diseases states (e.g. fatty liver disease).²⁸¹ Advantages of CSI include a larger total coverage and higher spatial resolution compared with single-voxel methods. In combination with hyperpolarisation methods, such as d-DNP, ^{13}C CSI has been used to

spatially map the distribution of hyperpolarised pyruvate and lactate signals thereby tracking real time metabolism in prostate cancer patients.⁴

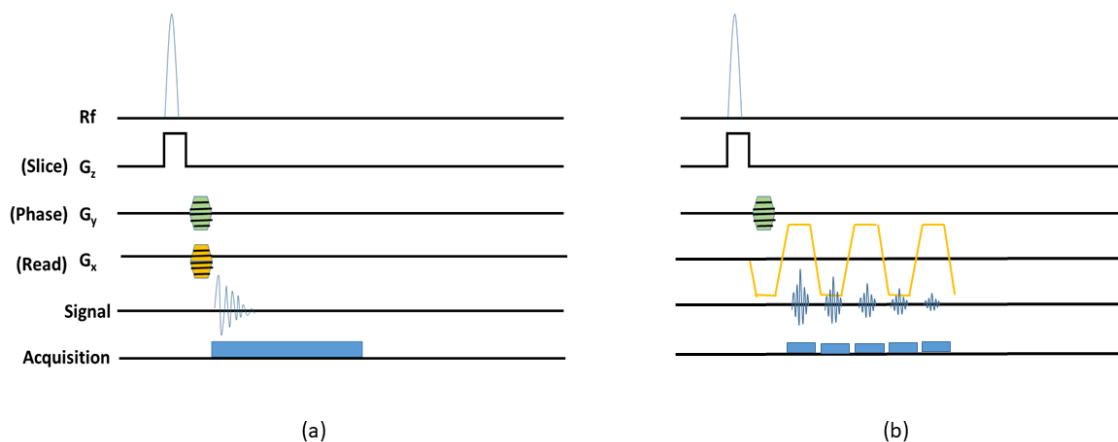


Figure 5.14: (a) A typical schematic of an FID-based CSI pulse sequence and (b) EPSI pulse sequence for MRI.

There are still some limitations to using CSI, particularly with hyperpolarised signals, which are susceptible to fast T_1 relaxation. The main problem lies with within the length of the acquisition sequence. As CSI involves two spatial dimensions, space and chemical shift (time), phase encoding is required in both dimensions. Due to these limitations, the scan time for CSI is often long (order of minutes). Furthermore, achieving high spatial resolution can be a problem when considering a hyperpolarised agent with a relatively short T_1 (order of tens of seconds).

To reduce the long acquisition time required for spatial encoding in CSI, faster spectroscopic pulse sequences can be applied, one of which is echo planar spectroscopic imaging (EPSI) (Figure 5.14 b). This was first described by Mansfield in 1984.⁶⁹ The basis of EPSI is that an alternating gradient, which is able to simultaneously encode for both space and chemical shift /spectral (time), is applied along one of the spatial (readout) directions. In this way the number of dimensions for phase-encoding is reduced by one which therefore increases the overall speed of the sequence (acquisition time). With an increase in speed, EPSI permits a relatively high spatial resolution (compared to CSI) within acquisition times that are practical for clinical application.²⁸² However, for many standard spectroscopic applications the improved spatial resolution is offset by limitations in signal to noise ratio (S/N). This is where strongly hyperpolarised signals with high signal to noise ratio could be a real benefit.

The RARE, CSI and EPSI capability of hyperpolarised T[2,3-*d*]P with [IrCl(COD)(*d*₂₂SIMes)] was tested in methanol-*d*₄ at 7 T, 9.4 T and clinical 3 T magnetic field strengths. Samples prepared using both 1:4 and 1:20 catalyst to substrate ratios were imaged.

5.5.2 RARE imaging

RARE imaging capability was tested on the hyperpolarised solutions contained in 10 mm J. Young's tubes at 9.4 T and results are shown in Figure 5.15.

For MRI it is the overall signal which is important as opposed to the signal enhancement. System noise is inherently higher than NMR. Increased absolute signal is therefore beneficial, with the aim of detecting signal in line with other ¹H pools (e.g., water at 1 M). Hence testing a high substrate to catalyst (e.g., 1:20) ratio was essential here. This is clearly demonstrated in Figure 5.15 a and d which show thermal images for the 1:4 and 1:20 sample ratio with S/N values of 1 ± 1 and 3 ± 1 , respectively. The 1:4 sample is clearly at the limit of detection (at thermal polarisation). Figure 5.15 c and f show the hyperpolarised images after shaking with 3 bar(g) of *p*-H₂. Resultant image S/N values were 42 and 58 for the 1:4 and 1:20 ratio, respectively. Hyperpolarisation of the signal is clearly observed. Although the 1:20 has the highest absolute signal (as expected due to increased baseline levels), actual signal gain, upon normalisation to the thermal signal is lower (19.41) compared to the 1:4 ratio (41.75). This agrees with the observations made in chapter 2.4.1, which demonstrated that the 1:4 ratio presents the highest NMR signal enhancement. Direct comparison of enhancements is difficult. MRI measures are confounded by the thermal signal for the 1:4 being at the limit of detection. Equally, quantification (using a 400 MHz NMR) of signal enhancement at 1:20 was not possible. Due to the higher absolute baseline signal, upon polarisation with SABRE the signal clipped the receiver gain and resulted in radiation dampening.

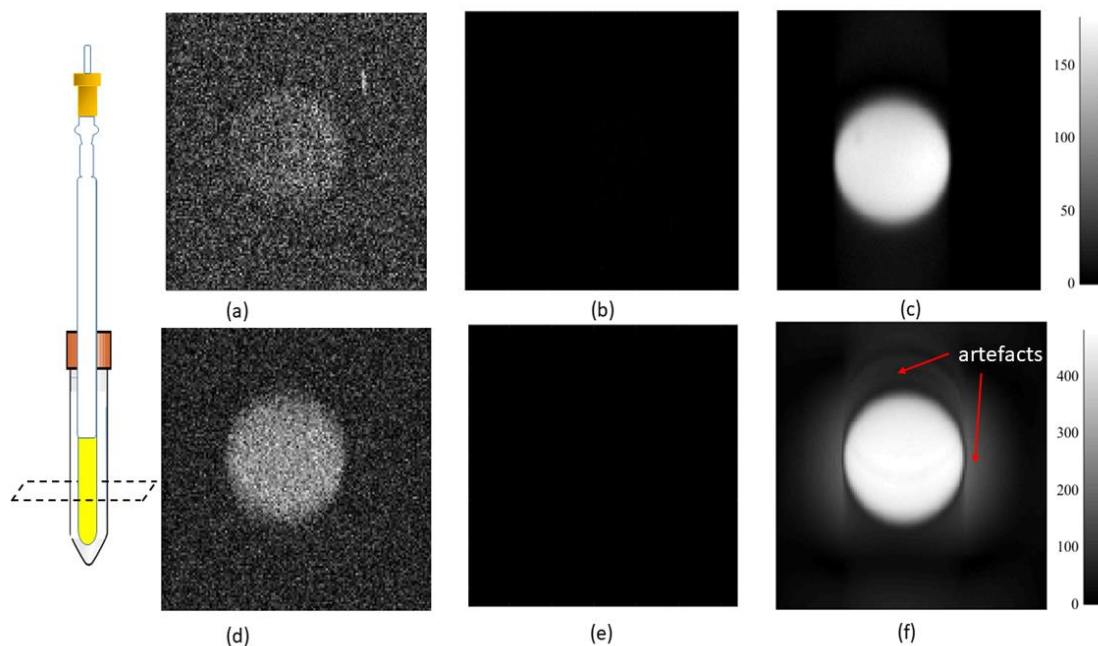


Figure 5.15: Thermally polarised RARE images of (a) 1 to 4 ratio of $[\text{IrCl}(\text{COD})(d_{22}\text{SIMes})]$ and $\text{T}[2,3-d]\text{P}$ in methanol- d_4 , (d) 1 to 20 ratio; (b) and (e) are the same thermal images as (a) and (d) but normalised with respect to the hyperpolarised images (c) and (f). In the hyperpolarised images (c) and (f) 3 bar(g) of $p\text{-H}_2$ was used and the sample shaken for 10 s in a 60 G shaker prior to measurement at 9.4 T. The diagram shows the experimental set up of the SABRE mixture within a 10 mm J. Young tube housed within a standard falcon tube.

Capability at clinical field strengths (3T) was also tested with the aim of distinguishing the hyperpolarised signal within a Siemens standard water/oil-based head coil phantom. This Siemens phantom has two holes within to house two 10 mm J. Young tubes. One contained the SABRE mixture (either 1:4 or 1:20 catalyst to substrate ratio) and one contained water as a reference. Results are shown in Figure 5.16.

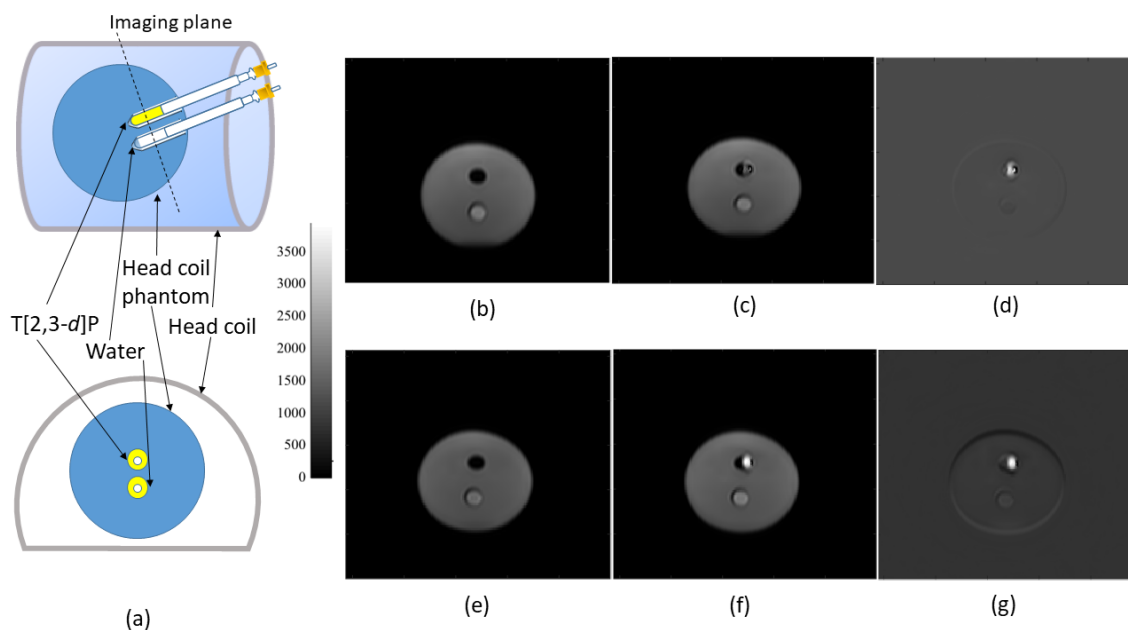


Figure 5.16: (a) Experimental set up for RARE imaging using a head coil and a Siemens water/oil based head coil phantom with two inserts to house two 10 mm J. Young tubes containing the SABRE mixture (top) and water (bottom); (b) thermal RARE with 1:4 ratio of substrate to catalyst; (c) hyperpolarised RARE with 1:4 ratio of substrate to catalyst; (d) difference image between the hyperpolarised and thermal signals with 1:4 ratio of substrate to catalyst; (e) thermal RARE with 1:20 ratio of substrate to catalyst; (f) hyperpolarised RARE with 1:20 ratio of substrate to catalyst; (g) difference image between the hyperpolarised and thermal signals with 1:20 ratio of substrate to catalyst. Images (b), (c), (e) and (f) are signal normalised relative to the head coil phantom response.

Again, the sample with 1:20 catalyst to substrate ratio gave the best overall image (Figure 5.16 f & g) with S/N of 2323 compared with 668 for the 1:4 sample. Contrasting to the results at 9.4 T, it is the 1:20 sample that has the biggest signal gain (13.5-fold) over the 1:4 (2.6-fold). This reflects the larger sample volume and greater p -H₂ loading.

These results clearly show that RARE can be used to detect a hyperpolarised signal. However, these images contain artefacts, which arise from using a hyperpolarised compound (Figure 5.17) with multiple frequency responses. At both high and low field there is evidence of image blurring with edges, being poorly defined (Figure 5.17 d). This results from the centric encoding scheme used for single shot RARE imaging. The outer lines of k-space, which contain high frequency information (therefore object edges when Fourier transformed) are captured last when there is little signal left because of T_2 decay.

A more pertinent problem is the artefact caused by chemical shift effects. RARE is able to measure the total concentration of a nuclei, in this case ¹H, however it is not designed to distinguish between the different ¹H resonances, which contribute. In terms of MR imaging, spatial position is assigned along the frequency-encode direction based on resonant frequency

being at $x = 0$. If the resonant frequency shifts the centre point of the resulting image will therefore shift along the x axis. If protons arising from both fat and water, for example, are present in a single voxel, the signal emitted by the fat/lipid protons will have a lower frequency than that of the water. Therefore, if the system frequency is set to water, the signal from the lipid protons will appear to arise from water protons from another voxel in a lower part of the field. The location of the lipid protons is therefore spatially misaligned towards the lower part of the readout gradient field (Figure 5.17a). This leads to an artefact of white and dark bands on either side of the object (Figure 5.17b). As observed in the T[2,3-*d*]P samples using the head phantom there is a clear chemical shift based image distortion caused by the $\Delta\delta = 5$ between H7 of T[2,3-*d*]P and the protons in the head phantom (Figure 5.17c).

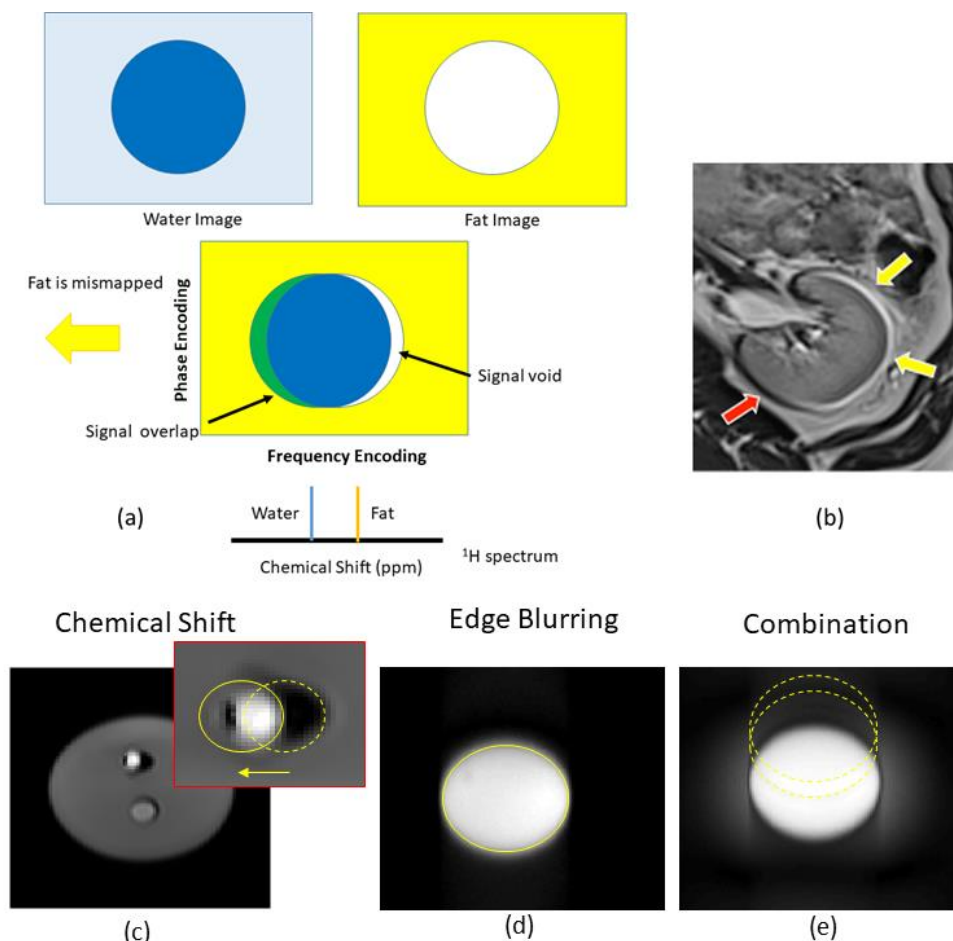


Figure 5.17: Chemical Shift artefacts (a) conceptually described and (b) MRI of a kidney showing dark bands and white bands that are characteristic of chemical shift artefacts;²⁸³ (c) chemical shift based image distortion caused by the 4.7 ppm and 8 ppm shifts of the resonant T[2,3-*d*]P peaks respectively (1:20 ratio at 3T); (d) image blurring (1:4 ratio at 9.4 T); (e) combination of image blurring and chemical shift artefacts (9.4 T)

These chemical shift artefacts are also compounded with a hyperpolarised sample such as T[2,3-*d*]P where there are four hyperpolarised resonances to consider. The image/signal observed originates from combination of the four hyperpolarised signals. However, this difference in precession frequency is difficult for the RARE sequence to overcome without selective RF saturation or long frequency specific excitation pulses. If these precessional frequency shifts are large enough, a measurable alteration in MR signal intensity as a function of frequency encoding will be observed and result in essentially overlapping images (Figure 5.17e) or chemical shift artefacts.²⁸⁴

S/N values were calculated using a region of interest (ROI) approach. However, as is evident from the fast acquisition and chemical shift artefacts there was a lot of signal bleed into noise ROIs. Despite this, images clearly show the large signal gains obtained with SABRE hyperpolarisation.

Although hyperpolarised RARE experiments have been carried out on hyperpolarised ¹H¹³⁵ and ¹³C nuclei,²⁸⁵ it is more common to use hyperpolarised Magnetic Resonance Spectroscopy (MRS) to create metabolite maps, which have the benefit of including chemical shift data without the problems leading to image artefacts. The negative aspect of MRS is that spatial resolution is sacrificed to gain spectral resolution.

5.5.3 Chemical Shift Imaging of T[2,3-*d*]P

To investigate the spectral imaging response a chemical shift-based sequence was tested on a preclinical 7 T MRI system (see section 8.6.3). A 1:20 T[2,3-*d*]P sample was prepared as above. The Young's tube was placed within a falcon tube containing water/agar to aid automated shimming. A ¹H single pulse experiment was completed using a 20° FA. The resulting spectrum Figure 5.18 shows that all four hyperpolarised proton resonances of hyperpolarised T[2,3-*d*]P were still visible against the background of the large water peak. The expansion shows the spectrum alongside the ¹H hyperpolarised spectrum recorded on a 400 MHz NMR system. Although there is slight offset in chemical shift due to field shimming of the imaging system it is clear that all four ¹H resonances of the free hyperpolarised T[2,3-*d*]P can be seen with the bound signals of H7 and H4 just visible too.

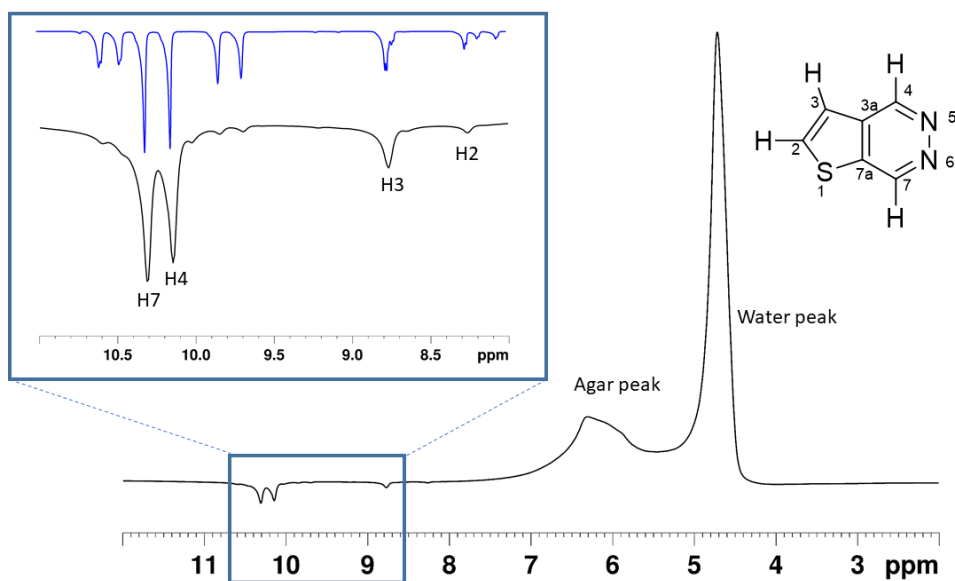


Figure 5.18: ^1H 20° single pulse NMR spectrum showing hyperpolarised peaks from T[2,3-*d*]P alongside the peaks from the water/agar mixture measured using the preclinical 7T MRI system. Expansion shows the hyperpolarised T[2,3-*d*]P peaks measured using the preclinical 7T MRI system (black) and hyperpolarised T[2,3-*d*]P peaks measured using a 400 MHz NMR system (blue).

Subsequent spectra-spatial data captured using CSI (16 x 16 grid across a FOV of 35 mm²) is shown in Figure 5.19. The small flip angle (FA) of 10° used ensured enough polarised signal remained for spatial encoding. Even with just a 16 x 16-voxel grid there will be 256 RF excitation pulses that will cause artificial decay of the hyperpolarised magnetisation vector. Using a FA of 10° , at the end of the experiment only $(\cos 10)^\{256\} = 0.5\%$ of the polarisation remains, which in reality would be even less due to T_1 decay. In linear encoding the central part of k-space, which generates the most important data in terms of signal magnitude, is only reached halfway through the experiment when only $(\cos 10)^\{128\} = 7.5\%$ of the signal remain which is by no means ideal. For this reason, centric encoding was used so that the middle part of k-space is sampled first when signal strength is on the order of 100-95%. The advantage of this is that we image the signal more readily. The disadvantage is that the edges are less resolved, and a blurry edge results. In the CSI sequence for each of the voxels an FID is recorded from which a spectrum is produced by Fourier transform.

Peaks of interest were selected and data superimposed onto thermal ^1H Fast Low Angle Shot (FLASH) images.

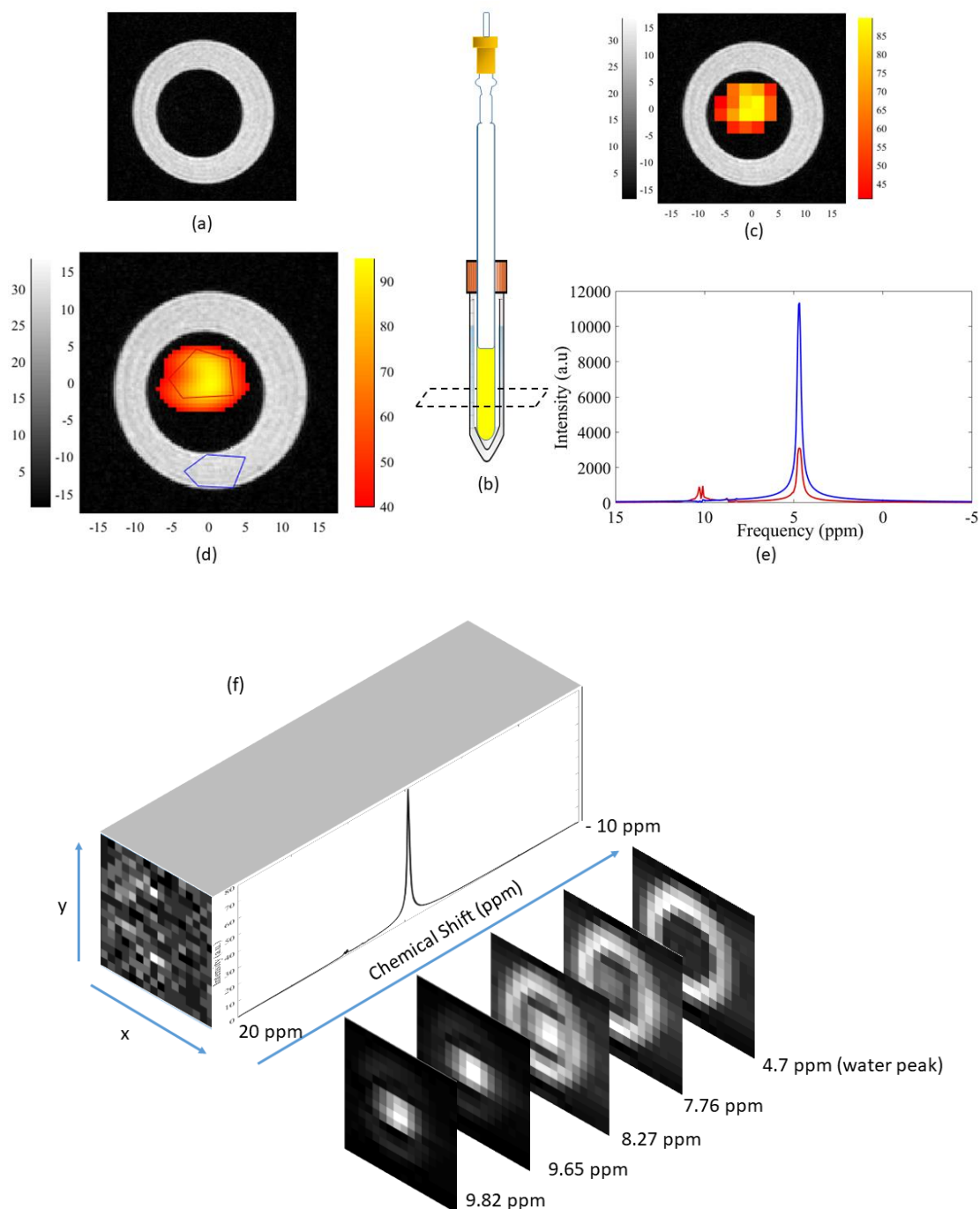


Figure 5.19: Set up of the hyperpolarised MR experiment on a 7 T preclinical scanner. a) ^1H high resolution FLASH reference scan shows the signal from the water before hyperpolarisation took place. **b)** Experimental set up with 10 mm Young's tube containing the sample surrounded by a falcon tube containing a water/agar mixture. **c)** Hyperpolarised CSI of sample in a 16 x 16 grid with a 20 mm slice thickness. Integral analysis across the δ 9.82 and 9.65 peaks was overlaid (as a heat map) on ^1H FLASH reference data. **d)** Hyperpolarised CSI heat map with cubic spline interpolation of the original data using a factor of 4 to give a 64 x 64 grid with ROI's of water (blue) and hyperpolarised sample (red). **e)** Spectra produced from the ROI of the hyperpolarised sample (red) and the ROI of the water (blue). **f)** Image blocks showing the x,y and frequency domain of the hyperpolarised sample with hyperpolarised peaks at δ 9.82, 9.65, 8.27 and 7.76.

A 3D (frequency, space - x, space - y) image block results. The raw spectral data appears as in Figure 5.19 f. Peaks of interest for T[2,3-*d*]P are located and the integral taken over an appropriate

spectral range. Regions covering the peaks at δ 9.82 and 9.65 (H7 & H4 respectively) clearly showed a localised hyperpolarised response. Integral images for the smaller peaks at δ 8.27 and 7.76 appeared noisy and confounded with background water signals.

Representative spectra from the region of interest within the T[2,3-*d*]P sample (red) and the water/agar phantom (blue) are shown in Figure 5.19 e. The spectral response was similar to that seen during single pulse excitation. Note the water peak is so large and broad explaining the “leakage” of water signal in the hyperpolarised images. The peak is broad because of poor automatic shimming across the large irregular water volume.

To probe the minimum concentration of T[2,3-*d*]P that could potentially be imaged with a CSI approach a series of experiments were carried out with varying slice thicknesses from 20 mm to 0.5 mm. The results are shown in Figure 5.20. Data demonstrate that CSI is capable of producing hyperpolarised images of T[2,3-*d*]P with concentrations as low as 0.08 mM/pixel. S/N remains fairly consistent (\sim 23) across the different slice thicknesses imaged. This indicates that the residual water is confounding the estimates of the background noise.

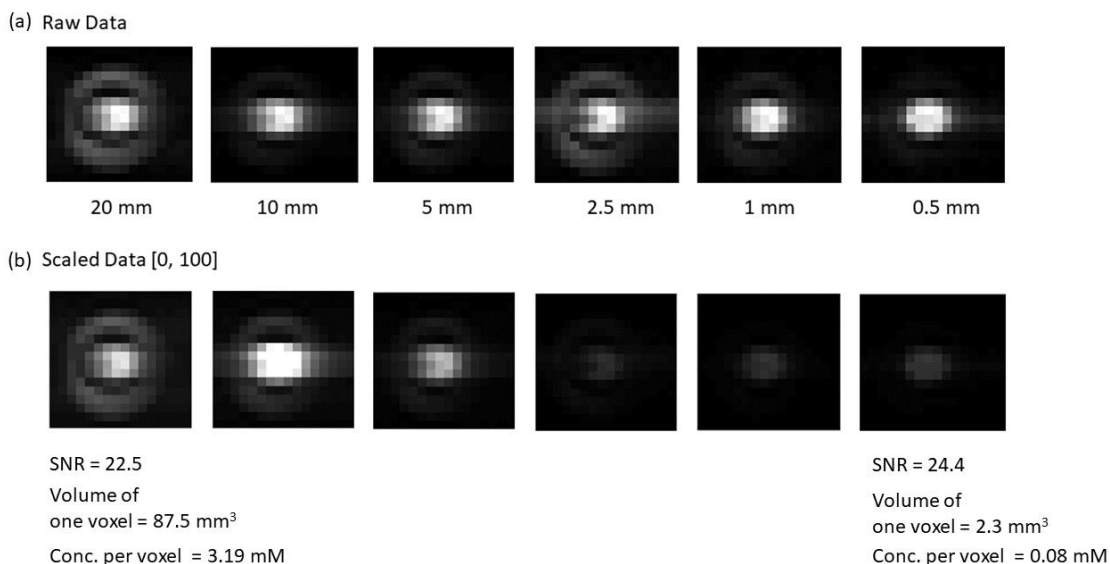


Figure 5.20: Hyperpolarised ¹H MR signal of thienopyridazine (90 mM) at slice thicknesses from 20 mm to 0.5 mm. (a) Gives the summed raw data of the hyperpolarised peaks (b) Gives the data on the same relative scale from 0 to 100.

With ¹H hyperpolarised imaging, the huge contribution from the water resonance can sometimes mask the low contributions from the substrates of interest and thus presents a challenge. Furthermore, the heterogeneous field distortions induced by the tissue and air pockets within the

body *in-vivo* can widen the water peak. Ideally imaging sequences for hyperpolarisation should utilise water suppression. However, water suppression modules often use strong RF pulses, which would destroy the hyperpolarised signal one is attempting to measure and can be somewhat ineffective due to the peak broadening caused by inherent magnetic susceptibility differences.

Another approach to water suppression from the signal can be done via post-processing. By running a thermal scan with identical parameters to the hyperpolarised scan, the difference between the two should leave just the hyperpolarised signal (Figure 5.21).

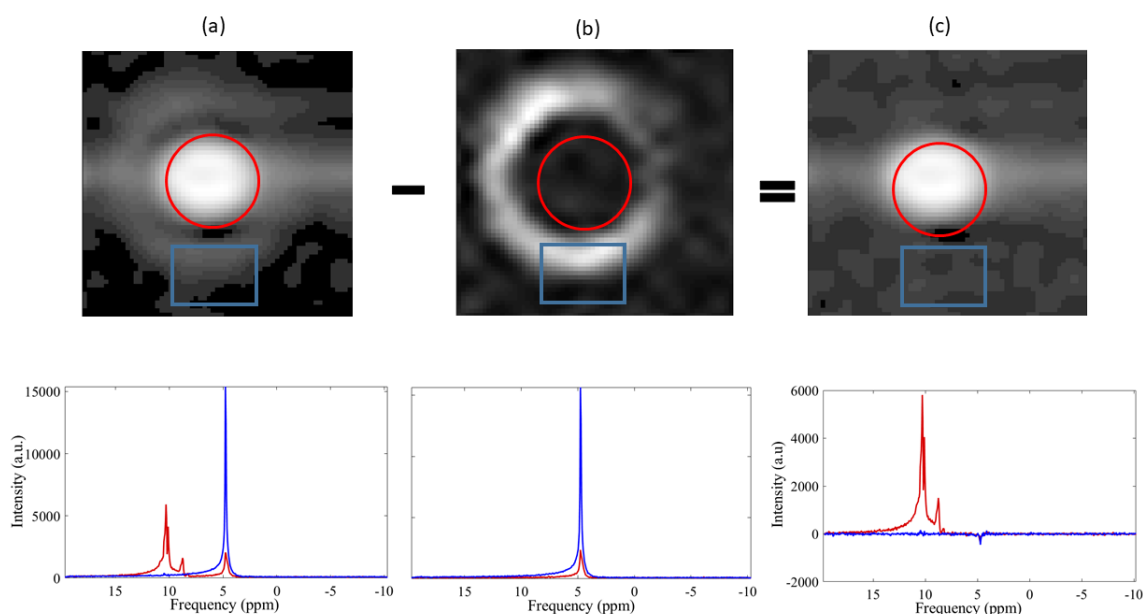


Figure 5.21:(a) Hyperpolarised CSI signal from T[2,3-*d*]P with a slice thickness of 0.5 mm (b) Signal at thermal equilibrium of T[2,3-*d*]P with a slice thickness of 0.5 mm showing only water (c) The difference from hyperpolarised signal – thermal signal leaving only the hyperpolarised T[2,3-*d*]P signal.

It is important to note that the CSI image/matrix size was 16 x 16; a total of 256 voxels. In essence, a separate FID was recorded for each of these 256 voxels. With a repetition time (TR) of ~290 ms, total scan time was $256 \times 290 \text{ ms} \approx 74 \text{ s}$. This was much longer than the T[2,3-*d*]P T_1 value of $38.21 \pm 0.18 \text{ s}$ for H7 (see 2.4.3); thus the chemical shift image is compromised due to excessive hyperpolarisation decay to thermal equilibrium over the duration of the experiment.

As mentioned above (5.5.1) an echo planar approach can vastly speed up this acquisition time by using switching/alternating gradients to simultaneously encode space and chemical shift. This is known as EPSI.

5.5.4 Echoplanar Spectroscopic Imaging EPSI of T[2,3-*d*]P.

The imaging time saved by implementing EPSI is important because the subsequent acquisition would be well within the T_1 limit of T[2,3-*d*]P. The spectra produced should therefore have a much better S/R, which in turn can be sacrificed to increase the spatial resolution of the desired image.

An EPSI experiment was completed on a 7 T preclinical MR scanner (section 8.6.3). Total scan time was 6 s and the sequence parameters resulted in a 4-fold increase in spatial resolution over the CSI equivalent (at a slight cost of spectral resolution and width, 18 Hz/pt across 15 ppm, compared with 15 Hz/pt across 30 ppm).

A direct comparison between resulting CSI and EPSI acquisitions for detection of hyperpolarised T[2,3-*d*]P was made (Figure 5.22 a and b respectively). The EPSI results show that there is much better signal to noise (x 2 relative intensity to water) with less “leakage”/bleeding artefacts from the background water signal (see insert Figure 5.22 a). The clear advantage of EPSI over CSI is the spatial resolution (0.3 mm² compared to 4.78 mm² per pixel in-plane resolution respectively).

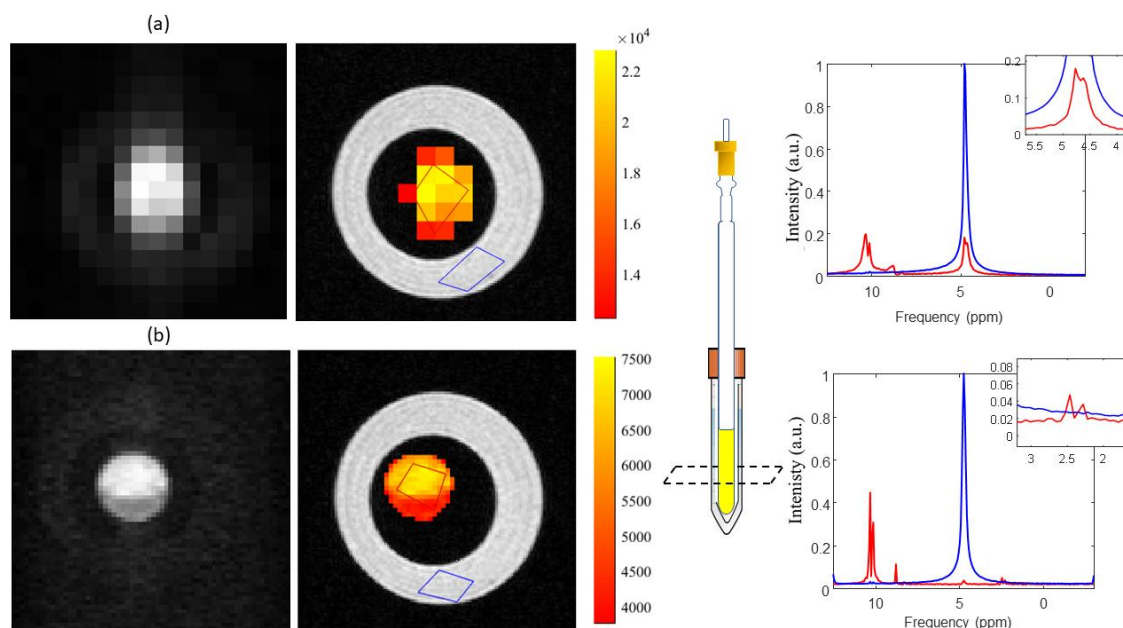


Figure 5.22: Comparison of (a) CSI (1 mm slice thickness) and (b) EPSI (1 mm slice thickness) showing image maps of hyperpolarised T[2,3-*d*]P and spectra normalised to the water peak. Insert in CSI spectrum (a) shows the incurrence of the water peak within the hyperpolarised spectrum with a similar amplitude to the peak of interest. Insert in EPSI spectrum (b) shows a Nyquist ghost of the T[2,3-*d*]P peaks at δ 2.4. Experimental set up shows a 10 mm J. Young tube containing the SABRE solution surrounded by water in a falcon tube.

For these EPSI experiments, the centre frequency of the scanner was set on the water signal at δ 4.7. Automatic shimming, RF power calibration and N/2 Nyquist ghost correction were completed upon the water phantom. As shown in the spectrum of Figure 5.22 b, a small 4% ghosting artefact is present at $\sim \delta$ 2.4 demonstrating one of the disadvantages of the EPSI approach.

When the centre frequency was set to δ 8 (centre of the hyperpolarised T[2,3-*d*]P peaks) the automatic N/2 Nyquist ghost correction failed (due to incorrect parametrisation of the gradient delay times), as can be seen in Figure 5.23 a-c. Spectra show T[2,3-*d*]P ghost peaks at $\sim \delta$ 4.7 - 6.5 with approximately equal magnitude to the actual peaks located at $\sim \delta$ 8.5 - 10.25 (Figure 5.23 c).

Such artefacts are detrimental because ghost peaks can shift/alias over other peaks of interest (Figure 5.23 c, water peak ghost artefact overlying T[2,3-*d*]P peak for H3 and H2), altering the linewidth and making integral quantification difficult; and ii) the intensity of the peak of interest is reduced because of signal leakage into the N/2 ghost.

Hyperpolarisation signal decay with T_1 does not allow enough time for the long automatic parameterisation step. Future use of this sequence would require manual setting of gradient delay times to reduce Nyquist ghosting. Alternatively, the problem can be solved by post-processing, analysing the odd and even echoes separately to correct for the N/2 ghost artefacts, at the cost of halving the sweep width (Figure 5.23 d).²⁸⁶ Nuisance peaks (e.g. water in this case) will however still alias into the detection window. It is easy to post process the spectra to manually correct the peak position (as the water and T[2,3-*d*]P peaks are in spatially distinct areas, Figure 5.23 e). *In-vivo* this would not be the case and more sophisticated correction methods would be required.²⁸⁷

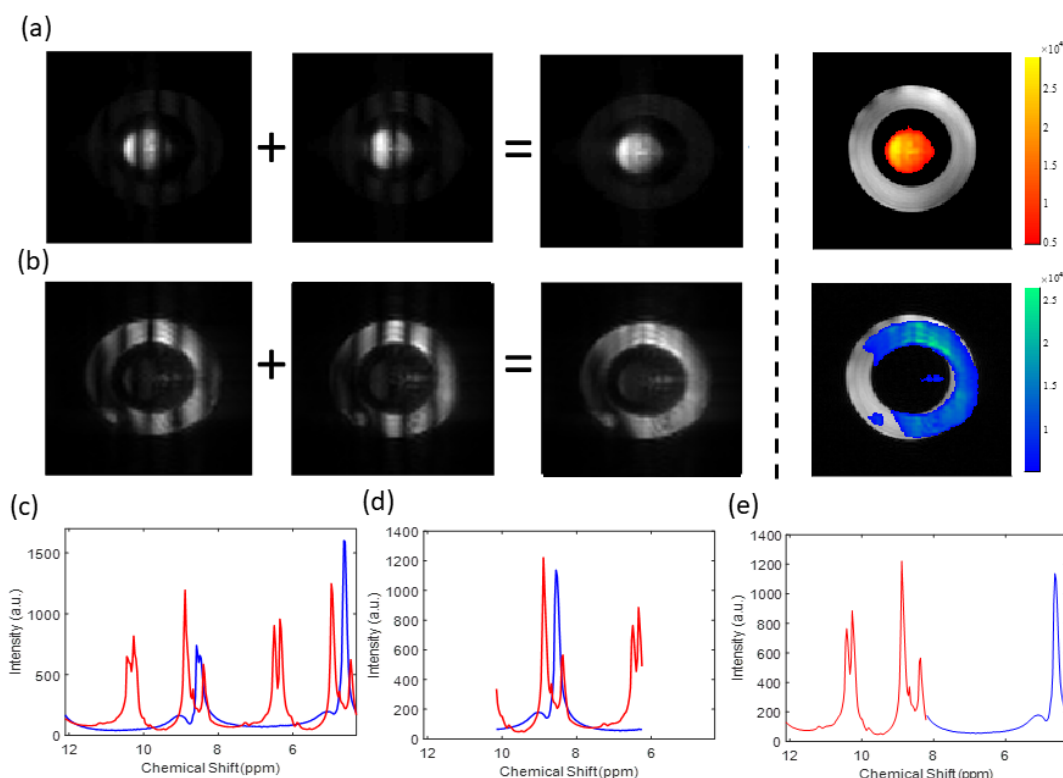


Figure 5.23: EPI a) odd and even echo analysis for T[2,3-*d*]P b) odd and even echo analysis for water c) Raw spectra showing N/2 ghost artefacts. d) Corrected spectra following odd/even analysis.²⁸⁶ Water peak is aliased to approximately δ 8.7, T[2,3-*d*]P peaks (H4 and H7) are aliased to approximately δ 6 - 6.5 as spectral width has been halved. e) Manual correction based on spatial position results in an adequate overall spectrum.

5.5.5 Ex-Vivo Imaging

An *ex-vivo* subcutaneous (SC) image in a rat was completed using the 1:20 sample of [IrCl(COD)(*d*₂₂-SIMes)] and T[2,3-*d*]P. After SABRE hyperpolarisation the sample was injected (via a cannula) into the subcutaneous space above the neck (as indicated in Figure 5.24 a). Data were acquired with an EPI sequence (section 8.6.3). Experiments were carried out immediately after injection (Figure 5.24b) and repeated 5 minutes later (Figure 5.24 c). A large water peak was observed with an N/2 Nyquist ghost at $\sim \delta$ 14.5. The four expected T[2,3-*d*]P peaks were not spectrally clear. A difference analysis between the two spectra (Figure 5.24 d) shows a dynamic spectral change centred on δ 8. This difference was greatest in the SC space (image map Figure 5.24 a). More in-depth analysis (of the spectrum immediately following injection) used a general linear model (GLM) approach and a suitable design matrix (separate model columns for DC offset M_1 , a ramp M_2 , and the expected spectral peak positions of water/Nyquist M_3 , and T[2,3-*d*]P M_4 , as independent variables in the GLM equation: $y = \sum \beta_n * M_n + \text{error}$, see Figure 5.24 e). Resultant parameter β maps further highlighted that

signals associated with T[2,3-*d*]P were indeed constrained to the SC space (see associated parameter map β_4 - Figure 5.24 g). Data is confounded by dissolved *p*-H₂ coming out of solution and creating a ‘bubble’ in the SC space (and large areas of null signal with the signal of interest pushed to the edges). This therefore raises further questions about safety and the need to ensure *p*-H₂ is removed by degassing or by using the extracted aqueous layer from a biphasic system (*p*-H₂ is 10 times more soluble in methanol than in water).

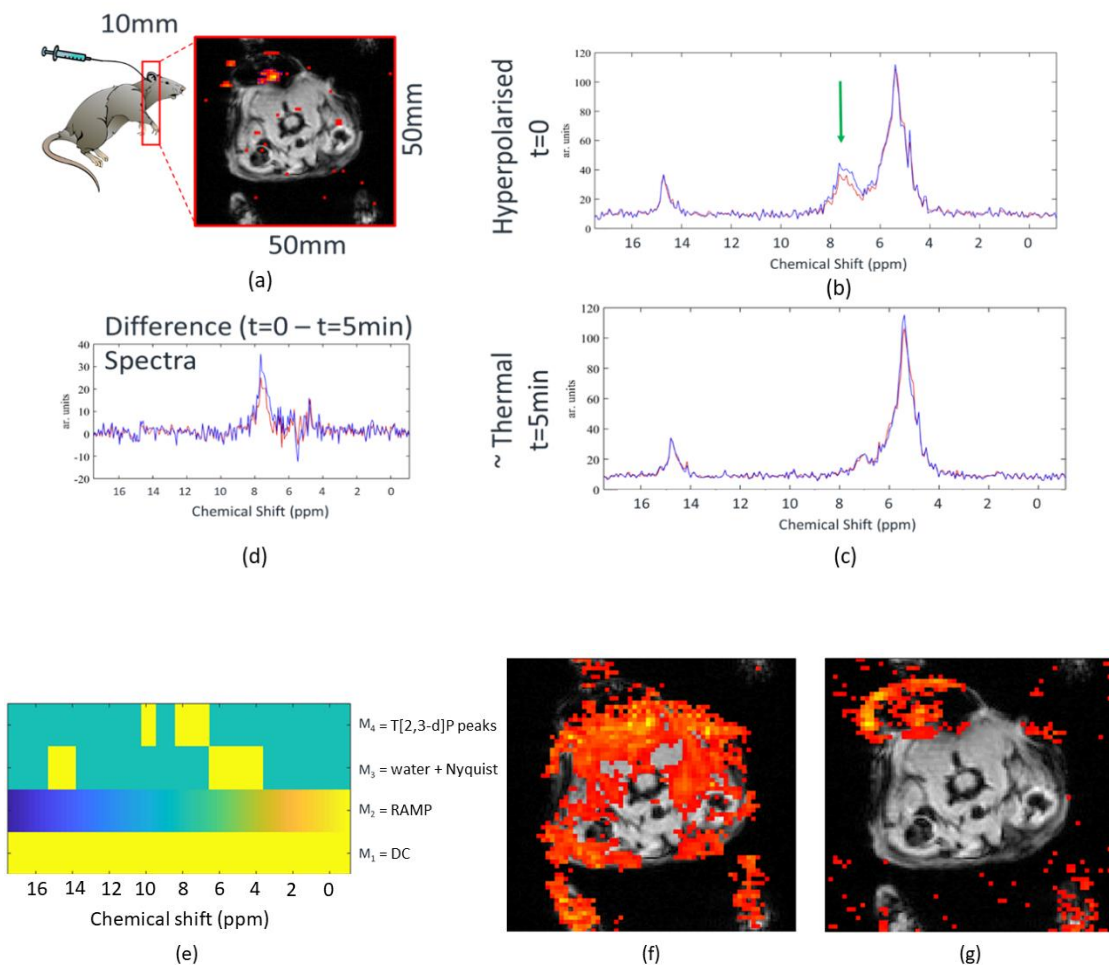


Figure 5.24: Ex-vivo subcutaneous injection of T[2,3-*d*]P. (a) Site of injection into rat and ¹H structural scan of cross section of torso overlaid with hyperpolarised T[2,3-*d*]P. (b) Hyperpolarised spectrum immediately after injection. (c) Thermal spectrum 5 minutes after injection. (d) Difference between hyperpolarised and thermal spectra (e) Design matrix for GLM analysis using $y = \beta_1 * M_1 + \beta_2 * M_2 + \beta_3 * M_3 + \beta_4 * M_4 + \text{error}$. Resultant fitted parameter maps of (f) β_3 showing water and associated Nyquist ghost peak signal originates in surrounding soft muscle tissue (as expected) and (g) β_4 showing T[2,3-*d*]P signal localised to the subcutaneous space where the bolus hyperpolarised solution was injected.

5.6 Conclusion and Discussions

This chapter has focused on solving the challenges of *in-vivo* SABRE detection and generating a usable framework for translation of the SABRE method from the laboratory benchtop to the imaging facility (specifically for ^1H).

SABRE-CASH was successfully implemented for the target T[2,3-*d*]P substrate. A hyperpolarised signal was detected in the aqueous layer thereby demonstrating that this is a viable route to improve SABRE biocompatibility. This approach simultaneously removes the heavy metal catalyst and detrimental organic solvents for the injection bolus. Thus, this overcomes one of the major disadvantages of the SABRE process which traditionally uses toxic iridium catalysts and methanol-*d*₄ as the solvent. However, further optimisation is needed as the signal enhancement measured in the aqueous layer was one third (940-fold signal enhancement, 3% polarisation for H7) of that achieved under standard SABRE conditions (3142-fold signal enhancement, 9.8% polarisation for H7 using non-biocompatible methanol-*d*₄ as the solvent).

It is noted that for successful SABRE-CASH addition of 0.65 μl HCl was required for promotion of the T[2,3-*d*]P agent into the aqueous phase. Unfortunately, the reversible nature of the SABRE process was subsequently inhibited. The presence of the acid degrades the catalyst and thus subsequent polarisation transfers show decreased signal enhancement. This being said, a one-shot hyperpolarisation process with acidic extraction could be envisaged to obtain the hyperpolarised bolus with a 940-fold signal enhancement. An additional neutralisation step would be required with pH testing as part of the QA process before considering *in vivo* injection. However, it is noted that phase catalysis separation followed by acidic extraction, neutralisation and pH testing all require time. During this time spin polarisation will decay (with a time constant T_1) reducing detectable signal levels at the time of injection. While it is proven that these processes can be done relatively quickly, in the case of pyruvate with d-DNP,⁴ initial polarisation levels using that technique are already much higher (see chapter 6). Therefore, further optimisation of polarisation would be needed for the SABRE process to realistically enable these QA steps.

Biocompatibility of the extracted aqueous layer was tested with cytotoxicity assays using two cell lines (MCF7 and A549). Results showed that there was no cell toxicity caused by the aqueous layers at T[2,3-*d*]P concentrations <3.6 mM. At concentrations of >10 mM of T[2,3-*d*]P cell death was evidenced. However, it is currently not known if the observed cell death is caused by the

toxicity of the aqueous SABRE layer or the actual anti-cancer properties of this agent. This would require a more in-depth investigation in the future.

A proof of concept study was completed to explore the imaging potential of the SABRE hyperpolarised T[2,3-*d*]P across a range of relevant magnetic field strengths (3-9.4T; clinical to preclinical respectively). As the signal enhancement of T[2,3-*d*]P was reduced by a third within the aqueous layer it was decided to return to the original methanol-*d*₄ for exploring the imaging potential. Once SABRE polarisation in the biphasic system has been optimised further to match the enhancements achieved in organic solvents, imaging protocols developed here will be ready for rollout.

Results show that ¹H hyperpolarised imaging of the synthesised T[2,3-*d*]P is achievable either through high resolution single shot RARE or spectral imaging using CSI/EPSI. It is noted that T[2,3-*d*]P concentrations of 18mM, with polarisation levels of ~10% (in methanol-*d*₄), are entirely suitable for imaging.

High hyperpolarised signal intensities (brighter than water) were observed with a single shot ¹H RARE imaging approach (at both low and high field). RARE does not encode chemical shift information and resultant images exhibit chemical shift artefacts (between water and the molecules of interest). Such artefacts would be problematic when considering the large water pool present during *in-vivo* scanning. To overcome chemical shift artefacts magnetic resonance spectroscopic imaging can be employed. Both CSI and EPSI techniques allow chemical shift information to be mapped spatially. It is noted that utilising a more spectroscopic imaging approach, hyperpolarised signals of up to 40% of the background ¹H water signal were detected (even when said background protons were saturated with the fast RF pulsing regimes applied to overcome hyperpolarisation T₁ decay).

In both cases, RF suppression of the water pool could be employed to ease the detection of the hyperpolarised signal. Such approaches are standard in thermal based MRS, but successful implementation takes time, requires a localised voxel shimming approach, and uses high flip angle pulses.²⁸⁹⁻²⁹³ High flip angle RF pulses, when applied during a SABRE based experiment could potentially attenuate the desired hyperpolarisation signal (especially *in-vivo* where field shimming is compromised) and therefore would be somewhat detrimental.

When considering hyperpolarised MR imaging, overall scan time and image resolution are very important considerations. CSI as applied here, has a long >1-minute scan time, with low in plane spatial resolution (16 x 16 pixels). Long scan times are a problem when considering a hyperpolarised agent with a relatively short T_1 . To overcome this limitation centric encoding schemes should always be employed (as they were here). It is the edges of k-space which encode the high frequency information required for edge mapping and therefore to improve overall image sharpness. If this information is captured once the spins have decayed back to thermal conditions, there is little to no signal and therefore resultant images are blurred (as demonstrated here with both CSI and single shot RARE). Fast radial/spiral acquisition of the data from the centre can also be used.^{294, 295}

EPSI has a relatively short scan time in comparison (~6 s). This is achieved by using alternating gradients for simultaneous encoding of chemical shift and space. Fast scan times result, albeit at the slight expense of spectral resolution and potential N/2 Nyquist ghosting. The reduction in spectral resolution is not a major problem for ^1H MRS as the spectral width is narrow (12 ppm). This would not be true for X nuclei, such as ^{13}C , where the spectral width required for metabolic mapping is much wider (~200 ppm).³ Nyquist ghosting occurred in the EPSI results presented here due to incorrect parametrisation of the gradient delay times. Analysing the odd and even echoes separately correction for the N/2 ghost artefacts was possible but resulted in half the sweep width.²⁸⁶ The water peak was aliased into the detection window and confounded the T[2,3-*d*]P peak identification. This can be manually corrected when the peaks arise in spatially distinct areas, but *in-vivo* this would not be the case and more sophisticated correction methods would have to be implemented.^{287, 288}

Using the EPSI approach successful imaging detection of 90 mM T[2,3-*d*]P *ex-vivo* was achieved; although peaks were not spectrally clear. GLM analysis was required to identify hyperpolarised regions and these were confined to the SC space. It was recognised that the time taken from SABRE polarisation through injection to subsequent scanning took 42 s. This process will need to be optimised to avoid unnecessary loss of polarisation due to T_1 .

As discussed in section 3.5 there are many advantages of using ^1H as the nuclei of choice for both thermal and hyperpolarised (spectroscopic) imaging. While this work demonstrates that detection of hyperpolarised T[2,3-*d*]P with concentrations ~18-90 mM is plausible, some hurdles remain before SABRE ^1H polarisation can be translated. Strong background signals from protons of

water and lipids, relative to those of relevant metabolites, overwhelm the resulting spectra and can be difficult to suppress (see above). Another problem with using ^1H is the limited chemical shift range ($\Delta\delta \sim 10$ ppm) of metabolites of interest in the ^1H spectrum.⁵⁴ This leads to complicated spectra as many of the resonances may overlap and pulses sequences with high spectral resolution, or higher field detection, would be required. Furthermore outer voxel suppression and spectral editing techniques can be used to further improve spectroscopic detection.^{292, 296}

Successful *in vivo* hyperpolarised ^{13}C MRS has been carried out, despite its low gyromagnetic ratio and natural abundance, giving dynamic information on metabolic processes. This was made possible through d-DNP.^{3, 297} Peaks corresponding to ^{13}C metabolites of interest occur over a much larger range, approximately 200 ppm. In addition, with most X-nuclei, there are no strong background signals to contend with.

With d-DNP now reaching clinical application, much focus on better MR pulse sequencing for imaging has been given. Recent work reported by Muller et al. (2020)²⁹⁸ used a multi-echo balanced steady-state free precession (me-bSSFP) sequence with Iterative Decomposition with Echo Asymmetry and Least squares estimation (IDEAL) reconstruction to acquire fast 2D and 3D metabolic imaging of ^{13}C - pyruvate to ^{13}C -lactate in pre-clinical studies. A large field of view ($180 \times 180 \times 48$ mm³) and high spatial resolution ($5.6 \times 5.6 \times 2$ mm³) was achieved in a scan time of 8.2 s thereby improving both spatial and temporal resolution for metabolic imaging of ^{13}C -pyruvate to ^{13}C -lactate conversion compared with either FID-CSI or EPSI methods reported at 3T. In earlier work by Chen et al. (2018), a 3D dynamic compressed sensing (CS)-EPSI sequence with spectral-spatial excitation was developed to give first-ever simultaneous volumetric and dynamic images of the metabolic conversion of ^{13}C pyruvate to ^{13}C lactate in a prostate cancer patient with full gland coverage.²⁹⁹ Spatial resolution of 0.5 cm³ was achieved within 18 s time frames, 2 s temporal resolution and 36 s total acquisition time. Application of some of these advanced techniques for ^1H hyperpolarisation may afford better detection of SABRE agents.

Future work would involve use of such sequences and would aim to image the biphasic bolus of thienopyridazines (following further polarisation optimisation). Here, increasing the number of equivalents from 4 to 20 and scaling up from an NMR sample (0.6 mL) to an MRI sample (3 mL) proved difficult as the separation was much slower and therefore attempts to image the sample proved difficult.

With advances in d-DNP methodologies and subsequent detection one should aim to benchmark SABRE detection against this existing literature. Chapter 6 will explore the ^{13}C hyperpolarisation of SABRE applicable substrates with d-DNP to set minimum limits on SABRE substrate polarisation.



Chapter 6: Hyperpolarisation and MRS of ^{13}C nicotinamide using d-DNP and SABRE

6.1 Introduction

This chapter benchmarks SABRE against existing d-DNP technology; both in terms of polarisation level and magnetic resonance spectroscopic imaging (MRSI) capability.

d-DNP is a low temperature, solid state electron paramagnetic resonance (EPR) technique, utilising continuous microwave irradiation to transfer spin polarization from electrons to target nuclei. Once sufficient polarisation of the target is achieved (often over several hours), a dissolution step delivers a bolus for subsequent detection via NMR/MRI. Akin to SABRE, the resulting signal enhancement is many orders of magnitude higher than the Boltzmann equilibrium³. Over the last decade, d-DNP has seen huge investment which has driven a wide range of successful applications.³⁰⁰⁻³⁰² Of particular relevance here are *in vivo* studies permitting MR based metabolic imaging in health and disease.^{4, 91, 96, 97}

In contrast to SABRE, the primary target nuclei for d-DNP are generally ^{13}C or ^{15}N , rather than ^1H . ^1H polarisation is less efficient with d-DNP due to relatively short T_1 values of ^1H nuclei and the strong interaction with the free radical leading to more efficient relaxation. The dissolution process, the transfer from the polariser to the magnet of measurement and settling causes signal loss due to the decay of polarisation. This polarisation loss arises from dipolar relaxation particularly when the magnetic field is low during the transfer from one magnet to another.²²⁶ d-DNP only enhances single quantum ^1H signals by approximately 600 fold with respect to thermal equilibrium (measured at 11.7 T).³⁰³ While it has been reported that d-DNP can boost intermolecular multiple-quantum coherence based ^1H in solvents, this advanced technical approach is yet to find clinical application.^{303, 304} Recent research has seen the development of pulse sequences based on a reverse INEPT to transfer polarisation from ^{13}C and ^{15}N to ^1H . This takes advantage of i) the high polarisation achieved with d-DNP (and the inherently longer T_1) in the low- γ X nuclei; and ii) the superior sensitivity (high- γ and high natural abundance) of ^1H .³⁰⁵⁻³⁰⁷ However, the majority of d-DNP studies remain based on ^{13}C and ^{15}N polarisation. Therefore, for a fair comparison, it was decided to also target low- γ ^{13}C labelled biomolecules with SABRE.

Synthesis of a ^{13}C labelled version of T[2,3-*d*]P proved difficult (chapter 3.5.2). Therefore ^{13}C -labelled nicotinamide (Figure 6.1), synthesised in house, was used for this study instead. Extensive ^1H SABRE studies have already been completed on nicotinamide and its deuterated counterparts ¹³⁵. This is the first time ^{13}C nicotinamide has been developed for polarisation with two different hyperpolarisation techniques.

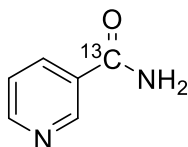


Figure 6.1: Chemical structure of ^{13}C -nicotinamide.

A closer examination of the biochemistry and metabolism of nicotinamide will be taken to establish how a hyperpolarised version of this important biomolecule could be important for clinical imaging (section 6.2). A summary of the *d*-DNP technique (introduced in chapter 1) focusing on the optimum conditions required for this process will be given in section 6.3. Optimisation of the *d*-DNP polarisation levels of ^{13}C nicotinamide will be discussed followed by subsequent use of a hyperpolarised bolus in a murine cancer model with MRS in section 6.4. Section 6.5 explores the T_1 lifetime *in vivo* and further investigations into the effects on T_1 in deuterated versions of nicotinamide will be made. A final study in section 6.6 benchmarked the two techniques by hyperpolarising ^{13}C -nicotinamide with SABRE and investigating imaging potential. Conclusions were drawn by comparing the two techniques and giving their relative advantages and limitations.

6.2 Theory: Nicotinamide

Nicotinamide (also known as NAM/niacinamide) has been previously targeted as a SABRE hyperpolarised contrast agent as it contains an N-heterocyclic ring and is an endogenous human metabolite which exhibits low toxicity (even after it has been through the SABRE process).¹⁶⁴ Therefore subsequent *in-vivo* injection will be free of side effects and tolerated by humans at very high doses (3.5-6 g).¹⁶⁵ Importantly, NAM plays a critical role in cellular biology as a precursor to Nicotinamide Adenine Dinucleotide (NAD)¹⁶⁶ and has been used as a therapeutic for the prevention of neurocognitive conditions¹⁶⁷ (see below). Therefore, hyperpolarised *in-vivo* detection could find application across a range of disease states.

6.2.1 Biomedical applications of Nicotinamide

NAM is a water-soluble amide derivative of nicotinic acid (niacin; vitamin B₃). It is widely distributed throughout the body in all tissue types. Rutkowski et al. (2008) showed that in rats, NAM is present in the plasma, erythrocytes, lungs, liver, heart and brain but only in very low quantities in fat tissue. Accumulation of NAM metabolites were found in the liver, lungs and skeletal muscle but not in fatty tissue or the brain³⁰⁸.

In the 1930's it was discovered that the deficiency of NAM caused pellagra³⁰⁹. As a supplement it is now used as a general preventative measure for neurocognitive diseases¹⁶⁷. It is used clinically to treat schizophrenia³¹⁰ and Alzheimer's³¹¹. Outside of neurology it finds use, alongside radiosensitization^{312, 313}, in the treatment of hyperphosphatemia in dialysis patients³¹⁴. Findings suggest that it can reverse plasma tryptophan depletion in HIV.³¹⁵ It is also in phase III clinical trials for skin cancer prevention.³¹⁶

Interestingly, NAM can also be used as a hydrotrope, improving the solubility of many water-insoluble drugs, including diazepam, testosterone and progesterone.³¹⁷ The broad range of potential clinical applications for NAM reflects the important role it plays in mediating cellular metabolism.

6.2.2 Nicotinamide biochemistry and metabolism

As a precursor to the cofactors nicotinamide adenine dinucleotide (NADH/NAD⁺) and nicotinamide adenine dinucleotide phosphate (NADPH/NADP⁺), nicotinamide is found in major metabolic pathways within the body. NAD⁺ and NADP⁺ act as coenzymes in a wide variety of oxidation and reactions, most importantly in glycolysis, the Tricarboxylic acid (TCA) cycle and the electron transport chain.³¹⁸ When nicotinamide is ingested it will undergo a series of reactions until it is transformed into NAD⁺ and later NADP⁺. In the liver, metabolism of NAM occurs by cytochrome P450 to form nicotinamide-*N*-oxide, 6-hydroxy-nicotinamide and *N*-methyl-nicotinamide (MNA). MNA is further metabolised to *N*-methyl-2-pyridone-5-carboxamide or *N*-methyl-4-pyridone-5-carboxamide³¹⁴. The main pathway for the biosynthesis of NAD in mammalian cells is a salvage pathway by the phosphorylation of nicotinamide by the enzyme, nicotinamide phosphoribosyltransferase (NAMPT). This represents the rate-limiting step of NAD biosynthesis³¹⁹⁻³²¹ (Figure 6.2). The human body can create NAD itself however, through other pathways including the metabolism of niacin or tryptophan³²² (Figure 6.2).

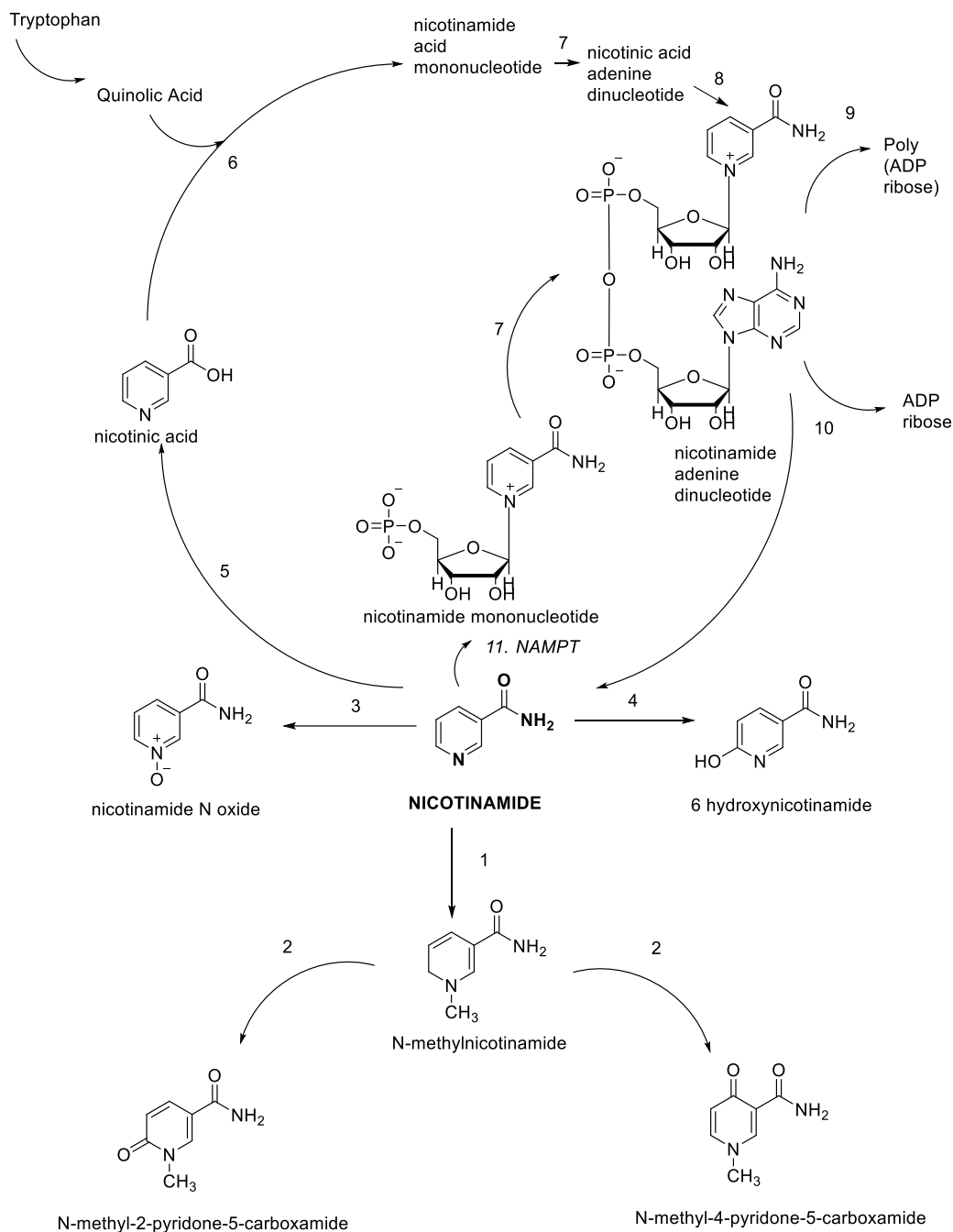


Figure 6.2: Schematic description of nicotinamide metabolism³¹⁴ Enzymes **1 = nicotinamide-N-methyltransferase**, **2 = aldehyde oxidase**, **3-5 = nicotinamide deamidase**, **6 = nicotinamide phosphoribosyltransferase**, **7 = NAMN adenylltransferase**, **8 = nicotinamide synthetase**, **9 = poly(ADP-ribose) synthetase**, **10 = nicotinamide glycohydrolase**, **11 = nicotinamide phosphoribosyltransferase (NAMPT)**.

6.2.3 Nicotinamide and cancer

As described above NAD has an essential role in cellular metabolism. One of its most important roles is as a cofactor for the redox reactions of glycolysis. Cancers exhibiting the Warburg effect³²³⁻³²⁵, i.e. increased aerobic glycolysis and decreased oxidative phosphorylation, demonstrate an increased rate of NAD^+ turnover to meet the demand for Adenosine Triphosphate (ATP). In addition, other enzymes requiring NAD such as poly ADP-ribose polymerases (PARPs)

have higher activity in cancer cells, hence a higher turnover of NAD and consequently NAM might be indicated in cancer.

NAMPT inhibitors have been developed for cancer treatment as they have been found to block nicotinamide metabolism which results in cell death in some cancers.^{166, 326} This process has already been monitored using d-DNP hyperpolarised pyruvate.²³⁴ The bio-imaging of hyperpolarised nicotinamide itself, via SABRE or d-DNP, could present as a novel future probe for mapping altered cellular metabolism. For context a brief description of d-DNP follows.

6.3 Theory: d-DNP

Nuclear spins in the solid state are polarised at low temperature (1–2 K), in a high magnetic field (3–7 T) via transfer from a free radical (as the source of unpaired electrons). Under these conditions, electron spin polarisation is almost unity. Microwave irradiation close to the paramagnetic resonance causes nuclear spin populations to redistribute and approach the electron spin polarisation. This process is slow at low temperature (tens of minutes to hours), but when high solid-state polarisation has been achieved, the sample can be dissolved quickly using a hot solvent. This process is rapid (a few seconds) with respect to nuclear relaxation, and a solution of polarised spins results.²⁹⁷ However, this strong nuclear spin polarisation, as with all hyperpolarisation methods, relaxes back to thermal equilibrium with the time constant T_1 . While d-DNP MRI is a very exciting clinically proven development, there are several critical features that need to be considered and optimised if an agent is to be successful both in terms of polarisation and disease profiling.

6.3.1 Biological Properties

The substrate of interest needs low toxicity to ethically inject into a living system. Hence, many DNP agents are chemically labelled endogenous metabolites. However, even then, the correct dosage is required. Concentrations used in a typical DNP experiment are 10^7 - 10^8 times higher when compared with Positron-emission tomography (PET).²³⁴ However, the tracer in PET is radioactive which limits its use in repeated/longitudinal screening.

The physiological pH at the injected concentrations must also be considered. For example, pyruvic acid necessitates the use of an alkaline buffer, pH 12, to counteract pH 2 of the acid when used clinically.⁴

Due to the time constraints of the experiment (which is predominately dictated by the apparent T_1 of the hyperpolarised molecule and delivery time), it is essential that transportation of the substrate to the site of interest and the metabolism of the substrate is sufficiently rapid to allow observation of the metabolites. This usually means that catabolic reactions rather than slower anabolic reactions are monitored by this technique.⁷²

Metabolically inert compounds, such as ^{13}C urea, which was the first reported substrate to be hyperpolarised via *d*-DNP³, have also been used as probes for perfusion imaging³²⁷; however such agents have attracted less clinical interest.

6.3.2 Physical Properties

One of the essential requirements for successful MRS is a long longitudinal (spin-lattice) relaxation time (T_1) for the detected nuclei. This is because if a signal is to be detected, the time for sample transportation and metabolism need to lie within the same timeframe as T_1 . Consequently, smaller rapidly tumbling molecules having a low molecular weight (<200-300 Da) have been the most successful for *d*-DNP (pyruvic acid = 89 Da). This reflects the fact T_1 decreases as a function of increasing correlation time (τ_c) and increasing molecular size (Figure 6.3). T[2,3-*d*]P if it could be labelled would fit, having a low molecular weight of 136 Da. ^{13}C nicotinamide also fits with a molecular weight of 123 Da. Smaller molecules also have the benefit of being more water-soluble.

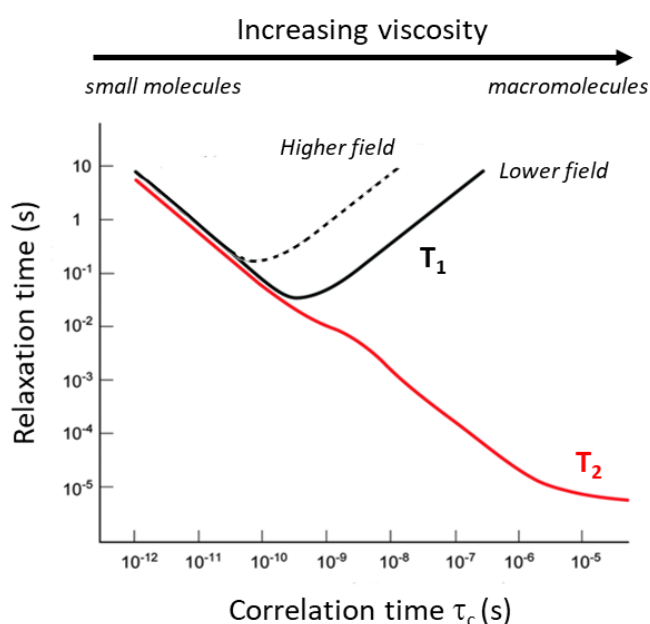


Figure 6.3: Relationship between relaxation time vs correlation time T_1 and T_2 ^{234, 328}.

In addition, it has proven usual to label the quaternary carbons (for example carbonyl carbons) within a structure, to extend T_1 values by avoiding as many pathways to relaxation as possible. Partial³²⁹⁻³³¹, or even full^{332,331}, deuteration of a structure and the use of deuterated solvents have also been employed to further reduce relaxation.⁹³

6.3.3 DNP Sample Preparation

For effective transfer of polarisation from the electron to the nuclei, the EPR spectrum of the radical requires a line width which exceeds the Larmor frequency of the nuclear spin in question. Nitroxides such as TEMPO (Figure 6.4) have a broad EPR spectrum and therefore cover the Larmor frequency range for all nuclear spins.³³³ The broad linewidth in nitroxyl radicals is due to *g*-anisotropy and the interaction of the unpaired electron with ^{14}N and ^1H .³³⁴

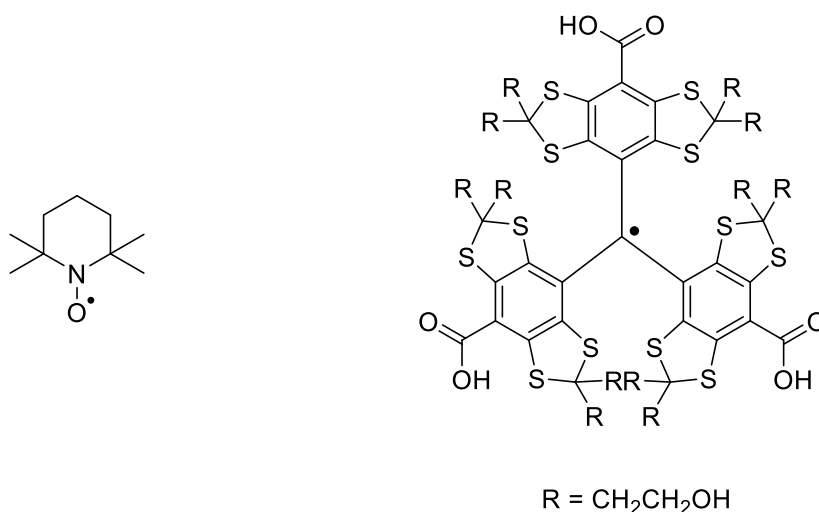


Figure 6.4: Radicals used in DNP a) TEMPO and b) OX063.

Although the EPR spectrum of the radical needs to be wider than the Larmor frequency of the nuclear spin to be hyperpolarised, a narrower width allows more efficient nuclear polarisation. Trityls³³⁵, such as OX063 (Figure 6.4) meet this requirement and are highly successful for polarising ^{13}C and ^{15}N (low gamma nuclei).³³⁶ The narrow line width is brought about by the fact the radical centre is surrounded by $I = 0$ nuclei thereby preventing any hyperfine coupling. Broadening due to *g*-anisotropy is also limited due to the symmetrical nature of the radical.³³⁴ OX063 is also water-soluble.

Radicals themselves however provide a route to relaxation. Consequently, studies where radicals are produced *in situ* through the UV irradiation of a suitable organic material have been

completed.³³⁷ In the case of pyruvic acid, it was shown that UV irradiation of a frozen sample for an hour led to enough free radicals to achieve high ^{13}C polarisation. The radicals were then proposed to recombine on dissolution. This would mean that the filtering and pharmacological tests (to ensure the potentially toxic radicals have been removed) would no longer be required.³³⁷

One further problem associated with the frozen solution is the need for a homogeneous distribution of radical. If the sample contains crystals, the radical becomes concentrated in domains and the DNP process is inhibited.⁷² The required amorphous solid is achieved by the addition of a glassing agent in a process that must be optimised. Such agents include glycerol and dimethylsulphoxide (DMSO).⁸⁷ The choice and ratios of the solvent and glassing agent is essential for achieving the highest molarity possible of the substrate. As the dissolution process involves dissolving the frozen sample in hot solvent (usually 6 mL), the concentration of the substrate is automatically reduced so it is important that the substrate is soluble at high initial concentrations.³³⁸ A higher concentration allows also for increased ^{13}C - ^{13}C spin diffusion during polarisation.⁷² Spin diffusion describes the allowed transitions whereby individual spins undergo an exchange of energy via a mutual flip-flop. This process is driven by the dipolar coupling interactions which are dependent on the spin-spin distance and the gyromagnetic ratios of the coupled spins.³³⁹

Gadolinium chelates have been found to increase polarisation and shorten the polarisation build-up times. This chelate improves the rate of pyruvic acid polarisation build up leading to increased final polarisation levels. This phenomenon, produced by the presence of Gd^{3+} species, can be attributed to the shortening of the electronic spin-lattice relaxation time T_{1e} .^{234, 340} Gadolinium (Dotarem, Figure 6.5) is FDA approved and remains in the final solution to be injected.

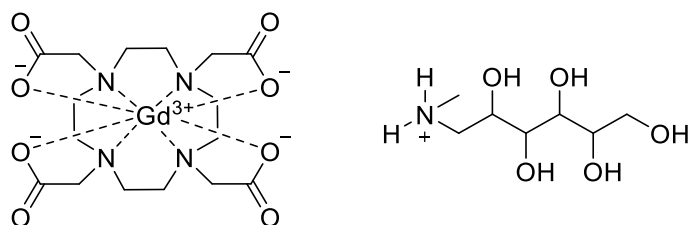


Figure 6.5: Dotarem – Gadolinium Chelate used in DNP to increase polarisation and shorten polarisation build up times.

6.4 d-DNP polarisation of nicotinamide and *in vivo* application

This study represented the first time ^{13}C -labelled nicotinamide was hyperpolarised with d-DNP. Sample preparation therefore needed to be optimised (based on the above conditions). 100 μl

aliquots of the formulations outlined in Table 6.1 were hyperpolarised on a commercial Hypersense DNP system (Oxford instruments; Model number: MCQ, Abingdon, UK) operating at 3.35 T and 1.4 K with a 100-mW microwave source.

The formulations tested allowed exploration of the effects of different glassing agents, agent concentration and Dotarem. Formulation A (25 mg of ^{13}C labelled agent, with 15 mg of OX063 radical in 200 μl of both water and glycerol) was based upon a recommended recipe³⁴¹ for the *d*-DNP of fumarate.

Table 6.1: Formulations of differing volumes of glycerol:water ratio and nicotinamide showing K_{BU} and the expected maximum amplitude. Maximum amplitude can be estimated after 60% of build up.

Formulation	NAM Conc. (M)	Water (μl)	Glycerol (μl)	OX063 (mg)	Optimum Frequency (GHz)	Ampl. after 5 min	Build up time constant K_{BU} (min)	Expected maximum amplitude
A (blue)	0.50	50	50	3.7		350		
B (red)	2.03	50 DMSO	50 methanol	2.7		330		
C (orange)	4.06	70	30	2.7	94.105	1728	55	10,000
D (green)	3.41	60	40	2.7	94.110	660	44	3,690
E (purple)	4.06	80	20	2.7	94.100	2340	25	6,600
F (black)	4.06	70	30	2.7 + 1 μl of 50 mM Dotarem	94.105	1379	43	11923

6.4.1 ^{13}C DNP of nicotinamide in the solid-state

In *d*-DNP the electron spin resonance (ESR) properties of the free radical, OX063, influence the efficiency of the polarisation transfer.³⁴² A broad microwave sweep, near the ESR Larmor frequency of the free radical (5 MHz increments between 94.080 - 94.160 GHz), was carried out to determine the approximate polarisation efficiency (after 300s) and optimum frequency for transfer. Between point measures, a series of three hard 90° RF excitation pulses were applied to

destroy the residual electron polarisation. Figure 6.6 shows the resultant ^{13}C microwave DNP based power spectrum (arbitrary units), measured with the built-in solid-state NMR detector, for qualitative analysis of each formulation investigated. The enhancement profiles (Figure 6.6 insert) are closely related to the shape of the first derivative ESR spectrum.³⁴³ Positive P(+) and negative P(-) polarisation peaks were observed, corresponding to minimum positive and negative spin temperatures, respectively.

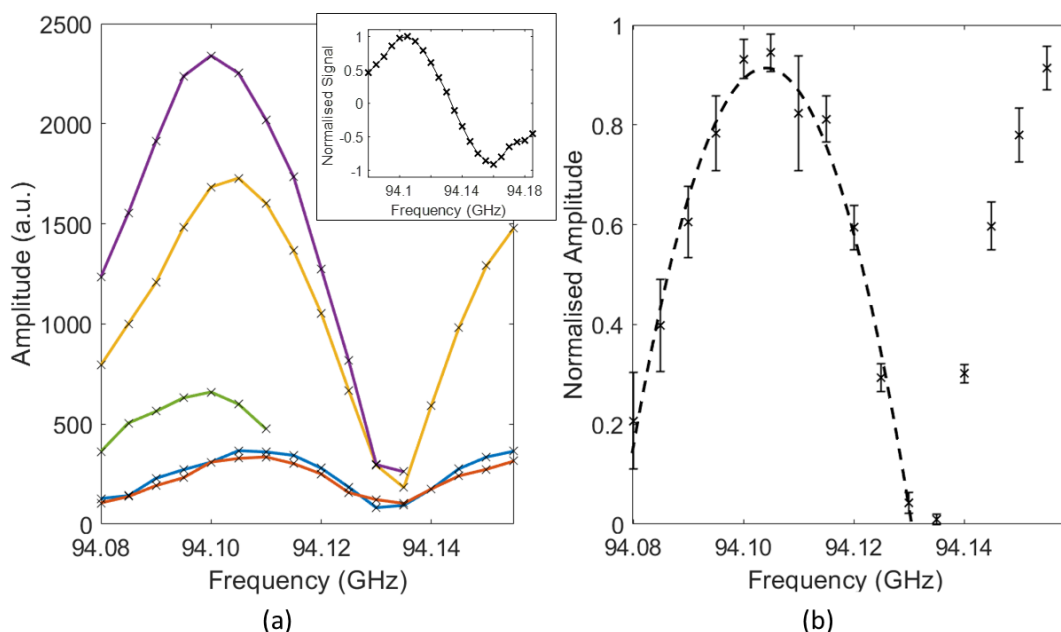


Figure 6.6: Power spectrum of microwave frequency to determine optimum for polarisation. A starting frequency of 94.080 GHz was used through to 94.160 GHz. The step size used was 5 MHz and the step duration 300 s. a) Absolute sweep amplitude recorded using: Formulation A (light blue), Formulation B (red), Formulation C (orange), Formulation D (green), Formulation E (purple). Insert shows normalised raw signal showing positive and negative polarisation peaks related to the shape of the first derivative ESR spectrum. b) Normalised amplitude of combined sweeps with errors indicating optimum frequency was 94.105 GHz. Dotted line shows least square fitting across all samples to estimate peak frequency.

Maximum enhancement for direct ^{13}C polarisation is observed at low-microwave frequencies (positive P(+) polarisation peak). A normalised power spectrum across all formulations (Figure 6.6 b) was used to estimate the optimal microwave frequency for efficient polarisation (94.105 GHz). The frequency (at 5 MHz resolution) was independent of the medium formulation. The polarisation peak separation $|P(+)-P(-)|$ for nicotinamide samples was approximately 50 MHz. This value reflects the size of the corresponding ESR line-shape, in qualitative agreement with the Borghini model of DNP spectra.³⁴⁴

Although direct quantification in terms of ‘enhancement value’ was not completed,³⁴¹ it was known that at 300 s, a power amplitude of ~ 4000 (arb. units) on a pyruvic acid ¹³C microwave spectrum (in a Hypersense MCQ model) enables subsequent *in-vivo* study.

Interestingly, in terms of potential ‘polarisation’, formulation A (optimised for fumarate) gave the poorest signal enhancement after 5 minutes (~350 arb. units.). This is evidence that no single recipe can be used for similar molecular weight probes. Formulation B using improved glassing agents (DMSO & methanol)^{72, 87} also resulted in low signal amplitudes (~330 arb. units).

In line with other d-DNP studies, the data here show that higher levels of polarisation result simply from a higher concentration of the metabolite (formulations C- F).^{72, 338} Note, a series of solubility studies (in water) were carried out using unlabelled nicotinamide to confirm maximum concentration (50 mg in 100 µl) before sample make-up for d-DNP experiments. The resulting concentration of nicotinamide was 3.41 - 4.06 M (dependent on formulation see Table 6.1). Following 300 s of d-DNP build up signal amplitudes of between 660 and 2340 (arb. units) were achieved. It is noted under similar conditions pyruvate achieves a signal amplitude of 4000 (arb. units).³⁴¹ Hence, it was hypothesized that *in vivo* signal detection of ¹³C labelled nicotinamide (in the absence of relaxation) would be feasible after further optimisation.

With adequate polarisation achieved (in 300 s), formulations C-E underwent polarisation build-up profiling at the optimum microwave frequency (Figure 6.7). Polarisation was allowed to build up over time until an accurate build-up time constant (k_{BU}) and maximum amplitude could be estimated (single exponential increase function – see equation 1.6).

As shown in Figure 6.7, the higher proportion of water to glycerol in formulation E lead to faster initial build-up (2340 after 5 minutes) with a build-up time constant of $K_{BU} = 25$ min but lower final amplitude/polarisation level (6,600). When using a lower proportion of water to glycerol in formulation D, the quantity of nicotinamide also had to be reduced slightly (from 50 mg to 42 mg) to ensure solubility. Despite the ability to readily form a glass, overall performance was reduced (3,690). Of the formulations tested the 70:30 water/glycerol mix of formulation C resulted in the highest final signal ~10,000 (after 5 hours of build-up). The addition of Dotarem, a gadolinium chelate, in formulation F proved to have a beneficial effect on ¹³C-nicotinamide polarisation both in terms of rate ($K_{BU} = 43$ min compared with 55 min without) and maximum amplitude (12,000 compared to 10,000 without).

It is noted that in all cases the hyperpolarised dissolution solution with ^{13}C labelled nicotinamide was pH 7. Thus, unlike pyruvate-based preparations, no further physical steps for correction of pH prior to liquid injection were needed. This had the advantage of preventing further unwanted signal loss due to T_1 relaxation back to thermal equilibrium.

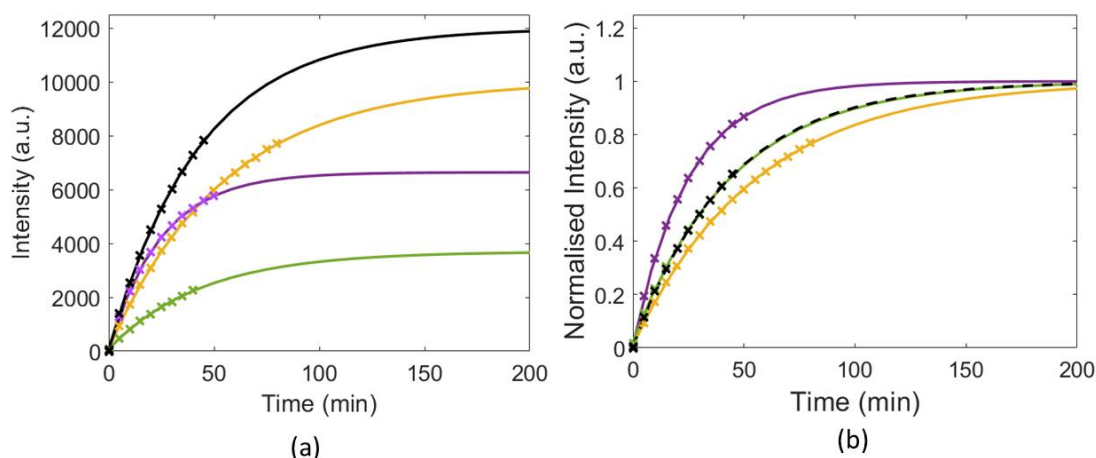


Figure 6.7: (a) Polarisation build up curves at 94.105 GHz using 100 μl aliquots of Formulation C (orange), Formulation D (green), Formulation E (purple) and Formulation F (black) (b) Corresponding normalised build up profiles.

With a suitable formulation (F) for efficient polarisation of ^{13}C labelled nicotinamide identified, the T_1 of the subsequent dissolution was estimated. Dissolution was carried out using 6 mL of distilled water and the sample placed into a 400MHz (9.4T) NMR system. A ‘hyperpolarised’ T_1 value of 17 ± 1 s (at 298 K) was determined (data not shown) using a variable flip angle protocol^{125, 345} (section 8.7.4). This value was confirmed using a standard inversion recovery approach on a thermal sample. Following confirmation of a suitably long T_1 value, a murine cancer model was used to determine i) if ^{13}C –nicotinamide could be detected *in vivo*; ii) if so, probe nicotinamide distribution in the body following injection and iii) confirm if any metabolism of the nicotinamide could be detected in the form of emerging NMR peaks.

6.4.2 *d*-DNP- MRS *in vivo* experiments with ^{13}C -nicotinamide

In vivo experiments used non-scid gamma (NSG) female mice (n=3). Full methods are described in section 8.7.2. Briefly, patient derived xenografts (human breast cancer cell line STG195) were implanted subcutaneously. The cells were allowed to grow for six months to form tumours of dimensions approx. 1 x 1 cm. An oestrogen pellet was implanted to encourage tumour growth.

On the day of MR imaging the mouse was anaesthetised with 2% isoflurane (in 100% oxygen). A tail vein catheter (PTFE tubing 60 cm in length; prefilled with heparinised saline, 50 units/ml)

was inserted for hyperpolarised bolus IV injection. The mouse was then positioned within a 7T small bore MRI system (Agilent, Varian). A 20mm ¹³C TX/RX single turn based surface coil (Rapid Biomedical GmbH, Rimpfing, Germany) was fitted above the flank of the animal allowing the tumour to protrude.

Standard ¹H fast low angle shot (FLASH) based images were taken of the animals prior to injection to ensure that they were positioned correctly magnet iso-centre. These images were used as a reference base image for subsequent CSI/MRS mapping (section 8.7.3.2). Animals were split into two groups: i) assessing non localised spectral build up, decay and potential metabolism of ¹³C nicotinamide from point of injection (n = 1) and ii) assessing spatial distribution of the biomolecule using CSI across the torso of the mouse (n = 2).

i) Slice selective single pulse spectroscopy

A slice selective ¹³C single pulse experiment, with 180 repetitions over 3 minutes, was used to assess the time course of hyperpolarised bolus arrival, associated metabolism, and subsequent decay. The hypothesis was that if any metabolism of ¹³C labelled nicotinamide occurred within the time frame of the overall *T*₁ decay and experiment, additional ¹³C NMR peaks would become apparent. The carbonyl carbon for NAD = 167.8 (D₂O), NADPH = 175.5 (D₂O) and Nicotinamide N-oxide = 168.2 (D₂O) ppm.

Formulation F was prepared and polarised via d-DNP (section 8.7) at the established optimum microwave frequency for 1 h 36 m. Following dissolution with 6 mL of PBS, pH was measured as 7.5. This was within acceptable pH range for bolus administration (pH 4-9)³⁴⁶ and also within normal physiological values (pH 7-8).³⁴⁶ ¹³C spectra were recorded for 3 minutes, starting immediately after administration (t = 0) with TR = 1 s using a 5° FA (to limit excitation attenuation). A ¹³C nicotinamide response was observed as expected at 171 ppm (Figure 6.8 a). Signal intensity peaked at 12 s post injection. There was evidence for molecular probe arrival (~6 s) and decay due to transport, relaxation and signal utilisation. Signal is lost by 70 s. Only a single peak was evidenced. It can therefore be concluded that no metabolism of the injected compound has taken place within the tumour in this timeframe.

However, it is noted that the peak at δ 171 was broad (Full Width Half Maximum = 1.21 ppm). Possible metabolic derivatives have similar chemical shifts to ¹³C nicotinamide (167.8 to 175.5 ppm). It could be possible that there is some overlapping and improved shimming may help

address this. However, it is hypothesised that the metabolism of NAM could be too slow to be seen within this timeframe.^{347, 348}

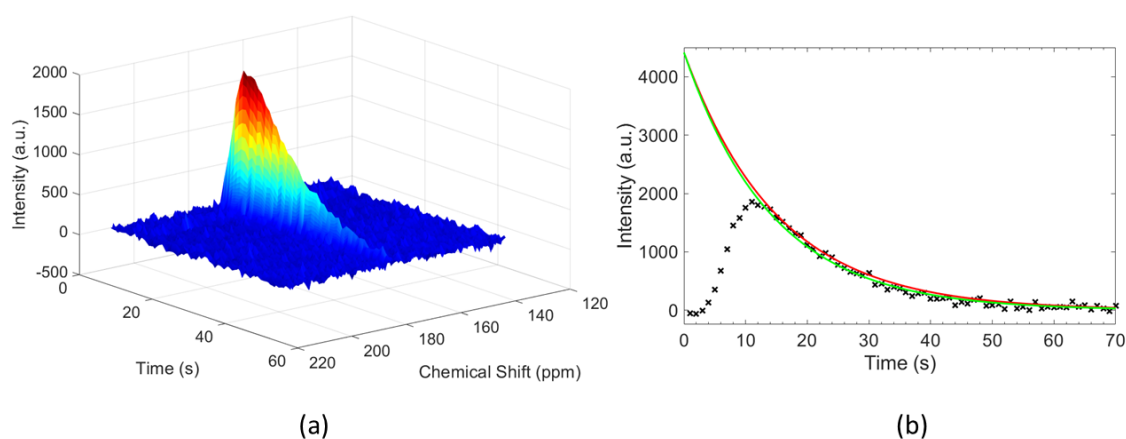


Figure 6.8: (a) 3D surface map of the flux of hyperpolarised ^{13}C -nicotinamide in PDX breast tumour (formulation F). Series of 180 ^{13}C magnetic resonance spectra recorded through the tumour starting immediately after the injection of 0.4 ml of 67 mM hyperpolarised ^{13}C nicotinamide. Spectra were collected every second for a total of 3 minutes with TE = 1 s. (b) 1D plot (through δ 171) of arterial input of the hyperpolarised ^{13}C -nicotinamide and the subsequent decay. The crosses indicate the experimental values. The red line indicates a theoretical T_1 decay of 14 s. The green line indicates a T_1 decay of 14 with the loss of hyperpolarisation due to the 5° FA being used. Experimental points from 14 s to 60 s fit with an exponential decay accounting for a 5° FA to give a T_1 of 14.7 s.

A 2D plot (Figure 6.8 b) through δ 171 was fitted to a mono-exponential decay function (with and without accounting for multiple 5° RF excitations). A T_1 of 14.7 s was estimated. The similar length of T_1 *in vitro* (400 MHz NMR spectrometer) and *in vivo* (300MHz / 7 T MRI scanner) suggest that there is no detrimental effect on the relaxation time due to blood (susceptibility) and associated flow.

ii) Spatial distribution

A Chemical Shift Imaging (CSI) based experiment ($n = 2$) was carried out to evaluate the distribution and relative intensity of the ^{13}C nicotinamide across the abdomen/tumour of the mouse (Figure 6.9a). Formulation F was prepared and polarised via DNP (section 8.7) at the established optimum microwave frequency for 1 h 30 m. Following dissolution, pH was measured as 7.

Representative CSI data, acquired 12-15 seconds after bolus injection, are shown in Figure 6.9. The resulting spatial map for ^{13}C nicotinamide at 170 ppm (Figure 6.9 b) is interpolated and

overlaid on the ^1H structural reference scan (Figure 6.9 c). This time was chosen to account for the arterial input function of ^{13}C nicotinamide (based on non-localised spectroscopy data above – which peaked at 12 s post injection). The CSI sequence used a spiral centre out k-space encoding scheme⁹⁷. This encoding regime ensured that the centre of k-space was acquired under maximum polarisation signal; under sampling outer areas of k-space (reducing image edge definition).

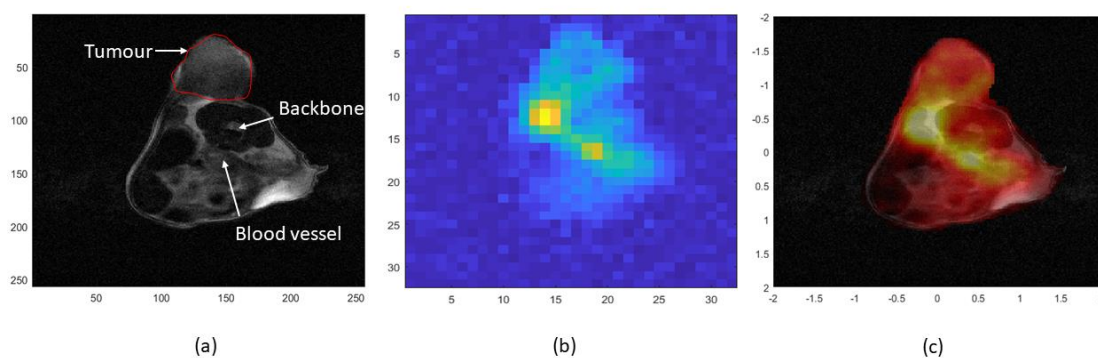


Figure 6.9: (a) ^1H MRI scan of the axial cross section of tumour bearing mouse (6 mm slice). (b) CSI map of 32 x 32 points showing the distribution of the ^{13}C -nicotinamide across the axial cross section through tumour and mouse torso (40 mm x 40 mm 2D plane, 6 mm slice). The yellow colour shows the areas of most intensive hyperpolarised signal whilst the dark blue colour shows the areas of little or no hyperpolarised signal. (c) CSI image of original 32 x 32 interpolated to 128 x 128 overlaid on a ^1H anatomical MRI scan. The white/yellow colour shows the areas of most intensive hyperpolarised signal.

Clear perfusion was observed with signal arriving in almost all tissue throughout the axial cross section of the animal. The signal was particularly high within the blood supply to the tumour. No other metabolic derivatives of NAM were observed in the spectra. Again, improved shimming would be beneficial, due to the close proximity of the chemical shifts of NAD metabolic derivatives (167.8 to 175.5 ppm). Equally cellular uptake of NAD is relatively slow³⁴⁷ and longer hyperpolarised signal lifetimes may be required. Deuteration of the molecule and the use of a deuterated solvent may help to extend the lifetime present as a future route to achieve this^{93, 330-332}.

In the absence of any useful metabolic markers, hyperpolarised ^{13}C nicotinamide could still be used as a probe for perfusion imaging (similar to ^{13}C urea). Hyperpolarised ^{13}C urea experiments have been used to determine tissue perfusion, in both static and dynamic studies.³²⁷ Urea has also been used as a co-polarized agent i.e. administered together with other polarising agents. It could be used to normalise for delivery in *d*-DNP studies as it is not metabolised on the time scale of the hyperpolarisation experiment.^{106, 349} Urea however has an apparent T_1 of 44 s at 11.7 T) and 35 s at 14.1 T which is longer than that of ^{13}C nicotinamide. Again, deuteration may help.

It is noted that the percentage polarisation achieved (via d-DNP and permitting *in-vivo* imaging) on protonated ^{13}C labelled nicotinamide (formulation F) was 13.5% (Figure 6.10 a - confirmed via high field NMR at 9.4 T). Dissolution and transfer to a 10 mm NMR tube followed by fast imaging with steady state free precession (FISP) using a 9.4 T Bruker NMR/Imaging system resulted in the hyperpolarised image shown in Figure 6.10b.

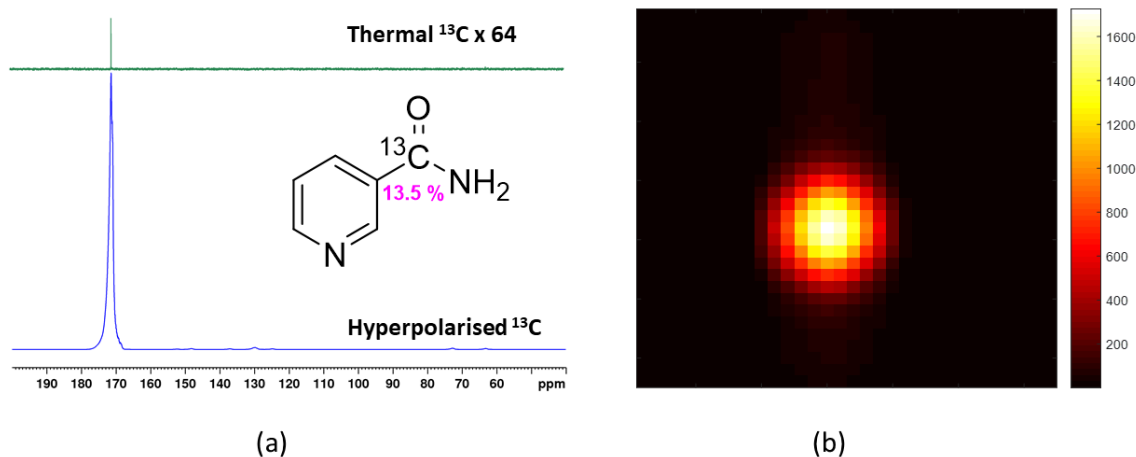


Figure 6.10: (a) Thermal spectrum of ^{13}C -nicotinamide vertically multiplied 64 times to be seen alongside the hyperpolarised spectrum using d-DNP. (b) ^{13}C FISP image of ^{13}C nicotinamide using d-DNP. Both the spectra and the image were measured on a 9.4 T magnet.

6.4.3 ^{13}C nicotinamide using d-DNP and the effect of deuteration on T_1 values

A further study was carried out to synthesise and study the deuterated forms of nicotinamide, including 2,4- d_2 -nicotinamide, 2,5- d_2 -nicotinamide and 4,6- d_2 -nicotinamide. Deuteration is known to extend the magnetic state lifetime of molecules.^{93, 330-332} It is noted that these isotopologues of nicotinamide were not ^{13}C -labelled and T_1 measures were thermal based (using inversion recovery) and completed on a 400 MHz NMR system. Synthesis of labelled and deuterated compounds took a relatively long time (order of weeks). Furthermore, there is a considerable cost involved to using labelled compounds in such quantities as is required for d-DNP (<50 mg per experiment).

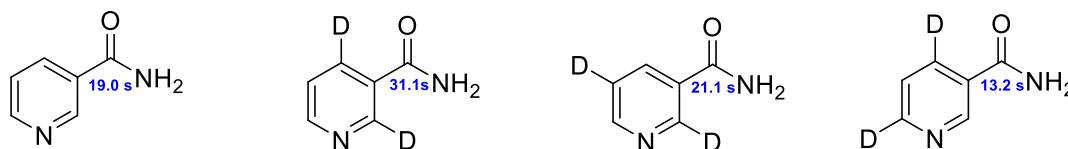


Figure 6.11: T_1 values the carbonyl carbon of nicotinamide, 2,4- d_2 -nicotinamide, 2,5- d_2 -nicotinamide and 4,6- d_2 -nicotinamide measured in ethanol- d_6 using thermal inversion recovery (400 MHz NMR system).

Comparative T_1 values to the protonated parent molecule are shown in Figure 6.11. As shown deuteration of the proton sites (2, 4) closest to the target carbonyl carbon nucleus, thus exhibiting the strongest coupling and acting as a polarisation sink, approximately doubles the T_1 lifetime. This clearly demonstrates the advantages of selected deuteration.

It is hypothesised that deuteration of the whole molecule would also be beneficial for d-DNP polarisation. However, again synthesis was expected to be lengthy, have high cost implications and therefore was not completed here.

It is noted that all the above measurements used an ethanol- d_6 solvent. An experiment was completed to confirm that changing the solvent to water/glycerol (for d-DNP use) did not affect T_1 . Only 4,6- d_2 -nicotinamide was available in enough quantity (>50mg) and was soluble in the water/glycerol mixture to make the subsequent DNP formulation and test this hypothesis. A T_1 of 13.2 s was measured confirming that the T_1 was independent of the two solvents tested (Figure 6.11 and Figure 6.12). Interestingly, when polarised with d-DNP a slightly smaller polarisation level (10.4%) was achieved compared to the protonated version (13.7%). It is hypothesised that this more reflects the ~4s shorter T_1 time and slight differences in time between manual sample insertion into the NMR and data acquisition.

Another way to extend T_1 lifetime is by varying the functional group bonded to the carbonyl carbon. Upon changing the amide (nicotinamide) to an ester (methyl-nicotinate), lifetime again approximately doubled to 33 s (Figure 6.12). Unfortunately, final achieved d-DNP polarisation level of the carbonyl carbon almost halved.

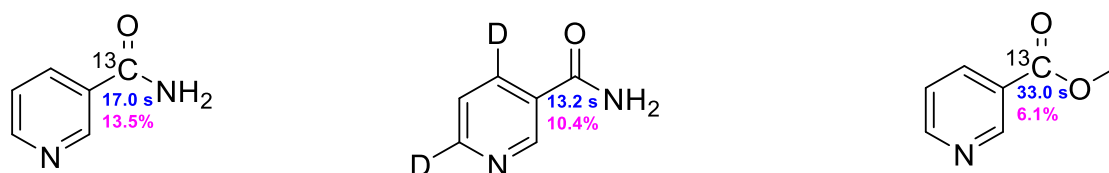


Figure 6.12: T_1 and percentage polarisation of ^{13}C nicotinamide, 4,6- d_2 -nicotinamide and ^{13}C methyl nicotinate in water/glycerol mixture. Hyperpolarisation was carried out using *d*-DNP and T_1 values were measured using a 1 shot hyperpolarised T_1 with variable flip angle protocol (400 MHz).

This confirms that the amide must play a large role in the relaxation processes of this target. The methyl nicotinate, in terms of magnetic lifetime, would be favourable for *in vivo* studies (permitting QA tests and time for injection), however nicotinamide gave the higher polarisation level and its biochemistry/toxicology is well known.¹⁶⁴ The biochemistry/toxicology of methyl nicotinate would need to be assessed more rigorously than the literature currently indicates if any human measurements were to be made.

6.5 SABRE hyperpolarisation of ^{13}C nicotinamide

The target ^{13}C -labelled nicotinamide was hyperpolarised with SABRE and benchmarked against the *d*-DNP data above.

In SABRE, the relay of hyperpolarisation from *p*- H_2 through the iridium catalyst to the substrate of interest requires reversible binding via the nitrogen of the heterocyclic ring. As can be seen in Figure 6.13, the carbonyl carbon site is distant from the source of polarisation (being 5 bonds away from the hydrides). The optimum field for ^{13}C SABRE polarisation was previously calculated as $\sim 2.5\text{ mG}$ (section 3.5.1).

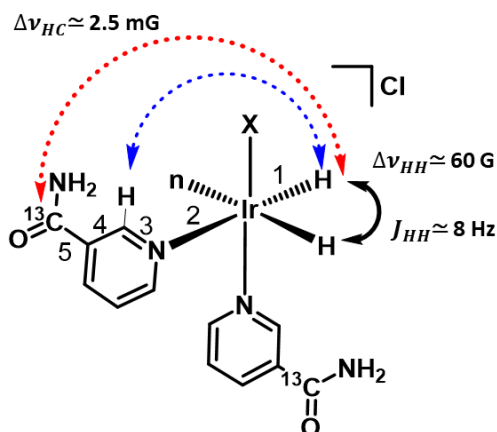


Figure 6.13: Iridium complex formed during SABRE with ^{13}C nicotinamide and $[\text{IrCl}(\text{COD})(\text{X})]$. The red dotted line shows the transfer of polarisation directly to the carbon and the blue dotted line shows the transfer of polarisation to the protons in nicotinamide. The black line indicates the coupling between the hydrides. (*n* is second in plane nicotinamide that is missed to aid the reader).

6.5.1 ^{13}C SABRE – NMR optimisation

A sample was prepared using 5 mM of $[\text{IrCl}(\text{COD})(\text{X})]$ catalyst precursor in a 1:10 ratio with ^{13}C nicotinamide in methanol- d_4 . Methanol- d_4 was used for preliminary investigations as this solvent usually affords the best signal enhancements with SABRE. PTF was tested using a solenoid in a mu metal shield. The current in the solenoid was varied to achieve different fields. In all fields tested (0 G, 2 mG and 9 mG, an anti-phase peak was created for the carbonyl resonance at $\sim\delta$ 168.4 (Figure 6.14). This is indicative of the creation of a two-spin order term involving ^1H and ^{13}C nuclei. Under normal conditions the two protons adjacent to the ^{13}C resonance will lead to a doublet of doublets but as the couplings are almost identical the appearance resembles a triplet splitting in a fully coupled spectrum. Under SABRE, longitudinal 2 spin order is created between the carbon and hydrogen nuclei. The appearance of this signal should therefore reflect an antiphase multiplet where the peak separation is $J_{\text{CH}1}$ and $J_{\text{CH}2}$. The middle line in this multiplet vanishes because the two overlapping contributions are anti phase. However, the observed antiphase peaks did not have equal intensity. This is because normal Zeeman polarisation is also created, which leads to a simple in-phase doublet of doublets. Experimentally, both sum together to yield the result which therefore depends on their relative amplitudes (proportion). Figure 6.14 establishes that this proportion can change with field.

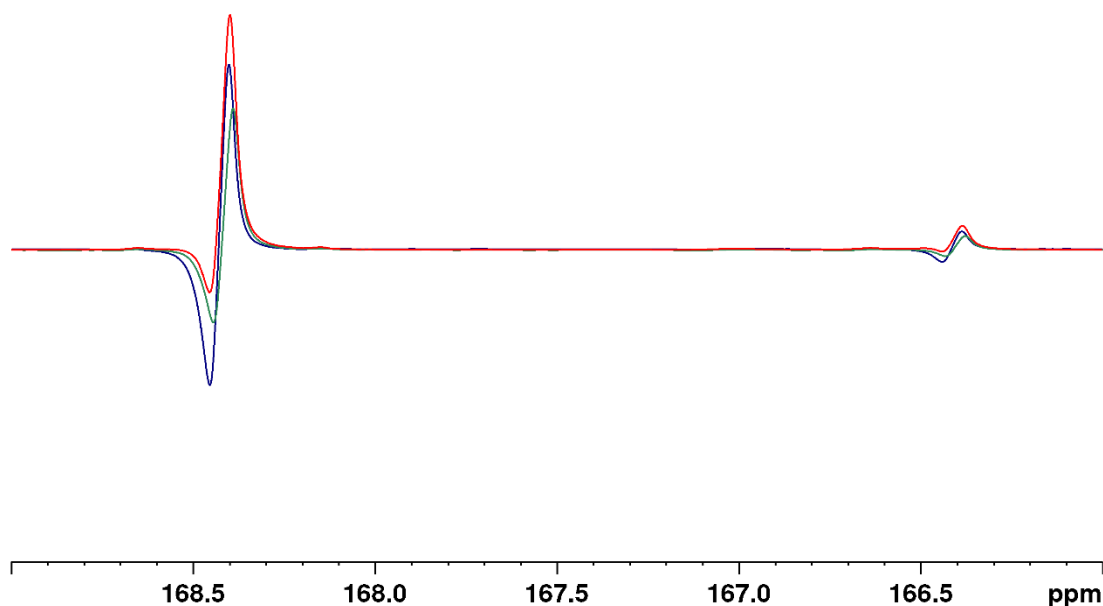


Figure 6.14: SABRE hyperpolarised ^{13}C signal from a sample containing ^{13}C nicotinamide and $[\text{IrCl}(\text{COD})(\text{X})]$ (5mM) in a 10 to 1 ratio in methanol- d_4 with 3 bar G of $p\text{-H}_2$ using different polarisation transfer fields: mu metal shield, 8-fold signal enhancement (red), -2mG, 18-fold signal enhancement (green) and -9mG, 24-fold signal enhancement (blue).

The signal gain for both of these terms relative to the Boltzmann derived response indicates an 8 to 24-fold enhancement (0.009% - 0.025%). Hence, the efficiency of direct transfer to ^{13}C was confirmed to be low.

A better potential route to polarising ^{13}C could be through transfer via hyperpolarised protons. INEPT (insensitive nuclei enhanced by polarisation transfer) is a pulse sequence, originally created to do this, thereby increasing the signal intensity of low gyromagnetic ratio nuclei (e.g. ^{13}C).⁶⁵ An INEPT protocol was used with refocusing for multiplicity and decoupling. The ^1H NMR polarisation levels of the protons on the ^{13}C labelled nicotinamide achieved reached 1.24% in methanol- d_4 and 0.9% in ethanol- d_6 (10 s shaking time). As the overall aim was to try to image *in vivo*, the “more biocompatible” ethanol- d_6 was chosen as the solvent for further optimisation.

A coupling of 20 Hz was used to set the evolution delay to transfer this magnetisation to ^{13}C . A series of experiments were then carried out to see how the signal intensity changed with shaking time. The optimum shaking time was found to be 40 seconds in terms of S/N, however 50 seconds in terms of signal enhancement (see Figure 6.15 a). This discrepancy can be explained in that S/N is calculated from the maximum peak value and signal enhancement from the area under the

curve. S/N is more relevant to MRI. After consecutive shake and drops when the peaks may become wider this may result in slightly differing trends.

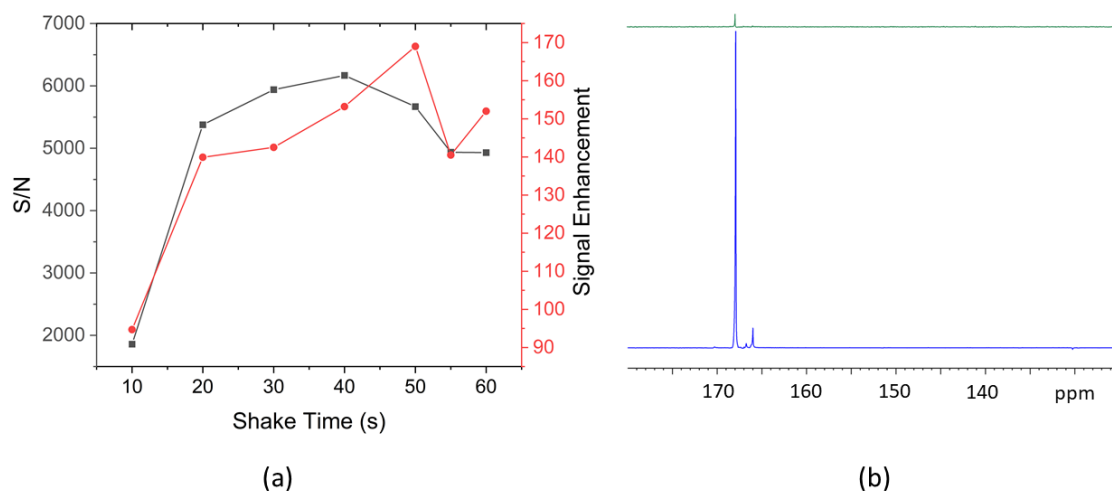


Figure 6.15: ^{13}C nicotinamide and $[\text{Ir}(\text{COD})\text{Cl}(\text{X})]$ (5 mM) in a 10 to one ratio in ethanol- d_6 with 3 bar(g) of *p*- H_2 . (a) Signal to noise ratios (black) and signal enhancement (red) at different shaking times using SABRE (b) Hyperpolarised ^{13}C signal resulting from a 50 s shake and drop experiment giving S/N = 5667 and signal enhancement = 169 (0.17% polarisation). Thermal signal is vertically multiplied $\times 2$ (green) to be seen alongside the hyperpolarised signal (blue).

The ^{13}C signal enhancement level (following INEPT transfer) for labelled nicotinamide in ethanol- d_6 was calculated as 169 using a 50 s shake time, which is equivalent to 0.17% polarisation (based on INEPT thermal data). A comparison of the thermal signal and the hyperpolarised signal can be seen in Figure 6.15 b. The polarisation measured with *d*-DNP was 13.5%, 70 times this observed SABRE value.

It was assumed that ^{13}C SABRE polarisation was low because initial proton polarisation values (0.9% in ethanol- d_6) were low. Much higher levels of ^1H polarisation in nicotinamide have been achieved in ^1H SABRE by selectively deuterated positions within the aromatic ring. In 4,6- d_2 -nicotinamide 2.0% polarisation was measured on H2 and 2.1% on H5 (in ethanol- d_6). In the parent nicotinamide only 1.1% and 0.1 % was achieved respectively.¹³⁵ However, these substrates were not available in a ^{13}C labelled form.

There will of course be some natural spin diffusion/thermal mixing or NOE transfer of polarisation from ^1H to ^{13}C sites. A final investigation looked at this natural transfer. The results showed surprisingly that better signal enhancement values were achieved without the use of the INEPT sequence. The resulting signal enhancement was subsequently estimated to be 211 ± 7 at

40 second shake time compared with 144 ± 9 using the INEPT sequence. The signal appears as an in-phase doublet thereby revealing that Zeeman polarisation is created.

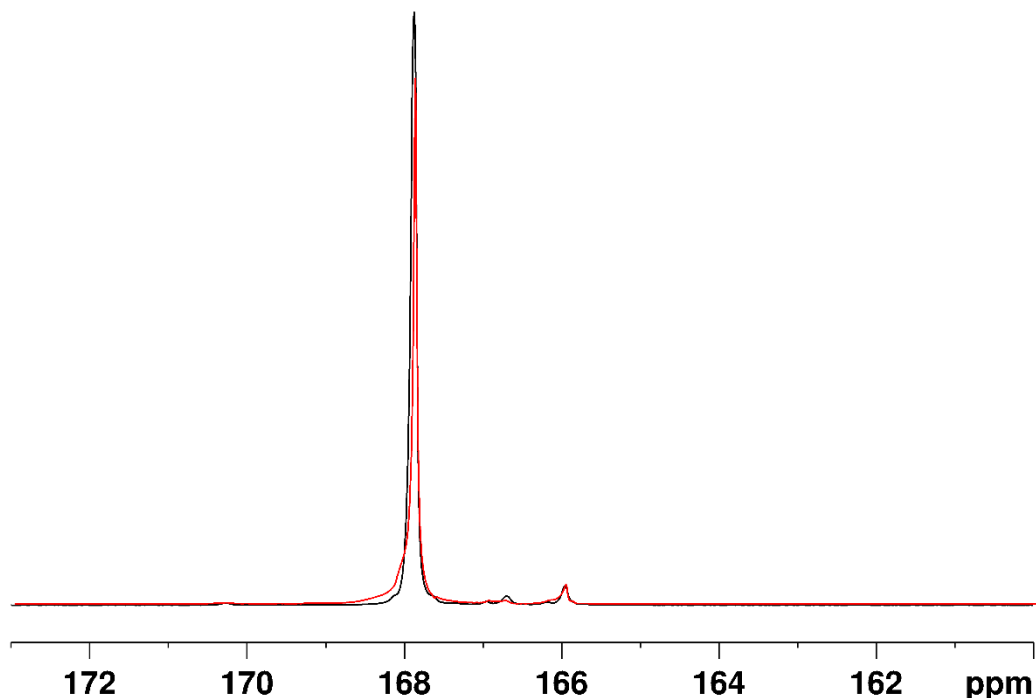


Figure 6.16: Ir(COD)Cl(X)] (5 mM) with 10 eq. of ^{13}C nicotinamide with SABRE PTF 60G (black) 211 ± 7 fold signal enhancement (based on thermal shake and drop experiment) and SABRE INEPTRD 60G (red) 144 ± 9 fold signal enhancement (based on thermal INEPTRD experiment).

Signal to noise is the defining factor in any measurement. It relates to polarisation level and concentration. As SABRE is a complex process, utilising the finite level of *p*-H₂ in the sample as the source of polarization, the two terms will not vary linearly. Hence there is a need to probe the S/N as a function of concentration. Two samples were prepared to test this involving 10 and 20 equivalents of substrate relative to a 5 mM precatalyst loading. These yielded almost identical S/N ratios or 7236 and 6999 respectively (Figure 6.17) and hence suggest that *p*-H₂ excess dominates in rapid measurements. However, the *T*₁ of the 20 equivalent sample should be longer and therefore ultimately this sample will result in a stronger signal at a fixed measurement time.

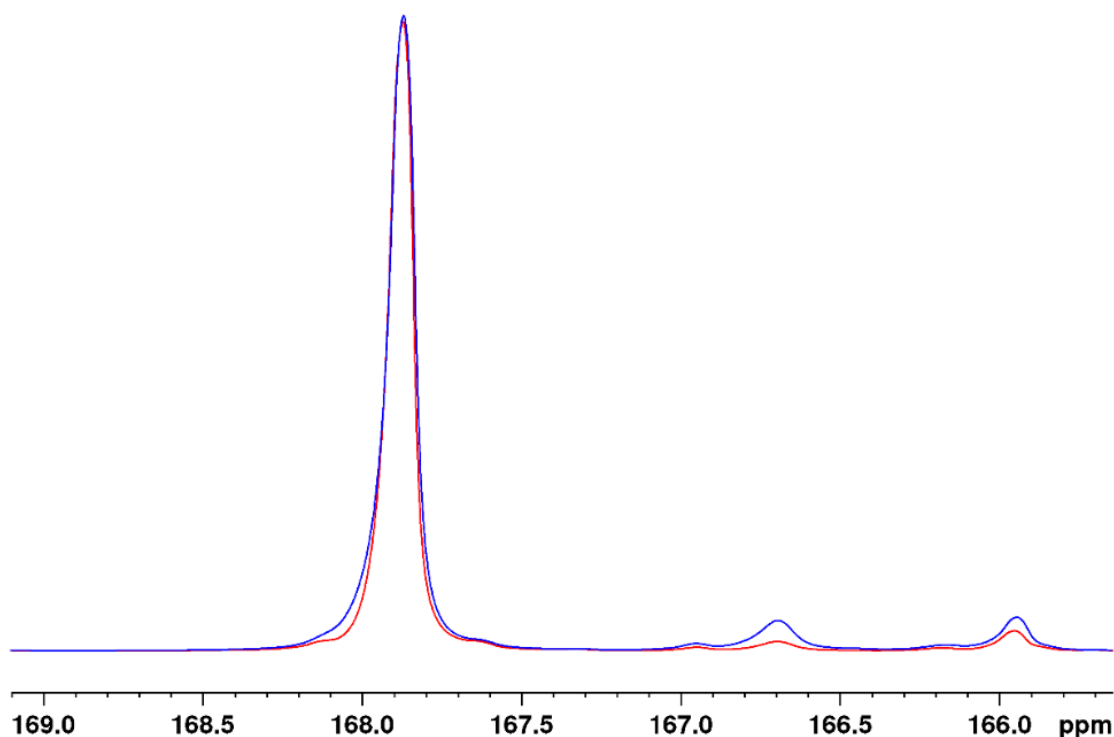


Figure 6.17: Comparison of hyperpolarised ^{13}C signals resulting from 40 s shake and drop experiments using $[\text{Ir}(\text{COD})\text{Cl}(\text{X})]$ (5 mM) with 10 eq. (blue) and 20 eq. (red) of ^{13}C nicotinamide in ethanol- d_6 at 60 G and 3 bar of $p\text{-H}_2$.

6.5.2 MRI/S

9.4 T Clinical Scanner

FISP (hyperpolarised and thermal), CSI and EPSI sequences were each carried out on the SABRE ^{13}C nicotinamide sample at 9.4 T. The FISP sequence (Figure 6.18 a hyperpolarised and b thermal) was not the optimum imaging sequence to use here. Only a 4-fold increase in S/N was found compared with the 500-fold increase in S/N for the ^{13}C nicotinamide *d*-DNP sample. Both the CSI and the EPSI work well (Figure 6.18 c and d) with the latter giving higher resolution. However, Nyquist ghosting is present once again resulting in an additional peak in the spectrum at 200 ppm (Figure 6.18 d spectrum).

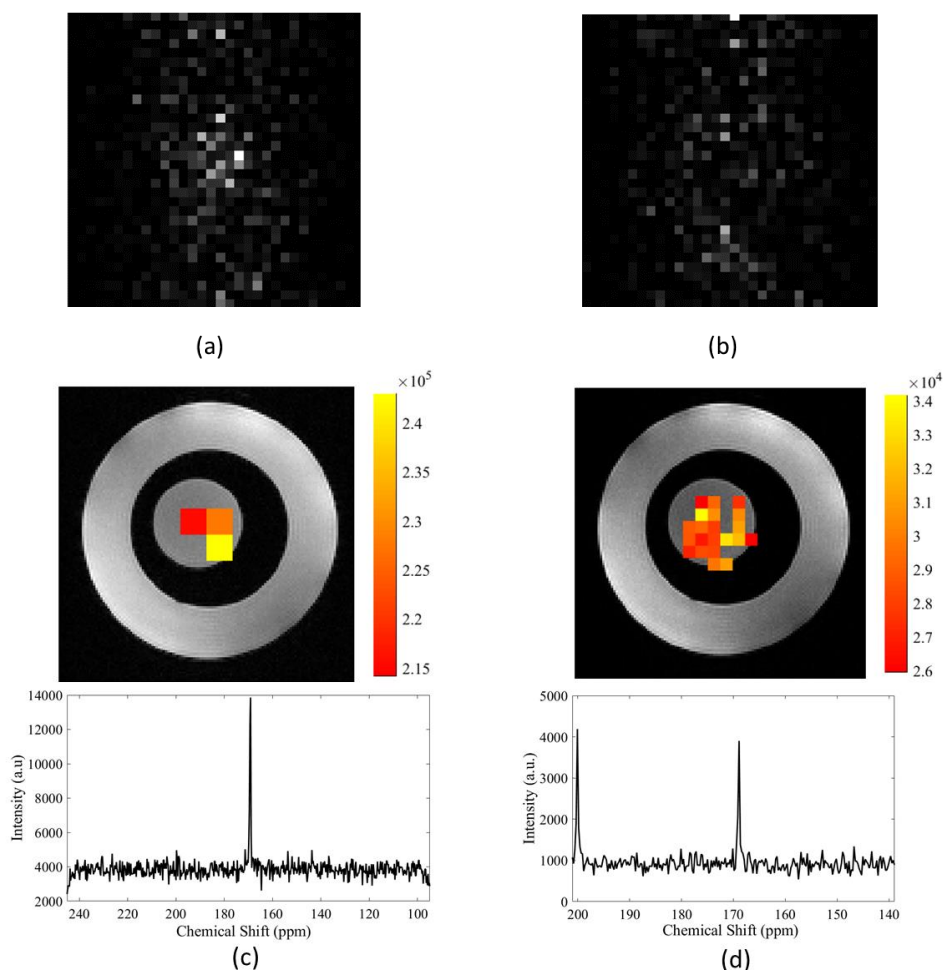


Figure 6.18: Images of SABRE hyperpolarised ^{13}C nicotinamide using $[\text{Ir}(\text{COD})\text{Cl}(\text{X})]$ (5 mM) with 10 eq. of ^{13}C nicotinamide in ethanol- d_6 at 60 G and 3 bar(g) of *p*- H_2 . (a) FISP hyperpolarised image. (b) FISP thermal image. (c) CSI image with corresponding spectrum of ^{13}C nicotinamide peak. (d) EPSI image with corresponding spectrum of ^{13}C nicotinamide peak revealing Nyquist ghost peak at ~ 200 ppm.

3T Clinical scanner

To test imaging potential at clinical field strength, ^{13}C nicotinamide (protonated) samples were analysed using a Siemens 3T MRI scanner. Imaging setup included a 1M acetic acid ^{13}C reference (178 ppm), a H_2O proton reference and a tube housing the 10 mm Young's containing the polarised sample, surrounded by H_2O to ensure good, automated shimming.

In-line with *d*-DNP measurements (Section 6.4) i) non-localised single pulse experiments and ii) CSI spatial mapping were completed. Unfortunately, due to the solvent used (100% ethanol- d_6) only *in-vitro* phantom studies could be completed.

i) 5° flip angle single pulse experiments were repeated (TR = 200, Repetitions = 512). ^{13}C signal from both the acetate phantom and hyperpolarised nicotinamide were observed (Figure 6.19 a).

The nicotinamide peak/decay curve at 168 ppm was integrated and T_1 estimated (Figure 6.19b). A T_1 of 14.5 s resulted after accounting for RF attenuation despite the presence of the catalyst, in agreement with previous measures using *d*-DNP.

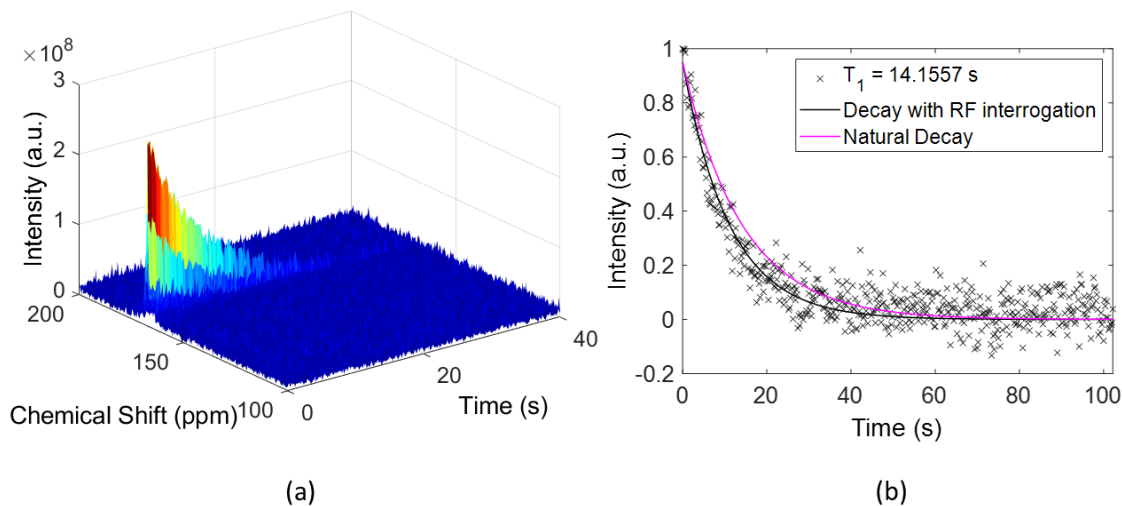


Figure 6.19: (a) ^{13}C 3D decay of ^{13}C nicotinamide under SABRE conditions (shaking at 60 G) measured at 3T. (b) Estimated T_1 calculation of decay = 14 s.

ii) Spatial mapping utilising a CSI approach is shown in Figure 6.20. Mapping was assessed across different spatial resolutions. In all cases a detectable signal was observed and located appropriately.

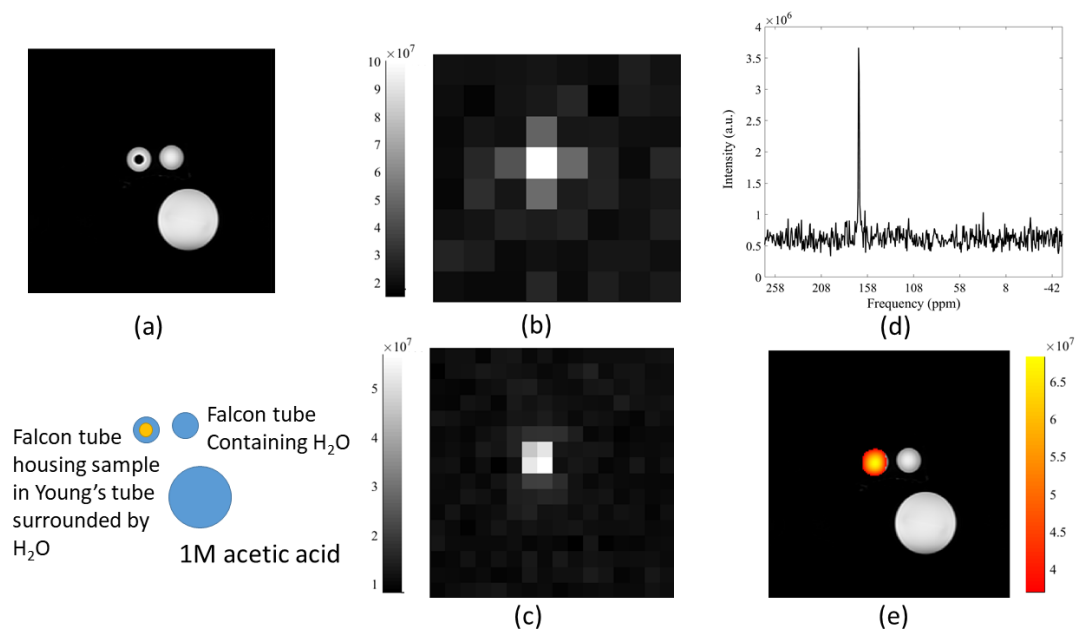


Figure 6.20: Images of SABRE hyperpolarised ^{13}C nicotinamide using $[\text{Ir}(\text{COD})\text{Cl}(\text{X})]$ (5 mM) with 10 eq. of ^{13}C nicotinamide in ethanol- d_6 at 60 G and 3 bar of *p*- H_2 at 3 T. (a) ^1H reference scan including sketch of set up. (b) CSI raw data using 8 x 8 voxels, (c) CSI raw data using 16 x 16 voxels, (d) spectrum from CSI showing ^{13}C nicotinamide hyperpolarised peak. (e) overlay of CSI (using 16 x 16 voxels) on ^1H reference scan with interpolation (8x).

In line with NMR findings, novel implementation of INEPT on the 3T Siemens system provided no increase in signal magnitude (data not shown).

6.6 Conclusions and Discussions

This is the first time a quantitative comparison between SABRE and DNP has been completed for NAM. d-DNP is now being used in the clinic for *in vivo* metabolic mapping with MRI. This technique delivers high levels of polarisation on X nuclei and therefore is a useful benchmark against which to compare SABRE data. d-DNP benchmarks show that detection of ^{13}C nicotinamide is possible *in vivo* with polarisation levels of ~ 13% and an apparent T_1 of 14 s (7 T MRI). For d-DNP the optimum formulation found was a 70:30 water: glycerol ratio with 50 mg of nicotinamide. For SABRE the optimum formulation found to date was found to be 5 mM of $[\text{IrCl}(\text{COD})(\text{X})]$ with 10 eq/20 eq of ^{13}C nicotinamide in ethanol- d_6 . Equivalent SABRE metrics are 0.17% and 14 s (3T).

This study demonstrates that for ^{13}C nicotinamide, polarisation levels achieved with d-DNP were over ten times higher than those achieved with SABRE. ^{13}C labelled nicotinamide on the carbonyl carbon would not be the optimum molecule of choice for SABRE as the ^{13}C labelled carbon of interest is distant from the nitrogen binding site. In terms of receiving the most polarisation, the aryl carbons in the 2 or 6 positions adjacent to the nitrogen binding site would undoubtedly be more favourable especially if relying on spin transfer from the proton.

Interestingly, SABRE studies found that there was no need for complex low field polarisation transfer measurements or INEPT sequences and that simply shaking at the optimum PTF for ^1H (60 G) gave similar values to those achieved with INEPT.

Upon considering the toxicity of the two different methods, d-DNP has the obvious advantage of the formulation and dissolution solution being water/glycerol and phosphate buffer solution (all of which are biocompatible). With SABRE, measurements here were made using 100% ethanol- d_6 solvents. Such solvents are not biocompatible and would need replacement. A biphasic system¹³⁸ could be considered (introduced in chapter 5); however the potential 70% reduction in signal enhancement level (compared to the corresponding data using methanol- d_4 as the solvent – as evidenced with T[2,3- d]P) would limit detection, especially *in-vivo*. Subsequent extraction of the hyperpolarised aqueous layer would also incur time constraints and would lead to further reduction in measurable polarisation levels.

At the 13.5% polarisation levels achieved with d-DNP it was possible to detect ^{13}C labelled nicotinamide *in vivo* in a murine cancer model and observe the ^{13}C nicotinamide signal distribution within the body and in the tumour. Polarisation levels of ^{13}C nicotinamide with SABRE were not sufficient to conduct *in vivo* studies but were observed *in vitro* using CSI and EPSI. The only published imaging data on PHIP based polarisation techniques is PHIP-SAH for pyruvate which was completed at 3.5% polarisation.¹¹¹

Unfortunately, even with d-DNP methods, only a single peak was detected *in vivo*. No peaks arising from metabolic derivatives were observed such as the catabolic conversion of NAM to NAD. This could limit application of this substrate. In metabolic profiling it is typical for faster catabolic reactions such as the conversion from pyruvate to lactate to be detected.

An optimised shimming strategy could reduce signal broadening and possibly reveal hidden peaks. Selective deuteration at the 2 and 4 position showed an increase in T_1 to 31 s. With deuteration of all proton sites combined with the use of deuterated solvents both in the aliquot and in the dissolution solution this magnetic lifetime could be extended even further. This could also lead to higher levels of ^{13}C polarisation. With an increase in polarisation and a longer observable window of time it may well become possible to observe relevant biochemical changes. Further analysis of T_1 effects could be envisaged when NAM is converted into the much larger molecules of nicotinamide mononucleotide and nicotinamide adenine dinucleotide. However, it is recognised that the anabolic reactions required to form these are slower than catabolic reactions.³⁴⁷

In the future, even in the absence of metabolic fingerprints ^{13}C nicotinamide could be used as perfusion agent, like urea.³²⁷ Without deuteration the T_1 is not quite as long as that of urea but a full deuterated version could offer a longer time constant. The advantage of using nicotinamide as a perfusion agent is that it has the ability to pass the blood/brain barrier³⁵⁰ and is harmless as it would be essentially a vitamin B injection.

The magnetic lifetime of 14 s *in vivo* is relatively short compared with existing probes (e.g. pyruvate 30-40 s *in vivo*^{72,97}). Selective deuteration was explored as a route to extend lifetime and it was found that deuteration in positions 2 and 4 immediately adjacent to the labelled carbonyl carbon had the greatest effect. Whilst lifetime was nearly doubled it is unknown if polarisation would remain the same in a ^{13}C labelled version.

The results show that the SABRE method can be used to successfully give hyperpolarised ¹³C *in vitro* images through chemical shift imaging. One of the main advantages of using ¹³C is the lack of any background signal due to water. The disadvantage is that ¹³C labelling can be expensive and synthetically challenging to do (as was the case for the target thienopyridazines). However, when compared with d-DNP, polarisation is significantly lower with the optimisation steps taken to date and the results shown here are still not in a biocompatible solution. Further optimisation steps could be taken by trying different catalysts, increasing *p*-H₂ pressure, using co-ligands etc. Traditional SABRE relies on the substrate being able to bind to the catalyst which limits the range of applicable metabolites. Using co-ligands and the new SABRE relay method involving proton exchange has extended the range of molecules that can be polarised using SABRE including pyruvate.^{241, 243}

The difficulties encountered studying these molecules by d-DNP, highlight the method is time consuming and expensive as there is significant waste even when the experiment is successful (only 0.4 mL was used for injection out of a total of 6 mL). The one-shot nature of d-DNP means that if there is a technical fault the whole ~ 2-hour process needs to begin again wasting time and 50 mg of expensive ¹³C labelled material. The Hypersense is undoubtedly an impressive piece of engineering able to handle extremes of temperatures but inevitably there are often technical problems that arise. When comparing with the SABRE method the relative simplicity of the experiment, the reduced costs involved and the ability to polarise within a matter of seconds (40 s as opposed to 1.5 h) can only be viewed advantages over the established d-DNP method.

Chapter 7: Conclusions and Outlook

NMR and MRI play a vital role in science, industry and medicine⁶⁰; but under standard Boltzmann (thermal) conditions only use a minute fraction of their potential signal. Cutting-edge hyperpolarisation technologies^{3, 5, 108, 109, 111, 112} can open up new applications via non-destructive manipulation of quantum spin state populations. Indeed, in the field of biomedicine, d-DNP is emerging as leading methodology for real-time in-vivo metabolomics^{4, 6, 7, 72} (with a particular focus in oncology and cardiology). Unfortunately, wider clinical uptake is currently limited by high equipment costs (£1M+) and long polarisation build-up times. It is recognised that hyperpolarisation is still a relatively new field and that there are still many advantages to thermal NMR/MRI.

It has been previously demonstrated that SABRE is an alternative and promising hyperpolarisation approach.^{112, 130, 132, 135} Unlike d-DNP, SABRE provides a simple, rapid and inexpensive route, capable of polarising a wide range of molecules containing NMR active nuclei (¹H, ¹³C, ¹⁵N, ³¹P). The fast polarisation build-up and reversible nature of the SABRE process means that potential hyperpolarised probes can be produced in a continuous nature as opposed to a batch/single-shot mode. This approach, alongside the use of low-field portable detectors, can empower reaction monitoring of industrial processes.^{125, 132, 133}

This multidisciplinary project concerned the initial research and development stages for creating novel SABRE hyperpolarised probes for future *in vivo* clinical based Magnetic Resonance Spectroscopy (MRS) rollout. Methods for the optimisation of this catalytic process for thienopyridazines (motifs found in some anti-cancer drugs¹⁶¹) were implemented. Novel ¹⁵N labelling was used to identify eight SABRE active complexes formed aiding future optimisation of this catalytic process. The presence of a ¹⁵N singlet state was also demonstrated, however further work would be required to optimise the storage field. Following optimisation, the functionalisation of SABRE hyperpolarised thienopyridazines were tested across a range of MRI field strengths – from clinically relevant 3 Tesla up to high field (9.4 T+). Furthermore, next generation SABRE methods cascading polarisation from *p*-H₂, *via* an *N*-heterocyclic substrate, to platinum-phosphine complexes were developed, and resulted in strong ³¹P signal detection. Together data support that, with continued on-going development, SABRE has the potential to aid clinical diagnosis and complement PET/CT for metabolic profiling.

7.1 Key findings

For any MR hyperpolarisation study, one aims for the highest achievable polarisation level (or signal enhancement) coupled with the longest magnetic state lifetime; to give the largest possible window of NMR/MRI observation. For clinical MRI one must also consider biocompatibility.

7.1.1 Polarisation level

Here, for the first time, a group of synthesised thienopyridazines were hyperpolarised using the Signal Amplification by Reversible Exchange (SABRE) technique. Through an extensive optimisation process (see below), ^1H signal enhancement for T[2,3-*d*]P of -10,130-fold \pm 230 (H7) was achieved over those obtained under Boltzmann conditions (which equates to 33% polarisation). Maximum ^1H longitudinal (T_1) lifetimes were found to be 38 s (H7 without catalyst) and 10 s (H7 with catalyst). On a structural basis the thienopyridazines were interesting molecules because of the presence of the sulfur and nitrogen nuclei. Here hyperpolarised NMR data proved that binding to the catalyst was exclusively through the nitrogen sites. This has implications for the design of future target substrates.

Targeting ^1H as the probe nucleus (as opposed to ^{13}C or ^{15}N) is beneficial because it (i) has the highest gyromagnetic ratio of all nuclei and therefore high NMR sensitivity; (ii) has a 99.98% natural abundance (negating the need for expensive/complicated synthetic pathways to generate the agents); and (iii) can be used with existing clinical ^1H MRI systems without the need for expensive hetero-nuclei RF coils/system upgrades.

Results showed that through optimisation of PTF, substrate to catalyst ratios, nature of the carbene on the iridium catalyst, increased *p*-H₂ pressure, and deuteration of both the carbene and co-ligand lead to increased polarisation levels with 33% (H7) recorded for T[2,3-*d*]P. Whilst use of a handheld magnetic array²⁰⁶ enabled polarisation at a precise PTF, resulting in more reliable and increased signal enhancements, there are practical limitations to using these (e.g. increased weight for manual shaking). In addition, data demonstrated a linear relation between enhancement and *p*-H₂ pressure. However, care must be taken when using high pressure H₂. While pressure is not substrate specific the other optimisation steps are. To date a large body of work has been carried out however it remains difficult to establish optimum conditions for specific substrates without completing optimisation studies like those described here.

It is noted that while achieving 33% polarisation for T[2,3-*d*]P represents an impressive increase in potential sensitivity for *in-vivo* detection, the reduced magnetic lifetime of the compound in

the presence of the catalyst (9 s H7 at catalyst:substrate ratio of 1:4) is a limiting factor. Furthermore, these levels of polarisation were achieved in a methanol- d_4 solvent which is toxic and not suitable for subsequent *in vivo* injection.

7.1.2 Magnetic Lifetimes

To extend T_1 lifetime and ease detection, long-lived state (LLS) pulse sequences were implemented to force spins into pseudo-singlet states, bypassing dipole-dipole relaxation, and storing the polarisation for longer.²¹⁰⁻²¹² 3,6-substituted pyridazines were used as a simple proof of principle model to demonstrate LLS application. Neighbouring ^1H nuclei in three pyridazine based molecules could be extended to up to three times their individual T_1 lifetimes. 3-Chloro-6-methoxypyridazine having already substantial individual T_1 values of 31 and 29 seconds yielded a T_{LLS} value of over 100 seconds. However, SABRE hyperpolarisation of these pyridazines molecules was found to be limited or non-existent (under the transfer conditions used).

The long-lived singlet state pulse sequence was applied to the target thienopyridazines. Only one of the regioisomers (T[2,3- d]P) showed an extension in magnetic lifetime in the proton pair of interest (between H2 and H3 from T_1 of 18 and 28 s to T_{LLS} of 40 s). Although there was an increase it did not extend the overall lifetime of the molecule as H7 already exhibited a 40 s T_1 . It was recognised that a potential pathway to further relaxation could exist if protons of the singlet state pair are scalar coupled to other protons within the same molecule.

A novel doubly labelled ^{15}N version of T[2,3- d]P was successfully synthesised and through a series of long range and short range HMQC experiments the existence of the eight SABRE active complexes were confirmed. This reflected the two possible binding sites of T[2,3- d]P to the SABRE catalyst and the unsymmetrical nature of the substrate. Data demonstrates that upon binding, the catalyst breaks the symmetry of the thienopyridazine ligand giving for the first time definitive proof of the existence of the singlet state (all ^{15}N signals were readily visible). This data adds to our fundamental understanding of SABRE chemistry.

Novel synthetic steps were also taken to synthesise the fully deuterated version, d_4 -T[2,3- d]P- $^{15}\text{N}_2$, in an effort to increase polarisation levels and increase magnetic lifetimes. Hyperpolarisation at -7 mG showed a large signal enhancement of -8291 (2.7% polarisation and S/N 2697.16) compared with -2167 (0.71% polarisation and S/N 1063.80) for the non-deuterated version. Interestingly the existence of a singlet state was observed in $^{15}\text{N}_2$ -thienopyridazine however further work would be needed to optimise the SABRE conditions (in particular the correct storage

field for the singlet state). Recent research into ^{15}N signal enhancements has shown that the use of a co-ligand in the form of d_9 -benzylamine³⁵¹ could also potentially increase the ^{15}N polarisation levels that were achieved here.

7.1.3 Biocompatibility & Imaging Potential

While SABRE has proven to deliver high levels of polarisation^{135, 140} across a range of molecules, often this is within organic solvents (for increased dissolution of both $p\text{-H}_2$ and the Ir based catalyst) not suitable for biomedical use. A biphasic approach, SABRE-CASH¹³⁸ was explored to extract the hyperpolarised T[2,3- d]P into a D_2O saline bolus. A hyperpolarised signal was successfully observed in the aqueous layer; albeit under acidic conditions (pH 1.5) with a reduced level of polarisation (940-fold signal enhancement, 3% polarisation for H7) compared with those in methanol- d_4 (3142-fold signal enhancement, 9.8% polarisation for H7. N.B. without the presence of a coligand and at 3 bar (g) $p\text{-H}_2$). This represented a 60% reduction in SABRE polarisation efficiency; it is hypothesised that this is mainly reflective of the extra preparation time required for phase separation. Although the biphasic route appears to be an effective route to biocompatible SABRE there are alternative methods to consider including the use of water-soluble catalysts,^{139, 266-268} and phase extraction using scavenging agents²⁷¹ or chelating ligands.²⁶³

Although absolute polarisation was reduced, biocompatibility of the extracted aqueous layer was confirmed through an in-depth cytotoxicity assays on two cell lines (MCF7 and A549). Results showed that there was no cell toxicity caused by the aqueous layers at T[2,3- d]P concentrations <3.6 mM. At concentrations of >10 mM of T[2,3- d]P cell death was evidenced but it was not confirmed if this was a direct cause of contamination in the aqueous SABRE layer or the actual anti-cancer properties T[2,3- d]P.

Data show that SABRE-CASH is a potential promising route to eventual clinical application of hyperpolarised T[2,3- d]P; however it is recognised that polarisation levels would have to increased further to make this a reality (see below).

Due to the reduction in polarisation levels in the SABRE-CASH preparation, proof of concept magnetic resonance spectroscopy/imaging utilised standard SABRE with a methanol- d_4 solvent. Imaging potential of ^1H polarised T[2,3- d]P was showcased across a range of valid field strengths (3 - 9.4 T) and pulse sequences. In all cases, following SABRE hyperpolarisation there was dramatic improvement in *in-vitro* detection potential compared to thermal base imaging. ^1H Spectroscopic imaging, to identify the multi peaks within hyperpolarised T[2,3- d]P used both

Chemical Shift (CSI) and Echo Planar spectroscopic Imaging (EPSI). Total acquisition time under CSI was long (74 s) compared with the estimated maximum T_1 value (~40 s). Although a centric encoding approach was used, resultant images remained low resolution and qualitatively blurred (spatial resolution ~ 2.2 mm²). EPSI was implemented to demonstrate that this problem could be overcome (by using alternating gradients to achieve simultaneous encoding for both chemical shift and space). Total scan time was reduced to ~6 s and spatial resolution was ~0.5 mm², images were sharper and better resolved than CSI equivalents. Note there was a slight reduction in spectral resolution (18 Hz/pt across 15 ppm, versus 15 Hz/pt across 30 ppm) but also images were confounded with N/2 Nyquist ghosting (due to the fast switching gradients). Moving forward with ¹H, EPSI is ideal for SABRE, but it is recognised that advanced post-processing (phase correction of interleaved gradient directions) is required to fix such ghosting artefacts.

Following successful *in-vitro* detection, *ex-vivo* detection in a rodent model was only possible on a 2 mL large bolus injected into the subcutaneous space in organic solvent. Again, detection in saline was not possible due to the low polarisation levels (see above). In all cases the vast background signal from the water pool was identified as one of the main difficulties for hyperpolarised ¹H imaging. Although there are many water suppression sequences used in thermal MRI, the use of RF to attenuate the signal could result in unwanted attenuation of the hyperpolarised signal (water suppression in MRS is usually only possible on small, localised voxels after extensive shimming procedures).

It is noted that the above concept imaging studies did not utilise a fully deuterated co-ligand (which delivers the highest polarisation levels). Synthesis of the fully deuterated ligand was only completed on a small scale. Synthetic protocols to increase yield would have to be developed; but this would increase the overall cost of the technique and so may not be ideal. A cost benefit study would be required.

7.1.4 Benchmarking

For the first time ¹³C labelled nicotinamide (NAM) was polarised and imaged using two hyperpolarisation techniques, both SABRE and d-DNP. Results from this study allow benchmarking of SABRE against an established technique already finding footing in a clinical forum. *In vitro* imaging was conducted using both methods however only with d-DNP was polarisation high enough (13%) to allow *in vivo* imaging in a murine cancer model. *In vitro* images were obtained with SABRE however polarisation was inferior (0.17%) to those obtained with d-

DNP. In terms of lifetime, an apparent T_1 of 14 s, combined with 13% d-DNP polarisation was sufficient to observe a NAM response in tumour tissue using single pulse and CSI based MR acquisition. However, it is noted that no metabolic mode of action was observed (i.e., no peaks for other metabolites beyond the injected NAM were recorded). It is recognised that conversion of NAM is slower than the usual catabolic reactions observed with d-DNP.⁷² However, metabolic derivatives for NAM (δ 171 D₂O) are of similar chemical shift (carbonyl carbon for NAD = 167.8 (D₂O), NADPH = 175.5 (D₂O) and Nicotinamide N-oxide = 168.2 (D₂O)) and even at 9.4 T spectral resolution in terms of FWHM (1.21 ppm) is poor due to shimming.

While this result was disappointing it iterated that NAM can also be used as a hydrotrope. NAM improves the solubility of many water-insoluble drugs, including diazepam, testosterone and progesterone.³¹⁷ Therefore MRI detection of NAM as a solvent hydrotrope could aid future drug delivery/distribution based studies.³⁵²

From the data presented here it can be concluded that d-DNP excels in ¹³C polarisation of labelled nicotinamide. To date no SABRE study has matched the polarisation potential of d-DNP for X nuclei but SABRE still excels in ¹H polarisation. Literature reports of ¹H d-DNP state only 600 fold enhancements.³⁰³ However it is noted, as an additional benchmark, that d-DNP polarisation build-up time took ~ 1 hour. SABRE polarisation build-up is rapid (tens of seconds). If SABRE polarisation levels can be increased (on X-nuclei) to the 13% mark (see below) then on build-up time alone SABRE can potentially supersede d-DNP. It is clear that there are advantages and disadvantages of both methods of hyperpolarisation discussed here. There are also advantages and disadvantages of ¹H over X nuclei. Either way hyperpolarisation has interesting application not only in the medical field³⁵³ but across a range of industry also.¹²⁶ It is the reversible nature³⁵⁴ of SABRE that makes it ideal for industrial NMR application. Hence continued research and development is essential.

7.1.5 Next generation catalysis for polarisation transfer

A final investigation developed a novel technique to relay polarisation to a second metal catalyst and thus to widen the range of ligands accessible to SABRE hyperpolarisation.¹⁶⁸ Polarisation was cascaded from the source *p*-H₂, via the traditional SABRE iridium catalyst, through a substrate intermediate to a remote ligand (dppm/dppe and dppp) on a platinum complex. It is noted that this platinum complex is not directly involved in the *p*-H₂ hyperpolarisation step (confirmed with NMR). Hyperpolarisation of a substrate (pyrimidine, pyrazine, methyl

nicotinate) through traditional SABRE followed by displacement of one or both of the labile ligands on a second complex with the hyperpolarised substrate and subsequent relay of polarisation onto ^{31}P nuclei within the fixed ligand on the second complex. The whole process was achievable in a matter of seconds in a one shot experiment producing hyperpolarised ^{31}P signals with clearly visible platinum satellites and S/N of up to 99 (using methyl nicotinate as the substrate). Substrates with high polarisation and long lifetimes (like 4,6- d_2 -methyl nicotinate) proved to be the most effective in relaying the polarisation. The major finding of this study was that the process could be carried out under simple SABRE conditions at a PTF of 65 G. Furthermore data confirmed that the creation of a singlet state in the hyperpolarised substrate was not a requirement for the SABRE-relay process to take place (as was previously hypothesised);¹⁶⁸ but a long T_1 combined with high polarisation was favourable.

7.2 Relevance

On a wider level hyperpolarised imaging has proven to be a powerful tool in many pre-clinical studies and clinical trials.^{4,7} It is non-radioactive (compared with its main competitor PET), and non-toxic (as synthetically made endogenous metabolites are used). Due to these characteristics, it could be used routinely and regularly at all stages of disease (i.e early detection, screening of drug effectiveness and as a tool for distinguishing necrotic from healthy tissue).

To date only d-DNP hyperpolarised imaging has transferred to the clinic. Its great strength lies in the fact that it achieves high polarisation levels (of 50% or more) which consequently result in large signal enhancements and make tracking of metabolic flux in tumours a realistic possibility.^{4,7} It can be applied to a broad range of nuclei and chemical motifs but there are still several limitations to the process that may prevent it from becoming a routinely used tool by clinicians. The first is that there is a significant infrastructure cost involved. Not only is there the initial expense of the polariser itself (SPINlab clinical polariser ~£1M) but there is the high running cost, particularly the vast quantities of helium required.⁹³ This problem is in part being solved by the invention of polarisers, which recycle the helium they use^{355,356} and the recent Covid-19 pandemic allowing global stocks to be replenished.³⁵⁷

The ^{13}C labelled metabolites used are expensive to buy (e.g., pyruvic acid £1/g, ^{13}C pyruvic acid £474/g) and can be difficult to synthesise (e.g., use of ^{13}C labelled CO gas in the synthesis of ^{13}C nicotinamide). The high concentrations and large volumes that are required accentuate this problem. Alternatives to make this process more cost-effective are required.³⁵⁸ In pre-clinical

research a significant proportion of the resulting dissolution solution is wasted as only a tiny fraction of it is injected into the animal. The polarisation build up is time-consuming even with the addition of gadolinium chelates. In this work the build-up still took approximately 45 min to 1 hour. This problem has recently been addressed through implementation of a multi-sample polariser.³⁵⁶ The polariser itself is a complex instrument and although the operation of it is relatively straight forward problems can often arise. Through first-hand experience I have witnessed that the d-DNP can often have technical difficulties which through the knowledge of trained operators may be tackled and overcome but often require the expensive and time-consuming expertise of the manufacturer (Oxford Instruments/GE) engineers. The use of ^{13}C as a probe, which has been the usual probe of choice in DNP, has the advantage that there are no background signals (due to low natural abundance), but it does have several disadvantages (especially for clinical based imaging). The first is that an extra RF transmitters and receivers are required in addition to the standard ^1H channel found on clinical scanners. A more powerful gradient coil system is also required as the gyromagnetic ratio of ^{13}C is a quarter of ^1H . This smaller gyromagnetic ratio also means that the signal-to-noise ratio is lower than for ^1H . Due to the “one-shot” nature of the hyperpolarisation reaction, signal averaging cannot be performed to overcome this. ^1H imaging has however been achieved with DNP using an indirect polarisation method where ^{13}C hyperpolarisation is transferred to ^1H via a reverse INEPT sequence.³⁰⁵

On a practical level SABRE polarisation is a much simpler method compared to d-DNP. The sample (containing the substrate, $p\text{-H=}$ and the Ir catalyst) simply needs to be shaken in the appropriate stray fringe field of the MR system for efficient polarisation transfer. While the process can be automated data show that the current engineering solution results in ~40% reduction in polarisation efficiency and the system requires more work. It is hypothesised that this is due to the inability to de-gas the sample prior to usage.

When manually shaking in the stray field it is difficult to maintain a constant PTF throughout the process. The strength and rigour of shake process and position in the stray field can vary from person to person which all increase repeatability errors. It is noted that there is an increase in SABRE signal enhancement level when moving from shaking in the stray field to using a handheld magnetic array²⁰⁶ at a pre-defined magnetic field. However, even with implementing the magnetic arrays with pre-defined magnetic fields there can still be discrepancies as the strength of the shake can still vary (data not shown). Often the user can do 30-50 shakes a day or may need to shake for long periods such as when polarising carbon (in chapter 6 – 50 s shake was

found to be optimum for ^{13}C nicotinamide) which can be physically demanding and may affect the overall results.

With an aim to translate SABRE to the clinic it is clear that an automated polariser would be required. If the existing automated method cannot at least match the polarisation levels achieved through shake and drop then this presents as a major hurdle.

Leading on from this there also needs to be an automated delivery system²⁹⁷ coupled to the automated polariser. When carrying out SABRE *ex vivo* experiments in chapter 5 it was recognised that over 50 s were required from the end of shaking until the introduction of the hyperpolarised bolus and the start of the imaging. This represented more than one T_1 time for T[2,3-*d*]P and therefore a loss of >63% of the magnetisation. Despite this relatively lengthy process (and consequent loss of signal) to remove excess $p\text{-H}_2$ it still resulted in a large air bubble being created in the subcutaneous layer due to the remaining $p\text{-H}_2$ dissolving out of solution.

In summary, with further research and development built on from this work, direct ^1H SABRE hyperpolarisation could provide a simple, cost effective alternative to d-DNP for clinical applications. All potential imaging agent agents will undoubtedly have multiple proton sites in their structure and therefore not require expensive labelling. Thus, clinical translation should be smooth when/if SABRE polarisation levels are increased (see section 7.3).

It has been observed that with all methods of hyperpolarisation and with all nuclei the limitation of T_1 decay is a major hurdle to overcome. This is especially true for slower metabolic processes like the usage of NAM *in vivo*. Hyperpolarised detection has been proven for fast processes, such as the conversion from pyruvate to lactate, but for wider usage, storage of polarisation by exploiting singlet states should continue to be a future research priority.

Although a broad range of heterocyclic containing molecules had been polarised with SABRE¹¹² it was only with the recent development of SABRE-relay²⁴³ that the process has now been extended to include a much wider range of structures and functionalities. This development now provides a breakthrough for the hyperpolarisation of metabolically relevant endogenous substances, characteristic of disease states. Disease, in particular, cancer, can manifest itself very differently from patient to patient and consequently this is reflected in the often-inconsistent treatment responses to chemotherapy.³⁵⁹ The possibility of early detection and tailor-made treatment with frequent monitoring is an essential and thus far unmet clinical requirement which

hyperpolarised MRI could meet. Whichever route to hyperpolarisation is taken, and in whichever disease it finds its niche, it will aid diagnostics; moving from reactive care to proactive detection will save lives.

7.3 Summary and Future Directions

Here theinopyridazines have been successfully synthesised and polarised for the first time using SABRE hyperpolarisation. In addition, a novel SABRE process for relaying polarisation to a second metal complex, widening the range of target substrates, has been developed. These early stage developments form a solid springboard for continued research and eventual clinical application of this technology. While the challenges for moving towards *in-vivo* application are highlighted in depth (in terms of biocompatibility i.e., removal of the heavy metal catalyst, H₂ gas and organic solvent), the rapid, easy nature of the SABRE process coupled with the high polarisation levels already achieved *in vitro* could now be advanced in the medical field for metabolic testing/profiling of bio-fluids. The ability to identify low concentrations of metabolites in a matter of seconds (using existing NMR hardware) could allow better molecular fingerprinting within biofluids to aid longitudinal assessment of disease.^{126, 360}

For *in-vivo* roll-out, next stage developments should concentrate on increasing the achievable polarisation levels in biocompatible solvents. d-DNP benchmark studies completed here show that *in-vivo* detection with ¹³C polarisation levels of ~13% is entirely plausible. PHIP-SAH demonstrated that 3.5% polarisation was sufficient for imaging but combined with a *T*₁ of 54 s in [1-¹³C]pyruvate. Any agent developed in a bio-compatible solvent should reach these levels before *in-vivo* studies are considered. The polarisation level for ¹H detection may need to be even higher due to the abundant proton pool in body water (unless novel pulse sequencing for whole body water suppression can be established).

Future work to improve SABRE signal enhancement further, could be carried out within the design of the catalyst.¹²³ Synthetic research has been carried out on the carbene IMes introducing electron withdrawing or donating groups at different positions to see how they affect the polarisation transfer.¹²³ Although the best performing catalysts from this study were tried using T[2,3-*d*]P as substrate they did not succeed in making any improvements in terms of polarisation. It is believed that this is because the SIMes carbene backbone is more favourable for T[2,3-*d*]P. If a similar synthetic detailed study could be carried out on SIMes it is possible that the introduction of different functional groups may increase overall polarisation transfer

performance. In terms of catalyst design there is always the problem that there are three vacant binding sites through which the substrate may ligate. In this respect the polarisation is diluted over the spins of three substrates. Here, the use of a deuterated co-ligand demonstrated that with only one protio substrate bound, the polarisation could be channelled solely to this one target, thereby increasing overall signal enhancement. The ideal scenario would be that the catalyst has only one binding site available. It is recognised that selective deuteration of the substrate could have multiple advantages; i) concentrating polarisation in one resonance, ii) increasing T_1 of this resonance and iii) leading to less complicated spectra for imaging. However, synthetic attempts to do so in T[2,3-*d*]P were not successful here (unreported data). Overcoming synthetic problems with selective deuteration are non-trivial and would require more research.

Although the 3,6- substituted pyridazines were not the main target substrates for this thesis it is recognised that they exhibited superior magnetic lifetimes (~ 100 s) using long-lived state strategies. However, SABRE enhancements were poor. Developments in catalyst chemistry and variation (electronically and sterically) of the substituents in the pyridazine molecules could be beneficial for achieving SABRE polarisation.

In terms of X-nuclei SABRE hyperpolarisation, further work could attempt full deuteration of the ^{13}C labelled substrate. Although this may increase sample costs considerably it was observed that even with partial deuteration of ^{13}C -nicotinamide, the lifetime of the carbonyl carbon was extended. One could also consider isotopic labelling the nitrogen site. Barskiy et al (2007) observed that ^{13}C SABRE polarisation in pyridine- ^{14}N was much lower than that achieved with pyridine- ^{15}N . This phenomenon was thought to arise from significant quadrupolar ^{14}N -relaxation in the micro-tesla fields.¹⁴⁶ All avenues should be explored to increase SABRE polarisation, while constantly investigating levels in biocompatible solvents of *in-vivo* application.

Although the focus of this thesis is on *in vivo* applications of hyperpolarised molecules, it is recognised that hyperpolarised NMR is a rapidly growing field of research. In an industrial setting reaction monitoring is an integral part of synthetic design, optimisation and scale up. High field NMR spectrometers (9.4 T +) are both costly to buy and run and considerable space is required to house one. Benchtop spectrometers (1-2 T) are a much cheaper and compact alternative however, these instruments suffer from lower sensitivity. This low sensitivity is confounded by often small amounts of available analyte or when detecting trace impurities for example in the pharmaceutical industry. Hyperpolarisation through a simple method such as SABRE could be

the answer to this insensitivity.¹²⁵⁻¹²⁷ Recent research by Lehmkuhl *et al.* (2020) showed how high resolution ^1H , ^{13}C , ^{15}N and ^{19}F were detected with a single scan in complex, high resolved spectra at magnetic fields between 1 mT and 10 mT.¹³¹ Research by Hill-Casey *et al.* (2019) showed how *in situ* SABRE can be achieved where PT (at a few mT) and detection (at Earth's field) are carried out on a simple, commercially-available Earth's field NMR detector. ^1H polarisation levels of up to 3.3% were reported.¹³²

Since the start of my PhD there has been a considerable amount of research published on SABRE both within the group and externally. Progress has been made to extend the range of possible substrates with the two SABRE-Relay methods and different ways of achieving biocompatible SABRE have been investigated including the CASH-SABRE technique. In this project optimisation was carried out in methanol- d_4 solutions. For future projects involving SABRE hyperpolarised agents for *in vivo* MRI, it would be advisable to start with the now established CASH-SABRE system and optimise conditions from there. When choosing new target molecules, interdisciplinary discussions carried out with medical specialist/biochemists earlier on in the process would provide insight into which key pathways could be successfully monitored in a specific disease process. This is particularly important considering the time constraints with a temporary hyperpolarised state.

This research aimed to satisfy the reader that SABRE hyperpolarisation is an important cost effective imaging tool, offering a wide range of target compounds which have the potential (with further research) to aid clinical diagnosis.

Chapter 8: Experimental

8.1 General Methods

Water is distilled water. Tetrahydrofuran (THF) was dried using a Grubbs solvent purification system. All reactions were carried out using oven-dried glassware. Flash column chromatography was carried out using Fluka Chemie GmbH silica (220-440 mesh). Thin layer chromatography was carried out using Merck F254 aluminium-backed silica plates. ^1H (400 /500 MHz) and ^{13}C (101/126 MHz) ^{15}N (41/51 MHz) ^{31}P (162/202) ^{19}F (376/471) NMR spectra were recorded on Bruker-400/500 Avance III series instruments with internal deuterium locks. Chemical shifts are quoted as parts per million and referenced to CHCl_3 (δH 7.27), $(\text{CH}_3)_2\text{SO}$ (δH 2.54), CDCl_3 (δC 77.0) or $(\text{CD}_3)_2\text{SO}$ (δC 40.45). ^{13}C NMR spectra were recorded with broadband proton decoupling. Coupling constants (J) are quoted in Hertz. Electrospray high- and low-resolution mass spectra were recorded on a Bruker Daltonics micrOTOF spectrometer. IR spectra were recorded using a Bruker Tensor 37 IR machine. All compounds were purchased from Sigma-Aldrich, Fluorochem or Alfa-Aesar and used as supplied unless otherwise stated.

The following compounds were synthesised in house according to literature procedures; $[\text{IrCl}(\text{COD})(\text{IMes})]$,¹²¹ $[\text{IrCl}(\text{COD})(\text{SIMes})]$,¹²¹ $[\text{IrCl}(\text{COD})(d_{22}\text{-IMes})]$,¹⁹⁷ $[\text{IrCl}(\text{COD})(d_{22}\text{SIMes})]$,¹³⁵ $[\text{IrCl}(\text{COD})(1,3\text{-bis}(4\text{-chloro-2,6-dimethylphenyl)imidazol-2-ylidene})]$,¹³⁵ $[\text{IrCl}(\text{COD})(1,3\text{-bis}(4\text{-(dimethylamino)-2,6-dimethylphenyl)imidazol-2-ylidene})]$,¹³⁵ 2,5- d_2 -pyrimidine,¹³⁵ and 2,4- d_2 -nicotinamide.¹³⁵

Remaining compounds 5- d -pyrimidine, 4,6- d_2 -pyrimidine, 4,5,6- d_3 -pyrimidine, and ^{13}C -nicotinamide were synthesised in house following unpublished methods.

8.2 General Procedures

8.2.1 NMR SABRE experiments

SABRE polarisation experiments were conducted in either i) a 5mm NMR tube, equipped with a J. Young Tap, manually shaken and dropped into the spectrometer (Method 1); or ii) with an automated polariser (Method 2).

Samples for SABRE polarization transfer experiments were normally based on using 5 mM solutions of $[\text{IrCl}(\text{COD})(\text{IMes})]$ and the specified substrate in methanol- d_4 (0.6 mL). For method 1 the samples were degassed using three freeze-pump-thaw cycles to remove dissolved oxygen in

the solution. *p*-H₂ was subsequently introduced into the tube at 3 bar(g) (unless otherwise stated). Samples were then shaken for 10 s (unless otherwise specified) in the specified fringe field of an NMR spectrometer or with the use of a hand-held magnet array²⁰⁶ before, in both cases, being manually dropped for rapid transport into the magnet for subsequent interrogation by NMR spectroscopy. Unless otherwise stated, a single NMR scan was collected, with a receiver gain of 1, and a pulse flip angle of 90°.

In method 1 the source of the *p*-H₂ was a custom-made *p*-H₂ rig.³⁶¹ Hydrogen gas is introduced into the rig and cooled to 30 K using a closed cycle helium refrigeration unit. The gas is passed over an Fe₂O₃ catalyst, to convert *o*-H₂ to *p*-H₂.

For the automated polarizer measurements, samples consisted of [IrCl(COD)(IMes)] and the substrate in methanol-*d*₄ solution (3mL). The Mixing Chamber (MC) is housed within a tuneable copper coil (0.5 to ± 150 G). The coil was situated in a magnetic field which has the components *x* 4.9 – 5.1 G, *y* 3.3 – 3.6 G and *z* 1.5 – 2.1 G. All magnitudes of the magnetic fields in which polarization transfer occurs (PTF) are stated without correction for this local field. The MC houses the solvent, catalyst and substrate. Liquid and gas flow are computer controlled via 5V (transistor-transistor logic, TTL) triggers within a custom edited pulse sequence program (Bruker, Topspin 3.1). *p*-H₂ is introduced into the MC first to activate the catalyst. Nitrogen gas is used to shuttle the hyperpolarized solution from the MC to the NMR probe head for measurement.¹¹⁵ The automatic polariser contains a microcontroller that sets the desired parameters (e.g., *p*-H₂ bubbling time, mixing field, time to transfer etc.) required for the specific experimental purpose. More details about this procedure can be found in Cowley *et. al.* (2011).¹⁹²

The source of H₂ in the flow system is a FDGS-Alliance hydrogen generator that electrolyses water. The H₂ is converted to *p*-H₂ in a Bruker *p*-H₂ generator through cooling.

8.2.2 Signal Enhancement Factors Calculations and Errors

To calculate the enhancements of NMR signals the formula in equation 8.1 was used.

$$\varepsilon = \frac{SI(hyp)}{SI(thermal)} \quad [8.1]$$

Where ε = Signal enhancement, $SI(hyp)$ = Integral of signal from the hyperpolarised sample, $SI(thermal)$ = Integral of signal from the unpolarised sample at thermal equilibrium. Both spectra were recorded using identical acquisition parameters including the receiver gain which

was set at 1 unless otherwise stated. The integrals of each of the individual resonances in the hyperpolarised and thermal spectra were then used to calculate the enhancement levels. Standard errors were calculated from the standard deviation (SD) using equation 8.2 where n is the number of experiments (typically between 5 and 8)

$$\sigma = \frac{SD}{\sqrt{n}} \quad [8.2]$$

When normalised data was used the enhancement factors ε were divided through the maximum signal for each condition ε_m as shown in equation 8.3. ε_n = Normalised signal enhancement

$$\varepsilon_n = \frac{\varepsilon_x}{\varepsilon_m} \quad [8.3]$$

Standard errors were propagated accordingly.

A slightly modified approach was followed for measuring X nuclei enhancement factors. Since a single scan thermal measurement was found to be insufficient to detect any observable signal, a large number of acquisitions were usually performed in each case of thermal X nuclei detection. The enhancement factor was then calculated using equation 8.4.

$$\varepsilon = \left(\frac{S_{HP}}{S_{Ref}} \right) * N_{Ref} \quad [8.4]$$

where S_{HP} denotes the hyperpolarized signal intensity, acquired in a single transient of 90° pulse. S_{Ref} represents the thermally polarized signal intensity added over N_{Ref} number of transients. Thermal signal was acquired by a specified number of 90° pulses with sufficient (at least 5 times T_1) relaxation delay between each scan. All NMR experimental parameters, except the number of scans, remained the same for hyperpolarized and thermal measurements.

8.2.3 Percentage Polarisation

The polarisation, P for any nuclei is given by equation 8.5 where γ is the gyromagnetic ratio of the nuclei, B_0 = Static magnetic field of measurement, \hbar = reduced Planck's constant, k_B = Boltzmann constant and T = temperature at which the measurement takes place.

$$P = \frac{\gamma B_0 \hbar}{2 k_B T} \quad [8.5]$$

The percentage hyperpolarised polarisation, %*P* is calculated using equation 8.6 where ϵ = enhancement factor

$$\%P = P \cdot \epsilon \cdot 100 \quad [8.6]$$

8.2.4 T_1 measurements using Inversion Recovery

T_1 was determined by a standard inversion recovery experiment. Integrated data points are fitted to equation 8.7 where $M_z(\tau)$ are the amplitudes at times τ and M_0 is a constant. τ is varied between 0 and $5 \cdot T_1$ over a series of experiments. A minimum delay of $5 \cdot T_1$ (estimated) was used to ensure full magnetisation relaxation and thereby improve the estimate of T_1 .

$$M_z(\tau) = M_0 \left(1 - 2e^{-\frac{\tau}{T_1}} \right) \quad [8.7]$$

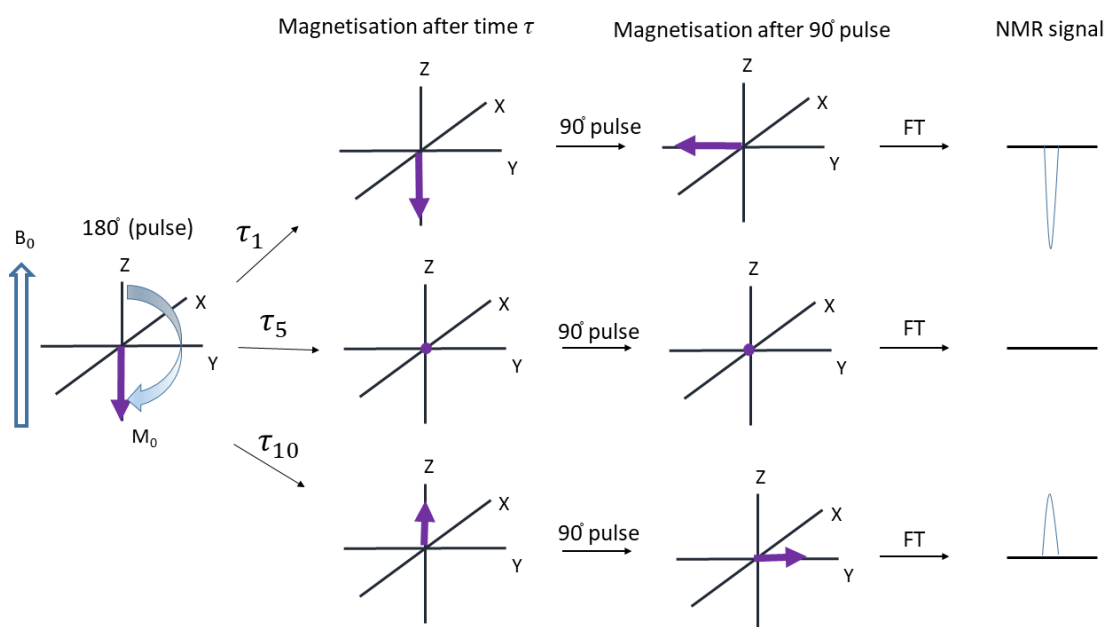


Figure 8.1: Inversion recovery experiment to measure T_1 . A 180° pulse flips the bulk magnetisation into the $-z$ plane. As the signal relaxes the bulk magnetisation builds back up into the $+z$ plane. Interrogation with a 90° pulse at various time intervals τ and fourier transform (FT) gives rise to an NMR peak. Analysis of the integral of this peak as a function of τ yields T_1 .

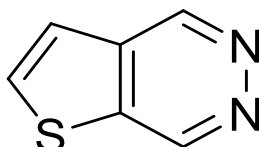
8.2.5 Characterisation NMR experiments

Standard 1D and 2D NMR methods (COSY, NOESY, HMQC) used for characterisation as described in the chapters.

8.3 Chapter 2 Methods: Synthesis of Thienopyridazines and Furopyridazines

Following synthesis all products were confirmed analytically. Spectroscopic data were consistent with those reported in the literature unless otherwise stated.

8.3.1 Synthesis of Thieno[2,3-*d*]pyridazine¹⁸¹

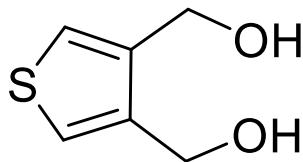


A solution of 2,3-thiophenedicarboxaldehyde (0.6315g, 4.505 mmol, 1 eq.) in 1:1 CH₂Cl₂:EtOH (10 mL) was added dropwise to a solution of hydrazine hydrate (0.65 ml of a 55% solution in H₂O, 13.5 mmol, 3 eq.) in EtOH (7 mL) at 0 °C. The reaction was stirred at room temperature for 16 hours. A saturated solution of NaHCO₃ (aq.) (20 mL) was added. CH₂Cl₂ was added (20 mL) and the two layers separated. The aqueous layer was extracted using CH₂Cl₂ (2 x 20 mL) and the combined organic layers were dried (MgSO₄) and concentrated under reduced pressure. Purification by flash column chromatography on silica gel using 100% EtOAc to 90:10 EtOAc-MeOH as eluent gave thieno[2,3-*d*]pyridazine (0.4767g, 3.500 mmol, 77% yield) as a white solid. R_f (0.18 in 100% EtOAc); **IR** (ATR, cm⁻¹) ν_{max} 3086w, 3055m, 1459m, 1278s, 962m, 789m, 739m; **¹H NMR** (500 MHz, CD₃OD, 298 K) δ 9.79 (*pseudo* s br, 1H), 9.63 (d, *J*=1.43 Hz, 1H), 8.25 (d, *J* = 5.34 Hz, 1H), 7.75 (dd, *J* = 5.34, 0.60 Hz, 1H); **¹³C NMR** (126 MHz, CD₃OD, 298 K) δ 146.4, 146.3, 139.9, 136.9, 135.2, 122.2; **¹⁵N NMR** (51 MHz, CD₃OD, 298 K) δ 355.04, 354.36; **MS** (ESI) *m/z* 137 [(M+H)⁺, 100]; **HRMS** (ESI) *m/z* [M+H]⁺ calculated for C₆H₅N₂S 137.0168, found 137.0170 (-1.6 ppm Mean error).

Lab Book Ref: EJF-1-15-30

8.3.2 Synthesis of Thieno[3,4-*d*]pyridazine¹⁸¹

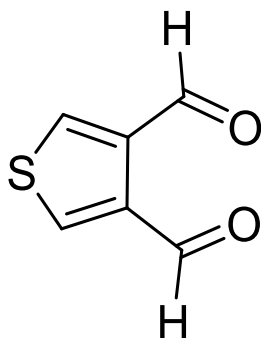
8.3.2.1 Synthesis of Thieno[3,4-*d*]pyridazine (Stage 1- Reduction of Dicarboxylic Acid- Synthesis of Thiophene-3,4-diyldimethanol)



3,4-thiophenedicarboxylic acid (0.200 g, 1.16 mmol) was added to dry THF (20 ml). The solution was cooled to 0°C and BH₃.DMS (0.286 ml of a 10M solution, 3.02 mmol, 2.6 eq.) was added dropwise. After gas evolution had ceased the mixture was heated to 65°C for one hour. After cooling to room temperature, MeOH (10 mL) was added and the resulting suspension was concentrated under reduced pressure. Purification by flash column chromatography on silica gel using 80:20 CH₂Cl₂-EtOAc as eluent gave thiophene-3,4-diyldimethanol (0.143 g, 85% yield) as a clear oil. ¹H NMR (500 MHz, CDCl₃, 298 K) δ 7.27 (s, 2H), δ 4.72 (s, 4H).

Lab Book Ref: EJF-1-17-38

8.3.2.2 Synthesis of Thieno[3,4-*d*]pyridazine (Stage 2- Swern Oxidation- Synthesis of Thiophene-3,4-dicarbaldehyde)

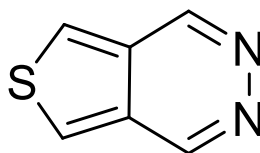


Oxalyl chloride (0.19 mL, 2.2 mmol, 2.2 eq.) was added to dry CH₂Cl₂ (10 mL) under N₂. The resulting solution was cooled to -78°C. A solution of DMSO (0.31 mL, 4.4 mmol, 4.4 eq.) in CH₂Cl₂ (5 mL) was added dropwise and the mixture was stirred for a further ten minutes after the final addition of DMSO. A solution of thiophene-3,4-diyldimethanol (0.1426g, 0.99 mmol, 1 eq.) in dry CH₂Cl₂ (10ml) was added dropwise and the resulting mixture was stirred for 30 minutes. Et₃N (2.41 mL, 0.0173mol, 17.5 eq.) was added dropwise and the mixture was stirred at -78°C

for a further ten minutes and at 0°C for two hours. Following warming to room temperature, the reaction mixture was quenched with water (30 mL). The organic layer was collected and the aqueous layer was extracted using CH₂Cl₂ (2 x 20 mL). The combined organic layers were washed with a saturated solution of NaHCO₃ (aq.) (20 mL) and a saturated solution of NaCl (20 mL). The combined organic layers were dried (MgSO₄) and concentrated under reduced pressure. The crude product was carried onto the final stage of synthesis without further purification.

Lab Book Ref: EJF-1-18-42

8.3.2.3 Synthesis of Thieno[3,4-d]pyridazine (Stage 3- Synthesis of Thieno[3,4-d]pyridazine)

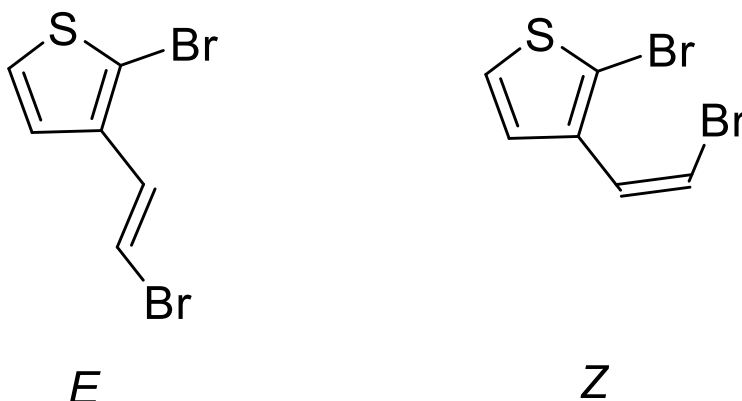


A solution of the crude 3,4-thiophenedicarboxaldehyde (0.1426 g, 0.0010174 mol, 1eq. assumed that previous reaction went to 100% completion) in 1:1 CH₂Cl₂:EtOH (10 mL) was added dropwise to a solution of hydrazine hydrate (0.2 mL of a 55 % solution in H₂O, 13.5 mmol, 3eq.) in EtOH (7 mL) at 0 °C. The reaction was stirred at room temperature for 16 hours. A saturated solution of NaHCO₃ (aq) (20 mL) was added. CH₂Cl₂ was added (10 mL) and the two layers separated. The aqueous layer was extracted using CH₂Cl₂ (2 x 10 mL) and the combined organic layers were dried (MgSO₄) and concentrated under reduced pressure. Purification by flash column chromatography on silica gel using 100% EtOAc to 90:10 EtOAc-MeOH as eluent gave thieno[3,4-d]pyridazine (64.1 mg, 46% yield across step 2 and 3) as brown crystals. R_f (0.21 in 90:10 EtOAc-MeOH); **IR** (ATR, cm⁻¹) ν_{max} 3095m, 2922w, 1574m, 1492m, 1457m, 1229m, 926m, 891m 779s, 663m; **¹H NMR** (500 MHz, CDCl₃, 298 K) δ 9.37 (s, 2H), 8.15 (s, 2H); **¹³C NMR** (126 MHz, CDCl₃, 298 K) δ 147.0 (2C), 130.7 (2C), 123.3 (2C); **¹⁵N NMR** (51 MHz, CDCl₃, 298 K) δ 347.4 (2N); **MS** (ESI) *m/z* 137 [(M+H)⁺, 100]; **HRMS** (ESI) *m/z* [M+H]⁺ calculated for C₆H₅N₂S 137.0168, found 137.0165 (0.9 ppm Mean error).

Lab Book Ref: EJF-1-19-46

8.3.3 Synthesis of Thieno[2,3-*c*]pyridazine¹⁸⁴

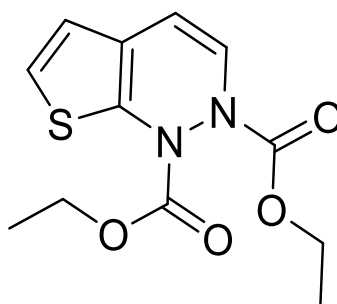
8.3.3.1 Synthesis of Thieno[2,3-*c*]pyridazine -Scale up (Stage 1- Synthesis of (*Z*)-2-Bromo-3-(2-bromovinyl)thiophene)



Potassium *tert*-butoxide (0.4405 g, 3.92 mmol, 1.5 eq.) was added portion-wise to a stirred solution of bromomethyltriphenylphosphonium bromide (1.712 g, 3.92 mmol, 1.5 eq.) in dry THF (50 mL) at -78°C under N₂. The reaction was stirred at room temperature for 1 hour before 2-bromothiophene-3-carbaldehyde (0.500 g, 2.6 mmol, 1 eq.) was added portion-wise. The reaction mixture was stirred at room temperature for 18 hours. Hexane (25 mL) was added to the white suspension which was then poured onto further hexane (75 mL). The resulting suspension was filtered through celite and washed with further hexane (50 mL). The filtrate was concentrated under reduced pressure. Purification by flash column chromatography on silica gel using 100% hexane as eluent gave a mixture of the *E* and *Z* alkenyl bromide (0.573 g, 83 %) as a pale, yellow oil. NMR confirmed the products showing integrals of *Z*:*E* = 2:1 (*Z*)-isomer: ¹H NMR (500 MHz, CDCl₃, 298 K) δ 7.26 (d, *J* = 6 Hz, 1H), 7.13 (d, *J* = 15 Hz, 1H), 7.01 (d, *J* = 6 Hz, 1H), 6.79 (d, *J* = 15 Hz, 1H); ¹³C NMR (126 MHz, CDCl₃, 298 K) δ 135.3, 127.1, 125.7, 125.2, 114.9, 107.4; (*E*)-isomer: ¹H NMR (500 MHz, CDCl₃, 298 K) δ 7.84 (d, *J* = 6 Hz, 1H), 7.32 (d, *J* = 6 Hz, 1H), 7.10 (d, *J* = 8 Hz, 1H), 6.48 (d, *J* = 8 Hz, 1H); ¹³C NMR (126 MHz, CDCl₃, 298 K) δ 136.4, 129.8, 126.6, 124.3, 111.4, 108.7.

Lab Book Ref: EJF-1-26-85

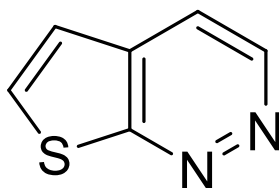
8.3.3.2 Synthesis of Thieno[2,3-*c*]pyridazine - Scale up (Stage 2- Synthesis of *N,N'*Diethyl thieno[2,3-*c*]dihydropyridazine-1,2-dicarboxylate)



A mixture of (*E*) (*Z*)-2-bromo-3-(2-bromovinyl)thiophene (0.573 g (*Z*:*E*/2:1) 2.16 mmol, 1 eq.) was dissolved in 1,4-dioxane (8mL) and transferred to a vial. Diethyl hydrazine-1,2-dicarboxylate (0.760 g, 4.31 mmol, 2 eq.), K_2CO_3 (0.745 g, 5.39 mmol, 2.5 eq.) and CuI (0.041 g, 2.16×10^{-4} moles, 0.1 eq.) were added. The vial was sealed and flushed with nitrogen. *N,N'*-dimethylethylenediamine (DMEDA) (46 μ L, 38mg, 4.31×10^{-4} moles, 0.2 eq.) was added via a glass syringe. The vial was covered in foil and the reaction mixture stirred in a pre-heated sand bath at 90°C for 18 hours. After cooling to room temperature, the reaction mixture was diluted with CH_2Cl_2 then run through a silica plug. Purification by flash column chromatography on silica gel using 95:5 hexane-acetone as eluent gave *N,N'*-diethylthieno[2,3-*c*]dihydropyridazine-1,2-dicarboxylate (0.132 g, 22% from *E&Z* mixture, 32% from *Z* isomer) as a clear oil. **1H NMR** (500 MHz, DMSO, 363K) δ 7.27 (d, $J = 5.5$, 1H), 6.90 (d, $J = 5.5$ Hz, 1H), 6.88 (d, $J = 7$ Hz, 1H), 6.36 (d, $J = 7$ Hz, 1H), 4.24 (m, $J = 7$ Hz, 4H), 1.25 (t, $J = 7$ Hz, 6H); **^{13}C NMR** (126 MHz, $CDCl_3$) δ 154.2, 152.9, 135.7, 127.1, 125.6, 122.1 (2C), 110.9, 63.9, 63.3, 14.6, 14.5; **MS** (ESI) m/z 305 [$(M + Na)^+$, 100]; **HRMS** (ESI) m/z [$M + Na$] $^+$ calculated for $C_{12}H_{14}N_2NaO_4S^+$ 305.0566, found 305.0556 (4.1 ppm Mean error).

Lab Book Ref: EJF-1-27-91

8.3.3.3 Synthesis of Thieno[2,3-*c*]pyridazine - (Stage 3- Synthesis of Thieno[2,3-*c*]pyridazine)

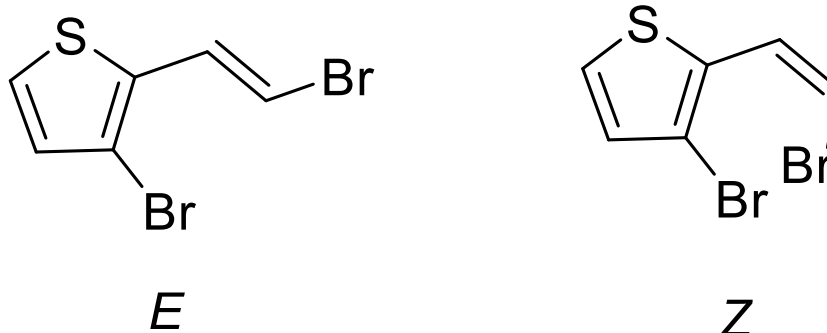


Sodium hydroxide (5M, 0.4 mL, 5.0 eq.) was added drop-wise to a stirred solution of diethylthieno[2,3-*c*]dihydropyridazine-1,2-dicarboxylate (0.1315 g, 4.6×10^{-4} mol, 1.0 eq.) in EtOH (2mL). The resulting solution was heated under reflux at 70°C for 16 hours left open to air. Further sodium hydroxide was added (5M, 0.4 mL, 2.3 x mmol, 5.0 eq.) and the reaction was left to reflux at 70°C for a total of seven days. After cooling to room temperature, the reaction mixture was partitioned between water (15 mL) and CH₂Cl₂ (15 mL). The organic layer was separated and the aqueous layer extracted with CH₂Cl₂ (2 x 15 mL). The combined organic phases were dried (MgSO₄) and concentrated under reduced pressure. Purification by flash column chromatography on silica gel using (97.5:2.5) EtOAc-triethylamine as eluent gave thieno[2,3-*c*]pyridazine (44.6 mg, 71%) as a pale yellow solid. R_f (0.33) ; **¹H NMR** (500 MHz, CD₃OD, 298 K) δ 9.18 (d, *J* = 5.65 Hz, 1H), 8.21 (d, *J* = 5.92 Hz, 1H), 8.17 (d *J* = 5.65 Hz , 1H), 7.54 (d, *J* = 5.92 Hz , 1H); **¹³C NMR** (126 MHz, CD₃OD, 298 K) δ 165.90, 145.00, 135.04, 135.01, 120.96, 120.93; **¹⁵N NMR** (51 MHz, CD₃OD, 298K) δ 373.88, 376.93; **MS** (ESI) *m/z* 137 [(M+H)⁺, 100]; **HRMS** (ESI) *m/z* [M+H]⁺ calculated for C₆H₅N₂S 137.0168, found 137.0172 (-3.5 ppm Mean error).

Lab Book Ref: EJF-1-29-99

8.3.4 Synthesis of Thieno[3,2-c]pyridazine (adapted from literature procedure Ball *et al.*, 2012)¹⁸⁴

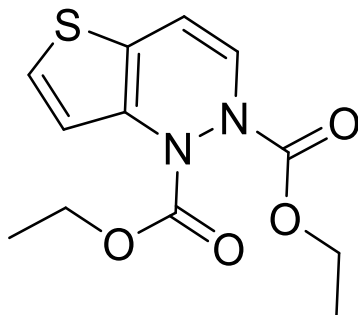
8.3.4.1 Synthesis of Thieno[3,2-c]pyridazine – Scale up (Stage 1- Synthesis of (Z)-3-Bromo-2-(2-bromovinyl)thiophene)



Potassium tert-butoxide (2.20 g, 19.6 mmol, 1.5 eq.) was added portion-wise to a stirred solution of bromomethyltriphenylphosphonium bromide (8.56 g, 19.6 mmol, 1.5eq.) in dry THF (250 mL) at -78°C under N_2 . Stirring at this temperature was maintained for 1 hour before 3-bromothiophene-2-carbaldehyde (1.42 mL, 2.50 g, 13 mmol, 1 eq.) in dry THF was added portion-wise. The reaction mixture was allowed to warm to room temperature and stirred for 16 hours. The resulting white suspension was diluted with hexane (100 mL) and poured onto further hexane (300 mL). The suspension was filtered through celite and washed with further hexane (100 mL). The filtrate was concentrated under reduced pressure to leave a white solid plus an oil. This was then dissolved in hexane and passed through a silica plug. Purification by flash column chromatography on silica gel using 100% hexane to 95:5 hexane-EtOAc as eluent gave a mixture of the (E Z) alkenyl bromide (2.40 g, 69 %) as a pale, yellow oil. NMR confirmed the products showing integrals Z:E/2.6:1) Rf (0.6 both *E* and *Z* in 95:5 hexane:EtOAc) (*Z*)-isomer: $^1\text{H NMR}$ (500MHz, CDCl_3 , 298K) δ 7.49 (d, $J = 8.0$ Hz, 1H), 7.42 (d, $J = 5.5$ Hz, 1H), 7.08 (d, $J = 5.5$ Hz, 1H), 6.50 (d, $J = 8.0$ Hz, 1H); $^{13}\text{C NMR}$ (126 MHz, CD_3OD , 298 K) δ 132.8, 129.6, 126.7, 125.1, 114.3, 106.5; (*E*)-isomer: $^1\text{H NMR}$ (500MHz, CDCl_3 , 298K) δ 7.27 (d, $J = 14$ Hz, 1H), 7.20 (d, $J = 5.5$ Hz, 1H), 6.97 (d, $J = 5.5$ Hz, 1H), 6.76 (d, $J = 14$ Hz, 1H); $^{13}\text{C NMR}$ (126 MHz, CD_3OD , 298 K) δ 134.6, 130.8, 128.8, 124.8, 110.6, 107.6; **MS** (ESI) m/z [(M - Br) $^+$, 188.92], [(M - CHBr) $^+$, 174.92].

Lab Book Ref: EJF-3-4-25/EJF-1-28-93

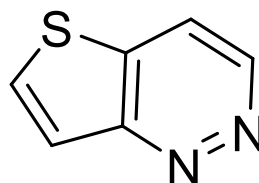
8.3.4.2 Synthesis of Thieno[3,2-c]pyridazine-Scale up (Stage 2- Synthesis of *N,N'*Diethyl thieno[3,2-c]dihydropyridazine-1,2-dicarboxylate)



A mixture of (*E*) (*Z*)-3-bromo-2-(2-bromovinyl)thiophene (2.0 g (*Z*:*E*/2.6:1) 7.52 x mmol, 1 eq.) was dissolved in 1,4-dioxane (8 mL) and transferred to a vial. Diethyl hydrazine-1,2-dicarboxylate (2.65 g, 15 mmol, 2 eq.), K_2CO_3 (2.41 g, 18.8 mmol, 2.5 eq.) and CuI (0.143 g, 0.75 mmol, 0.1 eq.) were added. The vial was sealed and flushed with nitrogen. *N,N'*-Dimethylethylenediamine (DMEDA) (162 μ l, 0.133 g, 1.51 mmol, 0.2 eq.) was added via a glass syringe. The vial was covered in foil and the reaction mixture stirred in a pre-heated sand bath at 90°C for 72 hours. After cooling to room temperature, the reaction mixture was diluted with CH_2Cl_2 (50 mL) then run through a silica plug washing with further CH_2Cl_2 . Purification by flash column chromatography on silica gel using 95:5 EtOAc-hexane to 80:20 EtOAc-hexane as eluent gave *N,N'*diethylthieno[3,2-c]dihydropyridazine-1,2-dicarboxylate (0.694 g, 33 % from *E*&*Z* mixture, 45 % from *Z* isomer) as a pale yellow oil. R_f (0.3 70:30 EtOAc-Hexane) 1H NMR (500 MHz, DMSO, 363K) δ 7.46 (d, $J = 5.3$ Hz, 1H), 7.11 (dd, $J = 5.3$ Hz, 0.5, 1H), 6.92 (d, $J = 7.1$ Hz, 1H), 6.43 (d, $J = 7.1$ Hz, 1H), 4.22 (m, $J = 7.1$ Hz, 4H), 1.26 (t, $J = 7.1$ Hz, 3H), 1.23 (t, $J = 7.1$ Hz, 3H); ^{13}C NMR (126 MHz, $CDCl_3$) δ 154.6, 152.6, 135.8, 125.4, 124.9, 124.6, 123.3, 108.7, 63.5, 63.1, 14.6, 14.5; MS (ESI) m/z 305 [$(M + Na)^+$, 100]; HRMS (ESI) m/z [$M + Na$] $^+$ calculated for $C_{12}H_{14}N_2NaO_4S^+$ 305.0566, found 305.0567 (3.8 ppm Mean error).

Lab Book Ref: EJF-3-5-29/EJF-3-1-3

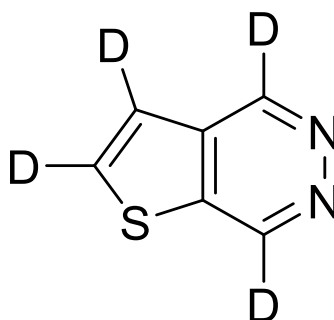
8.3.4.3 Synthesis of Thieno[3,2-*c*]pyridazine – (Stage 3- Synthesis of Thieno[3,2-*c*]pyridazine)



Sodium hydroxide (5M, 0.9 mL, 4.5 x mmol, 5.0 eq.) was added drop-wise to a stirred solution of *N-N'*diethylthieno[3,2*c*]dihydropyridazine-1,2-dicarboxylate (0.255 g, 9 x mmol, 1.0 eq.) in EtOH (8 mL). The resulting solution was heated under reflux at 70°C for 20 hours left open to air. After cooling to room temperature, the reaction mixture was partitioned between water (30 mL) and CH₂Cl₂ (30 mL). The organic layer was separated, and the aqueous layer extracted with CH₂Cl₂ (2 x 30 mL). The combined organic phases were dried (MgSO₄) and concentrated under reduced pressure. Purification by flash column chromatography on silica gel using (97.5:2.5) EtOAc-triethylamine as eluent gave thieno[2,3-*c*]pyridazine (78.4 mg, 64%) as a dark green solid. R_f (0.18) ; ¹H NMR (500 MHz, CDCl₃, 298 K) δ 9.14 (d, *J* = 5.74 Hz, 1H), 8.04 (dd, *J* = 5.74 Hz, 0.74, 1H), 7.91 (dd *J* = 5.65 Hz, 0.74, 1H), 7.87 (d, *J* = 5.65 Hz, 1H); ¹³C NMR (126 MHz, CDCl₃, 298 K) δ 159.89, 143.74, 136.99, 132.57, 124.28, 120.07; ¹⁵N NMR (51 MHz, CDCl₃, 298 K) δ 391.62, 393.95; MS (ESI) *m/z* 137 [(M+H)⁺, 100]; HRMS (ESI) *m/z* [M+H]⁺ calculated for C₆H₅N₂S 137.0168, found 137.0173 (-3.2 ppm Mean error).

Lab Book Ref: EJF-3-6-36

8.3.5 Novel synthesis of *d*₄-thieno[2,3-*d*]pyridazine

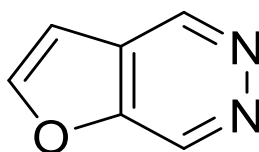


Thieno[2,3-*d*]pyridazine (100 mg, 0.73 mmol) was added to D₂O (10 mL) with K₂CO₃ (245 mg, 1.7 mmol) and refluxed for 4 weeks. During this time, the deuteration reaction was followed by LC-MS. When there was little further conversion, the D₂O was removed under reduced pressure and replenished with fresh D₂O (15 mL x 6) and additional K₂CO₃. After cooling to room temperature, CH₂Cl₂ (20 mL) was added. The organic layer was separated and the aqueous layer extracted with CH₂Cl₂ (2 x 20 mL). The combined organic phases were dried (MgSO₄) and concentrated under reduced pressure to give *d*₄-thieno[2,3-*d*]pyridazine (77.8 mg, 0.55 mmol, 75% with 94% deuteration) as a white solid; **IR** (ATR, cm⁻¹) ν_{\max} 2693w, 2917w, 2849w, 2317w, 2274m, 1422m, 1241s, 1018s, 797s 609m; **¹³C NMR** (126 MHz, CD₃OD, 298 K) δ 146.4 (t, *J* = 28.36 Hz), 146.3 (t, *J* = 28.36 Hz), 139.9 (s), 136.9 (s), 135.2 (t, *J* = 26.20 Hz), 121.9 (t, *J* = 27.2 Hz); **MS** (ESI) *m/z* 141 [(M+H)⁺, 100], ; **HRMS** (ESI) *m/z* [M+H]⁺ calculated for C₆HD₄N₂S 141.0419, found 141.0416 (3 ppm Mean error) *m/z* [M+H]⁺ calculated for C₆D₄N₂NaS 163.0238, found 163.0236 (3 ppm Mean error). Synthesis of this product is novel and no existing literature was found.

23% is 140 C₆H₂D₃N₂S – divided across 4 proton sites therefore 94 % deuteration

Lab Book Ref: EJF-3-13-63/64

8.3.6 One-Pot Synthesis of Furo[2,3-*d*]pyridazine¹⁸³



n-BuLi (3.2 mL, 6.40 mmol, 2M in hexane, 1.07 eq.) was added dropwise under nitrogen to a stirred solution of NNN'-trimethylethyldiamine (0.858 mL, 0.674g, 6.60 mmol, 1.10 eq.) in a mixture of dry hexane (10 mL) and THF (2.5 mL) at -25°C. The mixture was stirred at -20°C for 30 minutes to form the lithium amide. Furan-3-carbaldehyde (0.52 mL, 6.00 mmol, 1 eq.) was added dropwise at -20°C. The reaction mixture was stirred for 45 minutes and further *n*-BuLi (4.5 mL) was added at -20°C. The mixture was allowed to warm to room temperature and stirred for a further 2 hours. After cooling to -78°C THF (5 mL) and DMF (1.40 mL, 18.0 mmol, 3 eq.) were added and the reaction mixture was stirred for 10 minutes. The mixture was allowed to warm to 0°C and stirred for 1.5 hours. The reaction was then quenched with a solution of NH₄Cl (0.96

g, 18.0 mmol, 3 eq.) and $\text{N}_2\text{H}_4\cdot\text{H}_2\text{O}$ (1.03 mL, 11.5 mmol, 35%, 1.90 eq.) in H_2O (5mL). The reaction was allowed to warm to room temperature and stirred for 14 hours. After completion, the mixture was diluted with EtOAc (15 mL) and the organic layer was separated. The aqueous layer was extracted with EtOAc (3 x 20 mL) and the combined organic layers were dried (MgSO_4) and concentrated under reduced pressure. Purification was carried out using a silica plug followed by flash chromatography on silica gel using (40:60 – 50:50) acetone-hexane as eluent. Hexane was added to dissolve residual impurities and the hexane was removed under reduced pressure to give furo[2,3-*d*]pyridazine (273 mg, 2.28 mmol, 38%) as an orange powder. Rf (0.20 in 50:50 acetone-hexane); **IR** (ATR, cm^{-1}) ν_{max} 3157w, 3115w, 1602w, 1518m, 1465m, 1007m, 886m, 776m, 697m; **^1H NMR** (500 MHz, CD_3OD , 298 K) δ 9.62 (d, $J=1.23$ Hz, 1H), 9.59 (dd, $J=0.97, 1.29$ Hz, 1H), 8.25 (d, $J = 2.14$ Hz, 1H), 7.19 (dd, $J = 2.14, 0.94$ Hz, 1H); **^{13}C NMR** (126 MHz, CD_3OD , 298 K) δ 153.2, 150.1, 146.7, 137.7, 126.7, 104.7; **^{15}N NMR** (51 MHz, CD_3OD , 298K) δ 362.7, 367.3 (**MS** (ESI) m/z 121 [(M+H) $^+$, 100]; **HRMS** (ESI) m/z [M+H] $^+$ calculated for $\text{C}_6\text{H}_5\text{N}_2\text{S}$ 121.0396, found 121.0395 (1.2 ppm error).

Lab Book Ref: EJF-3-10-49

Samples for shake and drop experiments were made up to 4.5 mM concentration of catalyst with 0.7 mL of solvent.

8.4 Chapter 3 Methods: Long-Lived States

The following methods support the application of long-lived states to store polarisation and extend lifetime in chapter 3.

8.4.1 T_{LLS} measurements

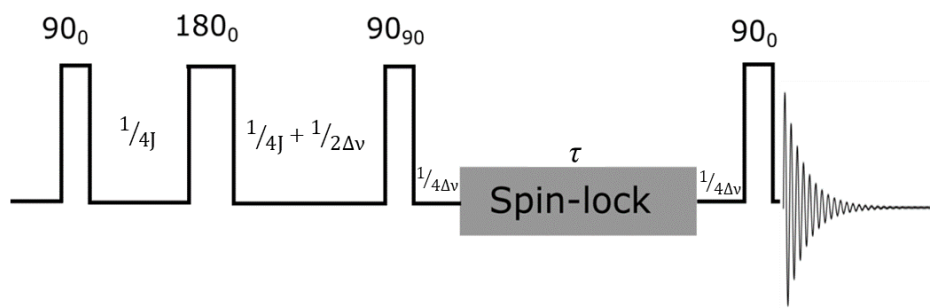


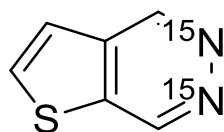
Figure 8.2: LLS pulse sequence with delays $1/4J$; $1/4J + 1/2\Delta\nu$; $1/4\Delta\nu$ and τ where J and $\Delta\nu$ denote the scalar-coupling constant and chemical shift difference between the associated spin pair in Hertz respectively. A Waltz-16 composite pulse of 1 KHz amplitude was used as the spin-lock (with duration τ) in all cases.

T_{LLS} measurements were carried out by varying the spin-lock durations (τ) while keeping all other parameters unchanged during the experiment. Integrated amplitudes $M_z(\tau)$ were fitted to simple mono (equation 8.8) and bi-exponentials.

$$M_z(\tau) = M_0 e^{-\tau/T_{LLS}} \quad [8.8]$$

where M_0 is a constant.

8.4.2 Novel synthesis of ^{15}N labelled thieno[2,3-*d*]pyridazine

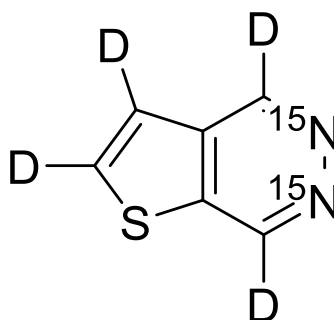


^{15}N -labelled hydrazine sulfate (94.2 mg, 7.134×10^{-4} mol) was added to a 1 M NaOH solution (1.4 mL) at 0°C . A solution of 2,3-thiophenedicarboxaldehyde (100 mg, 7.134×10^{-4} mol 1 eq.) in EtOH (5 mL) was added dropwise to the hydrazine sulfate solution at 0°C . The reaction was stirred at room temperature for 2 hours. A saturated solution of $\text{NaHCO}_3(\text{aq})$ (10 mL) was added to quench the hydrazine. CH_2Cl_2 was added (10 mL) and the organic layer was separated. The aqueous layer was extracted using CH_2Cl_2 (2 x 10 mL) and the combined organic layers were dried (MgSO_4) and concentrated under reduced pressure. Purification by flash column chromatography on silica gel using 100% EtOAc to 90:10 EtOAc-MeOH as eluent gave ^{15}N -

thieno[2,3-*d*]pyridazine (89 mg, 6.44×10^{-4} moles, 90% yield) as a pale yellow solid. Rf (0.16 in 100% EtOAc); **IR** (ATR, cm^{-1}) ν_{max} 3060w, 3034w, 1493m, 1455m, 1029m, 775m, 697s; **^1H NMR** (500 MHz, CD_3OD , 298 K) δ 9.79 (dddd, $J_{\text{HH}} = 1.5, 0.8$ Hz, $J_{\text{NH}} = 10.7, 5.0$ Hz, 1H), 9.63 (ddd, $J_{\text{HH}} = 1.5$ Hz, $J_{\text{NH}} = 10.7, 5.0$ Hz, 1H), 8.25 (d, $J = 5.34$ Hz, 1H), 7.75 (dd, $J = 5.34, 0.80$ Hz, 1H); **^{13}C NMR** (126 MHz, CD_3OD , 298 K) δ 146.1 (tt, $J_{\text{CD}} = 27.8$ Hz, $J_{\text{CN}} = 4.27$ Hz, 1C), 146.3 (tt, $J_{\text{CD}} = 27.8$ Hz, $J_{\text{CN}} = 5.19$ Hz, 1C), 139.8 (d, $J_{\text{CN}} = 4.74$ Hz, 1C), 136.8 (d, $J_{\text{CN}} = 4.79$ Hz, 1C), 134.9 (d, $J_{\text{CD}} = 28.8$ Hz), 121.9 (d, $J_{\text{CD}} = 26.8$ Hz); **^{15}N NMR** (51 MHz, CD_3OD , 298K) δ 355.1, 354.5 (AB d $J_{\text{NN}} = 22.5$ Hz.); **MS** (ESI) m/z 139 [(M+H) $^+$, 100]; **HRMS** (ESI) m/z [(M+H) $^+$] calculated for $\text{C}_6\text{H}_5^{15}\text{N}_2\text{S}$ 139.0109, found 139.0102 (4.3 ppm error)

Lab Book Ref: EJF-3-12-60

8.4.3 Novel synthesis of fully deuterated *d*₄-thieno[2,3-*d*]pyridazine- $^{15}\text{N}_2$



Thieno[2,3-*d*]pyridazine- $^{15}\text{N}_2$ (25 mg, 0.18 mmol) was added to D_2O (10 mL) with K_2CO_3 (50 mg) and refluxed for 4 weeks. During this time the deuteration reaction was followed by LC-MS. When there was little conversion being observed the D_2O was removed under reduced pressure and replenished with fresh D_2O (15mL x 6) and additional K_2CO_3 (spatula) for further reflux. After cooling to room temperature, CH_2Cl_2 (20 mL) was added. The organic layer was separated and the aqueous layer extracted with CH_2Cl_2 (2 x 20 mL). The combined organic phases were dried (MgSO_4) and concentrated under reduced pressure to give *d*₄-thieno[2,3-*d*]pyridazine- $^{15}\text{N}_2$ (26 mg, 0.18 mmol, 100 % with 92% deuteration) as a white solid. **IR** (ATR, cm^{-1}) ν_{max} 2918w, 2849w, 2317w, 2275m, 1530w, 1422m, 1232s, 847m. **^{13}C NMR** (126 MHz, CD_3OD , 298 K) δ 146.4 (t, $J_{\text{CN}} = 4.94$ Hz, 1C), 146.3 (t, $J_{\text{CN}} = 5.19$ Hz, 1C), 139.9 (d, $J_{\text{CN}} = 5.05$ Hz, 1C), 136.9 (d, $J_{\text{CN}} = 4.60$ Hz, 1C), 135.2, 122.2; **^{15}N NMR** (50.7 MHz, CD_3OD , 298K) δ 355.1, 354.5 (AB dd $J_{\text{NN}} = 22.5$ Hz) **MS** (ESI) m/z 143 [(M+H) $^+$, 100]; **HRMS** (ESI) m/z [(M+H) $^+$] calculated for C_6HD_4

$^{15}\text{N}_2\text{S}$ 143.0360, found 143.0359 (2.6 ppm error) m/z $[\text{M}+\text{H}]^+$ calculated for $\text{C}_6\text{D}_4^{15}\text{N}_2\text{NaS}$
165.0179, found 165.0179 (1.9 ppm error)

30% is $^{142}\text{C}_6\text{H}_2\text{D}_3\text{N}_2\text{S}$ – divided across 4 proton sites therefore 92 % deuteration was achieved.

Lab Book Ref: EJF-3-14-71

8.5 Chapter 4 Methods: Synthesis of platinum complexes for SABRE-Relay

8.5.1 Synthesis of $[\text{Pt}(\text{Cl})_2(\text{PhCN})_2]$

PtCl_2 (1 g, 3.76 mmol) was added to benzonitrile (40 ml) and the resulting solution heated to 110 °C for 2 hours. After cooling, hexane was added to encourage precipitation and the resulting pale-yellow precipitate was filtered, washed with hexane and dried *in vacuo*. $[\text{Pt}(\text{Cl})_2(\text{PhCN})_2]$ (1.628 g, 3.45 mmol) was isolated as a pale-yellow solid in 92% yield. $^1\text{H NMR}$ (400 MHz, CD_3Cl): 7.83 (d, $J_{\text{HH}} = 7.83$ Hz, 4H, PtNCCCH), 7.77 (ps-t, $J_{\text{HH}} = 7.7$ Hz, 2H, PtNCCCHCHCH), 7.59 (t, $J_{\text{HH}} = 7.7$ Hz, 4H, PtNCCCHCH). $^{13}\text{C NMR}$ (101 MHz, CDCl_3): 135.32 (PtNCCCHCHCH), 133.78 (PtNCCCH), 129.48 (PtNCCCHCH), 116.81 (PtNC), 109.06 (PtNCC).

8.5.2 Synthesis of $[\text{Pt}(\text{Cl})_2(\text{dppm})]$

$[\text{Pt}(\text{Cl})_2(\text{C}_6\text{H}_5\text{CN})_2]$ (400 mg, 0.847 mmol) and diphenylphosphinomethane (342 mg, 0.889 mmol, 1.05 eq.) were each dissolved in the minimum volume of dichloromethane (DCM, ~ 20 mL each). The solution of diphenylphosphinomethane was then added dropwise to that of $[\text{Pt}(\text{Cl})_2(\text{C}_6\text{H}_5\text{CN})_2]$. The solution was stirred for 1 hr, after which time a clear pale-yellow solution was observed but no precipitate formed. Hexane (~ 40 mL) was added to encourage precipitation, and the resulting white solid was filtered, washed with hexane, and dried *in vacuo*. $[\text{Pt}(\text{Cl})_2(\text{dppm})]$ (542 mg, 0.833 mmol) was isolated in 98% yield. $^1\text{H NMR}$ (500 MHz, CD_2Cl_2): 7.98 (d.d. $J_{\text{HP}} = 12.2$, $J_{\text{HH}} = 7.0$, 8H, PCCH), 7.59 (ps-t. $J_{\text{HH}} = 7.3$, 4H, PCCHCHCH), 7.53 (ps-t. $J_{\text{HH}} = 7.1$, 8H, PCCHCH), 4.53 (m. 2H, PCH_2). $^{13}\text{C NMR}$ (126 MHz, CD_2Cl_2): 133.24 (s, PCCHCH), 133.0 (t, $J_{\text{CP}} = 6.2$, PCCH), 132.50 (PCCHCHCH), 126.97 (t, $J_{\text{CP}} = 29$, PC) 44.3 (PCH_2). $^{31}\text{P NMR}$ (202 MHz, CDCl_3): -64.21 (s, $J_{\text{Pt}} = 3066$)

8.5.3 Synthesis of $[\text{Pt}(\text{OTf})_2(\text{dppm})]$

$[\text{Pt}(\text{Cl})_2(\text{dppm})]$ (156 mg, 0.240 mmol) and AgOTf (198 mg, 0.769 mmol) were added to a Schlenk tube under nitrogen and dry DCM was added. The resulting suspension was stirred under

nitrogen for 60 hours. Foil was used around the reaction vessel due to the light sensitivity of AgOTf. The solution containing the product was syringe filtered and transferred to a second Schlenk tube under nitrogen. The DCM was reduced to approximately half the volume using the vacuum of the Schlenk line and dry hexane was added to encourage precipitation. Cannula filtration was employed to remove excess solvent and the remaining white solid was dried *in vacuo*. [Pt(OTf)₂(dppm)] (123 mg, 0.140 mmol) was isolated in 58 % yield] ¹H NMR (500 MHz, CD₂Cl₂): 7.85 (dd, $J_{HP} = 14.0$, $J_{HH} = 7.0$, 8H, PCCH), 7.74 (*ps-t*, $J_{HH} = 7.4$, 4H, PCCHCHCH), 7.63 (*ps-t*, $J_{HH} = 7.5$, 8H, PCCHCH), 4.59 (m, 2H, PCH₂). ¹³C NMR (126 MHz, CD₂Cl₂): 134.1 (s, PCCHCHCH), 133.3 (s, PCCH), 130.6 (m, PCCHCH), 28.9 (m, PCH₂). ¹⁹F NMR (471 MHz, CD₂Cl₂): -78.1, ³¹P NMR (202 MHz, CD₂Cl₂): -70.8 (s, $J_{PPt} = 3492$)

8.5.4 Synthesis of [Pt(Cl)₂(dppe)]:

[Pt(Cl)₂(C₆H₅CN)₂] (400 mg, 0.847 mmol) and diphenylphosphinoethane (354 mg, 0.889 mmol, 1.05 eq.) were each dissolved in the minimum volume of DCM (~ 20 mL each). The solution of diphenylphosphinoethane was then added dropwise to that of [Pt(Cl)₂(C₆H₅CN)₂]. The solution was stirred for 1 hr, during which time a white precipitate was observed to form. Hexane (~ 40 mL) was added to encourage further precipitation, and the resulting white solid was sinter filtered, washed with hexane, and dried *in vacuo*. A mixture of [Pt(Cl)₂(dppe)] (193 mg, 34%) and [Pt(dppe)₂]Cl₂ (386 mg, 43%) was collected in a ratio of 0.8: 1 ratio respectively. ¹H NMR (400 MHz, CDCl₃): 7.89 (dd, $J_{HP} = 14.0$, $J_{HH} =$, 8H, PCCH), 7.55 (m, $J_{HH} = 7.5$, 4H, PCCHCHCH), 7.55 (m, $J_{HH} = 7.5$, 8H, PCCHCH), 2.37 (m, $J_{HP} = 18.2$, 4H, PCH₂), ¹³C NMR (101 MHz, CDCl₃): 133.5 (s, PCCH), 132.1 (s, PCCCH), 130.6 (m, PCCHCHCH), 28.9 (m, PCH₂). ³¹P NMR (162 MHz, CDCl₃): 41.28 (s, $J_{PPt} = 3626$).

8.5.5 Synthesis of [Pt(OTf)₂(dppe)]:

The mixture was carried forward to the next stage and an equivalent of [Pt(Cl)₂(dppe)] (72 mg, 0.108 mmol) and AgOTf (193g, 0.753 mmol) added to a Schlenk tube under nitrogen and dry DCM added. The resulting suspension was stirred under nitrogen for 60 hours. Foil was placed around the reaction vessel due to the light sensitivity of AgOTf. The solution containing the product was syringe filtered and transferred to a second Schlenk tube under nitrogen. The DCM was reduced to approximately half the volume using the vacuum of the Schlenk line and dry hexane added to encourage precipitation. Cannula filtration was employed to remove excess solvent and the remaining grey solid was dried *in vacuo*. A mixture of [Pt(OTf)₂(dppe)] (76mg, 84%) and [Pt(dppe)₂]Cl₂ (12 mg, 9%) was collected in a ratio of 1: 0.15. ¹H NMR (500 MHz,

CD₂Cl₂): 7.82 (dd, $J_{HP} = 14.0$, $J_{HH} = 7.0$, 8H, PCCH), 7.75 (*ps*-t, $J_{HH} = 7.4$, 4H, PCCHCHCH), 7.66 (*ps*-t, $J_{HH} = 7.5$, 8H, PCCHCH), 2.54 (m, 2H, PCH₂). ¹³C NMR (126 MHz, CD₂Cl₂): 134.1 (s, PCCHCHCH), 133.3 (s, PCCH), 130.6 (m, PCCHCH), 28.9 (m, PCH₂). ¹⁹F NMR (471 MHz, CD₂Cl₂): -78.53, ³¹P NMR (202 MHz, CD₂Cl₂): 36.4 (s, $J_{PPt} = 3492$).

8.6 Chapter 5 Methods: Translation of SABRE from benchtop to imaging facility

8.6.1 Biphasic- CASH-SABRE

All 1D MRI experiments were performed using a 400 MHz Bruker Avance spectrometer equipped with a z-gradient of maximum strength of 0.536 T/m. The experiments can be separated into two categories:

1D projections of the ²H signal amplitude on the z direction (parallel to the magnet bore and the NMR sample tube). These experiments were performed with the purpose of observing the spatial distribution of the two solvents.

1D projections of the ¹H signal amplitude on the z direction (parallel to the magnet bore and the NMR sample tube). In a typical experiment, 128 projections were acquired immediately after the shaking process with TR = 400 ms. These experiments were performed with the purpose of observing the spatial distribution of the substrate and decay to thermal equilibrium, after shaking in the presence of *p*-H₂.

8.6.2 Cytotoxicity Assays

Cell culture: Human alveolar adenocarcinoma cells (A549) and breast cancer cells (MCF7) were provided by Prof. Christoph Borner (IMMZ, Freiburg, Germany). All cell lines were grown in Dulbecco's Modified Eagle Medium (DMEM) supplemented with 10% foetal calf serum (FCS), penicillin (100 U mL⁻¹), streptomycin (100 μg mL⁻¹), and L-glutamine (2 mM,) (supplied by Gibco Life Technologies) and filter sterilized (0.22 μm). The cells were incubated under standard conditions (37 °C, 5 % CO₂). The media were changed at regular intervals, and upon reaching appropriate confluence (90 %) the cells were passaged after brief exposure to a trypsin/Ethylenediaminetetraacetic acid (EDTA) solution (Invitrogen).

Treatment of cells: Immediately after trypsin/EDTA treatment, viable cells were counted in a hemocytometer by Trypan blue (Sigma) exclusion. The required number of cells (normally

10^4 per well in a 96-well tissue culture plate (Nunc)) was seeded 24 h before treatment so that they were in an exponential growth phase at the start of the experiment. Before treatment various volumes of the bolus from substrate, or the SABRE reaction mixture were diluted to a maximum of 10 μL in the same solvent from which the compounds were originally prepared. For cell assays, throughout this study (unless otherwise indicated) the final amount of the solvent was maintained at 10 % in the total volume of the cell growth medium (i.e., 10 μL in 100 μL).

MTT assay: MTT tetrazolium was reduced to insoluble formazan crystals through the enzyme mitochondrial dehydrogenase found in living cells and therefore directly proportional to the number of living cells. Cells (normally 10^4 cells per well in a 96-well plate) were taken in triplicates and treated with the various solutions (illustrate above) or kept as a cell viability control with no treatment (untreated) in cell growth media. After incubation at desired time points (usually 1 h, 3h, 6 h and 24 h) the cell media was replaced with fresh media (100 μL) containing 10 μL of MTT. A 5 mg mL^{-1} stock solution of MTT is normally prepared in cell growth media and filter sterilized (0.22 μm). Cells were incubated further for 4 h in a humidified atmosphere at 37 °C. The medium with MTT was then carefully aspirated, and the formed formazan crystals were solubilized in 100 μL of dimethyl sulfoxide (DMSO). The absorbance of the coloured (purple) solution was then measured at 570 nm using a microplate reader (MultiskanGO, ThermoFisher). The absorbance values found (averaged out of the triplicate wells) were blanked against DMSO. The absorbance of cells exposed to cell growth medium only (i.e., untreated) was taken as 100 % viable (i.e. control). The cell viability of the treated samples was then calculated by normalizing to the untreated control sample and expressed as percent of control. Each assay was repeated a minimum of three times for statistical analysis of the data.

8.6.3 MRI and MRS

A variety of imaging systems were used with varying fields: a 9.4 T Bruker vertical bore imaging system equipped with a micro imaging gradient system (1 T/m) and a standard 30 mm inner diameter (ID) $^1\text{H}/^{13}\text{C}$ double resonance birdcage For RF transmission & reception; a 7 T preclinical Bruker horizontal bore (BioSpec 70/30) imaging system with a preinstalled BGA-12S gradient coil (600 mT/m) and a 82 mm ID ^1H quadrature birdcage resonator; a 3 T clinical Siemens horizontal bore (MAGNETOM Prisma) parallel transmission imaging system with XR gradient coils (80 mT/m) and a 64 channel ^1H head-array coil for RF reception.

For SABRE experiments, 10 mm Young's tubes were prepared with 4.5 mM of [Ir(COD)(Cl)(*d*₂₂-SIMes)] and T[2,3-*d*]P in a 1:4 or 1:20 ratio catalyst to substrate ratio in 3.5 mL of methanol-*d*₄. The Young's tubes were filled with 3 bars of *p*-H₂ (unless otherwise stated) and shaken in the stray field of the MRI magnet (ca. optimised PTF ~65 G- gauged using a gauss meter, Hirst Magnetics).

9.4 T- Hyperpolarised RARE (*T*₂) Experiments

If not otherwise stated, RARE imaging experiments used the following parameters: Matrix size 128*128; FOV 20*20 mm; slice thickness 10mm; centric encoded, RARE factor 128. Minimum TE = 20ms.

7 T – MRS (CSI/EPSI) Experiments

CSI MRS experiments were completed with the following parameters: Image size 16*16; FOV 35*35 mm; Data points = 604 Band/Sweep width = 30 ppm; Centre Frequency/O1P = 4.7 ppm; TE = 1.099 ms; TR = 289.021 ms. FA = 10 degrees. Slice thickness was varied from 0.5 mm to 20 mm.

EPSI MRS experiments (*in vitro* & *ex vivo*) were completed with the following parameters: Image size 64*64; Data points = 256; FOV 35*35 mm; Band/Sweep width = 15.6 ppm; Centre Frequency/O1P = 4.7 ppm; TE = 4 ms; TR = 93.75 ms. FA= 15 degrees. Slice thickness was varied from 0.5 mm to 20 mm.

Peak integrals were calculated in MATLAB (MathWorks) to generate a signal map, which was overlaid onto appropriate reference ¹H spin-echo/gradient echo images.

Subcutaneous Ex vivo

EPSI MRS experiments were completed with the following parameters: Image size 64*64; Data points = 256; FOV 50*50 mm; Band/Sweep width = 18.58 ppm; Centre Frequency/O1P = 4.7 ppm; TE = 4 ms; TR = 93.75 ms; FA= 15 degrees Slice thickness =10 mm. RG = 64

8.7 Chapter 6 Methods: d-DNP hyperpolarisation

8.7.1 Cell Culture (CRUK)

Patient derived xenograph (PDX) (breast cancer cells) were grown to a maximum cell density of $\sim 5 \times 10^7$ cells mL⁻¹.

8.7.2 Hyperpolarisation of ¹³C nicotinamide (CRUK)

155 mg of ¹³C nicotinamide (synthesised in CHyM, University of York) was dissolved in 217 μ l:93 μ l H₂O/glycerol containing 8.4 mg of trityl radical (OX063; GE Healthcare, Amersham, UK) and 3.1 μ l of (0.05 M) gadolinium chelate (Dotarem; Guerbet, Roissy, France). The solution was sonicated and centrifuged and a 114 mg (100 μ l) aliquot was hyperpolarised. The sample was rapidly cooled under liquid helium in a Hypersense hyperpolariser at a pressure of \sim 1mBar to \sim 1.2 K. Polarisation of the electron spins on the radical were transferred to the ¹³C label using microwave irradiation at 94.105 GHz over 1 hour. Following hyperpolarisation, the frozen samples were dissolved rapidly in 6 g (\sim 6 mL) of Phosphate Buffer Solution (PBS) pressurised to 10 bar and at 180 °C to yield a final pH in the physiological range pH 7-7.5.

8.7.3 Hyperpolarised ¹³C Spectroscopy (MRS) CSI *In Vivo* at 7 T (CRUK)

8.7.3.1 *Animals*

All animal experimentation was conducted in accordance with project and personal licences issued under the United Kingdom Animals (Scientific Procedures) Act, 1986. Protocols were approved by the Cancer Research UK, Cambridge Institute Animal Welfare and Ethical Review Body.

Tumours were established by subcutaneous inoculation of a suspension of 5×10^6 PDX breast cancer cells (in a volume of 200 μ L) in the right dorsal flank of NSG mice (n = 3, The Jackson Laboratory). PDX cells were implanted (5×10^6) in a single animal. MRI/CSI was performed when the tumours had grown to a size of approx. 1 x 1 cm³, which for PDX cells was 6 months after implantation (Table 8.1). A slow-release oestrogen pellet was also implanted subcutaneously in the left dorsal flank to encourage tumour growth.

Table 8.1: *In vivo* murine tumour size used for imaging

	Cage Number	Mouse ID	Weight (g)	Tumour Size (cm)	Experiment
1	11853	33192	29.7	1.2 x 1.1	SSBUILDUP3964 15 secs then acquisition CSI
2	11871	33280	27.7	1.0 x 0.9	SSBUILUP3965 Immediate acquisition Time course
3	11871	33279	24.7	1.1 x 0.9	SSBUILDUP3966 20 secs then acquisition High Resolution CSI

Animals were anaesthetised by inhalation of 3% isoflurane (Isoflo, Abbotts Laboratories Ltd.) in air/O₂ (75/25%, 2 L min⁻¹) and was maintained during the insertion of the tail vein cannula. A cannula was inserted into the tail vein with a 0.28 mm diameter tube (~600 mm in length) and syringe containing heparin diluted in sterile physiological saline (10 units/mL) in preparation for administration of the hyperpolarised solution. Animals were taped into the cradle to minimize breathing-related motions. Body temperature was maintained by blowing warm air directly to the animal through a tube within the magnet bore. Breathing rate (~60 bpm) and body temperature (37°C) were monitored during the entire experiment by a Biotrig physiological monitor (Small Animal Instruments, Stony Brook, NY). During imaging isoflurane level was reduced to 1-2 %.

8.7.3.2 *Magnetic resonance imaging and spectroscopy in vivo*

For *in vivo* experiments, a 20 mm diameter curved receive only surface coil (Rapid Biomedical GmbH, Rimpar, Germany) tuned to ¹³C was placed over the animal with a circle removed allowing the tumour to protrude. This was placed in a 42 mm ID transmit ¹³C/¹H birdcage volume coil (Rapid Biomedical, Germany), in a 7T Agilent horizontal bore magnet (Varian NMR instruments, gradient strength 400 mT/m) (Figure 8.3).

Transverse ¹H spin-echo images (Scout, axial_fsems, sagittal_fsems and coronal_fsems) were acquired to localize the tumour and plan the voxels for Chemical Shift Imaging (CSI).

In the first experiment data acquisition of the CSI was started 15 s after the start of administration of ^{13}C -nicotinamide (0.4 mL, 0.045 M, 7.4 mg/kg) with a total time between dissolution and data acquisition of ~ 30 s.

In the second experiment a slice selective pulse acquire sequence⁹⁷ was used to acquire single transient ^{13}C spectra every second for 180 seconds using a nominal FA of 5° (predetermined power amplitude from phantom experiments) Data acquisition started immediately from the point of injection of ^{13}C -nicotinamide (0.4 mL, x 0.067 M, x 7.9 mg/kg). There is a short wait of 0.83 ms then the acquisition train starts with 6010 Hz spectral width and 1024 data points.

In the third experiment data acquisition was started 20 s after administration of ^{13}C -nicotinamide (0.4 mL, x 0.067 M, x 8.9 mg/kg) and Chemical Shift Imaging (CSI)/ Magnetic Resonance Spectroscopy Imaging (MRSI)⁹⁷ was carried out. In this sequence k space is filled spiral centre out. This is a 2D image using an axial slice selective pulse. A 6 mm slice was used through the tumour and mouse torso (field of view 40 mm x 40 mm, repetition time 30 ms, echo time 22 ms, spectral width 6010 Hz, data matrix 32 x 32, nominal flip angle 9°).

Peak integrals were calculated in MATLAB (MathWorks) to generate a signal map, which was overlaid on reference ^1H spin-echo images.

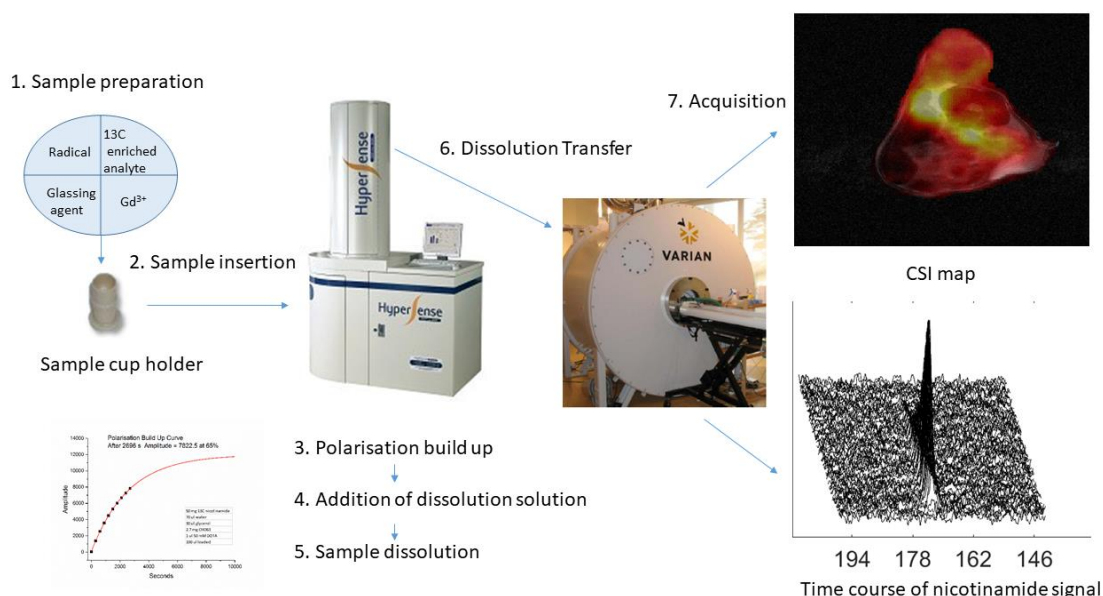


Figure 8.3: Schematic of the d-DNP-MRI process used to measure a hyperpolarised time course experiment of ^{13}C -nicotinamide within a tumour and a CSI distribution map of HP ^{13}C -nicotinamide within the mouse torso.

8.7.4 Hyperpolarised T_1 of ^{13}C nicotinamide (CHyM)

50 mg of ^{13}C nicotinamide (synthesised in CHyM, University of York) was dissolved in 70 μl :30 μl H_2O /glycerol containing 2.7 mg of trityl radical (OX063; GE Healthcare, Amersham, UK). The solution was sonicated and centrifuged, and a 114 mg (100 μl) aliquot was hyperpolarised. The sample was rapidly cooled under liquid helium in a Hypersense hyperpolariser at a pressure of ~ 1 mbar to ~ 1.2 K. Polarisation of the electron spins on the radical were transferred to the ^{13}C label using microwave irradiation at 94.035 GHz for 1 hour. Following hyperpolarisation, the frozen sample was dissolved rapidly in 6 mL of water pressurised to 10 bar and at 180 $^\circ\text{C}$ and transferred to a 400 MHz (9.4T) NMR spectrometer (Bruker). See Figure 8.4 for experimental set up. A series of ^{13}C -decoupled spectra were run every 2.5 seconds using a varied flip angle. The flip angles used were taken from previous shake and drop ^1H hyperpolarised T_1 experiments^{125, 345} and converted for ^{13}C (Table 8.2). NB: No Dotarem was added here.

Table 8.2: Variable FA used to estimate hyperpolarised ^{13}C T_1

Experiment	Flip Angle (θ)	Pulse Length (μs) when 90° is 9.25 μs
1	15.04	1.55
2	15.48	1.59
3	16.13	1.66
4	16.79	1.73
5	17.45	1.79
6	18.44	1.90
7	19.54	2.01
8	20.74	2.13
9	22.17	2.28
10	24.15	2.48
11	26.56	2.73
12	29.96	3.08
13	35.23	3.62
14	44.89	4.61
15	86.16	8.86

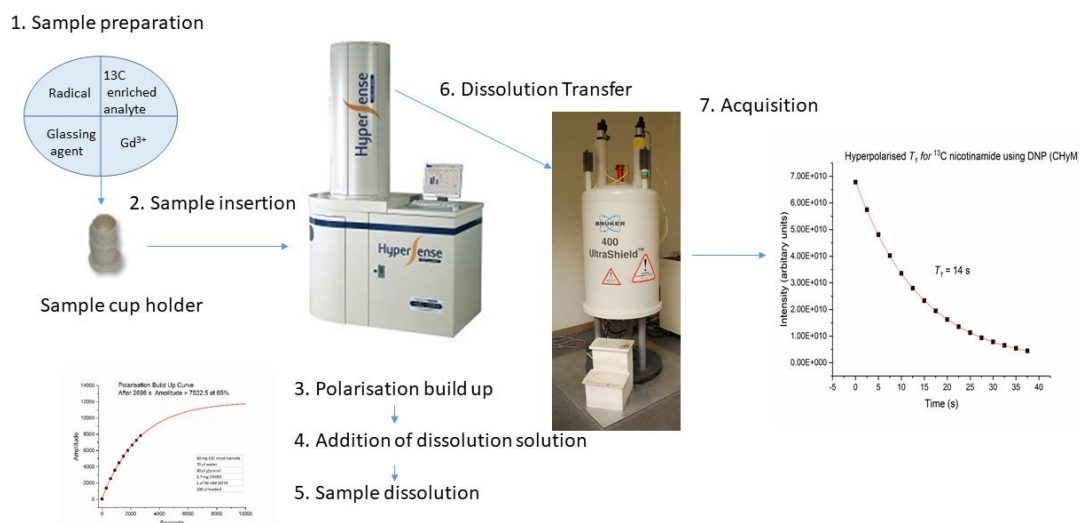


Figure 8.4: Schematic of the d-DNP-NMR process used to measure polarisation levels and hyperpolarised T_1 .

8.7.5 Hyperpolarised SABRE Imaging Experiments

Typical imaging parameters for experiments are given below.

9.4 T

FLASH ^1H – TR = 100 ms, TE = 2.3 ms, image size = 160 x 160, Slice thickness = 1 mm FOV 50 x 50 mm, 3 slices

FISP ^{13}C – TR = 410.7 ms, TE = 1.015 ms, Repts = 1, FA = 90°, Image size = 32 x 32, slice thickness = 10 mm FOV 40 x 40

EPSI ^{13}C - TR = 100 ms, TE = 3.7 ms, Repts = 1, FA = 30°, Image size = 32 x 32, slice thickness = 10 mm, FOV 40 x 40, SW = 62 ppm, No. of spectral points = 256

CSI ^{13}C - TR = 100 ms, TE = 1.22 ms, Repts = 1, FA = 30°, Image size = 16 x 16, slice thickness = 10 mm, FOV 40 x 40, SW = 150 ppm, No. of spectral points = 604

3T

Non-localised single pulse experiments ^{13}C – TR = 200, FA = 5°, Repts = 512

CSI ^{13}C - TR = 200 ms, TE = 2.3 ms, Repts = 8, FA = 5°, Image size = 16 x 16/ 8 x 8, slice thickness = 20 mm, FOV 200 x 200, SW = 322 ppm, No. of spectral points = 512



Table A 1: ^1H , ^{13}C and ^{15}N resonances of pre-catalyst A measured at 233 K in methanol- d_4 .

Resonance position	^1H – NMR (ppm)	^{13}C - NMR (ppm)	^{15}N – NMR (ppm)
a		-	
b			195.34
c	7.42, 2H overlap	124.76	
f	7.26 broad, 4H	129.1	
g			
h +j	2.40, br s, 12H		
i	2.45		
k CH^{COD}	3.70, 2H	64.4	
l CH^{COD}			
m CH^{COD}	3.38, 2H	80.5	
n CH^{COD}			
o CH_2^{COD}	1.93, 1.67	32.15	
p CH_2^{COD}	2.03, 1.65 v broad	28.76	
q CH_2^{COD}	2.03, 1.65 v broad	28.76	
$\text{RCH}_2^{\text{COD}}$	1.93, 1.67	32.15	
2	8.42	137.24	
3	7.48	122.54	
3a		139.98	
4	8.31	150.03	
5			286.63 (bound)
6			356.96
7	9.68	146.77	
7a		138.83	

Table A 2: ^1H , ^{13}C and ^{15}N resonances of pre-catalyst B measured at 233 K in methanol- d_4 .

Resonance position	^1H – NMR (ppm)	^{13}C - NMR (ppm)	^{15}N – NMR (ppm)
a		-	
b			195.34
c	7.42, 2H overlap	124.76	
f	6.72 br, 4H	Missing as very broad	
g			
h & j	2.40, br s, 12H		
i	2.43, s, 6H Rapid exchange		
k CH^{COD}	3.70, 2H	64.4	
l CH^{COD}			
m CH^{COD}	3.37, 2H	80.5	
n CH^{COD}			
o CH_2^{COD}	1.93, 1.67	32.15	
p CH_2^{COD}	2.03, 1.65 v broad	28.76	
q CH_2^{COD}	2.03, 1.65 v broad	28.76	
r CH_2^{COD}	1.93, 1.67	32.15	
2	7.76	121.15	
3	8.44	138.1	
3a		141.66	
4	9.51	146.67	
5			359.97
6			285.52 (bound)
7	8.43	150.0	
7a		135.94	

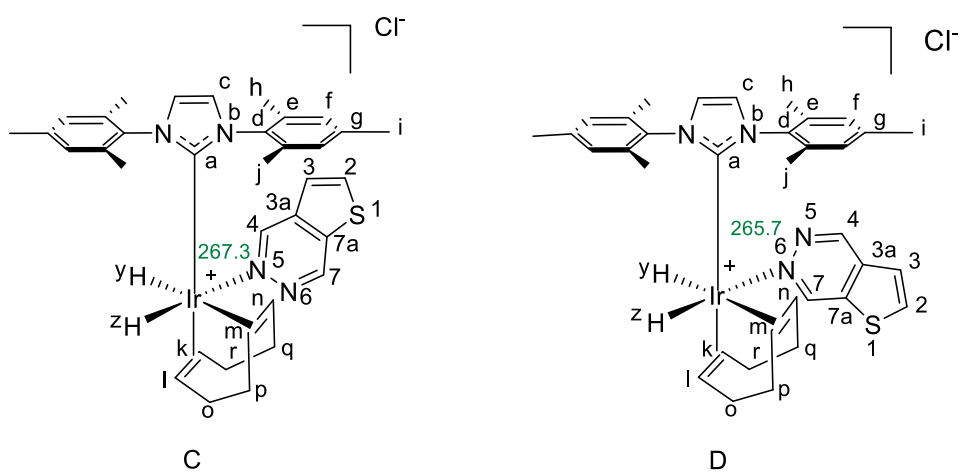


Figure A 2: Structures of intermediates $[\text{Ir}(\text{COD})(\text{H})_2(\text{IMes})(\text{T}[2,3\text{-}d]\text{P})]\text{Cl}$ C and D.

Table A 3: ^1H , ^{13}C and ^{15}N resonances of intermediate C $[\text{Ir}(\text{COD})(\text{H})_2(\text{IMes})(\text{T}[2,3\text{-d}]\text{P})]\text{Cl}$ measured at 233 K in methanol- d_4 (500 MHz spectrometer).

Resonance position	^1H – NMR (ppm)	^{13}C - NMR (ppm)	^{15}N – NMR (ppm)
a			
b			198
c	7.30	124.0	
d			
e		138.50	
e''		137.48	
f	6.82		
f''	7.00		
g			
h	1.67		
i	2.35		
j	2.25		
k CH^{COD}	4.36	95.39	
l CH^{COD}	5.20	97.97	
m CH^{COD}	5.16	78.5	
n CH^{COD}	3.83	82.88	
o CH_2^{COD}	1.73, 1.96	27.3	
p CH_2^{COD}	2.71, 2.20	35.5	
q CH_2^{COD}	1.90, 1.32	28.01	
r CH_2^{COD}	1.70, 1.80	30.0	
Y	-13.87, d $J_{\text{HH}} = 2.56$ Hz		
Z	-17.62 d $J_{\text{HH}} = 2.56$ Hz		
2	8.42	137.0	
3	7.64	122.5	
3a			
4	9.38	157.89	
5			267.3 (bound)
6			
7	9.65	147.85	
7a			

Table A 4: ^1H , ^{13}C and ^{15}N resonances of intermediate D $[\text{Ir}(\text{COD})(\text{H})_2(\text{IMes})(\text{T}[2,3\text{-}d]\text{P})]\text{Cl}$ measured at 233 K in methanol- d_4 (500 MHz spectrometer).

Resonance position	^1H – NMR (ppm)	^{13}C - NMR (ppm)	^{15}N – NMR (ppm)
a			
b	-	-	198.0
c	7.30	124	
d			
e			
e''			
f	6.84		
f''	7.02		
g			
h	1.63		
i	2.36		
j	2.26		
k CH^{COD}	4.33	95.39	-
l CH^{COD}	5.22	97.97	-
m CH^{COD}	5.16	78.5	-
n CH^{COD}	3.82	82.88	-
o CH_2^{COD}	1.73, 1.96	27.3	-
p CH_2^{COD}	2.71, 2.20	35.5	-
q CH_2^{COD}	1.90, 1.32	28.01	-
r CH_2^{COD}	1.70, 1.80	30.0	-
y	-13.92, d $J_{\text{HH}} = 2.6$ Hz	-	-
z	-17.70, d $J_{\text{HH}} = 2.6$ Hz	-	-
2	8.45	138.7	-
3	7.84	122.2	-
3a	-	?	-
4	9.50	147.9	-
5	-		
6	-		265.7 (bound)
7	9.53	157.7	-
7a	-		-

Appendix 2 Characterisation data for eight SABRE active complexes.

Table A 5: Characterisation data for eight SABRE active complexes E-L

Reson./ Complex	Equatorial 1								Equatorial 2								Axial								Hydrides			
	H2	H3	H4	H7	N1	N2	H2	H3	H4	H7	N1	N2	H2	H3	H4	H7	N1	N2	H2	H3	H4	H7	N1	N2	H1	H2		
E			9.355	9.981	302.09	361.557																						
F	8.26*	7.585	9.988*	9.3551	301.978	361.525	8.26*	7.585	9.988*	9.355	301.978	361.525	8.168	7.374	8.5764	10.2393	364.89	281.783										
G	8.282	7.704	9.2025	10.141	363.294	301.086	8.282	7.704	9.2025	10.141	363.294	301.086	8.168	7.374*	8.5654*	10.2365	364.49	281.393										
H				10.138	363.334	301.209				10.138	363.334	301.209	8.148	7.658	8.713	10.094	282.726	362.48										
I			9.3511	10.0154	301.307	361.358				10.104	363.556	301.989	7.658	8.148	8.718	10.091	282.941	362.66										
J			9.3511	10.0154	301.307	361.358				10.104	363.556	301.989	7.658	8.148	8.718	10.091	282.941	362.66										
K	8.26	7.593	9.3511	10.02	301.176	361.302	8.282	7.704*	9.2044*	10.105	363.518	301.890	7.374	8.168	8.5707	10.2378	281.598	364.67										
L	8.26	7.593	9.3511	10.02	301.176	361.302	8.282	7.704*	9.2044*	10.105	363.518	301.890	7.374	8.168	8.5707	10.2378	281.598	364.67										

Appendix 3: Characterisation data of complexes formed during SABRE-Relay

 ^1H NMR characterisation of $[\text{Ir}(\text{H})_2(d_{22}\text{-IMes})(2,4\text{-}d_2\text{-nicotinamide})_3]\text{Cl}$:

^1H NMR (500 MHz, CD_3OD): 8.58 (d. $J_{\text{HH}} = 5.3$, 1H, *ortho* NCH nicotinamide *trans* to Hydride, equatorial position), 8.03 (d. $J_{\text{HH}} = 5.5$, 1H, *ortho* NCH nicotinamide *trans* to NHC, axial position), 7.35 (d. $J_{\text{HH}} = 5.3$ *meta* NCHCH nicotinamide *trans* to Hydride, equatorial position), 7.13 (s. 2H, NCH d_{22} -IMes), 7.06 (d. $J_{\text{HH}} = 5.5$, 1H, *meta* NCHCH nicotinamide *trans* to NHC, axial position), -22.65 (s. 2H, IrH). Note – the protons of the amide rapidly exchange with the deuterium of the d_4 -methanol solvent, thus they are not observed in ^1H NMR spectra. (245K)

 ^1H and ^{31}P NMR characterisation of $[\text{Pt}(\text{OTf})(\text{dppm})(2,4\text{-}d_2\text{-nicotinamide})]\text{OTf}$:

^1H NMR (400 MHz, CD_3OD , 243K): δ 8.83 (d.d. $J_{\text{HH}} = 5.5$, $J_{\text{HP}} = 3.4$, 1H, *ortho* NCH nicotinamide on platinum), 8.12 (d.d. $J_{\text{HP}} = 13.9$, $J_{\text{HH}} = 7.5$, 4H, *ortho* PCCH (phenyl rings) *trans* to nicotinamide), 7.75 (d. $J_{\text{HH}} = 5.5$, 1H, *meta* NCHCH nicotinamide on platinum), 7.70 (m. 4H, *meta* PCCHCH (phenyl rings) *trans* to nicotinamide), 7.67 (*ps-t.* $J_{\text{HH}} = 6.8$, 4H, *ortho* PCCH (phenyl rings) *trans* to triflate), 7.57 (m. $J_{\text{HH}} = 8.1$, 4H, *meta* PCCHCH (phenyl rings) *trans* to triflate), 4.59 (s. 2H, PCH₂). ^{31}P NMR (500 MHz, CD_3OD): -57.35 (d. $J_{\text{PP}} = 69.6$, $J_{\text{PPt}} = 2900$, P *trans* to triflate), -64.39 (d. $J_{\text{PP}} = 69.6$, $J_{\text{PPt}} = 2900$, P *trans* to nicotinamide).

Abbreviations

% V _{bur}	Percentage buried volume
3-Cl-6-CF ₃ -py	3-chloro-6-(trifluoromethyl)pyridazine
3-Cl-6-OCH ₃ -p	3-chloro-6-methoxypyridazine
3-NH ₂ -6-Cl-py	3-amino-6-chloropyridazine
ALTADENA	Adiabatic Longitudinal Transport After Dissociation Engenders Net Alignment
BH ₃ .DMS	borane dimethylsulfide
BH ₃ .THF	borane-tetrahydrofuran
CA	Contrast agent
CASH-SABRE	Catalyst separated hyperpolarisation
COA	Cyclooctane
COD	1,5-Cyclooctadiene
COSY	Correlation Spectroscopy
CSI	Chemical Shift Imaging
CT	Computerised Tomography
DCM	Dichloromethane
d-DNP	Dissolution DNP
DEAE	Diethylaminoethyl
DMG	directed ortho-metalation group
DMSO	Dimethyl sulfoxide
DNP	Dynamic Nuclear Polarisation
dppe	1,3-bis(diphenylphosphino)ethane
dppm	1,3-bis(diphenylphosphino)methane
dppp	1,3-bis(diphenylphosphino)propane
EEG	electroencephalography
EPR	Electron paramagnetic resonance
EPSI	Echoplanar Spectroscopic Imaging
EXSY	EXchange SpectroscopY
F[2,3- <i>d</i>]P	Furo[2,3- <i>d</i>]pyridazine
FA	Flip angle
FDG	2-deoxy-2(¹⁸ F)fluoro-D-glucose
FID	Free Induction Decay
FISP	Fast Imaging with Steady state free Precession
FLASH	Fast low-angle shot
FOV	Field of View
FPG	fasting plasma glucose
HMQC	Heteronuclear Multiple Quantum Coherence
ICP-MS	Inductively Coupled Plasma – Mass Spectrometry
IKK	IκB kinases
IMes	1,3-Bis(2,4,6-trimethylphenyl)-imidazol-2-ylidene
INEPT	Insensitive Nuclei Enhanced by Polarisation Transfer
IR	Infrared
LAC	Level Anti-Crossing
LIGHT-SABRE	Low Irradiation Generation of High Tesla-SABRE
m/z	Mass/Charge ratio
MEGA-PRESS	MEscher-Garwood Point RESolved Spectroscopy
MRI	Magnetic Resonance Imaging
MRS	Magnetic Resonance Spectroscopy
MS	Mass Spectrometry
NAD	Nicotinamide Adenine Dinucleotide
nBuLi	n-Butyllithium

NHC	<i>N</i> -heterocyclic Carbene
NMR	Nuclear Magnetic Resonance
NOESY	Nuclear Overhauser Effect spectroscopy
<i>o</i> -H ₂	<i>Ortho</i> -hydrogen
OTf	Triflate
PARPS	poly ADP-ribose polymerases
PASADENA	<i>Para</i> -H ₂ And Synthesis Allow Dramatically Enhanced Nuclear Alignment
PDX	Patient Derived Xenograft
PET	Positron Emission Tomography
Ph	Phenyl
<i>p</i> -H ₂	<i>Para</i> -hydrogen
PHIP	<i>Para</i> -H ₂ Induced Polarisation
PHIP-SAH	<i>Para</i> -H ₂ Induced Polarisation-Side Arm Hydrogenation
PTF	Polarisation Transfer Field
PTT	Polarisation Transfer Time
pz	Pyrazine
RARE	Rapid Acquisition with Refocused Echoes
RF	Radiofrequency Pulse
Rf	Retention factor values
S/N	Signal to Noise Ratio
SABRE	Signal Amplification By Reversible Exchange
SEOP	Spin Exchange Optical Pumping
SIMes	1,3-bis(2,3,6-trimethylphenyl)-4,5-dihydroimidazol-2-ylidene
SPECT	single photon emission computed tomography
T[2,3- <i>c</i>]P	Thieno[2,3- <i>c</i>]pyridazine
T[2,3- <i>d</i>]P	Thieno[2,3- <i>d</i>]pyridazine
T[3,2- <i>c</i>]P	Thieno[3,2- <i>c</i>]pyridazine
T[3,4- <i>d</i>]P	Thieno[3,4- <i>d</i>]pyridazine
TCA	Tricarboxylic Acid
TE	Echo Time
TEMPO	(2,2,6,6-Tetramethylpiperidin-1-yl)oxidanyl
THF	Tetrahydrofuran

References

1. J. L. Markley, R. Bruschweiler, A. S. Edison, H. R. Eghbalnia, R. Powers, D. Raftery and D. S. Wishart, *Curr. Opin. Biotechnol.*, 2017, **43**, 34-40.
2. T. Bezabeh, O. B. Ijare, A. E. Nikulin, R. L. Somorjai and I. C. Smith, *Magn. Reson. Insights*, 2014, **7**, 1-14.
3. J. H. Ardenkjaer-Larsen, B. Fridlund, A. Gram, G. Hansson, L. Hansson, M. H. Lerche, R. Servin, M. Thaning and K. Golman, *Proc. Natl. Acad. Sci. U. S. A.*, 2003, **100**, 10158-10163.
4. S. J. Nelson, J. Kurhanewicz, D. B. Vigneron, P. E. Z. Larson, A. L. Harzstark, M. Ferrone, M. van Criekinge, J. W. Chang, R. Bok, I. Park, G. Reed, L. Carvajal, E. J. Small, P. Munster, V. K. Weinberg, J. H. Ardenkjaer-Larsen, A. P. Chen, R. E. Hurd, L. I. Odegardstuen, F. J. Robb, J. Tropp and J. A. Murray, *Sci. Transl. Med.*, 2013, **5**.
5. P. Nikolaou, B. M. Goodson and E. Y. Chekmenev, *Chem. Eur. J.*, 2015, **21**, 3156-3166.
6. J. G. Skinner, L. Menichetti, A. Flori, A. Dost, A. B. Schmidt, M. Plaumann, F. A. Gallagher and J.-B. Hoenner, *Mol. Imaging. Biol.*, 2018, **20**, 902-918.
7. F. A. Gallagher, R. Woitek, M. A. McLean, A. B. Gill, R. M. Garcia, E. Provenzano, F. Riemer, J. Kaggie, A. Chhabra, S. Ursprung, J. T. Grist, C. J. Daniels, F. Zaccagna, M. C. Laurent, M. Locke, S. Hilborne, A. Frary, T. Torheim, C. Boursnell, A. Schiller, I. Patterson, R. Slough, B. Carmo, J. Kane, H. Biggs, E. Harrison, S. S. Deen, A. Patterson, T. Lanz, Z. Kingsbury, M. Ross, B. Basu, R. Baird, D. J. Lomas, E. Sala, J. Wason, O. M. Rueda, S. F. Chin, I. B. Wilkinson, M. J. Graves, J. E. Abraham, F. J. Gilbert, C. Caldas and K. M. Brindle, *Proc. Natl. Acad. Sci. U. S. A.*, 2020, **117**, 2092-2098.
8. J. W. Gordon, H. Y. Chen, N. Dwork, S. Y. Tang and P. E. Z. Larson, *J. Magn. Reson. Imaging*, 2020, **53**, 686-702.
9. I. Oransky, *Lancet*, 2004, **364**, 1032-1032.
10. G. N. Hounsfield, *Br. J. Radiol.*, 1973, **46**, 1016-1022.
11. P. C. Lauterbur, *Nature*, 1973, **242**, 190-191.
12. D. J. Brenner, *Rev Environ Health*, 2010, **25**, 63-68.
13. H. E. Davies, C. G. Wathen and F. V. Gleeson, *Br. Med. J.*, 2011, **342**.
14. R. Mathew, K. Haque and W. Woothipoom, *Br. Med. J.*, 2006, **333**, 539-540.
15. B. F. Hutton, *Eur. J. Nucl. Med. Mol. Imaging.*, 2014, **41**, S3-S16.
16. D. E. Kuhl and R. Q. Edwards, *Radiology*, 1963, **80**, 653-662.
17. M. D. Devous, R. A. Thisted, G. F. Morgan, R. F. Leroy and C. C. Rowe, *J. Nucl. Med.*, 1998, **39**, 285-293.
18. R. B. Schwartz, A. L. Komaroff, B. M. Garada, M. Gleit, T. H. Doolittle, D. W. Bates, R. G. Vasile and B. L. Holman, *Am. J. Roentgenol.*, 1994, **162**, 943-951.
19. L. W. Dobrucki and A. J. Sinusas, *Nat. Rev. Cardiol.*, 2010, **7**, 38-47.
20. A. Prasad, A. Chaichi, D. P. Kelley, J. Francis and M. R. Gartia, *Rsc Advances*, 2019, **9**, 24568-24594.
21. R. Nutt, *Mol. Imaging. Biol.*, 2002, **4**, 11-26.
22. E. J. Hoffman, M. E. Phelps, N. A. Mullani, C. S. Higgins and M. M. Terpogossian, *J. Nucl. Med.*, 1976, **17**, 493-502.
23. W. Wadsak and M. Mitterhauser, *Eur. J. Radiol.*, 2010, **73**, 461-469.
24. P. Som, H. L. Atkins, D. Bandoyadhyay, J. S. Fowler, R. R. Macgregor, K. Matsui, Z. H. Oster, D. F. Sacker, C. Y. Shiue, H. Turner, C. N. Wan, A. P. Wolf and S. V. Zabinski, *J. Nucl. Med.*, 1980, **21**, 670-675.
25. K. Brindle, *Nat. Rev. Cancer*, 2008, **8**, 94-107.

26. M. F. Di Carli, S. Dorbala, Z. Curillova, R. J. Kwong, S. Z. Goldhaber, F. J. Rybicki and R. Hachamovitch, *J. Nucl. Cardiol.*, 2007, **14**, 799-809.
27. A. Newberg, A. Alavi and M. Reivich, *Semin. Nucl. Med.*, 2002, **32**, 13-34.
28. G. Kelloff, J. M. Hoffman, B. Johnson, H. I. Scher, B. A. Siegel, E. Y. Cheng, B. D. Cheson, J. O'Shaughnessy, K. Z. Guyton, D. A. Mankoff, L. Shankar, S. M. Larson, C. C. Sigman, R. L. Schilsky and D. C. Sullivan, *Clin. Cancer Res.*, 2005, **11**, 2785-2808.
29. B. P. Burke, C. S. Miranda, R. E. Lee, I. Renard, S. Nigam, G. S. Clemente, T. D'Huys, T. Ruest, J. Domarkas, J. A. Thompson, T. J. Hubin, D. Schols, C. J. Cawthorne and S. J. Archibald, *J. Nucl. Med.*, 2020, **61**, 123-128.
30. N. Oriuchi, T. Higuchi, T. Ishikita, M. Miyakubo, H. Hanaoka, Y. Iida and K. Endo, *Cancer Sci.*, 2006, **97**, 1291-1297.
31. R. Hustinx, F. Benard and A. Alavi, *Semin. Nucl. Med.*, 2002, **32**, 35-46.
32. S. Stroobants, J. Goeminne, M. Seegers, S. Dimitrijevic, P. Dupont, J. Nuyts, M. Martens, B. van den Borne, P. Cole, R. Sciot, H. Dumez, S. Silberman, L. Mortelmans and A. van Oosterom, *Eur. J. Cancer*, 2003, **39**, 2012-2020.
33. I. Sobhani, E. Tiret, R. Lebtahi, T. Aparicio, E. Itti, F. Montravers, C. Vaylet, P. Rougier, T. Andre, J. M. Gornet, D. Cherqui, C. Delbaldo, Y. Panis, J. N. Talbot, M. Meignan and D. Le Guludec, *Br. J. Cancer*, 2008, **98**, 875-880.
34. S. Sebastian, S. I. Lee, N. S. Horowitz, J. A. Scott, A. J. Fischman, J. F. Simeone, A. F. Fuller and P. F. Hahn, *Abdom. Imaging*, 2008, **33**, 112-118.
35. O. Warburg, F. Wind and E. Negelein, *J. Gen. Physiology*, 1927, **8**, 519-530.
36. A. Shetty and J. D. Carter, *Radiol. Case Rep.*, 2011, **6**, 409-409.
37. M. E. Juweid and B. D. Cheson, *N. Engl. J. Med.*, 2006, **354**, 496-507.
38. P. D. Shreve, Y. Anzai and R. L. Wahl, *Radiographics*, 1999, **19**, 61-77.
39. G. B. Saha, W. J. Macintyre and R. T. Go, *Semin. Nucl. Med.*, 1992, **22**, 150-161.
40. B. Fischer, U. Lassen, J. Mortensen, S. Larsen, A. Loft, A. Bertelsen, J. Ravn, P. Clementsen, A. Hogholm, K. Larsen, T. Rasmussen, S. Keiding, A. Dirksen, O. Gerke, B. Skov, I. Steffensen, H. Hansen, P. Vilmann, G. Jacobsen, V. Backer, N. Maltbaek, J. Pedersen, H. Madsen, H. Nielsen and L. Hojgaard, *N. Engl. J. Med.*, 2009, **361**, 32-39.
41. T. Beyer, D. W. Townsend, T. Brun, P. E. Kinahan, M. Charron, R. Roddy, J. Jerin, J. Young, L. Byars and R. Nutt, *J. Nucl. Med.*, 2000, **41**, 1369-1379.
42. D. W. Townsend, T. Beyer, P. Kinahan, C. C. Meltzer, T. Brun and R. Nutt, *Radiology*, 1998, **209P**, 169-170.
43. G. K. von Schulthess, H. C. Steinert and T. F. Hany, *Radiology*, 2006, **238**, 405-422.
44. S. Zou and X. Zhu, *Radiology*, 2020, **296**, E118.
45. L. Setti, M. Kirienko, S. C. Dalto, M. Bonacina and E. Bombardieri, *Eur. J. Nucl. Med. Mol. Imaging.*, 2020, **47**, 1649-1656.
46. Y. P. Shao, S. R. Cherry, K. Farahani, K. Meadors, S. Siegel, R. W. Silverman and P. K. Marsden, *Phys. Med. Biol.*, 1997, **42**, 1965-1970.
47. N. J. Shah, A. M. Oros-Peusquens, J. Arrubla, K. Zhang, T. Warbrick, J. Mauler, K. Vahedipour, S. Romanzetti, J. Felder, A. Celik, E. Rota-Kops, H. Iida, K. J. Langen, H. Herzog and I. Neuner, *J. Magn. Reson.*, 2013, **229**, 101-115.
48. M. A. Jacobs, R. Ouwerkerk, A. C. Wolff, E. Gabrielson, H. Warzecha, S. Jeter, D. A. Bluemke, R. Wahl and V. Stearns, *Breast Cancer Res.Tr.*, 2011, **128**, 119-126.
49. D. W. Townsend, *J. Nucl. Med.*, 2008, **49**, 938-955.
50. J. Kurhanewicz, M. G. Swanson, S. J. Nelson and D. B. Vigneron, *J. Magn. Reson. Imaging*, 2002, **16**, 451-463.

51. J. M. N. Duarte, H. X. Lei, V. Mlynarik and R. Gruetter, *Neuroimage*, 2012, **61**, 342-362.
52. C. D. Rae and S. R. Williams, *Anal. Biochem.*, 2017, **529**, 127-143.
53. M. G. Saleh, G. Oeltzschner, K. L. Chan, N. A. J. Puts, M. Mikkelsen, M. Schar, A. D. Harris and R. A. E. Edden, *Neuroimage*, 2016, **142**, 576-582.
54. H. Zhu and P. B. Barker, *Methods Mol. Biol.*, 2011, **711**, 203-226.
55. R. G. Shulman, T. R. Brown, K. Ugurbil, S. Ogawa, S. M. Cohen and J. A. D. Hollander, *Science*, 1979, **205**, 160-166.
56. Y. C. Liu, Y. N. Gu and X. Yu, *Quant. Imag. Med. Surg.*, 2017, **7**, 707-726.
57. A. D. Hendriks, W. J. M. van der Kemp, P. R. Luijten, N. Petridou and D. W. J. Klomp, *NMR Biomed.*, 2019, **32**.
58. V. D. Schepkin, B. D. Ross, T. L. Chenevert, A. Rehemtulla, S. Sharma, M. Kumar and J. Stojanovska, *Magn. Reson. Med.*, 2005, **53**, 85-92.
59. F. Wetterling, D. M. Corteville, R. Kalayciyan, A. Rennings, S. Konstandin, A. M. Nagel, H. Stark and L. R. Schad, *Phys. Med. Biol.*, 2012, **57**, 4555-4567.
60. E. R. Andrew, *British Medical Bulletin*, 1984, **40**, 115-&.
61. F. Bloch, W. W. Hansen and M. Packard, *Phys. Rev.*, 1946, **69**, 127-127.
62. E. M. Purcell, H. C. Torrey and R. V. Pound, *Phys. Rev.*, 1946, **69**, 37-38.
63. P. T. Callaghan, *Principles of Nuclear Magnetic Resonance Microscopy*, Oxford University Press, Oxford, 1993.
64. P. J. Hore, in *Nuclear Magnetic Resonance*, Oxford University Press, New York, U.S., 32 edn., 1995, ch. 1.
65. M. H. Levitt, *Spin Dynamics: Basics of Nuclear Magnetic Resonance*, John Wiley & Sons Ltd, Second edn., 2008.
66. H. H. Mitchell, T. S. Hamilton, F. R. Steggerda and H. W. Bean, *J. Biol. Chem.*, 1945, **158**, 625-637.
67. S. Currie, N. Hoggard, I. J. Craven, M. Hadjivassiliou and I. D. Wilkinson, *Postgrad. Med. J.*, 2013, **89**, 209-223.
68. D. C. Preston, Magnetic Resonance Imaging (MRI) of the Brain and Spine: Basics, <https://case.edu/med/neurology/NR/MRI%20Basics.htm>.
69. P. Mansfield, *Magn. Reson. Med.*, 1984, **1**, 370-386.
70. A. N. Garroway, P. K. Grannell and P. Mansfield, *J. Phys. C.*, 1974, **7**, L457-L462.
71. B. R. J. Friedman, J.P.; Chavez-Munoz, G.; Salmon, A.P.; Merritt, C.R.B., *Principles of MRI*, McGraw Hill Book Co; New York, NY (USA), 1221 Avenue of the Americas, New York, NY 10020 (USA), 1989.
72. K. M. Brindle, *J. Am. Chem. Soc.*, 2015, **137**, 6418-6427.
73. M. N. Hopkinson, C. Richter, M. Schedler and F. Glorius, *Nature*, 2014, **510**, 485-496.
74. A. W. Overhauser, *Phys. Rev.*, 1953, **92**, 411-415.
75. M. Kirby, A. Ouriadov, S. Svenningsen, A. Owrangi, A. Wheatley, R. Etemad-Rezai, G. E. Santyr, D. G. McCormack and G. Parraga, *Physiol. Rep.*, 2014, **2**.
76. J. P. Mugler and T. A. Altes, *J. Magn. Reson. Imaging*, 2013, **37**, 313-331.
77. B. M. Goodson, *J. Magn. Reson.*, 2002, **155**, 157-216.
78. E. E. de Lange, J. P. Mugler, J. R. Brookeman, J. Knight-Scott, J. D. Truwit, C. D. Teates, T. M. Daniel, P. L. Bogorad and G. D. Cates, *Radiology*, 1999, **210**, 851-857.
79. X. J. Xu, G. Norquay, S. R. Parnell, M. H. Deppe, S. Ajraoui, R. Hashoian, H. Marshall, P. D. Griffiths, J. Parra-Robles and J. M. Wild, *Magn. Reson. Med.*, 2012, **68**, 1900-1904.

80. G. Norquay, S. R. Parnell, X. J. Xu, J. Parra-Robles and J. M. Wild, *J. Appl. Phys.*, 2013, **113**.
81. J. M. Wild, H. Marshall, X. X. Xu, G. Norquay, S. R. Parnell, M. Clemence, P. D. Griffiths and J. Parra-Robles, *Radiology*, 2013, **267**, 251-255.
82. R. R. Rizi, I. E. Dimitrov, A. Thompson, G. Jones, T. R. Gentile, M. Ishii, R. Reddy, M. D. Schnall and J. S. Leigh, *Magn. Reson. Med.*, 1998, **39**, 865-868.
83. S. D. Swanson, M. S. Rosen, B. W. Agranoff, K. P. Coulter, R. C. Welsh and T. E. Chupp, *Magn. Reson. Med.*, 1997, **38**, 695-698.
84. M. J. Couch, I. K. Ball, T. Li, M. S. Fox, S. L. Littlefield, B. Biman and M. S. Albert, *Radiology*, 2013, **269**, 903-909.
85. S. J. Kruger, S. K. Nagle, M. J. Couch, Y. Ohno, M. Albert and S. B. Fain, *J. Magn. Reson. Imaging*, 2016, **43**, 295-315.
86. T. R. Carver and C. P. Slichter, *Phys. Rev.*, 1956, **102**, 975-980.
87. Y. Lee, *Appl. Spectrosc. Rev.*, 2016, **51**, 190-206.
88. C. D. Jeffries, *Phys. Rev.*, 1957, **106**, 164-165.
89. M. Borghini and K. Scheffler, *Phys. Rev. Lett.*, 1971, **26**, 1362-+.
90. C. F. Hwang and D. A. Hill, *Phys. Rev. Lett.*, 1967, **19**, 1011-&.
91. J. Kurhanewicz, D. B. Vigneron, K. Brindle, E. Y. Chekmenev, A. Comment, C. H. Cunningham, R. J. DeBerardinis, G. G. Green, M. O. Leach, S. S. Rajan, R. R. Rizi, B. D. Ross, W. S. Warren and C. R. Malloy, *Neoplasia*, 2011, **13**, 81-97.
92. F. A. Gallagher, S. E. Bohndiek, M. I. Kettunen, D. Y. Lewis, D. Soloviev and K. M. Brindle, *J. Nucl. Med.*, 2011, **52**, 1333-1336.
93. U. L. Gunther, in *Modern Nmr Methodology*, eds. H. Heise and S. Matthews, 2013, vol. 335, pp. 23-69.
94. J. Kurhanewicz, R. Bok, S. J. Nelson and D. B. Vigneron, *J. Nucl. Med.*, 2008, **49**, 341-344.
95. D. Mayer, Y. F. Yen, J. Tropp, A. Pfefferbaum, R. E. Hurd and D. M. Spielman, *Magn. Reson. Med.*, 2009, **62**, 557-564.
96. A. Comment, *J. Magn. Reson.*, 2016, **264**, 39-48.
97. S. E. Day, M. I. Kettunen, F. A. Gallagher, D. E. Hu, M. Lerche, J. Wolber, K. Golman, J. H. Ardenkjaer-Larsen and K. M. Brindle, *Nat. Med. (N. Y., NY, U. S.)*, 2007, **13**, 1382-1387.
98. A. P. Chen, M. J. Albers, C. H. Cunningham, S. J. Kohler, Y. F. Yen, R. E. Hurd, J. Tropp, R. Bok, J. M. Pauly, S. J. Nelson, J. Kurhanewicz and D. B. Vigneron, *Magn. Reson. Med.*, 2007, **58**, 1099-1106.
99. F. A. Gallagher, M. I. Kettunen, D. E. Hu, P. R. Jensen, R. in't Zandt, M. Karlsson, A. Gisselsson, S. K. Nelson, T. H. Witney, S. E. Bohndiek, G. Hansson, T. Peitersen, M. H. Lerche and K. M. Brindle, *Proc. Natl. Acad. Sci. U. S. A.*, 2009, **106**, 19801-19806.
100. K. Golman, J. S. Petersson, P. Magnusson, E. Johansson, P. Akeson, C. M. Chai, G. Hansson and S. Mansson, *Magn. Reson. Med.*, 2008, **59**, 1005-1013.
101. M. E. Merritt, C. Harrison, C. Storey, F. M. Jeffrey, A. D. Sherry and C. R. Malloy, *Proc. Natl. Acad. Sci. U. S. A.*, 2007, **104**, 19773-19777.
102. M. A. Schroeder, L. E. Cochlin, L. C. Heather, K. Clarke, G. K. Radda, D. J. Tyler and R. G. Shulman, *Proc. Natl. Acad. Sci. U. S. A.*, 2008, **105**, 12051-12056.
103. M. S. Dodd, H. J. Atherton, C. A. Carr, D. J. Stuckey, J. A. West, J. L. Griffin, G. K. Radda, K. Clarke, L. C. Heather and D. J. Tyler, *Circ. Cardiovasc. Imaging*, 2014, **7**, 895-+.
104. S. Mansson, E. Johansson, P. Magnusson, C. M. Chai, G. Hansson, J. S. Petersson, F. Stahlberg and K. Golman, *Eur. Radiol.*, 2006, **16**, 57-67.

105. J. Svensson, S. Mansson, E. Johansson, J. S. Petersson and L. E. Olsson, *Magn. Reson. Med.*, 2003, **50**, 256-262.
106. D. M. Wilson, K. R. Keshari, P. E. Z. Larson, A. P. Chen, S. Hu, M. Van Criekinge, R. Bok, S. J. Nelson, J. M. Macdonald, D. B. Vigneron and J. Kurhanewicz, *J. Magn. Reson.*, 2010, **205**, 141-147.
107. K. F. Bonhoeffer and P. Harteck, *Z. Phys. Chem B-Chem E*, 1929, **5**, 292-292.
108. C. R. Bowers and D. P. Weitekamp, *Phys. Rev. Lett.*, 1986, **57**, 2645-2648.
109. C. R. Bowers and D. P. Weitekamp, *J. Am. Chem. Soc.*, 1987, **109**, 5541-5542.
110. F. Reineri, T. Boi and S. Aime, *Nat. Commun.*, 2015, **6**.
111. E. Cavallari, C. Carrera, M. Sorge, G. Bonne, A. Muchir, S. Aime and F. Reineri, *Sci. Rep.*, 2018, **8**.
112. R. W. Adams, J. A. Aguilar, K. D. Atkinson, M. J. Cowley, P. I. P. Elliott, S. B. Duckett, G. G. R. Green, I. G. Khazal, J. Lopez-Serrano and D. C. Williamson, *Science*, 2009, **323**, 1708-1711.
113. K. D. Atkinson, M. J. Cowley, S. B. Duckett, P. I. P. Elliott, G. G. R. Green, J. Lopez-Serrano, I. G. Khazal and A. C. Whitwood, *Inorg. Chem.*, 2009, **48**, 663-670.
114. B. J. A. van Weerdenburg, S. Glogglar, N. Eshuis, A. H. J. Engwerda, J. M. M. Smits, R. de Gelder, S. Appelt, S. S. Wymenga, M. Tessari, M. C. Feiters, B. Blumich and F. Rutjes, *Chem. Commun. (Cambridge, U. K.)*, 2013, **49**, 7388-7390.
115. M. J. Cowley, R. W. Adams, K. D. Atkinson, M. C. R. Cockett, S. B. Duckett, G. G. R. Green, J. A. B. Lohman, R. Kerssebaum, D. Kilgour and R. E. Mewis, *J. Am. Chem. Soc.*, 2011, **133**, 6134-6137.
116. S. Diez-Gonzalez and S. P. Nolan, *Coord. Chem. Rev.*, 2007, **251**, 874-883.
117. P. J. Rayner and S. B. Duckett, *Angew. Chem., Int. Ed.*, 2018, **57**, 6742-6753.
118. E. B. Ducker, L. T. Kuhn, K. Munnemann and C. Griesinger, *J. Magn. Reson.*, 2012, **214**, 159-165.
119. R. W. Adams, S. B. Duckett, R. A. Green, D. C. Williamson and G. G. R. Green, *J. Chem. Phys.*, 2009, **131**.
120. K. L. Ivanov, A. N. Pravdivtsev, A. V. Yurkovskaya, H.-M. Vieth and R. Kaptein, *Prog. Nucl. Magn. Reson. Spectrosc.*, 2014, **81**, 1-36.
121. L. S. Lloyd, A. Asghar, M. J. Burns, A. Charlton, S. Coombes, M. J. Cowley, G. J. Dear, S. B. Duckett, G. R. Genov, G. G. R. Green, L. A. R. Highton, A. J. J. Hooper, M. Khan, I. G. Khazal, R. J. Lewis, R. E. Mewis, A. D. Roberts and A. J. Ruddlesden, *Catal. Sci. Technol.*, 2014, **4**, 3544-3554.
122. M. J. Burns, P. J. Rayner, G. G. R. Green, L. A. R. Highton, R. E. Mewis and S. B. Duckett, *J. Phys. Chem. B*, 2015, **119**, 5020-5027.
123. P. J. Rayner, P. Norcott, K. M. Appleby, W. Iali, R. O. John, S. J. Hart, A. C. Whitwood and S. B. Duckett, *Nat. Commun.*, 2018, **9**, 4251.
124. A. S. Rathore, R. Bhambure and V. Ghare, *Anal. Bioanal. Chem.*, 2010, **398**, 137-154.
125. O. Semenova, P. M. Richardson, A. J. Parrott, A. Nordon, M. E. Halse and S. B. Duckett, *Anal. Chem.*, 2019, **91**, 6695-6701.
126. N. K. J. Hermkens, N. Eshuis, B. J. A. van Weerdenburg, M. C. Feiters, F. P. J. T. Rutjes, S. S. Wijmenga and M. Tessari, *Anal. Chem.*, 2016, **88**, 3406-3412.
127. N. Eshuis, N. Hermkens, B. J. A. van Weerdenburg, M. C. Feiters, F. Rutjes, S. S. Wijmenga and M. Tessari, *J. Am. Chem. Soc.*, 2014, **136**, 2695-2698.
128. Q. X. Gong, A. Gordji-Nejad, B. Blumich and S. Appelt, *Anal. Chem.*, 2010, **82**, 7078-7082.

129. S. Glogglar, M. Emondts, J. Colell, R. Muller, B. Blumich and S. Appelt, *Analyst*, 2011, **136**, 1566-1568.
130. L. S. Lloyd, R. W. Adams, M. Bernstein, S. Coombes, S. B. Duckett, G. G. R. Green, R. J. Lewis, R. E. Mewis and C. J. Sleigh, *J. Am. Chem. Soc.*, 2012, **134**, 12904-12907.
131. S. Lehmkuhl, M. Siefert, A. Kentner, Y. F. Yen, B. Blumich, M. S. Rosen, S. Appelt and T. Theis, *J. Chem. Phys.*, 2020, **152**.
132. F. Hill-Casey, A. Sakho, A. Mohammed, M. Rossetto, F. Ahwal, S. B. Duckett, R. O. John, P. M. Richardson, R. Virgo and M. E. Halse, *Molecules*, 2019, **24**.
133. T. Theis, M. P. Ledbetter, G. Kervern, J. W. Blanchard, P. J. Ganssle, M. C. Butler, H. D. Shin, D. Budker and A. Pines, *J. Am. Chem. Soc.*, 2012, **134**, 3987-3990.
134. H. F. Zeng, J. D. Xu, J. Gillen, M. T. McMahon, D. Artemov, J. M. Tyburn, J. A. B. Lohman, R. E. Mewis, K. D. Atkinson, G. G. R. Green, S. B. Duckett and P. C. M. van Zijl, *J. Magn. Reson.*, 2013, **237**, 73-78.
135. P. J. Rayner, M. J. Burns, A. M. Oлару, P. Norcott, M. Fekete, G. G. R. Green, L. A. R. Highton, R. E. Mewis and S. B. Duckett, *Proc. Natl. Acad. Sci. U. S. A.*, 2017, **114**, E3188-E3194.
136. P. Norcott, M. J. Burns, P. J. Rayner, R. E. Mewis and S. B. Duckett, *Magn. Reson. Chem.*, 2018, **56**, 663-671.
137. R. V. Shchepin, D. A. Barskiy, A. M. Coffey, T. Theis, F. Shi, W. S. Warren, B. M. Goodson and E. Y. Chekmenev, *Acs Sensors*, 2016, **1**, 640-644.
138. W. Iali, A. M. Oлару, G. G. R. Green and S. B. Duckett, *Chem. Eur. J.*, 2017, **23**, 10491-10495.
139. H. F. Zeng, J. D. Xu, M. T. McMahon, J. A. B. Lohman and P. C. M. van Zijl, *J. Magn. Reson.*, 2014, **246**, 119-121.
140. P. Norcott, P. J. Rayner, G. G. R. Green and S. B. Duckett, *Chem. Eur. J.*, 2017, **23**, 16990-+.
141. K. M. Appleby, R. E. Mewis, A. M. Oлару, G. G. R. Green, I. J. S. Fairlamb and S. B. Duckett, *Chem. Sci.*, 2015, **6**, 3981-3993.
142. A. N. Pravdivtsev, A. V. Yurkovskaya, H. M. Vieth and K. L. Ivanov, *J. Phys. Chem. B*, 2015, **119**, 13619-13629.
143. A. N. Pravdivtsev, A. V. Yurkovskaya, H. M. Vieth and K. L. Ivanov, *Phys. Chem. Chem. Phys.*, 2014, **16**, 24672-24675.
144. J. B. Hovener, N. Schwaderlapp, R. Borowiak, T. Lickert, S. B. Duckett, R. E. Mewis, R. W. Adams, M. J. Burns, L. A. R. Highton, G. G. R. Green, A. Oлару, J. Hennig and D. von Elverfeldt, *Anal. Chem.*, 2014, **86**, 1767-1774.
145. M. L. Truong, T. Theis, A. M. Coffey, R. V. Shchepin, K. W. Waddell, F. Shi, B. M. Goodson, W. S. Warren and E. Y. Chekmenev, *J. Phys. Chem. C*, 2015, **119**, 8786-8797.
146. D. A. Barskiy, R. V. Shchepin, C. P. N. Tanner, J. F. P. Colell, B. M. Goodson, T. Theis, W. S. Warren and E. Y. Chekmenev, *Chemphyschem*, 2017, **18**, 1493-1498.
147. S. S. Roy, P. Norcott, P. J. Rayner, G. G. R. Green and S. B. Duckett, *Chem. Eur. J.*, 2017, **23**, 10496-10500.
148. T. Theis, M. L. Truong, A. M. Coffey, R. V. Shchepin, K. W. Waddell, F. Shi, B. M. Goodson, W. S. Warren and E. Y. Chekmenev, *J. Am. Chem. Soc.*, 2015, **137**, 1404-1407.
149. J. F. P. Colell, A. W. J. Logan, Z. Zhou, R. V. Shchepin, D. A. Barskiy, G. X. Ortiz, Jr., Q. Wang, S. J. Malcolmson, E. Y. Chekmenev, W. S. Warren and T. Theis, *J. Phys. Chem. C*, 2017, **121**, 6626-6634.

150. A. W. J. Logan, T. Theis, J. F. P. Colell, W. S. Warren and S. J. Malcolmson, *Chem. Eur. J.*, 2016, **22**, 10777-10781.
151. T. Theis, G. X. Ortiz, A. W. J. Logan, K. E. Claytor, Y. Feng, W. P. Huhn, V. Blum, S. J. Malcolmson, E. Y. Chekmenev, Q. Wang and W. S. Warren, *Sci. Adv.*, 2016, **2**.
152. K. Shen, A. W. J. Logan, J. F. P. Colell, J. Bae, G. X. Ortiz, T. Theis, W. S. Warren, S. J. Malcolmson and Q. Wang, *Angew. Chem., Int. Ed.*, 2017, **56**, 12112-12116.
153. V. V. Zhivonitko, I. V. Skovpin and I. V. Koptuyug, *Chem. Commun. (Cambridge, U. K.)*, 2015, **51**, 2506-2509.
154. A. M. Olaru, T. B. R. Robertson, J. S. Lewis, A. Antony, W. Iali, R. E. Mewis and S. B. Duckett, *Chemistryopen*, 2018, **7**, 97-105.
155. R. V. Shchepin, B. M. Goodson, T. Theis, W. S. Warren and E. Y. Chekmenev, *Chemphyschem*, 2017, **18**, 1961-1965.
156. P. J. Rayner, P. M. Richardson and S. B. Duckett, *Angew. Chem., Int. Ed.*, 2020, **59**, 2710-2714.
157. A. M. Olaru, A. Burt, P. J. Rayner, S. J. Hart, A. C. Whitwood, G. G. R. Green and S. B. Duckett, *Chem. Commun. (Cambridge, U. K.)*, 2016, **52**, 14482-14485.
158. T. Theis, M. Truong, A. M. Coffey, E. Y. Chekmenev and W. S. Warren, *J. Magn. Reson.*, 2014, **248**, 23-26.
159. D. A. Barskiy, R. V. Shchepin, A. M. Coffey, T. Theis, W. S. Warren, B. M. Goodson and E. Y. Chekmenev, *J. Am. Chem. Soc.*, 2016, **138**, 8080-8083.
160. A. K. El-Ansary, A. M. Kamal and M. A. Al-Ghorafi, *Med. Chem. Res.*, 2013, **22**, 2589-2601.
161. Z. Wu, 2015, *Thienopyridazine compounds, their preparations, pharmaceutical compositions and uses*, US 8,962,626 B2
162. S. Labadie, E.B. Sjogren, 2006, *Thienopyridazines as IKK inhibitors*, US 7,135,470 B2.
163. S. O'Hagan and D. B. Kell, *J. Cheminformatics*, 2017, **9**.
164. I. V. Linnik, P. J. Rayner, R. A. Stow, S. B. Duckett and G. M. T. Cheetham, *Eur. J. Pharm. Sci.*, 2019, **135**, 32-37.
165. V. Libri, C. Yandim, S. Athanasopoulos, N. Loyse, T. Natisvili, P. P. Law, P. K. Chan, T. Mohammad, M. Mauri, K. T. Tam, J. Leiper, S. Piper, A. Ramesh, M. H. Parkinson, L. Huson, P. Giunti and R. Festenstein, *Lancet*, 2014, **384**, 504-513.
166. D. Sampath, T. S. Zabka, D. L. Misner, T. O'Brien and P. S. Dragovich, *Pharmacol. Ther.*, 2015, **151**, 16-31.
167. G. Rennie, A. C. Chen, H. Dhillon, J. Vardy and D. L. Damian, *Nutr. Neurosci.*, 2015, **18**, 193-200.
168. S. S. Roy, K. M. Appleby, E. J. Fear and S. B. Duckett, *J. Phys. Chem. Lett.*, 2018, **9**, 1112-1117.
169. F. Bray, J. Ferlay, I. Soerjomataram, R. L. Siegel, L. A. Torre and A. Jemal, *Cancer J. Clin.*, 2018, **68**, 394-424.
170. W. A. Weber, *J. Nucl. Med.*, 2009, **50**, 1S-10S.
171. J. Czernin, W. A. Weber and H. R. Herschman, in *Annu. Rev. Med.*, 2006, vol. 57, pp. 99-118.
172. M. M. F. Goodarz Danaei, Yuan Lu, Gitanjali M Singh, Melanie J Cowan, Christopher J Paciorek, John K Lin, Farshad Farzadfar, Young-Ho Khang, Gretchen A Stevens, Mayuree Rao, Mohammed K Ali, Leanne M Riley, Carolyn A Robinson, Majid Ezzati, *The Lancet*, 2011, **378**, 31-40.
173. A. K. M. Tewari, A., *Biorg. Med. Chem. Lett.*, 2001, **9**, 715-718.

174. K. Ozadali, F. Ozkanli, S. Jain, P. P. N. Rao and C. A. Velazquez-Martinez, *Biorg. Med. Chem.*, 2012, **20**, 2912-2922.
175. S. Zhou, H. Liao, C. He, Y. Dou, M. Jiang, L. Ren, Y. Zhao and P. Gong, *Eur. J. Med. Chem.*, 2014, **83**, 581-593.
176. K. A. M. Abouzid, N. A. Khalil, E. M. Ahmed and K. O. Mohamed, *Arch. Pharmacol Res.*, 2013, **36**, 41-50.
177. Z. Wang, M. Wang, X. Yao, Y. Li, J. Tan, L. Wang, W. Qiao, Y. Geng, Y. Liu and Q. Wang, *Eur. J. Med. Chem.*, 2012, **54**, 33-41.
178. F. El-Mariah, M. Hosny and A. Deeb, *Phosphorus Sulfur Silicon Relat. Elem.*, 2006, **181**, 809-818.
179. D. F. Lee and M. C. Hung, *Clin. Cancer Res.*, 2008, **14**, 5656-5662.
180. A. Bishayee and K. Block, *Semin. Cancer Biol.*, 2015, **35**, S1-S4.
181. T. J. Montavon, Y. E. Turkmen, N. A. Shamsi, C. Miller, C. S. Sumaria, V. H. Rawal and S. A. Kozmin, *Angew. Chem., Int. Ed.*, 2013, **52**, 13576-13579.
182. R. O. Hutchins and F. Cistone, *Org. Prep. Proced. Int.*, 1981, **13**, 225-240.
183. S. N. Kessler and H. A. Wegner, *Org. Lett.*, 2012, **14**, 3268-3271.
184. C. J. Ball, J. Gilmore and M. C. Willis, *Angew. Chem., Int. Ed.*, 2012, **51**, 5718-5722.
185. R. V. Shchepin, D. A. Barskiy, A. M. Coffey, B. M. Goodson and E. Y. Chekmenev, *Chemistryselect*, 2016, **1**, 2552-2555.
186. B. J. Tickner, R. O. John, S. S. Roy, S. J. Hart, A. C. Whitwood and S. B. Duckett, *Chem. Sci.*, 2019, **10**, 5235-5245.
187. D. A. Barskiy, A. N. Pravdivtsev, K. L. Ivanov, K. V. Kovtunov and I. V. Koptuyug, *Phys. Chem. Chem. Phys.*, 2016, **18**, 89-93.
188. R. E. Mewis, R. A. Green, M. C. R. Cockett, M. J. Cowley, S. B. Duckett, G. G. R. Green, R. O. John, P. J. Rayner and D. C. Williamson, *J. Phys. Chem. B*, 2015, **119**, 1416-1424.
189. G. R. E. S.S. Eaton, R.H. Holm, *J. Organomet. Chem.*, 1972, **39**, 179-195.
190. M. Fekete, P. J. Rayner, G. G. R. Green and S. B. Duckett, *Magn. Reson. Chem.*, 2017, **55**, 944-957.
191. A. J. Ruddlesden and S. B. Duckett, *Chem. Commun. (Cambridge, U. K.)*, 2016, **52**, 8467-8470.
192. R. E. Mewis, K. D. Atkinson, M. J. Cowley, S. B. Duckett, G. G. R. Green, R. A. Green, L. A. R. Highton, D. Kilgour, L. S. Lloyd, J. A. B. Lohman and D. C. Williamson, *Magn. Reson. Chem.*, 2014, **52**, 358-369.
193. D. A. Barskiy, S. Knecht, A. V. Yurkovskaya and K. L. Ivanov, *Prog. Nucl. Magn. Reson. Spectrosc.*, 2019, **114-115**, 33-70.
194. A. N. Pravdivtsev, A. V. Yurkovskaya, H. M. Vieth, K. L. Ivanov and R. Kaptein, *Chemphyschem*, 2013, **14**, 3327-3331.
195. N. Eshuis, R. Aspers, B. J. A. van Weerdenburg, M. C. Feiters, F. Rutjes, S. S. Wijmenga and M. Tessari, *J. Magn. Reson.*, 2016, **265**, 59-66.
196. M. Fekete, S. S. Roy and S. B. Duckett, *Phys. Chem. Chem. Phys.*, 2020, **22**, 5033-5037.
197. M. Fekete, O. Bayfield, S. B. Duckett, S. Hart, R. E. Mewis, N. Pridmore, P. J. Rayner and A. Whitwood, *Inorg. Chem.*, 2013, **52**, 13453-13461.
198. H. Clavier and S. P. Nolan, *Chem. Commun. (Cambridge, U. K.)*, 2010, **46**, 841-861.
199. R. A. Kelly, H. Clavier, S. Giudice, N. M. Scott, E. D. Stevens, J. Bordner, I. Samardjiev, C. D. Hoff, L. Cavallo and S. P. Nolan, *Organometallics*, 2008, **27**, 202-210.
200. O. Torres, M. Martin and E. Sola, *Organometallics*, 2009, **28**, 863-870.

201. R. E. Mewis, M. Fekete, G. G. R. Green, A. C. Whitwood and S. B. Duckett, *Chem. Commun. (Cambridge, U. K.)*, 2015, **51**, 9857-9859.
202. H. Kwart, L. P. Kuhn and E. L. Bannister, *J. Am. Chem. Soc.*, 1954, **76**, 5998-6001.
203. L. Konermann, J. X. Pan and Y. H. Liu, *Chem. Soc. Rev.*, 2011, **40**, 1224-1234.
204. Y. Sawama, Y. Monguchi and H. Sajiki, *Synlett*, 2012, **7**, 959-972.
205. H. Sajiki, N. Ito, H. Esaki, T. Maesawa, T. Maegawa and K. Hirota, *Tetrahedron Lett.*, 2005, **46**, 6995-6998.
206. P. M. Richardson, S. Jackson, A. J. Parrott, A. Nordon, S. B. Duckett and M. E. Halse, *Magn. Reson. Chem.*, 2018, **56**, 641-650.
207. Asif.M, *Eur. J. Biol.*, 2016, **8**, 142-157.
208. A. S. Singh, N, *Journal of Nepal Chemical Society* 2013, **30**, 66-70.
209. L. S. Liebeskind and R. W. Fengl, *J. Org. Chem.*, 1990, **55**, 5359-5364.
210. M. Carravetta and M. H. Levitt, *J. Am. Chem. Soc.*, 2004, **126**, 6228-6229.
211. M. Carravetta, O. G. Johannessen and M. H. Levitt, *Phys. Rev. Lett.*, 2004, **92**.
212. M. H. Levitt, in *Annual Review of Physical Chemistry, Vol 63*, eds. M. A. Johnson and T. J. Martinez, 2012, vol. 63, pp. 89-105.
213. I. Marco-Rius, M. C. D. Tayler, M. I. Kettunen, T. J. Larkin, K. N. Timm, E. M. Serrao, T. B. Rodrigues, G. Pileio, J. H. Ardenkjaer-Larsen, M. H. Levitt and K. M. Brindle, *NMR Biomed.*, 2013, **26**, 1696-1704.
214. G. Pileio, M. Carravetta and M. H. Levitt, *Proc. Natl. Acad. Sci. U. S. A.*, 2010, **107**, 17135-17139.
215. H. A. I. Yoshihara, E. Can, M. Karlsson, M. H. Lerche, J. Schwitter and A. Comment, *Phys. Chem. Chem. Phys.*, 2016, **18**, 12409-12413.
216. M. Carravetta and M. H. Levitt, *J. Chem. Phys.*, 2005, **122**, 214505.
217. G. Pileio and M. H. Levitt, *J. Chem. Phys.*, 2009, **130**.
218. E. Terreno, D. Delli Castelli, A. Viale and S. Aime, *Chem. Rev.*, 2010, **110**, 3019-3042.
219. C. Cudalbu, A. Comment, F. Kurdzesau, R. B. van Heeswijk, K. Uffmann, S. Jannin, V. Denisov, D. Kirik and R. Gruetter, *Phys. Chem. Chem. Phys.*, 2010, **12**, 5818-5823.
220. J. Eills, PhD, University of Southampton, 2019.
221. P. Hakansson, *Phys. Chem. Chem. Phys.*, 2017, **19**, 10237-10254.
222. R. E. D. McClung, *Encycl. Magn. Reson.*, 2007, **1961**, 1.
223. M. C. D. Tayler and M. H. Levitt, *Phys. Chem. Chem. Phys.*, 2011, **13**, 9128-9130.
224. G. Pileio, M. Carravetta, E. Hughes and M. H. Levitt, *J. Am. Chem. Soc.*, 2008, **130**, 12582-12583.
225. W. S. Warren, E. Jenista, R. T. Branca and X. Chen, *Science*, 2009, **323**, 1711-1714.
226. R. Sarkar, P. Ahuja, D. Moskau, P. R. Vasos and G. Bodenhausen, *Chemphyschem*, 2007, **8**, 2652-2656.
227. A. Bornet, P. Ahuja, R. Sarkar, L. Fernandes, S. Hadji, S. Y. Lee, A. Haririnia, D. Fushman, G. Bodenhausen and P. R. Vasos, *Chemphyschem*, 2011, **12**, 2729-2734.
228. S. Cavadini, J. Dittmer, S. Antonijevic and G. Bodenhausen, *J. Am. Chem. Soc.*, 2005, **127**, 15744-15748.
229. S. S. Roy, P. J. Rayner, P. Norcott, G. G. R. Green and S. B. Duckett, *Phys. Chem. Chem. Phys.*, 2016, **18**, 24905-24911.
230. G. Stevanato, S. S. Roy, J. Hill-Cousins, I. Kuprov, L. J. Brown, R. C. D. Brown, G. Pileio, M. H. Levitt, *Phys. Chem. Chem. Phys.*, 2015, **17**, 5913-5922.

231. S. S. Roy, P. Norcott, P. J. Rayner, G. G. R. Green and S. B. Duckett, *Angew. Chem., Int. Ed.*, 2016, **55**, 15642-15645.
232. G. H. Glover, *J. Magn. Reson. Imaging*, 1991, **1**, 521-530.
233. I. Bezsonova, J. Forman-Kay and R. S. Prosser, *Concept. Magn. Reson. A*, 2008, **32A**, 239-253.
234. K. R. Keshari and D. M. Wilson, *Chem. Soc. Rev.*, 2014, **43**, 1627-1659.
235. G. A. Morris and R. Freeman, *J. Am. Chem. Soc.*, 1979, **101**, 760-762.
236. K. D. Atkinson, M. J. Cowley, P. I. P. Elliott, S. B. Duckett, G. G. R. Green, J. Lopez-Serrano and A. C. Whitwood, *J. Am. Chem. Soc.*, 2009, **131**, 13362-13368.
237. G. Stevanato, J. T. Hill-Cousins, P. Hakansson, S. S. Roy, L. J. Brown, R. C. D. Brown, G. Pileio and M. H. Levitt, *Angew. Chem., Int. Ed.*, 2015, **54**, 3740-3743.
238. G. Pileio and M. H. Levitt, *J. Magn. Reson.*, 2007, **187**, 141-145.
239. P. J. Ross, L. M. Broche and D. J. Lurie, *Magn. Reson. Med.*, 2015, **73**, 1120-1124.
240. B. Procacci, S. S. Roy, P. Norcott, N. Turner and S. B. Duckett, *J. Am. Chem. Soc.*, 2018, **140**, 16855-16864.
241. W. Iali, S. S. Roy, B. Tickner, F. Ahwal, A. J. Kennerley and S. B. Duckett, *Angew. Chem., Int. Ed.*, 2019, **58**, 10271-10275.
242. M. E. Gemeinhardt, M. N. Limbach, T. R. Gebhardt, C. W. Eriksson, S. L. Eriksson, J. R. Lindale, E. A. Goodson, W. S. Warren, E. Y. Chekmenev and B. M. Goodson, *Angew. Chem., Int. Ed.*, 2020, **59**, 418-423.
243. W. Iali, P. J. Rayner and S. B. Duckett, *Sci. Adv.*, 2018, **4**.
244. I. E. Dimitrov, R. Reddy and J. S. Leigh, *J. Magn. Reson.*, 2000, **145**, 302-306.
245. K. L. Ivanov, A. V. Yurkovskaya and H. M. Vieth, *J. Chem. Phys.*, 2008, **128**.
246. F. J. J. Dekanter and R. Kaptein, *Chem. Phys. Lett.*, 1979, **62**, 421-426.
247. G. K. Anderson, H. C. Clark and J. A. Davies, *Inorg. Chem.*, 1981, **20**, 1636-1639.
248. H. B. G. C.H. Langford, *Ligand Substitution Processes*, New York 1965.
249. D. T. Richens, *Chem. Rev.*, 2005, **105**, 1961-2002.
250. P. W. A. D. F. Shriver, C.H. Langford, *Inorganic Chemistry*, Oxford University Press, Oxford, Second edn., 1994.
251. R. J. Cross, *Adv. Inorg. Chem.*, 1989, **34**, 219-292.
252. R. J. Cross, *Chem. Soc. Rev.*, 1985, **14**, 197-223.
253. F. Basolo, in *Mechanisms of Inorganic Reactions* ed. J. Kleinberg, Kent Murmann, R. Fraser, R.T.M, Bauman, J, 1965, vol. 49, ch. 4, pp. 81-106.
254. P. van Leeuwen, P. C. J. Kamer, J. N. H. Reek and P. Dierkes, *Chem. Rev.*, 2000, **100**, 2741-2769.
255. K. Issleib and D. W. Muller, *Chem. Ber. Recl.*, 1959, **92**, 3175-3182.
256. E. Szlyk and M. Barwiolek, *Thermochim. Acta*, 2009, **495**, 85-89.
257. S. Fallis, G. K. Anderson and N. P. Rath, *Organometallics*, 1991, **10**, 3180-3184.
258. Y. J. You, J. T. Chen, M. C. Cheng and Y. Wang, *Inorg. Chem.*, 1991, **30**, 3621-3625.
259. T. Makovec, *Radiol. Oncol.*, 2019, **53**, 148-158.
260. J. Brent, K. McMartin, S. Phillips, C. Aaron, K. Kulig and S. Methylpyrazole Toxic Alcohols, *N. Engl. J. Med.*, 2001, **344**, 424-429.
261. D. Jacobsen and K. E. McMartin, *Med. Toxicol. Adverse Drug*, 1986, **1**, 309-334.
262. Purwanto, R. M. Deshpande, R. V. Chaudhari and H. Delmas, *J. Chem. Eng. Data*, 1996, **41**, 1414-1417.
263. A. Manoharan, P. J. Rayner, W. Iali, M. J. Burns, V. H. Perry and S. B. Duckett, *ChemMedChem*, 2018, **13**, 352-359.

264. B. S. Shin, Y. S. Do, H. S. Cho, T. S. Hahm, C. S. Kim, W. S. Sim, C. J. Lee, S. H. Lee, H. S. Jin, H. G. Song, K. B. Park, H. S. Park and S. T. Kim, *J. Vasc. Interv. Radiol.*, 2010, **21**, 1867-1872.
265. F. L. Fort, I. A. Heyman and J. W. Kesterson, *Journal of Parenteral Science and Technology*, 1984, **38**, 82-87.
266. M. Fekete, C. Gibard, G. J. Dear, G. G. R. Green, A. J. J. Hooper, A. D. Roberts, F. Cisnetti and S. B. Duckett, *Dalton Trans.*, 2015, **44**, 7870-7880.
267. F. Shi, P. He, Q. A. Best, K. Groome, M. L. Truong, A. M. Coffey, G. Zimay, R. V. Shchepin, K. W. Waddell, E. Y. Chekmenev and B. M. Goodson, *J. Phys. Chem. C*, 2016, **120**, 12149-12156.
268. J. F. P. Colell, M. Emondts, A. W. J. Logan, K. Shen, J. Bae, R. V. Shchepin, G. X. Ortiz, P. Spannring, Q. Wang, S. J. Malcolmson, E. Y. Chekmenev, M. C. Feiters, F. Rutjes, B. Blumich, T. Theis and W. S. Warren, *J. Am. Chem. Soc.*, 2017, **139**, 7761-7767.
269. F. Shi, A. M. Coffey, K. W. Waddell, E. Y. Chekmenev and B. M. Goodson, *Angew. Chem., Int. Ed.*, 2014, **53**, 7495-7498.
270. K. V. Kovtunov, L. M. Kovtunova, M. E. Gemeinhardt, A. V. Bukhtiyarov, J. Gesiorski, V. I. Bukhtiyarov, E. Y. Chekmenev, I. V. Koptuyug and B. M. Goodson, *Angew. Chem., Int. Ed.*, 2017, **56**, 10433-10437.
271. D. A. Barskiy, L. A. Ke, X. Y. Li, V. Stevenson, N. Widarman, H. Zhang, A. Truxal and A. Pines, *J. Phys. Chem. Lett.*, 2018, **9**, 2721-2724.
272. S. Sareen, G. Mathew and L. Joseph, *Int. J. Pharm. Investig.*, 2012, **2**, 12-17.
273. J. E. LeBeau, *Regul. Toxicol. Pharmacol.*, 1983, **3**, 71-74.
274. L. R. Depass, *Toxicol. Lett.*, 1989, **49**, 159-170.
275. E. de Kerviler, A. Leroy-Willig, O. Clement and J. Frija, *Biomed. Pharmacother.*, 1998, **52**, 69-75.
276. M. Mescher, H. Merkle, J. Kirsch, M. Garwood and R. Gruetter, *NMR Biomed.*, 1998, **11**, 266-272.
277. D. Hong, S. R. Rankouhi, J. W. Thielen, J. J. A. van Asten and D. G. Norris, *PLoS One*, 2019, **14**.
278. J. T. Grist, J. J. Miller, F. Zaccagna, M. A. McLean, F. Riemer, T. Matys, D. J. Tyler, C. Laustsen, A. J. Coles and F. A. Gallagher, *J. Cerebr. Blood. F. Met.*, 2020, **6**, 1137-1147.
279. S. J. Nelson, *NMR Biomed.*, 2011, **24**, 734-749.
280. L. Brateman, *Am. J. Roentgenol.*, 1986, **146**, 971-980.
281. B. R. Rosen, E. A. Carter, I. L. Pykett, B. R. Buchbinder and T. J. Brady, *Radiology*, 1985, **154**, 469-472.
282. S. Sarkar, K. Heberlein, G. J. Metzger, X. D. Zhang and X. P. Hu, *J. Magn. Reson. Imaging*, 1999, **10**, 1-7.
283. A. D. Elster, Chemical shift artifact, <http://mriquestions.com/chemical-shift-artifact.html>).
284. M. N. Hood, V. B. Ho, J. G. Smirniotopoulos and J. Szumowski, *Radiographics*, 1999, **19**, 357-371.
285. A. B. Schmidt, S. Berner, W. Schimpf, C. Muller, T. Lickert, N. Schwaderlapp, S. Knecht, J. G. Skinner, A. Dost, P. Rovedo, J. Hennig, D. von Elverfeldt and J. B. Hovener, *Nat. Commun.*, 2017, **8**.
286. W. L. Du, Y. P. Du, X. B. Fan, M. A. Zamora and G. S. Karczmar, *Magn. Reson. Med.*, 2003, **49**, 1113-1120.
287. G. Metzger and X. P. Hu, *J. Magn. Reson.*, 1997, **125**, 166-170.
288. A. Ebel, A. A. Maudsley, M. W. Weiner and N. Schuff, *Magn. Reson. Med.*, 2005, **54**, 697-701.

289. R. A. de Graaf and K. Nicolay, *Magn. Reson. Med.*, 1998, **40**, 690-696.
290. R. J. Ogg, P. B. Kingsley and J. S. Taylor, *J. Magn. Reson., Ser B*, 1994, **104**, 1-10.
291. J. StarLack, S. J. Nelson, J. Kurhanewicz, L. R. Huang and D. B. Vigneron, *Magn. Reson. Med.*, 1997, **38**, 311-321.
292. A. Haase, J. Frahm, W. Hanicke and D. Matthaei, *Phys. Med. Biol.*, 1985, **30**, 341-344.
293. H. Zhu, R. Ouwerkerk and P. B. Barker, *Magn. Reson. Med.*, 2010, **63**, 1486-1492.
294. M. S. Ramirez, J. Lee, C. M. Walker, V. C. Sandulache, F. Hennel, S. Y. Lai and J. A. Bankson, *Magn. Reson. Med.*, 2014, **72**, 986-995.
295. A.-i. Oun, J. Lechner-Scott, K. Ribbons and S. Ramadan, *J. Biomed. Sci.*, 2017, **24**.
296. E. Prost, P. Sizun, M. Piotto and J. M. Nuzillard, *J. Magn. Reson.*, 2002, **159**, 76-81.
297. J. H. Ardenkjaer-Larsen, *J. Magn. Reson.*, 2016, **264**, 3-12.
298. C. A. Muller, C. Hundhammer, M. Braeuer, J. G. Skinner, S. Berner, J. Leupold, S. Duwel, S. G. Nekolla, S. Mansson, A. E. Hansen, D. von Elverfeldt, J. H. Ardenkjaer-Larsen, F. Schilling, M. Schwaiger, J. Hennig and J.-B. Hovener, *NMR Biomed.*, 2020, **33**, e4291-e4291.
299. H. Y. Chen, P. E. Z. Larson, J. W. Gordon, R. A. Bok, M. Ferrone, M. van Criekinge, L. Carvajal, P. Cao, J. M. Pauly, A. B. Kerr, I. Park, J. B. Slater, S. J. Nelson, P. N. Munster, R. Aggarwal, J. Kurhanewicz and D. B. Vigneron, *Magn. Reson. Med.*, 2018, **80**, 2062-2072.
300. S. Jannin, J.-N. Dumez, P. Giraudeau and D. Kurzbach, *J. Magn. Reson.*, 2019, **305**, 41-50.
301. Y. Kim and C. Hilty, in *Biological Nmr, Pt B*, ed. A. J. Wand, 2019, vol. 615, pp. 501-526.
302. I. J. Day, J. C. Mitchell, M. J. Snowden and A. L. Davis, *J. Magn. Reson.*, 2007, **187**, 216-224.
303. M. Mishkovsky, U. Eliav, G. Navon and L. Frydman, *J. Magn. Reson.*, 2009, **200**, 142-146.
304. R. A. Wind and J. H. Ardenkjaer-Larsen, *J. Magn. Reson.*, 1999, **141**, 347-354.
305. J. Z. Wang, F. Kreis, A. J. Wright, R. L. Hesketh, M. H. Levitt and K. M. Brindle, *Magn. Reson. Med.*, 2018, **79**, 741-747.
306. F. Kreis, A. J. Wright, V. Somai, R. Katz-Brull and K. M. Brindle, *Magn. Reson. Med.*, 2020, **84**, 1844-1856.
307. R. Sarkar, A. Comment, P. R. Vasos, S. Jannin, R. Gruetter, G. Bodenhausen, H. Hall, D. Kirik and V. P. Denisov, *J. Am. Chem. Soc.*, 2009, **131**, 16014-+.
308. P. Rutkowski, E. M. Slominska, W. Wolyniec, R. T. Smolenski, M. Szolkiewicz, J. Swierczynski and B. Rutwoski, *J. Ren. Nutr.*, 2008, **18**, 56-59.
309. P. G. A. Cecil Alport, G. Hanna, *The Lancet*, 1938, **232**, 1460-1463.
310. A. Hoffer, H. Osmond, M. J. Callbeck and I. Kahan, *J. Clin. Exp. Psychopathol.*, 1957, **18**, 131-158.
311. C. Reitz, *Int. J. Alzheimers Dis.*, 2012, **2012**, 11.
312. M. R. Horsman, D. J. Chaplin and J. M. Brown, *Radiat. Res.*, 1987, **109**, 479-489.
313. M. R. Horsman, P. J. Wood, D. J. Chaplin, J. M. Brown and J. Overgaard, *Radiotherapy and Oncology*, 1990, **18**, 49-57.
314. A. Lenglet, S. Liabeuf, P. Guffroy, A. Fournier, M. Brazier and Z. A. Massy, *Drugs in R&D*, 2013, **13**, 165-173.
315. M. F. Murray, M. Langan and R. R. MacGregor, *Nutrition*, 2001, **17**, 654-656.

316. A. C. Chen, A. J. Martin, B. Choy, P. Fernandez-Penas, R. A. Dalziel, C. A. McKenzie, R. A. Scolyer, H. M. Dhillon, J. L. Vardy, A. Krickler, G. St George, N. Chinniah, G. M. Halliday and D. L. Damian, *N. Engl. J. Med.*, 2015, **373**, 1618-1626.
317. A. A. Rasool, A. A. Hussain and L. W. Ditter, *J. Pharm. Sci.*, 1991, **80**, 387-393.
318. P. Belenky, K. L. Bogan and C. Brenner, *Trends Biochem. Sci.*, 2007, **32**, 12-19.
319. K. R. Keshari, D. M. Wilson, M. Van Criekinge, R. Sriram, B. L. Koelsch, Z. J. Wang, H. F. VanBrocklin, D. M. Peehl, T. O'Brien, D. Sampath, R. A. D. Carano and J. Kurhanewicz, *Prostate*, 2015, **75**, 1601-1609.
320. J. R. Revollo, A. A. Grimm and S. Imai, *J. Biol. Chem.*, 2004, **279**, 50754-50763.
321. A. Rongvaux, M. Galli, S. Denanglaire, F. Van Gool, P. L. Dreze, C. Szpirer, F. Bureau, F. Andris and O. Leo, *J. Immunol.*, 2008, **181**, 4685-4695.
322. A. C. Williams, L. S. Cartwright and D. B. Ramsden, *Qjm-Int. J. Med.*, 2005, **98**, 215-226.
323. M. G. V. Heiden, L. C. Cantley and C. B. Thompson, *Science*, 2009, **324**, 1029-1033.
324. R. A. Gatenby and R. J. Gillies, *Nat. Rev. Cancer*, 2004, **4**, 891-899.
325. O. Warburg, *Science*, 1956, **123**, 309-314.
326. K. Tateishi, H. Wakimoto, A. J. Iafrate, S. Tanaka, F. Loebe, N. Lelic, D. Wiederschain, O. Bedel, G. J. Deng, B. L. Zhang, T. He, X. Shi, R. E. Gerszten, Y. Y. Zhang, J. R. J. Yeh, W. T. Curry, D. Zhao, S. Sundaram, F. Nigim, M. V. A. Koerner, Q. Ho, D. E. Fisher, E. M. Roider, L. V. Kemeny, Y. Samuels, K. T. Flaherty, T. T. Batchelor, A. S. Chi and D. P. Cahill, *Cancer Cell*, 2015, **28**, 773-784.
327. K. Golman, J. H. Ardenaer-Larsen, J. S. Petersson, S. Mansson and I. Leunbach, *Proc. Natl. Acad. Sci. U. S. A.*, 2003, **100**, 10435-10439.
328. N. Bloembergen, E. M. Purcell and R. V. Pound, *Phys. Rev.*, 1948, **73**, 679-712.
329. A. W. Barb, S. K. Hekmatyar, J. N. Glushka and J. H. Prestegard, *J. Magn. Reson.*, 2013, **228**, 59-65.
330. T. Doura, R. Hata, H. Nonaka, K. Ichikawa and S. Sando, *Angew. Chem., Int. Ed.*, 2012, **51**, 10114-10117.
331. H. Allouche-Arnon, T. Wade, L. F. Waldner, V. N. Miller, J. M. Gomori, R. Katz-Brull and C. A. McKenzie, *Contrast Media Mol. Imaging*, 2013, **8**, 72-82.
332. S. Meier, M. Karlsson, P. R. Jensen, M. H. Lerche and J. O. Duus, *Mol. BioSyst.*, 2011, **7**, 2834-2836.
333. S. Jannin, A. Comment, F. Kurdzesau, J. A. Konter, P. Hautle, B. van den Brandt and J. J. van der Klink, *J. Chem. Phys.*, 2008, **128**.
334. L. Lumata, A. K. Jindal, M. E. Merritt, C. R. Malloy, A. D. Sherry and Z. Kovacs, *J. Am. Chem. Soc.*, 2011, **133**, 8673-8680.
335. T. J. Reddy, T. Iwama, H. J. Halpern and V. H. Rawal, *J. Org. Chem.*, 2002, **67**, 4635-4639.
336. R. E. Hurd, Y. F. Yen, A. Chen and J. H. Ardenkjaer-Larsen, *J. Magn. Reson. Imaging*, 2012, **36**, 1314-1328.
337. T. R. Eichhorn, Y. Takado, N. Salameh, A. Capozzi, T. Cheng, J. N. Hyacinthe, M. Mishkovsky, C. Roussel and A. Comment, *Proc. Natl. Acad. Sci. U. S. A.*, 2013, **110**, 18064-18069.
338. A. Comment, B. van den Brandt, K. Uffmann, F. Kurdzesau, S. Jannin, J. A. Konter, P. Hautle, W. T. H. Wenckebach, R. Gruetter and J. J. van der Klink, *Concept. Magn. Reson. B*, 2007, **31B**, 255-269.
339. A. C. Pinon, PhD, École Polytechnique Federale de Lausanne, 2018.

340. J. H. Ardenkjaer-Larsen, S. Macholl and H. Johannesson, *Appl. Magn. Reson.*, 2008, **34**, 509-522.
341. B. Group, personal communication.
342. L. Lumata, Z. Kovacs, A. D. Sherry, C. Malloy, S. Hill, J. van Tol, L. Yu, L. K. Song and M. E. Merritt, *Phys. Chem. Chem. Phys.*, 2013, **15**, 9800-9807.
343. T. Maly, A. F. Miller and R. G. Griffin, *Chemphyschem*, 2010, **11**, 999-1001.
344. M. Borghini, *Phys. Rev. Lett.*, 1968, **20**, 419-&.
345. R. Kaptein, K. Dijkstra and C. E. Tarr, *J. Magn. Reson.*, 1976, **24**, 295-300.
346. Y. C. Lee, P. D. Zocharski and B. Samas, *Int. J. Pharm.*, 2003, **253**, 111-119.
347. L. Liu, X. Y. Su, W. J. Quinn, S. Hui, K. Krukenberg, D. W. Frederick, P. Redpath, L. Zhan, K. Chellappa, E. White, M. Migaud, T. J. Mitchison, J. A. Baur and J. D. Rabinowitz, *Cell Metab.*, 2018, **27**, 1067-+.
348. A. Olsson, T. Olofsson and R. W. Pero, *Biochem. Pharmacol.*, 1993, **45**, 1191-1200.
349. C. von Morze, P. E. Z. Larson, S. Hu, H. A. I. Yoshihara, R. A. Bok, A. Goga, J. H. Ardenkjaer-Larsen and D. B. Vigneron, *Magn. Reson. Imaging*, 2012, **20**, 305-311.
350. R. Spector, *Neurochem. Res.*, 1987, **12**, 27-31.
351. M. Fekete, F. Ahwal and S. B. Duckett, *J. Phys. Chem. B*, 2020, **124**, 4573-4580.
352. H. Metz and K. Maeder, *Int. J. Pharm.*, 2008, **364**, 170-175.
353. J.-B. Hoevener, A. N. Pravdivtsev, B. Kidd, C. R. Bowers, S. Gloeggler, K. V. Kovtunov, M. Plaumann, R. Katz-Brull, K. Buckenmaier, A. Jerschow, F. Reineri, T. Theis, R. V. Shchepin, S. Wagner, P. Bhattacharya, N. M. Zacharias and E. Y. Chekmenev, *Angew. Chem., Int. Ed.*, 2018, **57**, 11140-11162.
354. J.-B. Hoevener, S. Knecht, N. Schwaderlapp, J. Hennig and D. von Elverfeldt, *Chemphyschem*, 2014, **15**, 2451-2457.
355. R. Radebaugh, *J. Phys. Condens. Matter*, 2009, **21**.
356. T. Cheng, A. P. Gaunt, I. Marco-Rius, M. Gehrung, A. P. Chen, J. J. van der Klink and A. Comment, *NMR Biomed.*, 2020, **33**.
357. D. Kramer, Helium Shortage has Ended at Least for now, <https://physicstoday.scitation.org/doi/10.1063/PT.6.2.20200605a/full/>, DOI: 10.1063/PT.6.2.20200605a).
358. F. G. A. Fernandez, J. M. F. Sevilla, T. A. Egorova-Zachernyuk and E. M. Grima, *Biomol. Eng*, 2005, **22**, 193-200.
359. Z. Ai, X. Gao, S. Zheng and C. Lu, *Clin. Nurs. Res.*, 2018, **0**, 1-16.
360. I. Reile, N. Eshuis, N. K. J. Hermkens, B. J. A. van Weerdenburg, M. C. Feiters, F. P. J. T. Rutjes and M. Tessari, *Analyst*, 2016, **141**, 4001-4005.
361. P. M. Richardson, R. O. John, A. J. Parrott, P. J. Rayner, W. Iali, A. Nordon, M. E. Halse and S. B. Duckett, *Phys. Chem. Chem. Phys.*, 2018, **20**, 26362-26371.